

ENCLOSURE 3

UAP-HF-10145

**Revision 1 to Topical Report MUAP-07013
'Small Break LOCA Methodology for US-APWR'**

May 2010
(Non-Proprietary)

Small Break LOCA Methodology for US-APWR

Non-Proprietary Version

May 2010

**© 2010 Mitsubishi Heavy Industries, Ltd.
All Rights Reserved**

Revision History

Revision	Page	Description
0	All	Original issue
1	5.2.2.2-1	Descriptions of the integral effects test, ROSA/LSTF SB-CL-09, newly adopted for the M-RELAP5 assessment. (Section 5.2.2.2)
	5.2.2.3-1	Descriptions of the integral effects test, ROSA/LSTF IB-CL-02, newly adopted for the M-RELAP5 assessment. (Section 5.2.2.3)
	5.2.2.4-1	Descriptions of the integral effects test, LOFT L3-1, newly adopted for the M-RELAP5 assessment. (Section 5.2.2.4)
	5.2.2.5-1	Descriptions of the integral effects test, Semiscale S-LH-1, newly adopted for the M-RELAP5 assessment. (Section 5.2.2.5)
	8.1.2-1 8.1.3-1	Revised code assessment results using the ORNL/THTF void profile, uncovered-bundle heat transfer, and high-pressure reflood test data in response to minor corrections in M-RELAP5 input decks. (Sections 8.1.2 and 8.1.3)
	8.2.1-14	Three additional sensitivity calculations for the ROSA/LSTF SB-CL-18 test to investigate M-RELAP5 ability to predict core liquid level behaviors. (Section 8.2.1.8).
	8.2.1-17	A sensitivity calculation for the ROSA/LSTF SB-CL-18 test, where the break flow and the secondary system behaviors are explicitly simulated using the code models. (Section 8.2.1.9)
	8.2.1-18	Modifications to conclusions obtained from the M-RELAP5 assessment using ROSA/LSTF SB-CL-18. (Section 8.2.1.10)
	8.2.2-1	New M-RELAP5 assessment results using the ROSA/LSTF SB-CL-09 test. (Section 8.2.2)
	8.2.3-1	New M-RELAP5 assessment results using the ROSA/LSTF IB-CL-02 test. (Section 8.2.3)
	8.2.4-1	New M-RELAP5 assessment results using the LOFT L3-1 test. (Section 8.2.4)
	8.2.5-1	New M-RELAP5 assessment results using the Semiscale S-LH-1 test. (Section 8.2.5)
	8.4-1	Modifications to the plant nodding scheme equivalent to that used for US-APWR DCD SBLOCAs. (Section 8.4)
E-1	Modifications to the sample calculation in response to changes in the applied nodding scheme (Appendix E).	

© 2010
MITSUBISHI HEAVY INDUSTRIES, LTD.
All Rights Reserved

This document has been prepared by Mitsubishi Heavy Industries, Ltd. ("MHI") in connection with its request to the U.S. Nuclear Regulatory Commission ("NRC") licensing review of MHI's US-APWR nuclear power plant design. No right to disclose, use or copy any of the information in this document, other than that by the NRC and its contractors in support of MHI's pre-application review of the US-APWR, is authorized without the express written permission of MHI.

This document contains technology information and intellectual property relating to the US-APWR and it is delivered to the NRC on the express condition that it not be disclosed, copied or reproduced in whole or in part, or used for the benefit of anyone other than MHI without the express written permission of MHI, except as set forth in the previous paragraph.

This document is protected by the laws of Japan, U.S. copyright law, international treaties and conventions, and the applicable laws of any country where it is being used.

Mitsubishi Heavy Industries, Ltd.
16-5, Konan 2-chome, Minato-ku
Tokyo 108-8215 Japan

ABSTRACT

This report describes the analysis methodology and evaluation of emergency core cooling system (ECCS) cooling performance for design-basis small break loss-of-coolant accidents (SBLOCAs) in the US-APWR. The content of this report is in accordance with the process shown in the Regulatory Guide 1.203, "Transient and Accident Analysis Methods." Regulatory Guide 1.203 identified four elements with a total of 20 steps for the development and assessment of the evaluation methodology.

For the US-APWR small-break LOCA analysis, MHI specifically selected RELAP5-3D and modified it as M-RELAP5 in order to meet the requirements in 10CFR Part 50 Appendix K, "ECCS Evaluation Models".

First, the PIRT for small break LOCA of the US-APWR was developed for the modification and validation plans of M-RELAP5. The approach used for the US-APWR SBLOCA PIRT was to utilize the expertise at MHI and also the independent experts. For conservative M-RELAP5, some Appendix K requirements are achieved through the implementation of new models or the modification, although RELAP5-3D has a number of models that enable it to meet many of the Appendix K requirements with no modification.

Then, M-RELAP5 capability to analyze the small break LOCA was confirmed by the validation analyses with integral effect tests and separate effect tests focused on the models related to the important phenomena identified in the PIRT as follows: CHF/core dryout, uncovered core heat transfer, rewet, core mixture level, water hold up in SG primary side, SG primary and secondary heat transfer, water level in the SG outlet piping, loop seal formation and clearance, downcomer mixture level/downcomer void distribution.

The calculation results for the ROSA/LSTF void profile test using M-RELAP5 show good agreement with the test data for both the axial void fraction profile and the averaged void fraction. M-RELAP5 was assessed by the comparison with the ORNL/THTF two-phase mixture level swell test and the uncovered-bundle heat transfer test. The assessment shows that the M-RELAP5 code reasonably predicts these parameters. Rewetting modeling was assessed against the ORNL/THTF high-pressure reflood tests. M-RELAP5 conservatively predicts the rod heat transfer and rewet behavior during reflood. M-RELAP5 was assessed by the comparison with the UPTF CCFL test data and Dukler Air-Water Flooding Test. It is

confirmed that M-RELAP5 with the CCFL parameters is applicable to CCFL behavior of the hot leg and the SG plenum, and SG U-tube in the US-APWR.

M-RELAP5 was assessed by the comparison with the ROSA/LSTF small break (5%) LOCA integral test (SB-CL-18) and with the ROSA/LSTF small break (10%) LOCA integral test (SB-CL-09) for confirmation of integral system behavior. A cold leg break (17%) test, scaled to the 1-ft² break of US-APWR, has been recently performed using the ROSA/LSTF with technical support of JAEA (Japan Atomic Energy Agency), and was used to assess M-RELAP5 applicability to SBLOCAs with relatively larger break sizes. In addition, M-RELAP5 was validated using small break LOCA test data obtained in the LOFT (L3-1, 2.5%) and Semiscale (S-LH-1, 5%) facilities in compliance to requirements specified in the TMI Action Plan. Against these various experimental tests performed in the different test facilities, M-RELAP5 predicted excellently the following important parameters: water hold up in SG primary side, condensation drainage to inlet plenum, SG primary and secondary heat transfer, water level in SG outlet piping, and loop seal formation and clearance. M-RELAP5 also provided conservative or reasonable predictions of peak cladding temperature for all the integral experiments.

The modeling capabilities of M-RELAP5 were also examined and concluded to be applicable to the important phenomena specified in the PIRT with the constitutive equations. Time step sensitivity analyses also show that M-RELAP5 is able to control the numerical error to be sufficiently small. Finally, modeling and nodalization of M-RELAP5 for the US-APWR SBLOCA analysis were discussed in detail.

With these results, M-RELAP5 is concluded to be able to applicable to the Chapter 15 small break LOCA analysis of the US-APWR against the acceptance criteria specified in 10 CFR Part 50 Section 50.46, "Acceptance Criteria for Emergency Core Cooling System for Light-Water Nuclear Power Reactors."

Table of Contents

List of Tables	
List of Figures	
List of Acronyms	
1.0 INTRODUCTION	1-1
1.1 Roadmap for the Process of Development and Assessment of the M-RELAP5 Evaluation Model	1-2
1.2 References	1-4
2.0 COMPLIANCE WITH 10CFR 50.46	2-1
2.1 Analysis Purpose	2-1
2.2 Power Plant Class	2-1
2.3 Transient Class	2-2
2.4 Figures of Merit	2-3
2.5 References	2-4
3.0 SYSTEMS, COMPONENTS, PHASES, GEOMETRIES, FIELDS, AND PROCESSES THAT MUST BE MODELED	3-1
3.1 US-APWR Systems to Be Modeled	3-1
3.2 Components to be Modeled	3-1
3.2.1 Primary System Components	3-2
3.2.2 Secondary System Components	3-16
3.2.3 Containment Vessel	3-19
3.3 Phases to be Modeled	3-20
3.4 Geometries	3-21
3.5 Field Equations	3-22
3.6 Processes to be Considered	3-22
4.0 IDENTIFY AND RANK KEY PHENOMENA AND PROCESSES	4-1
4.1 Introduction	4-1
4.1.1 Target Plant / US-APWR	4-1

4.1.2	Accident Scenario	4-2
4.1.3	Measure of Merit for the PIRT	4-2
4.2	Small Break LOCA Scenario	4-3
4.3	Phenomena Identification and Ranking Table (PIRT)	4-7
4.3.1	Definition of Rankings	4-7
4.3.2	Discussions on Rankings	4-8
4.4	Validation Plan of M-RELAP5	4-29
4.4.1	Phenomena Modeling based on Appendix-K requirements	4-29
4.4.2	Confirmation plan	4-29
4.5	References	4-32
5.0	ASSESSMENT BASE	5.1-1
5.1	Introduction	5.1-1
5.1.1	References	5.1-1
5.2	Proposed IETs and SETs for US-APWR SBLOCA Assessment	5.2.1.1-1
5.2.1	SETs	5.2.1.1-1
5.2.2	IETs	5.2.2.1-1
6.0	DEVELOPMENT AND ASSESSMENT OF THE RELAP5-3D-BASED FRAMEWORK OF THE M-RELAP5 EVALUATION MODEL	6.1-1
6.1	Selection of a RELAP5-Based Code with Inclusion of Appendix K	
Conservative Models		6.1-1
6.1.1	General Selection Process	6.1-1
6.1.2	Selection Criteria Based on the Specific NRC Guidelines	6.1-3
6.1.3	Overview of RELAP5 and RELAP5-3D	6.1-5
6.2	Evaluation Model Structure	6.2.1-1
6.2.1	Systems and Components	6.2.1-1
6.2.2	Constituents and Phases	6.2.2-1
6.2.3	Field Equations	6.2.3-1
6.2.4	Closure Relationships	6.2.4-1
6.2.5	Numerics	6.2.5-1
6.2.6	Additional Features	6.2.6-1
6.3	References	6.3-1

7.0	<u>DEVELOP OR INCORPORATE CLOSURE MODELS</u>	7.1.1-1
7.1	Appendix-K compliant models	7.1.1-1
7.1.1	Selection for Appendix-K requirements	7.1.1-1
7.1.2	Gap Conductance Model	7.1.2-1
7.1.3	Fission Product Decay	7.1.3-1
7.1.4	Metal Water Reaction Model	7.1.4-1
7.1.5	Cladding Swelling and Rupture Model	7.1.5-1
7.1.6	Discharge Model	7.1.6-1
7.1.7	Critical Heat Flux and Post-CHF Heat Transfer Model	7.1.7-1
7.2	Advanced Accumulator	7.2-1
7.2.1	Advanced Accumulator Model	7.2-1
7.2.2	Model Validation	7.2-2
7.3	References	7.3-1
8.0	ASSESSMENT OF EM ADEQUACY	8.1.1-1
8.1	Prepare Input and Perform Calculations To Assess Model Fidelity or Accuracy	8.1.1-1
8.1.1	ROSA/LSTF Void Profile Test	8.1.1-1
8.1.2	ORNL/THTF Void Profile and Uncovered-Bundle Heat Transfer Tests	8.1.2-1
8.1.3	ORNL/THTF High-Pressure Reflood test	8.1.3-1
8.1.4	UPTF CCFL	8.1.4-1
8.1.5	Dukler Air-Water Flooding Test	8.1.5-1
8.2	Prepare Input and Perform Calculations To Assess System Interaction and Global Capability	8.2.1-1
8.2.1	ROSA/LSTF small break (5%) LOCA test (SB-CL-18)	8.2.1-1
8.2.2	<u>ROSA/LSTF small break (10%) LOCA test (SB-CL-09)</u>	8.2.2-1
8.2.3	<u>ROSA/LSTF small break (17%) LOCA test (IB-CL-02)</u>	8.2.3-1
8.2.4	<u>LOFT small break (2.5%) LOCA test (L3-1)</u>	8.2.4-1
8.2.5	<u>Semiscale small break (5%) LOCA test (S-LH-1)</u>	8.2.5-1
8.3	Determine Capability of Field Equations to Represent Processes and Phenomena and Ability of Numeric Solution to Approximate Equation Set	8.3.1-1
8.3.1	The Field Equations Evaluation	8.3.1-1
8.3.2	The Numeric Solution Evaluation	8.3.2-1
8.4	Determine Applicability of Evaluation Model to Simulate System	8.4-1

8.4.1	Reactor Vessel Modeling	8.4-4
8.4.2	Reactor Coolant System Modeling	8.4-14
8.4.3	References	8.4-26
8.5	Determination of Evaluation Model	8.5-1
9.0	CONCLUSIONS	9-1
9.1	References	9-2
APPENDIX-A	Resumes of peer reviewer for PIRT	A-1
APPENDIX-B	Cladding Swelling and Rupture Effect on Cladding Heat Conduction Calculation	B-1
APPENDIX-C	Validation of Discharge Model	C-1
APPENDIX-D	Implementation of Advanced Accumulator Model	D-1
APPENDIX-E	Sample Analyses of Small Break LOCA	E-1

List of Tables

Table 1.1-1	Roadmap for the Presentation of M-RELAP5 Evaluation Model	1-5
Table 4.3.2-1	PIRT for Small Break LOCA	4-25
Table 4.3.2-2	PIRT for Small Break LOCA (High rank)	4-28
Table 4.4.2-1	Validation Tests for High Ranking Phenomena for Small Break LOCA	4-31
Table 5.2.1.1-1	Summary of LSTF Rod Bundle Design	5.2.1.1-5
Table 5.2.1.1-2	Summary of Test Conditions	5.2.1.1-6
Table 5.2.1.1-3	Total Heat Loss	5.2.1.1-6
Table 5.2.1.2-1	THTF Design Summary	5.2.1.2-8
Table 5.2.1.2-2	Rod-Sheath Thermocouple Designations	5.2.1.2-8
Table 5.2.1.2-3	Nomenclature for Thermocouples in THTF	5.2.1.2-9
Table 5.2.1.2-4	Summary of Void Profile Test Conditions	5.2.1.2-13
Table 5.2.1.2-5	Instrument Uncertainty Analysis for the THTF Loop Summary of Results	5.2.1.2-14
Table 5.2.1.3-1	THTF Design Summary	5.2.1.3-7
Table 5.2.1.3-2	Rod-Sheath Thermocouple Designations	5.2.1.3-7
Table 5.2.1.3-3	Nomenclature for Thermocouples in THTF	5.2.1.3-8
Table 5.2.1.3-4	Summary of Uncovered-Bundle Heat Transfer Test Conditions	5.2.1.3-12
Table 5.2.1.3-5	Instrument Uncertainty Analysis For The THTF Loop Summary of Results	5.2.1.3-13
Table 5.2.1.4-1	THTF Design Summary	5.2.1.4-7
Table 5.2.1.4-2	Rod-Sheath Thermocouple Designations	5.2.1.4-7
Table 5.2.1.4-3	Nomenclature for Thermocouples in THTF	5.2.1.4-8
Table 5.2.1.4-4	High-Pressure Reflood Test Matrix	5.2.1.4-12

Table 5.2.1.4-5	Summary of Initial Conditions for High-Pressure Reflood Tests	5.2.1.4-12
Table 5.2.1.4-6	Instrument Uncertainty Analysis For The THTF Loop Summary of Results	5.2.1.4-13
Table 5.2.1.5-1	Comparison of UPTF Hot Leg Configuration with Typical Westinghouse and Combustion Engineering (CE) PWR's	5.2.1.5-4
Table 5.2.1.6-1	The Four Different Input Liquid Flow Rates	5.2.1.6-4
Table 5.2.2.1-1	Major Design Characteristics of LSTF and PWR	5.2.2.1-15
Table 5.2.2.1-2	Materials for Primary Loop Components	5.2.2.1-15
Table 5.2.2.1-3	Primary Characteristics of the Pressure Vessel	5.2.2.1-16
Table 5.2.2.1-4	Comparison of Various Elevations	5.2.2.1-17
Table 5.2.2.1-5	Pressure Vessel Nozzles	5.2.2.1-18
Table 5.2.2.1-6	Primary Characteristics of the Upper Plenum Structures	5.2.2.1-19
Table 5.2.2.1-7	Major Core Characteristics	5.2.2.1-20
Table 5.2.2.1-8	Heater Rod Specification	5.2.2.1-21
Table 5.2.2.1-9	Pressurizer Characteristics	5.2.2.1-22
Table 5.2.2.1-10	Characteristics of Primary Loop Piping	5.2.2.1-23
Table 5.2.2.1-11	Comparison of Major Design Specification of Primary Coolant Pumps between LSTF and PWR	5.2.2.1-24
Table 5.2.2.1-12	List of Major Components in Secondary Coolant System in LSTF ..	5.2.2.1-24
Table 5.2.2.1-13	Comparison of Major Design Characteristics of LSTF and PWR Steam Generators	5.2.2.1-25
Table 5.2.2.1-14	Major Design Parameters of Jet Condenser	5.2.2.1-28
Table 5.2.2.1-15	Major Design Parameters of Cooling Towers CT-1 and CT-2	5.2.2.1-28
Table 5.2.2.1-16	Major Design Parameters of Main and Auxiliary Feedwater Pumps PF and PA	5.2.2.1-28
Table 5.2.2.1-17	Major Design Parameters of Piping in Secondary Coolant System ..	5.2.2.1-29

Table 5.2.2.1-18	Initial Conditions for Run SB-CL-18	5.2.2.1-30
Table 5.2.2.1-19	Specified Operational Setpoints and Conditions for Run SB-CL-18	5.2.2.1-31
Table 5.2.2.1-20	Core Power Decay Curve	5.2.2.1-32
Table 5.2.2.1-21	ECCS Conditions for Run SB-CL-18	5.2.2.1-33
Table 5.2.2.1-22	Total Heat Loss	5.2.2.1-34
<u>Table 5.2.2.2-1</u>	<u>Initial Conditions for Run SB-CL-09</u>	<u>5.2.2.2-4</u>
<u>Table 5.2.2.2-2</u>	<u>Specified Operational Setpoints and Conditions for Run SB-CL-09</u>	<u>5.2.2.2-5</u>
<u>Table 5.2.2.2-3</u>	<u>ECCS Conditions for Run SB-CL-09</u>	<u>5.2.2.2-6</u>
<u>Table 5.2.2.3-1</u>	<u>Characteristics of Pressurizer used for Run IB-CL-02</u>	<u>5.2.2.3-3</u>
<u>Table 5.2.2.3-2</u>	<u>Initial Conditions for Run IB-CL-02</u>	<u>5.2.2.3-4</u>
<u>Table 5.2.2.3-3</u>	<u>Specified Operational Setpoints and Conditions for Run IB-CL-02</u>	<u>5.2.2.3-5</u>
<u>Table 5.2.2.3-4</u>	<u>ECCS Conditions for Run IB-CL-02</u>	<u>5.2.2.3-6</u>
<u>Table 5.2.2.4-1</u>	<u>Operational Setpoints and Conditions for Experiment L3-1</u>	<u>5.2.2.4-8</u>
<u>Table 5.2.2.4-2</u>	<u>ECCS Conditions for Experiment L3-1</u>	<u>5.2.2.4-9</u>
<u>Table 5.2.2.4-3</u>	<u>Initial Conditions for Experiment L3-1</u>	<u>5.2.2.4-10</u>
<u>Table 5.2.2.5-1</u>	<u>Initial Conditions for Experiment S-LH-1</u>	<u>5.2.2.5-4</u>
<u>Table 5.2.2.5-2</u>	<u>Specified Operational Setpoints and Conditions for Experiment S-LH-1</u>	<u>5.2.2.5-5</u>
<u>Table 5.2.2.5-3</u>	<u>ECCS Conditions for Experiment S-LH-1</u>	<u>5.2.2.5-6</u>
Table 6.1-1	RELAP5/MOD3 Code Assessment Matrix for PWR SBLOCAs	6.1-7
Table 6.2.1-1	Hydrodynamic Components Typically Used for PWR Applications	6.2.1-6
Table 6.2.1-2	Types of Valves	6.2.1-7
Table 6.2.1-3	List and Description of the Special Process Models	6.2.1-8
Table 6.2.1-4a	General Hydrodynamic Components Applicable for US-APWR	6.2.1-9
Table 6.2.1-4b	<u>General Hydrodynamic Components Applicable for US-APWR</u>	6.2.1-10
Table 6.2.4-1	Drift Flux Correlations Used for Vertical Bubbly-Slug Flow	6.2.4-13

Table 6.2.4-2	Drift Flux Correlation Used for Vertical Bubbly-Slug Flow	6.2.4-14
Table 6.2.4-3	Wall Heat Transfer Correlations	6.2.4-15
Table 6.2.4-4	Expressions Used in Correlations	6.2.4-16
Table 6.2.4-5	Examples of the Expressions Used for Bubbly and Dispersed Flows	6.2.4-17
Table 7.1.1-1	Appendix K Required and Acceptable Features of Evaluation Models and Approach for Acceptance	7.1.1-63
Table 7.1.3-1	Energy yields and decay constants for ANS 1971	7.1.3-4
Table 7.1.3-2	Analysis Results When Assuming the Yield of ^{239}U as 0.7	7.1.3-5
Table 7.1.3-3	Effect of the Yield of ^{239}U on the Decay Heat	7.1.3-6
Table 7.2-1	Test Conditions of Full Height 1/2 Scale Test	7.2-5
Table 8.1.1-1	Characteristics of LSTF rod bundle	8.1.1-6
Table 8.1.1-2	Summary of test conditions	8.1.1-7
Table 8.1.2-1	ORNL/THTF 3.09.10 Series ; Void Profile and Uncovered-Bundle Heat Transfer Test Conditions	8.1.2-8
Table 8.1.3-1	ORNL/THTF High-Pressure Reflood Test Conditions	8.1.3-6
Table 8.1.4-1	Flow Rate Conditions for UPTF CCFL Test Analysis	8.1.4-4
Table 8.1.4-2	Results of UPTF CCFL Test Analysis (15bar)	8.1.4-4
Table 8.1.4-3	Results of UPTF CCFL Test Analysis (3 bar)	8.1.4-4
Table 8.1.5-1	Experimental results	8.1.5-4
Table 8.2.1-1	Major Design Characteristics of LSTF and PWR	8.2.1-4421
Table 8.2.1-2	Steady-State Parameter Checklist	8.2.1-4522
Table 8.2.1-3	Operational Setpoints for Run SB-CL-18	8.2.1-4623
Table 8.2.1-4	Core Power Decay Curve	8.2.1-4724
Table 8.2.1-5	ECCS Conditions for Run SB-CL-18	8.2.1-4825
Table 8.2.1-6	Transient Results Summary for 5-Percent Cold Leg Side Break	8.2.1-4926
Table 8.2.1-7	Transient Results Summary for 5-Percent Cold Leg Side Break (Calculation	

	with Simulated Secondary System and Break Flow Behavior)	8.2.1-27
Table 8.2.1-8	Comparison of PCT (Calculation with Simulated Secondary System and Break Flow Behavior).....	8.2.1-27
Table 8.2.2-1	Steady-State Parameter Checklist	8.2.2-8
Table 8.2.2-2	Operational Setpoints for Run SB-CL-09.....	8.2.2-9
Table 8.2.2-3	Core Power Decay Curve	8.2.2-10
Table 8.2.2-4	ECCS Conditions for Run SB-CL-09	8.2.2-11
Table 8.2.2-5	Transient Results Summary for 10-Percent Cold Leg Side Break	8.2.2-12
Table 8.2.3-1	Steady-State Parameter Checklist	8.2.3-8
Table 8.2.3-2	Core Power Decay Curve	8.2.3-9
Table 8.2.3-3	Pump Coastdown Curve	8.2.3-10
Table 8.2.3-4	Transient Results Summary for 17-Percent Cold Leg Side Break	8.2.3-11
Table 8.2.4-1	Steady-State Parameter Checklist for Experiment L3-1.....	8.2.4-8
Table 8.2.4-2	Primary Test Chronology for Experiment L3-1	8.2.4-9
Table 8.2.5-1	Steady-State Parameter Checklist for Experiment S-LH-1	8.2.5-9
Table 8.2.5-2	Primary Test Chronology for Experiment S-LH-1	8.2.5-10
Table 8.2.5-3	Summary of PCTs during Loop Seal for Experiment S-LH-1	8.2.5-11

Appendix

Table D-1	Total Uncertainty of Experimental Equation for Safety Analysis of US-APWR	D-14
Table E-1	Analysis Conditions for US-APWR	E-6
Table E-2	Sequence of Events in US-APWR Sample Analysis	E-7

List of Figures

Figure 3.2.1-1	Reactor General Assembly	3-4
Figure 3.2.1-2	Reactor Coolant System	3-8
Figure 3.2.1-3	Reactor Vessel	3-9
Figure 3.2.1-4	Steam Generator	3-10
Figure 3.2.1-5	Reactor Coolant Pump	3-11
Figure 3.2.1-6	Pressurizer	3-12
Figure 3.2.1-7	Emergency Core Cooling System	3-15
Figure 3.2.2-1	Emergency Feedwater System	3-18
Figure 4.2-1	Pressure and Core Liquid Level Responses of Small Break LOCA	4-6
Figure 5.2.1.1-1	Schematic of ROSA-IV Large Scale Test Facility (LSTF)	5.2.1.1-7
Figure 5.2.1.1-2	Axial Power Profile and Location of Differential Pressure Measurements and Grid Spacers	5.2.1.1-8
Figure 5.2.1.1-3	Core Grid	5.2.1.1-9
Figure 5.2.1.1-4	Comparison of Calculated and Measured Void Fraction Profiles, Test ST-VF-01D	5.2.1.1-10
Figure 5.2.1.1-5	Definition of Heat Loss for Each Component in LSTF System	5.2.1.1-11
Figure 5.2.1.2-1	THTF in Small-break Test Configuration	5.2.1.2-15
Figure 5.2.1.2-2	Cross Section of THTF Test Section	5.2.1.2-16
Figure 5.2.1.2-3	Cross Section of THTF	5.2.1.2-17
Figure 5.2.1.2-4	Axial Location of Spacer Grids and FRS Thermocouples.	5.2.1.2-18
Figure 5.2.1.2-5	Simplified Cross Section of a Typical Fuel Rod Simulator	5.2.1.2-19

Figure 5.2.1.2-6	Shroud-wall Thermocouple Configuration.....	5.2.1.2-20
Figure 5.2.1.2-7	Axial Location of Shroud-Wall Thermometry.....	5.2.1.2-21
Figure 5.2.1.2-8	THTF In-Bundle Pressure Instrumentation	5.2.1.2-22
Figure 5.2.1.2-9	Schematic of a Nuclear Reactor Subchannel in a Partially Uncovered Configuration.....	5.2.1.2-23
Figure 5.2.1.3-1	THTF in Small-break Test Configuration.....	5.2.1.3-14
Figure 5.2.1.3-2	Cross Section of THTF Test Section.....	5.2.1.3-15
Figure 5.2.1.3-3	Cross Section of THTF	5.2.1.3-16
Figure 5.2.1.3-4	Axial Location of Spacer Grids and FRS Thermocouples.....	5.2.1.3-17
Figure 5.2.1.3-5	Simplified Cross Section of a Typical Fuel Rod Simulator.....	5.2.1.3-18
Figure 5.2.1.3-6	Shroud-wall Thermocouple Configuration.....	5.2.1.3-19
Figure 5.2.1.3-7	Axial Location of Shroud-wall Thermometry	5.2.1.3-20
Figure 5.2.1.3-8	THTF In-Bundle Pressure Instrumentation	5.2.1.3-21
Figure 5.2.1.4-1	THTF in Small-break Test Configuration.....	5.2.1.4-14
Figure 5.2.1.4-2	Cross Section of THTF Test Section.....	5.2.1.4-15
Figure 5.2.1.4-3	Cross Section of THTF	5.2.1.4-16
Figure 5.2.1.4-4	Axial Location of Spacer Grids and RRS Thermocouples.....	5.2.1.4-17
Figure 5.2.1.4-5	Simplified Cross Section of a Typical FRS.....	5.2.1.4-18
Figure 5.2.1.4-6	Shroud-Wall Thermocouple Configuration.	5.2.1.4-19
Figure 5.2.1.4-7	Axial Location of Shroud-Wall Thermometry.....	5.2.1.4-20
Figure 5.2.1.4-8	THTF In-Bundle Pressure Instrumentation	5.2.1.4-21
Figure 5.2.1.5-1	Overall View of UPTF	5.2.1.5-5
Figure 5.2.1.5-2	UPTF Hot Leg Configuration.....	5.2.1.5-6
Figure 5.2.1.5-3	Configuration of International ECC Injection Pipe (Hutze) in UPTF Hot Leg	5.2.1.5-7
Figure 5.2.1.5-4	UPTF Hot Leg Separate Effect Test Overall Flow Conditions.....	5.2.1.5-8

Figure 5.2.1.5-5	UPTF Hot Leg Separate Effects Test Comparison of UPTF Hot Leg Void Fractions to Wallis Correlation	5.2.1.5-9
Figure 5.2.1.6-1	Flooding/Upflow Test Loop Schematic Diagram.	5.2.1.6-5
Figure 5.2.1.6-2	Air Inlet Section	5.2.1.6-6
Figure 5.2.1.6-3	Liquid Entrance Device	5.2.1.6-7
Figure 5.2.1.6-4	Exit Section	5.2.1.6-8
Figure 5.2.1.6-5	Flooding Velocities for Air and Water in Vertical Tubes Designed to Minimize End Effects. All Data at Atmospheric Pressure.	5.2.1.6-9
Figure 5.2.2.1-1	General View of LSTF	5.2.2.1-35
Figure 5.2.2.1-2	Comparison of PWR and LSTF	5.2.2.1-36
Figure 5.2.2.1-3	Comparison of LSTF and PWR Pressure Vessel Dimensions	5.2.2.1-37
Figure 5.2.2.1-4	Pressure Vessel Assembly	5.2.2.1-38
Figure 5.2.2.1-5	Vessel Major Nozzle Locations	5.2.2.1-39
Figure 5.2.2.1-6	Coolant Flow Path in Pressure Vessel	5.2.2.1-40
Figure 5.2.2.1-7	Pressure Vessel Internals (Upper Plenum)	5.2.2.1-41
Figure 5.2.2.1-8	Core and Lower Plenum	5.2.2.1-42
Figure 5.2.2.1-9	Partial Core Cross Sections	5.2.2.1-43
Figure 5.2.2.1-10	Core Cross Section and Heater Rod Arrangement	5.2.2.1-43
Figure 5.2.2.1-11	Axial Core Power Profile	5.2.2.1-44
Figure 5.2.2.1-12	Pressurizer	5.2.2.1-45
Figure 5.2.2.1-13	Head-Flow Curves for PC-A and PC-B	5.2.2.1-46
Figure 5.2.2.1-14	Single-phase Head Homologous Curves for PC-A ($a>0$)	5.2.2.1-47
Figure 5.2.2.1-15	Single-phase Torque Homologous Curves for PC-A	5.2.2.1-48
Figure 5.2.2.1-16	Frictional Torque Characteristics of PC-A	5.2.2.1-49
Figure 5.2.2.1-17	Flow Diagram of LSTF Secondary Coolant System	5.2.2.1-50
Figure 5.2.2.1-18	Configuration of Steam Generator SG-A with Internals	5.2.2.1-51

Figure 5.2.2.1-19	Coolant Flow in SG Secondary Side	5.2.2.1-52
Figure 5.2.2.1-20a	Details of SG Plenum and Tube Sheet	5.2.2.1-53
Figure 5.2.2.1-20b	Details of Middle Part of SG Vessel and U-tubes	5.2.2.1-54
Figure 5.2.2.1-20c	Details of Top Part of SG Vessel	5.2.2.1-55
Figure 5.2.2.1-20d	Details of Downcomer Piping	5.2.2.1-56
Figure 5.2.2.1-21	Comparison of LSTF and PWR SGs	5.2.2.1-57
Figure 5.2.2.1-22	Details of U-Tube Support Plate	5.2.2.1-58
Figure 5.2.2.1-23	Details of Flow Distributor	5.2.2.1-58
Figure 5.2.2.1-24	Details of Primary Steam Separator	5.2.2.1-59
Figure 5.2.2.1-25	Configuration of Secondary Steam Separator	5.2.2.1-60
Figure 5.2.2.1-26	Design Flow Characteristics for Secondary Steam Separator	5.2.2.1-60
Figure 5.2.2.1-27	Details of Jet Condenser JC	5.2.2.1-61
Figure 5.2.2.1-28.a	Details of Cooling Tower CT-1	5.2.2.1-62
Figure 5.2.2.1-28.b	Design Performance for CT-1	5.2.2.1-62
Figure 5.2.2.1-29.a	Details of Cooling Tower CT-2	5.2.2.1-63
Figure 5.2.2.1-29.b	Design Performance for CT-2	5.2.2.1-63
Figure 5.2.2.1-30	Pump Characteristics of PWR Main Feedwater Pump	5.2.2.1-64
Figure 5.2.2.1-31	Pump Characteristics of PWR Auxiliary Feedwater Pump	5.2.2.1-64
Figure 5.2.2.1-32	Definition of Heat Loss for Each Component in LSTF System	5.2.2.1-65
<u>Figure 5.2.2.4-1</u>	<u>Schematic of LOFT Major Components</u>	<u>5.2.2.4-11</u>
<u>Figure 5.2.2.4-2</u>	<u>LOFT Core Configuration</u>	<u>5.2.2.4-12</u>
<u>Figure 5.2.2.4-3</u>	<u>Small Break Orifice Configuration for LOFT L3-1</u>	<u>5.2.2.4-13</u>
<u>Figure 5.2.2.5-1</u>	<u>Schematic of Semiscale Mod-2C Major Components</u>	<u>5.2.2.5-7</u>
<u>Figure 5.2.2.5-2</u>	<u>Small Break Orifice Configuration for Semiscale S-LH-1</u>	<u>5.2.2.5-8</u>
<u>Figure 5.2.2.5-3</u>	<u>Semiscale Mod-2C Core Heater Rod Configuration</u>	<u>5.2.2.5-9</u>
Figure 6.2.1-1	Thermal Hydraulic Volume	6.2.1-11

Figure 6.2.1-2	Connecting Volumes with Junctions	6.2.1-11
Figure 6.2.1-3	Example of Vessel Nodalization for One Dimensional Flow in the Core	6.2.1-12
Figure 6.2.1-4	Example of the Nodalization Used for the Primary System Piping and Components.....	6.2.1-13
Figure 6.2.1-5	Example of the Nodalization Used for the Steam Generator	6.2.1-14
Figure 6.2.1-6	Heat Structure with the Hydrodynamic Volumes Connected to the Two Surfaces	6.2.1-15
Figure 6.2.1-7	Multiple Heat Structures Connected to a Single Hydrodynamic Volume	6.2.1-15
Figure 6.2.3-1	Interface Heat Transfer in the Bulk and Near the Wall for Subcooled Boiling	6.2.3-5
Figure 6.2.4-1	Schematic of the Vertical Flow Regime Map	6.2.4-18
Figure 6.2.4-2	Schematic of the Horizontal Flow Regime Map	6.2.4-18
Figure 6.2.4-3	Schematic of the Flow Regime Map Using in a High Mixing Region	6.2.4-19
Figure 6.2.4-4	Boiling and Condensation Curve Regions	6.2.4-19
Figure 7.1.3-1	Decay heat power obtained by applying the ANS_1971 decay heat model	7.1.3-5
Figure 7.1.3-2	Integral decay heat power.....	7.1.3-6
Figure 7.1.5-1	Burst Temperature of ZIRLO.....	7.1.5-3
Figure 7.1.5-2	Burst Strain of ZIRLO.....	7.1.5-4
Figure 7.1.5-3	Assembly Blockage of ZIRLO.....	7.1.5-5
Figure 7.1.6-1	Maximum steam/water flow rate and local stagnation properties	7.1.6-5
Figure 7.1.6-2	Local static pressure and stagnation properties at maximum steam/water flow rate.....	7.1.6-65
Figure 7.2-1	The Flow Characteristics of the Flow Damper	7.2-6

Figure 7.2-2	Noding diagram	7.2-7
Figure 7.2-3	Injection volumetric flow rate (analysis result of 1/2-scale test: case 1)	7.2-8
Figure 7.2-4	Tank pressure (analysis result of 1/2-scale test: case 1)	7.2-8
Figure 7.2-5	Tank water level (analysis result of 1/2-scale test: case 1)	7.2-9
Figure 7.2-6	Injection volumetric flow rate (analysis result of 1/2-scale test: case 2)	7.2-9
Figure 7.2-7	Tank pressure (analysis result of 1/2-scale test: case 2)	7.2-10
Figure 7.2-8	Tank water level (analysis result of 1/2-scale test: case 2)	7.2-10
Figure 7.2-9	Injection volumetric flow rate (analysis result of 1/2-scale test: case 3)	7.2-11
Figure 7.2-10	Tank pressure (analysis result of 1/2-scale test: case 3)	7.2-11
Figure 7.2-11	Tank water level (analysis result of 1/2-scale test: case 3)	7.2-12
Figure 7.2-12	Injection volumetric flow rate (analysis result of 1/2-scale test: case 4)	7.2-12
Figure 7.2-13	Tank pressure (analysis result of 1/2-scale test: case 4)	7.2-13
Figure 7.2-14	Tank water level (analysis result of 1/2-scale test: case 4)	7.2-13
Figure 8.1.1-1	Schematic of ROSA-IV Large Scale Test Facility (LSTF)	8.1.1-8
Figure 8.1.1-2	Axial power profile and locations of differential pressure Measurements and grid spacers	8.1.1-9
Figure 8.1.1-3	Schematic of M-RELAP5 modeling regions	8.1.1-10
Figure 8.1.1-4	Nodalization of M-RELAP5 model	8.1.1-11
Figure 8.1.1-5	Simulated void fraction transient for test ST-NC-06E	8.1.1-12
Figure 8.1.1-6	Simulated void fraction profile for test ST-NC-06E	8.1.1-13
Figure 8.1.1-7	Simulated averaged void fraction profile for 7.3 MPa tests	8.1.1-14
Figure 8.1.2-1	THTF in Small-Break Test Configuration	8.1.2-9
Figure 8.1.2-2	Cross Section of THTF Test Section	8.1.2-10
Figure 8.1.2-3	Cross Section of a typical Fuel Rod Simulator	8.1.2-11
Figure 8.1.2-4	Axial Location of Spacer Grids and FRS Thermocouples	8.1.2-12

Figure 8.1.2-5	THTF In-Bundle Pressure Instrumentation	8.1.2-13
Figure 8.1.2-6	M-RELAP5 Noding Scheme for ORNL/THTF Tests	8.1.2-14
Figure 8.1.2-7	Comparison of Predicted and Measured Void Fraction Profiles for ORNL/THTF Test 3.09.10J	8.1.2-15
Figure 8.1.2-8	Comparison of Predicted and Measured FRS Surface Temperature Profiles for ORNL/THTF Test 3.09.10J	8.1.2-16
Figure 8.1.2-9	Comparison of Predicted and Measured Vapor Temperature Profiles for ORNL/THTF Test 3.09.10J	8.1.2-17
Figure 8.1.2-10	Comparison of Predicted and Measured Heat Transfer Coefficient Profiles for ORNL/THTF Test 3.09.10J	8.1.2-18
Figure 8.1.2-11	Comparison of Predicted and Measured Void Fraction Profiles for ORNL/THTF Test 3.09.10K	8.1.2-19
Figure 8.1.2-12	Comparison of Predicted and Measured FRS Surface Temperature Profiles for ORNL/THTF Test 3.09.10K	8.1.2-20
Figure 8.1.2-13	Comparison of Predicted and Measured Vapor Temperature Profiles for ORNL/THTF Test 3.09.10K	8.1.2-21
Figure 8.1.2-14	Comparison of Predicted and Measured Heat Transfer Coefficient Profiles for ORNL/THTF Test 3.09.10K	8.1.2-22
Figure 8.1.2-15	Comparison of Predicted and Measured Void Fraction Profiles for ORNL/THTF Test 3.09.10M	8.1.2-23
Figure 8.1.2-16	Comparison of Predicted and Measured FRS Surface Temperature Profiles for ORNL/THTF Test 3.09.10M	8.1.2-24
Figure 8.1.2-17	Comparison of Predicted and Measured Vapor Temperature Profiles for ORNL/THTF Test 3.09.10M	8.1.2-25
Figure 8.1.2-18	Comparison of Predicted and Measured Heat Transfer Coefficient Profiles for ORNL/THTF Test 3.09.10M	8.1.2-26

Figure 8.1.2-19	Comparison of Predicted and Measured Void Fraction Profiles for ORNL/THTF Test 3.09.10N	8.1.2-27
Figure 8.1.2-20	Comparison of Predicted and Measured FRS Surface Temperature Profiles for ORNL/THTF Test 3.09.10N	8.1.2-28
Figure 8.1.2-21	Comparison of Predicted and Measured Vapor Temperature Profiles for ORNL/THTF Test 3.09.10N	8.1.2-29
Figure 8.1.2-22	Comparison of Predicted and Measured Heat Transfer Coefficient Profiles for ORNL/THTF Test 3.09.10N	8.1.30
Figure 8.1.2-23	Comparison of Predicted and Measured Void Fraction Profiles for ORNL/THTF Test 3.09.10AA	8.1.2-31
Figure 8.1.2-24	Comparison of Predicted and Measured Void Fraction Profiles for ORNL/THTF Test 3.09.10BB	8.1.2-32
Figure 8.1.2-25	Comparison of Predicted and Measured Void Fraction Profiles for ORNL/THTF Test 3.09.10CC	8.1.2-33
Figure 8.1.2-26	Comparison of Predicted and Measured Void Fraction Profiles for ORNL/THTF Test 3.09.10DD	8.1.2-34
Figure 8.1.2-27	Comparison of Predicted and Measured Void Fraction Profiles for ORNL/THTF Test 3.09.10EE	8.1.2-35
Figure 8.1.2-28	Comparison of Predicted and Measured Void Fraction Profiles for ORNL/THTF Test 3.09.10FF	8.1.2-36
Figure 8.1.2-29	Comparison of Predicted and Measured Collapsed Liquid Levels for ORNL/THTF Tests	8.1.2-37
Figure 8.1.2-30	Comparison of Predicted and Measured Mixture Levels for ORNL/THTF Tests	8.1.2-38
Figure 8.1.2-31	Sensitivity 1: Comparison of Predicted and Measured Collapsed Liquid Levels for ORNL/THTF Tests (1.2 x nominal power cases)	8.1.2-39

Figure 8.1.2-32	Sensitivity 1: Comparison of Predicted and Measured Mixture Levels for ORNL/THTF Tests (1.2 x nominal power cases)	8.1.2-40
Figure 8.1.2-33	Sensitivity 2: Comparison of Predicted and Measured Mixture Levels for ORNL/THTF Tests (CHF modification cases)	8.1.2-41
Figure 8.1.3-1	M-RELAP5 Noding Diagram for ORNL/THTF High-Pressure Reflood Test	8.1.3-7
Figure 8.1.3-2	Comparison of Inputted and Measured Test Section Inlet Flows for ORNL/THTF Test 3.09.10P	8.1.3-8
Figure 8.1.3-3	Comparison of Inputted and Measured Test Section Inlet Temperatures for ORNL/THTF Test 3.09.10P	8.1.3-9
Figure 8.1.3-4	Comparison of Inputted and Measured Test Section Outlet Pressures for ORNL/THTF Test 3.09.10P	8.1.3-10
Figure 8.1.3-5	Comparison of Inputted and Measured Test Section Inlet Flows for ORNL/THTF Test 3.09.10Q	8.1.3-11
Figure 8.1.3-6	Comparison of Inputted and Measured Test Section Inlet Temperatures for ORNL/THTF Test 3.09.10Q	8.1.3-12
Figure 8.1.3-7	Comparison of Inputted and Measured Test Section Outlet Pressures for ORNL/THTF Test 3.09.10Q	8.1.3-13
Figure 8.1.3-8	Comparison of Predicted and Measured FRS and Fluid Temperatures at Level F for ORNL/THTF Test 3.09.10P	8.1.3-14
Figure 8.1.3-9	Comparison of Predicted and Measured FRS Temperatures at Level G for ORNL/THTF Test 3.09.10P	8.1.3-15
Figure 8.1.3-10	Comparison of Predicted and Measured Collapsed Liquid Level for ORNL/THTF Test 3.09.10P	8.1.3-16
Figure 8.1.3-11	Comparison of Predicted and Measured Quench Level for ORNL/THTF	

Test 3.09.10P	8.1.3-17
Figure 8.1.3-12 Comparison of Predicted and Measured FRS and Fluid Temperatures at Level F for ORNL/THTF Test 3.09.10Q	8.1.3-18
Figure 8.1.3-13 Comparison of Predicted and Measured FRS Temperatures at Level G for ORNL/THTF Test 3.09.10Q	8.1.3-19
Figure 8.1.3-14 Comparison of Predicted and Measured Collapsed Liquid Level for ORNL/THTF Test 3.09.10Q	8.1.3-20
Figure 8.1.3-15 Comparison of Predicted and Measured Quench Level for ORNL/THTF Test 3.09.10Q	8.1.3-21
Figure 8.1.4-1 UPTF CCFL Test Analysis, Geometry of a Broken Loop Hot Leg	8.1.4-5
Figure 8.1.4-2 Regression Analysis Results of the UPTF CCFL Parameters β , c and m for M-RELAP5	8.1.4-6
Figure 8.1.4-3 Nodalization Diagram Used for the UPTF CCFL Test Analysis	8.1.4-7
Figure 8.1.4-4 UPTF CCFL Test Analysis, Comparison of the Flooding Curves of Analysis Results and Test Results	8.1.4-8
Figure 8.1.5-1 Schematic of the Dukler Air/Water Test Facility	8.1.5-5
Figure 8.1.5-2 Nodalization Diagram of the Dukler Air/Water Flooding Experiment	8.1.5-6
Figure 8.1.5-3 Comparison of Calculated and Measured Results Using the Wallis Flooding Correlation Constants(c=0.88,m=1.0)	8.1.5-7
Figure 8.1.5-4 Comparison of Calculated and Measured Results Using the Wallis Flooding Correlation Constants(c=0.88,m=1.0)	8.1.5-8
Figure 8.2.1-1 General Structure of Large Scale Test Facility (LSTF)	8.2.1-2028
Figure 8.2.1-2 Pressure Vessel Assembly	8.2.1-2429
Figure 8.2.1-3 Break Assembly	8.2.1-2230
Figure 8.2.1-4 Break Orifice	8.2.1-2331
Figure 8.2.1-5 M-RELAP5 Noding Diagram of a Cold Leg Break LOCA for the LSTF	8.2.1-2432

Figure 8.2.1-6	Vessel Noding	8.2.1-2533
Figure 8.2.1-7	Hot Leg Noding	8.2.1-2634
Figure 8.2.1-8	SG Primary and Secondary Side Noding	8.2.1-2735
Figure 8.2.1-9	Cross-Over Leg Noding	8.2.1-2836
Figure 8.2.1-10	Total Core Power (Base Case)	8.2.1-2937
Figure 8.2.1-11	Reactor Coolant Pump in Primary Loop-A Rotation Speed	8.2.1-3038
Figure 8.2.1-12	Reactor Coolant Pump in Primary Loop-B Rotation Speed	8.2.1-3139
Figure 8.2.1-13	SGA Steam Dome Pressure	8.2.1-3240
Figure 8.2.1-14	SGB Steam Dome Pressure	8.2.1-3341
Figure 8.2.1-15	Break Flowrate	8.2.1-3442
Figure 8.2.1-16	Pressurizer Pressure	8.2.1-3543
Figure 8.2.1-17	Core Differential Pressure (Base Case)	8.2.1-3644
Figure 8.2.1-18	Loop-A Cross-Over Leg Flowrate	8.2.1-3745
Figure 8.2.1-19	Loop-B Cross-Over Leg Flowrate	8.2.1-3846
Figure 8.2.1-20	Loop-A Hot Leg to U-Tube Top Differential Pressure	8.2.1-3947
Figure 8.2.1-21	Loop-B Hot Leg to U-Tube Top Differential Pressure	8.2.1-4048
Figure 8.2.1-22	Loop-A Hot Leg to SG Inlet Plenum Bottom Differential Pressure	8.2.1-4149
Figure 8.2.1-23	Loop-B Hot Leg to SG Inlet Plenum Bottom Differential Pressure	8.2.1-4250
Figure 8.2.1-24	Loop-A SG Inlet Plenum Differential Pressure	8.2.1-4351
Figure 8.2.1-25	Loop-B SG Inlet Plenum Differential Pressure	8.2.1-4452
Figure 8.2.1-26	Loop-A SG U-tube Uphill Side Differential Pressure	8.2.1-4553
Figure 8.2.1-27	Loop-B SG U-tube Uphill Side Differential Pressure	8.2.1-4654
Figure 8.2.1-28	Loop-A SG U-tube Downhill Side Differential Pressure	8.2.1-4755
Figure 8.2.1-29	Loop-B SG U-tube Downhill Side Differential Pressure	8.2.1-4856
Figure 8.2.1-30	Loop-A Cross-over Leg Downhill Side Differential Pressure	8.2.1-4957
Figure 8.2.1-31	Loop-B Cross-over Leg Downhill Side Differential Pressure	8.2.1-5058

Figure 8.2.1-32	Loop-A Cross-over Leg Uphill Side Differential Pressure	8.2.1-5459
Figure 8.2.1-33	Loop-B Cross-over Leg Uphill Side Differential Pressure	8.2.1-5260
Figure 8.2.1-34	Downcomer Differential Pressure	8.2.1-5361
Figure 8.2.1-35	Loop-A Accumulator Injection Flowrate	8.2.1-5462
Figure 8.2.1-36	Loop-B Accumulator Injection Flowrate	8.2.1-5563
Figure 8.2.1-37	Heater Rod Surface Temperature (Test Data)	8.2.1-5664
Figure 8.2.1-38	Heater Rod Surface Temperature (M-RELAP5, Base Case)	8.2.1-5765
Figure 8.2.1-39	Heater Rod Surface Temperature at 3.61m (Test Data) and at 3.57m (M-RELAP5, Base Case)	8.2.1-5866
Figure 8.2.1-40	Heater Rod Surface Temperature at 3.05m (Test Data) and at 3.17m (M-RELAP5, Base Case)	8.2.1-5967
Figure 8.2.1-41	Heater Rod Surface Temperature at 2.24m (Test Data) and at 2.23m (M-RELAP5, Base Case)	8.2.1-6068
Figure 8.2.1-42	Heater Rod Surface Temperature at 1.83m (Test Data) and at 1.82m (M-RELAP5, Base Case)	8.2.1-6169
Figure 8.2.1-43	Heater Rod Surface Temperature at 1.02m (Test Data) and at 1.11m (M-RELAP5, Base Case)	8.2.1-6270
Figure 8.2.1-44	Heater Rod Surface Temperature at 0.05m (Test Data) and at 0.07m (M-RELAP5, Base Case)	8.2.1-6371
Figure 8.2.1-45	Void Fraction at 3.57m (High Power Channel)	8.2.1-6472
Figure 8.2.1-46	Void Fraction at 3.17m (High Power Channel)	8.2.1-6573
Figure 8.2.1-47	Heater Rod Surface Temperature at 3.61m (Test Data) and at 3.57m (M-RELAP5, Sensitivity-1)	8.2.1-6674
Figure 8.2.1-48	Heater Rod Surface Temperature at 3.05m (Test Data) and at 3.17m (M-RELAP5, Sensitivity-1)	8.2.1-6775
Figure 8.2.1-49	Heater Rod Surface Temperature at 2.24m (Test Data) and at 2.23m	

	(M-RELAP5, Sensitivity-1)	8.2.1-6876
Figure 8.2.1-50	Heater Rod Surface Temperature at 1.83m (Test Data) and at 1.82m (M-RELAP5, Sensitivity-1)	8.2.1-6977
Figure 8.2.1-51	Heater Rod Surface Temperature at 1.02m (Test Data) and at 1.11m (M-RELAP5, Sensitivity-1)	8.2.1-7078
Figure 8.2.1-52	Heater Rod Surface Temperature at 0.05m (Test Data) and at 0.07m (M-RELAP5, Sensitivity-1)	8.2.1-7479
Figure 8.2.1-53	Total Core Power (Sensitivity-2)	8.2.1-7280
Figure 8.2.1-54	Core Differential Pressure (Sensitivity-2)	8.2.1-7381
Figure 8.2.1-55	Heater Rod Surface Temperature at 3.61m (Test Data) and at 3.57m (M-RELAP5, Sensitivity-2)	8.2.1-7482
Figure 8.2.1-56	Heater Rod Surface Temperature at 3.05m (Test Data) and at 3.17m (M-RELAP5, Sensitivity-2)	8.2.1-7583
Figure 8.2.1-57	Heater Rod Surface Temperature at 2.24m (Test Data) and at 2.23m (M-RELAP5, Sensitivity-2)	8.2.1-7684
Figure 8.2.1-58	Heater Rod Surface Temperature at 1.83m (Test Data) and at 1.82m (M-RELAP5, Sensitivity-2)	8.2.1-7785
Figure 8.2.1-59	Heater Rod Surface Temperature at 1.02m (Test Data) and at 1.11m (M-RELAP5, Sensitivity-2)	8.2.1-7886
Figure 8.2.1-60	Heater Rod Surface Temperature at 0.05m (Test Data) and at 0.07m (M-RELAP5, Sensitivity-2)	8.2.1-7987
Figure 8.2.1-61	Upper Plenum Differential Pressure.....	8.2.1-88
Figure 8.2.1-62	Upper Head Liquid Level	8.2.1-89
Figure 8.2.1-63	ROSA/LSTF Noding Diagram (Sensitivity-3 Upper Head Nodalization Sensitivity Study).....	8.2.1-90
Figure 8.2.1-64	Upper Head Liquid Level (Sensitivity-3).....	8.2.1-91

<u>Figure 8.2.1-65</u>	<u>Core Differential Pressure (Sensitivity-3)</u>	<u>8.2.1-92</u>
<u>Figure 8.2.1-66</u>	<u>Downcomer Differential Pressure (Sensitivity-3)</u>	<u>8.2.1-93</u>
<u>Figure 8.2.1-67</u>	<u>Upper Plenum Differential Pressure (Sensitivity-3)</u>	<u>8.2.1-94</u>
<u>Figure 8.2.1-68</u>	<u>Loop-A Cross-Over Leg Uphill Side Differential Pressure (Sensitivity-4)</u>	<u>8.2.1-95</u>
<u>Figure 8.2.1-69</u>	<u>Loop-B Cross-Over Leg Uphill Side Differential Pressure (Sensitivity-4)</u>	<u>8.2.1-96</u>
<u>Figure 8.2.1-70</u>	<u>Core Differential Pressure (Sensitivity-4)</u>	<u>8.2.1-97</u>
<u>Figure 8.2.1-71</u>	<u>Upper Plenum Collapsed Liquid Level (Sensitivity-4)</u>	<u>8.2.1-98</u>
<u>Figure 8.2.1-72</u>	<u>Break Flowrate (Sensitivity-5)</u>	<u>8.2.1-99</u>
<u>Figure 8.2.1-73</u>	<u>Pressurizer Pressure (Sensitivity-5)</u>	<u>8.2.1-100</u>
<u>Figure 8.2.1-74</u>	<u>Loop-A Hot Leg to SG Inlet Plenum Bottom Differential Pressure (Sensitivity-5)</u>	<u>8.2.1-101</u>
<u>Figure 8.2.1-75</u>	<u>Loop-B Hot Leg to SG Inlet Plenum Bottom Differential Pressure (Sensitivity-5)</u>	<u>8.2.1-102</u>
<u>Figure 8.2.1-76</u>	<u>Core Differential Pressure (Sensitivity-5)</u>	<u>8.2.1-103</u>
<u>Figure 8.2.1-77</u>	<u>Upper Plenum Collapsed Liquid Level (Sensitivity-5)</u>	<u>8.2.1-104</u>
<u>Figure 8.2.1-78</u>	<u>Heater Rod Surface Temperature (Sensitivity-3)</u>	<u>8.2.1-105</u>
<u>Figure 8.2.1-79</u>	<u>Heater Rod Surface Temperature (Sensitivity-4)</u>	<u>8.2.1-106</u>
<u>Figure 8.2.1-80</u>	<u>Heater Rod Surface Temperature (Sensitivity-5)</u>	<u>8.2.1-107</u>
<u>Figure 8.2.1-81</u>	<u>M-RELAP5 Noding Diagram for ROSA-IV/LSTF around Break</u>	<u>8.2.1-108</u>
<u>Figure 8.2.1-82</u>	<u>Pressurizer Pressure (Calculation with Simulated Secondary System and Break Flow Behavior)</u>	<u>8.2.1-109</u>
<u>Figure 8.2.1-83</u>	<u>SG-A Steam Dome Pressure (Calculation with Simulated Secondary System and Break Flow Behavior)</u>	<u>8.2.1-110</u>
<u>Figure 8.2.1-84</u>	<u>SG-B Steam Dome Pressure (Calculation with Simulated Secondary System and Break Flow Behavior)</u>	<u>8.2.1-111</u>
<u>Figure 8.2.1-85</u>	<u>Break Flowrate (Calculation with Simulated Secondary System and Break</u>	

<u>Flow Behavior)</u>	8.2.1-112
<u>Figure 8.2.1-86 Loop-A Accumulator Injection Flowrate (Calculation with Simulated Secondary System and Break Flow Behavior)</u>	8.2.1-113
<u>Figure 8.2.1-87 Loop-B Accumulator Injection Flowrate (Calculation with Simulated Secondary System and Break Flow Behavior)</u>	8.2.1-114
<u>Figure 8.2.1-88 Loop-A Cross-over Leg Downhill Side Differential Pressure (Calculation with Simulated Secondary System and Break Flow Behavior)</u>	8.2.1-115
<u>Figure 8.2.1-89 Loop-B Cross-over Leg Downhill Side Differential Pressure (Calculation with Simulated Secondary System and Break Flow Behavior)</u>	8.2.1-116
<u>Figure 8.2.1-90 Loop-A Cross-over Leg Uphill Side Differential Pressure (Calculation with Simulated Secondary System and Break Flow Behavior)</u>	8.2.1-117
<u>Figure 8.2.1-91 Loop-B Cross-over Leg Uphill Side Differential Pressure (Calculation with Simulated Secondary System and Break Flow Behavior)</u>	8.2.1-118
<u>Figure 8.2.1-92 Core Differential Pressure (Calculation with Simulated Secondary System and Break Flow Behavior)</u>	8.2.1-119
<u>Figure 8.2.1-93 Heater Rod Surface Temperature at 3.61m (M) and 3.57m (P) (Calculation with Simulated Secondary System and Break Flow Behavior)</u>	8.2.1-120
<u>Figure 8.2.1-94 Heater Rod Surface Temperature at 3.05m (M) and 3.17m (P) (Calculation with Simulated Secondary System and Break Flow Behavior)</u>	8.2.1-121
<u>Figure 8.2.1-95 Heater Rod Surface Temperature at 2.24m (M) and 2.23m (P) (Calculation with Simulated Secondary System and Break Flow Behavior)</u>	8.2.1-122
<u>Figure 8.2.1-96 Heater Rod Surface Temperature at 1.83m (M) and 1.82m (P) (Calculation with Simulated Secondary System and Break Flow Behavior)</u>	8.2.1-123
<u>Figure 8.2.1-97 Heater Rod Surface Temperature at 1.02m (M) and 1.11m (P) (Calculation with Simulated Secondary System and Break Flow Behavior)</u>	8.2.1-124
<u>Figure 8.2.1-98 Heater Rod Surface Temperature at 0.05m (M) and 0.07m (P) (Calculation</u>	

<u>with Simulated Secondary System and Break Flow Behavior)</u>	8.2.1-125
<u>Figure 8.2.1-99 Integral of Vapor Mass Released from SGs (Calculation with Simulated</u>	
<u>Secondary System and Break Flow Behavior)</u>	8.2.1-126
<u>Figure 8.2.2-1 Break Assembly</u>	8.2.2-13
<u>Figure 8.2.2-2 Break Orifice</u>	8.2.2-14
<u>Figure 8.2.2-3 Total Core Power</u>	8.2.2-15
<u>Figure 8.2.2-4 Reactor Coolant Pump in Primary Loop-A Rotation Speed</u>	8.2.2-16
<u>Figure 8.2.2-5 Reactor Coolant Pump in Primary Loop-B Rotation Speed</u>	8.2.2-17
<u>Figure 8.2.2-6 Pressurizer Pressure</u>	8.2.2-18
<u>Figure 8.2.2-7 SGA Steam Dome Pressure</u>	8.2.2-19
<u>Figure 8.2.2-8 SGB Steam Dome Pressure</u>	8.2.2-20
<u>Figure 8.2.2-9 Break Flowrate</u>	8.2.2-21
<u>Figure 8.2.2-10 Core Differential Pressure</u>	8.2.2-22
<u>Figure 8.2.2-11 Loop-A SG Inlet Plenum Differential Pressure</u>	8.2.2-23
<u>Figure 8.2.2-12 Loop-B SG Inlet Plenum Differential Pressure</u>	8.2.2-24
<u>Figure 8.2.2-13 Loop-A SG U-tube Uphill Side Differential Pressure</u>	8.2.2-25
<u>Figure 8.2.2-14 Loop-B SG U-tube Uphill Side Differential Pressure</u>	8.2.2-26
<u>Figure 8.2.2-15 Loop-A SG U-tube Downhill Side Differential Pressure</u>	8.2.2-27
<u>Figure 8.2.2-16 Loop-B SG U-tube Downhill Side Differential Pressure</u>	8.2.2-28
<u>Figure 8.2.2-17 Loop-A Cross-over Leg Downhill Side Differential Pressure</u>	8.2.2-29
<u>Figure 8.2.2-18 Loop-B Cross-over Leg Downhill Side Differential Pressure</u>	8.2.2-30
<u>Figure 8.2.2-19 Loop-A Cross-over Leg Uphill Side Differential Pressure</u>	8.2.2-31
<u>Figure 8.2.2-20 Loop-B Cross-over Leg Uphill Side Differential Pressure</u>	8.2.2-32
<u>Figure 8.2.2-21 Downcomer Differential Pressure</u>	8.2.2-33
<u>Figure 8.2.2-22 Upper Plenum Differential Pressure</u>	8.2.2-34
<u>Figure 8.2.2-23 Loop-A Accumulator Injection Flowrate</u>	8.2.2-35

Figure 8.2.2-24	Loop-B Accumulator Injection Flowrate	8.2.2-36
Figure 8.2.2-25	Heater Rod Surface Temperature at 3.61m (M) and at 3.57m (P)	8.2.2-37
Figure 8.2.2-26	Heater Rod Surface Temperature at 3.05m (M) and at 3.17m (P)	8.2.2-38
Figure 8.2.2-27	Heater Rod Surface Temperature at 2.64m (M) and at 2.68m (P)	8.2.2-39
Figure 8.2.2-28	Heater Rod Surface Temperature at 2.24m (M) and at 2.23m (P)	8.2.2-40
Figure 8.2.2-29	Heater Rod Surface Temperature at 1.83m (M) and at 1.82m (P)	8.2.2-41
Figure 8.2.2-30	Heater Rod Surface Temperature at 1.42m (M) and at 1.37m (P)	8.2.2-42
Figure 8.2.2-31	Heater Rod Surface Temperature at 1.02m (M) and at 1.11m (P)	8.2.2-43
Figure 8.2.2-32	Heater Rod Surface Temperature at 0.61m (M) and at 0.64m (P)	8.2.2-44
Figure 8.2.2-33	Heater Rod Surface Temperature at 0.05m (M) and at 0.07m (P)	8.2.2-45
Figure 8.2.3-1	Break Assembly	8.2.3-12
Figure 8.2.3-2	Break Orifice	8.2.3-13
Figure 8.2.3-3	Break Modeling of IB-CL-02	8.2.3-14
Figure 8.2.3-4	Total Core Power	8.2.3-15
Figure 8.2.3-5	Reactor Coolant Pump in Primary Loop-A Rotation Speed	8.2.3-16
Figure 8.2.3-6	Reactor Coolant Pump in Primary Loop-B Rotation Speed	8.2.3-17
Figure 8.2.3-7	Pressurizer Pressure	8.2.3-18
Figure 8.2.3-8	SGA Steam Dome Pressure	8.2.3-19
Figure 8.2.3-9	SGB Steam Dome Pressure	8.2.3-20
Figure 8.2.3-10	Break Flowrate	8.2.3-21
Figure 8.2.3-11	Integral of Break Flow	8.2.3-22
Figure 8.2.3-12	Core Differential Pressure	8.2.3-23
Figure 8.2.3-13	Loop-A SG Inlet Plenum Differential Pressure	8.2.3-24
Figure 8.2.3-14	Loop-B SG Inlet Plenum Differential Pressure	8.2.3-25
Figure 8.2.3-15	Loop-A SG U-tube Uphill Side Differential Pressure	8.2.3-26
Figure 8.2.3-16	Loop-B SG U-tube Uphill Side Differential Pressure	8.2.3-27

<u>Figure 8.2.3-17</u>	<u>Loop-A SG U-tube Downhill Side Differential Pressure</u>	<u>8.2.3-28</u>
<u>Figure 8.2.3-18</u>	<u>Loop-B SG U-tube Downhill Side Differential Pressure</u>	<u>8.2.3-29</u>
<u>Figure 8.2.3-19</u>	<u>Downcomer Differential Pressure</u>	<u>8.2.3-30</u>
<u>Figure 8.2.3-20</u>	<u>Upper Plenum Differential Pressure</u>	<u>8.2.3-31</u>
<u>Figure 8.2.3-21</u>	<u>Accumulator Injection Flowrate</u>	<u>8.2.3-32</u>
<u>Figure 8.2.3-22</u>	<u>Safety Injection Flowrate</u>	<u>8.2.3-33</u>
<u>Figure 8.2.3-23</u>	<u>Heater Rod Surface Temperature at 3.61m (M) and at 3.57m (P)</u>	<u>8.2.3-34</u>
<u>Figure 8.2.3-24</u>	<u>Heater Rod Surface Temperature at 3.05m (M) and at 3.17m (P)</u>	<u>8.2.3-35</u>
<u>Figure 8.2.3-25</u>	<u>Heater Rod Surface Temperature at 2.64m (M) and at 2.68m (P)</u>	<u>8.2.3-36</u>
<u>Figure 8.2.3-26</u>	<u>Heater Rod Surface Temperature at 2.24m (M) and at 2.23m (P)</u>	<u>8.2.3-37</u>
<u>Figure 8.2.3-27</u>	<u>Heater Rod Surface Temperature at 1.83m (M) and at 1.82m (P)</u>	<u>8.2.3-38</u>
<u>Figure 8.2.3-28</u>	<u>Heater Rod Surface Temperature at 1.42m (M) and at 1.37m (P)</u>	<u>8.2.3-39</u>
<u>Figure 8.2.3-29</u>	<u>Heater Rod Surface Temperature at 1.02m (M) and at 1.11m (P)</u>	<u>8.2.3-40</u>
<u>Figure 8.2.3-30</u>	<u>Heater Rod Surface Temperature at 0.61m (M) and at 0.64m (P)</u>	<u>8.2.3-41</u>
<u>Figure 8.2.3-31</u>	<u>Heater Rod Surface Temperature at 0.05m (M) and at 0.07m (P)</u>	<u>8.2.3-42</u>
<u>Figure 8.2.4-1</u>	<u>M-RELAP5 Noding Diagram for LOFT L3-1</u>	<u>8.2.4-10</u>
<u>Figure 8.2.4-2</u>	<u>Break Flow Rate</u>	<u>8.2.4-11</u>
<u>Figure 8.2.4-3</u>	<u>Primary System Pressures</u>	<u>8.2.4-12</u>
<u>Figure 8.2.4-4</u>	<u>Secondary System Pressure</u>	<u>8.2.4-13</u>
<u>Figure 8.2.4-5</u>	<u>Pressurizer Liquid Level</u>	<u>8.2.4-14</u>
<u>Figure 8.2.4-6</u>	<u>Intact Loop Cross-over Leg Downhill Side Differential Pressure</u>	<u>8.2.4-15</u>
<u>Figure 8.2.4-7</u>	<u>Intact Loop Cross-over Leg Uphill Side Differential Pressure</u>	<u>8.2.4-16</u>
<u>Figure 8.2.4-8</u>	<u>Accumulator Tank Pressure</u>	<u>8.2.4-17</u>
<u>Figure 8.2.4-9</u>	<u>Accumulator Tank Liquid Level</u>	<u>8.2.4-18</u>
<u>Figure 8.2.4-10</u>	<u>Fuel Cladding Surface Temperature at 62-in from Core Bottom</u>	<u>8.2.4-19</u>
<u>Figure 8.2.5-1</u>	<u>M-RELAP5 Noding Diagram for Semiscale S-LH-1</u>	<u>8.2.5-12</u>

Figure 8.2.5-2	Break Flow Rate	8.2.5-13
Figure 8.2.5-3	Secondary System Pressure	8.2.5-14
Figure 8.2.5-4	Primary System Pressure	8.2.5-15
Figure 8.2.5-5	Collapsed Level in Uphill-Side of Intact Loop Crossover Leg	8.2.5-16
Figure 8.2.5-6	Collapsed Level in Uphill-Side of Broken Loop Crossover Leg	8.2.5-17
Figure 8.2.5-7	Collapsed Level in Intact Loop Hot Leg	8.2.5-18
Figure 8.2.5-8	Collapsed Level in Broken Loop Hot Leg	8.2.5-19
Figure 8.2.5-9	Collapsed Level in Uphill-Side of Intact Loop SG U-tubes	8.2.5-20
Figure 8.2.5-10	Collapsed Level in Uphill-Side of Broken Loop SG U-tubes	8.2.5-21
Figure 8.2.5-11	Core Collapsed Level	8.2.5-22
Figure 8.2.5-12	Heater Rod Cladding Temperature	8.2.5-23
Figure 8.3.2-1	Core Differential Pressure.....	8.3.2-4
Figure 8.3.2-2	Heater Rod Surface Temperature (2.23m).....	8.3.2-4
Figure 8.4-1	Overall Nodalization of Primary System for US-APWR	
	SBLOCA Analysis.....	8.4-3
Figure 8.4.1-1	Modeling Regions of Reactor Vessel and Internals	8.4-9
Figure 8.4.1-2	Nodalization of Reactor Vessel for US-APWR	8.4-10
Figure 8.4.1-3	Expanded Downcomer and Core Nodalization for US-APWR	8.4-11
Figure 8.4.1-4	Comparison of US-APWR and RELAP5-3D Guidelines for Reactor Vessel Nodalization	8.4-12
Figure 8.4.1-5	Comparison of US-APWR and RELAP5-3D Guidelines for Core and Downcomer Nodalization	8.4-12
Figure 8.4.1-6	Expanded View of Nodalization of Upper and Lower Plenum Regions of Reactor Vessel.....	8.4-13
Figure 8.4.2-1	Expanded View of Nodalization for Loop with Pressurizer.....	8.4-20
Figure 8.4.2-2	Expanded View of Nodalization for Loops without Pressurizer.....	8.4-21

Figure 8.4.2-3	Modeling Regions of Steam Generator	8.4-22
Figure 8.4.2-4	RELAP-3D Guidelines for Primary Loop Nodalization	8.4-23
Figure 8.4.2-5	Comparison of US-APWR and RELAP-3D Guidelines for Pressurizer Nodalization	8.4-23
Figure 8.4.2-6	Comparison of US-APWR and RELAP-3D Guidelines for Steam Generator Nodalization	8.4-24
Figure 8.4.2-7	ECCS Injection Nodalization	8.4-25
Figure 8.4.2-8	Nodalization of Feedwater and Steam Systems	8.4-25

Appendix

Figure B-1	Temperature Calculation Mesh Points and Intervals between them	B-3
Figure C-1	Noding Diagram of Moody Critical Flow Model Test Problem	C-3
Figure C-2	Maximum Steam/Water Flow Rate and Local Stagnation Properties	C-4
Figure C-3	Comparison of the Calculation Results with the Moody's Paper	C-5
Figure C-4	Connection of Moody's Critical Flow Model and Other Models	C-6
Figure D-1	Accumulator model	D-15
Figure D-2	Parameters required for the calculation of P_D	D-16
Figure E-1	Pressurizer Pressure	E-8
Figure E-2	SG Secondary Side Pressure	E-9
Figure E-3	<u>Normalized Core Power</u>	E-10
Figure E-4	<u>Average Core Channel Flow Rate</u> <u>Hot Assembly Exit Vapor and Liquid Mass Flowrates</u>	E-11
Figure E-5	DVI and Accumulator Injection Flow Rate	E-12
Figure E-6	Break Flow	E-13
Figure E-7	<u>Core and Upper Plenum Collapsed Level (Hot Channel)</u>	E-14
Figure E-8	Cladding Temperature of Hot Rod at All Elevations	E-15

Figure E-9 Heat Transfer Coefficient of Hot Rod at PCT Location E-16

List of Acronyms

ACC	Accumulator
APWR	Advanced Pressurized-Water Reactor
CCFL	Counter-Current Flow Limitations
CHF	Critical Heat Flux
CSS	Containment Spray System
CV	Containment Vessel
CVCS	Chemical and Volume Control System
DNB	Departure from Nucleate Boiling
DVI	Direct Vessel Injection
ECCS	Emergency Core Cooling System
EFWS	Emergency Feedwater System
ESF	Engineered Safety Feature
HHIS	High Head Injection System
LOCA	Loss Of Coolant Accident
LP	Lower plenum of reactor vessel
NR	Neutron Reflector
PCT	Peak Cladding Temperature

PIRT	Phenomena Identification and Ranking Table
PWR	Pressurized-water Reactor
PZR	Pressurizer
RCCA	Rod Cluster Control Assembly
RCP	Reactor Coolant Pump
RCS	Reactor Coolant system
RHR	Residual Heat Removal
RV	Reactor Vessel
RVH	Reactor Vessel Head
RVI	Reactor Vessel Internal
RWSP	Refueling Water Storage Pit
SBLOCA	Small Break LOCA
SG	Steam Generator
SRP	Standard Review Plan
SRV	Safety Relief Valve
UP	Upper Plenum of Reactor Vessel

1.0 INTRODUCTION

This report describes MHI's analysis methodology and evaluation of emergency core cooling system (ECCS) cooling performance for design-basis small break loss-of-coolant accidents (SBLOCAs) in the US-APWR. Both the analysis methodology and the plant analysis are performed in accordance with the requirements regarding applications specified in 10 CFR Part 50, "Domestic Licensing of Production and Utilization Facilities," Section 50.34, "Contents of Applications; Technical Information." (Ref. 1-1)

The purpose of the analysis is to determine the performance of the designed ECCS for the design-basis small break loss-of-coolant accidents (SBLOCAs) in the US-APWR against the acceptance criteria specified in 10 CFR Part 50 Section 50.46, "Acceptance Criteria for Emergency Core Cooling System for Light-Water Nuclear Power Reactors." (Ref. 1-2)

MHI specifically selected the RELAP5-3D computer code for the US-APWR small-break LOCA analysis and as a framework for M-RELAP5 based on two important principles.

- This approach was determined to be the most "straight-forward" way to satisfy the basic requirements for the development and assessment of a small-break LOCA evaluation model as described in Regulatory Guide 1.203. RELAP5 is a mature code, having evolved under the guidance of the US NRC and others. It incorporates the modeling approaches and specific models required to model a wide range of transients in different plant designs. In particular, RELAP5-3D abilities to model PWRs comparable in design to the US-APWR for SBLOCA conditions ~~has~~have been the subject of many studies. RELAP5-3D has been directly applied to most, if not all, of the experiments applicable to SBLOCAs in PWRs. The development of RELAP5-3D has followed quality assurance standards with independent peer review of a fundamental part of its development history. The RELAP5-3D reference manuals, along with supplementary material provided in this report, provide comprehensive, accurate, up-to-date documentation.
- RELAP5-3D is the culmination of a long series of RELAP5 versions developed at the Idaho National Laboratory (INL). Many of the current code development and application staffs have been associated with the code over much of its development history. RELAP5-3D models and correlations are based on the widely accepted and tested RELAP5/MOD3.2, and more recent RELAP5/MOD3.3, models and correlations first released in the US NRC versions of RELAP5. Many of the current user guidelines

have been prepared by staff members involved in development and validation of the code. The development history and configuration of the code has also been well documented from the original versions of RELAP5.

1.1 Roadmap for the Process of Development and Assessment of the M-RELAP5 Evaluation Model

The content of this report is in accordance with the process shown in the Regulatory Guide 1.203, "Transient and Accident Analysis Methods." (Ref. 1-3)

Regulatory Guide 1.203 identifies four elements with a total of 20 steps for the development and assessment of the evaluation methodology. This document follows the general roadmap of the 4 elements and associated 20 tasks as described in Table 1.1-1. The first element, *Establish Requirements for Evaluation Model Capability*, and the associated steps 1-4 are presented in Section 2 through 4 of this report. The second element, *Develop Assessment Base*, and associated steps 5-9, are presented in Section 5 of this report. The third element, *Develop Evaluation Model*, and associated steps 11-13 are presented in Sections 6 and 7 of this report. Section 6 provides a general assessment of the M-RELAP5-based part of evaluation model. Section 7 describes the development and general assessment of the "conservative" Appendix K (Ref. 1-4) methods used in the SBLOCA analysis. The fourth element, *Assess Evaluation Model Adequacy*, and associated steps 13-20, are presented in Sections 8. Section 8 provides a more detailed assessment of the small-break LOCA evaluation model which is called M-RELAP5. Section 9 is a summary of the overall assessment results for M-RELAP5.

The Regulatory Guidance on the use of a general purpose computer code also played a fundamental role in the final decision to develop the M-RELAP5 evaluation model combining the general framework of RELAP5-3D with "conservative" Appendix K methods. Specifically, the guidance noted the importance of generic reviews to minimize the amount of work required for plant- and event-specific reviews. It was also noted that a certain amount of generic assessments may be applied for part of the generic code development. The guidance also used the development of the US NRC system thermal hydraulic codes as an example of the development, assessment, and application of an evaluation model.

The decision was to use the conservative analysis methods defined in 10 CFR 50.46, Appendix K for the analysis of the US-APWR SBLOCA also simplified the assessment of the evaluation model because it was possible to perform code-to-data comparisons without the need for an

uncertainty analysis, as noted in the Regulatory Guide –

“An uncertainty methodology is not required for the original conservative Appendix K option in 10 CFR 50.46. Rather, the features required by Appendix K provide sufficient conservatism without the need for an uncertainty analysis. It should be noted that Section II.4 of Appendix K requires that “To the extent practicable, predictions of the EM, or portions thereof, shall be compared with applicable experimental information. Thus, Appendix K requires comparisons to data similar to those required for the best-estimate option, but without the need for an uncertainty analysis. However, poor comparisons with applicable data may prevent NRC acceptance of the Appendix K model.”

As a result, the evaluations of M-RELAP5, as presented in Section 8, are focused on the representative code-to-data comparisons and the verification that the M-RELAP5 application of the conservative Appendix K models is conservative.

1.2 References

- 1-1. 10 CFR 50.34, "Contents of Application; Technical Information."
- 1-2. 10 CFR 50.46, "Acceptance Criteria for Emergency Core Cooling System for Light-Water Nuclear Power Reactors."
- 1-3. Regulatory Guide 1.203, "Transient and Accident Analysis Methods," December 2005.
- 1-4. 10 CFR Part 50, Appendix K, "ECCS Evaluation Models."

Table 1.1-1 Roadmap for the Presentation of M-RELAP5 Evaluation Model

Steps in Evaluation Model Development and Assessment (Regulatory Guide 1.203)	Sections Presented
Step 1: Specify Analysis Purpose, Transient Class, and Power Plant Class	2
Step 2: Specify Figures of Merit	2
Step 3: Identify Systems, Components, Phases, Geometries, Fields, and Processes That Must Be Modeled	3
Step 4: Identify and Rank Key Phenomena and Processes	4
Step 5: Specify Objectives for Assessment Base	5
Step 6: Perform Scaling Analysis and Identify Similarity Criteria	5
Step 7: Identify Existing Data and/or Perform Integral Effects Tests (IETs) and Separate Effects Tests (SETs) To Complete the Database	5
Step 8: Evaluate Effects of IET Distortions and SET Scaleup Capability	5
Step 9: Determine Experimental Uncertainties as Appropriate	5
Step 10: Establish an Evaluation Model Development Plan	-
Step 11: Establish Evaluation Model Structure	6
Step 12: Develop or Incorporate Closure Models	7
Step 13: Determine Model Pedigree and Applicability To Simulate Physical Processes	6,7
Step 14: Prepare Input and Perform Calculations To Assess Model Fidelity or Accuracy	8
Step 15: Assess Scalability of Models	8
Step 16: Determine Capability of Field Equations To Represent Processes and Phenomena and the Ability of Numeric Solutions To Approximate Equation Set	8
Step 17: Determine Applicability of Evaluation Model To Simulate System Components	8
Step 18: Prepare Input and Perform Calculations To Assess System Interactions and Global Capability	8
Step 19: Assess Scalability of Integrated Calculations and Data for Distortions	8
Step 20: Determine Evaluation Model Biases and Uncertainties	8,9

2.0 COMPLIANCE WITH 10CFR 50.46

This report describes MHI's analysis methodology and evaluation of emergency core cooling system (ECCS) cooling performance for design-basis small break loss-of-coolant accidents (SBLOCAs) in the US-APWR. These analyses are performed in accordance with the requirements regarding applications specified in 10 CFR Part 50, "Domestic Licensing of Production and Utilization Facilities," Section 50.34, "Contents of Applications; Technical Information." (Ref. 2-1)

This report is prepared to conform with the process shown in Regulatory Guide 1.203, "Transient and Accident Analysis Methods." (Ref. 2-2)

2.1 Analysis Purpose

The purpose of the analysis is to show the evaluation and performance of the ECCS for the design-basis SBLOCAs in the US-APWR in accordance with the requirements specified in 10 CFR Part 50 Section 50.34, and the acceptance criteria specified in 10 CFR Part 50 Section 50.46, "Acceptance Criteria for Emergency Core Cooling System for Light-Water Nuclear Power Reactors." (Ref. 2-3).

2.2 Power Plant Class

The US-APWR is four-loop, pressurized-water reactor (PWR) with a thermal output of 4,451 MW. The fuel assembly has an about 14 ft heated length elements with 11 grid spacers in a 17x17 rod array. Each of the four loops consists of a steam generator, reactor coolant pump, associated piping, and ECCS.

The ECCS configuration of the US-APWR is similar to that for the conventional Westinghouse-designed PWRs in which the pumped safety injection and accumulator injection are provided. However, the ECCS for the US-APWR includes the following improvements:

- i) Four-train direct vessel safety Injection (DVI) system, which enhances safety and reliability.
- ii) Emergency water storage pit inside the containment, which eliminates switchover for pumped safety injection system.
- iii) Advanced accumulator, which is a passive component and enhances the safety

injection flow characteristics.

2.3 Transient Class

The SBLOCA events are categorized as one of postulated design-basis accidents that are specified in SRP 15.0 (Ref. 2-4). SRP 15.6.5 (Ref. 2-5) states in the "areas of review" section that a spectrum of both large and small break LOCA are to be evaluated and the limiting breaks are to be identified through sufficient analyses to determine the worst break peak clad temperature (PCT), the worst local clad oxidation, and the highest core wide oxidation percentage. Moreover, the SRP states that for the evaluation of the ECCS, the evaluation model must comply with acceptance criteria for ECCS given in 10 CFR 50.46. These criteria are described as figures of merit in the following section.

The postulated SBLOCA is defined as a break in the reactor coolant pressure boundary having a broken area that results in a loss of coolant at a rate in excess of the capability of the normal reactor coolant makeup system and is equal to or less than 1.0 ft² of the cross sectional area of the cold leg.

In the SBLOCA events, the RCS depressurization results in a pressure decrease in the pressurizer to the "pressurizer low-pressure" setpoint (1860 psia), actuating a reactor trip signal. Continuous depressurization generates a safety injection "S" signal and the ECCS is aligned for injection when the "pressurizer low-low pressure" setpoint (1760 psia) is reached.

The ECCS includes four redundant trains of the high-head safety injection system (direct vessel safety injection (DVI) system) and accumulator injection system. The safety injection (SI) pumps of the DVI system take suction from the refueling water storage pit in the containment and deliver borated water to the safety injection nozzles of the reactor vessel. Once the RCS pressure falls below the accumulator operating pressure, pressurized nitrogen gas forces borated water from the accumulator tanks to inject into the cold legs of RCS.

During a SBLOCA, the reactor system depressurizes and mass is lost out the break as the RCS drains to the break elevation, while mass is added from the SI pumps and the accumulators. Water injected by the SI pumps and accumulators provides core cooling and prevents excessive cladding temperature.

The US-APWR SBLOCA event can be divided into five periods that characterize the fluid transient behavior in the RCS. They are: Blowdown (BLD), Natural Circulation (NC), Loop Seal Clearance (LSC), Boil-Off (BO) and Core Recovery (REC) (Ref. 2-6). The duration of each period is break-size dependent. The above classification is useful in order to identify and rank various phenomena to develop a Phenomena Identification and Ranking Table (PIRT), which is discussed in the Section 4.

2.4 Figures of Merit

General Design Criterion 35 in Appendix A to 10 CFR Part 50 (Ref. 2-7) requires that a means of providing abundant emergency core cooling be provided that will transfer heat from the reactor core in the event of LOCA, and the evaluation of ECCS performance is required in accordance with 10 CFR 50.46 and Appendix K to 10 CFR Part 50 (Ref. 2-8).

10 CFR 50.46 and SRP 15.6.5 further defines acceptance criteria in terms of quantitative fuel and reactor system design limits for the events of interest that should be considered as figures of merits in the ECCS performance evaluation. The following five specific criteria for ECCS design are specified.

- i. *Peak cladding temperature (PCT)*: The calculated maximum fuel element cladding temperature shall not exceed 2200°F.
- ii. *Maximum cladding oxidation*: The calculated total oxidation of the cladding shall nowhere exceed 0.17 times the total cladding thickness before oxidation.
- iii. *Maximum hydrogen generation*: The calculated total amount of hydrogen generated from the chemical reaction of the cladding with water or steam shall not exceed 0.01 times the hypothetical amount that would be generated if all of the metal in the cladding cylinders surrounding the fuel, excluding the cladding surrounding the plenum volume, were to react.
- iv. *Coolable geometry*: Calculated changes in core geometry shall be such that the core remains amenable to cooling.
- v. *Long-term cooling*: After any calculated successful initial operation of the ECCS, the calculated core temperature shall be maintained at an acceptably low value and decay heat shall be removed for the extended period of time required by the long-lived radioactivity remaining in the core.

With respect to the above long-term cooling aspect, it is important to maintain vessel inventory to provide sufficient cooling, therefore vessel inventory is a key parameter that should be considered in the evaluation.

2.5 References

- 2-1. 10 CFR 50.34, "Contents of Application; Technical Information."
- 2-2. Regulatory Guide 1.203, "Transient and Accident Analysis Methods," December 2005.
- 2-3. 10 CFR 50.46, "Acceptance Criteria for Emergency Core Cooling System for Light-Water Nuclear Power Reactors."
- 2-4. NUREG-0800, "Standard Review Plan 15.0 Introduction-Transient and Accident Analyses," Revision 3 –March 2007.
- 2-5. NUREG-0800, "Standard Review Plan 15.6.5 Loss-of-Coolant-Accident Resulting from Spectrum of Postulated Piping Breaks within the Reactor Coolant Pressure Boundary," Revision 3 –March 2007.
- 2-6. Bajorek, S.M. et al., "SMALL BREAK LOSS OF COOLANT ACCIDENT PHENOMENA IDENTIFICATION AND RANKING TABLE (PIRT) FOR WESTINGHOUS PRESSURISED WATER REACTORS," Ninth International Topical Meeting on Nuclear Reactor Thermal Hydraulics (NURETH-9), October, 1999.
- 2-7. 10 CFR Part 50, Appendix A, "General Design Criteria for Nuclear Power Plants."
- 2-8. 10 CFR Part 50, Appendix K, "ECCS Evaluation Models."

3.0 SYSTEMS, COMPONENTS, PHASES, GEOMETRIES, FIELDS, AND PROCESSES THAT MUST BE MODELED

In the SBLOCA, the thermal-hydraulic transient is of longer duration than for a large break LOCA since the rate of discharged of flow and energy is relatively small to that in a large break LOCA. To ensure the accuracy of the thermal-hydraulic plant response, the reactor system model includes the reactor core, the RCS, the ECCS, and the secondary system. One-dimensional (1D) modeling enables constructing the integrated reactor system model by interconnecting 1D nodalized reactor system control volumes with flow the same paths as those that exist in the US-APWR.

The 1D thermal-hydraulic code M-RELAP5 used for SBLOCA analysis contains well-established two-phase flow regimes. The transient behavior of the system is analyzed using governing equations of mass, energy, and momentum, as modeled in the code. The code provides the multi-node capability to give the spatial representation of reactor core, and also includes the following models specific to SBLOCA transient:

- Critical flow correlations
- Heat transfer between the core and metal structures and fluid flow
- Response of components including pump coastdown, valve opening/closing, accumulator discharging behavior
- Signals to actuate or trip equipments

3.1 US-APWR Systems to Be Modeled

The US-APWR systems that must be modeled and analyzed includes:

- i) Primary System (Reactor and Core, Reactor Coolant System, Emergency core cooling system)
- ii) Secondary System (Main steam system, Main feedwater system, Emergency feedwater system)
- iii) Containment Vessel

3.2 Components to Be Modeled

The reactor primary and SG secondary systems are modeled in the SBLOCA calculations.

Primary system modeling includes the reactor internals and vessel, the steam generators, the reactor coolant pumps, the pressurizer, the reactor coolant piping and pressurizer surge line, the accumulators and the high-head safety injection system. Secondary system modeling includes the SG secondary side – main feedwater, main steam and emergency feedwater lines, their isolation valves, and safety and relief valves.

3.2.1 Primary System Components

3.2.1.1 Reactor and Core

The reactor's general configuration is shown in Figure 3.2.1-1. The reactor internals consist of two major assemblies, the lower core support assembly and the upper core support assembly. These support the core, maintain fuel assemblies alignment, limit fuel assemblies' movement, and maintain alignment between fuel assemblies and control rods. These structures also direct the coolant flowing through the fuel assemblies, transmit the loads from the core to the reactor vessel, provide radiation shielding of the reactor vessel, and guide the in-core instrumentation.

Lower Core Support Assembly

The lower core support assembly consists of the core barrel, the lower core support, the neutron reflector, the diffuser plate, and the energy absorber.

The core barrel is a long cylindrical structure with four outlet nozzles attached, and the flange is welded at the top of the cylinder. The bottom of the core barrel is horizontally supported by radial supports welded to the reactor vessel. The neutron reflector is located inside the core barrel.

The lower core support is welded to the bottom of the core barrel. The lower core support plate supports the fuel assemblies, the neutron reflector, the diffuser plate and the energy absorber. Four flow holes are provided for each fuel assembly.

The neutron reflector is located between the core barrel and the core, and lines the core cavity. The purposes of this reflector are to increase structural reliability by eliminating bolts in the high neutron influence region, to improve neutron utilization and thus fuel cycle cost, and to reduce

neutron irradiation of the reactor vessel.

Upper Core Support Assembly

The upper core support assembly consists of the upper core support, the upper core plate, the upper support columns and the guide tubes.

The upper core support is the major support structure for the upper internals, and consists of the flange, the cylindrical skirt and the thick forged plate. This structure separates the upper plenum of the core barrel from the reactor vessel upper head plenum region and supports the guide tubes and the upper support columns.

The upper core plate is connected to the upper core support by the upper support columns. The fuel assembly alignment pins are attached at the bottom of the upper core plate. The upper core plate is positioned in its proper location, with respect to the lower support assembly, by the upper core plate guide pins in the core barrel.

The upper support columns connect the upper core support and the upper core plate. The top and bottom are bolted to the upper core support and the upper core plate, respectively.

The guide tube assemblies guide the control rod drive shafts and the rod cluster control assemblies (RCCAs). The upper flange of the guide tubes is fastened to the upper core support in the upper head region and the bottom of guide tubes are restrained by pins in the upper core plate.

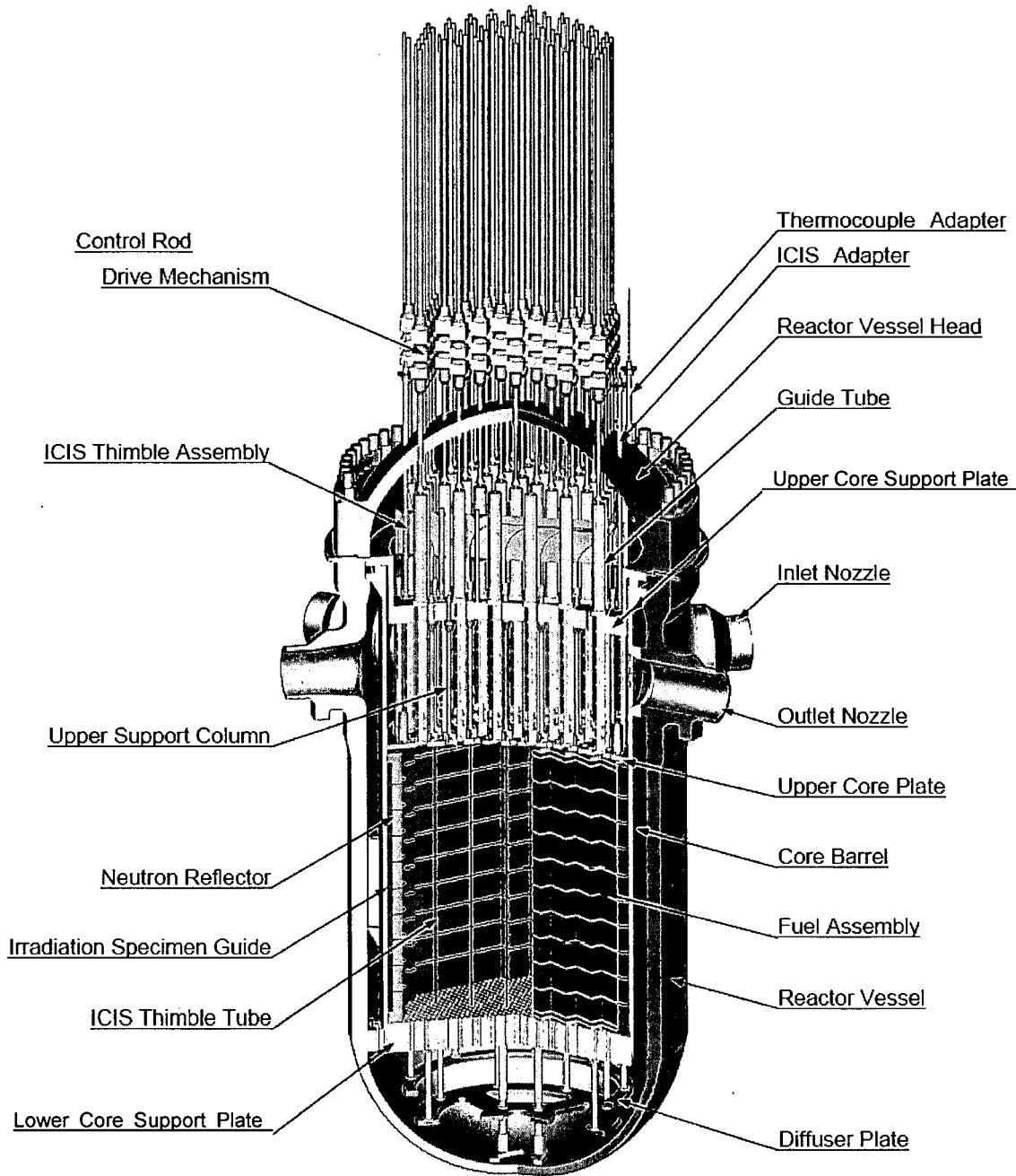


Figure 3.2.1-1 Reactor General Assembly

3.2.1.2 Components of the Reactor Coolant System

The reactor coolant system (RCS), shown in Figure 3.2.1-2, provides reactor cooling and energy transport functions. The RCS consists of the reactor vessel, the steam generators, the reactor coolant pumps, the pressurizer, and the reactor coolant pipes and valves.

The RCS performs the following functions:

- Circulates the reactor coolant through the reactor core and transfers heat to the secondary system via the steam generators.
- Cools the core sufficiently to prevent core damage during reactor operation.
- Provides the reactor coolant pressure boundary, which acts as a barrier to prevent radioactive materials in the reactor coolant from being released to the environment.
- Functions as a neutron moderator and reflector and as a solvent for boron.
- Controls the reactor coolant pressure.

Reactor Vessel

The reactor vessel (RV), shown in Figure 3.2.1-1 and 3.2.1-3, is a vertical vessel with hemispherical top and bottom heads.

The RV contains the fuel assemblies and reactor vessel internals, including the core support structures, control rods, neutron reflector and other structures associated with the core.

The RV is provided with four inlet nozzles, four outlet nozzles, and four safety injection nozzles, which are located between the upper reactor vessel flange and the top of the core, so as to be able to maintain coolant in the reactor vessel in the case of leakage in the reactor coolant loop.

During normal operations, coolant enters the vessel through the inlet nozzles, flows down the annulus between the core barrel and RV wall, turns at the bottom of the vessel, and flows upwards through the core to the outlet nozzles.

Steam Generator

The steam generator (SG), shown in Figure 3.2.1-4, is a vertical shell U-tube evaporator with integral moisture separating equipment.

The reactor coolant enters the channel head via the hot side primary coolant nozzle, flows through the inverted U-tubes, transferring heat from the primary side to the secondary side, and leaves from the channel head via the cold side primary coolant nozzle. The channel head is divided into inlet and outlet chambers by a vertical partition plate extending down from the apex of the head to the tube sheet.

Steam generated on the shell side (secondary side), flows upward, and exits through the outlet nozzle at the top of the vessel. Feedwater enters the steam generator at an elevation above the top of the U-tubes through a feedwater nozzle. The feedwater enters a feed-ring and is distributed through nozzles attached to the top of the feed-ring. After exiting the nozzles, the feedwater mixes with saturated water removed by the moisture separators. The flow then enters the downcomer annulus between the wrapper and the shell.

The support plates provide the tubes with support and maintain the proper tube spacing. The holes in the tube support plates are broached to increase the for flow area around tubes.

When water passes through the tube bundle, it is converted to a steam-water mixture. The steam-water mixture from the tube bundle then rises into the primary separators and the secondary separators.

Reactor Coolant Pump

The reactor coolant pump, shown in Figure 3.2.1-5, is vertical single-stage centrifugal pump of similar design as the 93A pump, which is used in four-loop PWRs, and is driven by three-phase induction motors. A flywheel on the shaft above the motor provides additional inertia to extend pump coastdown. The pump suction is located at the bottom, and the discharge on the side.

The reactor coolant that enters into the bottom of the casing is accelerated by the impeller, and is transformed to higher pressure through the diffuser, then is delivered through the discharge nozzle.

Pressurizer

The pressurizer, shown in Figure 3.2.1-6, functions to control the RCS pressure and to

Mitsubishi Heavy Industries, LTD.

accommodate any change in the coolant volume. The pressurizer is a vertical vessel with hemispherical top and bottom heads. Electrical immersion-type heaters are installed vertically through the bottom head of the vessel while the spray nozzle and relief line connections to relief and safety valves are located on the top head of the vessel.

The pressurizer is designed to accommodate positive and negative volume surges caused by load transients. The surge line, which is attached to the bottom of the pressurizer, connects to the hot leg of one of reactor coolant loops.

Reactor Coolant System Piping

The reactor coolant pipe work consists of the pipes connecting the reactor pressure vessel, steam generators, reactor coolant pumps, and pressurizer.

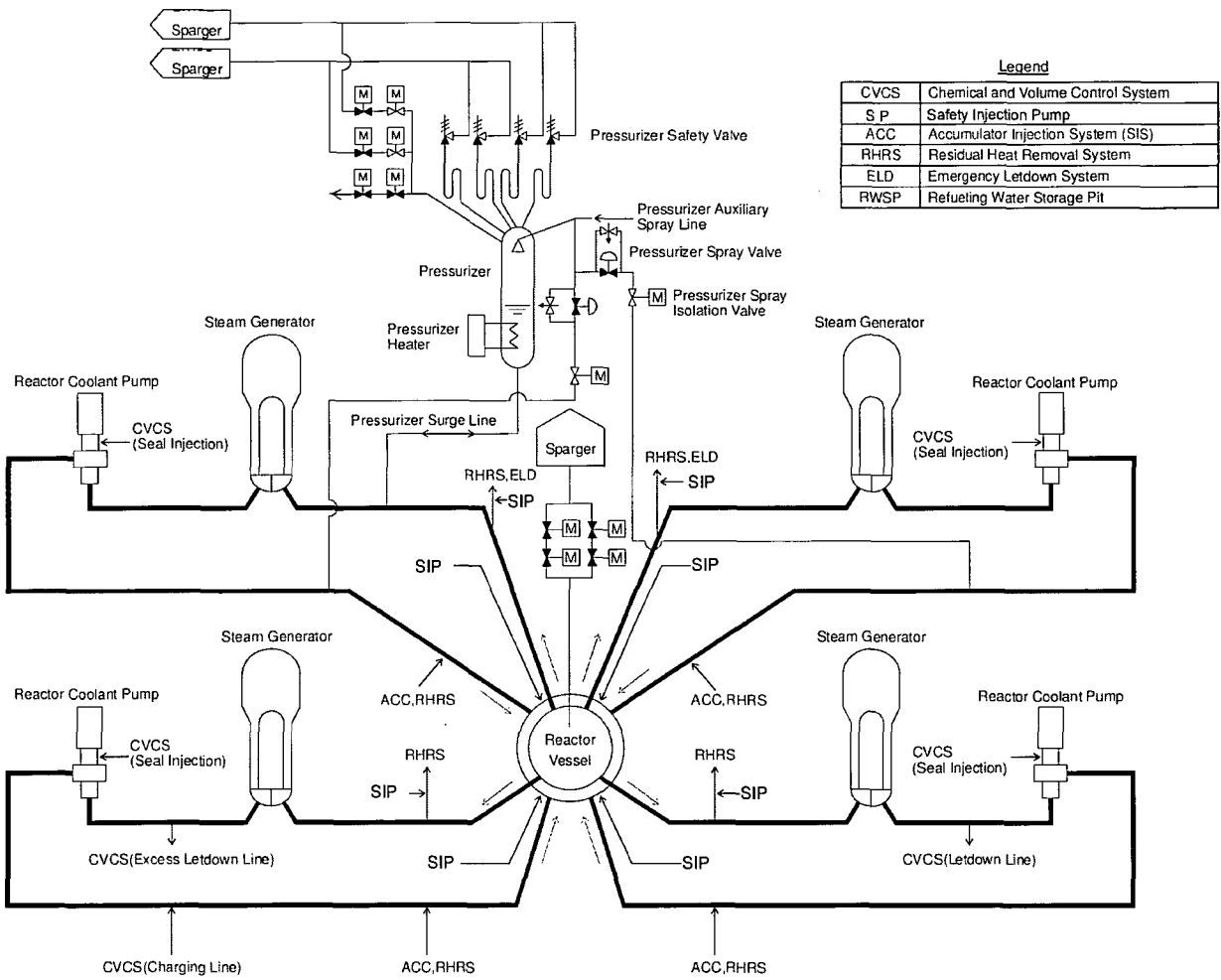


Figure 3.2.1-2 Reactor Coolant System

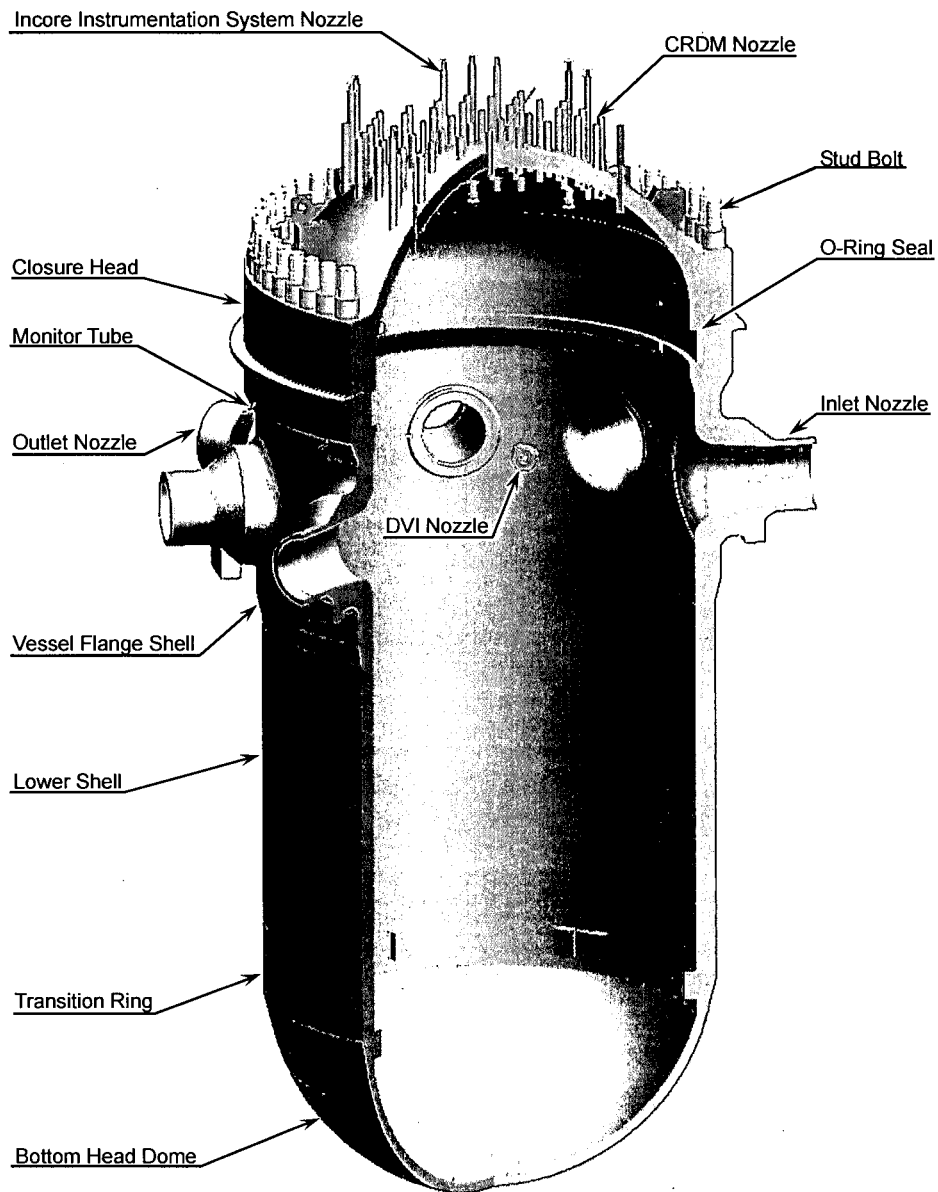


Figure 3.2.1-3 Reactor Vessel

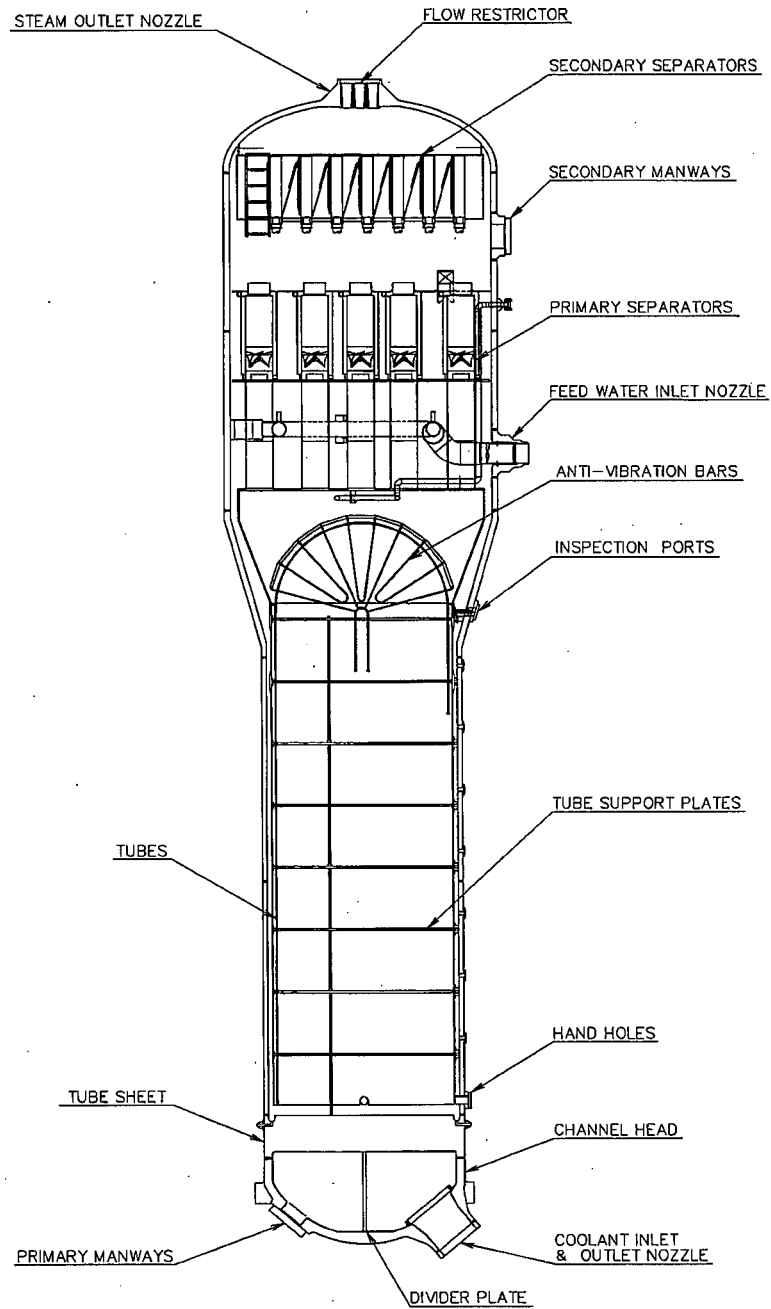


Figure 3.2.1-4 Steam Generator

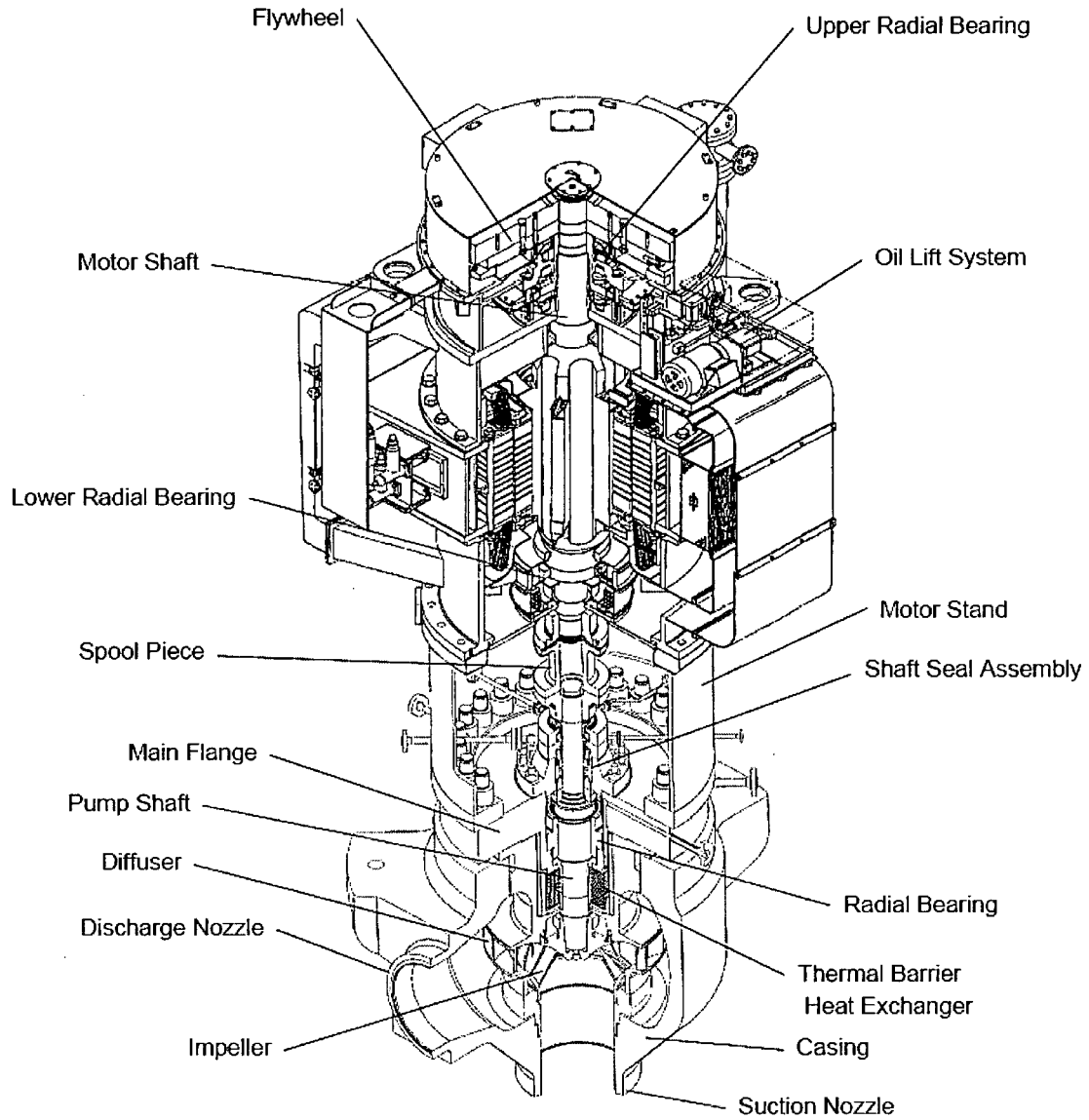


Figure 3.2.1-5 Reactor Coolant Pump

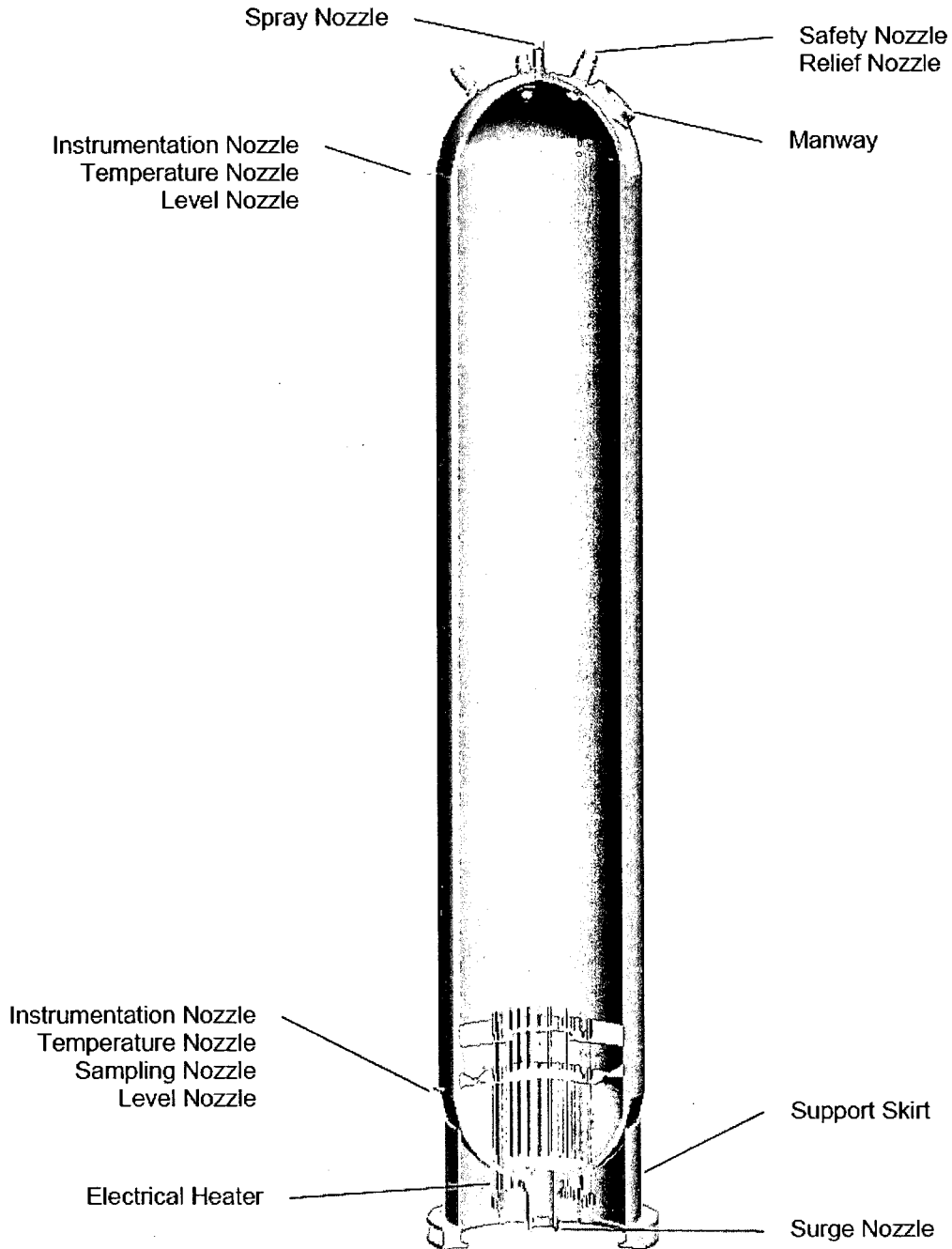


Figure 3.2.1-6 Pressurizer

3.2.1.3 Components of Emergency Core Cooling System

The emergency core cooling system (ECCS), shown in Figure 3.2.1-7, includes the accumulator system, the high-head safety injection system, and the emergency letdown system. The accumulator system and high-head safety injection system are included in the evaluation model.

The ECCS injects borated water into the reactor coolant system following a postulated accident and performs the following functions:

- Following a loss-of-coolant accident (LOCA), the ECCS cools the reactor core, prevents the fuel and fuel cladding from serious damage, and limits the zirconium-water reaction of the fuel cladding to a very small amount.
- Following a main steam line break (MSLB), the ECCS provides negative reactivity to shutdown the reactor.
- In the event that the normal CVCS letdown and boration capability is lost, the ECCS provides emergency letdown and boration of the RCS.

The ECCS design is based on the followings:

- In combination with control rod insertion, the ECCS is designed to shut down and cool the reactor during the following accidents:
 - Small break Loss-of Coolant Accidents of the primary piping,
 - Control rod ejection,
 - Main steam line break,
 - Steam generator tube rupture
- The ECCS is designed with sufficient redundancy (four trains) to accomplish the specified safety functions assuming a single failure of an active component in the short term following an accident with one train out of service for maintenance, or a single failure of an active component or passive component for the long term following an accident with one train out of service.
- The ECCS is automatically initiated by a safety injection signal.
- The emergency electrical power to the essential components is provided so that the design functions can be maintained during a loss of offsite power.

Accumulator System

The accumulator system stores borated water under pressure and automatically injects it if the reactor coolant pressure decreases significantly.

The accumulator system consists of four accumulators, and the associated valves and piping, for each RCS loop. The system is connected to the cold legs of the reactor coolant piping and injects borated water when the RCS pressure falls below the accumulator operating pressure. Pressurized nitrogen gas forces borated water from the tanks into the RCS. The accumulator system is a passive component.

The accumulator performs the large flow injection to refill the reactor vessel. After the large flow period the accumulator provides a smaller injection flow and during core reflooding in association with the high-head safety injection pumps. The high-head safety injection system provides long term core cooling for the core.

High-Head Injection System

The high-head injection system (HHIS) consists of four independent trains, each containing a safety injection pump and the associated valves and piping. The safety injection pumps start automatically upon receipt of the safety injection signal. One of four independent safety electrical buses is available to each safety injection pump.

The safety injection pumps are aligned to take suction from the refueling water storage pit and to deliver borated water to the safety injection nozzles on the reactor vessel. Two safety injection trains are capable of meeting the design cooling function for a large break LOCA, assuming a single failure in one train and a second train is out of service for maintenance.

The refueling water storage pit in the containment provides a continuous borated water source for the safety injection pumps. This configuration eliminates the need for realignment from the refueling water storage tank to the containment sump, which is employed in the existing PWR plants.

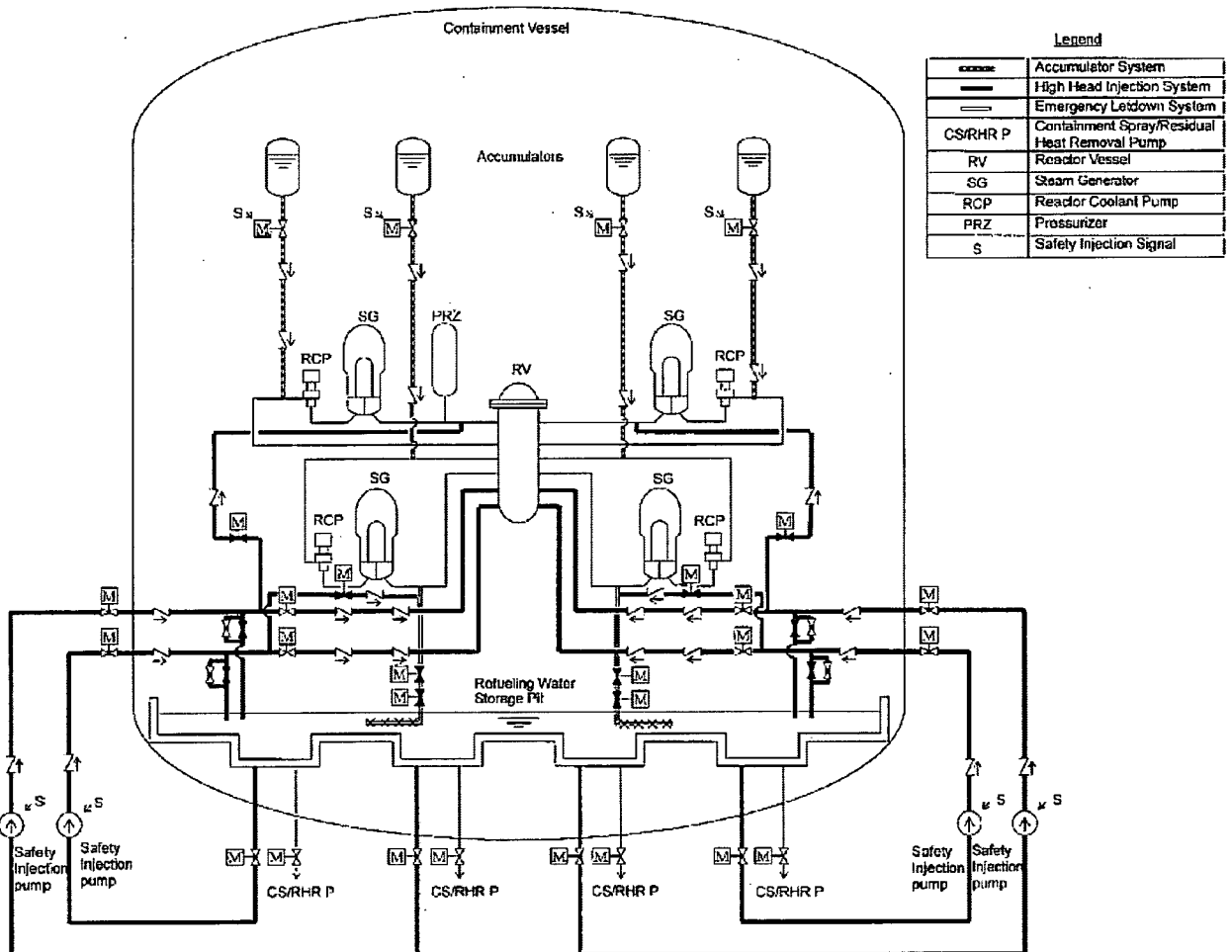


Figure 3.2.1-7 Emergency Core Cooling System

3.2.2 Secondary System Components

The secondary system consists of the main feedwater system, the main steam system, the emergency feedwater system, and the power conversion system.

3.2.2.1 Main Steam System Components

The main steam system includes the main steam pipes from the steam generator outlets to the turbine inlet steam chests and equipment and piping connected to the main steam pipes. The main steam relief and safety valves are installed upstream of the main steam isolation valve. They prevent excessive steam pressure and maintain cooling of RCS if the turbine bypass is not available. The total capacity of the main steam safety valves exceeds 100% of the rated main steam flow rate.

Branch pipes for driving the turbine-driven emergency feedwater pumps are connected upstream of the main steam isolation valves.

The secondary sides of SGs to the main steam isolation valves are included in the evaluation model.

3.2.2.2 Main Feedwater System Components

The main feedwater system supplies the steam generators with heated feedwater in a closed steam cycle using regenerative feedwater heating. The system is composed of the condensate subsystem, the feedwater subsystem, and a portion of the steam generator feedwater piping. The feedwater control valves, the feedwater bypass control valves, the steam generator water filling control valves, and the feedwater isolation valves are installed on the feedwater lines.

The feedwater isolation valves to the secondary sides of the SGs are included in the evaluation model.

3.2.2.3 Emergency Feedwater System Components

The emergency feedwater system (EFWS), shown in Figure 3.2.2-1, consists of two

Mitsubishi Heavy Industries, LTD.

motor-driven pumps, two steam turbine-driven pumps, two emergency feedwater pits, and associated piping and valves. The four emergency feedwater pumps take suction from two emergency feedwater pits.

The EFWS removes reactor decay heat and RCS residual heat through the steam generators following transient conditions or postulated accidents.

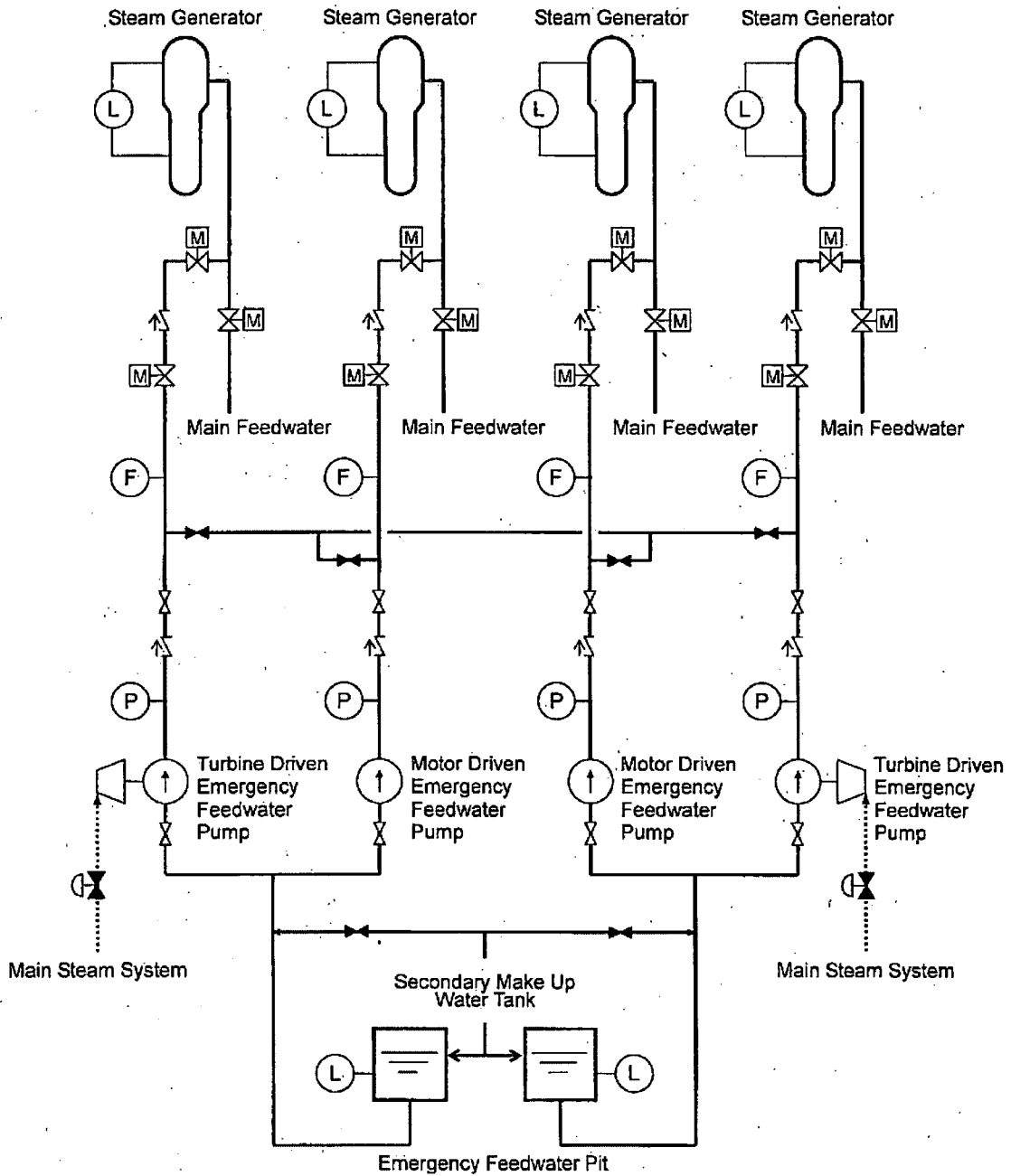


Figure 3.2.2-1 Emergency Feedwater System

3.2.3 Containment Vessel

The containment vessel is designed to completely enclose the reactor and RCS and to ensure that essentially no leakage of radioactive materials to the environment would result even if a major failure of the RCS were to occur.

The containment vessel is a pre-stressed, post-tensioned concrete structure with an inside steel lining. The containment vessel is designed to contain the energy and radioactive materials that could result from a postulated LOCA.

In the SBLOCA evaluation, an atmospheric condition inside the containment vessel is assumed as the boundary conditions for the break back-pressure in the system model.

3.3 Phases to be Modeled

A spectrum of small breaks is being evaluated for the US-APWR with a cold leg break assumed as the limiting break location in terms of core cooling. The behavior of the system is characterized by single phase, forced and natural circulation in the primary system, followed by two-phase, combined forced and natural circulation as depressurization and safety injection occur. The secondary side is also characterized by a combination of single phase and two phase natural convection as the secondary side is isolated and steam is released through the secondary side relief valves. The primary system will also have non-condensable gases present during part of the transient with the injection of nitrogen once the accumulators empty.

In the case of the US-APWR, the transition from single phase forced convection to two phase convection occurs during the blowdown phase of the transient as the result of the following sequence of events. As the break occurs, liquid will start to exit out of the break, resulting in the depressurization of the primary system. As the pressure in the pressurizer reaches the "pressurizer pressure low" set point (1860psia), the reactor is tripped and the steam generator secondary side will be isolated. As a result, the steam generator secondary side pressure rises to the safety valve set point and secondary side steam is released through the safety valves.

As the pressure in the pressurizer reaches the "pressurizer low-low pressure" set point (1760psia), a safety injection signal is generated. The safety injection will initiate after a specified delay time. This safety injection will be performed by the four train direct vessel injection system directly into the downcomer and by the four advanced accumulators into the cold leg. The accumulators will inject water into the cold leg once the primary system pressure falls below the accumulator operating pressure (600 psia).

The primary system liquid will remain as a single phase for much of the blowdown period, with phase separation first occurring in the upper head, upper plenum and hot legs. The break flow remains as liquid during this period. As the pressure continues to drop, the primary system pressures will reach the saturation point, terminating the subcooled phase of the blowdown. The saturated blowdown will continue as the primary side pressure approaches the secondary side pressure.

As the blowdown phase is completed, a period of two-phase natural circulation will predominate.

The two-phase natural circulation will continue because of condensation occurring in the steam generator tubes. At some point, natural circulation will stop as vapor builds up in the steam generator tubes and blocks the circulating flow. The next period is characterized by the clearance of the loop seal with the possibility of partial core uncover due to the static pressure imbalance in the primary system. After the loop seal clears, the static pressure imbalance will be removed and the water level in the vessel will rise again. The remaining phases will depend on the size of the break and the capacity of the water injection systems. If the break flows exceed the capacity of the water injection systems, the vessel water level will again start to decrease. Otherwise the vessel water levels will increase and the transient will be terminated.

The injection of non-condensable gases from the accumulators as they empty can occur although the specific timing and quantities of non-condensable gases present at any time will depend on the transient. Since the accumulators must empty before the non-condensable gas (nitrogen) is injected, the core should have been fully recovered before the nitrogen enters the primary system.

Both single phase and two-phase flow behavior including the influence of the pressure differences, heat transfer, and co-current and counter-current flow need to be modeled for a small-break LOCA. Specific models that represent each of the systems and components of the US-APWR are modeled as well as models specific to PWR fuel assemblies that will be used to describe the flow and heat transfer in core region. The core region can experience both single and two-phase flows as well as co- and counter-current flows including the influence of water drainage from the upper plenum region. Models that include the specific features of the other reactor vessel internals will also be used. Like the core region, these components include the downcomer, upper plenum, and lower plenum. During the transient, these components can also experience both single and two-phase mixtures with the presence of non-condensable gases. Single and two-phase co- and counter-current flow will also be modeled in the balance of the primary system and secondary system components. For example, the water held-up in the SG due to flooding will be modeled.

3.4 Geometries

All components of the primary system and portions of the secondary system are modeled for the SBLOCA. Where appropriate, portions of the emergency core cooling system (ECCS) and

containment will be included in the analysis, although the specific components of the ECCS and containment systems may be activated using appropriate time dependent boundary conditions. These systems and the structures associated with them are modeled primarily using one dimensional flow networks and heat structures, although multi-dimensional networks and structures may be used where appropriate.

The geometries of the flow paths and structures that make up the US-APWR primary system and components are modeled so that flow rates, pressure differences, and heat transfer can be calculated. Representative fuel assembly geometries are modeled in the core region including the fuel rod dimensions, fuel assembly pitch, and other physical characteristics of the fuel assemblies. The physical characteristics of the other reactor internal structures are modeled including (a) primary flow areas, (b) leakage paths such the paths between the upper plenum and downcomer, and (c) structural surface areas and volumes to insure the proper heat storage in these structures. The flow areas, orientation, and structural surface areas and thicknesses are modeled in the balance of the primary system and components to insure realistic flow and heat transfer calculations.

The geometries of the secondary system flow paths and structures that are important to SBLOCA conditions are modeled to insure the accuracy of the calculations of the secondary side heat transfer and flow conditions.

3.5 Field Equations

A non-equilibrium, separated two-phase flow model will be used to model the SBLOCA in the US-APWR. The model will also include influence of non-condensable gases. Although more simplistic field equations, using a simplified form of the momentum equations, have also been used for such analysis, the non-equilibrium, separated two-phase flow is now the commonly used approach. One dimensional formulation will be used in the balance of the primary and secondary system.

3.6 Processes to be Considered

All of the processes important to the analysis of SBLOCA will be considered along with those processes that are useful for the purposes of the analysis, such as the implementation of control system responses. The thermal hydraulic response of the primary and secondary

system, heat transfer within system structures and components, power generation associated with fission heating, decay heat, and oxidation of the fuel rod cladding, and the important features of the reactor control system will be modeled as needed for a specific transient. The deformation and rupture of the fuel rod cladding and its impact on flow within the core will be modeled as needed for a specific transient.

Specifically, the processes to be considered include:

- Single phase and two-phase convective flow and heat transfer,
- Subcooled, saturated two-phase and vapor break flows over a range of break sizes,
- Structural heat transfer as a heat sink and as a heat source,
- Reactor kinetics and decay heat as a heat source, and
- Cladding oxidation as a heat source.

The two-phase flow distribution will include the calculation of core void fraction, collapsed liquid level, and two-phase mixture levels in the core and balance of the reactor coolant system where appropriate. A full boiling curve will be used to describe the heat transfer in the core and steam generator, and elsewhere where appropriate. The heat transfer model will consider single phase convection, nucleate boiling, critical heat flux (CHF), and post-CHF behavior. The appropriate flow regimes will be considered including single phase convection, two-phase co-current and counter-current flows, and flooding in the core, reactor vessel, piping, steam generator, and other primary and secondary system components.

4.0 IDENTIFY AND RANK KEY PHENOMENA AND PROCESSES

4.1 Introduction

One of the most important steps in developing an analysis methodology is the identification of phenomena and processes that provide the most dominant influence on the specific transient of interest. A Phenomena Identification and Ranking Table (PIRT) lists key processes and specifies at which stage in the transient the process or phenomenon occurs. The PIRT developed for a small break Loss-of-Coolant Accident (LOCA) for a Mitsubishi US-APWR is similar to that developed by Bajorek et al. (Ref. 4-1) for a Westinghouse PWR. The ranking definitions for the phenomena are also consistent with those developed by Boyack (Ref. 4-2). The approach used for the US-APWR SBLOCA PIRT was to utilize the expertise at MHI to develop the initial SBLOCA PIRT. There were five individuals involved at MHI which had a total of 110 years experience in analyzing PWRs, performing safety related experiments, and conducting accident analyses for model development and plant analysis. Once this Preliminary SBLOCA PIRT was completed, it was reviewed independently and separately by Dr. Thomas George from Numerical Applications Incorporated and Dr. L.E. Hochreiter from The Pennsylvania State University. Once the review comments were assembled, a meeting was held between MHI, Dr. George and Dr. Hochreiter to review comments and resolve differences. The resumes for Drs. George and Hochreiter are given in Appendix-A. The result of these efforts is the SBLOCA PIRT described in Section 4.3.

In developing the PIRT, the phenomena are identified by major system components, and a ranking is assigned for the respective periods of small break LOCA using the definitions for "High, Medium, and Low" as developed by Boyack (Ref. 4-2). Since the PIRT depends on the plant and the accident scenario, the overview of the US-APWR plant and its small break LOCA transient are described below in Sections 4.1.1 and 4.1.2.

4.1.1 Target Plant / US-APWR

This PIRT applies to those phenomena and processes that would occur in a Mitsubishi US-APWR small break LOCA transient. The US-APWR is a four-loop PWR, in which the high pressure safety injection is directly injected into the downcomer (Direct Vessel Injection (DVI)), and advanced accumulators inject to the cold legs. It is assumed that the plant is in its normal, full power operation mode in accordance with its Technical Specifications at the time a small

break LOCA occurs.

4.1.2 Accident Scenario

The assumed accident is a small break LOCA with a most limiting single failure associated with the safeguard system. A cold leg break is assumed as the limiting break location in terms of core cooling, based on historical PWR experience.

During a small break LOCA transient, a reactor trip signal is generated when the RCS depressurizes to the "pressurizer low-pressure" set point (1860 psia). The US-APWR design employs a four-train direct vessel injection (DVI) system, which is activated by an S-signal which is generated when the RCS depressurizes to the "pressurizer low-low pressure" set point (1760 psia). The accumulator system consists of four advanced accumulators and the associated valves and piping, one for each cold leg. The system injects borated water when the RCS pressure falls below the accumulator operating pressure at a pressure of 600 psia.

During a small break LOCA, the reactor vessel depressurizes as the reactor vessel and RCS mass inventory is lost out the break. The DVI and accumulator systems add liquid mass to the RCS to maintain cooling for the core. The quantity and timing of the water injection must be such that the core is cooled to an acceptable level for a spectrum of small break LOCA transients.

4.1.3 Measure of Merit for the PIRT

When developing a PIRT a measure of merit it is necessary to judge the relative importance of the different phenomena expected during the transient. For the Small-Break LOCA PIRT, the main measure of merit that has been used in the past is the resulting Peak Cladding Temperature or PCT. The PCT has been used as the measure of merit for the large-break LOCA PIRTs as well as the Small-Break LOCA PIRT as developed by Bajorek et al (Ref. 4-1). The relative importance of the different phenomena that are identified is judged by the impact they can or could have on the measure of merit. This assessment determines the ranking of High, Medium, or Low. Other parameters could have been chosen such as vessel mixture level or inventory. However, since the most difficult Appendix K requirement to meet is the PCT, this parameter was chosen as the measure of merit when evaluating the different phenomena of interest.

4.2 Small Break LOCA Scenario

In order to identify various phenomena and provide importance rankings for them during the small break LOCA transient, it is useful to divide the transient into several periods. Some phenomena, which exhibit a significant importance in a certain period, may not necessarily exhibit such significance in other periods. However, simulations of these significant phenomena are required to accurately predict the overall US-APWR transient response. Small break LOCA transients can be divided into five time periods: Blowdown, Natural Circulation, Loop Seal Clearance, Boil-off and Core Recovery. The length of each time period depends on the break size and the performance of the ECC systems. Each is characterized as described below and schematically shown in Figure 4.2-1. It is assumed that the break is a small break located at the bottom of the reactor cold leg.

Blowdown (BLD):

Upon initiation of the break, the RCS primary side rapidly depressurizes until flashing of the hot coolant into steam begins. Reactor trip is initiated on the "pressurizer low-pressure" set point of 1860 psia. Closure of the condenser steam dump valves isolates the SG secondary side. As a result, the SG secondary side pressure rises to the safety valve set point, and the steam is released through the safety valves. A safety injection signal is generated at the time that the pressurizer pressure decreases to the "pressurizer low-low pressure" set point at 1760 psia, and the safety injection initiates after a set delay time.

The coolant in the RCS remains in the liquid phase throughout most of the blowdown period, although towards the end of the period, steam begins to form in the upper head, upper plenum and hot legs. The rapid depressurization ends when the pressure falls to just above the saturation pressure of the steam generator secondary side at the safety valve set point. At that time, the steam generation rate in the upper regions of the core and in the upper plenum increases. The break flow is single-phase liquid phase throughout the blowdown period.

Natural Circulation (NC):

When the blowdown period ends, the RCS pressure settles slightly above the SG secondary side pressure. Two-phase natural circulation is established through the RCS loops with the decay heat being removed by heat transfer (via condensation and convection) to the SG secondary side. Pressure rise in the secondary side is suppressed by frequent steam venting through the secondary side safety valves. Auxiliary feedwater flow is initiated to maintain the secondary side liquid inventory. As more coolant is lost from the RCS through the break, the

loop flow velocity decreases, natural circulation is broken, and steam accumulates in the downhill side of the SG tubes and the crossover leg. The circulation flow stops with the formation of single phase liquid plugs in the pump suction piping (loop seals).

Loop Seal Clearance (LSC):

The third period is the loop seal clearance period. With the loop seals filled, the break, located at the bottom of the cold leg, remains covered with water so that the water inventory continues to drop and the steam volume in the RCS increases. Water accumulates in the uphill side of the SG tubes and hot legs due to condensation in the SG and non-homogenous two-phase flow in the RCS loops. The relative pressure in the core increases to overcome the increasing gravitational and drag forces in the hot legs and uphill SG tubes. The increase of pressure at the top of the core causes the liquid level in the core to decrease. As the steam volume continues to increase, the liquid levels in the core and in the downhill side of the SG of the loop seals continue to decrease. When the liquid level on the downhill side of the SG is depressed to seal elevation, the loop seals clear and steam in the RCS is vented to the cold legs and the break flow changes from a low-quality mixture to primarily steam. This relieves the back pressure on the core and the core liquid level is restored to the cold leg elevation by flow from the downcomer.

If, during this process, the core mixture level drops below the top of the core, the cladding will experience a dryout and the cladding temperature in the upper part of the core will begin to rise rapidly. Typically, the temperature rise is not sufficient to challenge safety limits because the core is quickly recovered with water when the loop seals clear.

Boil-off (BO):

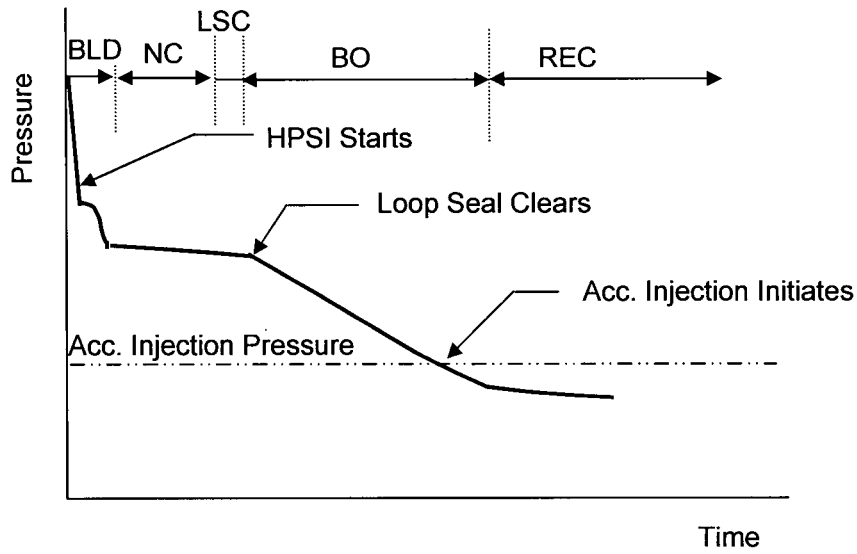
After the loop seal clears, the RCS primary side pressure falls below that of the secondary side due to the increase of the break flow quality resulting in a lower mass flow rate but a higher volumetric break flow leaving the break. This changes the direction of heat transfer in the SG so that the secondary side begins to supply heat to the primary side. For a medium break size, the vessel mixture level may decrease as a result of the core boiling-off. This occurs because the RCS pressure is too high for the injection system to make up for the boil-off rate.

For the US-APWR, the flow from one safety injection pump is sufficient to match the boil-off rate for the case of a DVI line (3.4-inch inner diameter) guillotine break. Equivalently, this is sufficient to maintain the vessel mixture level for the case of a cold leg break for the twice the

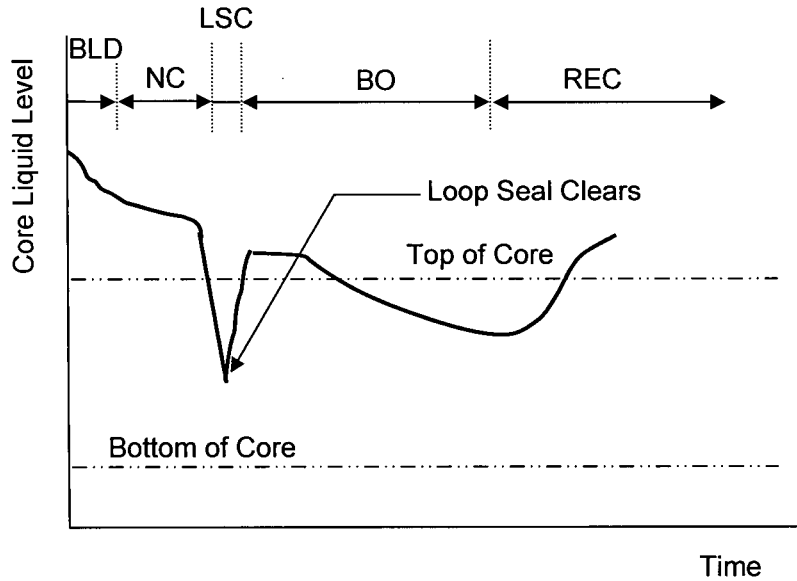
area of the DVI line, since two safety injection pumps are available. For larger breaks, the core might uncover before the RCS depressurizes to the point where the safety injection pumps and accumulators deliver ECC water to the RCS at a higher rate than the break flow.

Core Recovery (REC):

As the RCS pressure continues to fall, the SI flow increases and the accumulator eventually starts to inject such that total ECC flow exceeds the break flow. The vessel mass inventory increases and the core recovers. The transient terminates when the entire core is quenched and the ECC water delivery exceeds the break flow.



Primary Pressure Response



Core Collapsed Liquid Level Response

Figure 4.2-1 Pressure and Core Liquid Level Responses of Small Break LOCA

4.3 Phenomena Identification and Ranking Table (PIRT)

A PIRT directly applicable to the Mitsubishi US-APWR, which considers the plant design features was developed and independently reviewed for the US-APWR as discussed in Section 4.1.

4.3.1 Definition of Rankings

Relative to the impact on PCT, phenomena and processes were evaluated and assigned rankings with the following definitions as given by Boyack (Ref. 4-2), which are consistent with other accident analysis PIRTs.

H = The process is considered to have high importance. Accurate modeling of the process is considered to be crucial to the correct prediction of the transient. Models used to predict the process must be validated.

H* = The process is considered to potentially have high importance. It is break size dependent so in some cases it may be insignificant.

M = The process is considered to have medium importance. Modeling has to be made for appropriate process simulation, although the level of influence on the entire transient is expected to be lower than those ranked high (H) or (H*).

M* = The process is considered to potentially have medium importance. It is break size dependent so in some cases it may be insignificant.

L = The process is considered to have low importance. The phenomena need to be modeled in the code or explained in adequate detail in the methodology, although accuracy in modeling the process is not considered very influential to the analysis of the whole transient.

L* = The process is considered to have low importance. For some break sizes, however, the phenomena should be modeled in the code.

N/A = The process is considered not to occur at all.

4.3.2 Discussions on Rankings

Table 4.3.2-1 lists small break LOCA phenomena and their relative rankings. This section discusses key categories in the PIRT, explains the basis for the ranking, and defines the phenomena considered as the “process”. Table 4.3.2-2 lists processes by respective components that were ranked high (H) for at least one period in the transient.

4.3.2.1 Fuel Rod

1. Stored Energy/Initial stored energy:

2. Core Kinetics, Reactor Trip (Fission Power):

3. Decay heat:

4. Oxidation of Cladding:

[]

5. Cladding Deformation:

[]

6. Gap conductance:

[]

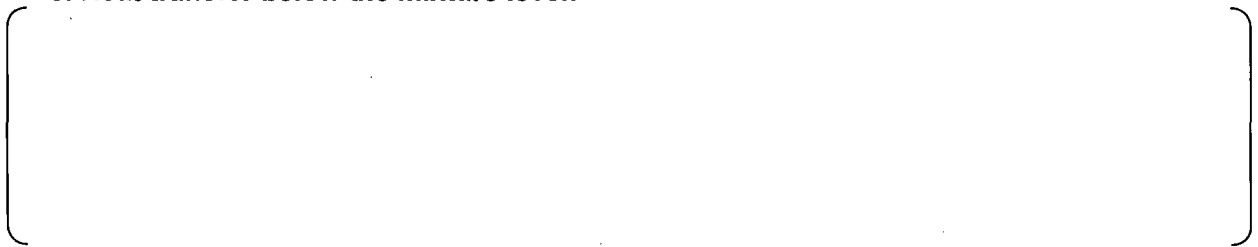
7. Local power:

[]



4.3.2.2 Core

8. Heat transfer below the mixture level:



9. CHF/Dryout:



10. Uncovered Core Heat Transfer:



11. Rewet (Heat transfer recovery):



12. Entrainment/De-entrainment:

13. 3-D Flow:

14. Mixture level:

15. Flow resistance:



16. 3-D Power Distribution:



17. Top Nozzle/Tie Plate CCFL:



4.3.2.3 Neutron Reflector

18. Steam and Droplet Generation in Flow Holes:



19. Water Storage and Boiling in Back Region:



()

20. Heat Transfer between Back Region and Core Barrel:

()

21. Core Bypass Flow:

()

4.3.2.4 Upper Head

22. Drainage to Core / Initial Fluid Temperature:

()

23. Bypass Flow from Upper Head to Downcomer (Cold Leg):

()

24. Metal Heat Release:

()

4.3.2.5 Upper Plenum

25. Mixture Level:



26. Draining to Core:



27. Entrainment/De-entrainment:

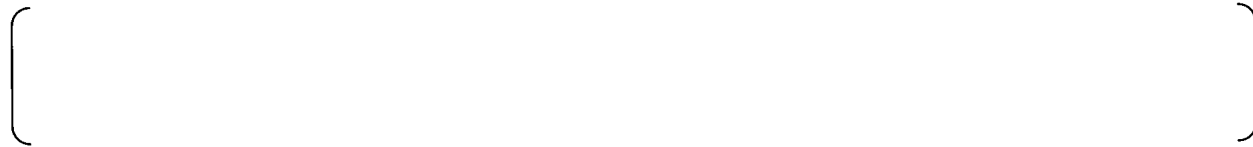




28. Bypass Flow/Hot Leg - Downcomer Gap:



29. Metal Heat Release:



4.3.2.6 Hot Leg

30. Horizontal Stratification/Counter-flow:



31. Entrainment/De-entrainment:

[]

32. Metal Heat Release:

[]

4.3.2.7 Pressurizer and Surge Line

33. Mixture Level:

[]

34. Out-Surge by Depressurization:

[]

35. Metal Heat Release:

[]

36. Location/Proximity to Break:

[]

4.3.2.8 Steam Generator (SG)

37. Water Hold-up in SG Inlet Plenum:

[]

38. Water Hold-up in U-Tube Uphill Side:

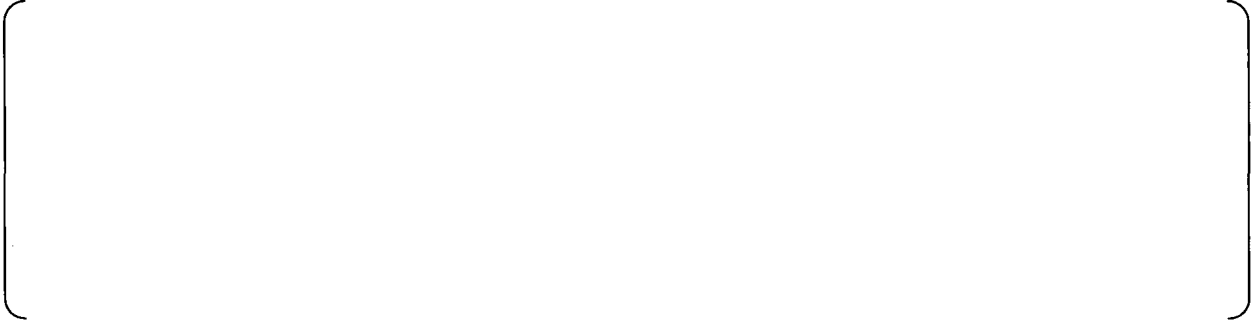
[]

39. Primary side Heat Transfer:

[]



40. Secondary side heat transfer (Water Level):



41. Metal heat release:



42. Multi-U-tube Behavior:



43. Auxiliary Feed Water Flow:



4.3.2.9 Crossover Leg

44. Water Level in SG Outlet Piping:

45. Loop Seal Formation and Clearance (Entrainment/Flow regime/Interfacial drag/Flow resistance):

46. Metal Heat Release:

4.3.2.10 RCP

47. Coastdown Performance:

[]

48. Two-phase Flow Performance:

[]

49. Reversal Flow of ECC Water:

[]

50. Metal heat release:

[]

4.3.2.11 Cold Leg

51. Stratified Flow:

[]

[]

52. Condensation by ACC water:

[]

53. Non-condensable Gas Effect:

[]

54. Metal heat release:

[]

4.3.2.12 Accumulator

55. Large Flow Injection/Flow Resistance:

[]

56. Small Flow Injection/Flow Resistance:

[]



57. Interfacial Heat Transfer:



58. Metal heat release:



59. Injection of Nitrogen gas Effects:



4.3.2.13 Downcomer Region/Lower Plenum

60. Mixture Level/Void Distribution:



61. Metal heat release:

[]

62. ECC Water/Mixing:

[]

63. 3-D Flow:

[]

64. DVI/SI Water/Flowrate:

[]

65. DVI/SI Water/Condensation:

[]

[]

66. DVI/SI Water/Injection Temperature:

[]

4.3.2.14 Break

67. Critical Flow:

[]

68. Break Flow Enthalpy:

[]

Table 4.3.2-1(1/3) PIRT for Small Break LOCA

Location Process / Phenomena		Small Break LOCA				
		Blowdown	Natural Circulation	Loop Seal Clearance	Boil-off	Recovery
Fuel Rod						
1	Stored Energy/Initial Stored Energy					
2	Core kinetics, Reactor Trip (fission power)					
3	Decay Heat					
4	Oxidation of Cladding					
5	Clad Deformation					
6	Gap Conductance					
7	Local Power					
Core						
8	Heat Transfer below the Mixture Level					
9	CHF/Dryout					
10	Uncovered Core Heat Transfer					
11	Rewet (Heat Transfer Recovery)					
12	Entrainment/De-entrainment					
13	3-D Flow					
14	Mixture Level					
15	Flow Resistance					
16	3-D Power Distribution					
17	Top Nozzle/Tie Plate CCFL					
Neutron Reflector						
18	Steam and Droplet Generation in Flow Holes					
19	Water Storage and Boiling in Back Region					
20	Heat Transfer between Back Region and Core Barrel					
21	Core Bypass Flow					
Upper Head						
22	Drainage to Core/Initial Fluid Temperature					
23	Bypass Flow between Upper Head and Downcomer (Cold Leg)					
24	Metal Heat Release					

Asterisk (*) denotes that the ranking is "break size dependent."

Table 4.3.2-1(2/3) PIRT for Small Break LOCA

Location Process / Phenomena		Small Break LOCA				
		Blowdown	Natural Circulation	Loop Seal Clearance	Boil-off	Recovery
Upper Plenum						
25	Mixture Level					
26	Drainage to Core					
27	Entrainment/De-entrainment					
28	Bypass Flow/Hot Leg -Downcomer Gap					
29	Metal Heat Release					
Hot leg						
30	Stratified Flow/Counter-flow					
31	Entrainment/De-entrainment					
32	Metal Heat Release					
Pressurizer and Surge Line						
33	Mixture Level					
34	Out-Surge by Depressurization					
35	Metal Heat Release/Heater					
36	Location/Proximity to Break					
Steam Generator						
37	Water Hold-Up in SG Inlet Plenum					
38	Water Hold-Up in U-Tube Uphill Side					
39	Primary Side Heat Transfer					
40	Secondary Side Heat Transfer (Water Level)					
41	Metal Heat Release					
42	Multi-U-tube Behavior					
43	AFW					
Crossover Leg						
44	Water Level in SG Outlet Piping					
45	Loop Seal Formation and Clearance (Entrainment/Flow Regime/ Interfacial Drag/Flow Resistance)					
46	Metal Heat Release					

Asterisk (*) denotes that the ranking is "break size dependent."

Table 4.3.2-1(3/3) PIRT for Small Break LOCA

Location Process / Phenomena		Small Break LOCA				
		Blowdown	Natural Circulation	Loop Seal Clearance	Boil-off	Recovery
Reactor Coolant Pump						
47	Coastdown Performance					
48	Two-Phase Flow Performance					
49	Reversal Flow of ECC Water					
50	Metal Heat Release					
Cold Leg						
51	Stratified Flow					
52	Condensation by ACC Water					
53	Non-condensable Gas Effect					
54	Metal Heat Release					
Accumulator						
55	Large Flow Injection/Flow Resistance					
56	Small Flow Injection/Flow Resistance					
57	Interfacial Heat Transfer					
58	Metal Heat Release					
59	Injection of N2 Gas Effect					
Downcomer/Lower Plenum						
60	Mixture Level/Void Distribution					
61	Metal Heat Release					
62	ECCS Water/Mixing					
63	3-D Flow					
64	DVI/SI Water/Flowrate					
65	DVI/SI Water/Condensation					
66	DVI/SI Water /Injection Temperature					
Break						
67	Critical Flow					
68	Break Flow Enthalpy					

Asterisk (*) denotes that the ranking is "break size dependent."

Table 4.3.2-2 PIRT for Small Break LOCA (High rank)

Location Process / Phenomena		Small Break LOCA				
		Blowdown	Natural Circulation	Loop Seal Clearance	Boil-off	Recovery
Fuel Rod						
3	Decay Heat					
7	Local Power					
Core						
9	CHF/Dryout					
10	Uncovered Core Heat Transfer					
11	Rewet (Heat Transfer Recovery)					
14	Mixture Level					
16	3-D Power Distribution					
Steam Generator						
37	Water Hold-Up in SG Inlet Plenum					
38	Water Hold-Up in U-Tube Uphill Side					
39	Primary Side Heat Transfer					
40	Secondary Side Heat Transfer (Water Level)					
Crossover Leg						
44	Water Level in SG Outlet Piping					
45	Loop Seal Formation and Clearance (Entrainment/Flow Regime /Interfacial Drag/Flow Resistance)					
Downcomer/Lower Plenum						
60	Mixture Level/Void Distribution					
64	DVI/SI Water/Flowrate					
Break						
67	Critical Flow					
68	Break Flow Enthalpy					

Asterisk (*) denotes that the ranking is "break size dependent."

4.4 Validation Plan of M-RELAP5

This section describes a plan to validate the M-RELAP5 code that ~~are~~is used for the US-APWR small break LOCA analysis.

To validate M-RELAP5, which is a modified version of RELAP5-3D, the Phenomena Identification and Ranking Table (PIRT) for small break LOCA of the US-APWR that is described in Section 4.3 has been developed. The phenomena that are ranked as High in the PIRT are shown in Table 4.3.2-2. These high-ranking phenomena are either conservatively modeled based on the Appendix-K requirements or are confirmed by the test calculations.

4.4.1 Phenomena Modeling based on Appendix-K requirements

The phenomena that are modeled conservatively based on the Appendix-K requirements are the followings:

- Decay heat: ANS-1971 x 1.2 decay heat curve is used.
- Local power of fuel rod: Highest peaking power is used.
- 3-D power distribution of core: Highest peaking power is used.
- Safety Injection flow rate: Most limiting single failure is assumed.
- Critical flow: Moody's critical flow model is used.

Requirement of the worst break location and orientation addresses Break flow enthalpy.

4.4.2 Confirmation plan

The following validation plan has been developed to confirm the other high-ranking phenomena, as shown in Table 4.4.2-1.

(1) Core mixture level related models

The core mixture level related models are confirmed by using the following tests results:

- ROSA/LSTF Void Profile test (Ref. 4-3)
Core mixture level is confirmed.
- ORNL/THTF Void Profile test (Ref. 4-4)
Core mixture level is confirmed.

-
- ORNL/THTF Uncovered heat transfer test (Ref. 4-4)
CHF/Core Dryout and Uncovered Core Heat Transfer are confirmed.
 - ORNL/THTF Reflood test (Ref. 4-5)
Uncovered Core Heat Transfer and Rewet (heat transfer recovery) is confirmed.

(2) SG primary side CCFL model

The CCFL model is confirmed by comparing the calculated values to the following test results:

- UPTF SG plenum CCFL test (Kutateladze type correlation) (Ref. 4-6)
Water hold-up in SG inlet plenum is confirmed.
- Dukler Air-Water Flooding test (Wallis type correlation) (Ref. 4-7)
Water hold-up in U-tube uphill side is confirmed.

(3) Integral test results

The calculated results by M-RELAP5 are compared with a small break LOCA integral tests:

- ROSA/LSTF small break (5%) LOCA test (SB-CL-18) (Ref. 4-8)
- ROSA/LSTF small break (10%) LOCA test (SB-CL-09) (Ref. 4-9)
- ROSA/LSTF small break (17%) LOCA test (IB-CL-02) (Ref. 4-10)
- LOFT small break (2.5%) LOCA test (L3-1) (Ref. 4-11)
- Semiscale small break (5%) LOCA test (S-LH-1) (Ref. 4-12)

Using these integral test calculation, integral system behavior as well as the following phenomena are confirmed: CHF/core dryout, uncovered core heat transfer, rewet, core mixture level, water hold up in SG primary side, SG primary and secondary heat transfer, water level in the SG outlet piping, loop seal formation and clearance, downcomer mixture level/downcomer void distribution.

**Table 4.4.2-1 Validation Tests for High Ranking
Phenomena for Small Break LOCA**

	CHF/Core Dryout	Uncovered core heat transfer	Rewet	Core mixture level	Water hold-up in SG Inlet plenum	Water hold-up in U-tube uphill side	SG primary and secondary heat transfer	Water level in SG outlet piping	Loop seal formation and clearance	Downcomer mixture level/void distribution
ROSA-IV/LSTF Void Profile test				X						
ORNL/THTF Void Profile test				X						
ORNL/THTF Uncovered heat transfer test	X	X								
ORNL/THTF Reflood test		X	X							
UPTF SG plenum CCFL test					X					
Dukler Air-Water Flooding test						X				
ROSA/LSTF small break (5%) LOCA test	X	X	X	X	X	X	X	X	X	X
ROSA/LSTF small break (10%) LOCA test	X	X	X	X	X	X	X	X	X	X
ROSA/LSTF small break (17%) LOCA test	X	X	X	X	X	X	X	X	X	X
LOFT small break (2.5%) LOCA test					X	X	X	X	X	X
Semiscale small break (5%) LOCA test	X	X	X	X	X	X	X	X	X	X

4.5 References

- 4-1. Bajorek, S.M. et al., "SMALL BREAK LOSS OF COOLANT ACCIDENT PHENOMENA IDENTIFICATION AND RANKING TABLE (PIRT) FOR WESTINGHOUS PRESSURISED WATER REACTORS," Ninth International Topical Meeting on Nuclear Reactor Thermal Hydraulics (NURETH-9), October, 1999.
- 4-2. Boyack, B., "AP600 Large Break Loss of coolant Accident phenomena Identification and ranking Tabulation," LA-UR-95-2718, August, 1995
- 4-3. Y. Anoda, Y. Kukita and K. Tasaka, "Void fraction distribution in rod bundle under high pressure conditions," HTD-Vol.155, Am. Soc. Mech. Eng., Winter Annual Meeting, Dallas, Nov. 25-30, 1990.
- 4-4. T. M. Anklam, R. J. Miller, and M. D. White, "Experimental Investigations of Uncovered-Bundle Heat Transfer and Two-Phase Mixture Level Swell Under High-Pressure Low Heat-Flux Conditions," NUREG-2456, ORNL-5848, March 1982.
- 4-5. C. R. Hyman, T. M. Anklam, and M. D. White, "Experimental Investigations of Bundle Boiloff and Reflood Under High-Pressure Low Heat-Flux Conditions," NUREG-2455, ORNL-5846, April 1982.
- 4-6. P.S. Damerell, et al., "USE OF FULL-SCALE UPTF DATA TO EVALUATE SCALING OF DOWNCOMER (ECC BYPASS) AND HOT LEG TWO-PHASE FLOW PHENOMENA", NUREG/CP-0091 vol4.
- 4-7. A. E. Dukler, L. Smith , " Two Phase Interactions in Counter-Current Flow : Studies of the Flooding Mechanism, Annual Report November 1975 – October 1977", NUREG/CR-0617, January 1979.
- 4-8. Kumamaru, H., et al., "ROSA-IV/LSTF 5% Cold Leg Break LOCA Experiment RUN SB-CL-18 Data Report," JAERI-M 89-027, 1989.
- 4-9. M. Suzuki and H. Nakamura, "A study on ROSA/LSTF SB-CL-09 Test Simulating

PWR 10% Cold Leg Break LOCA: Loop-Seal Clearing and 3D core Heat-Up Phenomena," JAEA-Research, October 2008.

4-10 JAEA, Experimental Report on Simulated Intermediate Break Loss-of-Coolant Accident using ROSA/LSTF, March 2010 (in Japanese).

4-11 P. D. Bayless et al., 'Experimental Data Report for LOFT Nuclear Small Break Experiment L3-1,' NUREG/CR-1145, EGG-2007, January 1980.

4-12 G. G. Loomis, 'Experimental Operating Specifications for Semiscale Mod-2C 5% Small Break Loss-of-Coolant Experiment S-LH-1,' EGG-SEMI-6813, February 1985.

5.0 ASSESSMENT BASE

5.1 Introduction

The Phenomena Identification and Ranking Table (PIRT) for small break LOCA of the US-APWR is developed as described in Section 4.3. The phenomena that are ranked High in the PIRT and also confirmed by the test calculations are the following: CHF/core dryout, uncovered core heat transfer, rewet, core mixture level, water hold up in SG primary side, SG primary and secondary heat transfer, water level in the SG outlet piping, loop seal formation and clearance, downcomer mixture level/downcomer void distribution.

To validate M-RELAP5 for the high-ranking phenomena, six Separate Effect Tests (SETs) and ~~one~~ five Integral Effects Tests (IETs), are selected as follows:

- (1) ROSA/LSTF Void Profile test (Ref. 5.1-1)
- (2) ORNL/THTF Void Profile test (Ref. 5.1-2)
- (3) ORNL/THTF Uncovered heat transfer test (Ref. 5.1-2)
- (4) ORNL/THTF Reflood test (Ref. 5.1-3)
- (5) UPTF SG plenum CCFL test (Ref. 5.1-4)
- (6) Dukler Air-Water Flooding test (Ref. 5.1-5)
- (7) ROSA/LSTF small break (5%) LOCA test (SB-CL-18) (Ref. 5.1-6)
- (8) ROSA/LSTF small break (10%) LOCA test (SB-CL-09) (Ref. 5.1-7)
- (9) ROSA/LSTF small break (17%) LOCA test (IB-CL-02) (Ref. 5.1-8)
- (10) LOFT small break (2.5%) LOCA test (L3-1) (Ref. 5.1-9)
- (11) Semiscale small break (5%) LOCA test (S-LH-1) (Ref. 5.1-10)

In this section, the following information about the tests are discussed from public reports: facility design, scaling, range of conditions, data to be compared, data uncertainty, distortion.

5.1.1 References

- 5.1-1. Y. Anoda, Y. Kukita and K. Tasaka, "Void fraction distribution in rod bundle under high pressure conditions," HTD-Vol.155, Am. Soc. Mech. Eng., Winter Annual Meeting, Dallas, Nov. 25-30, 1990.

-
- 5.1-2. T. M. Anklam, R. J. Miller, and M. D. White, "Experimental Investigations of Uncovered-Bundle Heat Transfer and Two-Phase Mixture Level Swell Under High-Pressure Low Heat-Flux Conditions," NUREG-2456, ORNL-5848, March 1982.
- 5.1-3. C. R. Hyman, T. M. Anklam, and M. D. White, "Experimental Investigations of Bundle Boiloff and Reflood Under High-Pressure Low Heat-Flux Conditions," NUREG-2455, ORNL-5846, April 1982.
- 5.1-4. P.S. Damerell, et al., "USE OF FULL-SCALE UPTF DATA TO EVALUATE SCALING OF DOWNCOMER (ECC BYPASS) AND HOT LEG TWO-PHASE FLOW PHENOMENA", NUREG/CP-0091 vol4.
- 5.1-5. A. E. Dukler, L. Smith , "Two Phase Interactions in Counter-Current Flow : Studies of the Flooding Mechanism, Annual Report November 1975 – October 1977", NUREG/CR-0617, January 1979.
- 5.1-6. Kumamaru, H., et al., "ROSA-IV/LSTF 5% Cold Leg Break LOCA Experiment RUN SB-CL-18 Data Report," JAERI-M 89-027, 1989.
- 5.1-7. M. Suzuki and H. Nakamura, "A study on ROSA/LSTF SB-CL-09 Test Simulating PWR 10% Cold Leg Break LOCA: Loop-Seal Clearing and 3D core Heat-Up Phenomena," JAEA-Research, October 2008.
- 5.1-8. JAEA, Experimental Report on Simulated Intermediate Break Loss-of-Coolant Accident using ROSA/LSTF, March 2010 (in Japanese).
- 5.1-9. P. D. Bayless et al., 'Experimental Data Report for LOFT Nuclear Small Break Experiment L3-1,' NUREG/CR-1145, EGG-2007, January 1980.
- 5.1-10. G. G. Loomis, 'Experimental Operating Specifications for Semiscale Mod-2C 5% Small Break Loss-of-Coolant Experiment S-LH-1,' EGG-SEMI-6813, February 1985.

5.2 Proposed IETs and SETs for US-APWR SBLOCA Assessment

5.2.1 SETs

5.2.1.1 ROSA/LSTF Void Profile Test

(1) Facility Design

a. Fundamental Design

The ROSA-IV LSTF (Ref. 5.2.2.1-1), shown schematically in Figure 5.2.1.1-1, is a volumetrically-scaled (1:48) full-height model of a Westinghouse-type 4-loop PWR. The facility includes a pressure vessel and two symmetric primary loops each one containing an active steam generator and an active coolant pump. Pressure vessel contains a 1104-rod (1008 electrically heated and 96 unheated rods), full-length (3.66m) bundle. Rod diameter and pitch are typical of a 17 X 17 fuel assembly. The heater rods are supported at ten different elevations by grid spacers with mixing vanes. The radial power distribution is uniform. The axial power profile is chopped-cosine with a peaking factor of 1.495. The differential pressures are measured for overall and seven vertical segments along the rod bundle. The location of the differential pressure measurements are compared with the axial power profile and the location of grid spacers in Figure 5.2.1.1-2. Approximately 500 thermocouples are installed in the bundle to measure fluid temperatures and rod surface temperatures. Major characteristics of the LSTF rod bundle are summarized in Table 5.2.1.1-1. The core grid located at the bottom of the heated zone is shown in Figure 5.2.1.1-3. The information above is from Reference 5.2.1.1-1.

b. System Break

System breaks in the reference PWR are simulated in the LSTF by using a break unit, which is attached to the appropriate component, and including an orifice plate and a break valve (Ref.5.2.1.1-2). The maximum break size was designed to be 10% of the 1/48-scaled cold leg flow area of the reference PWR. The 10% maximum area was chosen to provide sufficient break size margin such that a full spectrum of small breaks can be tested. System break locations are follows:

- Cold leg – oriented at 90 degree increments in the plane normal to the pipe axis (hereafter labeled : oriented at 90° increments)
- Crossover leg
- Hot leg – oriented at 90° increments

- Pressurizer power operated relief valve and pressurizer vessel wall
- Steam generator U-tube
- Main steam line
- Main feedwater line
- Pressure vessel wall: lower plenum, upper head

The valves were designed to open in less than 0.1 s.

(2) Scaling

- Elevations: preserved, i.e., one to one correspondence with the reference PWR. Because the LSTF hot and cold leg inner diameters (IDs) are smaller than those of the reference PWR, only the top of the primary hot and cold legs (IDs) were set equal to those of the reference PWR.
- Volumes: scaled by the facility scaling factor 1/48.
- Flow area: scaled by 1/48 in the pressure vessel and 1/24 in the steam generators. However, the hot and cold legs were scaled to conserve the ratio of the length to the square root of pipe diameter, i.e., L/\sqrt{D} for the reference PWR. Such an approach was taken to better simulate the flow regime transition in the primary loops.
- Core power: scaled by 1/48 at core powers equal to or less than 14% of the scaled reference PWR rated power. The LSTF rated and steady-state power is 10 MWt, i.e., 14% of the rated reference PWR core power scaled by 1/48.
- Fuel assembly: dimensions, i.e., fuel rod diameter, pitch and length, guide thimble diameter pitch and length, and ratio of number of fuel rods to number of guide thimbles, designed to be the same as the 17 x 17 fuel assembly of the reference PWR to preserve the heat transfer characteristics of the core. The total number of rods was scaled by 1/48 and is 1064 for heated and 104 for unheated rods.
- Design pressures: roughly the same as the reference PWR.
- Fluid flow differential pressures (ΔP s): designed to be equal to the reference PWR for scaled flow rates.
- Flow capacities; scaled by the overall scaling factor where practicable.
- Core and lower plenum: in comparison with the reference PWR, the length of the heated zone, fuel rod diameter and pitch, power peaking factor and number of spacers are conserved. The core volume and the number of fuel rods are scaled at a ratio of 1/48.

The information above is from Reference 5.2.1.1-2.

(3) Range of Conditions

Table 5.2.1.1-2 summarizes the test conditions. The tests were conducted at pressures

between 1.0 and 17.2 MPa, for rod bundle power from 0.5 to 7.2 MW corresponding to the average heat fluxes from 4.5 to 62 KW/m². For low pressures below 8 MPa and low powers below 4 MW, the void fraction distributions were measured under the steady-state reflux condensation conditions. The mixture level was kept constant at slightly below the hot leg bottom i.e. 2 m above the bundle outlet. For the higher pressures than 8 MPa or the higher powers than 4 MW, the data were obtained from the quasi-steady boil-off conditions. In any case, all data were taken at the conditions of small inlet flow for the bundle entirely covered by mixture. The information above is from Reference 5.2.1.1-1.

(4) Data to be compared

The void fraction data was derived from the differential pressures along the rod bundle, assuming negligible friction and form-loss pressure drop (Ref. 5.2.1.1-3). The bundle-averaged void fraction was obtained from the over-all bundle differential pressure (DP1 in Figure 5.2.1.1-2). It is noticed however that this range slightly includes unheated region at both inlet and outlet ends. The void fraction profile was obtained from the differential pressures measured for seven segments along the bundle (from DP2 to DP8). Because the DP call taps are located at the exact same elevation of the axial power steps, the volume averaged void fraction was assigned to the midpoint of the step.

(5) Data uncertainties

"In the figures (like Figure 5.2.1.1-4), the uncertainty of the measured void fraction is smaller than the diameter of the symbol" from Reference 5.2.1.1-1.

(6) Distortions

Thermal insulation and heat loss control system is intended to compensate heat loss from piping and vessels during an experiment by on-off control of heaters wound outside the surface of the piping and vessels (thermal insulation heaters). Thermal insulation heaters are wound on the outside surface of the following piping and vessels.

Pressure boundaries of the LSTF primary and secondary systems are covered by the thermal insulator made of rock wool or glass wool. As the thermal conductivity of the insulator is approximately 1/1000 of the structural metal (carbon steel), a total heat loss for the whole LSTF system is mainly controlled by thermal conduction through the insulators.

Total heat loss in a quasi-steady state of the primary and secondary system per unit time (Q_{HL}) is defined here as a sum of heat losses per unit time for the primary and secondary fluid system

(Q_F) and for the metal structures contacting with the fluid (Q_M) in addition to a heat input per unit time (Q_G) from the heater rod electric power or the operating primary pump power as,

$$Q_{HL} = Q_F + Q_M + Q_G.$$

Total heat loss per unit time through the insulators (Q_T), on the other hand, is given by Q_{HL} and a heat loss per unit time of the outer metal structures (Q_{Mo}), which are covered by the thermal insulators and contacting with the pressure boundary metal structures (see Figure 5.2.1.1-5) as:

$$Q_T = Q_{HL} + Q_{Mo}.$$

Heat losses in the fluid system (Q_F), metal structures (Q_M) and total system (Q_{HL}) were obtained as shown in Table 5.2.1.1-3. Heat input from the operating pumps was amended as 2.4 kW. Namely, $Q_F = 61.0$ kW (44%), $Q_M = 73.9$ kW (54%) and $Q_G = 2.4$ kW (2%). Therefore, the total heat loss was,

$$Q_{HL} = 137 \text{ kW.}$$

Heat losses for the primary system and two SGs were 49% and 51% of Q_{HL} .

The Information shown here is from the page 15 of Reference 5.2.1.1-3.

(7) References

- 5.2.1.1-1 Y. Anoda, Y. Kukita, and K. Tasaka, "Void Fraction Distribution in Rod Bundle under High Pressure Conditions," HTD-Vol.155, Am. Soc. Mech. Eng., Winter Annual Meeting, Dallas, Nov. 25-30, 1990.
- 5.2.1.1-2 "ROSA-IV Large Scale Test Facility(LSTF) System Description", JAERI-M 84-237, 1984.
- 5.2.1.1-3 "Supplemental Description of ROSA-IV/LSTF with No.1 Simulated Fuel-Rod Assembly", JAERI-M-89-113, 1989.

Table 5.2.1.1-1 Summary of LSTF Rod Bundle Design

Parameter	Quantity
Number of heated rods	1008
Number of unheated rods	96
Heated length (m)	3.66
Diameter of heated rod (mm)	9.5
Diameter of unheated rod (mm)	12.24
Lattice	Square
Pitch(mm)	12.6
Maximum Power (MW)	10.0
Axial peaking	1.495
Number of grid spacers	9
Inner diameter of shroud (m)	0.514
Flow area (m ²)	
Core (at spacer)	0.06774
Core (below spacer)	0.1134
Grid (or Lower nozzle)	0.06653
End box (or Upper nozzle)	0.08720

(From Ref. 5.2.1.1-1 "Void Fraction Distribution in Rod Bundle under High Pressure Conditions", Ref. 5.2.1.1-2 JAERI-M 84-237)

Table 5.2.1.1-2 Summary of Test Conditions

Test	Pressure (MPa)	Power (MW)	Heat Flux (KW/m ²)	Jg, exit (m/s)
ST-VF-01A	1.0	0.5	4.5	0.425
ST-VF-01B	1.0	1.0	9.1	0.851
ST-VF-01C	1.0	2.0	18.2	1.702
ST-VF-01D	1.0	3.5	31.8	2.978
ST-NC-08E	2.4	1.426	13.0	0.566
ST-NC-01	7.3	3.57	30.7	0.553
ST-NC-06E	7.3	3.95	34.0	0.612
SB-CL-16L	7.3	5.0	43.0	0.774
ST-SG-04	7.35	7.17	61.7	1.104
ST-VF-01E	15.0	1.0	9.1	0.091
ST-VF-01F	15.0	0.5	4.5	0.045
ST-VF-01G	15.0	2.0	18.2	0.182
ST-VF-01H	15.0	4.0	36.3	0.363
TR-LF-03	17.2	0.94	7.2	0.080

(From Ref. 5.2.1.1-1 "Void Fraction Distribution in Rod Bundle under High Pressure Conditions")

Table 5.2.1.1-3 Total Heat Loss

	Q _F [kW]	Q _M [kW]	Q _G [kW]	Q _{HL} [kW]
Primary System	31.3	33.2	2.4	66.9
SG/Secondary System	29.7	40.7	-	70.4
Total	61.0	73.9	2.4	137.3

(From JAERI-M-89-113)

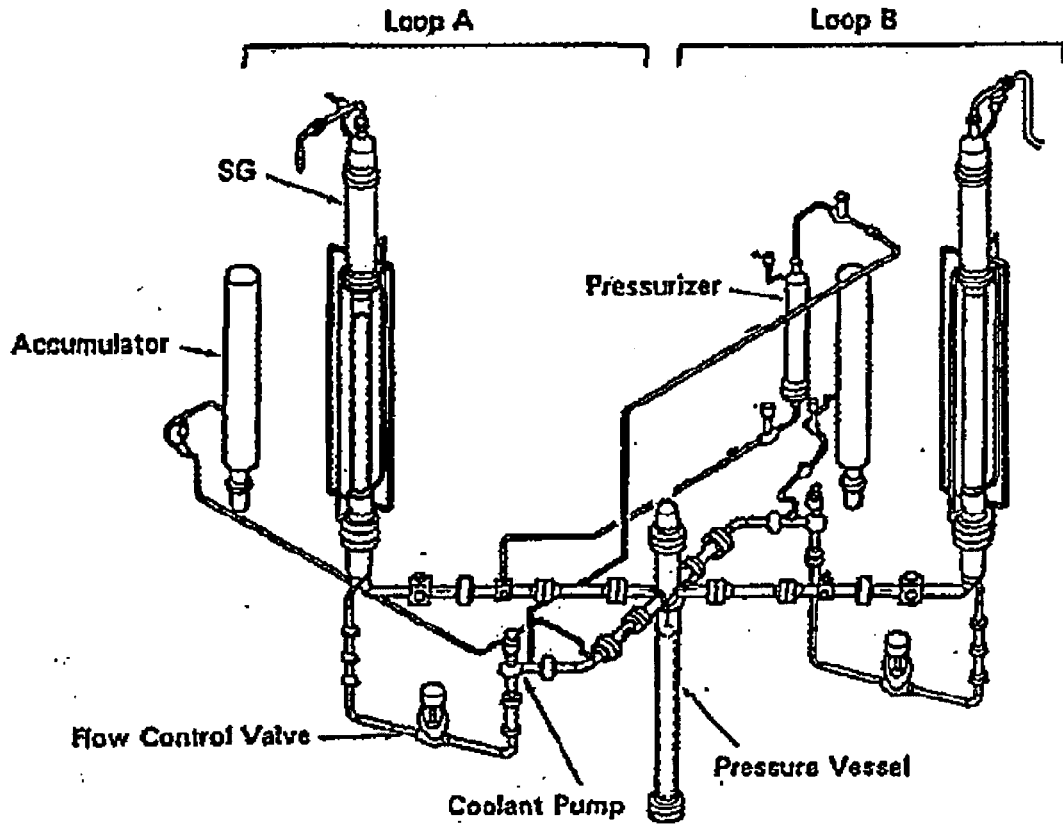


Figure 5.2.1.1-1 Schematic of ROSA-IV Large Scale Test Facility (LSTF)
 (From Ref. 5.2.1.1-1 "Void Fraction Distribution in Rod Bundle under High Pressure Conditions")

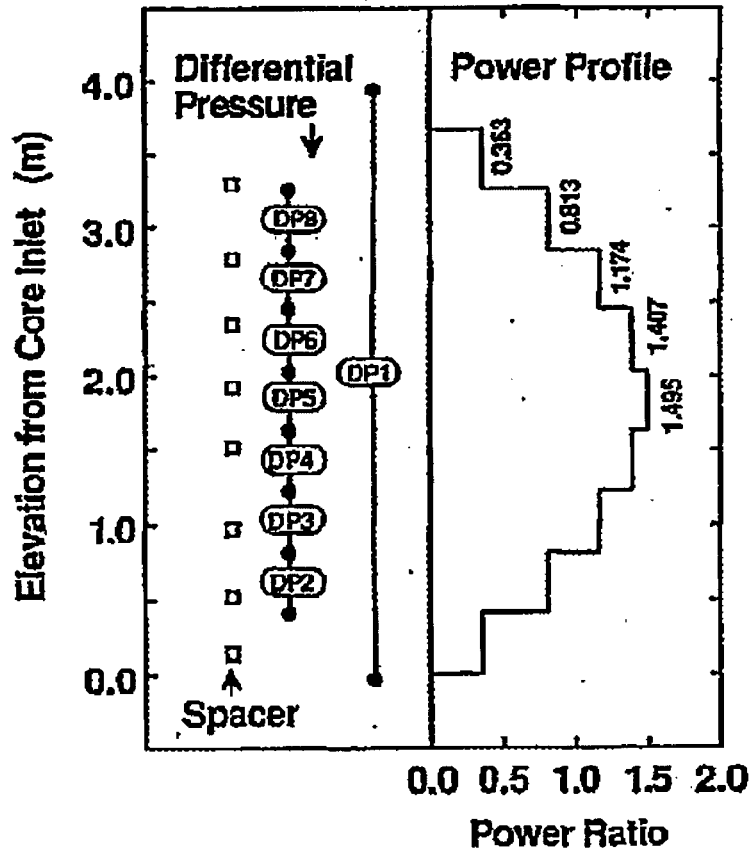


Figure 5.2.1.1-2 Axial Power Profile and Location of Differential Pressure Measurements and Grid Spacers

(From Ref. 5.2.1.1-1 "Void Fraction Distribution in Rod Bundle under High Pressure Conditions")

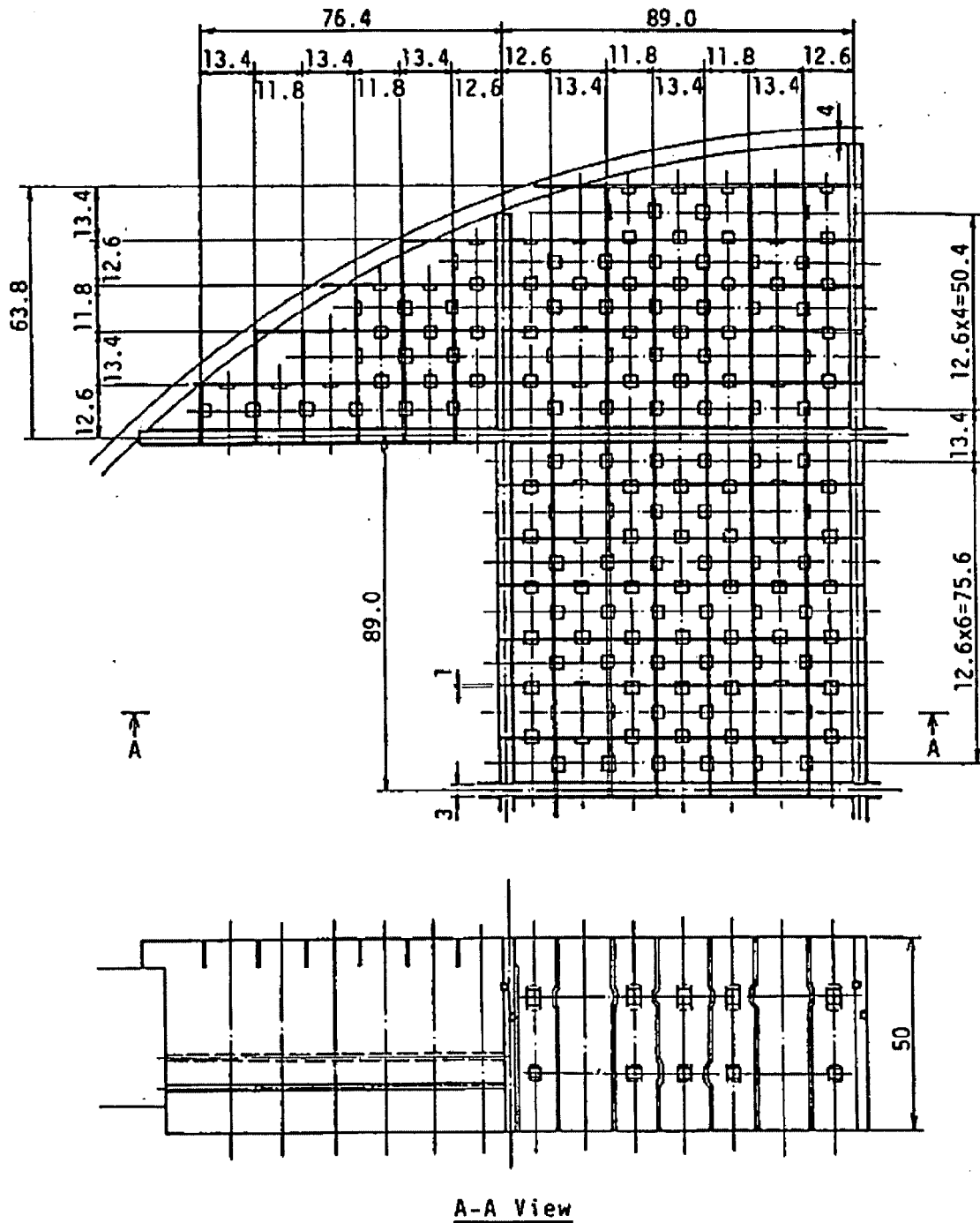


Figure 5.2.1.1-3 Core Grid
(From JAERI-M 84-237)

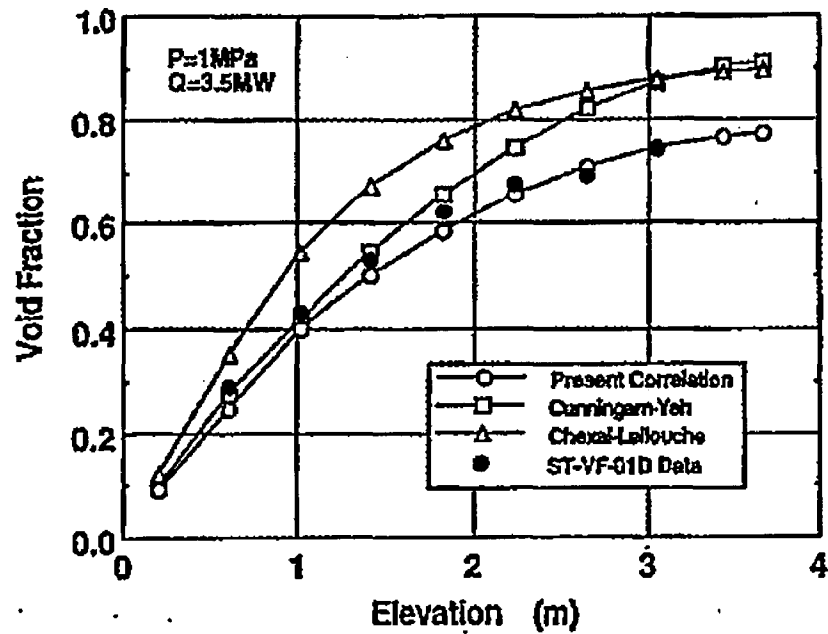
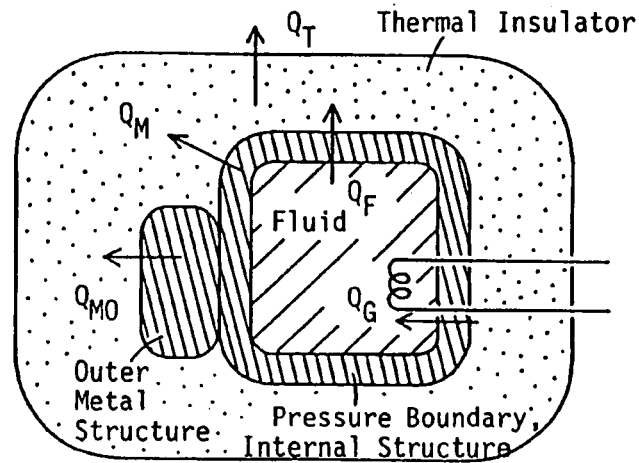


Figure 5.2.1.1-4 Comparison of Calculated and Measured Void Fraction Profiles, Test ST-VF-01D

(From Ref. 5.2.1.1-1 "Void Fraction Distribution in Rod Bundle under High Pressure Conditions")



$$Q_T = Q_F + Q_G + Q_M + Q_{MO}$$

Q_T : Total Energy Loss through Thermal Insulator

Q_F : Energy Loss in Fluid

Q_M : Energy Loss in Metal

Q_{MO} : Energy Loss in Outer Metal

Q_G : Energy Income from Heater or Operating Pumps

Figure 5.2.1.1-5 Definition of Heat Loss for Each Component in LSTF System

(From JAERI-M-89-113)

5.2.1.2 ORNL/THTF Void Profile Test

(1) Facility Design

The experiments of void profile test were performed at the THTF in ORNL. The THTF is a large high-pressure non-nuclear thermal hydraulics loop. System configuration was designed to produce a thermal-hydraulic environment similar to that expected in a small-break loss-of-coolant accident (SBLOCA). Key aspects of the THTF design have been summarized in Table 5.2.1.2-1.

a. Flow Circuit Description

Figure 5.2.1.2-1 is an illustration of the THTF in small-break test configuration. Flow leaves the main coolant pump and passes through FE-3, a 2-in. turbine meter. On leaving FE-3, flow enters the inlet flow manifold. The flow manifold is divided into two parallel flow lines: a 1/2 in. line used to meter very low flow rates and a 3/4-in. flooding line used for the higher flows experienced during reflood. The entire inlet-flow manifold was constructed of high-pressure stainless steel tubing. Volumetric flow rates in the low-flow 1/2 in. inlet line were measured by FE-18A (a low-flow orifice meter), and FE-250 and FE-260 (1/2-in. turbine meters). The two inlet lines converge at the injection manifold, from which fluid passes directly into the lower plenum. Fluid does not pass through a downcomer. Flow proceeds upward through the heated bundle and exits through the bundle outlet spool piece. Spool piece measurements include pressure, temperature, density, volumetric flow, and momentum flux. When outlet flow rates were very low the volumetric flow was measured by a bank of low-flow orifice meters downstream of the outlet spool piece. On leaving the orifice manifold, flow passes through a heat exchanger and returns to the pump inlet.

System pressure was controlled via the loop pressurizer. The pressurizer was partially filled with subcooled water, and nitrogen cover gas was used to control pressure. The system pressure could be controlled more easily by filling or venting nitrogen than by the conventional flashing and condensation of saturated water and steam.

Flow was injected directly into the lower plenum and did not pass through a downcomer. The shroud-plenum annulus (Figure 5.2.1.2-2) was used in earlier THTF testing as an internal downcomer but was isolated from the primary flow circuit in these tests. The shroud-plenum annulus pressure was equalized with the system pressure. This was accomplished by connecting the bottom of the annulus region to the pressurizer surge line and the top of the annulus to the test section outlet. The line between the annulus and pressurizer was opened,

and the line between the annulus and test section outlet was closed during the initial boiloff phase of steady-state testing. This allowed any vapor generated by boiling in the annulus to displace liquid into the pressurizer. Note that the displacement of liquid causes the mixture levels in the downcomer and bundle to equalize, which is why installation of a line between the pressurizer and downcomer was advantageous. However, once mixture levels had equalized, leaving this line open was no longer advantageous. The reason is that the steam flow through the outlet causes a substantial pressure drop between the test section and pressurizer. If the annulus was in communication with the pressurizer, then a large pressure difference between the test section bundle and the downcomer would exist. This large pressure difference has been observed to cause substantial leakage from the bundle to the annulus. To minimize this leakage, the line between the pressurizer and annulus was closed after mixture-level equalization had taken place. To maintain pressure equalization, the shroud bypass line, which connects the top of the shroud annulus to the test outlet, was opened (Figure 5.2.1.2-1). As a final step to minimize the possibility of leakage from bundle to annulus, the shroud bypass line was closed shortly before data were taken. The annulus was then completely isolated from the rest of the system, thus providing the least opportunity for undesired leakage.

b. Bundle Description

The THTF test section contains a 64-rod electrically heated bundle. Figure 5.2.1.2-3 is a cross section of the bundle. The four unheated rods were designed to represent control-rod guide tubes in a nuclear fuel assembly. Rod diameter and pitch are typical of a 17 x 17 fuel assembly.

Figure 5.2.1.2-4 is an axial profile of the THTF bundle that illustrates the positions of spacer grids and fuel rod simulator (FRS) thermocouples. The heated length is 3.66 m (12 ft), and a total of 25 FRS thermocouple levels are distributed over that length. An FRS thermocouple level refers to an axial location where a selected number of FRSs are instrumented with sheath thermocouples.* (*FRS thermocouple levels A,B,C,D,E,F, and G contain most of the FRS sheath thermocouples and are referred to as primary thermocouple levels. All other FRS thermocouple levels are referred to as intermediate thermocouple levels.) Note that the upper third of the bundle is more heavily instrumented than the lower portion. For most tests, the two-phase mixture level is in the top 1/3 of the heated length. The additional instrumentation in the top 1/3 of the bundle is used to better define the mixture-level position. In addition, the increased instrumentation near the spacer grids can be used to ascertain to what extent spacer grids affect heat transfer.

A drawing of an FRS cross section is shown in Figure. 5.2.1.2-5. Each FRS has 12 sheath and

4 center thermocouples. The thermocouples are either 0.05 cm (0.020 in.) or 0.04 cm (0.016 in.) in diameter and can have their junctions at any of the 25 axial levels mentioned previously. Each rod can have from 0 to 3 sheath thermocouple junctions at any particular axial level. When an FRS has three junctions at the same level, they are spaced evenly around the rod (i.e., 120° apart). Table 5.2.1.2-2 describes the FRS sheath thermocouple naming convention.

In addition to the FRS thermometry, there are a number of locations where fluid temperature is measured. In-bundle fluid temperature is measured by four different types of fluid thermocouples. The first type is a thermocouple array-rod thermocouple. These are exposed* fluid thermocouples that project from unheated rods. (* Exposed in this context does not mean that the thermocouple junction actually contacts the fluid. The junction is encased in a stainless steel sheath but does not have a droplet shield.) Thermocouple array-rod thermocouples are installed at 1.83, 2.41, 3.02, and 3.62 m (72, 95, 119, and 142.5 in.) above the beginning of the heated length (BOHL). The second type of fluid thermocouple is a shroud box fluid thermocouple. These are exposed fluid thermocouples that project from the bundle shroud into subchannels adjacent to the shroud. Shroud box fluid thermocouples are installed at 0.38, 0.64, 1.22, 1.83, 2.41, 3.02, and 3.61 m (15, 25, 48, 72, 95, 119, and 142 in.) above BOHL. The third type of fluid thermocouple is a spacer grid fluid thermocouple. These thermocouples are exposed fluid thermocouples that project from spacer grids. Spacer grid fluid thermocouples project slightly upstream of each spacer grid. The fourth and final type of fluid thermocouple is a subchannel rake thermocouple. These thermocouples are attached to a rake located several centimeters above the end of the heated length (EOHL). They are used in measuring the cross-sectional temperature distribution. Nomenclature and locations for fluid thermocouples are summarized in Table 5.2.1.2-3.

As previously noted, the THTF bundle is surrounded by a shroud box (Figure 5.2.1.2-2). The shroud box walls have been instrumented with thermocouples in order to estimate bundle heat losses. A typical instrumentation site consists of a pair of thermocouples embedded in the shroud box wall (Figure 5.2.1.2-6). Because the thermocouples are separated, the radial temperature gradient can be calculated and the bundle heat losses estimated. Figure 5.2.1.2-7 shows the axial locations where the shroud box walls have been instrumented.

c. Differential Pressure (ΔP) Instrumentation

A primary objective of this test series was to obtain mixture-level swell and void-fraction distribution data under high-pressure low heat-flux conditions. These data were obtained through the use of "stacked" ΔP cells. Figure 5.2.1.2-8 illustrates the ΔP measurement sites.

Differential pressure cells PdE-180 through 188 are ranged from 0.0 to 0.63m (0.0 to 25.0 in.) of standard water, and PdE-189 is ranged from 0.0 to 0.76 m (0.0 to 30.0 in.) of water. Spacing of the cells varies from 0.75 to 0.22 m (29.4 to 8.5 in.).

(2) Scaling

The THTF contains a 64-rod electrically heated bundle with internal dimensions typical of a 17 x 17 PWR fuel assembly. The scaling of the facility is fine since it is full length and prototypical dimensions

(3) Range of Conditions

Table 5.2.1.2-4 summarizes the test conditions for each of the 12 mixture-level swell and void distribution tests. For the sake of convenience, the tests can be divided into two pressure groups, one group of six tests run at roughly 4 MPa (580 psia) and another group of six at roughly 7.5 MPa (1088 psia).

(4) Data to Be Compared

The void fraction profiles, collapses liquid levels, and two-phase mixture levels are plotted against the axial position for the 7.5- and 4-MPa data sets.

Pictured in Figure 5.2.1.2-9 is a schematic of PWR subchannel during the uncovered phase of an SBLOCA. Void distribution was assumed to be radially uniform, and the Z-coordinate axis was taken parallel to the subchannel axis. The subchannel can be divided into three thermal-hydraulic regions: (1) a subcooled inlet region, (2) a saturated boiling region, and (3) a dry (or high-quality) steam-flow region. The subcooled boiling region was assumed to be negligibly small in comparison with the saturated boiling region, since surface heat fluxes typical of reactor decay-heat levels are low.

The zero coordinate was taken to be at Z_{sat} (i.e., $Z_{sat} = 0$), the elevation where saturated boiling begins. Other elevations important in the analysis are the two-phase mixture level ($Z_{2\phi}$) and the collapsed-liquid level (Z_{CLL}). The two-phase mixture level, assumed to coincide with the FRS dryout level, is the maximum height above Z_{sat} where liquid is the continuous phase. The collapsed-liquid level is the elevation to which the mixture level would fall if all boiling ceased. Steam velocities in the subject tests were low, causing little or no liquid entrainment. Friction and form-loss pressure drops were negligible; thus, the collapsed-liquid level may also be interpreted as the hydrostatic head of the coolant inventory between Z_{sat} and $Z_{2\phi}$, as measured by the ΔP cell.

The mixture-level swell, defined as

$$S = \frac{Z_{2\phi} - Z_{CLL}}{Z_{CLL}}, \quad (1)$$

is a convenient parameter that interpolates the elevations of interest. Mixture swell is equal to the relative vertical expansion of the boiling length caused by the presence of vapor voids. If the mass inventory M is written in terms of the collapsed-liquid level

$$M = \rho_f A_F Z_{CLL}, \quad (2)$$

then the relationship between the mass inventory, swell, and two-phase mixture level is given by

$$Z_{2\phi} = \frac{M}{\rho_f A_F} (S + 1). \quad (3)$$

This formulation is significant because it relates the mass inventory to the elevation where core uncovering occurs. Below the mixture level the core remains in nucleate boiling, and heat transfer is sufficient to prevent thermal damage. In the uncovered region, heat transfer by steam cooling alone may not be sufficient to prevent thermal damage. An assessment of the severity of a hypothetical accident is dependent on the ability to predict the amount of core uncovering that would occur for a given coolant inventory loss; if mixture-level swell and mass inventory are known, the above equation allows this prediction.

The mixture-level swell and the local void fraction $[\alpha(Z)]$ are related through the definition of the collapsed-liquid level:

$$Z_{CLL} = \int_0^{Z_{2\phi}} [1 - \alpha(z)] dz. \quad (4)$$

Substitution of Eq. (4) into Eq. (1) yields the swell expressed as a function of the local void fraction and the mixture level.

a. Void Fraction Profiles

The void fraction profile was calculated from the readings of the ΔP cells, assuming negligible friction and form loss pressure drops. This void fraction is a volume average. In comparing it with M-RELAP5 calculated void fraction, this volume average void fraction is assigned to the midpoint between the ΔP cell taps. The test facility had nine ΔP cells (Figure 5.2.1.2-8); therefore, nine data points were calculated. An average void fraction of zero was assigned to cells lying entirely below the saturation level.

Most of the experimental void profiles show several commonalities and parametric trends. All of the experimental profiles show very low or zero void fraction near the bottom of the heated length. This was expected because fluid in the lower portion of the bundle was either subcooled or of low quality. Void fraction then increased with elevation in a relatively linear or slightly parabolic manner. Slope of the void profile varied considerably from test to test with the steepest slopes associated with the highest volumetric vapor-generation rate tests. Finally, at a location near the two-phase mixture level, a sharp increase in void fraction with elevation occurred. In this region void fraction rapidly approached 1.0, and FRS dryout occurred.

b. Two-Phase Mixture-Levels

The two-phase mixture level was identified by observing the average temperature at the FRS thermocouple levels. The two-phase mixture level $Z_{2\phi}$ was assumed to be midway between highest level where the average temperature indicated nucleate boiling and the lowest where the average temperature indicated dryout. Those levels cooled by nucleate boiling had temperatures close to the saturation temperature, and temperature excursion occurring at the dryout level is large and easily recognized.

The experimentally derived two phase mixture level and collapsed level are plotted against the axial position for the 7.5- and 4- MPa data sets. These parameters together with the void profiles relate to interfacial momentum exchange.

c. Collapsed Liquid Levels

The collapsed-liquid level, as defined in Eq. (4) is the elevation to which the mixture level would fall if all boiling ceased.

(5) Data Uncertainties

Results of instrument uncertainty analysis for the THTF, reported in Reference 5.2.1.2-2, ~~is~~ are summarized in Table 5.2.1.2-5, and uncertainties in the mixture and collapsed-liquid levels

reported in Reference 5.2.1.2-1 are presented in Table 5.2.1.2-4.

In heavily instrumented top section of the bundle, the two-phase mixture level was determined to within $\sim\pm 8.0$ cm (± 3.1 in.). If the dryout occurred in the lower two-thirds of the bundle where the thermocouple levels are widely spaced, the uncertainty became as large as ± 30 cm (± 11.8 in.).

(6) Distortion

The heat loss to the environment from the rod bundle and housing was significant and could affect the experimental results. Only total bundle heat loss for each case is reported from shroud-wall thermocouple thermometry (Figures 5.2.1.2-6 and 7).

(7) References

5.2.1.2-1 T. M. Anklam, R. J. Miller, M. D. White, "Experimental Investigations of Uncovered-Bundle Heat Transfer and Two-Phase Mixture-Level Swell Under High-Pressure Low-Heat Conditions," NUREG/CR-2456, ORNL-5848

5.2.1.2-2 D. K. Felde et al., "Facility Description – THTF MOD3 ORNL PWR BDHT Separate-Effects Program," NUREG2640, ORNL/TM-2640, ORNL/TM-7842, September 1982

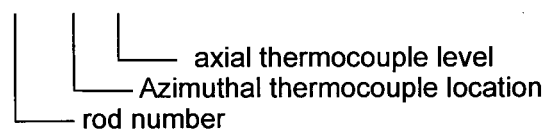
Table 5.2.1.2-1 THTF Design Summary^(Ref. 5.2.1.2-1)

Parameter	Quantity
Design pressure [MPa (psia)]	17.2 (2500)
Pump capacity [m ³ /s (gpm)]	0.044 (700)
Heated length [m (ft)]	3.66 (12.0)
Power profile	Flat
FRS diameter [cm (in.)]	0.95 (0.374)
Lattice	Square
Pitch [cm (in.)]	1.27 (0.501)
Subchannel hydraulic diameter [cm (in.)]	1.23 (0.48)
Number of heated rods	60
Number of unheated rods	4
Unheated rod diameter [cm (in.)]	1.02 (0.40)
Bundle shroud configuration	Square
Bundle shroud thickness 2 sides [cm (in.)]	2.54 (1.0)
2 sides [cm (in.)]	1.91 (0.75)
Number of grid spacers	7

Table 5.2.1.2-2 Rod-Sheath Thermocouple Designations^(Ref. 5.2.1.2-1)

Rod-sheath thermocouples are designed according to one of the following two schemes:

1. TE-3 17 A D



2. TE-3 54 F8



Thus, this first designation refers to the sheath thermocouple in rod 17 at level D, azimuthal location A. If the thermocouple designation ends with a number, this designation refers to the sheath thermocouple in rod 54 at level F8.

Table 5.2.1.2-3 Nomenclature for Thermocouples in THTF (1/4) ^(Ref. 5.2.1.2-2)**Subchannel Thermocouples**

The subchannel thermocouple rake is located ~2.3 cm above the upper end of the heated section. (Figure 5.2.1.2-8) The naming convention takes the following form:

TE-12nn,

Where

nn = a number between 01-81 that equals the number of the subchannel in which it is located. (Figure 5.2.1.2-3.)

Table 5.2.1.2-3 Nomenclature for Thermocouples in THTF (2/4) (Ref. 5.2.1.2-2)Spacer-Grid Thermocouples

The spacer-grid fluid thermocouples are attached to core grids No. 2-7. (Figure 5.2.1.2-4. Six grid locations are indicated.) The naming convention takes the following form:

TE-29na,

where

n = a number between 1-6 designating the spacer-grid level as follows:

<u>Number</u>	Between Thermocouple <u>levels</u>	<u>spacer-grid No.</u>
1	A & B	2
2	B & C	3
3	C & D	4
4	D & E	5
5	E & F	6
6	F & G	7,

and a = a letter "A-F" designating the subchannel into which the thermocouple projecting, as follows(Figure 5.2.1.2-3.):

<u>Letter</u>	<u>Subchannel No.</u>
A	32
B	43
C	57
D	70
E	17
F	38

Table 5.2.1.2-3 Nomenclature for Thermocouples in THTF (3/4) (Ref. 5.2.1.2-2)

Shroud-box Thermocouples

Shroud-box thermocouples protrude through the shroud wall into the fluid in the wall subchannels. The naming convention has the following form:

TE-18na,

where

n = a number 1-7 designating the level of the thermocouple in the shroud box as follows(Figure 5.2.1.2-4.)

<u>Number</u>	<u>Thermocouple levels</u>
1	A
2	B
3	C
4	D
5	E
6	F
7	G

and

a = a letter designating the side of the box through which the thermocouple protrudes, N, E, S, or W. (Figure 5.2.1.2-3.)

Table 5.2.1.2-3 Nomenclature for Thermocouples in THTF (4/4) (Ref. 5.2.1.2-2)Thermocouple-Array Rod Thermocouples

The thermocouple-array rods occupied grid positions 19 and 36. (Figure 5.2.1.2-3). Each array rod contains 14 thermocouples, and, at each axial level in the bundle where there is a primary FRS thermocouple level, two of these thermocouples protrude from the rod into the fluid. The naming convention has the following form:

TE-18nal,

where

n = the number 8 or 9 designating in which grid position the thermocouple array rod is located such that 8 denotes grid position 19 and 9 denotes grid position 36(Figure 5.2.1.2-3.);

a = a letter A and B designating which of two subchannels associated with that rod the thermocouple protrudes into (Figure 5.2.1.2-3.):

<u>Rod grid position</u>	<u>(a =) A subchannel</u>	<u>(a =) B subchannel</u>
(n=8→) 19	22	30
(n=9→) 36	41	49

l = the thermocouple level A-G. (same as FRS thermocouple level designation. Figure 5.2.1.2-4)

Table 5.2.1.2-4 Summary of Void Profile Test Conditions ^a (Ref. 5.2.1.2-1)

Test	System Pressure [MPa (psia)]	Linear Power/rod [kW/m(kw/ft)]	Vapor Superficial Velocity at Mixture Level [m/s (ft/s)]	Mixture Level [m(ft)]	Collapsed-Liquid Level [m(ft)]	Beginning of Boiling Length [m(ft)]	Mixture-Level Swell
3.09.10I	4.50 (650)	2.22 (0.68)	1.30±0.04 (4.25±0.13)	2.62±0.04 (8.60±0.13)	1.34±0.03 (4.39±0.1)	0.36±0.01 (1.18±0.03)	1.30±0.08
3.09.10J	4.20 (610)	1.07 (0.33)	0.61±0.02 (1.99±0.07)	2.47±0.04 (8.10±0.14)	1.62±0.03 (5.31±0.1)	0.27±0.01 (0.89±0.03)	0.63±0.05
3.09.10K	4.01 (580)	0.32 (0.10)	0.15±0.02 (0.50±0.05)	2.13±0.30 (6.98±0.98)	1.62±0.03 (5.31±0.1)	0.28±0.04 (0.92±0.13)	0.38±0.24
3.09.10L	7.52 (1090)	2.17 (0.66)	0.73±0.02 (2.39±0.06)	2.75±0.09 (9.02±0.29)	1.76±0.03 (5.77±0.1)	0.69±0.02 (2.26±0.07)	0.93±0.12
3.09.10M	6.96 (1010)	1.02 (0.31)	0.37±0.01 (1.20±0.03)	2.62±0.04 (8.60±0.13)	1.89±0.03 (6.20±0.1)	0.55±0.01 (1.80±0.03)	0.54±0.05
3.09.10N	7.08 (1030)	0.47 (0.14)	0.12±0.01 (0.40±0.04)	2.13±0.03 (6.98±0.98)	1.86±0.03 (6.10±0.1)	0.46±0.07 (1.51±0.23)	0.20±0.24
3.09.10AA	4.04 (590)	1.27 (0.39)	1.04±0.03 (3.40±0.10)	3.42±0.03 (11.23±0.09)	2.00±0.03 (6.56±0.1)	0.56±0.02 (1.84±0.07)	0.98±0.04
3.09.10BB	3.86 (560)	0.64 (0.20)	0.48±0.02 (1.59±0.07)	3.31±0.04 (10.85±0.12)	2.32±0.03 (7.61±0.1)	0.48±0.02 (1.57±0.07)	0.53±0.03
3.09.10CC	3.59 (520)	0.33 (0.10)	0.40±0.02 (1.31±0.07)	3.60±0.02 (11.80±0.08)	2.88±0.03 (9.45±0.1)	0.41±0.02 (1.34±0.07)	0.29±0.02
3.09.10DD	8.09 (1170)	1.29 (0.39)	0.46±0.01 (1.50±0.03)	3.23±0.04 (10.61±0.13)	2.39±0.03 (7.84±0.1)	0.90±0.02 (2.95±0.07)	0.57±0.04
3.09.10EE	7.71 (1120)	0.64 (0.19)	0.27±0.01 (0.88±0.03)	3.47±0.03 (11.40±0.08)	2.85±0.03 (9.35±0.1)	0.92±0.02 (3.02±0.07)	0.32±0.03
3.09.10FF	7.53 (1090)	0.32 (0.98)	0.12±0.01 (0.40±0.03)	3.23±0.04 (10.61±0.13)	2.90±0.03 (9.51±0.1)	0.86±0.02 (2.82±0.07)	0.16±0.03

^aSome rounding off of numbers has been done. Accordingly, conversions between metric and English and value of mixture-level swell may not appear to be exact.

Table 5.2.1.2-5 Instrument Uncertainty Analysis For The THTF Loop
Summary of Results (Ref. 5.2.1.2-2)

Two standard deviation uncertainty bands are described for critical instrumentation in the Thermal Hydraulic Test Facility (THTF). The analyzed instruments and their minimum, steady-state, 2σ error bands [root sum square (RSS), 95% confidence interval] include:

1.	Turbine flowmeter	4.1 % reading
2.	Gamma densitometer	10.4 % FS*
3.	Strain gage pressure cell	1.0% FS*
4.	Differential pressure cell	2.0% FS* min to 9.9% FS* max
5.	Thermocouple	3.7°C min to 10.3 °C max
6.	Rod power instrumentation	1.1% reading
7.	Strain gage drag disk	56% reading below 10% FS* 19% reading above 10% FS*

*Full-scale values

ORNL-DWG 81-7837R ETD

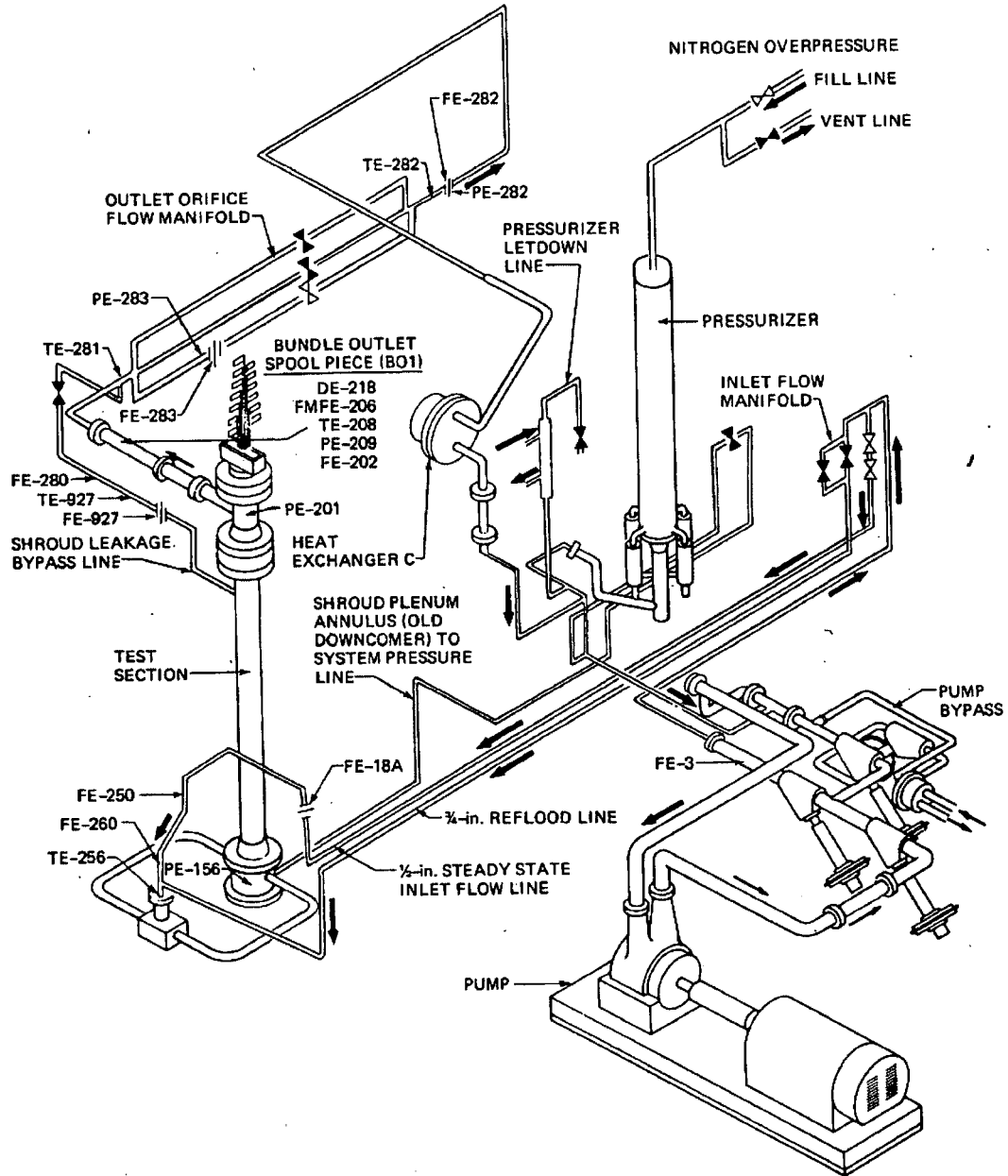


Figure 5.2.1.2-1 THTF in Small-break Test Configuration

ORNL-DWG 82-4875 ETD

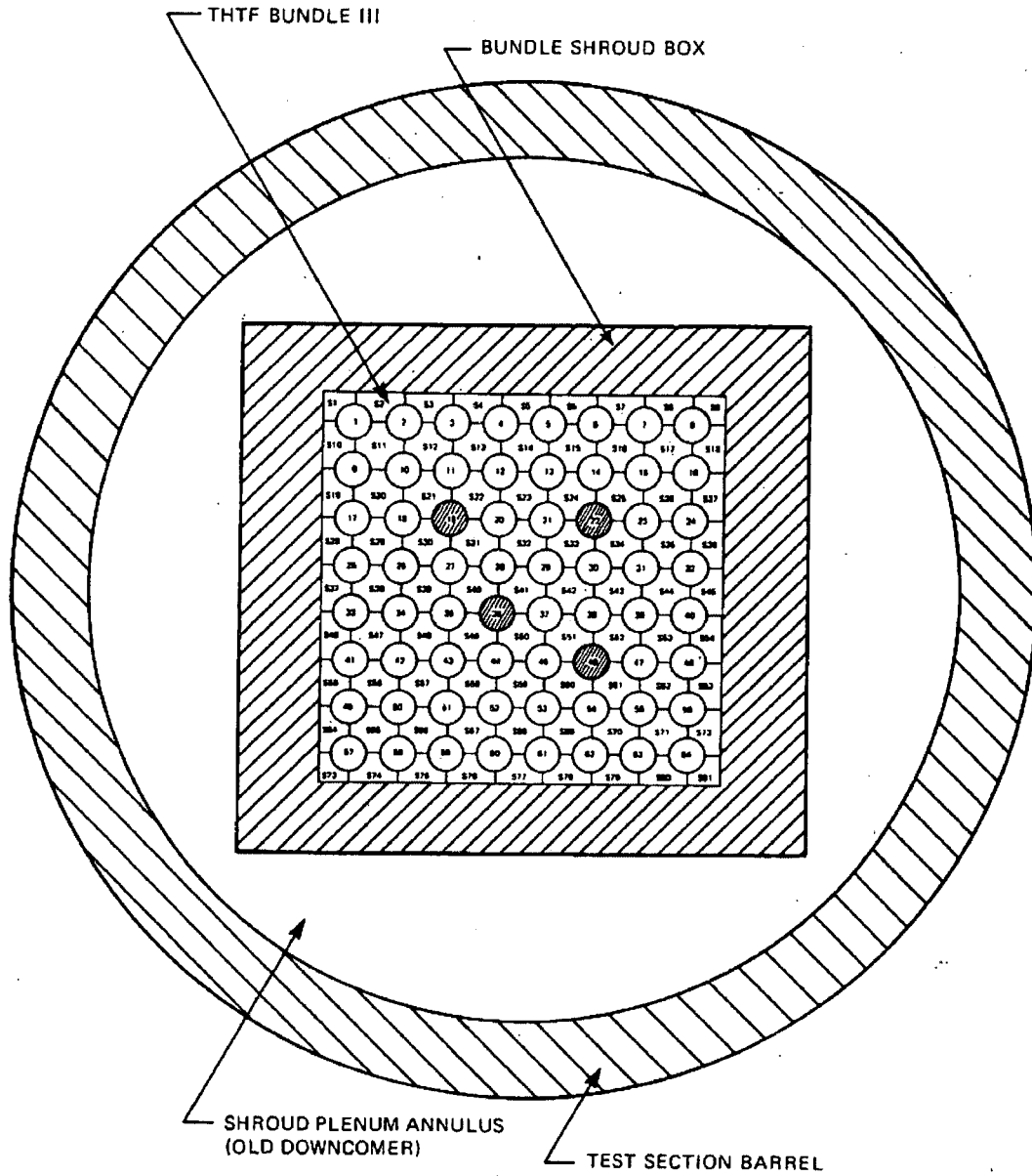


Figure 5.2.1.2-2 Cross Section of THTF Test Section

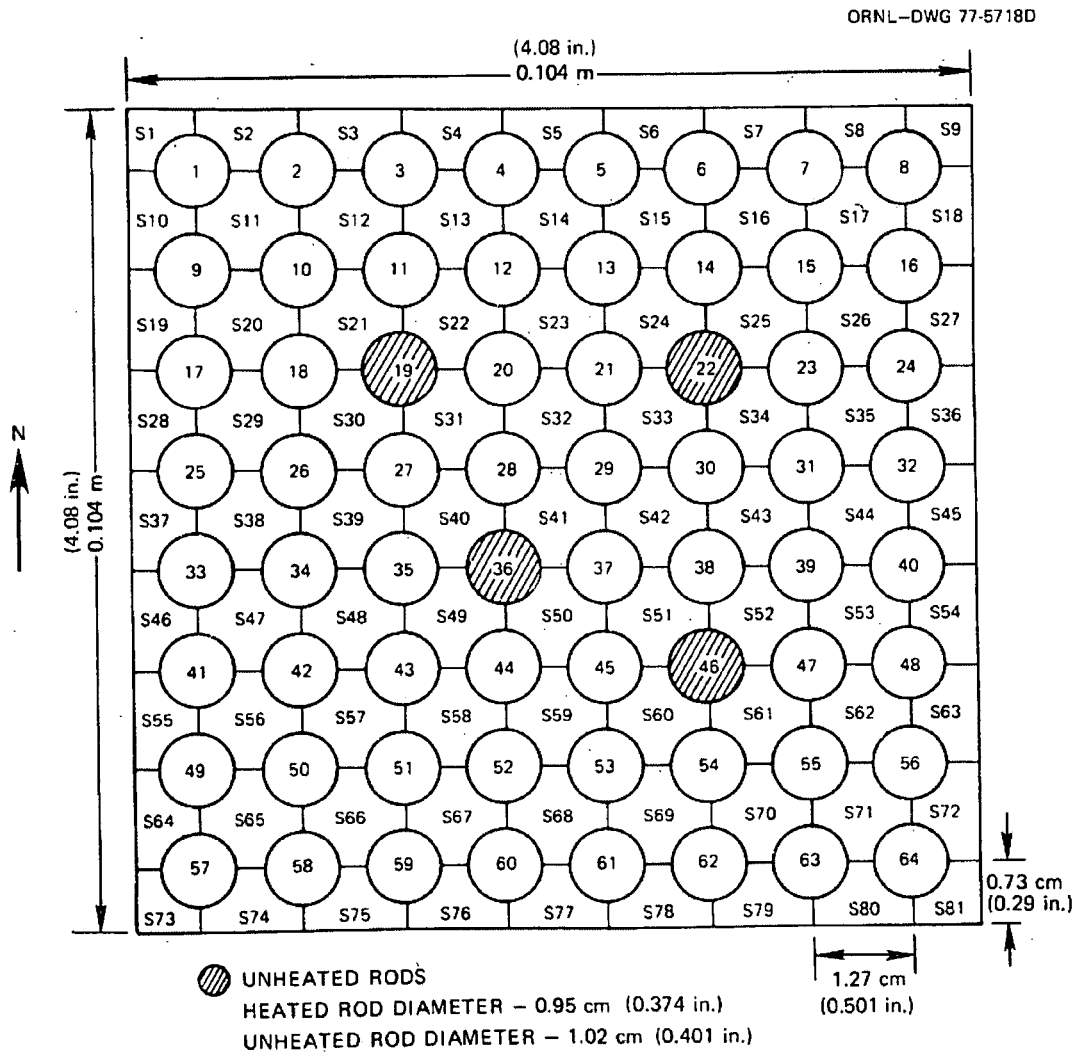


Figure 5.2.1.2-3 Cross Section of THTF

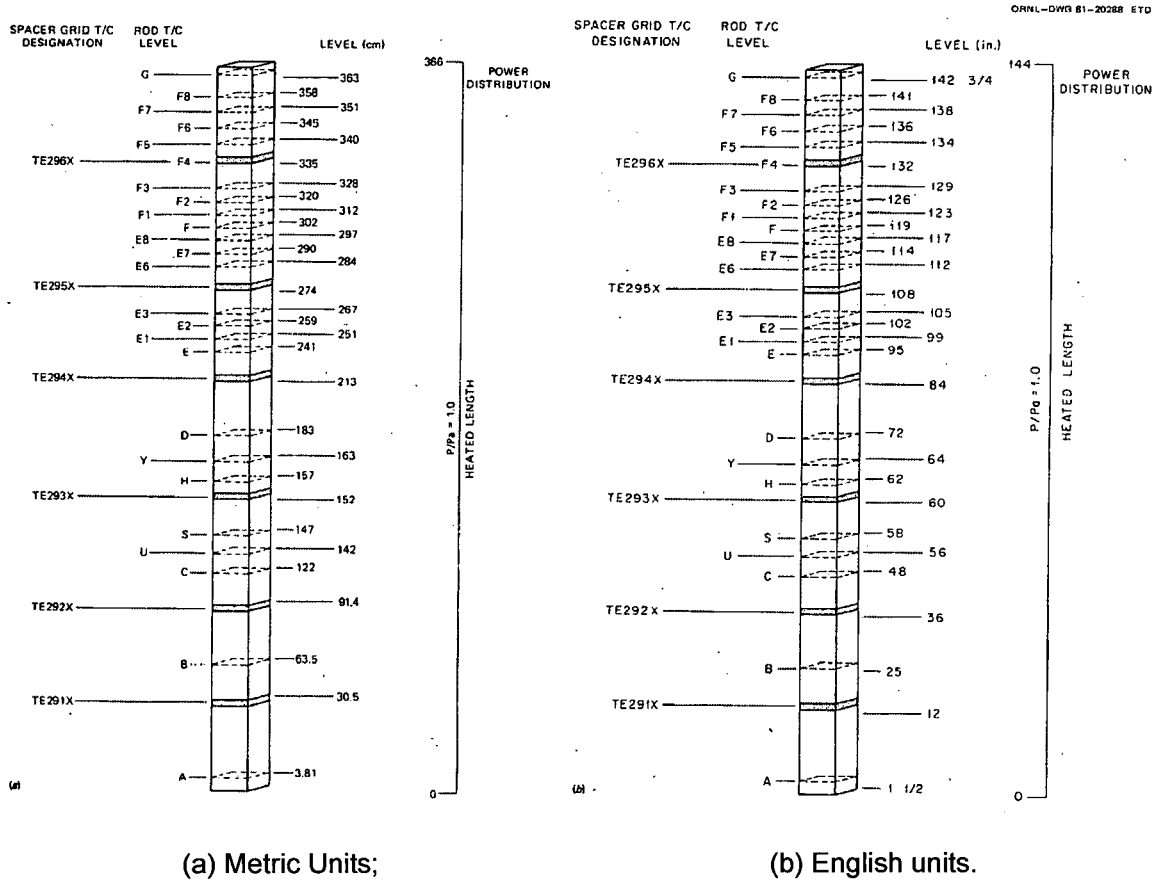


Figure 5.2.1.2-4 Axial Location of Spacer Grids and FRS Thermocouples

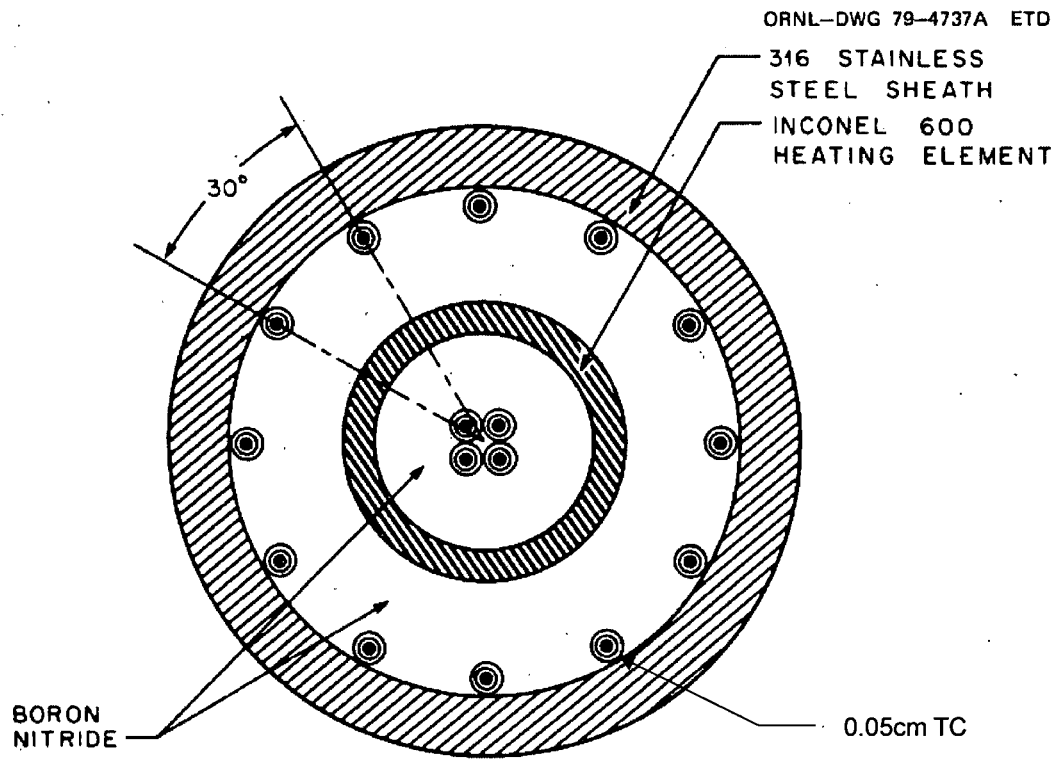


Figure 5.2.1.2-5 Simplified Cross Section of a Typical Fuel Rod Simulator

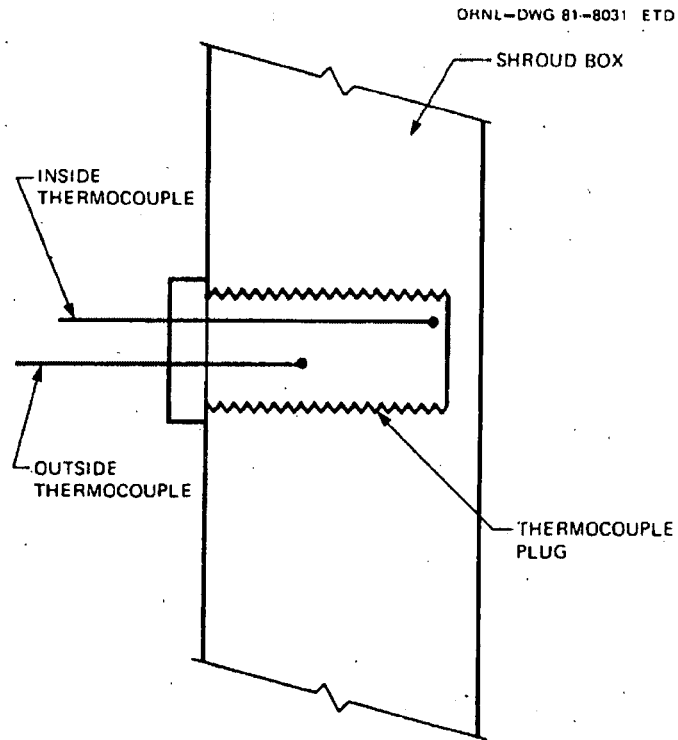


Figure 5.2.1.2-6 Shroud-wall Thermocouple Configuration

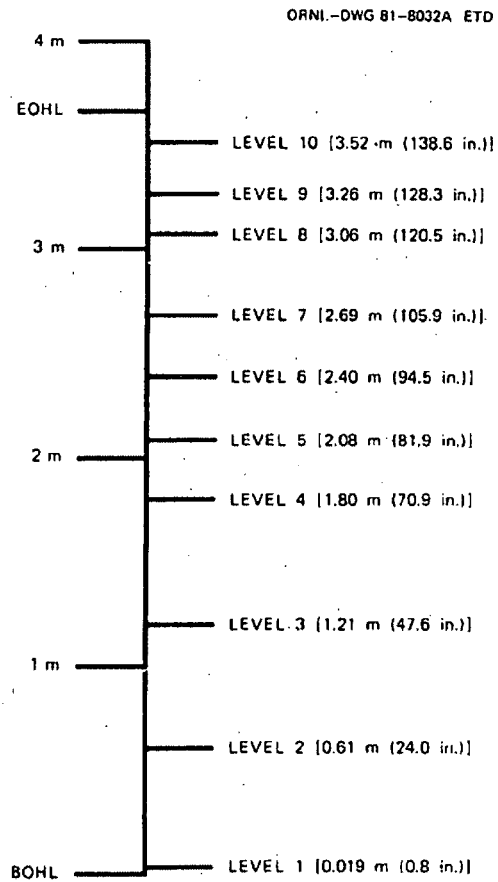


Figure 5.2.1.2-7 Axial Location of Shroud-Wall Thermometry

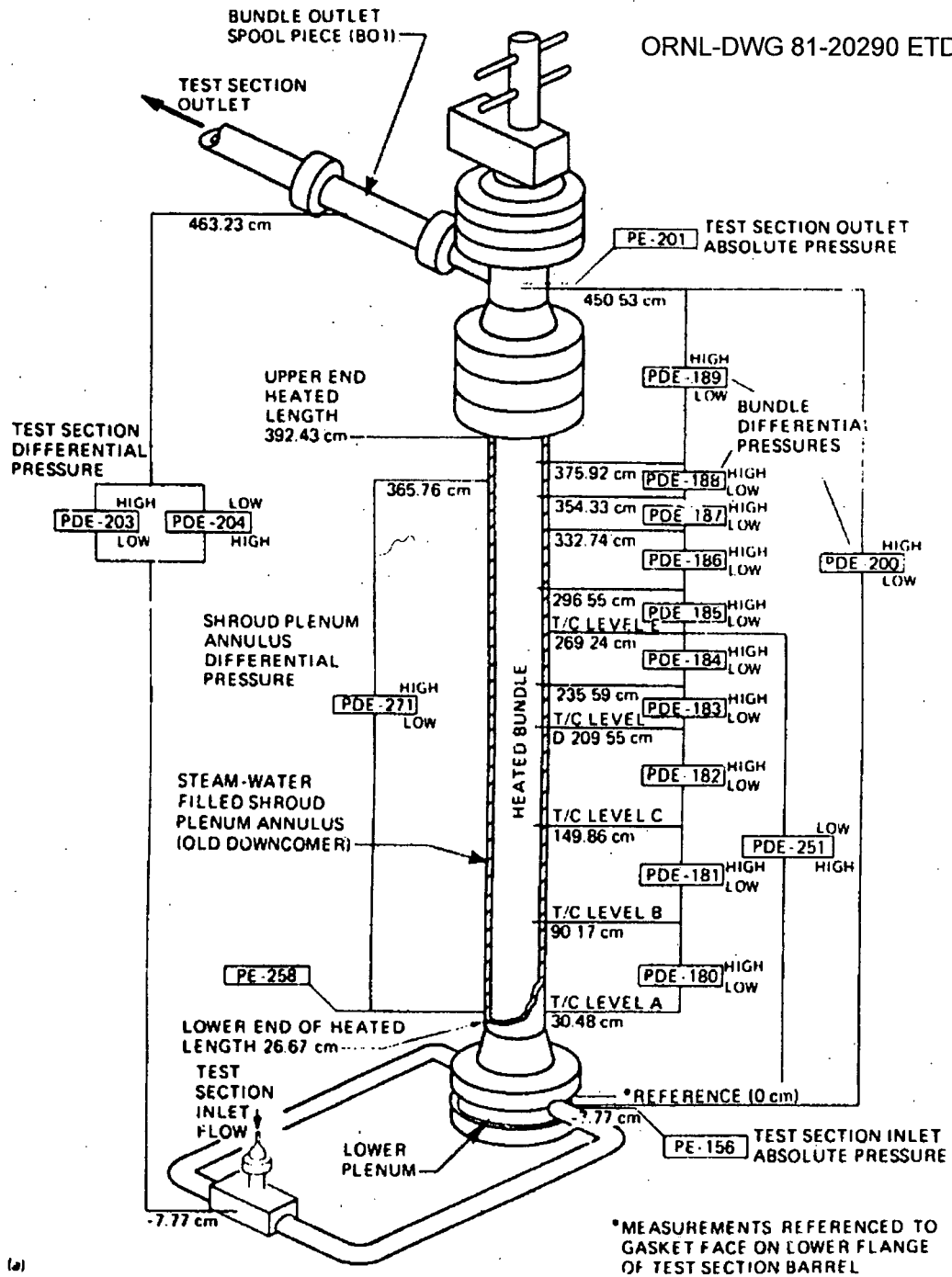


Figure 5.2.1.2-8 THTF In-Bundle Pressure Instrumentation

ORNL-DWG 80-5674 ETD

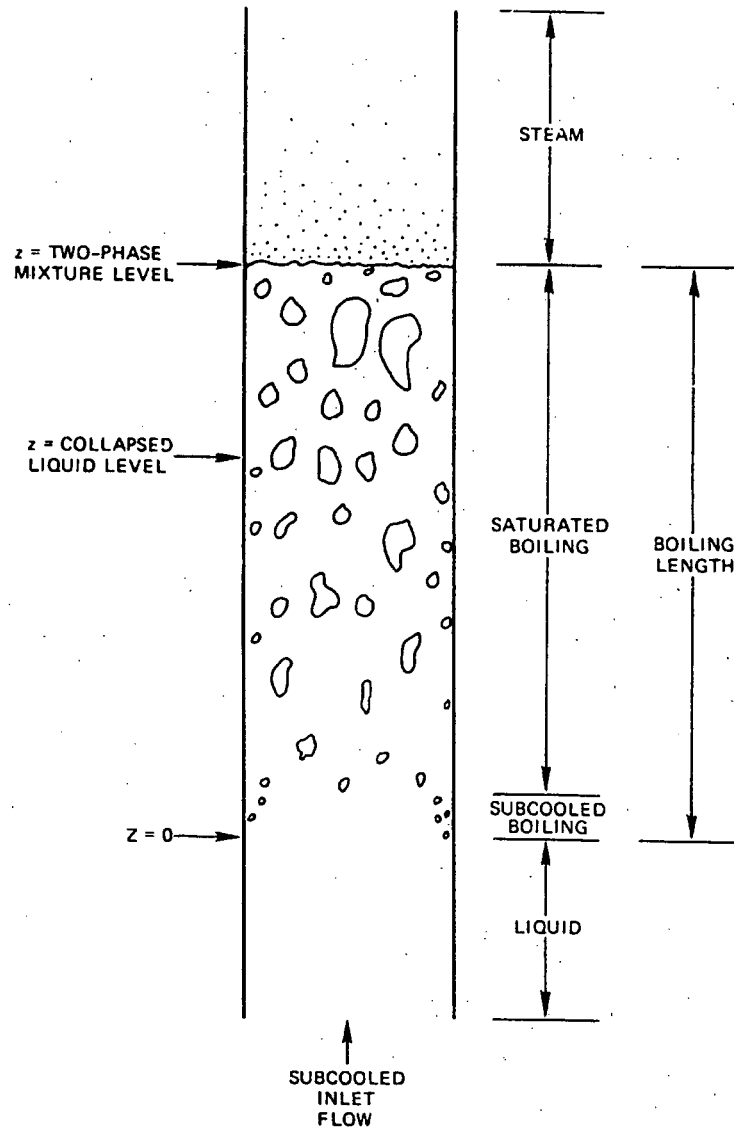


Figure 5.2.1.2-9 Schematic of a Nuclear Reactor Subchannel in a Partially Uncovered Configuration

5.2.1.3 ORNL/THTF Uncovered-Bundle Heat Transfer test

(1) Facility Design

Experiments of uncovered-bundle heat transfer test were performed at ORNL in the THTF. The THTF is a large high-pressure non-nuclear thermal hydraulics loop. System configuration was designed to produce a thermal-hydraulic environment similar to that expected in a small-break loss-of-coolant accident (SBLOCA). Key aspects of the THTF design have been summarized in Table 5.2.1.3-1.

a. Flow Circuit Description

Figure 5.2.1.3-1 is an illustration of the THTF in small-break test configuration. Flow leaves the main coolant pump and passes through FE-3, a 2-in. turbine meter. On leaving FE-3, flow enters the inlet flow manifold. The flow manifold is divided into two parallel flow lines: a 1/2 in. line used to meter very low flow rates and a 3/4-in. flooding line used for the higher flows experienced during reflood. The entire inlet-flow manifold was constructed of high-pressure stainless steel tubing. Volumetric flow rates in the low-flow 1/2 in. inlet line were measured by FE-18A (a low-flow orifice meter), and FE-250 and FE-260 (1/2-in. turbine meters). The two inlet lines converge at the injection manifold, from which fluid passes directly into the lower plenum. Fluid does not pass through a downcomer. Flow proceeds upward through the heated bundle and exits through the bundle outlet spool piece. Spool piece measurements include pressure, temperature, density, volumetric flow, and momentum flux. When outlet flow rates were very low the volumetric flow was measured by a bank of low-flow orifice meters downstream of the outlet spool piece. On leaving the orifice manifold, flow passes through a heat exchanger and returns to the pump inlet.

System pressure was controlled via the loop pressurizer. The pressurizer was partially filled with subcooled water, and nitrogen cover gas was used to control pressure. The system pressure could be controlled more easily by filling or venting nitrogen than by the conventional flashing and condensation of saturated water and steam.

Flow was injected directly into the lower plenum and did not pass through a downcomer. The shroud-plenum annulus (Figure 5.2.1.3-2) was used in earlier THTF testing as an internal downcomer but was isolated from the primary flow circuit in these tests. The shroud-plenum annulus pressure was equalized with the system pressure. This was accomplished by connecting the bottom of the annulus region to the pressurizer surge line and the top of the annulus to the test section outlet. The line between the annulus and pressurizer was opened,

and the line between the annulus and test section outlet was closed during the initial boiloff phase of steady-state testing. This allowed any vapor generated by boiling in the annulus to displace liquid into the pressurizer. Note that the displacement of liquid causes the mixture levels in the downcomer and bundle to equalize, which is why installation of a line between the pressurizer and downcomer was advantageous. However, once mixture levels had equalized, leaving this line open was no longer advantageous. The reason is that the steam flow through the outlet causes a substantial pressure drop between the test section and pressurizer. If the annulus was in communication with the pressurizer, then a large pressure difference between the test section bundle and the downcomer would exist. This large pressure difference has been observed to cause substantial leakage from the bundle to the annulus. To minimize this leakage, the line between the pressurizer and annulus was closed after mixture-level equalization had taken place. To maintain pressure equalization, the shroud bypass line, which connects the top of the shroud annulus to the test outlet, was opened (Figure 5.2.1.3-1). As a final step to minimize the possibility of leakage from bundle to annulus, the shroud bypass line was closed shortly before data were taken. The annulus was then completely isolated from the rest of the system, thus providing the least opportunity for undesired leakage.

b. Bundle Description

The THTF test section contains a 64-rod electrically heated bundle. Figure 5.2.1.3-3 is a cross section of the bundle. The four unheated rods were designed to represent control-rod guide tubes in a nuclear fuel assembly. Rod diameter and pitch are typical of a 17 x 17 fuel assembly. Figure 5.2.1.3-4 is an axial profile of the THTF bundle that illustrates the positions of spacer grids and fuel rod simulator (FRS) thermocouples. The heated length is 3.66 m, (12 ft), and a total of 25 FRS thermocouple levels are distributed over that length. An FRS thermocouple level refers to an axial location where a selected number of FRSs are instrumented with sheath thermocouples.* (*FRS thermocouple levels A,B,C,D,E,F, and G contain most of the FRS sheath thermocouples and are referred to as primary thermocouple levels. All other FRS thermocouple levels are referred to as intermediate thermocouple levels.) Note that the upper third of the bundle is more heavily instrumented than the lower portion. For most tests, the two-phase mixture level is in the top 1/3 of the heated length. The additional instrumentation in the top 1/3 of the bundle is used to better define the mixture-level position. In addition, the increased instrumentation near the spacer grids can be used to ascertain to what extent spacer grids affect heat transfer.

A drawing of an FRS cross section is shown in Figure 5.2.1.3-5. Each FRS has 12 sheath and 4 center thermocouples. The thermocouples are either 0.05 cm (0.020 in.) or 0.04 cm (0.016 in.)

in diameter and can have their junctions at any of the 25 axial levels mentioned previously. Each rod can have from 0 to 3 sheath thermocouple junctions at any particular axial level. When an FRS has three junctions at the same level, they are spaced evenly around the rod (i.e., 120° apart). Table 5.2.1.3-2 describes the FRS sheath thermocouple naming convention.

In addition to the FRS thermometry, there are a number of locations where fluid temperature is measured. In-bundle fluid temperature is measured by four different types of fluid thermocouples. The first type is a thermocouple array-rod thermocouple. These are exposed* fluid thermocouples that project from unheated rods. (* Exposed in this context does not mean that the thermocouple junction actually contacts the fluid. The junction is encased in a stainless steel sheath but does not have a droplet shield.) Thermocouple array-rod thermocouples are installed at 1.83, 2.41, 3.02, and 3.62 m (72, 95, 119, and 142.5 in.) above the beginning of the heated length (BOHL). The second type of fluid thermocouple is a shroud box fluid thermocouple. These are exposed fluid thermocouples that project from the bundle shroud into subchannels adjacent to the shroud. Shroud box fluid thermocouples are installed at 0.38, 0.64, 1.22, 1.83, 2.41, 3.02, and 3.61 m (15, 25, 48, 72, 95, 119, and 142 in.) above BOHL. The third type of fluid thermocouple is a spacer grid fluid thermocouple. These thermocouples are exposed fluid thermocouples that project from spacer grids. Spacer grid fluid thermocouples project slightly upstream of each spacer grid. The fourth and final type of fluid thermocouple is a subchannel rake thermocouple. These thermocouples are attached to a rake located several centimeters above the end of the heated length (EOHL). They are used in measuring the cross-sectional temperature distribution. Nomenclature and locations for fluid thermocouples are summarized in Table 5.2.1.3-3.

As previously noted, the THTF bundle is surrounded by a shroud box (Figure 5.2.1.3-2). The shroud box walls have been instrumented with thermocouples in order to estimate bundle heat losses. A typical instrumentation site consists of a pair of thermocouples embedded in the shroud box wall (Figure 5.2.1.3-6). Because the thermocouples are separated, the radial temperature gradient can be calculated and the bundle heat losses estimated. Figure 5.2.1.3-7 shows the axial locations where the shroud box walls have been instrumented.

c. Differential Pressure (ΔP) Instrumentation

Differential pressure data were obtained through the use of "stacked" ΔP cells. Figure 5.2.1.3-8 illustrates the ΔP measurement sites. Differential pressure cells PdE-180 through 188 are ranged from 0.0 to 0.63m (0.0 to 25.0 in.) of standard water, and PdE-189 is ranged from 0.0 to 0.76 m (0.0 to 30.0 in.) of water. Spacing of the cells varies from 0.75 to 0.22 m (29.4 to 8.5 in.).

The void fraction profile was calculated from the readings of the ΔP cells as described in 5.2.1.2 (4) (a).

(2) Scaling

The objective of heat transfer testing was to acquire heat transfer coefficient and fluid conditions in partially uncovered bundle.

The THTF contains a 64-rod electrically heated bundle with internal dimensions typical of a 17 x 17 PWR fuel assembly. The scaling of the facility is fine since it is full length and prototypical dimensions.

(3) Range of Conditions

Table 5.2.1.3-4 summarizes the test conditions for the quasi-steady-state uncovered-bundle heat transfer test series. The table indicates that three tests were run at roughly 4.1 MPa (600 psia) and three tests at roughly 7.2 MPa (1050 psia). The three tests at each of the primary pressure levels were designed to span a range of linear powers.

Mixture level varied considerably from test to test. This variation occurred because test procedure specified that the maximum core uncovering be achieved while maintaining a peak clad temperature of roughly 1033 K (1400°F). At high power levels this constraint allowed uncovering of only 25 to 30% of the bundle, while at low power roughly 50% of the bundle could be uncovered.

The steam-cooling region was defined as the region at or above the lowest primary thermocouple level experimentally indicating the presence of dry superheated vapor, but at or below the EOHL. The steam-cooling region corresponds to the portion of the bundle for which heat transfer calculations have been performed.

The entire steam-cooling region appears to be in simple forced-convection dominated turbulent flow in only two of the six tests. In the other four tests at least part of the steam-cooling region appears to be in mixed convection. Note that in three of the tests (10K, 10N, and 10J) a flow transition is indicated. Test 10K indicates laminarization in the upper part of the steam-cooling region. Test 10N indicates a movement from a mixed turbulent regime at the bottom of the steam-cooling region toward a mixed transition to laminar regime at the top of the bundle, and test 10J undergoes a transition to turbulent forced convection in the upper portion of the bundle.

(4) Data to be compared

The data to be compared are the bundle cross-section average vapor temperature and FRS temperature profiles and associated heat transfer coefficient profiles.

a. Rod Surface Temperature

Rod surface temperatures vary from a low of about 811 K (1000°F) to a high of 1061K (1450°F). The most notable feature of the FRS temperature profiles is the distinct drop in surface temperature at and downstream of spacer grids. The drop in temperature at the grid increases with an increasing Reynolds number. Test 10L (13,000 Re_v<math><17,700</math>) shows the greatest effect with a reduction of 128K (230°F). On the other hand, test 10K (1,100 Re_v<math><1,900</math>) shows no temperature drop at the grid.

b. Vapor Temperature

Vapor temperature profiles showed that vapor temperatures varied from a minimum of about 561K (550 °F) to a maximum of 950K (1250 °F). The profiles also show that, except for tests 10K and 10N, vapor temperature increased relatively linearly with elevation. The variation of vapor temperature with elevation was a result of both bundle heat input and heat losses. In tests 10I, J, L, and M bundle heat losses were small compared with the heat input (<math><5\%</math>). Accordingly, the axially uniform heat input dominated the temperature profile, and a relatively linear increase in vapor temperature with elevation occurred. This was not the case in tests 10K and N where heat losses were roughly 17% of bundle power. In tests 10K and N, the vapor temperature rise in the lower portion of the steam-cooling region was linear. However, as vapor temperature rose so did heat losses. Therefore, heat losses in the upper portion of the steam-cooling region were greater than in the lower portion. As a result, the rate of vapor temperature rise with elevation decreased in the upper portion of the steam-cooling region.

c. Heat Transfer Coefficient

The shape of the heat transfer profiles is the combined result of changes in convective heat transfer, radiative transfer, and grid effects. Spacer grids were observed to substantially increase heat transfer at, and downstream of, the grid. The effect was most pronounced in the high-flow tests. In many cases substantial enhancement of heat transfer occurred when the vapor was dry and highly superheated.

(5) Data uncertainties

Results of instrument uncertainty analysis for the THTF, reported in Reference 5.2.1.3-2, ~~is~~are

summarized in Table 5.2.1.3-5.

FRS and fluid temperature are measured by TE-300, TE-188, and TE-189 series thermocouples. Their range and error are 273-1309K(32-1900F) and 3.7K (6.7°F) for “ < 623K (662°F)” and 1% reading for “ >623K(662°F)”.

(6) Distortion

The heat loss to the environment from the rod bundle and housing, shown in Table 5.2.1.3-4, was significant and could affect the experimental results. Only total bundle heat loss for each case is reported based on the shroud-wall thermocouple thermometry (Figures 5.2.1.3-6 and 7).

(7) References

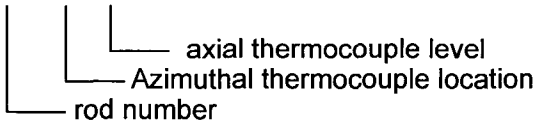
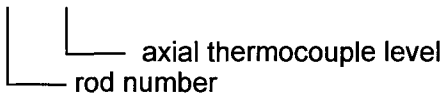
- 5.2.1.3-1 T. M. Anklam, R. J. Miller, M. D. White, Experimental Investigations of Uncovered-Bundle Heat Transfer and Two-Phase Mixture-Level Swell Under High-Pressure Low-Heat Conditions, NUREG/CR-2456, ORNL-5848
- 5.2.1.3-2 D. K. Felde et al., “Facility Description – THTF MOD3 ORNL PWR BDHT Separate-Effects Program, “NUREG2640, ORNL/TM-2640, ORNL/TM-7842, September 1982

Table 5.2.1.3-1 THTF Design Summary^(Ref. 5.2.1.3-1)

Parameter	Quantity
Design pressure [MPa (psia)]	17.2 (2500)
Pump capacity [m ³ /s (gpm)]	0.044 (700)
Heated length [m (ft)]	3.66 (12.0)
Power profile	Flat
FRS diameter [cm (in.)]	0.95 (0.374)
Lattice	Square
Pitch [cm (in.)]	1.27 (0.501)
Subchannel hydraulic diameter [cm (in.)]	1.23 (0.48)
Number of heated rods	60
Number of unheated rods	4
Unheated rod diameter [cm (in.)]	1.02 (0.40)
Bundle shroud configuration	Square
Bundle shroud thickness 2 sides [cm (in.)]	2.54 (1.0)
2 sides [cm (in.)]	1.91 (0.75)
Number of grid spacers	7

Table 5.2.1.3-2 Rod-Sheath Thermocouple Designations^(Ref. 5.2.1.3-1)

Rod-sheath thermocouples are designed according to one of the following two schemes:

- TE-3 17 A D

- TE-3 54 F8


Thus, this first designation refers to the sheath thermocouple in rod 17 at level D, azimuthal location A. If the thermocouple designation ends with a number, this designation refers to the sheath thermocouple in rod 54 at level F8.

Table 5.2.1.3-3 Nomenclature for Thermocouples in THTF (1/4) (Ref. 5.2.1.3-2)**Subchannel Thermocouples**

The subchannel thermocouple rake is located ~2.3 cm above the upper end of the heated section. (Figure 5.2.1.23-8) The naming convention takes the following form:

TE-12nn,

Where

nn = a number between 01-81 that equals the number of the subchannel in which it is located. (Figure 5.2.1.23-3.)

Table 5.2.1.3-3 Nomenclature for Thermocouples in THTF (2/4) (Ref. 5.2.1.3-2)Spacer-Grid Thermocouples

The spacer-grid fluid thermocouples are attached to core grids No. 2-7. (Figure 5.2.1.23-4. Six grid locations are indicated.) The naming convention takes the following form:

TE-29na,

where

n = a number between 1-6 designating the spacer-grid level as follows:

<u>Number</u>	<u>Between thermocouple levels</u>	<u>spacer-grid No.</u>
1	A & B	2
2	B & C	3
3	C & D	4
4	D & E	5
5	E & F	6
6	F & G	7,

and a = a letter "A-F" designating the subchannel into which the thermocouple projecting, as follows(Figure 5.2.1.23-3.):

<u>Letter</u>	<u>Subchannel No.</u>
A	32
B	43
C	57
D	70
E	17
F	38

Table 5.2.1.3-3 Nomenclature for Thermocouples in THTF (3/4) ^(Ref. 5.2.1.3-2)
Shroud-box Thermocouples

Shroud-box thermocouples protrude through the shroud wall into the fluid in the wall subchannels. The naming convention has the following form:

TE-18na,

where

n = a number 1-7 designating the level of the thermocouple in the shroud box as follows (Figure 5.2.1.23-4.)

<u>Number</u>	<u>Thermocouple levels</u>
1	A
2	B
3	C
4	D
5	E
6	F
7	G

and

a = a letter designating the side of the box through which the thermocouple protrudes, N, E, S, or W. (Figure 5.2.1.23-3.)

Table 5.2.1.3-3 Nomenclature for Thermocouples in THTF (4/4) (Ref. 5.2.1.3-2)Thermocouple-Array Rod Thermocouples

The thermocouple-array rods occupied grid positions 19 and 36. (Figure 5.2.1.23-3). Each array rod contains 14 thermocouples, and, at each axial level in the bundle where there is a primary FRS thermocouple level, two of these thermocouples protrude from the rod into the fluid. The naming convention has the following form:

TE-18naI,

where

n = the number 8 or 9 designating in which grid position the thermocouple array rod is located such that 8 denotes grid position 19 and 9 denotes grid position 36 (Figure 5.2.1.23-3.);

a = a letter A and B designating which of two subchannels associated with that rod the thermocouple protrudes into (Figure 5.2.1.23-3.):

<u>Rod grid position</u>	<u>(a =) A subchannel</u>	<u>(a =) B subchannel</u>
(n=8→) 19	22	30
(n=9→) 36	41	49

I = the thermocouple level A-G. (same as FRS thermocouple level designation. Figure 5.2.1.23-4)

Table 5.2.1.3-4 Summary of Uncovered-Bundle Heat Transfer Test Conditions^a (Ref. 5.2.1.3-1)

Test	System pressure [MPa (psia)]	Linear power/rod [kW/m(kw/ft)]	Mass flux [kg/m ² · s(lb/h · ft ²)x10 ⁻⁴]	Mixture level [m(ft)]	Steam cooling region [m(ft)]	Vapor Reynolds number (BOSCR) ^b	Vapor Reynolds number (EOSCR)	Fractional heat loss	Heat transfer regime (BOSCR) ^{b,d}	Heat transfer regime (EOSCR) ^{c,d}
3.0910I	4.5 (650)	2.22 (0.68)	29.7 (2.19)	2.62 (8.6)	3.02-3.62 (9.91-11.88)	16,600	12,200	0.018	FCT	FCT
3.0910J	4.2 (610)	1.07 (0.33)	12.7 (0.94)	2.47 (8.1)	3.02-3.62 (9.91-11.88)	6,700	5,000	0.052	MCT	FCT
3.0910K	4.0 (580)	0.32 (0.10)	3.1 (0.23)	2.13 (7.0)	2.42-3.62 (7.94-11.88)	1,900	1,100	0.176	MCT	FCT
3.0910L	7.5 (1090)	2.17 (0.66)	29.1 (2.15)	2.75 (9.0)	3.02-3.62 (9.91-11.88)	17,700	13,000	0.017	FCT	FCT
3.0910M	7.0 (1010)	1.02 (0.31)	12.6 (0.93)	2.62 (8.6)	3.02-3.62 (9.91-11.88)	6,500	5,100	0.042	MCT	MCT
3.0910N	7.1 (1030)	0.47 (0.14)	4.6 (0.34)	2.13 (7.0)	2.42-3.62 (7.94-11.88)	3,000	1,600	0.162	MCT	MCTR

^aNumbers in this table have been rounded off.^bBoscr-beginning of steam-cooling region.^cEOSCR-end of steam-cooling region^dAbbreviations are:
FCT - forced-convection turbulent
MCT - mixed-convection turbulent
FCL - forced convection laminar
MCTR - mixed convection transition to laminar

Table 5.2.1.3-5 Instrument Uncertainty Analysis For The THTF Loop
Summary of Results ^(Ref. 5.2.1.3-2)

Two standard deviation uncertainty bands are described for critical instrumentation in the Thermal Hydraulic Test Facility (THTF). The analyzed instruments and their minimum, steady-state, 2σ error bands [root sum square (RSS), 95% confidence interval] include:

1.	Turbine flowmeter	4.1 % reading
2.	Gamma densitometer	10.4 % FS*
3.	Strain gage pressure cell	1.0% FS*
4.	Differential pressure cell	2.0% FS* min to 9.9% FS* max
5.	Thermocouple	3.7°C min to 10.3 °C max
6.	Rod power instrumentation	1.1% reading
7.	Strain gage drag disk	56% reading below 10% FS* 19% reading above 10% FS*

*Full-scale values

ORNL-DWG 81-7837R ETD

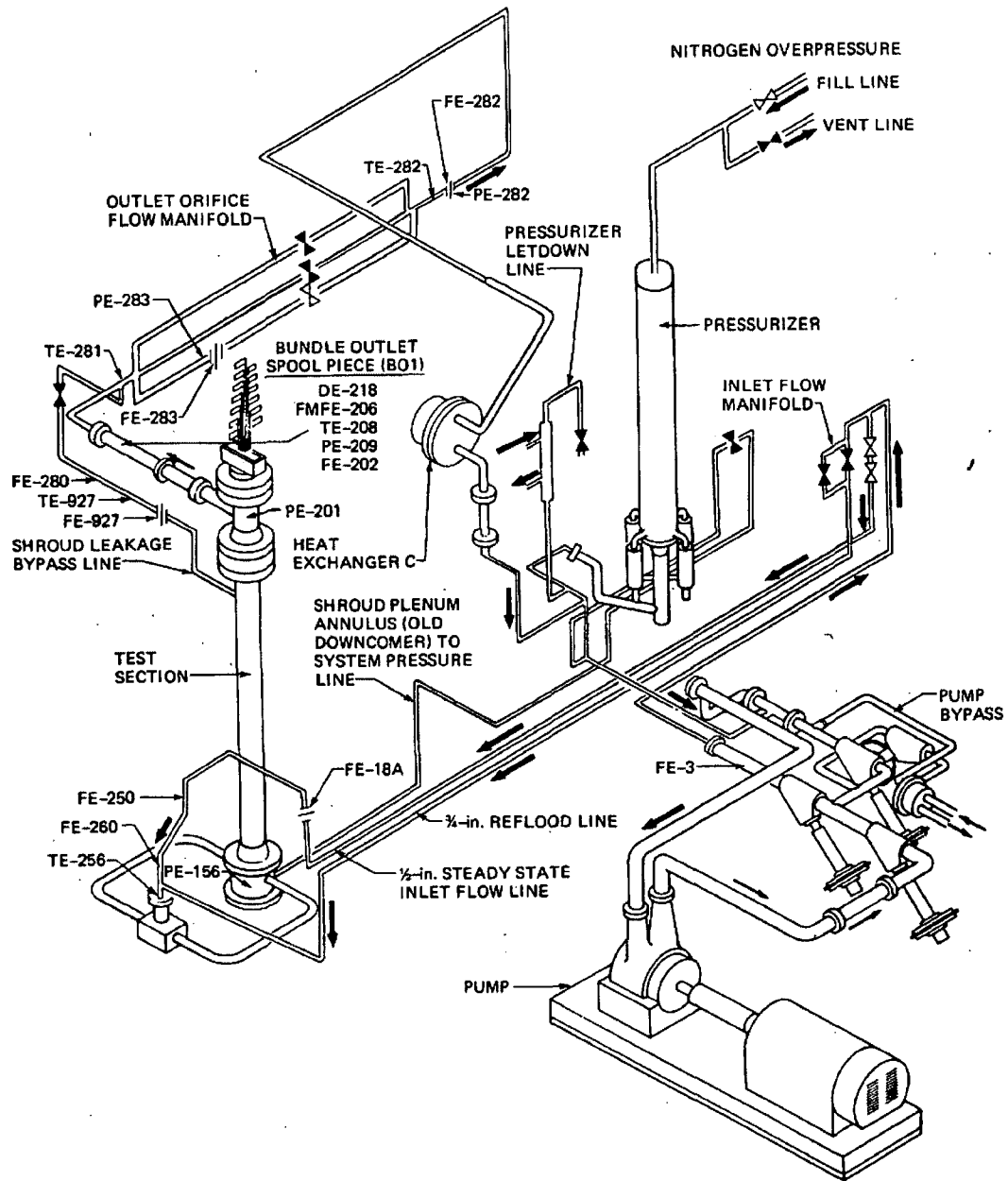


Figure 5.2.1.3-1 THTF in Small-break Test Configuration

ORNL-DWG 82-4875 ETD

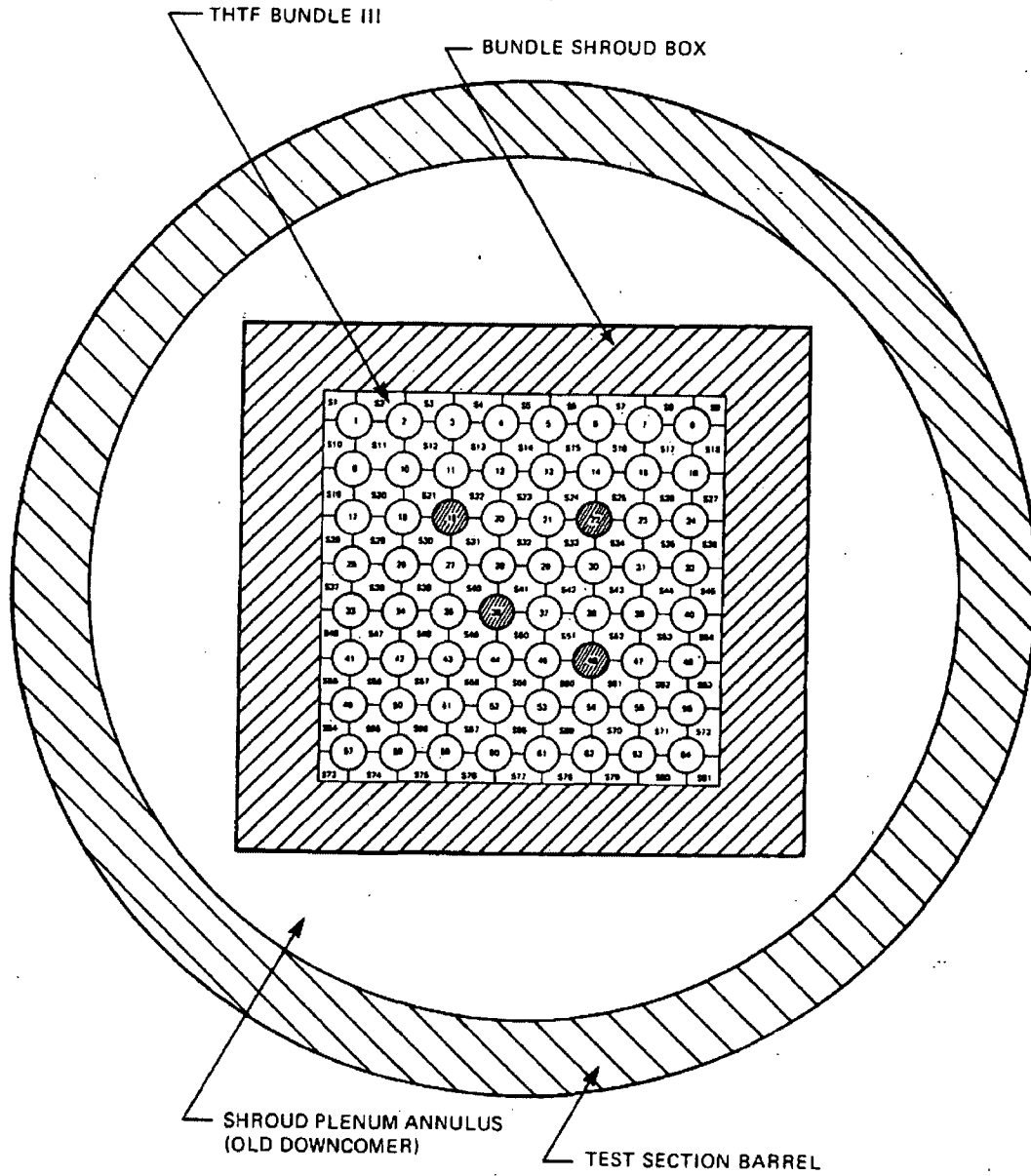


Figure 5.2.1.3-2 Cross Section of THTF Test Section

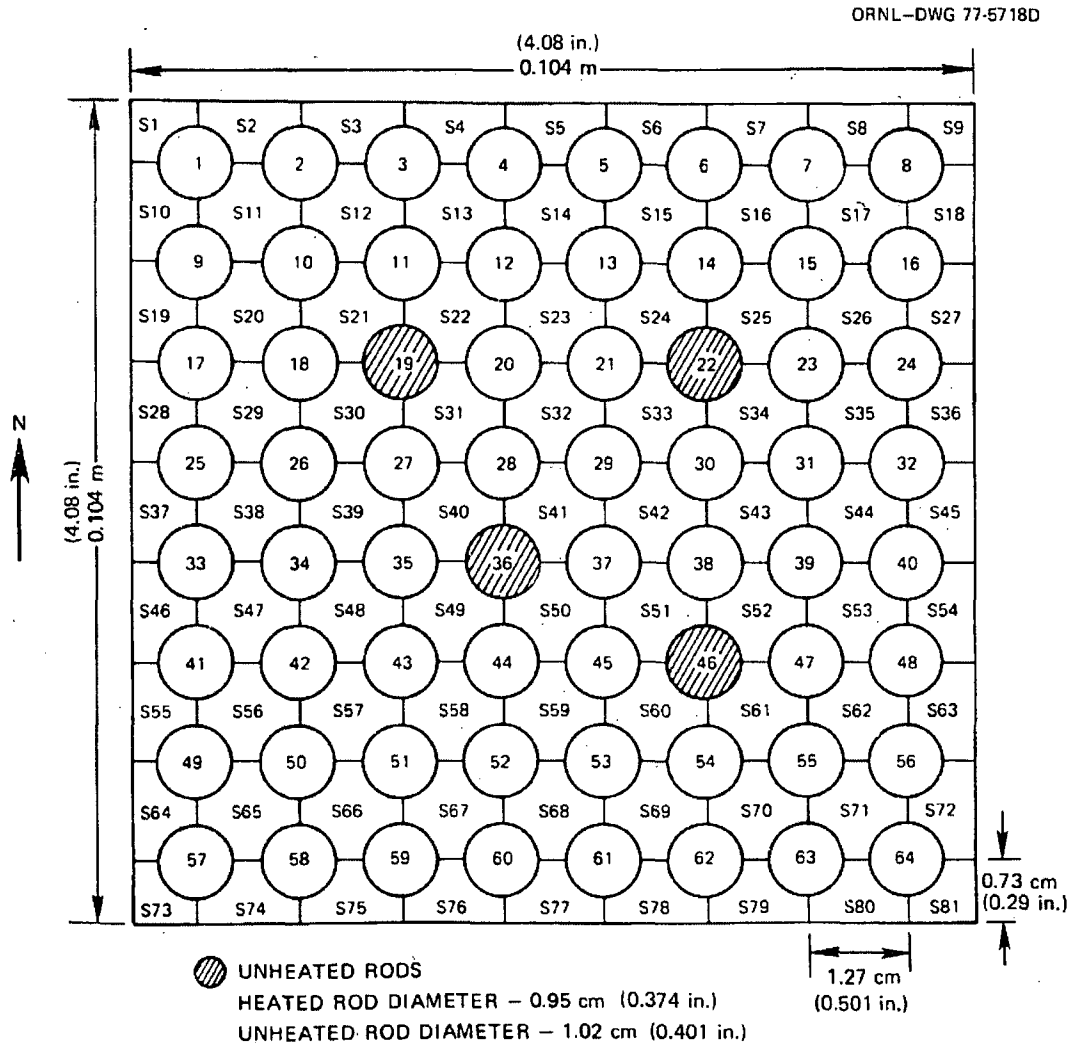


Figure 5.2.1.3-3 Cross Section of THTF

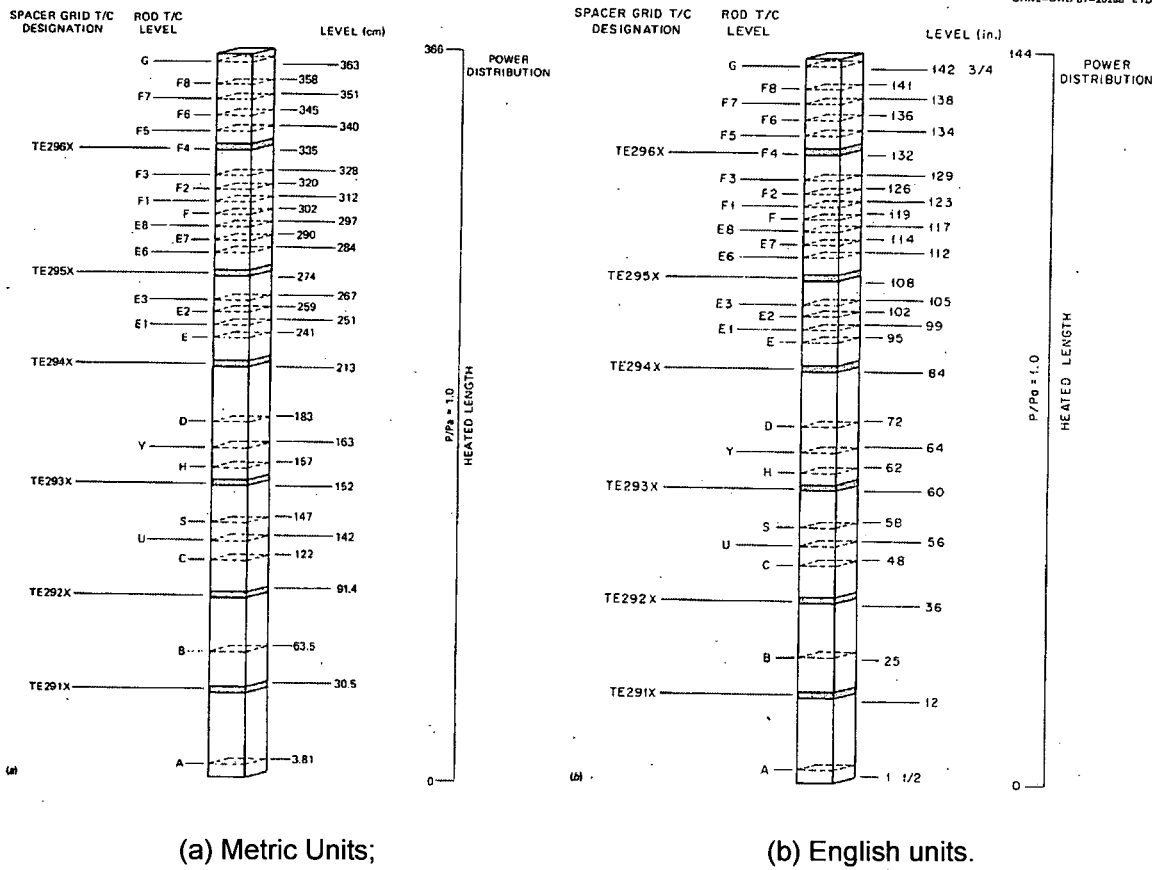


Figure 5.2.1.3-4 Axial Location of Spacer Grids and FRS Thermocouples

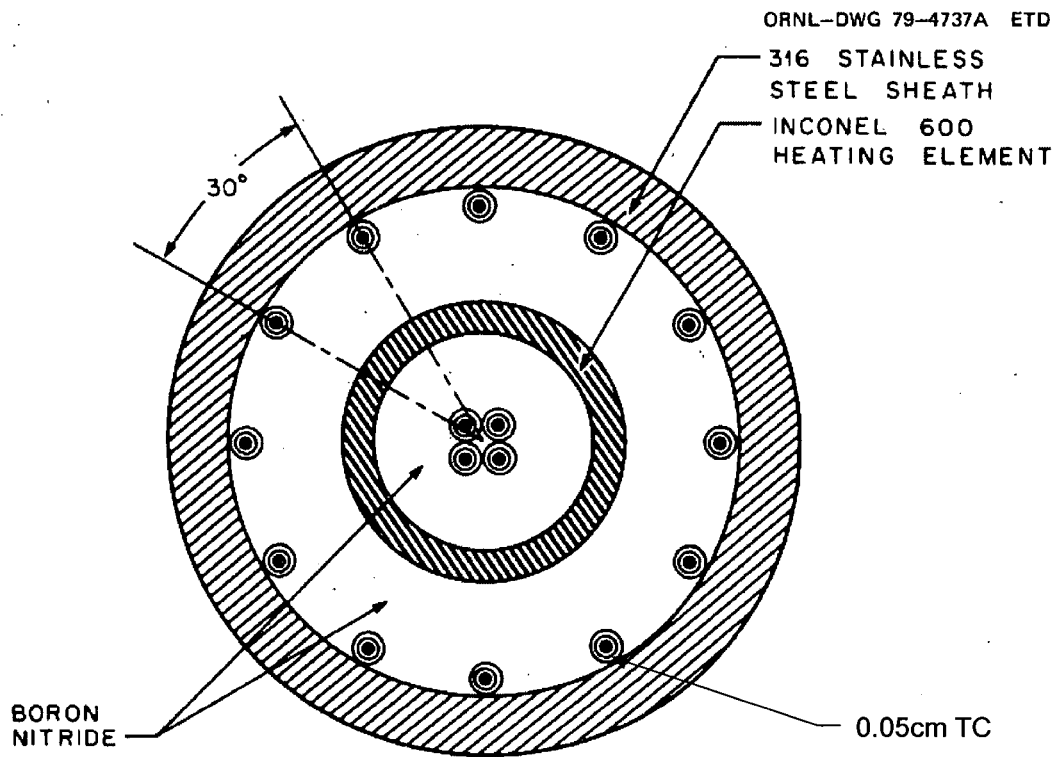


Figure 5.2.1.3-5 Simplified Cross Section of a Typical Fuel Rod Simulator

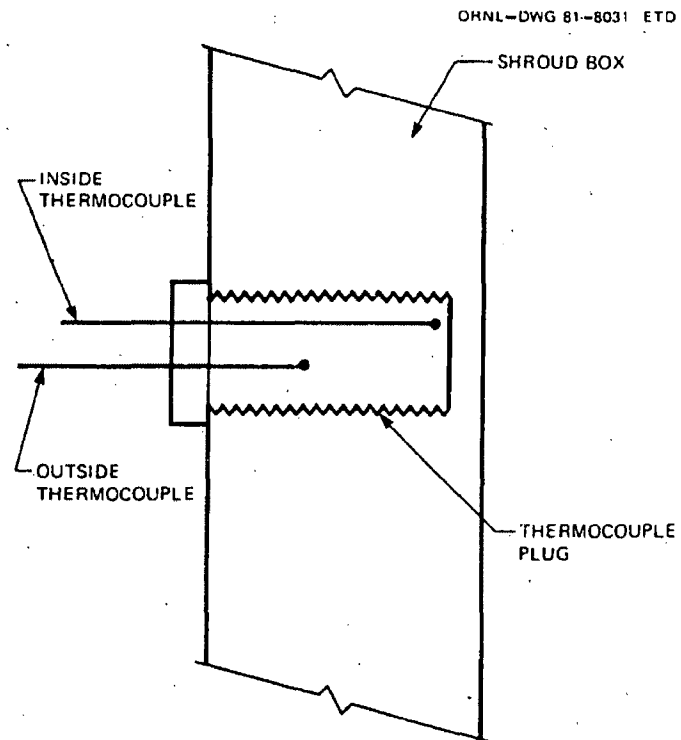


Figure 5.2.1.3-6 Shroud-wall Thermocouple Configuration

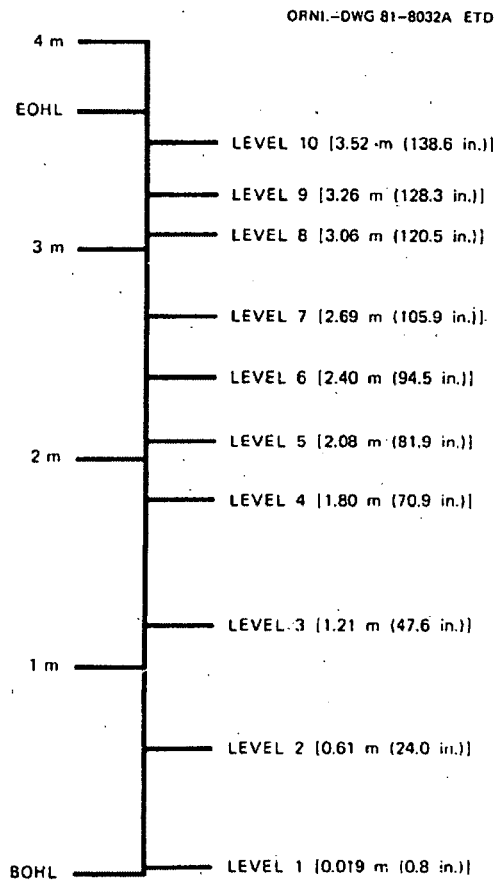


Figure 5.2.1.3-7 Axial Location of Shroud-wall Thermometry

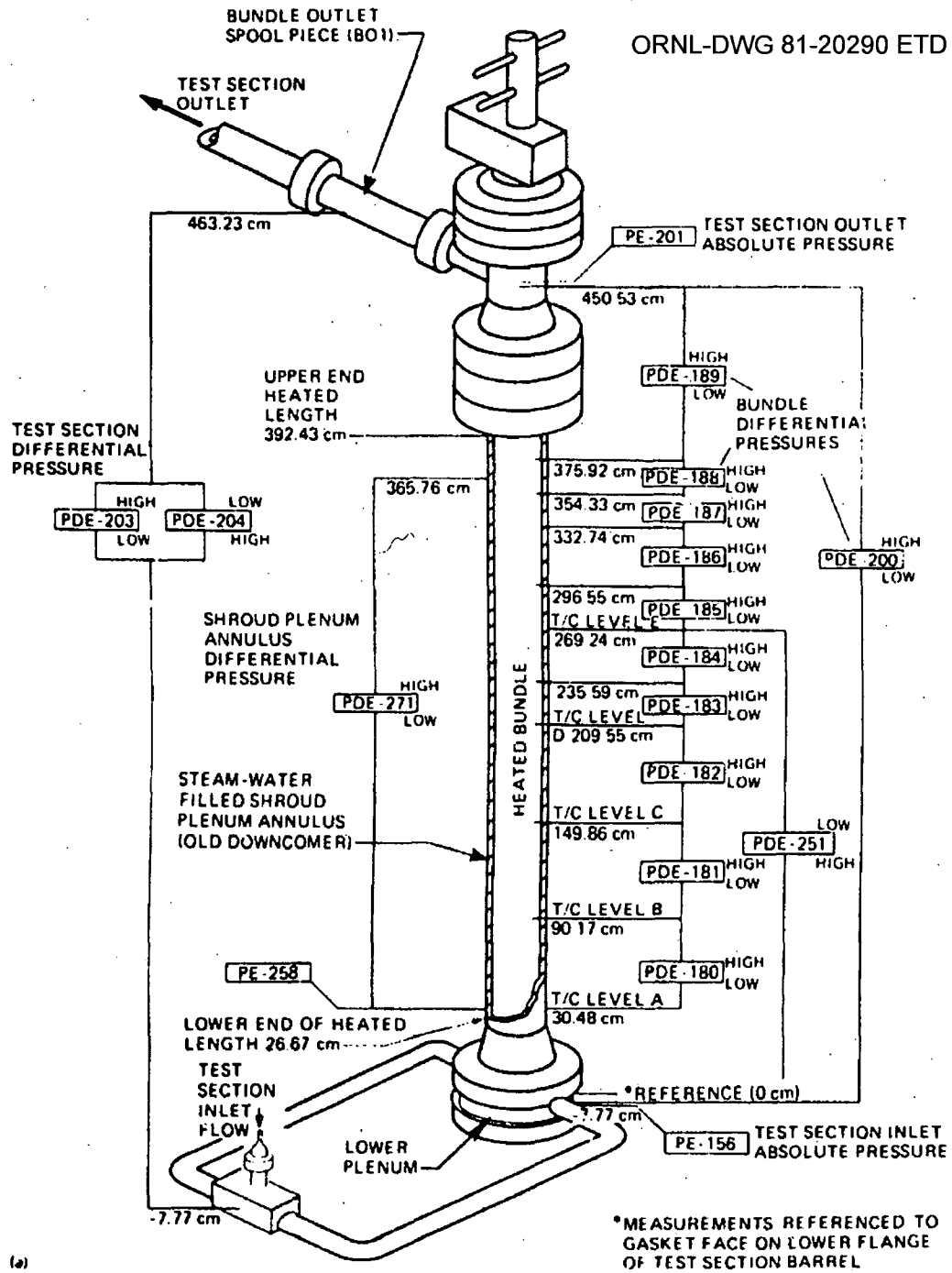


Figure 5.2.1.3-8 THTF In-Bundle Pressure Instrumentation

5.2.1.4 ORNL/THTF High-Pressure Reflood test

(1) Facility Design

The experiments of high-pressure reflood test were performed at the THTF in ORNL. The THTF is a large, high-pressure, non-nuclear thermal-hydraulic loop. System configuration was designed to produce a thermal-hydraulic environment similar to that expected in a SBLOCA. Key aspects of the THTF design have been summarized in Table 5.2.1.4-1.

a. Flow Circuit Description

Figure 5.2.1.4-1 is an illustration of the THTF in small-break test configuration. Flow leaves the main coolant pump and passes through FE-3, a 2-in, turbine meter. On leaving FE-3, flow enters flow lines: a 1/2-in. line used to meter very low flow rates and a 3/4 in. flooding line used for the higher flows experienced during reflood. The entire inlet flow manifold was constructed of high-pressure stainless steel tubing. Volumetric flow rates in the low-flow 1/2 in. inlet line were measured by FE-18A (a low-flow orifice meter), FE-250m and FE-260 (1/2 in. turbine meters). The two inlet lines converge at the injection manifold from which fluid passes directly into the lower plenum. Fluid does not pass through a downcomer. Flow proceeds upward through the heated bundle and exits through the bundle outlet spool piece. Spool piece measurements include pressure, temperature, density, volumetric flow, and momentum flux. At very low outlet flow rates, the volumetric flow was measured by a bank of low-flow orifice meters downstream of the outlet spool piece. On leaving the orifice manifold, flow passes through a heat exchanger and returned to the pump inlet.

System pressure was controlled via the loop pressurizer. The pressurizer was partially filled with subcooled water, and nitrogen cover gas was used to control pressure. By filling or venting nitrogen, the system pressure could be controlled easier than by the conventional flashing and condensation of saturated water and steam.

Flow was injected directly into the lower plenum and did not pass through a downcomer. The shroud plenum annulus (Figure 5.2.1.4-2) was used in earlier THTF testing as an internal downcomer but was isolated from the primary flow circuit in the present tests. The shroud plenum annulus pressure was equalized with the system pressure by connecting the bottom of the annulus region to the pressurizer surge line and the top of the annulus to the test section outlet. The line between the annulus and pressurizer was opened, and the line between the annulus and test section outlet was closed during the initial boiloff phase of steady-state testing. This allowed any vapor generated by boiling in the annulus to displace liquid into the pressurizer.

Because the displacement of liquid will cause the mixture levels in the downcomer and bundle to equalize, it was advantageous to install a line between the pressurizer and downcomer. However, once mixture levels had equalized, it was no longer advantageous to leave this line open because the steam flow through the outlet causes a substantial pressure drop between the test section and pressurizer. If the annulus was in communication with the pressurizer, then a large pressure difference between the test section bundle and downcomer would exist. This large pressure difference would cause substantial leakage from the bundle to the annulus. To minimize this leakage, the line between the pressurizer and annulus was closed after mixture level equalization had taken place. To maintain pressure equalization, the shroud bypass line, which connects the top of the shroud annulus to the test outlet, was opened (Figure 5.2.1.4-1). As a final step, to minimize the possibility of leakage from bundle to annulus, the shroud bypass line was closed shortly before data were taken. This completely isolated the annulus from the rest of the system, thus providing the least opportunity for undesired leakage.

b. Bundle Description

The THTF test section contains a 64-rod, electrically heated, rod bundle (Figure 5.2.1.4-3). The four unheated rods were designed to represent control-rod guide tubes in a nuclear fuel assembly. Rod diameter and pitch are typical of a 17 x 17 PWR fuel assembly.

Figure 5.2.1.4-4 is an axial profile of the THTF bundle that illustrates the positions of spacer grids and FRS thermocouples. The heated length is 3.66 m (12 ft), and a total of 25 FRS thermocouple levels are distributed 3.66 m (12 ft), and a total of 25 FRS thermocouple levels are distributed over that length. An FRS thermocouple level refers to an axial location where a selected number of FRSs are instrumented with sheath thermocouples. The upper third of the bundle is more heavily instrumented than the lower portion. For most tests the two-phase mixture level is in the top third of the heated length. The additional instrumentation in the top third of the bundle is used to better define the mixture level position. In addition, the increased instrumentation near the spacer grids can be used to ascertain to what extent spacer grids affect the heat transfer.

An FRS cross section (Figure 5.2.1.4-5) shows that each FRS has 12 sheaths and 4 center thermocouples. The thermocouples are either 0.05 or 0.04 cm (0.020 or 0.016 in.) in diameter. The thermocouples may have their junctions at any of the 25 axial levels. Each rod may have from zero to three sheath thermocouple junctions at any particular axial level. When an FRS has three junctions at the same level, they are spaced evenly around the rod (i.e., 120° apart).

Table 5.2.1.4-2 describes the FRS sheath thermocouple naming convention.

In addition to the FRS thermometry, fluid temperature is measured at a number of locations. In-bundle fluid temperature measurement uses four different types of fluid thermocouples. The first type, thermocouple-array rod thermocouples, are exposed* fluid thermocouples that project from unheated rods. (*"Exposed" in this context does not mean that the thermocouple junction actually contacts the fluid. The junction is encased in a stainless steel sheath but does not have a droplet shield.)

Thermocouple-array rod thermocouples are installed at 1.83, 2.41, 3.02, and 3.62 m (79, 95, 119, and 142.5 in.) above the beginning of the heated length (BOHL). The second type, shroud wall fluid thermocouples, are exposed fluid thermocouples that project from the bundle shroud into subchannels adjacent to the shroud. Shroud-box fluid thermocouples are installed at 0.38, 0.64, 1.22, 1.83, 2.41, 3.02, and 3.61 m (15, 25, 48, 72, 95, 119, and 142 in.) above BOHL. The third type, spacer-grid fluid thermocouples, are exposed fluid thermocouples that project slightly upstream of each spacer grid. The fourth and final type, subchannel thermocouple-rake thermocouples, are attached to a thermocouple rake located several inches above the end of the heated length. They are used in measuring the cross-sectional temperature distribution. Nomenclature and locations for fluid thermocouples are summarized in Table 5.2.1.4-3.

As previously noted, the THTF bundle is surrounded by a bundle shroud box (Figure 5.2.1.4-2). The shroud-box walls have been instrumented with thermocouples to estimate bundle heat losses. A typical instrumentation site consists of a pair of thermocouples embedded in the shroud-box wall (Figure 5.2.1.4-6). Since the thermocouples are separated, the temperature gradient can be calculated and the bundle heat losses estimated. Figure 5.2.1.4-7 shows the axial locations where the shroud-box walls have been instrumented.

c. Differential Pressure Instrumentation

Data were obtained through the use of "stacked" differential pressure cells. Figure 5.2.1.4-8 illustrates the differential pressure measurement sites. Cells PdE-180 through 188 are ranged from 0.0 to 0.64m (0.0 to 25.0 in.) of standard water, and PdE-189 is ranged from 0.0 to 0.76m (0.0 to 30.0 in.) of water. Spacing of the cells varies from 0.75 to 0.22m (29.4 to 8.5 in.).

(2) Scaling

Thermal Hydraulic Test Facility (THTF) has a 64-rod, full-length rod bundle heat transfer loop. Rod diameter and pitch are typical of a 17x17 PWR fuel assembly. The scaling of the facility is

fine since it is full length and prototypical dimensions.

(3) Range of Conditions

Table 5.2.1.4-4 summarizes main parameters for the tests. Average inlet flooding velocities ranged from a low of 5.92 to a high of 12.2 cm/s (2.33 to 4.82 in./s). Initial system pressure ranged from 3.88 to 7.53 MPa (563 to 1.92 psia). Linear power ranged from 0.994 to 2.16 kW/m (0.304 to 0.659 kW/ft).

Initial loop conditions were established so that the bundle was in a quasi-steady-state partially uncovered configuration. Flow-power matching was such that ~22 to 34 % of the bundle heated length would uncover. At ~20 s before initiation of reflood, a data scan started. The scanning frequency was ten points per second per instrument. At ~0.0 s, the inlet flooding valve was opened to a predetermined setpoint, and the reflood commenced.

Throughout the reflood, liquid flowed to the test section through both the 3/4-in. flooding line and the 1/2-in. steady-state flow line. Cover gas was injected into the pressurizer to maintain loop pressure high enough to prevent pump cavitation. Bundle power remained constant until completion of core recovery.

A summary of initial conditions present in all reflood tests is shown in Table 5.2.1.4-5. The bundle mass flows were calculated from measurements of the inlet volumetric flow and the inlet density as determined from test section pressure and inlet fluid temperature.

(4) Data to be compared

In view of bundle quenching behavior study, the following parameters are to be compared.

- FRS Temperature
- Fluid Temperature
- Collapsed Liquid Level in the Bundle
- Quench Level

Quench is defined the time when precursory cooling ends and a precipitous drop in surface temperature begins.

Collapsed liquid level ZCLL is defined as the elevation in the test section to which the liquid free surface would fall if boiling ceased. Thus:

$$Z_{CLL} = Z_{SAT} + \int_{z=Z_{SAT}}^{z=Z_M} [1 - \alpha(z)] dz ,$$

where

$\alpha(Z)$ - void fraction as a function of height Z , the void profile was obtained through the use of stacked differential pressure cells. Figure 5.2.1.4-8 illustrates the differential pressure measurement sites.

Z_{SAT} - height above the BOHL at which saturated boiling begins.

Z_M - two-phase mixture level. The uppermost level along the heated length where liquid is the continuous phase.

(5) Data uncertainties

Results of instrument uncertainty analysis for the THTF, reported in Reference 5.2.1.4-2, ~~is~~ are summarized in Table 5.2.1.4-6.

FRS and fluid temperature are measured by TE-300, TE-188, and TE-189 series thermocouples. Their range and error are 273-1309K(32-1900F) and 3.7K (6.7°F) for “ < 623K (662°F)” and 1% reading for “ >623K(662°F)”.

Test section pressure is defined as the pressure measured in the upper plenum by PE-201(strain gage pressure cell; Figure 5.2.1.4-1). Its range and error are 20, 700 kPa (3000psi) and 1%full-scale value, respectively.

There is a description in the data report Reference 5.2.1.4-1 that the inlet flow is measured upstream of the inlet manifold, and the only flow meter corresponds to this description in Figure 5.2.1.4-1 is FE-3(instrument spool piece turbine flowmeter). Its range and error are $\pm 1.3E-3$ m³/s (± 22 gpm) or $\pm 1.4E-2$ m³/s (± 225 gpm) and 4.1% reading, respectively.

Differential pressure is measured by PDE-180 series capacitive differential pressure cells. Their range and error are 37.5kPa (150 in.) and 1.9% full-scale value, 6.25 kPa (25 in.) and 1.1%full-scale value, and 7.5kPa (30 in.) and 1.1% full-scale value.

(6) Distortion

No information is found in the references.

(7) References

- 5.2.1.4-1 C. R. Hyman, T. M. Anklam, T. D. White, Experimental Investigations of Bundle Boiloff and Reflood under High-Pressure Low Heat Flux Conditions, NUREG/CR-2455, ORNL-5846
- 5.2.1.4-2 D. K. Felde et al., "Facility Description – THTF MOD3 ORNL PWR BDHT Separate-Effects Program, "NUREG/CR-2640, ORNL/TM-7842, September 1982

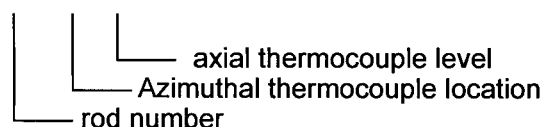
Table 5.2.1.4-1 THTF Design Summary (Ref. 5.2.1.4-1)

Parameter	Quantity
Design pressure [MPa (psia)]	17.2 (2500)
Pump capacity [m ³ /s (gpm)]	0.044 (700)
Heated length [m (ft)]	3.66 (12.0)
Power profile	Flat
FRS diameter [cm (in.)]	0.95 (0.374)
Lattice	Square
Pitch [cm (in.)]	1.27 (0.501)
Number of heated rods	60
Number of unheated rods	4
Unheated rod diameter [cm (in.)]	1.02 (0.40)
Bundle shroud configuration	Square
Bundle shroud thickness 2 sides [cm (in.)]	2.54 (1.0)
2 sides [cm (in.)]	1.91 (0.75)
Number of grid spacers	7

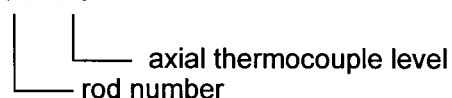
Table 5.2.1.4-2 Rod-Sheath Thermocouple Designations (Ref. 5.2.1.4-1)

Rod-sheath thermocouples are designed according to one of the following two schemes:

1. TE-3 17 A D



2. TE-3 54 F8



Thus, this first designation refers to the sheath thermocouple in rod 17 at level D, azimuthal location A. If the thermocouple designation ends with a number, this designation refers to the sheath thermocouple in rod 54 at level F8.

Table 5.2.1.4-3 Nomenclature for Thermocouples in THTF (1/4) ^(Ref. 5.2.1.4-2)**Subchannel Thermocouples**

The subchannel thermocouple rake is located ~2.3 cm above the upper end of the heated section. (Figure 5.2.1.4-8) The naming convention takes the following form:

TE-12nn,

Where

nn = a number between 01-81 that equals the number of the subchannel in which it is located. (Figure 5.2.1.4-3.)

Table 5.2.1.4-3 Nomenclature for Thermocouples in THTF (2/4) (Ref. 5.2.1.4-2)Spacer-Grid Thermocouples

The spacer-grid fluid thermocouples are attached to core grids No. 2-7. (Figure 5.2.1.4-4. Six grid locations are indicated.) The naming convention takes the following form:

TE-29na,

where

n = a number between 1-6 designating the spacer-grid level as follows:

<u>Number</u>	<u>Between thermocouple levels</u>	<u>spacer-grid No.</u>
1	A & B	2
2	B & C	3
3	C & D	4
4	D & E	5
5	E & F	6
6	F & G	7,

and a = a letter "A-F" designating the subchannel into which the thermocouple projecting, as follows(Figure 5.2.1.4-3.):

<u>Letter</u>	<u>Subchannel No.</u>
A	32
B	43
C	57
D	70
E	17
F	38

Table 5.2.1.4-3 Nomenclature for Thermocouples in THTF (3/4) (Ref. 5.2.1.4-2)

Shroud-box Thermocouples

Shroud-box thermocouples protrude through the shroud wall into the fluid in the wall subchannels. The naming convention has the following form:

TE-18na,

where

n = a number 1-7 designating the level of the thermocouple in the shroud box as follows(Figure 5.2.1.4-4.)

<u>Number</u>	<u>Thermocouple levels</u>
1	A
2	B
3	C
4	D
5	E
6	F
7	G,

and

a = a letter designating the side of the box through which the thermocouple protrudes, N, E, S, or W. (Figure 5.2.1.4-3.)

Table 5.2.1.4-3 Nomenclature for Thermocouples in THTF (4/4) ^(Ref. 5.2.1.4-2)Thermocouple-Array Rod Thermocouples

The thermocouple-array rods occupied grid positions 19 and 36. (Figure 5.2.1.4-3). Each array rod contains 14 thermocouples, and, at each axial level in the bundle where there is a primary FRS thermocouple level, two of these thermocouples protrude from the rod into the fluid. The naming convention has the following form:

TE-18nal,

where

n = the number 8 or 9 designating in which grid position the thermocouple array rod is located such that 8 denotes grid position 19 and 9 denotes grid position 36(Figure 5.2.1.4-3.);

a = a letter A and B designating which of two subchannels associated with that rod the thermocouple protrudes into (Figure 5.2.1.4-3.):

<u>Rod grid position</u>	<u>(a =) A subchannel</u>	<u>(a =) B subchannel</u>
(n=8→) 19	22	30
(n=9→) 36	41	49

l = the thermocouple level A-G. (same as FRS thermocouple level designation. Figure 5.2.1.4-4)

Table 5.2.1.4-4 High-Pressure Reflood Test Matrix^(Ref. 5.2.1.4-1)

Test	Series	Initial pressure [MPa (psia)]		Flooding Velocity [cm/s (in./s)]		Linear heat rate [kW/m (kW/ft)]	
3.0209.10O	II	3.88	(563)	12.2	(4.8)	2.03	(0.62)
3.0209.10P	II	4.28	(621)	9.2	(3.6)	0.997	(0.30)
3.0209.10Q	II	3.95	(573)	5.9	(2.3)	1.02	(0.31)
3.0209.10R	II	7.34	(1065)	11.7	(4.6)	2.16	(0.66)
3.0209.10S	II	7.53	(1092)	10.2	(4.0)	1.38	(0.42)

Table 5.2.1.4-5 Summary of Initial Conditions for High-Pressure Reflood Tests^(Ref. 5.2.1.4-1)

Test	Pressure		Linear heat rate		Bundle mass flow	
	[MPa (psia)]		[kW/m (kW/ft)]		[kg/s (1bm/s)]	
3.09.10O	3.88	(563)	2.03	(0.618)	0.156	(0.343)
3.09.10P	4.28	(621)	1.00	(0.304)	0.075	(0.164)
3.09.10Q	3.95	(573)	1.02	(0.311)	0.078	(0.172)
3.09.10R	7.34	(1065)	2.16	(0.659)	0.170	(0.373)
3.09.10S	7.53	(1092)	1.38	(0.421)	0.085	(0.188)
	Inlet subcooling		Outlet superheat		Maximum	FRS
	[K (°F)]		[K (°F)]		temperature	[K (°F)]
3.09.10O	74	(0.343)	198	(356)	1055	(1440)
3.09.10P	65	(0.164)	209	(377)	1089	(1500)
3.09.10Q	66	(0.172)	168	(303)	1027	(1390)
3.09.10R	113	(0.373)	133	(239)	1033	(1400)
3.09.10S	105	(0.188)	164	(295)	1077	(1480)

Table 5.2.1.4-6 Instrument Uncertainty Analysis For The THTF Loop
Summary of Results ^(Ref. 5.2.1.4-2)

Two standard deviation uncertainty bands are described for critical instrumentation in the Thermal Hydraulic Test Facility (THTF). The analyzed instruments and their minimum, steady-state, 2σ error bands [root sum square (RSS), 95% confidence interval] include:

1.	Turbine flowmeter	4.1 % reading
2.	Gamma densitometer	10.4 % FS*
3.	Strain gage pressure cell	1.0% FS*
4.	Differential pressure cell	2.0% FS* min to 9.9% FS* max
5.	Thermocouple	3.7°C min to 10.3°C max
6.	Rod power instrumentation	1.1% reading
7.	Strain gage drag disk	56% reading below 10% FS* 19% reading above 10% FS*

*Full-scale values

ORNL-DWG 81-7837R ETD

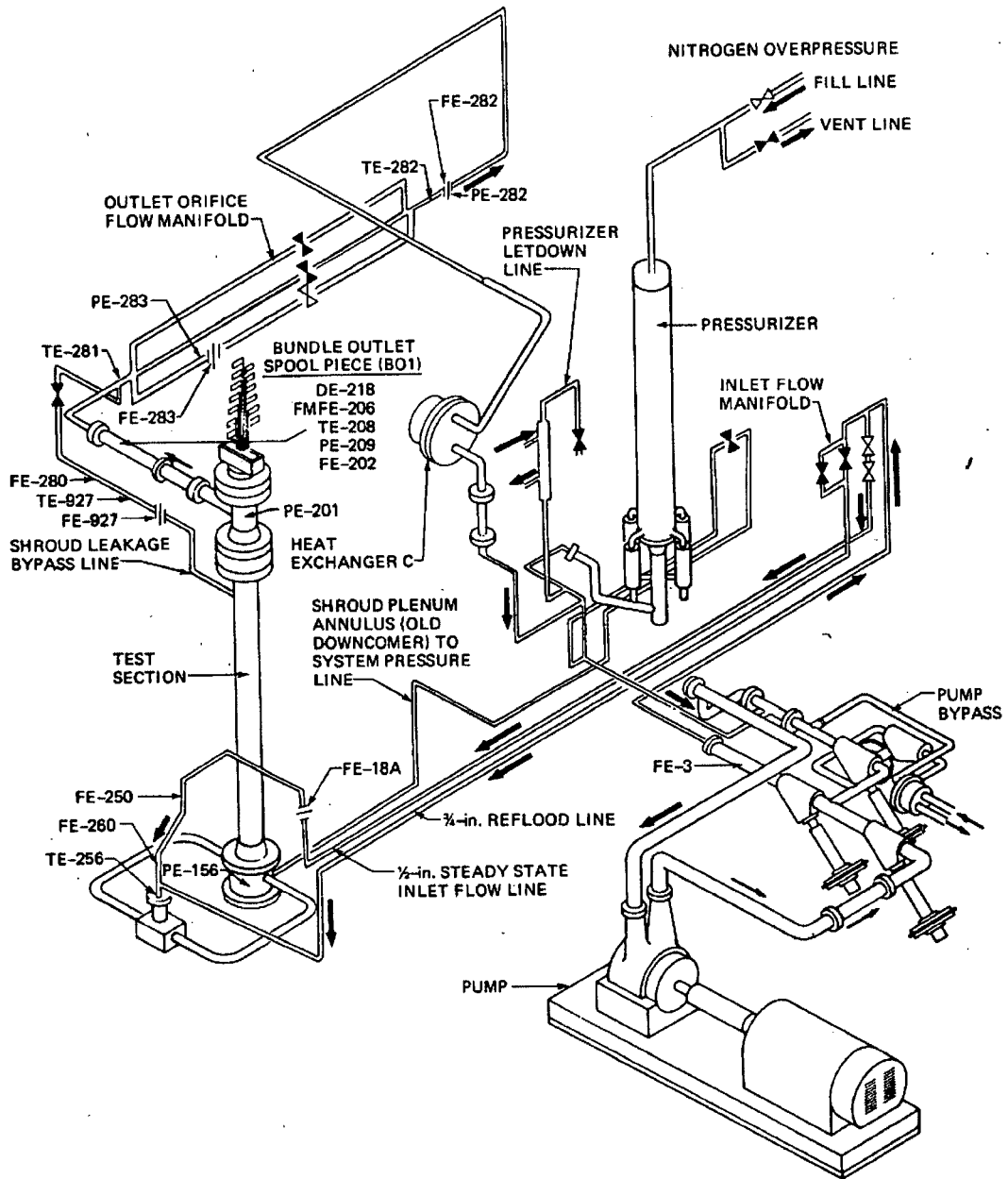


Figure 5.2.1.4-1 THTF in Small-break Test Configuration.

ORNL-DWG 82-4875 ETD

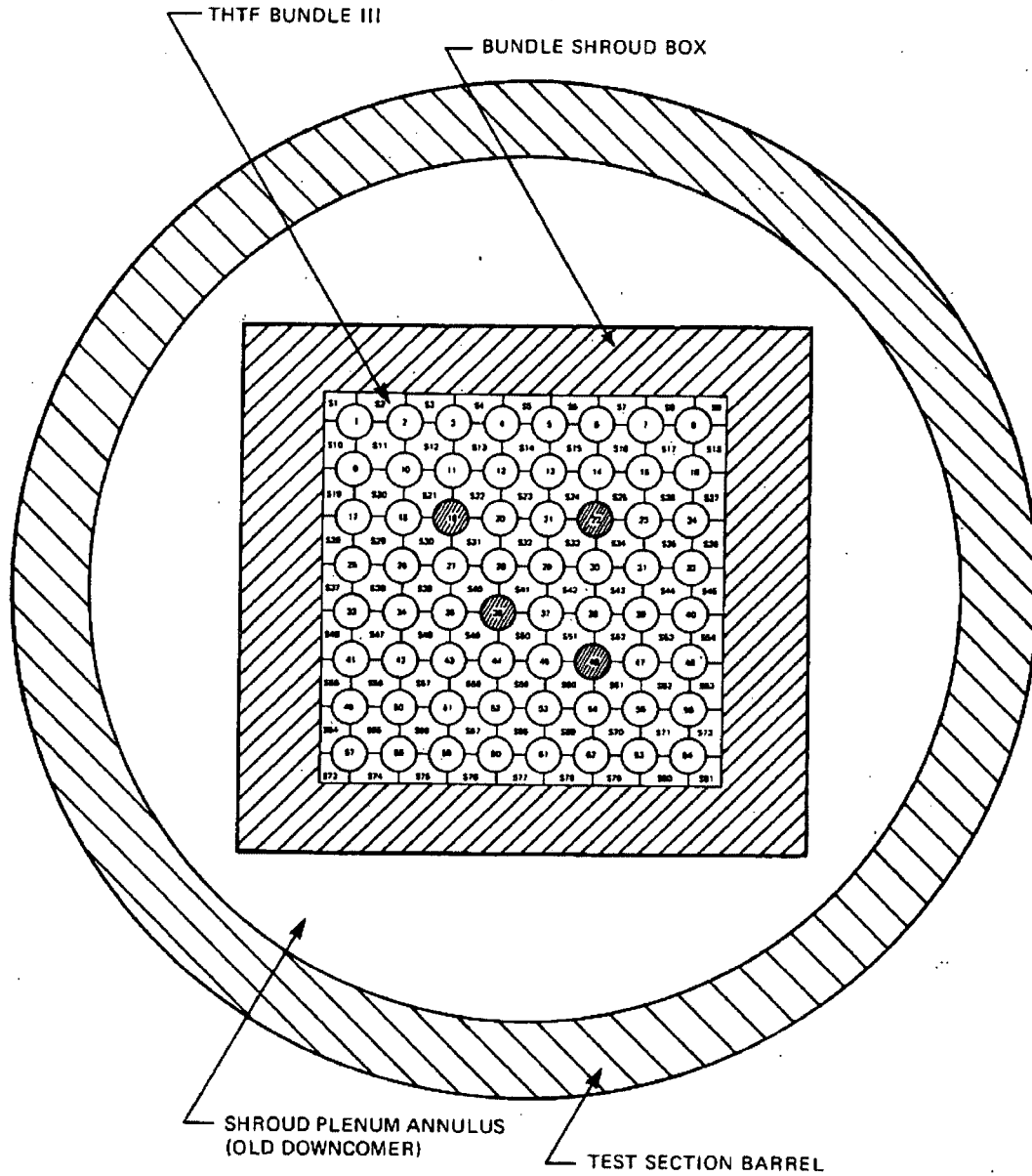


Figure 5.2.1.4-2 Cross Section of THTF Test Section

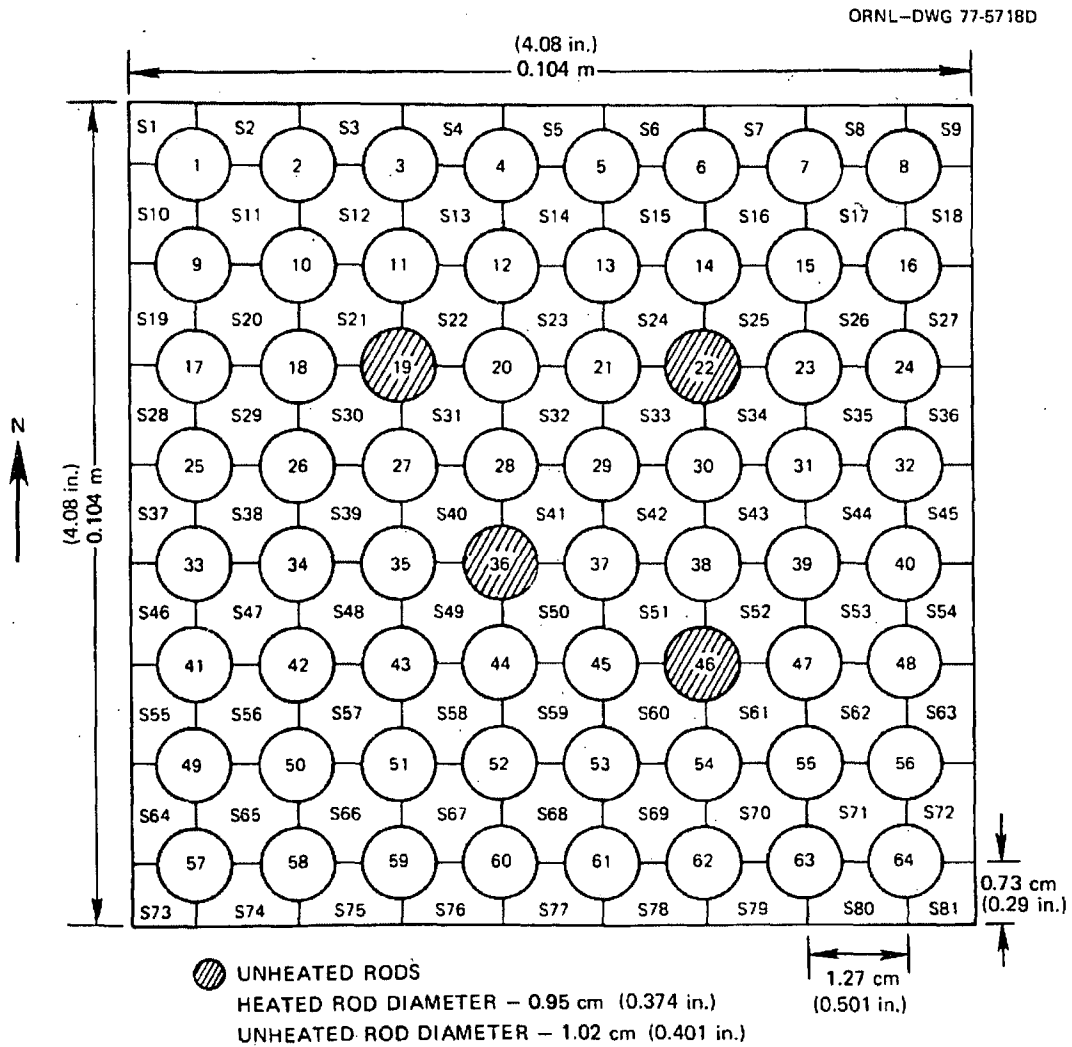


Figure 5.2.1.4-3 Cross Section of THTF

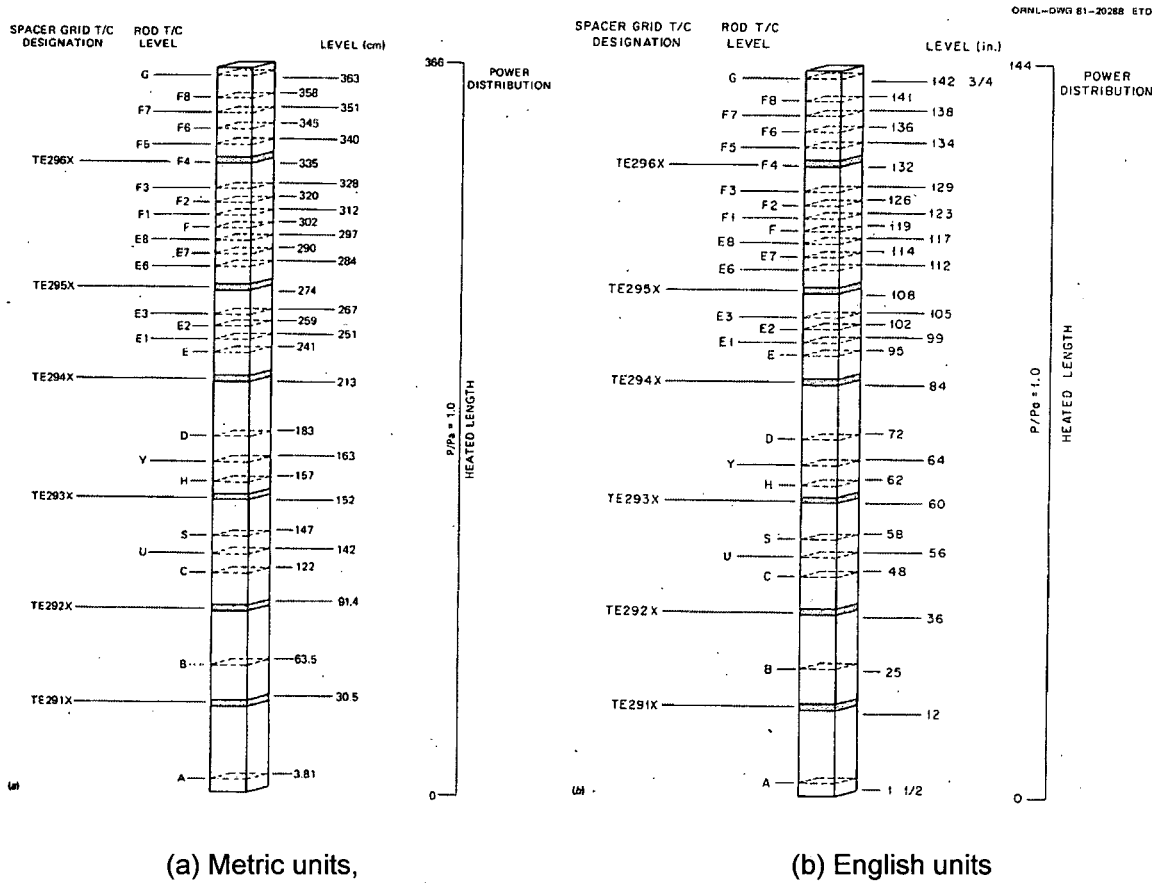


Figure 5.2.1.4-4 Axial Location of Spacer Grids and RRS Thermocouples.

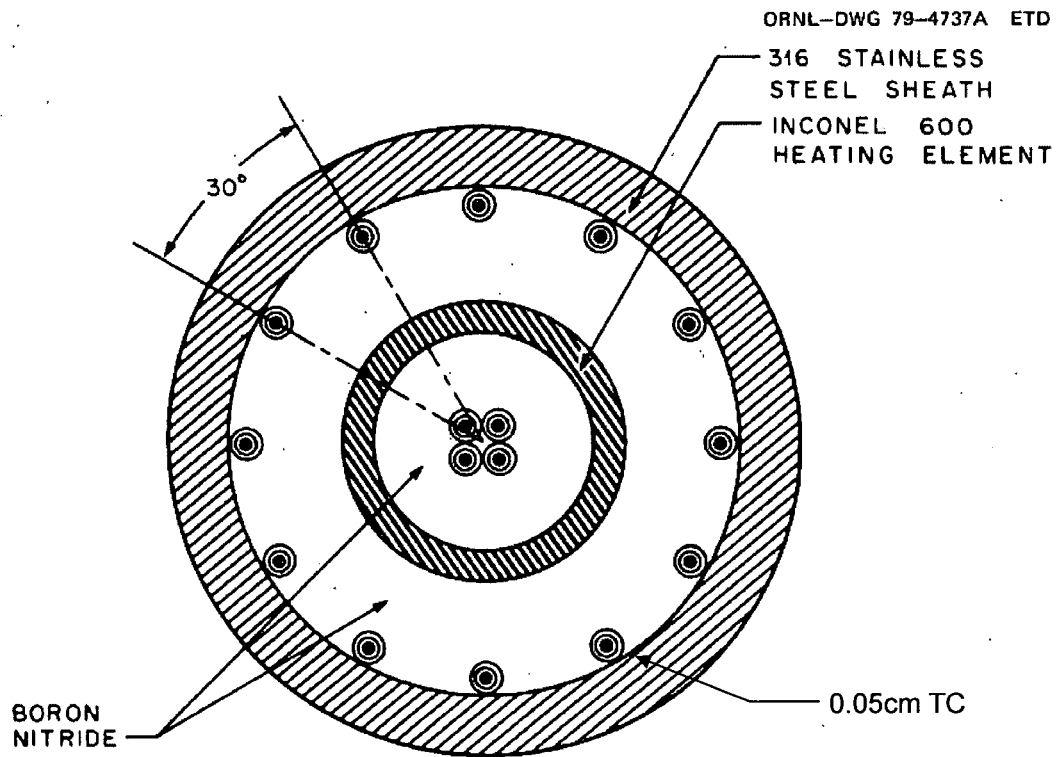


Figure 5.2.1.4-5 Simplified Cross Section of a Typical FRS

ORNL-DWG 81-8031 ETD

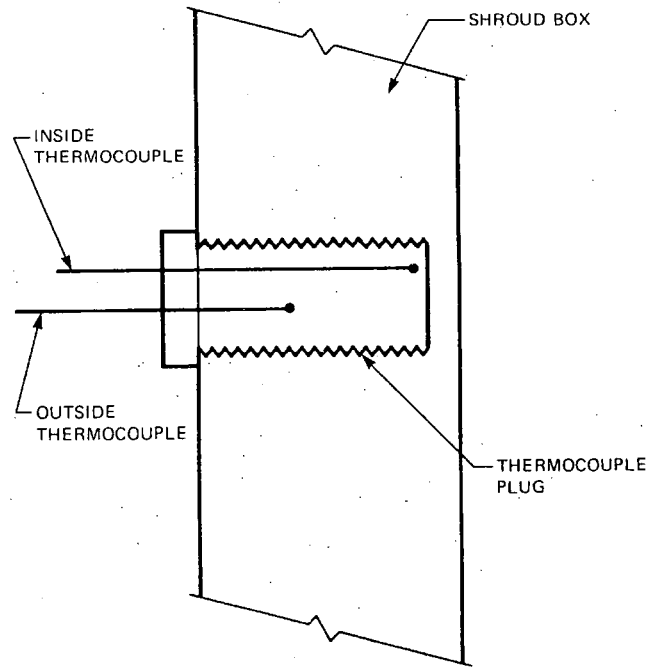


Figure 5.2.1.4-6 Shroud-Wall Thermocouple Configuration

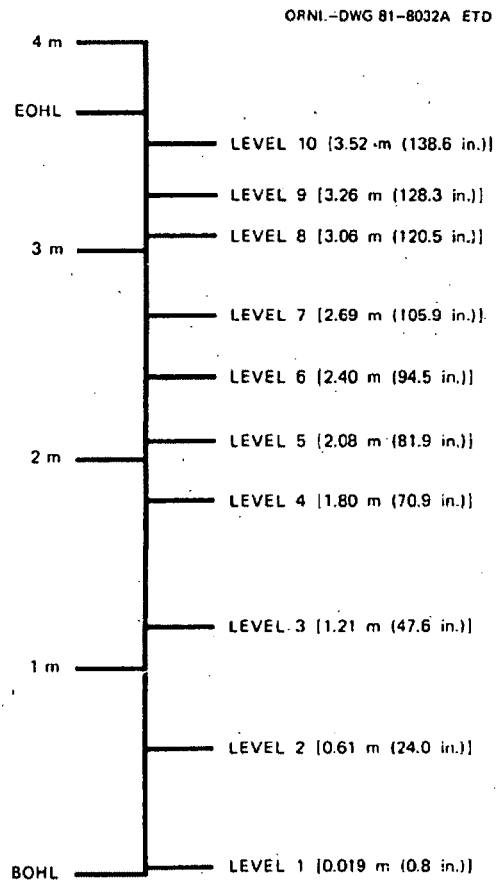


Figure 5.2.1.4-7 Axial Location of Shroud-Wall Thermometry

ORNL-DWG 81-20290 ETD

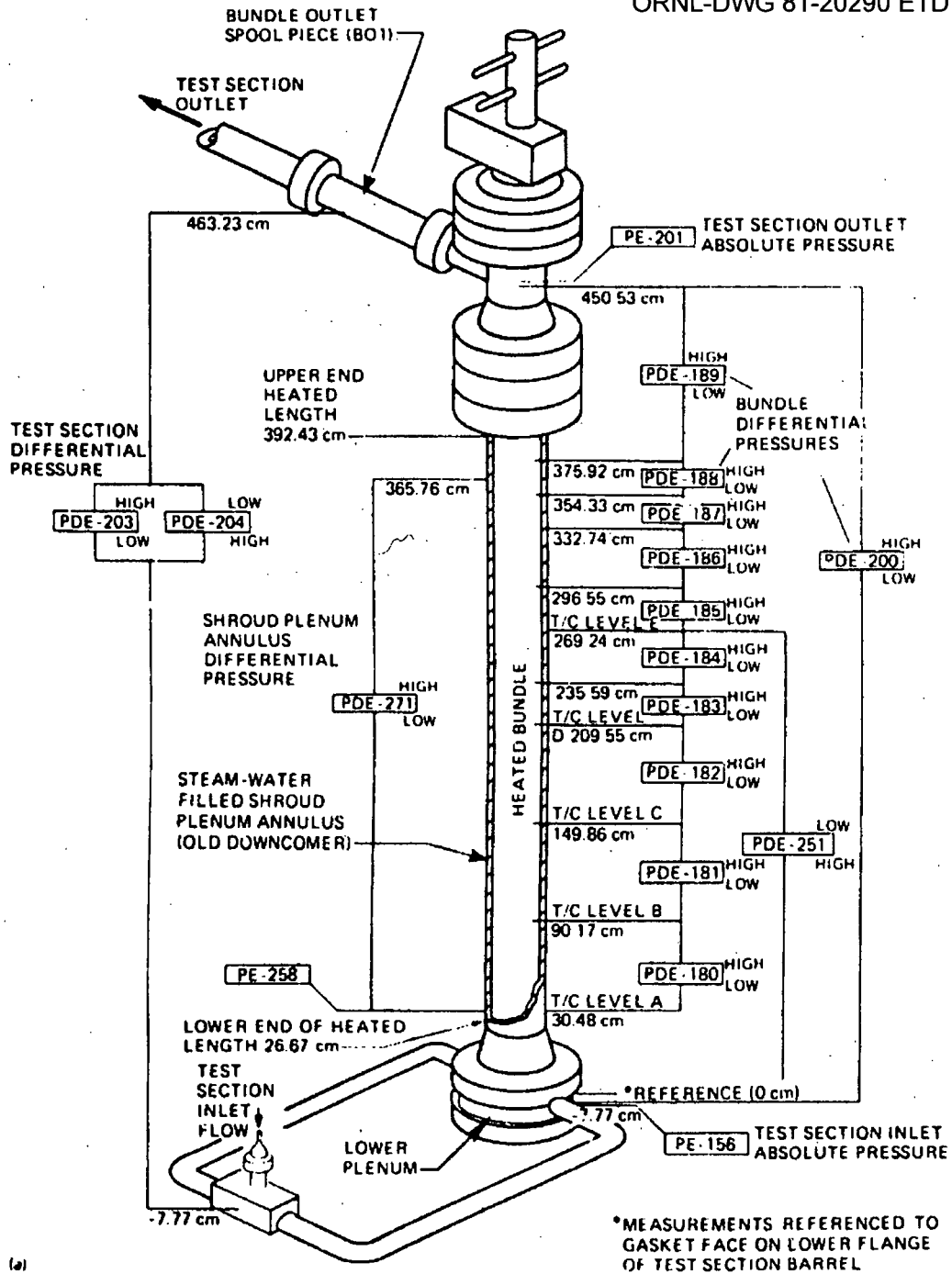


Figure 5.2.1.4-8 THTF In-Bundle Pressure Instrumentation

5.2.1.5 UPTF Full-scale SG Plenum CCFL Test

(1) Facility Design

UPTF simulates a 4-loop German PWR which is similar to a US 4-loop Westinghouse PWR (Figure 5.2.1.5-1). A full-size reactor vessel and piping (four hot legs and four cold legs) are included in UPTF. ECC can be injected in the hot and/or cold legs of all four loops, or in the downcomer. One of the four loops contains break valves which are piped to a large containment simulator tank. The four steam generators are simulated by four steam/water separators and the four reactor coolant pumps are simulated by four passive, adjustable resistances. The reactor vessel upper plenum internals and top-of-core are full-scale replicas. The core is simulated by a steam/water injection system with 193 nozzles, one for each active fuel assembly which would be present in a PWR. UPTF was originally designed as an integral system test facility covering the end-of-blowdown, refill and reflood phases of a large break LOCA. As discussed in Reference 5.2.1.5-1, it has also proven very useful as a full-scale separate effects facility covering both large and small break LOCA phenomena. UPTF can operate at up to 18 bar (260 psia) pressure and 220 °C (428 °F) temperature.

Each UPTF hot leg (Figure 5.2.1.5-2) is 750 mm (29.5 in) inner diameter and has a total lateral run from the vessel to the steam generator simulator of about 8 m (26 ft). A 50° riser section rises 0.91 m (3.0 ft) at the end of the hot leg attached to the steam generator simulator. In the horizontal section of hot leg, an internal ECC injection pipe ("Hutze") is located along the bottom edge of the pipe (Figure 5.2.1.5-3). There was no injection through the Hutze in the Counter-Current Flow Limitation (CCFL) tests, i.e., it is a dead space in the hot leg. The Hutze blocks an area of 0.0444 m² (0.478 ft²), about 10 percent of the total pipe area. A Hutze is present in German PWRs but not in US PWRs. Table 5.2.1.5-1 compares UPTF hot leg configuration with that of typical Westinghouse and CE US PWRs. The information above was obtained in Reference 5.2.1.5-1.

(2) Scaling

Since UPTF hot leg separate effect test is full scale model, scaling is not an issue.

(3) Range of Conditions

The test was run using only the broken loop hot leg of the UPTF. The test was performed as several steady phases, each consisting of steam injection into the primary vessel which flowed out the broken loop hot leg, and saturated water injection in the steam generator simulator plenum which could either flow back down the hot leg toward the vessel or out of the system

through the steam generator simulator (Figure 5.2.1.5-4). Six separate steady flows were obtained at 3 bar (44 psia) system pressure and 10 flows were obtained at 15 bar (218 psia) system pressure. In all cases water flow was established prior to steam flow. The intent of obtaining several flows at each pressure was to "map out" the CCFL boundary. Also, one of the flows at 15 bar simulated conditions in a Westinghouse 4-loop PWR during the reflux condensation mode, which can occur during an SBLOCA. The information above was obtained in Reference 5.2.1.5-1.

(4) Data to be compared

There is a comparison between the experimental results and Wallis correlation in Reference 5.2.1.5-1. In the Wallis correlation, which is a j^* /void fraction correlation, the comparison is on Figure 5.2.1.5-5. The results of the comparisons shown on Figures 5.2.1.5-5 are as follows:

Close agreement is obtained between the UPTF data and the Wallis correlation which is based on void fraction rather than liquid flow. This indicates that the basic approach of this correlation (once again, a j^* correlation) appears correct for scaling, but that implementing this model to calculate liquid flows is dependent on knowing an accurate void fraction.

Following correlation was obtained using the Wallis correlations:

$$\sqrt{j_f^*} = 0.7955 - 1.1564\sqrt{j_g^*} \quad (5.2.1.5-1)$$

The data on a dimensionless j^* were calculated, where

$$j_g^* = \frac{M_g \sqrt{\rho_g}}{\rho_g A \sqrt{(\rho_f - \rho_g)gD_h}} \quad (5.2.1.5-2)$$

$$j_f^* = \frac{M_f \sqrt{\rho_f}}{\rho_f A \sqrt{(\rho_f - \rho_g)gD_h}} \quad (5.2.1.5-3)$$

Where M = mass flow rate of gas or liquid

A = area

ρ = density

g = gravity

D_h = hydraulic diameter

The line drawn through the data is the "best-fit" experimental correlation to the UPTF data.

The results of this test provided direct demonstration that there is significant margin against hot leg CCFL during the reflux condensation phase of an SBLOCA. This is shown by the fact that the "typical" point is substantially below the CCFL boundary. This point was chosen based on conservative assumptions such as relatively high power and one steam generator inactive, etc. Accordingly, this result provides direct and convincing evidence that substantial margin exists.

Measured hot leg level and void fraction for all of the tests are plotted against j_g^* , the dimensionless gas flow. These data are from a three-beam gamma densitometer located just on the vessel side of the hot leg riser bend. There is no "Hutze" obstructing the bottom of the hot leg in this short section of hot leg. The data clearly indicated a stratified regime and show significant water presence in this region of the hot leg. These data appear to show that CCFL is being controlled by the hot leg (i.e., CCFL is not occurring in the riser or steam generator simulator), since water is not absent from the hot leg when there is zero net penetration to the vessel.

(5) Data Uncertainties

There is no available information in Reference 5.2.1.5-1.

(6) Distortion

There is no available information about heat loss in Reference 5.2.1.5-1.

(7) References

- 5.2.1.5-1 P. S. Damerell, N. E. Ehrich, K. A. Wolfe, "Use of Full-Scale UPTF Data to Evaluate Scaling of Downcomer (ECC Bypass) and Hot Leg Two-Phase Flow Phenomena," NUREG/CP-0091 Vol.4, CONF-8710111-Vol.4.

Table 5.2.1.5-1 Comparison of UPTF Hot Leg Configuration with Typical Westinghouse and Combustion Engineering (CE) PWR's

Parameter	UPTF Value	Westinghouse PWR Value	CE PWR Value
Diameter, m (in)	0.750(29.5)	0.737(29)	1.07(42)
Hydraulic Diameter, m (in)	0.639(25.2)	0.737(29)	1.07(42)
Flow Area, m ² (ft ²)	0.397(4.28)*	0.427(4.59)	0.894(9.62)

*0.4418m² within diameter minus 0.0444m² blocked by "Hutze".
(From NUREG/CP-0091 Vol.4, CONF-8710111-Vol.4)

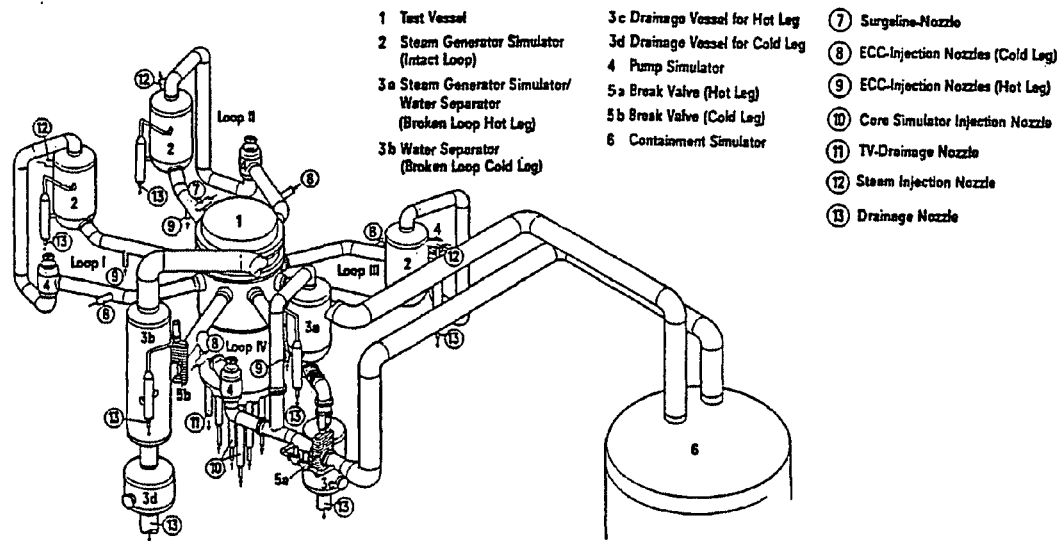
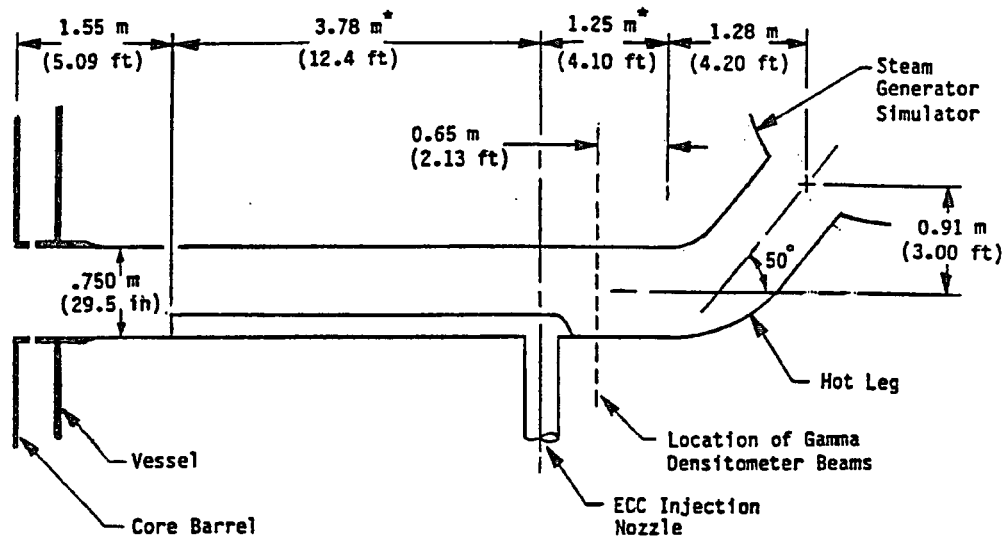


Figure 5.2.1.5-1 Overall View of UPTF
 (From NUREG/CP-0091 Vol.4, CONF-8710111-Vol.4)



* Note: These dimensions are for the UPTF broken loop hot leg, which was the only hot leg used in the Hot Leg Separate Effects Test. In the intact loops, these two dimensions are slightly larger (3.86 m and 1.34 m).

Figure 5.2.1.5-2 UPTF Hot Leg Configuration
(From NUREG/CP-0091 Vol.4, CONF-8710111-Vol.4)

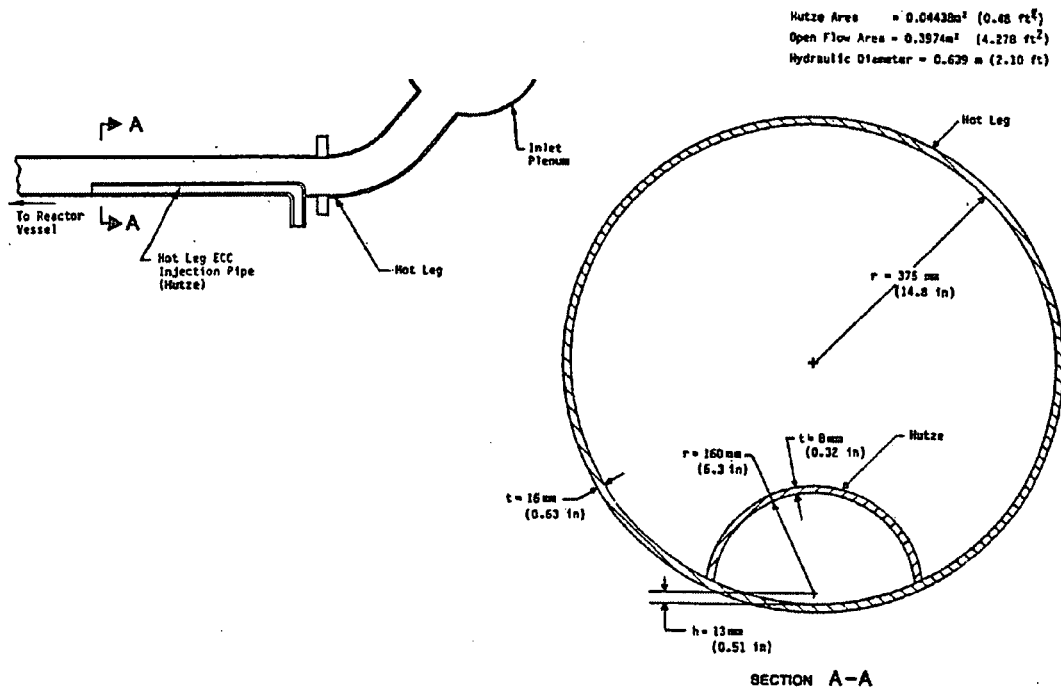


Figure 5.2.1.5-3 Configuration of International ECC Injection Pipe (Hutze) in UPTF Hot Leg
 (From NUREG/CP-0091 Vol.4, CONF-8710111-Vol.4)

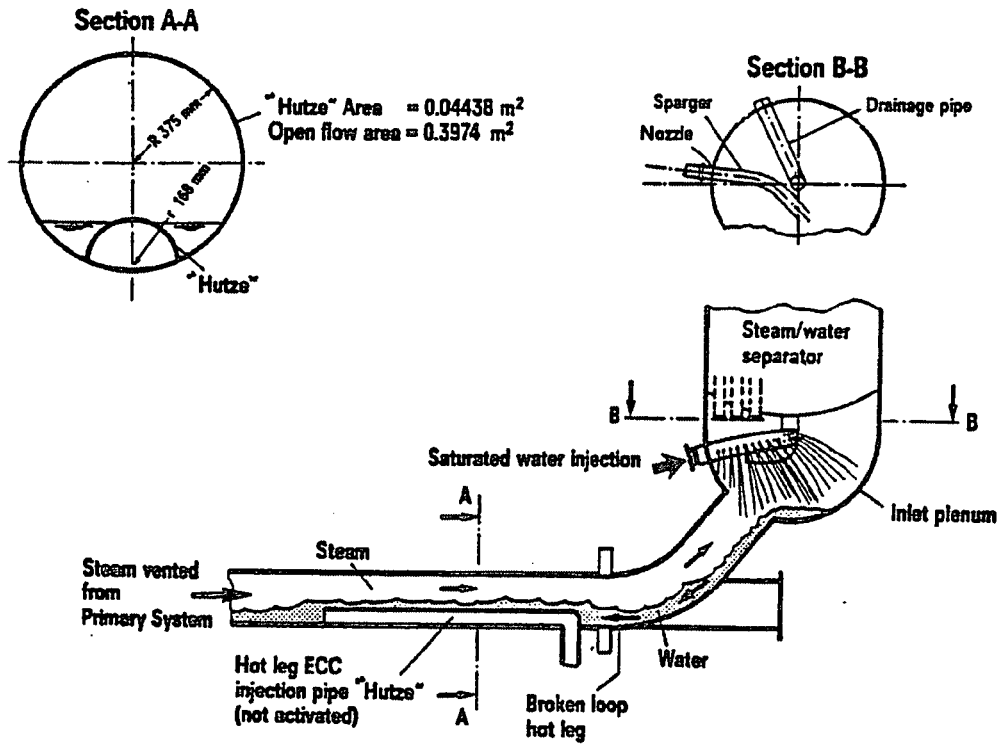


Figure 5.2.1.5-4 UPTF Hot Leg Separate Effect Test Overall Flow Conditions
 (From NUREG/CP-0091 Vol.4, CONF-8710111-Vol.4)

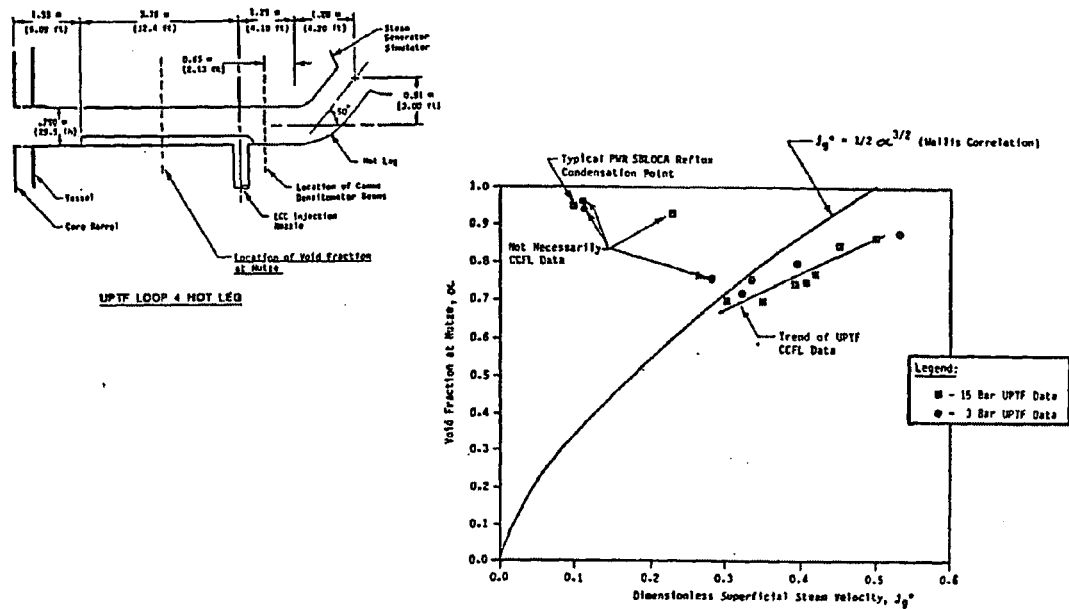


Figure 5.2.1.5-5 UPTF Hot Leg Separate Effects Test Comparison of UPTF Hot Leg Void Fractions to Wallis Correlation

(From NUREG/CP-0091 Vol.4, CONF-8710111-Vol.4)

5.2.1.6 Dukler Air-Water Flooding test

(1) Facility Design

The Information shown here is from Reference 5.2.1.6-1.

a. General Description of System

The flow system consisted of a 5-foot length of 2-inch I.D. plexiglass pipe used as a claming section for the incoming air, a 12-inch I.D. section of plexiglass pipe for both introducing the air to the test section and removing the falling liquid film, a 13-foot test section consisting of 2-inch plexiglass pipe, four pressure and film thickness measuring stations and a liquid entrance device, and an exit section for removing the air, entrainment and the liquid film flowing up. The entire system was supported by a unistrut structure and all air and water connections were by flexible tygon tubing to eliminate external vibrations. A schematic of the flow loop is shown in Figure 5.2.1.6-1.

b. Air-Inlet Section

A schematic drawing of the entrance section is shown in Figure 5.2.1.6-2. The air inlet section was designed to remove the liquid film falling counter to the air flow and to provide a smooth entrance for the air. The entrance consisted of a 12-inch I.D. section of plexiglass pipe containing a smooth flange at the top connecting to the test section and at the bottom a 2-inch I.D. section of pipe which could be moved vertically various distances from the smooth flange. In order to prevent undesirable pressure fluctuation in the entrance the liquid level had to be maintained constant. This was accomplished through the use of a liquid-level control system consisting of two metal electrodes, a rela, and a solenoid valve. The falling liquid film passed over an expansion nozzle which caused the outer diameter of the liquid sheet to expand from 2.00" to approximately 5.0". After leaving the nozzle the liquid sheet spread still farther thus avoiding interaction with the rising air jet. Visual observations indicated this was an excellent method of separating the film without creating entrainment. Liquid flowing out of this section was either weighed to determine the amount of downflow or recirculated to the system.

c. Liquid Entrance

A sketch of liquid entrance device is shown in Figure 5.2.1.6-3. The device was constructed to provide a smooth liquid film at the liquid entrance. Water entered an annulus whose inside wall was made of porous sintered metal and passed through the porous metal to form a smooth film. The inner wall of the porous metal was sized to coincide with the test section I.D. to prevent discontinuities.

d. Exit Section

A sketch of the exit section is shown in Figure 5.2.1.6-4. The exit section consisted of a smooth flange over which the liquid film flowing up was separated from the air steam containing entrained droplets. In a manner similar to that of the air entrance, the sheet of liquid was expanded in diameter across an expansion nozzle. The film passed around the air removal pipe and fall to the liquid surface in the tank. The air and entrained drops flowed out of the separator. In this way it was possible to distinguish between liquid upflow in the film and that which was entered. However, under churn flow conditions, a portion of the continuous liquid phase could be captured across the outlet pipe. Similarly, under lower liquid flow conditions, some of the air could be expected to flow into the reservoir before leaving in the air line. Thus the entrainment measurement must be considered only an approximate measure of the entrainment actually existing under upflow conditions in the test section. This section like the entrance, was equipped with a liquid level controller.

The air and entrained liquid passed into a Peerless Vane type separator from which the entrained liquid could be separated and weighed. The liquid upflow minus entrainment was withdrawn from the liquid pool while the entrainment was withdrawn from the separator and both were either recirculated or weighed to determine the respective flow rates.

e. Test Section

The test section consisted of length of plexiglass pipe individually machined to exactly 2,000 inch I.D. with error less than 0.001 inch and equipped with interlocking flanges.

(2) Scaling

Verification of the experimental results was carried out using general correlation using dimensionless parameters in Reference 5.2.1.6-2. Dimensionless groups which relate momentum fluxes are shown as follows:

$$j_g^* = j_g \rho_g^{1/2} [gD(\rho_f - \rho_g)]^{-1/2} \quad (5.2.1.6-1)$$

$$j_f^* = j_f \rho_f^{1/2} [gD(\rho_f - \rho_g)]^{-1/2} \quad (5.2.1.6-2)$$

Correlations for flooding in vertical tubes may be expressed in the general form

$$j_g^{*1/2} + mj_f^{*1/2} = C \quad (5.2.1.6-3)$$

For turbulent flow m is equal to unity. The value of C is found to depend on the design of the ends of the tubes and the way in which the liquid and gas are added and extracted. For tubes with sharp-edged flanges, $C = 0.725$, whereas when end effects are minimized, C lies between 0.88 and 1. Figure 5.2.1.6-5 shows the relation about the flooding velocities for air and water in vertical tubes designed to minimize end effects. In Reference 5.2.1.6-1, it is mentioned that Hewitt and Wallis found that for an air-water system the flooding velocities could be correlated by the equation

$$j_g^{*1/2} + j_f^{*1/2} = 0.88 \quad (5.2.1.6-4)$$

(3) Range of Conditions

Tests were conducted at four different liquid flow rates, with the flow varying between 100 lb_m/hr to 1000 lb_m/hr. The four different input liquid flow rates are shown in Table 5.2.1.6-1. Gas Flow rates ranged from 136 lb/h to 330 lb/h for the determination of pressure gradients and from 0 to 280 lb/h for film thickness data.

(4) Data to be compared

Experimental data was obtained which described the major feature of the system before and during flooding. Results included the following:

- Liquid Film Upflow
- Liquid Film Downflow

(5) Data uncertainties

There is no information available in Reference 5.2.1.6-1.

(6) Distortion

There is no information available in Reference 5.2.1.6-1.

(7) References

- 5.2.1.6-1 A. E. Dukler, L. Smith, "Two Phase Interactions in Counter-Current Flow: Studies of the Flooding Mechanism," NUREG/CR-0617
- 5.2.1.6-2 Graham B. Wallis, "One-dimensional Two-phase Flow," McGraw-Hill, 1969.

Table 5.2.1.6-1 The Four Different Input Liquid Flow Rates

W_L(lb/h)	100	250	500	1000
Re_L	310	776	1552	3105

(From NUREG/CR-0617)

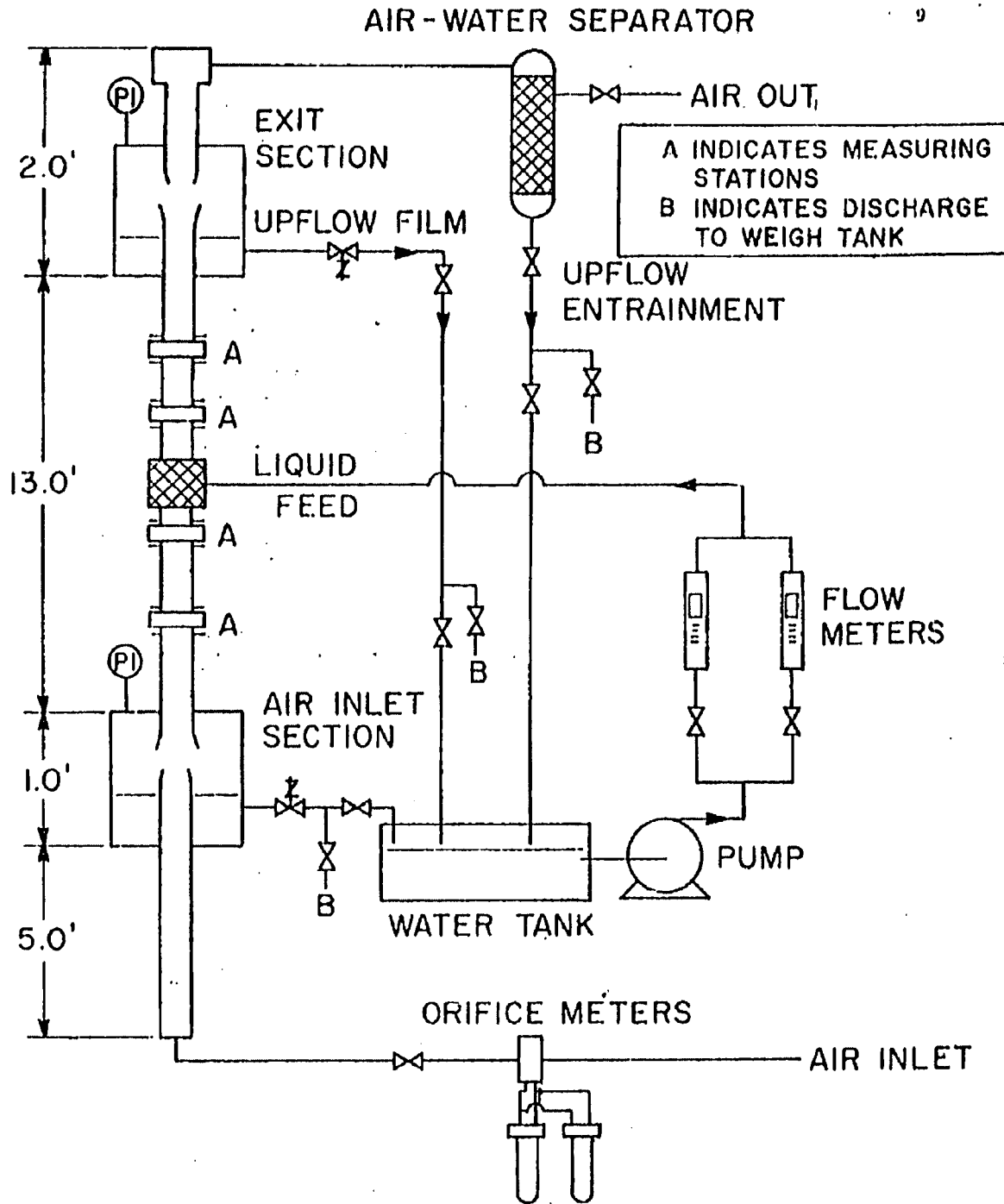


Figure 5.2.1.6-1 Flooding/Upflow Test Loop Schematic Diagram
(From NUREG/CR-0617)

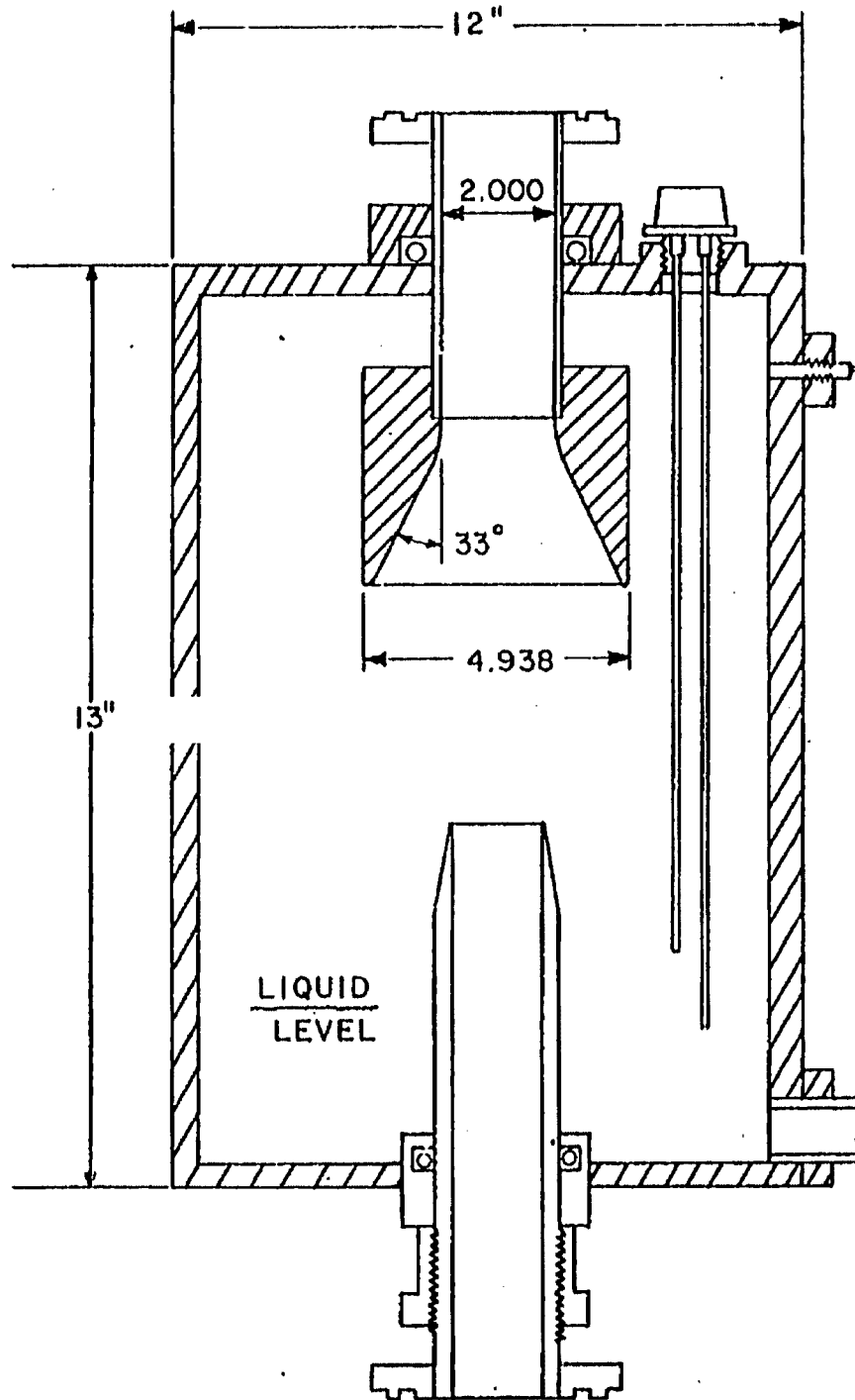


Figure 5.2.1.6-2 Air Inlet Section
(From NUREG/CR-0617)

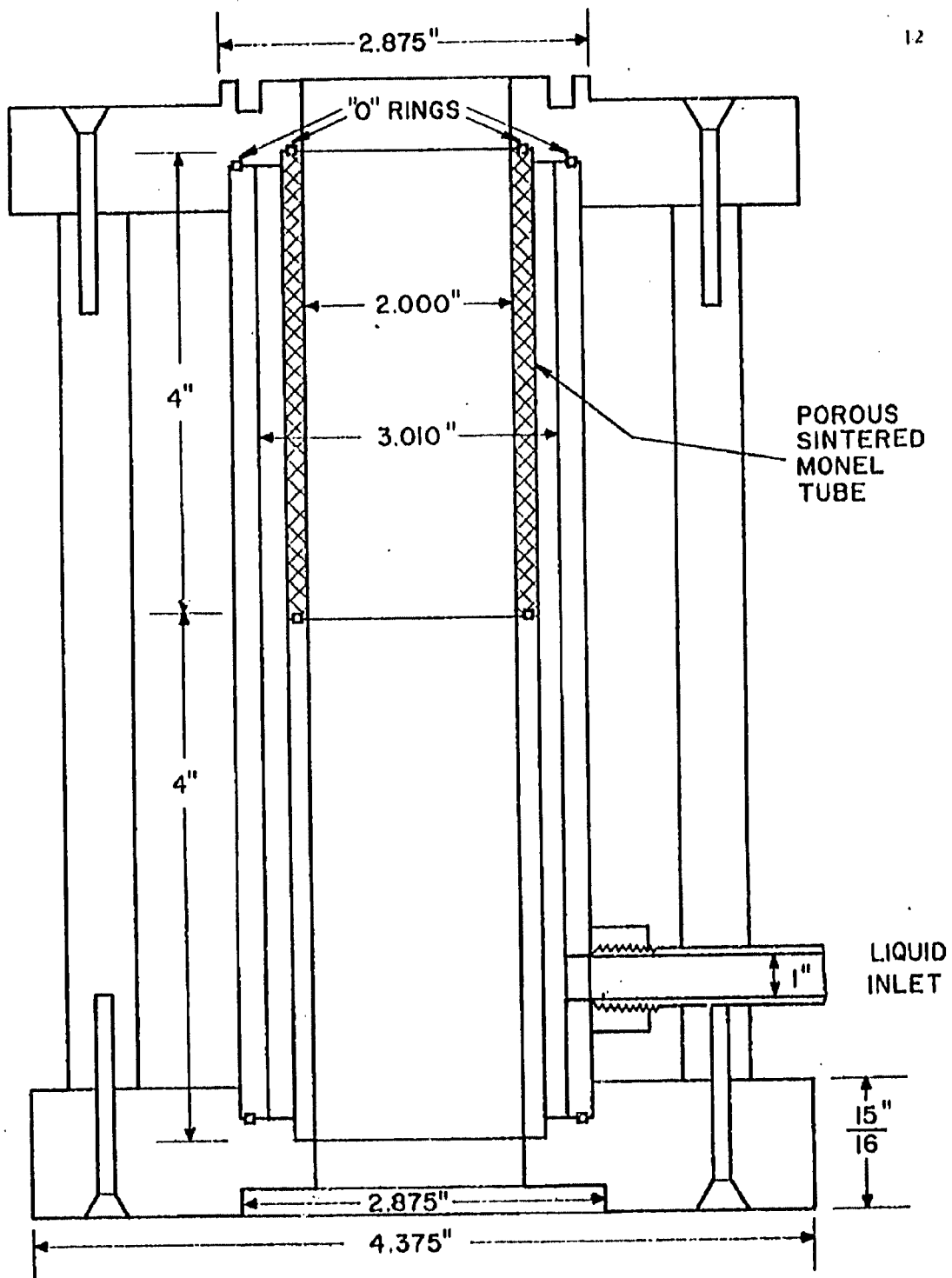


Figure 5.2.1.6-3 Liquid Entrance Device
(From NUREG/CR-0617)

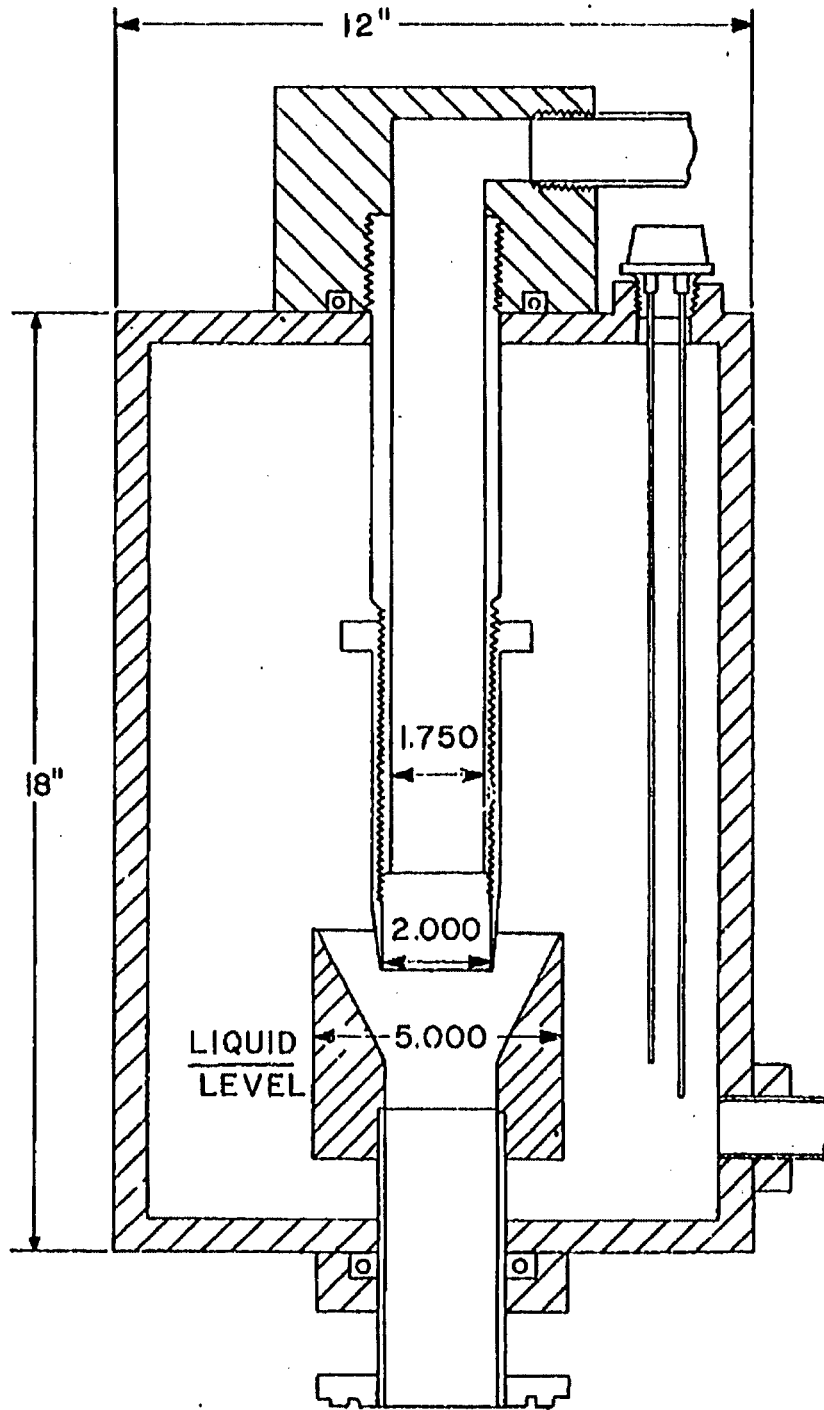
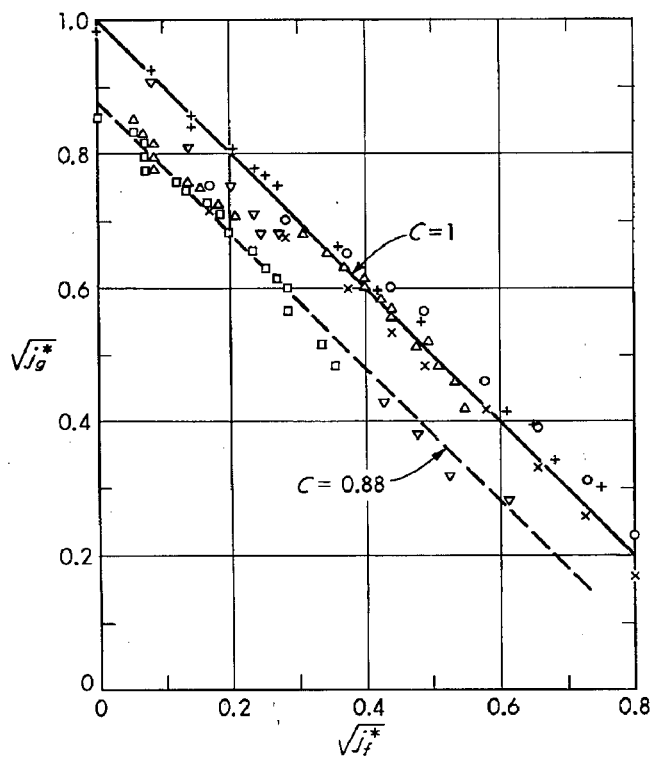


Figure 5.2.1.6-4 Exit Section

Two Phase Interactions in Counter-Current Flow: Studies of the Flooding Mechanism,
 NUREG/CR-0617



- 1"-dia. (Nicklin and Davidson²⁸) "short column" well-rounded air inlet design.
- × 1"-dia. (Nicklin and Davidson²⁸) "main column" well-rounded air inlet design.
- △ 1¼"-dia. (Hewitt and Wallis²¹) water injection and extraction through porous walls. Points where flooding starts with increasing flow.
- 1¼"-dia. (Hewitt and Wallis²¹) points where flooding stops with decreasing flow.
- + ¾"-dia. (Wallis, Steen, and Brenner²⁹) flooding starts.
- ▽ ¾"-dia. (Wallis, Steen, and Brenner²⁹) flooding stops.

Figure 5.2.1.6-5 Flooding Velocities for Air and Water in Vertical Tubes Designed to Minimize End Effects. All Data at Atmospheric Pressure.

(From Ref. 5.2.1.6-2 "One-dimensional Two-phase Flow")

5.2.2 IETs

5.2.2.1 ROSA-IV/LSTF small break (5%) LOCA test (SB-CL-18)

(1) Facility Design and Scaling Issues/Distortions

(a) Fundamental Design Requirements

The LSTF is an experimental facility designed to model a full height primary system of the reference PWR. The four primary loops of the reference PWR are represented by two equal-volume loops. The overall facility scaling factor is 1/48. The overall scaling factor was used as follows:

- Elevations: preserved, i.e., one to one correspondence with the reference PWR. Because the LSTF hot and cold leg inner diameters (IDs) are smaller than those of the reference PWR, only the top of the primary hot and cold legs (IDs) were set equal to those of the reference PWR.
- Volumes: scaled by the facility scaling factor 1/48.
- Flow area: scaled by 1/48 in the pressure vessel and 1/24 in the steam generators. However, the hot and cold legs were scaled to conserve the ratio of the length to the square root of pipe diameter, i.e., L/\sqrt{D} for the reference PWR. Such an approach was taken to better simulate the flow regime transition in the primary loops. In other words, The hot and cold legs were sized to conserve the volume scaling and the ratio of the length to the square root of pipe diameter, L/\sqrt{D} , for the reference PWR in expectation that the flow regime transitions in the primary loops can be simulated appropriately by taking this scaling approach.
- Core power: scaled by 1/48 at core powers equal to or less than 14% of the scaled reference PWR rated power. The LSTF rated and steady-state power is 10 MWt, i.e., 14% of the rated reference PWR core power scaled by 1/48.
- Fuel assembly: dimensions, i.e., fuel rod diameter, pitch and length, guide thimble diameter pitch and length, and ratio of number of fuel rods to number of guide thimbles, designed to be the same as the 17 x 17 fuel assembly of the reference PWR to preserve the heat transfer characteristics of the core. The total number of rods was scaled by 1/48 and is 1064 for heated and 104 for unheated rods.
- Design pressures: roughly the same as the reference PWR.
- Fluid flow differential pressures (ΔP s): designed to be equal to the reference PWR for scaled flow rates.
- Flow capacities: scaled by the overall scaling factor where practicable.

All information above is obtained in Reference 5.2.2.1-1.

(b) General Functions and Systems

The LSTF test facility is a scaled model of a LPWR with an electrically heated core. The intent of the facility is to model the thermal-hydraulic phenomena which would take place in a PWR during small break LOCAs and transients. The general philosophy in scaling coolant volumes and flow areas was to keep the scaling ratio of 1/48. The height and elevation of each component are designed to be the same as those of the reference PWR as practicable as possible. The components used in the LSTF test facility are similar in design to those of the reference PWR. Because of scaling and component design, the LSTF experiments are expected to closely model LPWR behavior during small break LOCAs and transients.

The general facility view is presented in Figure 5.2.2.1-1 in Reference 5.2.2.1-1. The major design characteristics are compared with those of the reference PWR in Table 5.2.2.1-1. Figure 5.2.2.1-2 gives comparison of the LSTF and reference PWR system configurations. Whole information described here are derived from Reference 5.2.2.1-1.

Nineteen break locations are provided in the LSTF. On (or two) break location(s) will be selected out of these depending on the test objectives. Several ECC injection locations typical and atypical of the reference PWR are also provided. The injection locations can be changed as test parameters.

(c) Primary Coolant System

The primary coolant system is composed of the pressure vessel containing an electrically heated core, primary loop piping, coolant pumps and a pressurizer. Materials used for major components in the primary coolant system are listed in Table 5.2.2.1-2 as shown in Reference 5.2.2.1-1. Each component is described in detail below.

1) Pressure Vessel and Internal Structures

a) Pressure Vessel Assembly

The pressure vessel houses a full-length core with 1064 electrically heated rods and 104 unheated rods. The vessel is fabricated out of stainless steel (SUS316L) clad carbon steel (SB49) and rated at a pressure of 17.95 MPa and temperature of 630.2 K. It is 11.0 m tall with an inside diameter of 0.64 m and wall thickness of 61 mm including the clad. Primary characteristics of the pressure vessel are summarized in Table 5.2.2.1-3. The LSTF pressure vessel and the reactor vessel of the reference PWR are compared graphically in Figure 5.2.2.1-3.

As shown in Figure 5.2.2.1-4, the vessel's internal space can be divided into the core, annular downcomer, lower plenum and upper plenum. The lengths of the core and downcomer as well as the elevations (EL) of various internal components relative to the bottom of the heated zone are conserved with respect to those of the reference PWR to the extent as practicably as possible. Relative elevations of the pressure vessel components in LSTF and PWR are compared in Table 5.2.2.1-4.

The major nozzles attached to the pressure vessel are shown in Figure 5.2.2.1-5 and listed in Table 5.2.2.1-5. The nozzles for the hot and cold leg piping are located at the same elevation above the top of the core. Two primary coolant loops are attached to the pressure vessel at these locations.

In addition to hot and cold leg nozzles, the pressure vessel has nozzles for:

- a) ECCS injection (upper plenum and lower plenum injection),
- b) Lower plenum and upper head break simulation,
- c) Nitrogen gas injection,
- d) Vent line connected to the top of the pressurizer,
- e) External piping to simulate core barrel vent valves,
- f) Plant safety and pressure relief valves,
- g) Auto-bleed system for volume control,
- h) Hot leg leakage simulation,
- i) Reflux flowmeter,
- j) Alternate pressurizer surge line connection,
- k) Instruments.

Nitrogen gas injection nozzles are intended for studying the effect of non-condensable gas generated in the core on the system behavior during a small-break LOCA. Nitrogen gas is injected directly into the upper head through a nozzle (N5) and into the lower plenum through hour tubes of 6.22 mm ID. The injection points in the lower plenum are located at a height of EL-1.01 m, and below the tie rods whose positions in the core bundle are B1466, B1626, and B1822. The vent line between the pressure vessel upper head and the pressurizer is expected to mitigate the effect of non-condensable accumulating in the upper head of the pressure vessel.

The core barrel vent valves are intended to reduce the upper plenum back pressure and enhance coolant penetration into the core via downcomer during ECC injection. In LSTF, nozzles are attached to the downcomer and upper plenum and connected to an external piping

to simulate the core barrel vent valve of a B&W reactor.

The auto-bleed nozzle is used to control the primary coolant volume together with a charging pump. Hot leg leakage nozzles are intended to simulate the leak flow between the hot leg and downcomer. The reflux flow meter is intended to measure the liquid condensate flow from the steam generator back to the core in the hot leg during the reflux condensation cooling mode. The pressurizer surge line nozzle attached to the pressure vessel upper head is used to test the effect of alternate surgeline location on the system behavior during LOCA and operational transients.

Additionally, there are many small diameter nozzles for attachment of various instruments to measure vessel pressure, structural and fluid temperatures, downcomer flow rate and liquid level.

In-core instruments to measure fuel rod surface and fluid temperatures, liquid level and power lead lines are routed through the pressure vessel and plate.

The coolant flow paths inside the vessel under normal and accident or transient conditions are shown in Figure 5.2.2.1-6.

b) Pressure Vessel Internals

The upper plenum internals is shown in Figure 5.2.2.1-7 and the characteristics summarized in Table 5.2.2.1-6. Each information is obtained from Reference 5.2.2.1-1. Most of the components are made of stainless steel (SUS304). The upper core support plate and upper core plate are located at respectively the same elevation as in the reference PWR. The upper core support plate is attached to the support barrel which is fixed to the pressure vessel shell head.

2) Core and Lower Plenum

The major characteristics of the core are summarized in Table 5.2.2.1-7, and the cross sections are shown in Figure 5.2.2.1-8 through 5.2.2.1-10. The information shown in tables or figures is obtained from Reference 5.2.2.1-1. In comparison with the reference PWR, the length of the heated zone, fuel rod diameter and pitch, power peaking factor and number of spacers are conserved. The core volume and the number of fuel rods are scaled at a ratio of 1/48.

The bottom section of the core barrel has openings which effectively form the flow channel

between the downcomer and the lower plenum. The top of the openings corresponds to the bottom of the downcomer and the elevation relative to the bottom of the heated zone is the same as in a PWR.

As shown in Figure 5.2.2.1-10, the core contains 16 square 17x17 bundles and 8 semi-crescent shaped bundles. The core power profile is chopped-cosine in shape with a peaking factor of 1.495 (Figure 5.2.2.1-11). As summarized in Table 5.2.2.1-8, eight bundles contain high power-density heater rods (1.4 kW), and the remaining bundles contain low power-density heater rods (0.97 kW). Each bundle contains heated fuel rods, both non-instrumented and instrumented types. The heater rods are connected to a 3-phase, 400 V AC power supply system.

3) Pressurizer

The function of pressurizer is to control the primary loop pressure and to accommodate any changes in the coolant volume during normal and abnormal plant conditions. All information is derived from Reference 5.2.2.1-1.

The pressurizer of LSTF is shown in Figure 5.2.2.1-12. It consists of a 4.19 m tall cylindrical vessel, immersion-type electrical heaters and nozzles used to connect the surge line, pressure vessel vent line, and safety and pressure relief valve lines. Major characteristics are summarized in Table 5.2.2.1-9.

The pressurizer of LSTF is scaled to have 1/48 of the volume and the same height-to-diameter ratio as the pressurizer of a PWR. The normal coolant volume is also scaled at 1/48, while the coolant level above the bottom of the core is the same as that of a PWR.

The pressurizer is normally connected through the surge line to the primary loop at the hot leg of the A loop. Provisions have also been made to allow connection of the effectiveness of system pressure control for this alternate method.

The vent line between the pressurizer and the pressure vessel is intended to provide a means of venting non-condensable gas accumulating in the pressure vessel out of the primary system. The power operated relief valve and safety valve are designed to simulate those in a PWR. The spray line is connected to the cold leg of loop A to provide relatively cooler primary coolant for pressure control.

The pressurizer control logic built into the LSTF is the same as that of the reference PWR as compared in Table 5.2.2.1-9. The system pressure is controlled by either heating the coolant in the pressurizer or by spraying relatively cooler primary coolant taken from the cold leg. Pressurizer spray pump is always turned on under normal operating conditions and turned off automatically by a safety injection signal. The spray flow rate is controlled by a combination of the main and bypass valves located in the spray line. The bypass valve is adjusted to supply a fixed rate of coolant flow at 0.011 kg/s. The main valve is operated according to the control logic shown in Table 5.2.2.1-9, and supplies additional coolant flow. The flow rate varies linearly from zero at pressures below 15.68 MPa and to a maximum of 0.98 kg/s at pressures above 16.03 MPa. The pressurizer heater consists of 21 heater rods with sheath made of SUS 316L. The heater rods are 1075 mm long with effective heated length of 850 mm located at the bottom of the pressurizer as shown in Figure 5.2.2.1-12. Both the backup and proportional heaters are switched on at a pressure below 15.34 MPa. Only the proportional heater is used to control the pressure between 15.41 MPa and 15.62 MPa.

4) Primary Coolant Loops

The LSTF's primary coolant loop consists of two identical loops each representing two loops of the reference four-loop PWR.

Major characteristics of the primary loop are summarized and also compared with those of a PWR in Table 5.2.2.1-10.

The diameters of the piping are listed in Table 5.2.2.1-10. Basically there are only two different diameter pipes used in the whole loop. Pipes with 207 mm ID and 295 mm OD are used for hot and cold legs, while those for the cross-over legs have 168.2 mm ID and 240.2 mm OD. All of the pipes are made out of stainless steel, SUS316L-TF. All information shown here is in Reference 5.2.2.1-1.

5) Reactor Coolant Pumps

The reactor coolant pumps (PCs) installed in both primary loops drive the primary coolant into the core to remove the heat generated in the core.

In order to simulate the pump characteristics of the reference PWR, the PC of LSTF was designed as follows.

- The type of PC is a canned-type centrifugal pump with configuration of the impeller, casing,

- inlet and outlet regions similar to those of the PWR reactor coolant pump.
- Pump speed can be controlled electrically to simulate the transient flow characteristics of the PWR reactor coolant pump.
 - The capacity of PC is larger than 14% of the 2/48 scaled cold leg flow rate of the reference PWR. The two PCs (PC-A and PC-B) have the same pump characteristics.
 - The reverse rotation of PC is not permitted as in the PWR.

The design specifications of PC are compared with those of the PWR reactor coolant pump in Table 5.2.2.1-11. The moment of inertia of the PC rotor is shown in Table 5.2.2.1-11. A latch mechanism is provided to the shaft to prevent reverse rotation.

Figure 5.2.2.1-13 shows the single-phase head-flow characteristics (Q-H curves) for normal and reverse flows under forward rotation at room temperature. Figure 5.2.2.1-14 shows non-dimensional homologous heat curves of PC-A derived from the Q-H curves and rated conditions shown in Table 5.2.2.1-11. The pump torque characteristics of PC-A were experimentally obtained for a single-phase water flow. Figures 5.2.2.1-15 and 5.2.2.1-16 show the torque homologous curves and frictional torque of PC-A, respectively. The pump torque was obtained by subtracting the frictional torque from the motor torque. The head and torque homologous curves for the reverse rotation are not prepared because the reverse rotation is not allowed in LSTF. The pump performance data for PC-A can also be used for PC-B, which has the same design specification. Whole information is in Reference 5.2.2.1-1.

(d) Secondary Coolant System

The secondary coolant system of LSTF is designed to simulate the steady state and transient responses of the steam and feedwater flows and primary-to-secondary heat transfer. The main components such as steam generators and main and auxiliary feedwater pumps of the reference PWR are simulated in LSTF as closely as possible including the control and trip logics. However, the LSTF has a steam condensing system instead of the turbine generator system in PWR. Information described here is in Reference 5.2.2.1-1.

Figure 5.2.2.1-17 and Table 5.2.2.1-12 shows a flow diagram and a list of major components in the secondary system of LSTF. There are two steam generators (SG-A and SG-B) each with maximum heat removal capacity of 35 MW, which is 1/24 scaled capacity of a PWR SG. The secondary coolant system consists of four subsystems, i.e., (1) steam generation system i.e., the SG secondary-side, (2) steam condensation system including a jet condenser (JC) and cooling towers, (3) feedwater system including main and auxiliary feedwater pumps and (4)

pipings and related components including valves, orifices and flow meters.

1) Steam Generator

The steam generators, SG-A and SG-B, have the same designed specification. Each SG consists of a vessel, U-tubes, primary and secondary steam separators and other internals as shown in Figure 5.2.2.1-18. The coolant flow in the secondary-side of SG is shown in Figure 5.2.2.1-19.

a) SG Vessel

Figures 5.2.2.1-20 (a) through 5.2.2.1-20 (c) show the SG vessel, U-tubes and plena with filler blocks. The design of the two SGs is identical except that a break unit for simulation of U-tube rupture is furnished only on SG-B. The SG vessel has 0.85 m I.D. and 18.3 m inner height. The vessel height is nearly the same as that of reference PWR as shown in Figure 5.2.2.1-21. Major design parameters of SG-A and SG-B are compared with those of PWR in Table 5.2.2.1-13.

The SG vessel consists of three parts connected to each other by flanges and is made of carbon steel with lining of stainless steel. Filler blocks made of aluminum with U-tubes flow paths are installed in the inlet and outlet plena in order to simulate height and coolant volume of the plena. The outer surface of SG vessel wall is covered by a layer of thermal insulating material. Wire heaters are at the outer surface to control the heat loss.

The main steam line nozzle is located at the top of the SG vessel. The feedwater inlet nozzle is located at the middle of the vessel. The downcomer consists of an upper annulus region and four pipes of 97.1 mm I.D. (Figure 5.2.2.1-20(d)) located outside the SG vessel. The external downcomer configuration facilitates measurement of the circulation flow rate.

b) U-tubes

There are 141 U-tubes made of stainless steel, SUS316, arranged in a square array in each SG as shown in Figure 5.2.2.1-22 and Figure 5.2.2.1-23. The inner diameter and wall thickness of the U-tubes are 197.6 mm and 2.9 mm, respectively. The U-tubes are classified by height into nine groups (see Figure 5.2.2.1-20(b)). The U-tubes are fixed to the tubesheet and supported by seven support plates. A flow distributor is fixed at the lower part of U-tubes. The flow area at each place is shown in Table 5.2.2.1-13.

The small break due to U-tube rupture is simulated by a valve at a pipe connecting the SG-B

inlet plenum and lower part of the SG-B secondary-side.

c) Primary and Secondary Steam Separators

Figures 5.2.2.1-24 and 5.2.2.1-25 show geometry of the primary and secondary steam separators, respectively. The primary steam separator is designed to simulate the configuration of that of reference PWR. The flow characteristics of the secondary steam separator shown in Figure 5.2.2.1-26 were designed to simulate that of the reference PWR. The secondary separator forms a steam path between two corrugated plates.

2) Steam Condensation System

Steam generated in the steam generators flows into the steam condensation system and is condensed rapidly by a spray system. The steam condensation system consists of the jet condenser (JC), spray system, auto-bleed and vent-condenser.

a) Jet Condenser (JC)

Figure 5.2.2.1-27 shows the vessel of JC made of carbon steel with stainless steel lining. The design specification of JC is shown in Table 5.2.2.1-14.

The piping for the spray line, the vent-condenser line and the auto-bleed are connected to the vessel of JC. The outer surface of the JC vessel is covered by a layer of thermal insulating material.

b) Supplement Components

The spray system, auto-bleed and vent-condenser are used for controlling the pressure and fluid mass in the secondary system. The spray water line from the cooling tower CT-2 is connected to JC at the nozzle. The spray header has four nozzles as shown in Figure 5.2.2.1-27. The steam condensing performance in the jet condenser is controlled by water flow rate and temperature difference between the steam and spray water.

The auto-bleed system connected to the lower part of JC vessel functions to control the water level in JC by discharging the water.

The vent-condenser system connected to the steam region of JC serves to control the pressure in the secondary system by discharging the steam from the JC.

A low pressure water supply system which fills up the secondary system by water prior to the test initiation is connected to a nozzle near the bottom of JC vessel. The water supply pump

(PS), check valve and air operated valve are also provided in the system.

A high pressure charging system is provided in the secondary coolant system. The charging pump (PJ) is used for water charging under high pressure condition. The charging line is connected to the nozzle of JC vessel wall. The water stored in RWST is supplied to the JC by both water supply system and high pressure charging system.

3) Feedwater System

The feedwater system supplies feedwater to the secondary-side of SGs. When the main feedwater is tripped off, the auxiliary feedwater system is in turn initiated. The feedwater flow rate and fluid temperature are test parameters of LSTF. Major components in the feedwater system are two cooling towers CT-1 and CT-2, a main feedwater pump (PF) and auxiliary feedwater pump (PA). The total cooling capacity of CT-1 and CT-2 can be controlled from 10% to 100% of 10 MW.

a) Cooling Towers

The CT-1 is used to cool the hot condensed water from the HC down to a desired feedwater temperature and has a cooling capacity of 8 MW. The CT-2 has a cooling capacity of 2MW and serves to control the sub-cooling of the spray water. Table 5.2.2.1-15 shows major design parameters of CT-1 and CT-2.

Figures 5.2.2.1-28(a) and 5.2.2.1-28 (b) show the configuration and designed cooling performance of CT-1. The feedwater temperature is mainly controlled by changing the bypass feedwater flow rate and the wind flow rate at CT-1. Figures 5.2.2.1-29 (a) and 5.2.2.1-29 (b) show the configuration and designed cooling performance of CT-2.

b) Main Feedwater Pump

The main feedwater pump (PF) is a canned type centrifugal pump with design specification shown in Table 5.2.2.1-16. The main feedwater pump drives the feedwater from the CT-1 to SG secondary-sides. The feedwater flow rate to each SG is controlled separately by a control valve located in each feedwater line. The PF pump characteristics are compared to those of the main feedwater pump of PWR which is shown in Figure 5.2.2.1-30.

c) Auxiliary Feedwater Pump

The auxiliary feedwater pump (PA) is a plunger type pump with design specification shown in Table 5.2.2.1-16. It delivers cold water from the simulated refueling water storage tank (RWST)

to the SG secondary regions when the main feedwater flow is tripped off. The auxiliary feedwater line is connected to the piping of main feedwater line between the PF and steam generators as shown in Figure 5.2.2.1-17. Designed maximum flow rate of PA is 3% of the maximum flow rate of PF. This capacity of PA is enough to simulate the 1/48 scaled auxiliary feedwater flow rate by the motor-driven auxiliary feedwater pump of the reference PWR. Figure 5.2.2.1-31 shows scaled Q-H characteristics of the auxiliary feedwater pumps of the PWR. The control and trip logics for PA simulate those of the reference PWR.

4) Piping in the Secondary System

Main piping in the secondary coolant system (see Figure 5.2.2.1-17) consists of three groups, i.e., main steam line, main feedwater line including piping around the jet condenser and auxiliary feedwater line. The other related components including various types of valves, orifices, and flow meters are also shown in Figure 5.2.2.1-17. The design specifications of the main piping are shown in Table 5.2.2.1-17. All the main piping are covered by a layer of thermal insulator.

(2) Range of Conditions

The major initial conditions of the LSTF 5% cold leg break test, Run SB-CL-18, are shown in Table 5.2.2.1-18. Both the initial steady state conditions and the test procedures were designed to minimize the effects of LSTF scaling compromises on the transients during the test. All information shown here is in Reference 5.2.2.1-2.

The most important design scaling compromise is the 10 MW maximum core power limitation, 14% of the scaled reference PWR rated power. The steady-state condition is restricted to a core mass flow rate that is 14% of the scaled value to simulate the reference PWR temperature distribution in the primary loop. The desired primary coolant flow rate was established by reducing the pump speed with the flow control valves (FCVs) in the cross-over legs fully open. The primary loop flow rate was then increased at the time of break to improve the similarity of the LSTF to the reference PWR by increasing the pump speed.

The primary-to-secondary heat transfer must also be maintained at 10 MW, i.e., 14% of the scaled value. Since the LSTF steam generators (SGs) are geometrically scaled to the reference PWR, the 14% primary-to-secondary heat transfer rate is established by raising the secondary temperature such that the primary pressure and temperature are representative of the reference PWR.

Major operational setpoints and conditions including emergency core cooling system (ECCS) actuation logic for this test are shown in Figure 5.2.2.1-32 and summarized in Table 5.2.2.1-19. After the break occurred at time zero, the primary system depressurizes quickly. At a pressurizer pressure of 12.97 MPa, the reactor scrams. Loss of offsite power concurrent with the reactor scram is assumed and the primary coolant pumps are tripped to begin coastdown and the core power begins to decrease along the preprogrammed decay curve. The power decay curve used in the test takes into account the actinides and delayed neutron effects and gives a slower decrease than the ANS standard. The core power decay curve used in the test is tabulated in Table 5.2.2.1-20. The SG auxiliary feedwater is assumed to fail to simplify the transient.

At a pressurizer pressure of 12.27 MPa, the safety injection signal is sent that trips ECCS to be actuated at respective pressure setpoints. However, the high pressure charging system and the high pressure injection system (HPIS) are assumed to fail in the test. The ECCS conditions are summarized in Table 5.2.2.1-21. The accumulator (ACC) system and the low pressure injection system (LPIS) are specified to initiate coolant injection into the primary system at pressures of 4.51 and 1.29 MPa, respectively. The accumulator-cold (ACC-Cold) system simulates ACC injection flow to the cold leg A and the accumulator-hot (ACC-Hot) system simulates ACC injection flow to the cold leg B. The water temperatures of ACC-Cold and ACC-Hot tanks are the same and the ratio of ACC injection flow rate to cold leg A and to cold leg B is 3:1. This injection method is adopted for good simulation of ACC injection flow rate to each cold leg in the LSTF.

(3) Data to be compared

The experimental results shown in figures were arranged as follows:

- 1) TE, fluid temperature,
- 2) DT, differential temperature,
- 3) TW, heater rod and structure temperatures,
- 4) FE, flow rate measured with conventional flow meter,
- 5) PE, pressure,
- 6) MI, miscellaneous instrument signal,
- 7) LE, liquid level,
- 8) DP, differential pressure,
- 9) CP, conductivity probe signal,
- 10) MF, momentum flux with drag disk in volt and engineering unit,
- 11) DE, density with gamma densitometer in volt and engineering unit,

12) RC, two-phase flow data calculated with MF, DE and others in engineering unit.

Information described here is in Reference 5.2.2.1-2 page 10.

(4) Data uncertainties

The flow rates measured with conventional flow meters using venturi, orifice or nozzle and DP cell are limited in accuracy in principle to single-phase liquid or vapor flow. In addition, when the reading is below about 20% of the measurement range, the accuracy is not satisfactory, since the flow rate is proportional to the square root of the differential pressure measured. For example, a zero-level drift of 1% in the DP cell output results in a flow rate reading of 10% the measurement range, even though the actual flow rate is zero. Hence, we should pay attention to the use of flow rate data below about 20% of the measurement range even though the DP cell data for the flow rates were corrected based upon a calibration test for static pressure effect as shown in Reference 5.2.2.1-2 page 11.

(5) Distortion

Thermal insulation and heat loss control system is intended to compensate heat loss from piping and vessels during an experiment by on-off control of heaters wound outside the surface of the piping and vessels (thermal insulation heaters). Thermal insulation heaters are wound on the outside surface of the following piping and vessels.

Pressure boundaries of the LSTF primary and secondary systems are covered by the thermal insulator made of rock wool or glass wool. As the thermal conductivity of the insulator is approximately 1/1000 of the structural metal (carbon steel), a total heat loss for the whole LSTF system is mainly controlled by thermal conduction through the insulators.

Total heat loss in a quasi-steady state of the primary and secondary system per unit time (Q_{HL}) is defined here as a sum of heat losses per unit time for the primary and secondary fluid system (Q_F) and for the metal structures contacting with the fluid (Q_M) in addition to a heat input per unit time (Q_G) from the heater rod electric power or the operating primary pump power as,

$$Q_{HL} = Q_F + Q_M + Q_G.$$

Total heat loss per unit time through the insulators (Q_T), on the other hand, is given by Q_{HL} and a heat loss per unit time of the outer metal structures (Q_{Mo}), which are covered by the thermal insulators and contacting with the pressure boundary metal structures (see Figure 5.2.2.1-32) as,

$$Q_T = Q_{HL} + Q_{Mo}.$$

Heat losses in the fluid system (Q_F), metal structures (Q_M) and total system (Q_{HL}) were obtained

as shown in Table 5.2.2.1-22. Heat input from the operating pumps was amended as 2.4 kW. Namely, $Q_F = 61.0$ kW (44%), $Q_M = 73.9$ kW (54%) and $Q_G = 2.4$ kW (2%). Therefore, the total heat loss was,

$$Q_{HL} = 137 \text{ kW.}$$

Heat losses for the primary system and two SGs were 49% and 51% of Q_{HL} . Information shown here is in Reference 5.2.2.1-3 page 15.

(6) References

- 5.2.2.1-1 "ROSA-IV Large Scale Test Facility(LSTF) System Description," JAERI-M 84-237.
- 5.2.2.1-2 "ROSA-IV/LSTF 5% Cold Leg Break LOCA Experiment Run SB-CL-18 Data Report," JAERI-M-89-027.
- 5.2.2.1-3 "Supplemental Description of ROSA-IV/LSTF with No.1 Simulated Fuel-Rod Assembly," JAERI-M-89-113.

Table 5.2.2.1-1 Major Design Characteristics of LSTF and PWR

		LSTF	PWR	PWR/ LSTF
Pressure	(MPa)	16	16	1
Temperature	(K)	598	598	1
No. of fuel rods		1064	50952	48
Core height	(m)	3.66	3.66	1
Fluid volume V	(m ³)	7.23	347	48
Core power P	(MW)	10	3423(t)	342
P/V	(MW/m ³)	1.4	9.9	7.1
Core inlet flow	(ton/s)	0.0488	16.7	342
Downcomer gap	(m)	0.053	0.260	4.91
Hot leg D	(m)	0.207	0.737	3.56
L	(m)	3.69	6.99	1.89
L/\sqrt{D}	(m ^{1/2})	8.15	8.15	1.0
$\frac{\pi}{4}D^2L$	(m ³)	0.124	2.98	24.0
No. of loops		2	4	2
No. of tubes in steam generator		141	3382	24
Length of steam generator				
Tube(average)	(m)	20.2	20.2	1.0

ROSA-IV Large Scale Test Facility(LSTF) System Description, JAERI-M 84-237

Table 5.2.2.1-2 Materials for Primary Loop Components

Components	Material
Pressure Vessel	SB49 + SUS316L clad
Primary Loop Piping	SCS13A
Pressurizer	SB49 + SUS316L clad
Pressurizer Piping	SUS316L – TP
Primary Coolant Pumps	SCS13A and SUS304

ROSA-IV Large Scale Test Facility(LSTF) System Description, JAERI-M 84-237

Table 5.2.2.1-3 Primary Characteristics of the Pressure Vessel

	LSTF	PWR	PWR/ LSTF
Total Volume (m ³)	2.6748	131.7	1/49.24
Upper Head Volume (m ³)	0.5100	24.6	1/48.23
Upper Plenum Volume(incl. Endbox) (m ³)	0.5472	28.4	1/51.90
Core Volume (m ³)	0.4078	17.5	1/42.91
Lower Plenum Volume (m ³)	0.5802	29.62	1/51.05
Downcomer + Core Bypass Vol. (m ³)		31.58	
Core Flow Area (at spacer) (m ²)	0.06774	3.70	1/54.62
Core Flow Area (m ²)	0.1134	4.75	1/41.89
Downcomer Flow Area (m ²)	0.09774	3.38	1/34.58
(incl. Bypass)		5.23	1/53.51
Downcomer Gap Width (m)	0.053	0.26	1/4.91
Spray Nozzle Flow Area (m ²)	72.63	3552	1/48.91
Normal Core Flow Rate (m ³ /s)	0.0651	22.30	1/342.9
Leakage bet. Hot Leg and D.C.		1% of Core Flow	
Leakage bet. D.C. and Upper Head		0.5% of Core Flow	
Press. Drop in PV (kPa)			
Cold Leg – Hot Leg		251.75	
Inlet Nozzle		39.83	
Downcomer		3.39	
Lower Plenum		56.78	
Core		137.30	
Outlet Nozzle		14.41	

ROSA-IV Large Scale Test Facility(LSTF) System Description, JAERI-M 84-237

Table 5.2.2.1-4 Comparison of Various Elevations

Location	LSTF	PWR
Shell Top	8600.2	9469.7
Upper Head Break Nozzle	8500.6	
Nitrogen Injection Nozzle	8145.	
Surge Line Nozzle	7936.	
Upper Core Support Plate (B)(t)	6170.2 (304)	6170.2 (304)
Vent Valve/Upper Plenum ECCS	6086.9	6086.9
Hot Leg Pipe Center (ID)	5502.8 (207)	5238. (736.6)
Cold Leg Pipe Center (ID)	5502.8 (207)	5238. (698.5)
Downcomer (T)	5399.3	4888.5
Upper Core Plate (B)(t)	3968. (76.2)	3968. (76.2)
Upper End Box (B)(t)	3864.5 (19.5)	3854.5 (19.5)
Spacer #9 (T)	3710.	3807.
Top of Heated Zone	3660.	3660.
Spacer #8 (T)	3299.	3299.
Spacer #7 (T)	2791.	2791.
Spacer #6 (T)	2338.	2338.
Spacer #5 (T)	1920.	1884.
Cross Over Leg (B)	1701.1	1701.1
Spacer #4 (T)	1514.	1431.
Spacer #3 (T)	977.	977.
Spacer #2 (T)	524.	524.
Spacer #1 (T)	140.	54.
Bottom of Heated Zone	EL 0.0	EL 0.0
Lower End Box (T)	-41.3	-41.3
Lower Core plate (T)(t)		-109. (50.8)
Lower Core Support Plate (T)(t)		-750.8 (508)
Downcomer (B)	-1258.8	-1258.8
Lower Plenum ECCS/Break Nozzle	-1735.	
Shell (B)	-2361	-3098.8

ROSA-IV Large Scale Test Facility(LSTF) System Description, JAERI-M 84-237

Table 5.2.2.1-5 Pressure Vessel Nozzles

Nozzle No.	Service	Inner Diameter (mm)	Qty
N-1 ^a _b	Hot Leg	265	2
N-2 ^a _b	Cold Leg	207	2
N-3	ECCS Injection	87.3	1
N-4	Safety Valve	66.9	1
N-5	N ₂ Gas Injection	12.3	1
N-6 ^a _b	Break	87.3	2
N-7 ^a _b	Vent Valve	87.3	2
	Vent Valve	87.3	2
N-8	Auto-bleed	21.2	1
N-9	Press. Relief Valve	12.3	1
N-10	PV-PR Ventline	43.1	1
N-11 ^a _b	Hot Leg Leakage	21.2	2
N-12	ECCS Injection	101.3	1
N-13	Spare (Surge line)	66.9	1

ROSA-IV Large Scale Test Facility(LSTF) System Description, JAERI-M 84-237

Table 5.2.2.1-6 Primary Characteristics of the Upper Plenum Structures

	LSTF	PWR	PWR/ LSTF
Upper Head Structures			
Control Rod Guide Tubes	8	57	
Upper Core Support Columns	10	50	
Orifice Plate	2	16	
Inlet Holes	12	70	
Upper Core Plate Opening (m ²) for			
Coolant Flow	0.03114	1.440	1/46.24
Control Rod Guide Tubes	0.03427	1.605	1/46.83
Support Columns	0.02017	0.9680	1/47.99
Coolant Flow Area between			
Upper Plenum and Upper Head (m ²)	0.001263	0.05778	1/45.75

ROSA-IV Large Scale Test Facility(LSTF) System Description, JAERI-M 84-237

Table 5.2.2.1-7 Major Core Characteristics

Item	LSTF	PWR	Ratio
Number of Rod Bundles	24	193	
Bundle Size	7 x 7 (square) 48 rods (semi-crescent)	17 x 17	
Total Number of Rods	1,168	55,777	(1/47.75)
Heater Rods	1,064	50,952	(1/47.89)
Non-Heating Rods	104	4,825	(1/46.39)
Rod Diameter (mm)			
Heater Rod	9.5	9.5	1/1
Non-Heating Rods	12.24	12.24	1/1
Rod Pitch (mm)	12.6	12.6	1/1
Effective Heated Length (m)	3.66	3.66	1/1
Output Power (MWth)	10.0	3,423	1/342.3
Peaking Factor	1.495	1.495	1/1
Cladding Thickness (mm)	1.0	0.57	1.754/1
Cladding Material	Inconel	Zr-4	
Number of Spacers in Core	9	9	1/1
Core Barrel			
Inner Diameter (mm)	514	3759	1/7.313
Outer Diameter (mm)	534	3,875	1/7.255
Thickness (mm)	10	57.5	1/5.75
Core Volume (m ³)	0.4078	17.5	1/42.91
Flow Area (m ²)			
Core (at spacer)	0.06774	3.70	1/54.62
Core (below spacer)	0.1134	4.75	1/41.89
Grid (or Lower nozzle)	0.06653	2.988	1/44.91
End Box (or Upper Nozzle)	0.08720	4.187	1/48.02

ROSA-IV Large Scale Test Facility(LSTF) System Description, JAERI-M 84-237

Table 5.2.2.1-8 Heater Rod Specification

High-Power Rod Specification					
DIVISION		DESIGN VALUES			
		Power Ratio	Output (kW)	Heat Flux (W/cm ²)	Resistance (Ω)
1	9	0.3632	0.568	4.7	0.155
2	8	0.8134	1.263	10.4	0.344
3	7	1.1737	1.823	15.0	0.496
4	6	1.4068	2.185	18.0	0.595
5		1.4950	2.322	19.2	0.632
TOTAL		Average 1.0000	14.0	Average 12.8	3.810

Total Number of Rods = 360

Location (Bundle Number) 13-20

Low Power Rod Specification					
DIVISION		DESIGN VALUES			
		Power Ratio	Output (kW)	Heat Flux (W/cm ²)	Resistance (Ω)
1	9	0.3632	0.394	3.2	0.223
2	8	0.8134	0.875	7.2	0.496
3	7	1.1737	1.263	10.4	0.716
4	6	1.4068	1.514	12.5	0.858
5		1.4950	1.608	13.3	0.912
TOTAL		Average 1.0000	9.700	Average 8.9	5.498

Total Number of Rods = 704

Location (Bundle Number) 1-12

21-24

ROSA-IV Large Scale Test Facility(LSTF) System Description, JAERI-M 84-237

Table 5.2.2.1-9 Pressurizer Characteristics

Parameter	LSTF	PWR	LSTF /PWR
Volume	1.147(m ³)	51(m ³)	1/44.5
Water Volume (at Normal Liquid Level)	0.764(m ³)	32(m ³)	1/41.9
Steam Volume (at Normal Liquid Level)	0.383(m ³) (0.401(m ³)In cluding piping)	19.2(m ³)	1/50.1 (1/47.9)
Inside Diameter	0.6m	2.1m	1/3.5
Vessel Height	4.187m	15.5m	1/3.7
Nominal Pressure	15.55MPa	15.52MPa	-
Nominal Temperature	618.1K	617.4K	-
Elevation from Bottom of Core Heated Zone			
PR Spray Nozzle Upper Surface	-	26.67m	-
PR Shell Top	21.4928m	-	-
Nominal Water Level	20.088m	20.088m	1/1
PR Shell Bottom	17.2828m	-	-
PR Surge Nozzle Lower Surface	-	10.488m	-
Spray Line Flow Rate (Max.)	-	0.0567(m ³ /s)	-
Spray Set Point Close	16.03MPa*	16.03MPa	-
Open	15.68MPa*	15.68 MPa	-
Proportional Heater Capacity	7.5kW	350kW	1/46.7
Backup Heater Capacity	112.5kW	1160kW	1/10.3
Proportional Heaters at Max. Power	15.41MPa*	15.41 MPa	-
Proportional Heaters Off	15.62MPa*	15.62 MPa	-
Backup Heaters On	15.34MPa*	15.34 MPa	-
Backup Heaters Off	15.4MPa*	15.4 MPa	-
Surge Line Flow Rate (Max.)	-	0.2384(m ³ /s)	-

ROSA-IV Large Scale Test Facility(LSTF) System Description, JAERI-M 84-237

Table 5.2.2.1-10 Characteristics of Primary Loop Piping

	LSTF	PWR	LSTF /PWR
Hot Leg Inner Diameter(D)	0.207m	0.7366m	
Hot Leg Length(L)	3.6860m	6.9927m	
Hot Leg Volume	0.1240m ³	2.980m ³	1/24.03
Hot Leg L/ \sqrt{D}	8.102	8.148	1/1.006
Cold Leg Inner Diameter(D)	0.207m	0.6985m	
Length	3.4381m	7.2465m	
Volume	0.1157m ³	2.777m ³	1/24.00
Cross Over Leg Inner Diameter(D)	0.1682m	0.7874m	
Length	9.5498m	8.3458m	
Volume ^{*1)}	0.2122m ³	4.064m ³	1/19.15
Surge Line Inner Diameter	0.0669m	0.2842m	
Length	20.15m	20.306m	
Volume	0.07081m ³	1.288m ³	1/18.19
Spray Line Inner Diameter	0.0212m	0.0873m	
Length	48.283m	69.701m	
Volume ^{*2)}	0.01855m ³	0.4172m ³	1/22.49
Vent Line Inner Diameter(PR~PV)	0.0431m	-	-
Length	39.03m	-	-
Volume	0.05695m ³	-	-
Safety Valve Line(PR~RΦ1-1)			
Inner Diameter	0.0431m	-	-
Length	23.97m	-	-
Volume	3.497×10 ⁻² m ³	-	-
Pressure Relief Valve Line(PR~RΦ1-2)			
Inner Diameter	0.0344m	-	-
Length	17.06m	-	-
Volume	1.585×10 ⁻² m ³	-	-
Normal Flow Rate(per loop)		5.5835m ³ /s	
Surge Line Max. Flow Rate		0.2384m ³ /s	
Spray Line Max. Flow Rate		0.05667m ³ /s	
Primary Loop Pressure Drop			
Core		137.3kPa	
PV inlet and outlet		245.2 kPa	
SG inlet and outlet		196.1 kPa	
Loop Piping		58.8 kPa	

ROSA-IV Large Scale Test Facility(LSTF) System Description, JAERI-M 84-237

Table 5.2.2.1-11 Comparison of Major Design Specification of Primary Coolant Pumps between LSTF and PWR

Items	LSTF	PWR
Number of Pumps	2	4
Pump Type	Centrifugal Pump Canned Type	Centrifugal Pump Shaft-Seal Type
Rated Flow Rate (m ³ /s)	0.054	5.58
Rated Pump Speed (rad/s)	188.5	124.6
Rated Pump Head (m)	10	84
Rated Pump Torque (N-m)	55.2	-
Moment of Inertia (kg· m ²)	0.54	-
Water Volume (m ³)	0.0235	2.4
Reverse Rotation	not allowed	not allowed

ROSA-IV Large Scale Test Facility(LSTF) System Description, JAERI-M 84-237

Table 5.2.2.1-12 List of Major Components in Secondary Coolant System in LSTF

1.	SG-A (Steam Generator in Primary Coolant Loop A)
2.	SG-B (Steam Generator in Primary Coolant Loop B)
3.	JC (Jet Condenser)
4.	CT-1 (Cooling Tower with 8 MW Capacity)
5.	CT-2 (Cooling Tower for JC Spray System)
6.	FF (Main Feedwater Pump)
7.	PA (Auxiliary Feedwater Pump)
8.	Secondary Auto-bleed
9.	Vent-condenser
10.	Break Lines for Steam Line Break, Feedwater Line Break and SG U-Tube Break (Ref. Section 5.5)
11.	Piping of Main Steam Line, Main Feedwater Line and Auxiliary Feedwater Line

ROSA-IV Large Scale Test Facility(LSTF) System Description, JAERI-M 84-237

Table 5.2.2.1-13 Comparison of Major Design Characteristics of LSTF and PWR Steam Generators

(a) Thermal Hydraulic Design for Steam Generator

Items	LSTF	PWR	LSTF /PWR
Number of SGs	2	4	1/2
Max. Heat Removal Rate*(MW)	35.7	856	1/24
Number of U-tubes*	141	3382	1/24
Feedwater Flow Rate* (kg/s)	2.76	469	1/170
Steam Flow Rate* (kg/s)	2.76	468	1/170
Pressure in SG Steam Dome (MPa)	7.34	6.13	1.20/1
Temperature in SG Steam Dome (K)	562.2	550.2	1.02/1
Primary Coolant Flow Rate* (kg/s)	24.5	8352	1/341
Pressure in Primary Loop (MPa)	15.61	15.61	1/1
Temperature at SG inlet (K)	598.1	598.1	1/1
Temperature at SG outlet (K)	562.4	562.4	1/1
Temperature Difference between SG Inlet and Outlet (K)	35.7	35.7	1/1
Inner Diameter of U-tube (mm)	19.6	19.6	1/1
Outer Diameter of U-tube (mm)	25.4	22.23	1.14/1
Total Inner S. Area of U-tubes* (m ²)	171	4214	1/25
Total Outer S. Area of U-tubes* (m ²)	222	4780	1/22
Average Length of U-tubes (m)	19.7	20.2	1/1
Wall Thickness of U-tube (mm)	2.9	1.3	2.23/1
Pitch of U-tubes (mm)	32.5	32.5	1/1

* Designed value per one SG

(b) Height and Elevation of SG

Items	LSTF	PWR	LSTF /PWR
Height			
Inner Height of SG Vessel (m)	19.840	19.972	1/1.0
Inner Height of Plenum (m) including fillerblock (m)	1.823	1.595	1/1.1
Inner Height of SG secondary side (m)	17.695	17.827	1/1.0
Height of U-tube (max.) (m)	10.620	10.620	1/1.0
Height of U-tube (min.) (m)	9.156	9.156	1/1.0
Height of downcomer (m)	14.101	14.101	1/1.0
Elevation from bottom of Active fuel zone (m)			
Bottom of Plenum	EL 5.819	EL 5.819	1/1.0
Bottom of Downcomer	EL 8.164	EL 8.164	1/1.0
Bottom of Secondary-side	EL 7.964	EL 7.964	1/1.0
Bottom of Support Plate (1)	EL 9.228	EL 9.228	1/1.0
Bottom of Support Plate (2)	EL 10.510	EL 10.510	1/1.0
Bottom of Support Plate (3)	EL 11.793	EL 11.793	1/1.0
Bottom of Support Plate (4)	EL 13.076	EL 13.076	1/1.0
Bottom of Support Plate (5)	EL 14.358	EL 14.358	1/1.0
Bottom of Support Plate (6)	EL 15.641	EL 15.641	1/1.0
Bottom of Support Plate (7)	EL 16.924	EL 16.924	1/1.0
Bottom of Downcomer Annulus	EL 19.115	-	-
Feedwater Inlet Nozzle	EL 19.761	EL 19.761	1/1.0
Bottom of Separator Skirt	EL 21.795	EL 21.637	1/1.0
Top of Separator	EL 22.065	EL 22.065	1/1.0
Normal Water Level	EL 20.792	EL 20.792	1/1.0
Bottom of Dryer	EL 23.237	EL 22.569	1/1.0
Top of Dryer	EL 24.512	EL 24.839	1/1.0

(c) Fluid Volume and Flow Area

Items	LSTF	PWR	LSTF /PWR
Fluid Volume (m³)			
Inlet Plenum	0.174	4.18	1/24
Outlet Plenum	0.174	4.18	1/24
Inside U-tube	0.8384	20.65	1/25
Inside Tubesheet	0.0468	1.12	1/24
Total Primary Coolant in SG	1.233	30.1	1/24
Lower Downcomer Piping	0.349	-	-
Total Secondary Coolant	7.480	163.1	1/22
Flow Area per One SG (m²)			
Inside Filler Block	0.0443	-	-
Inside U-tube	0.0425	1.02	1/24
Boiler Section	0.2293	5.101	1/22
U-tube support plate	0.0712	2.147	1/30
Flow Distributer	0.0771	1.9	1/25
Separator Vane	0.129	-	-
Downcomer Annulus	0.0743	-	-
Lower Downcomer	0.0296	0.6627	1/22
Main Steam Line	0.02862	0.3249	1/11
Main Feedwater Line	1.924×10 ⁻³	0.0460	2/24
Feedwater Sparger Nozzles	2.73×10 ⁻³	0.0654	1/24

ROSA-IV Large Scale Test Facility(LSTF) System Description, JAERI-M 84-237

Table 5.2.2.1-14 Major Design Parameters of Jet Condenser

Vessel Height	5.55m
Inner Diameter	1.50m
Free Volume	10m ³
Design Pressure	8.27 MPa
Design Temperature	571.2 K
Vessel Material	Carbon Steel (SB49) with Stainless Steel Clad (SUS316)

ROSA-IV Large Scale Test Facility(LSTF) System Description, JAERI-M 84-237

Table 5.2.2.1-15 Major Design Parameters of Cooling Towers CT-1 and CT-2

Item	CT-1	CT-2
Cooling Method	Air-cooling by Fin-tube and Fan	Air-cooling by Fin-tube and Fan
Design Pressure	8.27 MPa	8.27 MPa
Design Temperature	571.2 K	571.2 K
Cooling Capacity	8 MW	8 MW
Rated Flow Rate	25.37 kg/s	19.87 kg/s
Rated Inflow Temperature	560.1 K	495.2 K
Rated Outflow Temperature	495.2 K	473.2 K

ROSA-IV Large Scale Test Facility(LSTF) System Description, JAERI-M 84-237

Table 5.2.2.1-16 Major Design Parameters of Main and Auxiliary Feedwater Pumps PF and PA

Item	PF	PA
Type	Centrifugal Pump	Flunger Pump
Max. Flow	0.035 m ³ /s	0.0013 m ³ /s
Max. Head	100 m	950 m
Fluid Temperature	195.2 K	Room Temperature
Material	Stainless Steel SUSF316L for Casing and SCS13 for Impeller	Stainless Steel (SUSF304) for Wetted Surface

ROSA-IV Large Scale Test Facility(LSTF) System Description, JAERI-M 84-237

Table 5.2.2.1-17 Major Design Parameters of Piping in Secondary Coolant System**(a) Configuration of Piping and Long Elbow (SUS316LTP)**

Type	I.D.(mm)	Thickness (mm)	Weight (kg/m)
2B	49.5	5.5	7.46
3B	73.9	7.6	15.3
4B	97.1	8.6	22.4
5B	120.8	9.5	30.5
6B	143.2	11.0	41.8
8B	190.9	12.7	63.8

(b) Configuration of 1500# Flanges (SUS316LTP)

Type	Length (mm)	Weight (kg)
2B	108.0	11
3B	123.9	20
4B	130.2	30
6B	177.8	69
8B	219.1	118

ROSA-IV Large Scale Test Facility(LSTF) System Description, JAERI-M 84-237

Table 5.2.2.1-18 Initial Conditions for Run SB-CL-18

		Specified	Measured
Pressurizer pressure	(MPa)	15.5	15.5
Hot leg fluid temperature (A/B)	(K)	598/598	599/599
Cold leg fluid temperature (A/B)	(K)	562/562	563/564
Core power	(MW)	10	10
Core inlet flow rate	(kg/s)	48.6	48.7
Pressurizer water level	(m)	2.7	2.7
Primary coolant pump speed (A/B)	(rpm)	800/800	769/769
Primary coolant flow control valve		full open	full open
SG secondary pressure (A/B)	(MPa)	7.3/7.3	7.3/7.4
SG secondary liquid level (A/B)	(m)	10.3/10.3	10.8/10.6
SG feedwater temperature	(K)	495	494
SG feedwater and steam flow rates	(kg/s)	2.7	2.6-2.8
Break orientation		Side	Side
Break size	(mm/%)	22.5/5.0	22.5/5.0

ROSA-IV/LSTF 5% Cold Leg Break LOCA Experiment Run SB-CL-18 Data Report,
JAERI-M-89-027

Table 5.2.2.1-19 Specified Operational Setpoints and Conditions for Run SB-CL-18

Reactor scram signal	12.97 MPa
Initiation of RC pump coastdown	with reactor scram
Safety injection (SI) signal	12.27 MPa
High pressure charging	not actuated
Safety injection	not actuated
Accumulator injection	4.51 MPa
Low pressure injection	1.29 MPa
Main feedwater termination	with reactor scram
Turbine throttle valve closure	with reactor scram
Auxiliary feedwater	not actuated
Pressurizer Spray Valve Bypass Flow Rate	0.011 kg/s
Pressurizer Proportional-Heater off	1 m (PR Liquid Level)
Pressurizer Back-up-heater off	1 m (PR Liquid Level)
Pressurizer Relief Valve Orifice	6.83 mm
Pressurizer Relief Valve on/off	16.20/16.07 MPa
Pressurizer Safety Valve Orifice	14.5 mm
Pressurizer Safety Valve on/off	17.26/17.06 MPa
Core Power Profile	Case 3
Downcomer-to-Hot-Leg Leakage	0.049 kg/s/loop
Steam Generator Relief Valve Orifice	19.4 mm
Steam Generator Relief Valve on/off	8.03/7.82 MPa
Steam Generator Safety Valve Orifice	26.6 mm
Steam Generator Safety Valve on/off	8.68/7.69 MPa

ROSA-IV/LSTF 5% Cold Leg Break LOCA Experiment Run SB-CL-18 Data Report,
JAERI-M-89-027

Table 5.2.2.1-20 Core Power Decay Curve

Time s	Power MW	Time s	Power MW
0.000	10.000	100.000	5.200
1.000	10.000	150.000	3.632
2.000	10.000	200.000	2.848
3.000	10.000	400.000	1.776
4.000	10.000	600.000	1.568
5.000	10.000	800.000	1.488
6.000	10.000	1000.000	1.424
7.000	10.000	1500.000	1.280
8.000	10.000	2000.000	1.200
10.000	10.000	4000.000	.992
15.000	10.000	6000.000	.848
20.000	10.000	7980.000	.784
29.000	10.000	10020.000	.784
40.000	8.912	19980.000	.592
60.000	7.344	60000.000	.464
80.000	6.128	100020.000	.368

ROSA-IV/LSTF 5% Cold Leg Break LOCA Experiment Run SB-CL-18 Data Report,
JAERI-M-89-027

Table 5.2.2.1-21 ECCS Conditions for Run SB-CL-18

ECCS	Specification
High Pressure charging system Pump shut-off head Delay time from SI signal Flowrate Fluid temperature Injection Location (ratio)	not actuated
High pressure injection system Pump shut-off head Delay time from SI signal Flowrate Fluid temperature Injection Location (ratio)	not actuated
Low pressure injection system Pump shut-off head Delay time from SI signal Flowrate Fluid temperature Injection Location (ratio)	1.29 MPa 17 s scaled full capacity 310 K CLA, CLB (3:1)
ACC system Pressure setpoint Water temperature Injection Location (ratio) Initial tank level to loop-A : ACC-Cold to loop-B : ACC-Hot Terminal tank level to loop-A : ACC-Cold to loop-B : ACC-Hot	4.51 MPa 320 K CLA, CLB (3:1) 5.76 m 6.43 m 3.38 m 5.64 m

ROSA-IV/LSTF 5% Cold Leg Break LOCA Experiment Run SB-CL-18 Data Report,
JAERI-M-89-027

Table 5.2.2.1-22 Total Heat Loss

	Q_F [kW]	Q_M [kW]	Q_G [kW]	Q_{HL} [kW]
Primary System	31.3	33.2	2.4	66.9
SG/Secondary System	29.7	40.7	-	70.4
Total	61.0	73.9	2.4	137.3

Supplemental Description of ROSA-IV/LSTF with No.1 Simulated Fuel-Rod Assembly,
JAERI-M-89-113

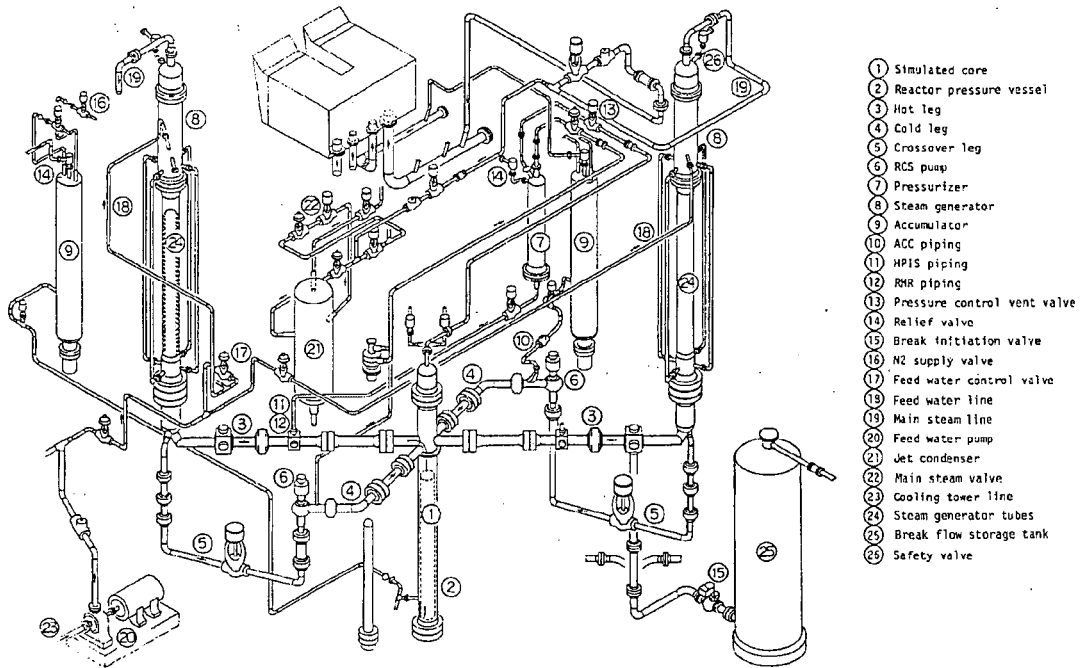


Figure 5.2.2.1-1 General View of LSTF

ROSA-IV Large Scale Test Facility(LSTF) System Description, JAERI-M 84-237

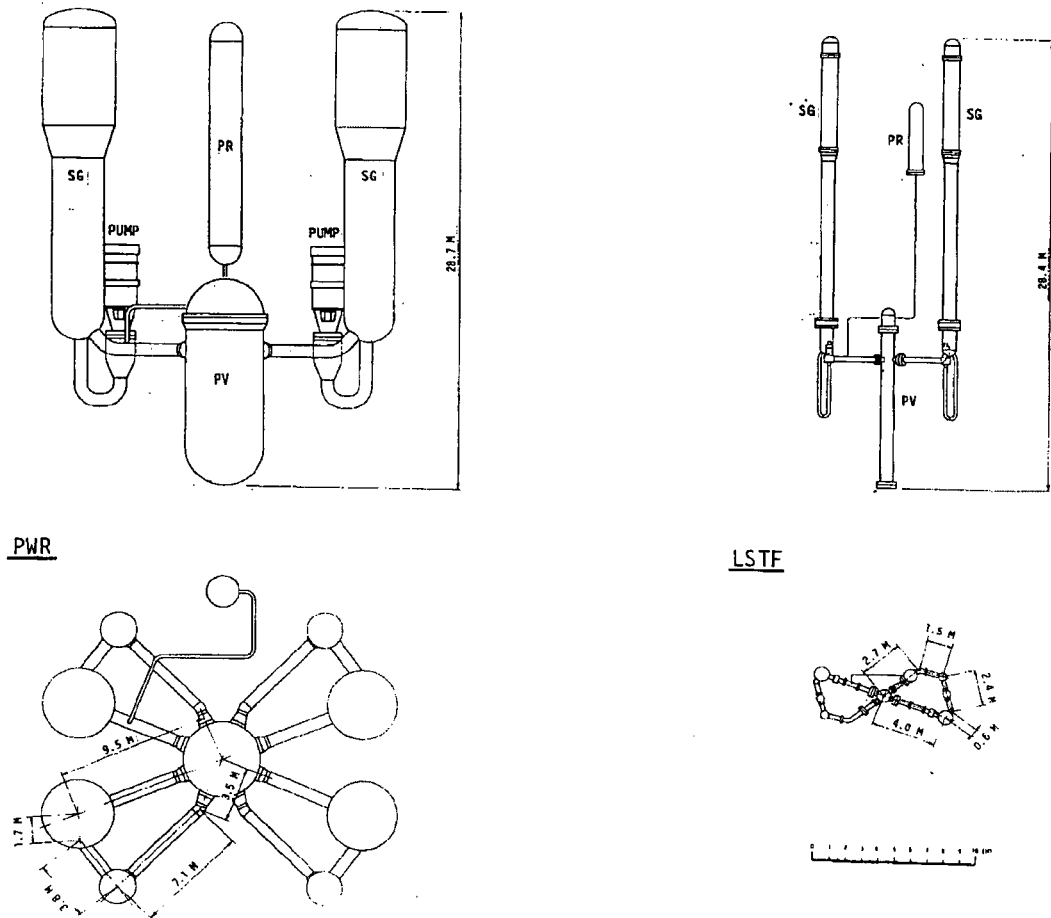


Figure 5.2.2.1-2 Comparison of PWR and LSTF

ROSA-IV Large Scale Test Facility(LSTF) System Description, JAERI-M 84-237

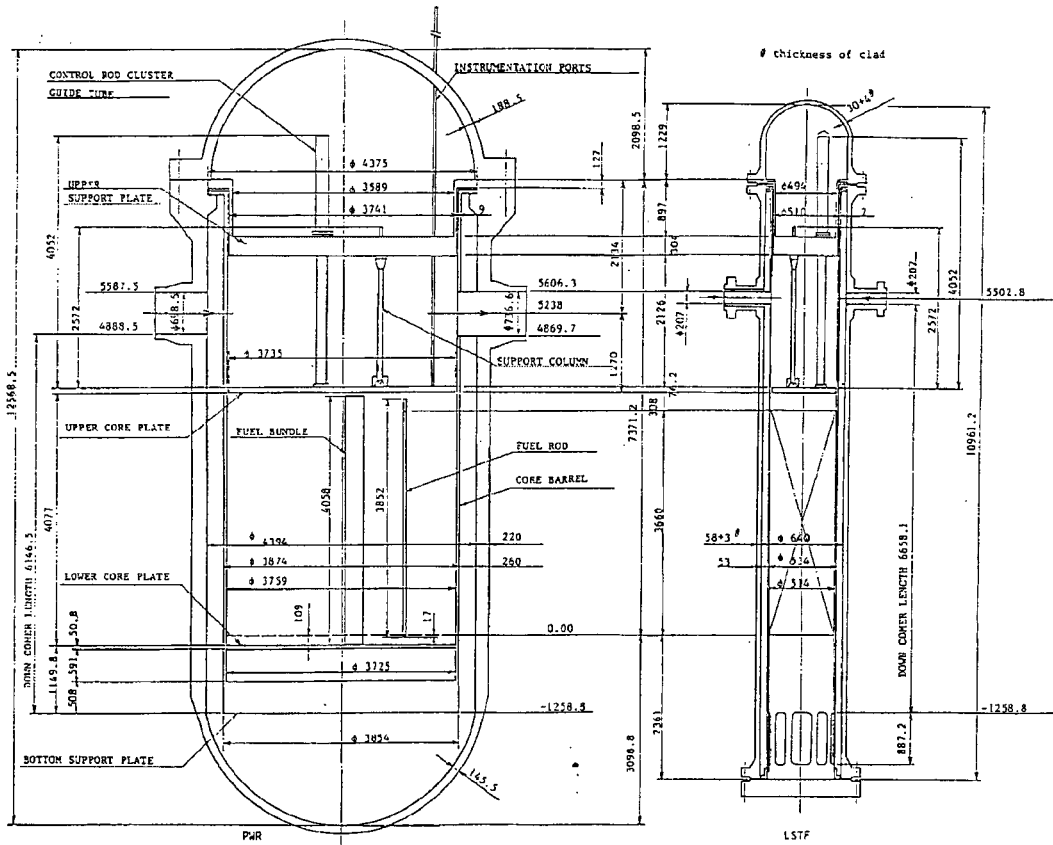


Figure 5.2.2.1-3 Comparison of LSTF and PWR Pressure Vessel Dimensions
ROSA-IV Large Scale Test Facility(LSTF) System Description, JAERI-M 84-237

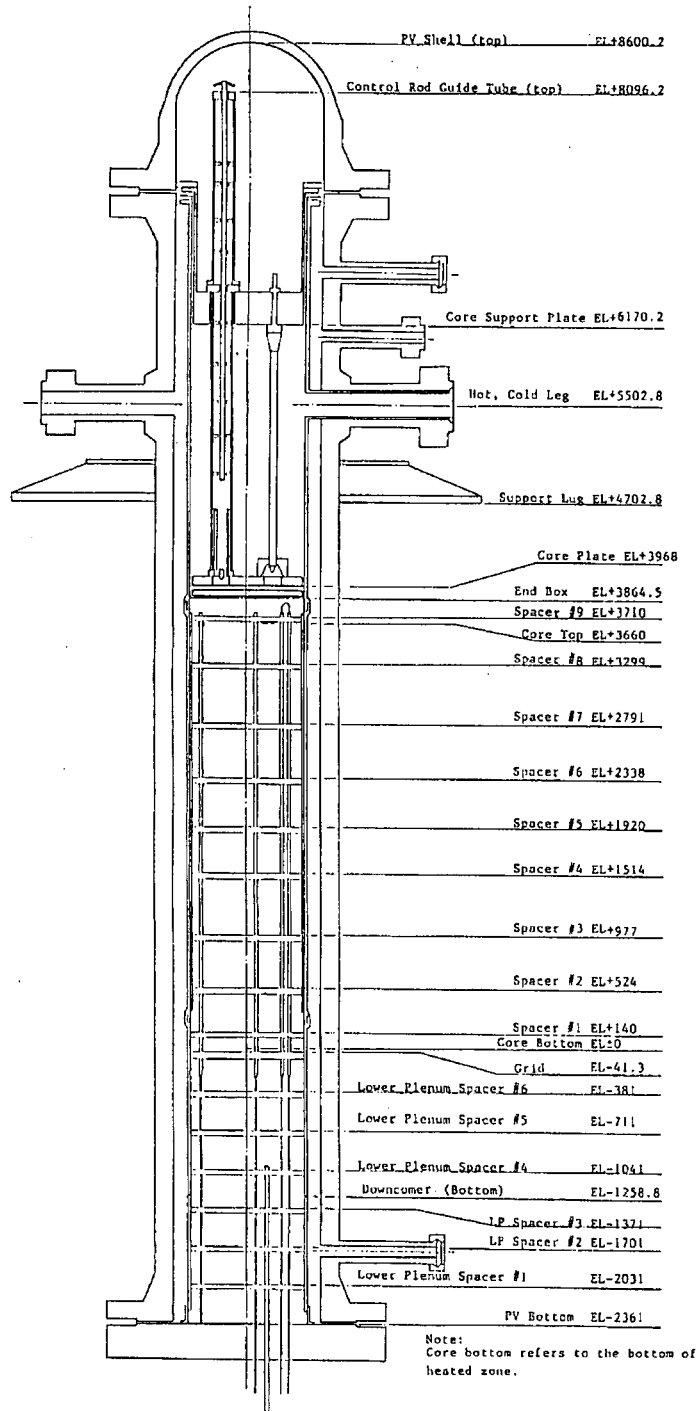


Figure 5.2.2.1-4 Pressure Vessel Assembly
 ROSA-IV Large Scale Test Facility(LSTF) System Description, JAERI-M 84-237

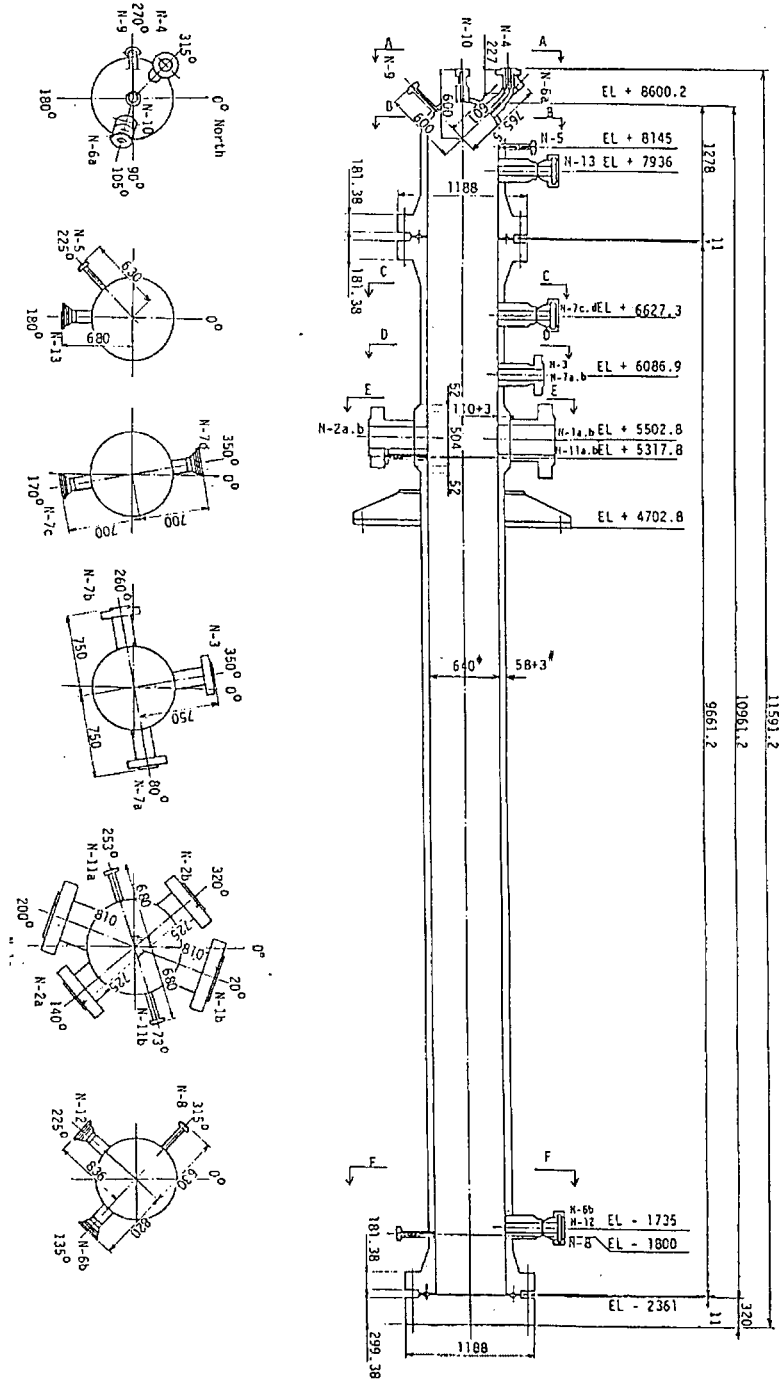


Figure 5.2.2.1-5 Vessel Major Nozzle Locations
 ROSA-IV Large Scale Test Facility(LSTF) System Description, JAERI-M 84-237

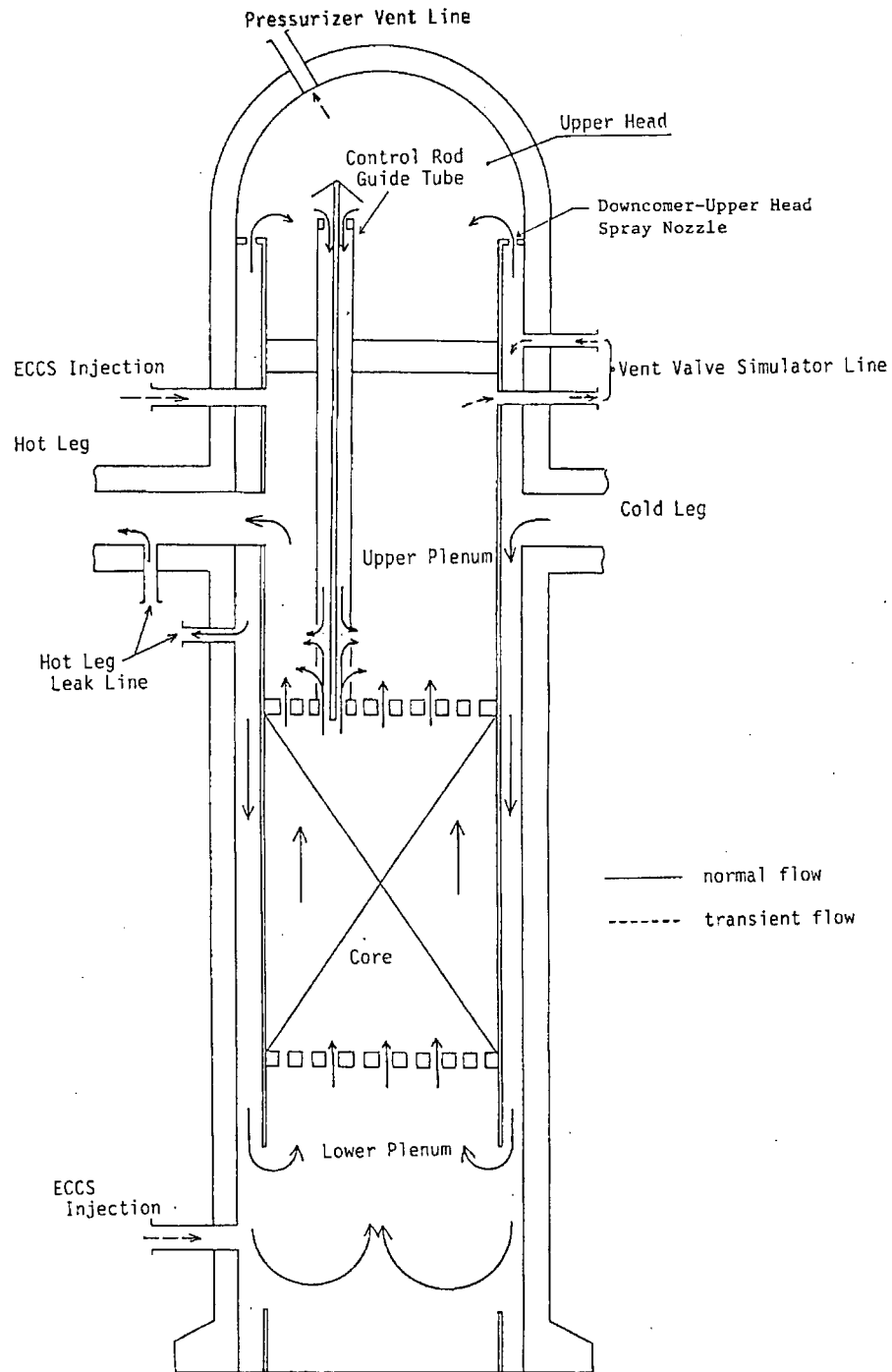


Figure 5.2.2.1-6 Coolant Flow Path in Pressure Vessel
 ROSA-IV Large Scale Test Facility(LSTF) System Description, JAERI-M 84-237

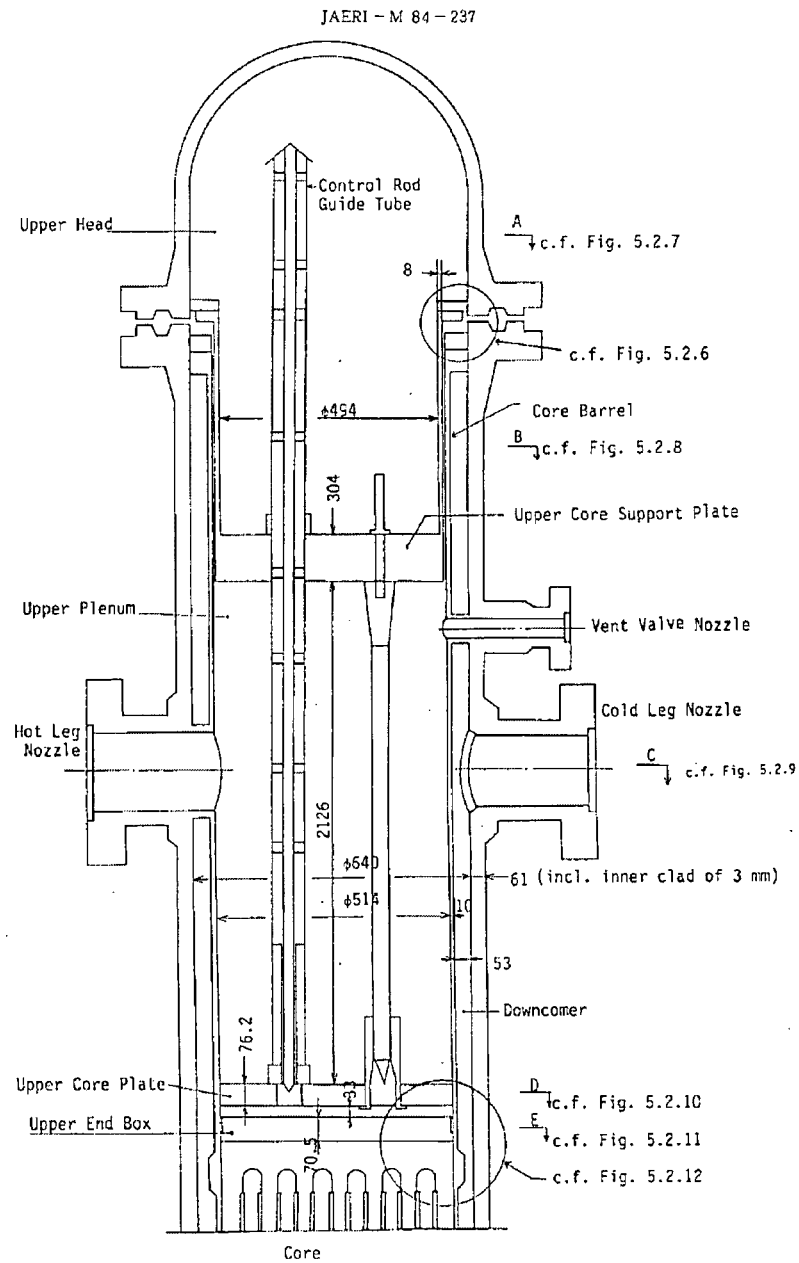


Figure 5.2.2.1-7 Pressure Vessel Internals (Upper Plenum)
 ROSA-IV Large Scale Test Facility(LSTF) System Description, JAERI-M 84-237

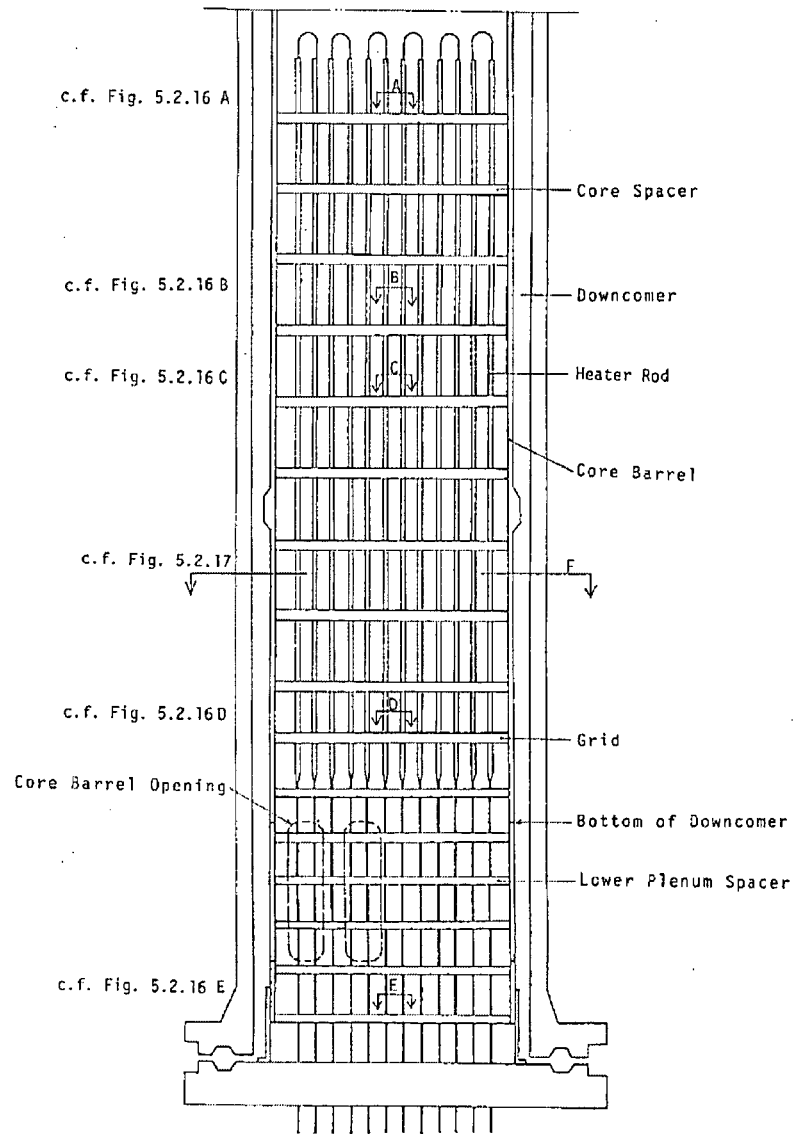


Figure 5.2.2.1-8 Core and Lower Plenum

ROSA-IV Large Scale Test Facility(LSTF) System Description, JAERI-M 84-237

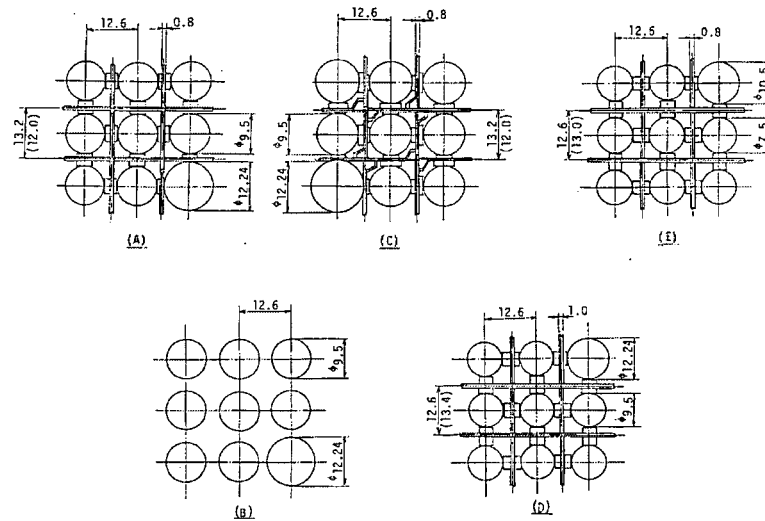


Figure 5.2.2.1-9 Partial Core Cross Sections
(Cross Section Locations shown in Figure 5.2.2.1-8)

ROSA-IV Large Scale Test Facility(LSTF) System Description, JAERI-M 84-237

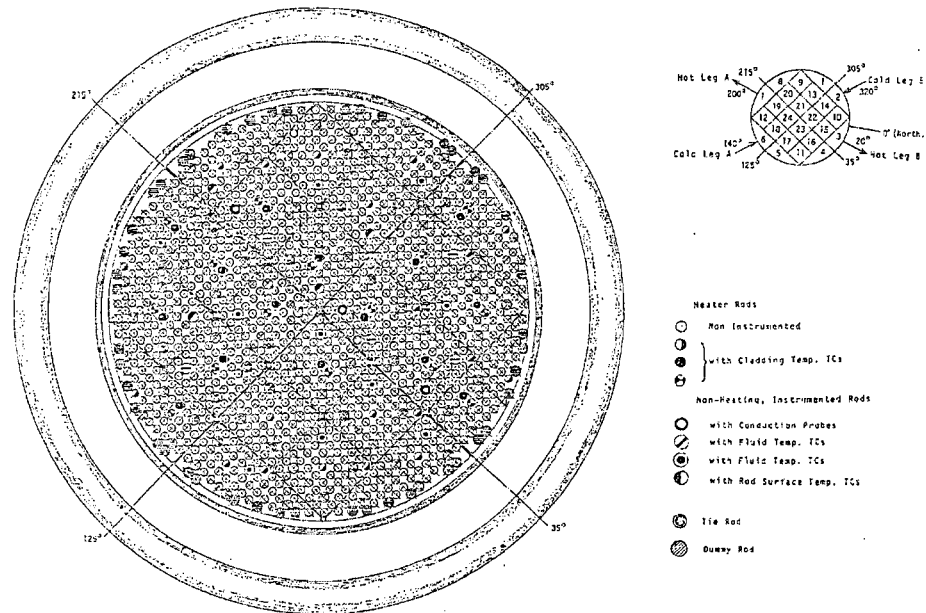


Figure 5.2.2.1-10 Core Cross Section and Heater Rod Arrangement
(Cross Section F in Figure 5.2.2.1-8)

ROSA-IV Large Scale Test Facility(LSTF) System Description, JAERI-M 84-237

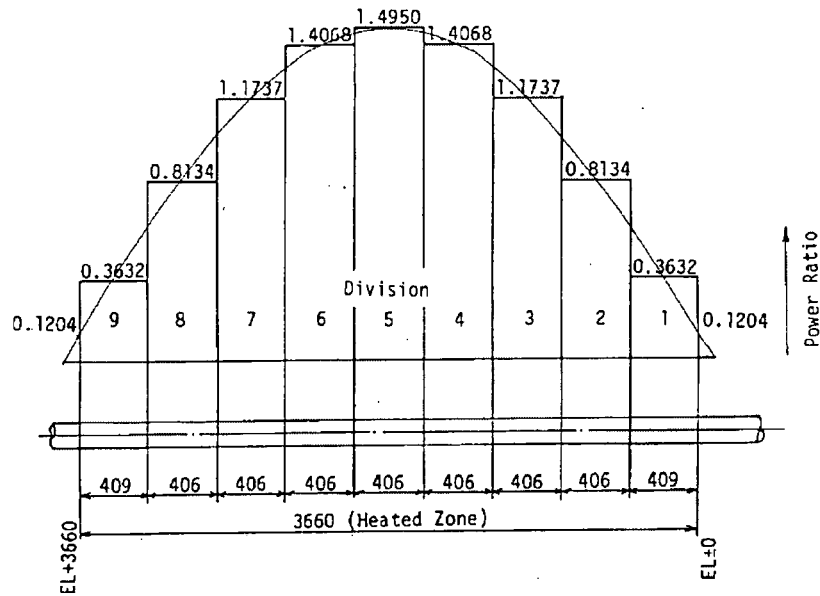


Figure 5.2.2.1-11 Axial Core Power Profile

ROSA-IV Large Scale Test Facility(LSTF) System Description, JAERI-M 84-237

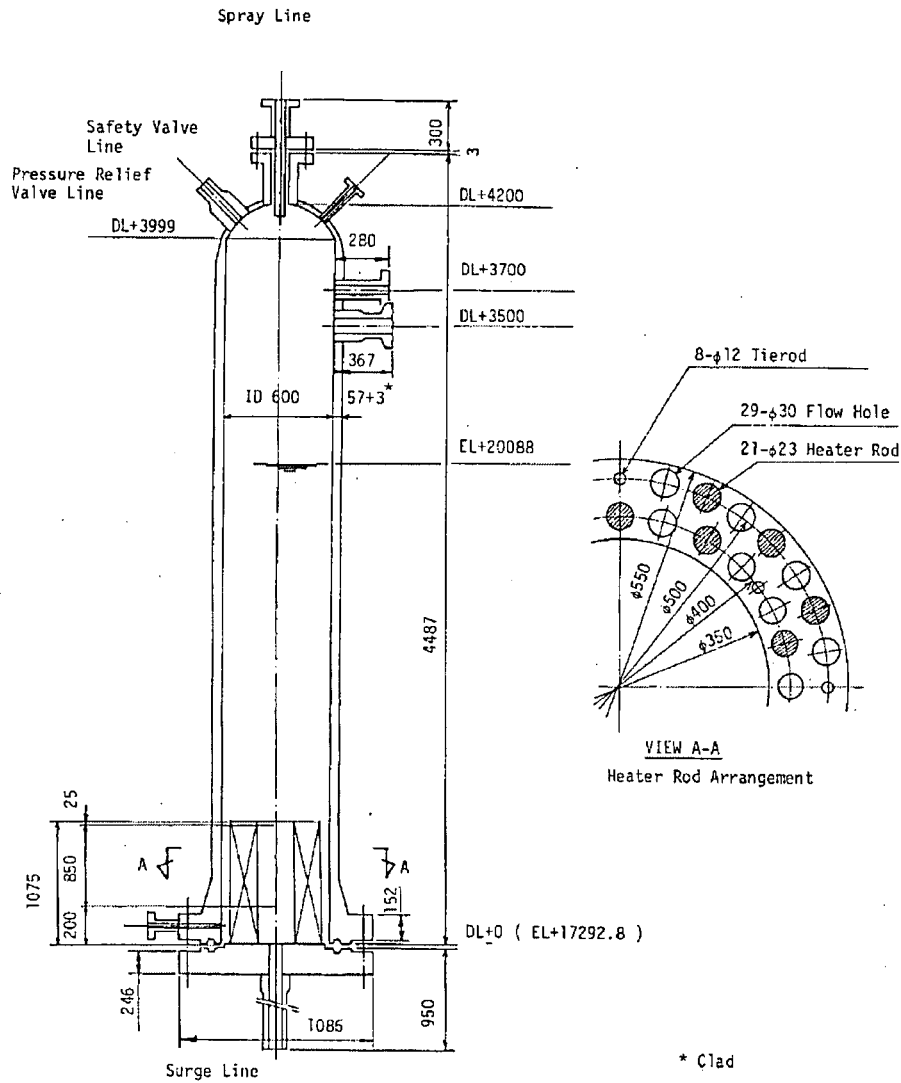


Figure 5.2.2.1-12 Pressurizer

ROSA-IV Large Scale Test Facility(LSTF) System Description, JAERI-M 84-237

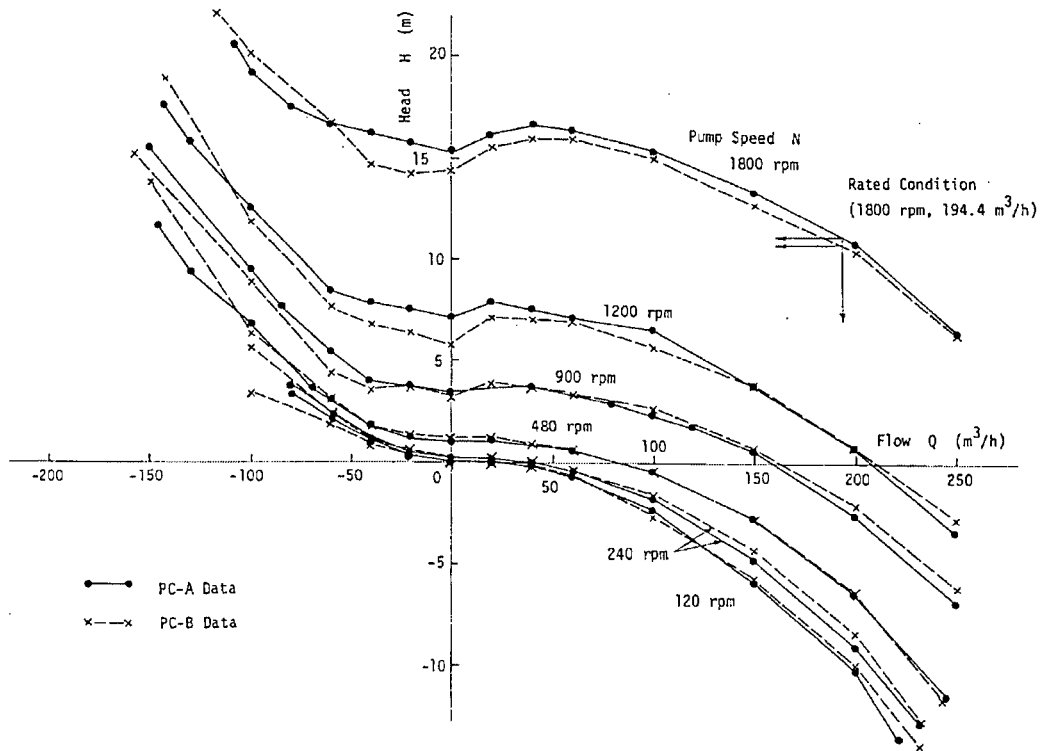


Figure 5.2.2.1-13 Head-Flow Curves for PC-A and PC-B
 ROSA-IV Large Scale Test Facility(LSTF) System Description, JAERI-M 84-237

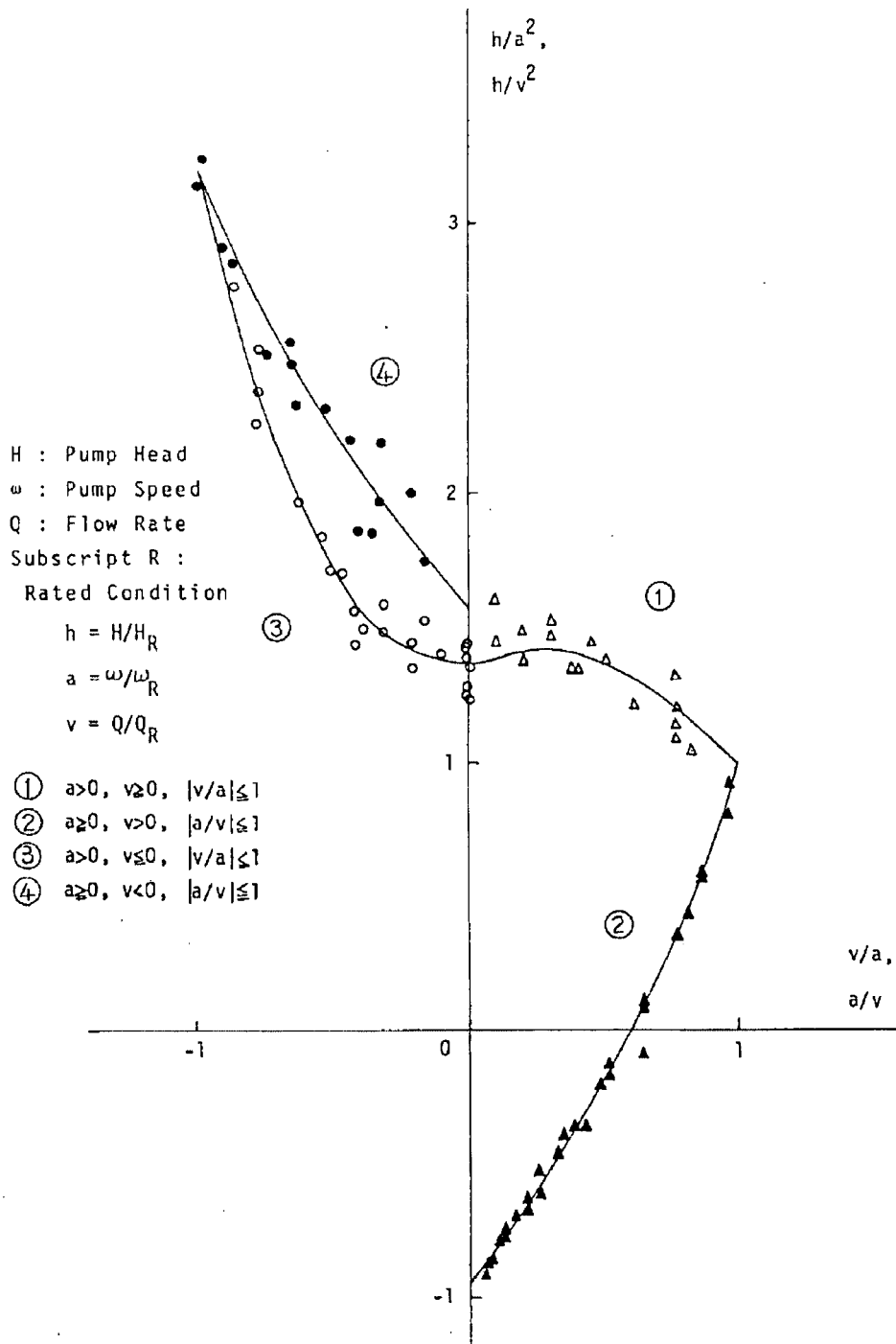


Figure 5.2.2.1-14 Single-phase Head Homologous Curves for PC-A ($a > 0$)
 ROSA-IV Large Scale Test Facility(LSTF) System Description, JAERI-M 84-237

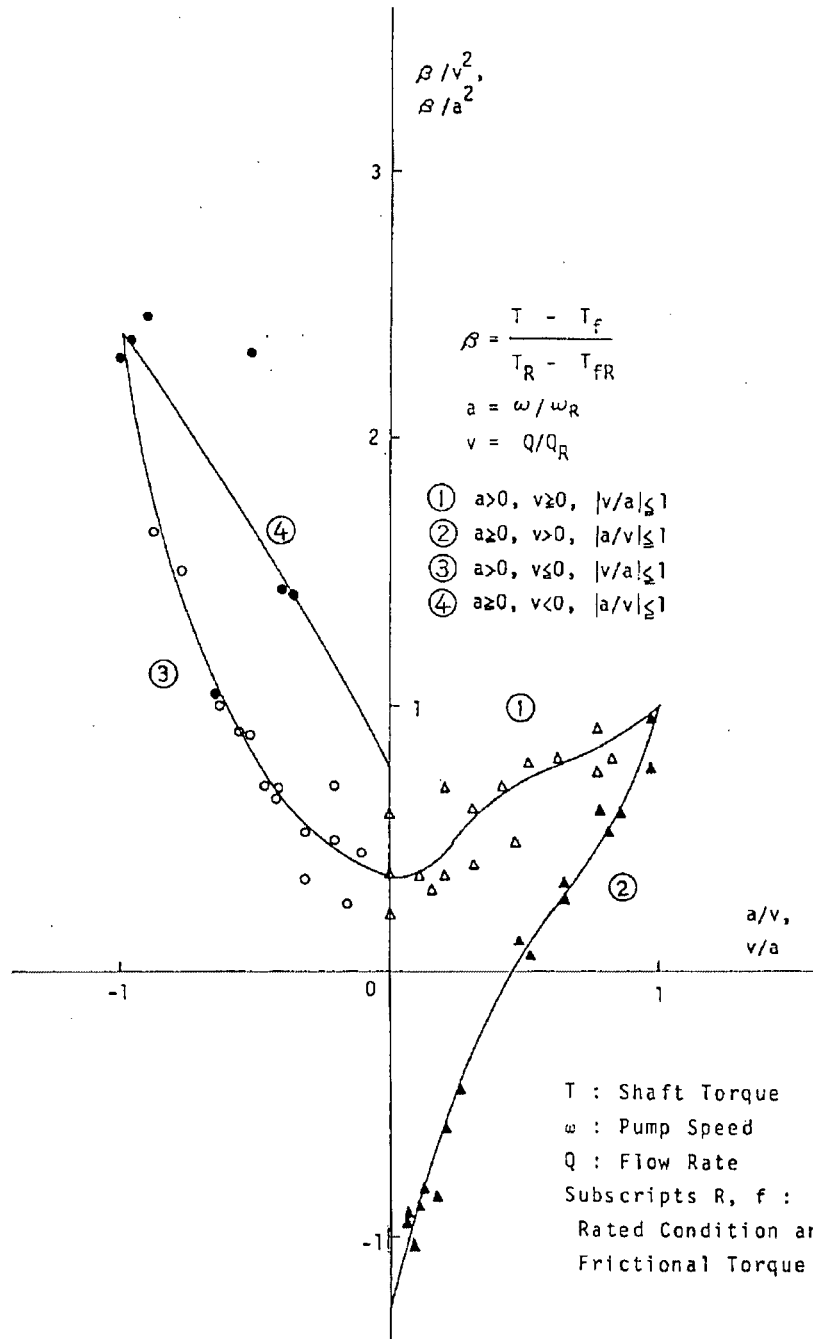


Figure 5.2.2.1-15 Single-phase Torque Homologous Curves for PC-A
 ROSA-IV Large Scale Test Facility(LSTF) System Description, JAERI-M 84-237

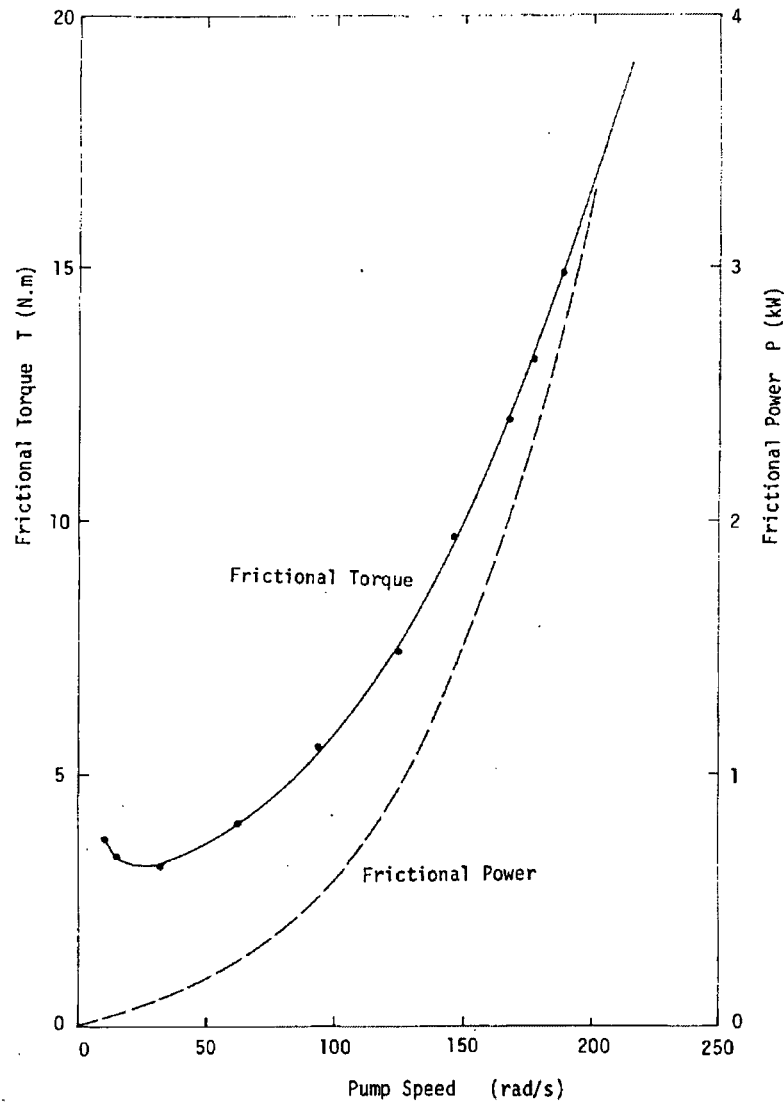


Figure 5.2.2.1-16 Frictional Torque Characteristics of PC-A
 ROSA-IV Large Scale Test Facility(LSTF) System Description, JAERI-M 84-237

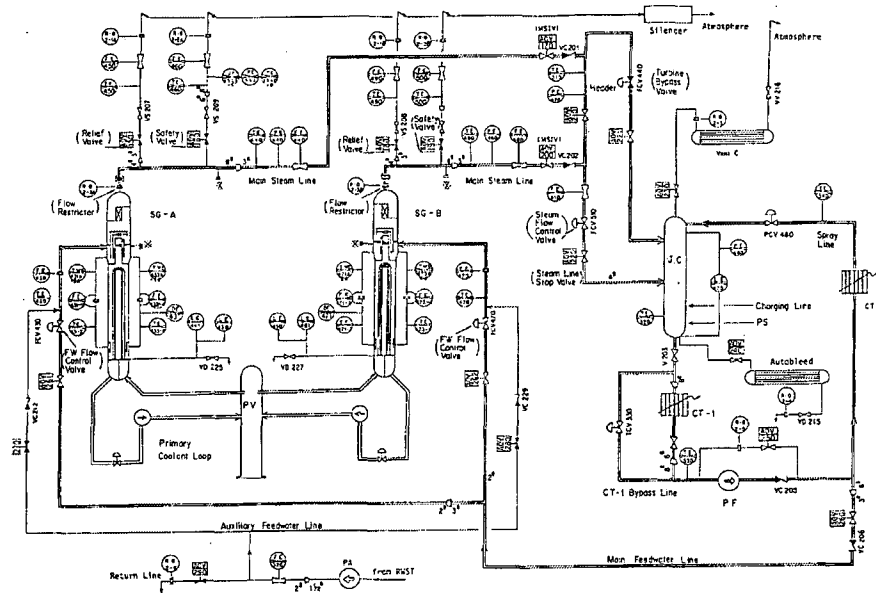


Figure 5.2.2.1-17 Flow Diagram of LSTF Secondary Coolant System
 ROSA-IV Large Scale Test Facility(LSTF) System Description, JAERI-M 84-237

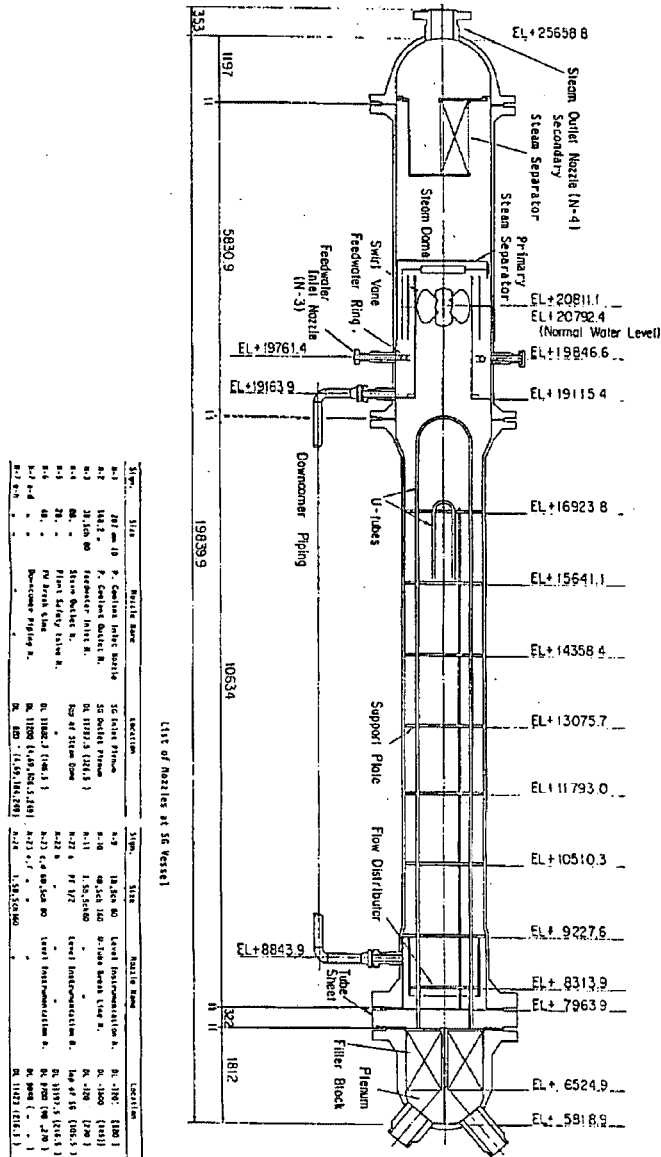


Figure 5.2.2.1-18 Configuration of Steam Generator SG-A with Internals
ROSA-IV Large Scale Test Facility(LSTF) System Description, JAERI-M 84-237

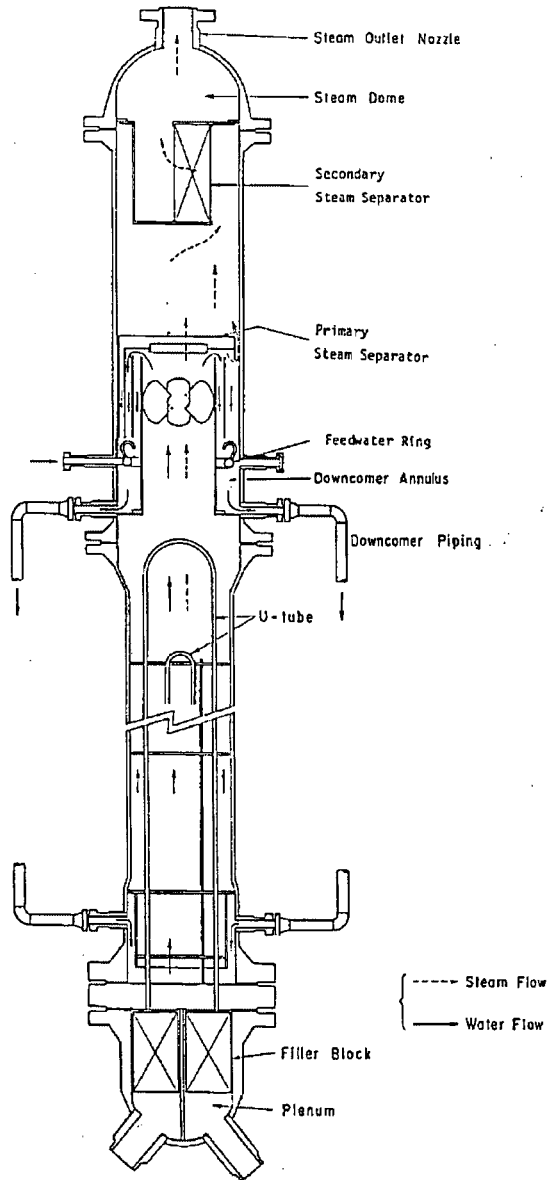


Figure 5.2.2.1-19 Coolant Flow in SG Secondary Side
 ROSA-IV Large Scale Test Facility(LSTF) System Description, JAERI-M 84-237

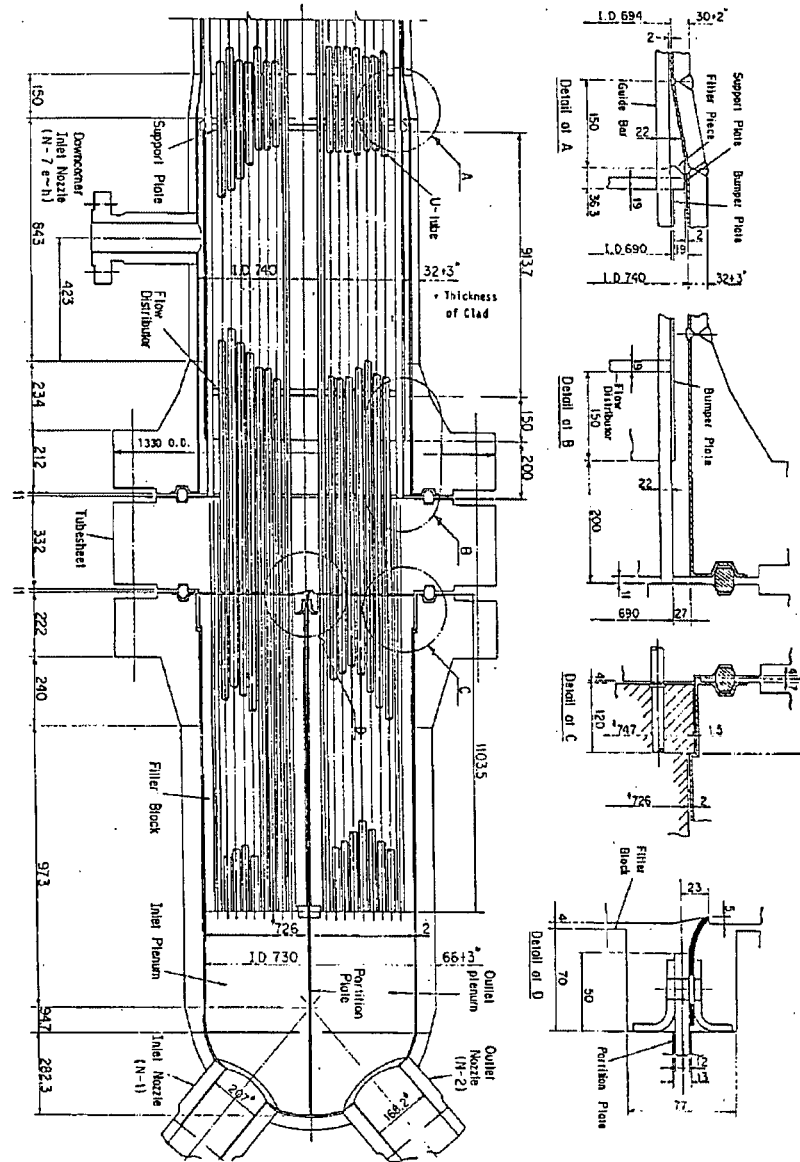


Figure 5.2.2.1-20a Details of SG Plenum and Tube Sheet
 ROSA-IV Large Scale Test Facility(LSTF) System Description, JAERI-M 84-237

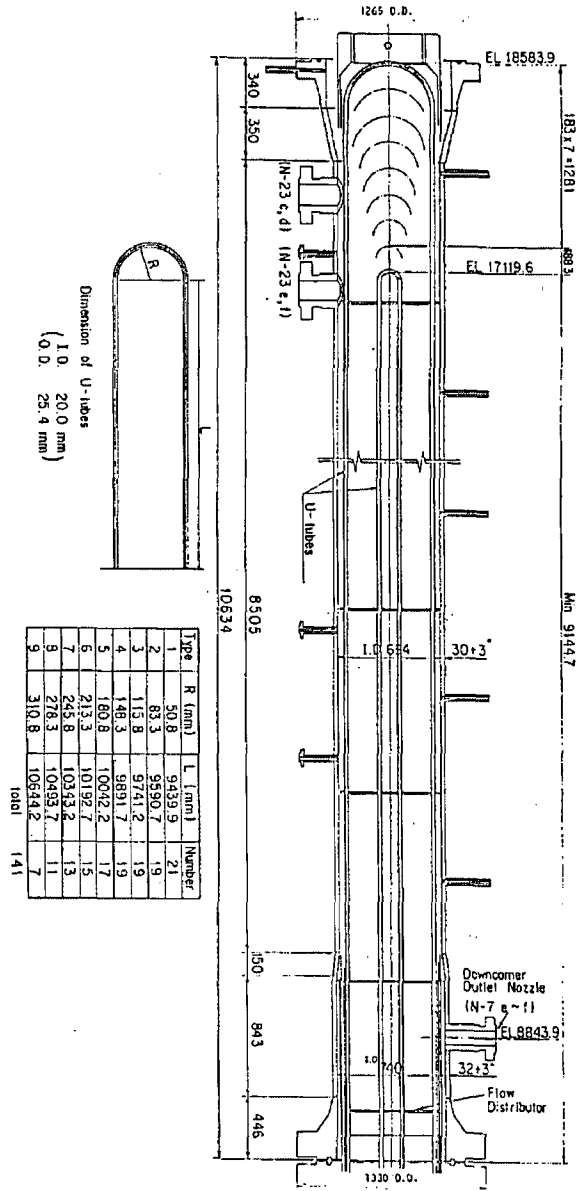


Figure 5.2.2.1-20b Details of Middle Part of SG Vessel and U-tubes
ROSA-IV Large Scale Test Facility(LSTF) System Description, JAERI-M 84-237

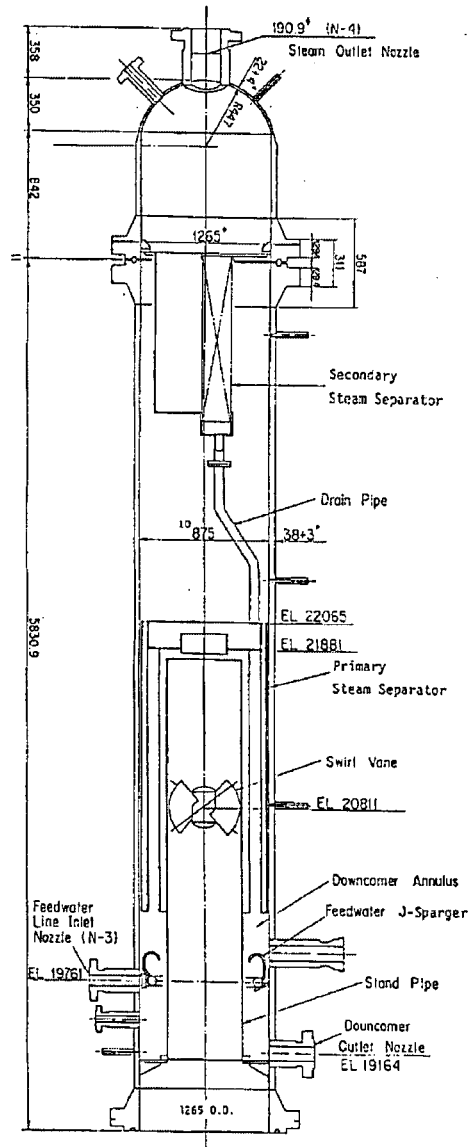


Figure 5.2.2.1-20c Details of Top Part of SG Vessel
 ROSA-IV Large Scale Test Facility(LSTF) System Description, JAERI-M 84-237

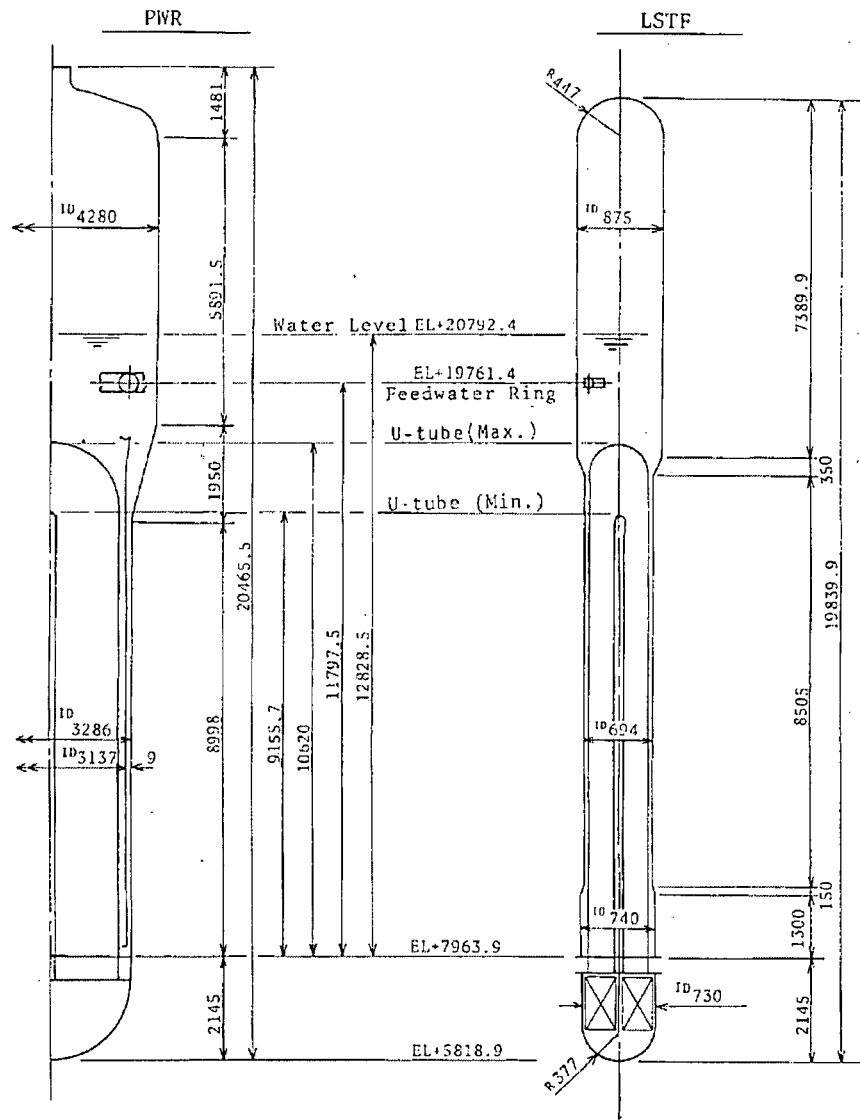


Figure 5.2.2.1-21 Comparison of LSTF and PWR SGs
 ROSA-IV Large Scale Test Facility(LSTF) System Description, JAERI-M 84-237

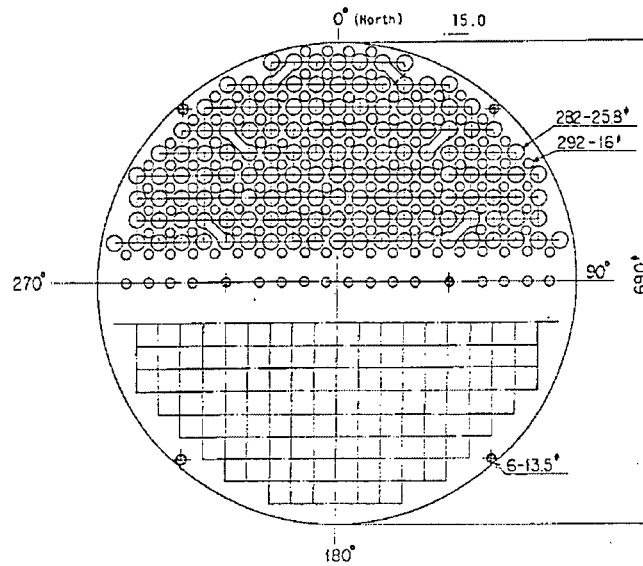


Figure 5.2.2.1-22 Details of U-Tube Support Plate
 ROSA-IV Large Scale Test Facility(LSTF) System Description, JAERI-M 84-237

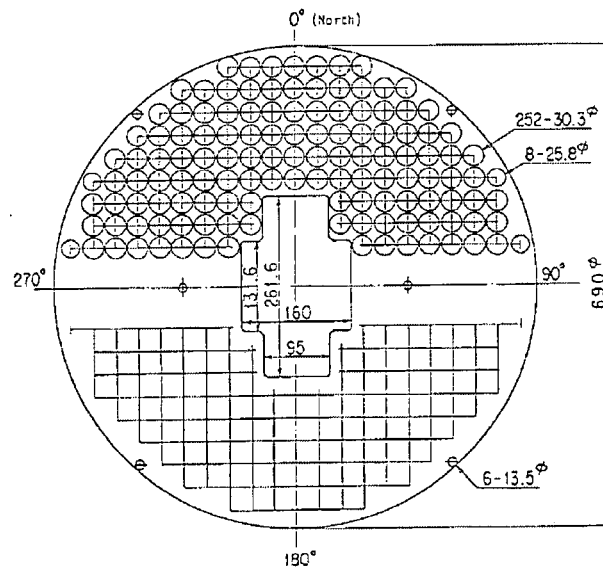


Figure 5.2.2.1-23 Details of Flow Distributor
 ROSA-IV Large Scale Test Facility(LSTF) System Description, JAERI-M 84-237

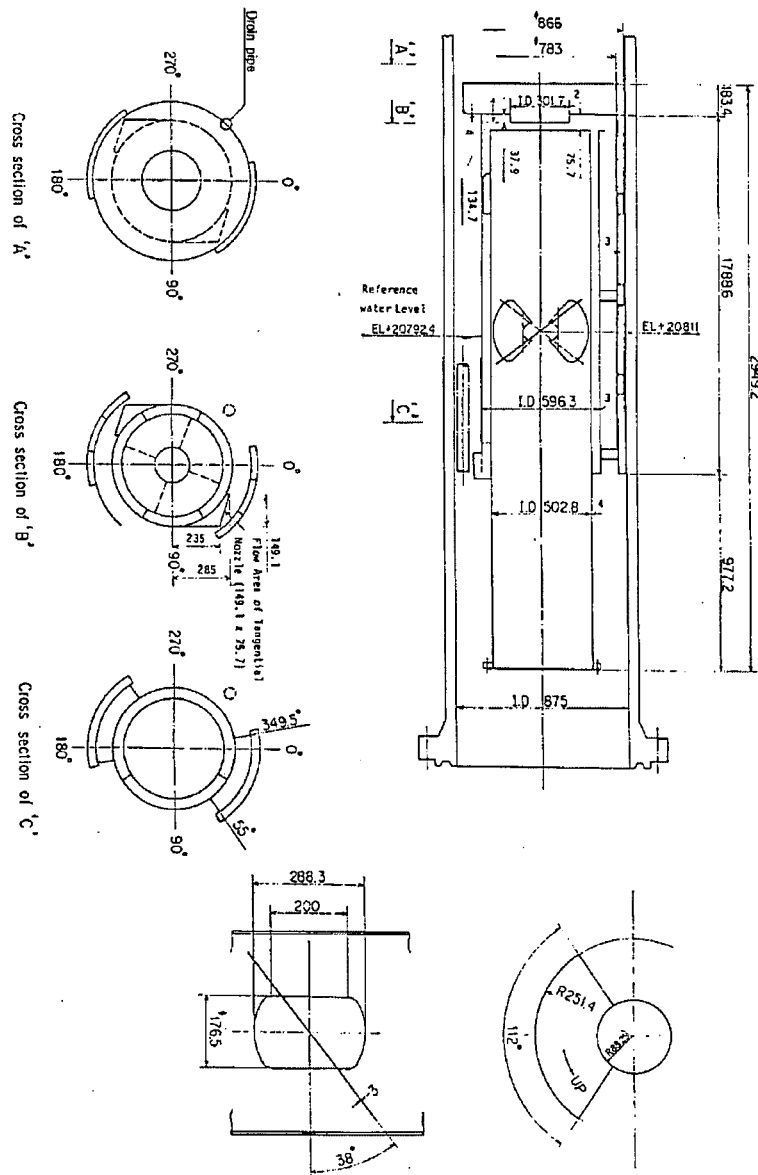


Figure 5.2.2.1-24 Details of Primary Steam Separator
 ROSA-IV Large Scale Test Facility(LSTF) System Description, JAERI-M 84-237

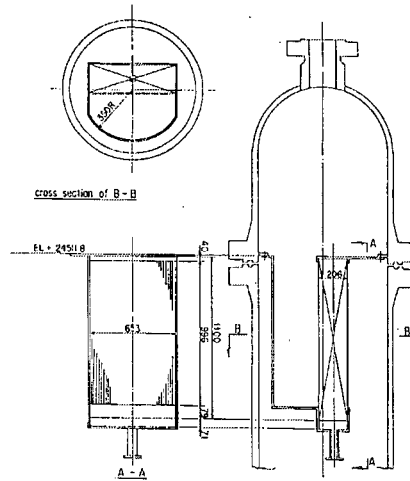


Figure 5.2.2.1-25 Configuration of Secondary Steam Separator
 ROSA-IV Large Scale Test Facility(LSTF) System Description, JAERI-M 84-237

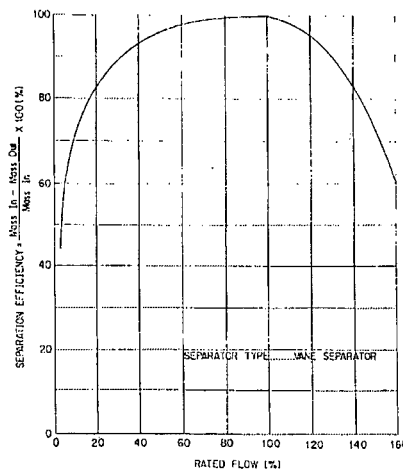


Figure 5.2.2.1-26 Design Flow Characteristics for Secondary Steam Separator
 ROSA-IV Large Scale Test Facility(LSTF) System Description, JAERI-M 84-237

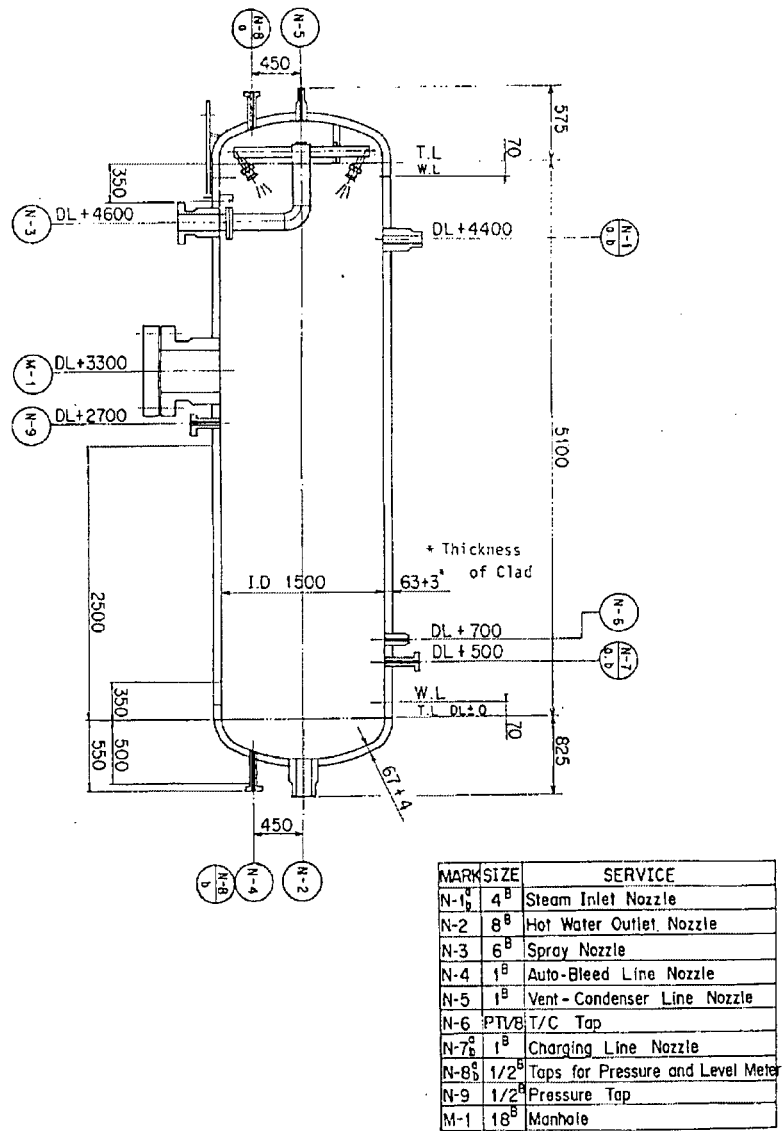


Figure 5.2.2.1-27 Details of Jet Condenser JC
 ROSA-IV Large Scale Test Facility(LSTF) System Description, JAERI-M 84-237

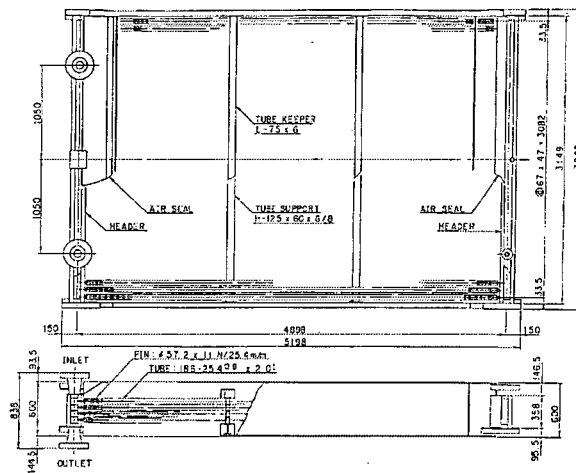


Figure 5.2.2.1-28.a Details of Cooling Tower CT-1
 ROSA-IV Large Scale Test Facility(LSTF) System Description, JAERI-M 84-237

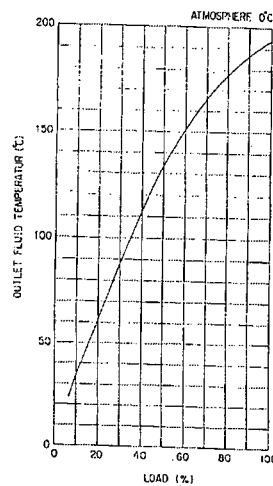


Figure 5.2.2.1-28.b Design Performance for CT-1
 ROSA-IV Large Scale Test Facility(LSTF) System Description, JAERI-M 84-237

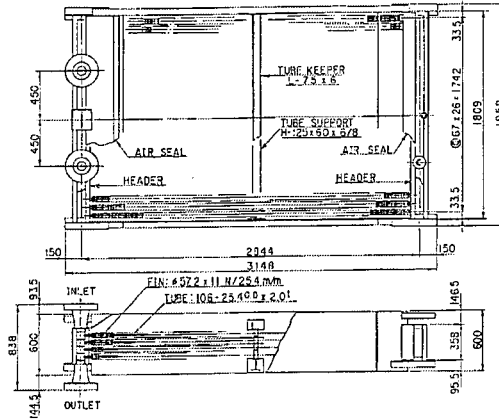


Figure 5.2.2.1-29.a Details of Cooling Tower CT-2
 ROSA-IV Large Scale Test Facility(LSTF) System Description, JAERI-M 84-237

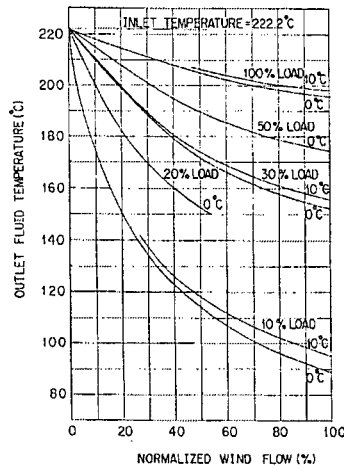


Figure 5.2.2.1-29.b Design Performance for CT-2
 ROSA-IV Large Scale Test Facility(LSTF) System Description, JAERI-M 84-237

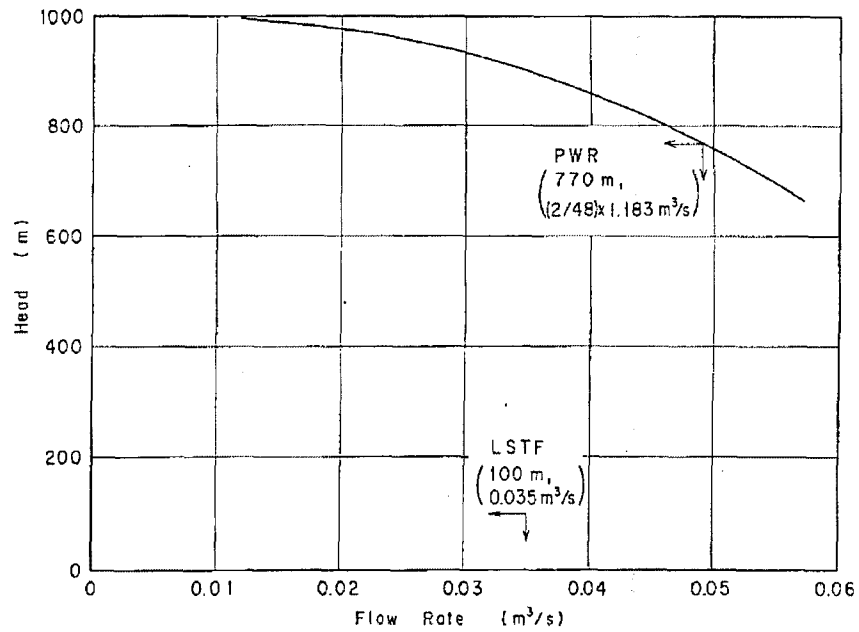


Figure 5.2.2.1-30 Pump Characteristics of PWR Main Feedwater Pump
 ROSA-IV Large Scale Test Facility(LSTF) System Description, JAERI-M 84-237

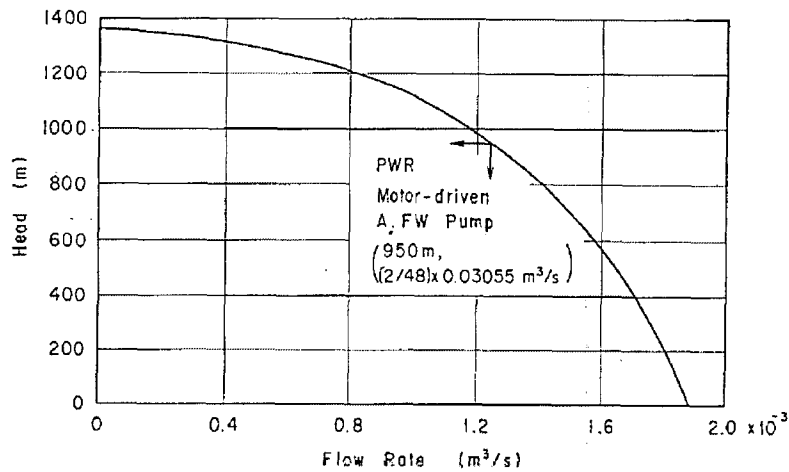
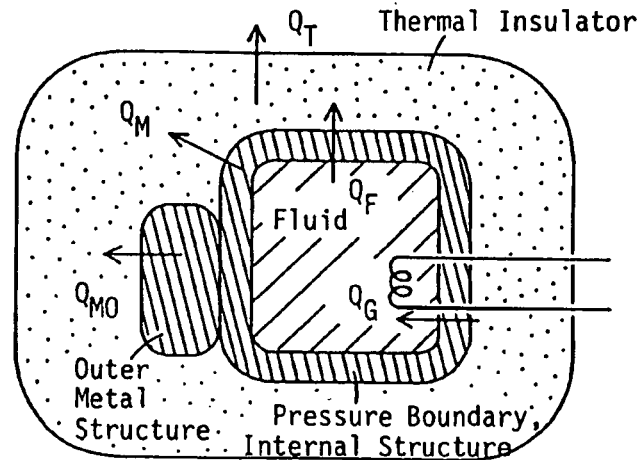


Figure 5.2.2.1-31 Pump Characteristics of PWR Auxiliary Feedwater Pump
 ROSA-IV Large Scale Test Facility(LSTF) System Description, JAERI-M 84-237



$$Q_T = Q_F + Q_G + Q_M + Q_{MO}$$

Q_T : Total Energy Loss through Thermal Insulator

Q_F : Energy Loss in Fluid

Q_M : Energy Loss in Metal

Q_{MO} : Energy Loss in Outer Metal

Q_G : Energy Income from Heater or Operating Pumps

Figure 5.2.2.1-32 Definition of Heat Loss for Each Component in LSTF System
 Supplemental Description of ROSA-IV/LSTF with No.1 Simulated Fuel-Rod Assembly,
 JAERI-M-89-113

5.2.2.2 ROSA-IV/LSTF small break (10%) LOCA test (SB-CL-09)**(1) Facility Design and Scaling Issues/Distortions**

A 10% cold leg break experiment (SB-CL-09) was conducted at the Large-Scale Test Facility (LSTF) on August 28 in 1986, at the early stage of the ROSA-IV Program, simulating a loss-of-coolant accident (LOCA) of pressurized water reactors (PWRs). The objective of SB-CL-09 test was to clarify thermal-hydraulic phenomena especially for the core cooling conditions under the small break LOCAs with relatively large break sizes. A break orifice with an inner diameter of 31.9 mm (1.26 in) was used to simulate 10% cold leg break. The high pressure injection (HPI) system was assumed to fail. Details of the experiment are given in Reference 5.2.2.2-1.

Features of facility design, scaling issues and distortions specific to ROSA-IV/LSTF are described in Section 5.2.2.1, and are applicable to the SB-CL-09 test.

(2) Range of Conditions

The measured initial steady-state conditions of the SB-CL-09 test are listed in Table 5.2.2.2-1, which were in reasonable agreement with the values specified for the test. As the LSTF initial core power of 10 MW was limited to 14% of the 1/48-scaled reference PWR rated core power (3423 MW), initial core flow rate was controlled to approximately 14% of the 1/48-scaled PWR core flow rate in order to obtain similar initial coolant enthalpy distributions across the core.

Initial steam generator (SG) secondary pressure was intended to be 7.3 MPa to limit the primary-to-secondary heat transfer rate at 10 MW, while 6.1 MPa is a nominal value in the reference PWR. The secondary pressures were actually about 7.5 MPa. Initial secondary-side liquid levels were set above the top of U-tubes and the main feedwater flow rate was controlled to maintain stable secondary water level. Initial main steam flow rate was 2.60 kg/s for both SGs.

Table 5.2.2.2-2 shows the specified control logic, operation set-points and boundary conditions. The experiment was initiated by quickly opening the break valve in the break unit connected to the cold leg B at time zero. At the same time, rotation speed of each primary coolant pump is raised up to 1500 rpm for better simulation of the transient pump coast-down characteristics from the rated PWR pump speed after the scram signal, as same as was done in Run SB-CL-18. Scram and safety injection (SI) signals are generated when the pressurizer (PR) pressure decreased to 12.97 MPa and 12.27 MPa, respectively.

The core power, which is initially maintained at 10 MW, is changed by the scram signal into the transient power curve (Table 5.2.2.1-20) and starts to decrease along the power decay simulation curve 29 seconds after the scram signal. The core power started to decrease from 10 MW at 42 seconds after the break initiation. The core power was tripped off at 111 seconds in this experiment in order to protect heater rods from overheat above 923 K according to the power control logic shown in Table 5.2.2.2-2. The threshold temperature for activating the LSTF core protection and power controlling system is also shown in Table 5.2.2.2-2.

The primary coolant pump speed is controlled to simulate reference PWR pump coast-down transient after the scram. The pump rotations in two loops were actually controlled and their electric powers were tripped at 250 seconds after the scram signal.

Table 5.2.2.2-3 shows the ECCS condition for SB-CL-09 test. As the HPI system was assumed to fail, the available ECCSs included the AIS (accumulator injection system) and the LPI (low pressure injection) system. The ECCS injection ratio to the primary loop is set as 3 for the cold leg A to simulate three intact primary loops and 1 for the cold leg B to simulate a broken loop. Initial pressure and coolant temperature of ACC (accumulator for cold leg A in loop with pressurizer) and ACH (accumulator for cold leg B in loop without pressurizer) tanks were actually 4.6 MPa and 322 to 323 K, respectively. The coolant temperature of LPI system was 310 K. Flow from the LPI system was allowed if the primary pressure was less than 1.29 MPa and more than 17 seconds had elapsed since the SI signal had been generated.

(3) Data to be compared

The same experimental measurements as described in Section 5.2.2.1 were obtained for the SB-CL-09 test, details of which are referred to Appendix A of Reference 5.2.2.2-1.

(4) Data uncertainties

After the data acquisition, some experimental data are calibrated. The high-range pressure data in the pressurizer (PR) and upper plenum (UO) are corrected by the low-range pressure data, which had lower uncertainty.

Collapsed water level derived from differential pressure (DP) data is calibrated if it includes a zero shift at a clearly steam-filled condition. Actually, some collapsed water levels in steam generator (SG) U-tubes showed apparent zero shifts when water level disappeared at the end of experiment and they were corrected as follows.

The collapsed water level at the inlet side of SG-A Tube-3 (RC 144) showed a constant zero shift of -0.25 m at 1100 seconds and it was corrected to be zero at 1100 seconds. Similarly, level shifts of -0.36 m at SG-A Tube-2 inlet side (RC 145), -0.18 m at SG-B Tube-2 inlet side (RC 161), +0.21 m at SG-B Tube-5 inlet side (RC 164), and +1.2 m at SG-B Tube-3 outlet side (RC 166) were corrected. The collapsed water level at the SG-B inlet rise region (RC 159) showed a slight shift of -0.05 m at 1100 seconds and it was also corrected. Other RC collapsed level data were estimated as good with lower zero-shifts than these corrected RC data.

(5) Distortion

Related information is described in Section 5.2.2.1.

(6) References

5.2.2.2-1 M. Suzuki and H. Nakamura, "A Study of ROSA/LSTF SB-CL-09 Test Simulating PWR 10% Cold Leg Break LOCA - Loop-seal Clearing and 3D Core Heat-up Phenomena," JAEA-Research 2008-087, October 2008.

Table 5.2.2.2-1 Initial Conditions for Run SB-CL-09

		<u>Specified</u>	<u>Measured</u>
<u>Pressurizer pressure</u>	<u>(MPa)</u>	<u>15.52</u>	<u>15.45</u>
<u>Hot leg fluid temperature (A/B)</u>	<u>(K)</u>	<u>598.1/598.1</u>	<u>600.6/600.3</u>
<u>Cold leg fluid temperature (A/B)</u>	<u>(K)</u>	<u>562/562</u>	<u>565.5/564.9</u>
<u>Core power</u>	<u>(MW)</u>	<u>10</u>	<u>10</u>
<u>Core inlet flow rate</u>	<u>(kg/s)</u>	<u>48.6</u>	<u>52.0</u>
<u>Pressurizer water level</u>	<u>(m)</u>	<u>2.7</u>	<u>2.67</u>
<u>SG secondary pressure (A/B)</u>	<u>(MPa)</u>	<u>7.3/7.3</u>	<u>7.45/7.48</u>
<u>SG secondary liquid level (A/B)</u>	<u>(m)</u>	<u>10.3/10.3</u>	<u>10.7/10.6</u>
<u>SG feedwater temperature</u>	<u>(K)</u>	<u>495</u>	<u>495.2</u>
<u>SG feedwater and steam flow rates</u>	<u>(kg/s)</u>	<u>2.74</u>	<u>2.60/2.95</u>
<u>ACC initial pressure (A/B)</u>	<u>(MPa)</u>	<u>4.51/4.51</u>	<u>4.6/4.6</u>
<u>ACC water temperature (A/B)</u>	<u>(K)</u>	<u>320/320</u>	<u>322.9/322.1</u>
<u>LPI water temperature</u>	<u>(K)</u>	<u>310</u>	<u>310.1</u>
<u>Break orientation</u>		<u>Side</u>	<u>Side</u>
<u>Break size</u>	<u>(mm/%)</u>	<u>31.9/10.0</u>	<u>31.9/10.0</u>

A Study on ROSA/LSTF SB-CL-09 Test Simulating PWR 10% Cold Leg Break LOCA,
JAEA-Research-2008-087

Table 5.2.2.2-2 Specified Operational Setpoints and Conditions for Run SB-CL-09

<u>Reactor scram signal</u>	<u>12.97 MPa</u>
<u>Initiation of RC pump coastdown</u>	<u>with reactor scram</u>
<u>Safety injection (SI) signal</u>	<u>12.27 MPa</u>
<u>High pressure charging</u>	<u>not actuated</u>
<u>Safety injection</u>	<u>not actuated</u>
<u>Accumulator injection</u>	<u>4.51 MPa</u>
<u>Low pressure injection</u>	<u>1.29 MPa</u>
<u>Main feedwater termination</u>	<u>with reactor scram</u>
<u>Turbine throttle valve closure</u>	<u>with reactor scram</u>
<u>Auxiliary feedwater</u>	<u>not actuated</u>
<u>Pressurizer heater power off</u>	<u>1 m (PR Liquid Level)</u>
<u>Downcomer-to-Hot-Leg Leakage</u>	<u>0.049 kg/s/loop</u>
<u>Steam Generator Relief Valve Orifice</u>	<u>19.4 mm</u>
<u>Steam Generator Relief Valve on/off</u>	<u>8.03/7.82 MPa</u>
<u>Steam Generator Safety Valve on/off</u>	<u>8.68/7.69 MPa</u>
<u>Core power limitation to prevent heater rod overheat</u>	<u>75 % for rod temperature \geq 908 K</u> <u>50 % for rod temperature \geq 918 K</u> <u>25 % for rod temperature \geq 919 K</u> <u>10 % for rod temperature \geq 920 K</u> <u>0 % for rod temperature \geq 923 K</u>

A Study on ROSA/LSTF SB-CL-09 Test Simulating PWR 10% Cold Leg Break LOCA,
JAEA-Research-2008-087

Table 5.2.2.2-3 ECCS Conditions for Run SB-CL-09

<u>ECCS</u>	<u>Specification</u>
<u>High Pressure charging system</u> <u>Pump shut-off head</u> <u>Delay time from SI signal</u> <u>Flowrate</u> <u>Fluid temperature</u> <u>Injection location (ratio)</u>	<u>not actuated</u>
<u>High pressure injection system</u> <u>Pump shut-off head</u> <u>Delay time from SI signal</u> <u>Flowrate</u> <u>Fluid temperature</u> <u>Injection location (ratio)</u>	<u>not actuated</u>
<u>Low pressure injection system</u> <u>Pump shut-off head</u> <u>Delay time from SI signal</u> <u>Flowrate</u> <u>Fluid temperature</u> <u>Injection location (ratio)</u>	<u>1.29 MPa</u> <u>17 s</u> <u>scaled full capacity</u> <u>310 K</u> <u>CLA, CLB (3:1)</u>
<u>ACC system</u> <u>Pressure setpoint</u> <u>Water temperature</u> <u>Injection location (ratio)</u> <u>Initial tank level</u> <u>to loop-A : ACC-Cold</u> <u>to loop-B : ACC-Hot</u> <u>Terminal tank level</u> <u>to loop-A : ACC-Cold</u> <u>to loop-B : ACC-Hot</u>	<u>4.51 MPa</u> <u>320 K</u> <u>CLA, CLB (3:1)</u> <u>5.76 m</u> <u>6.43 m</u> <u>3.38 m</u> <u>5.64 m</u>

A Study on ROSA/LSTF SB-CL-09 Test Simulating PWR 10% Cold Leg Break LOCA, JAEA-Research-2008-087

5.2.2.3 ROSA/LSTF small break (17%) LOCA test (IB-CL-02)**(1) Facility Design and Scaling Issues/Distortions**

A 17% cold leg break experiment (IB-CL-02) was conducted at the Large-Scale Test Facility (LSTF) on September 10 in 2009, at the MHI-JAEA joint program, simulating the 1-ft² cold leg break in the US-APWR. The objective of IB-CL-02 test was to confirm thermal-hydraulic phenomena experimentally, which are expected to occur in the scenario of US-APWR 1ft² cold leg break. [

] Details of the experiment are given in Reference 5.2.2.3-1 and in Section 8.2.3 of the present report.

Prior to conducting the IB-CL test series, the pressurizer used in the SB-CL test series was replaced by a new one with the design specifications listed in Table 5.2.2.3-1. It consists of a full-height cylindrical vessel constructed from three steel cylinders and a heater flange. A hemispherical head is welded to the top cylinder, and the heater flange is fastened to the bottom cylinder. Details of the design specifications are described in Reference 5.2.2.3-2.

Features of facility design, scaling issues and distortions described in Section 5.2.2.1 are applicable for the present test facility except for the pressurizer. The pressurizer design has been modified to the full-height without changing the ratio of water volume scaled from the 1/48-scaled reference PWR (Westinghouse-designed 4-loop PWR), which improves the scaling characteristics particularly from the gravitational point of view.

(2) Range of Conditions

The measured initial steady-state conditions of the IB-CL-02 test are listed in Table 5.2.2.3-2.

[

]

Table 5.2.2.3-3 shows the specified control logic, operation set-points and boundary conditions.

[

]

I

1

(3) Data to be compared

The same experimental measurements as described in Section 5.2.2.1 were obtained for the IB-CL-02 test, details of which are referred to Appendix A of Reference 5.2.2.3-1.

(4) Data uncertainties

Significant data uncertainties are not reported for the IB-CL-02 test.

(5) Distortion

Related information is described in Section 5.2.2.1.

(6) References

5.2.2.3-1 JAEA, "Experimental Report on Simulated Intermediate Break Loss-of-Coolant Accident using ROSA/LSTF," March 2010 (*in Japanese, proprietary*).

5.2.2.3-2 The ROSA-V Group, "ROSA-V Large Scale Test Facility (LSTF) System Description for the Third and Fourth Simulated Fuel Assemblies," JAERI-Tech 2003-037, March 2003.

Table 5.2.2.3-1 Characteristics of Pressurizer used for Run IB-CL-02

<u>Parameter</u>	<u>LSTF</u>	<u>Reference PWR</u>	<u>LSTF /PWR</u>
<u>Volume</u>	<u>1.2* (m³)</u>	<u>51(m³)</u>	<u>1/42.5</u>
<u>Water Volume</u> <u>(at Normal Liquid Level)</u>	<u>0.75 (m³)</u>	<u>32(m³)</u>	<u>1/42.7</u>
<u>Steam Volume</u> <u>(at Normal Liquid Level)</u>	<u>0.45 (m³)</u>	<u>19.2(m³)</u>	<u>1/42.7</u>
<u>Inside Diameter</u>	<u>0.372m</u>	<u>2.1m</u>	<u>1/5.6</u>
<u>Vessel Height</u>	<u>11*m</u>	<u>15.5m</u>	<u>1/1.4</u>
<u>Nominal Pressure</u>	<u>15.55MPa</u>	<u>15.52MPa</u>	<u>-</u>
<u>Nominal Temperature</u>	<u>618.1K</u>	<u>617.4K</u>	<u>-</u>
<u>Elevation from Bottom of Core Heated Zone</u>			<u>-</u>
<u>PR Spray Nozzle Upper Surface</u>	<u>-</u>	<u>26.67m</u>	<u>-</u>
<u>PR Shell Top</u>	<u>22* m</u>	<u>-</u>	<u>-</u>
<u>Nominal Water Level</u>	<u>18.243 m</u>	<u>20.088m</u>	<u>1/1.1</u>
<u>PR Shell Bottom</u>	<u>11* m</u>	<u>-</u>	<u>-</u>
<u>PR Surge Nozzle Lower Surface</u>	<u>-</u>	<u>10.488m</u>	<u>-</u>
<u>Spray Line Flow Rate (Max.)</u>	<u>-</u>	<u>0.0567(m³/s)</u>	<u>-</u>
<u>Spray Set Point Close</u>	<u>16.03** MPa</u>	<u>16.03MPa</u>	<u>-</u>
<u>Open</u>	<u>15.68** MPa</u>	<u>15.68 MPa</u>	<u>-</u>
<u>Proportional Heater Capacity</u>	<u>10.0 kW</u>	<u>350kW</u>	<u>1/35</u>
<u>Backup Heater Capacity</u>	<u>112.5 kW</u>	<u>1160kW</u>	<u>1/10.3</u>
<u>Proportional Heaters at Max. Power</u>	<u>15.41** MPa</u>	<u>15.41 MPa</u>	<u>-</u>
<u>Proportional Heaters Off</u>	<u>15.62** MPa</u>	<u>15.62 MPa</u>	<u>-</u>
<u>Backup Heaters On</u>	<u>15.34** MPa</u>	<u>15.34 MPa</u>	<u>-</u>
<u>Backup Heaters Off</u>	<u>15.4** MPa</u>	<u>15.4 MPa</u>	<u>-</u>
<u>Surge Line Flow Rate (Max.)</u>	<u>-</u>	<u>0.2384(m³/s)</u>	<u>-</u>

* Approximate values. ** Values may depend on type of tests.

Table 5.2.2.3-2 Initial Conditions for Run IB-CL-02



Table 5.2.2.3-3 Specified Operational Setpoints and Conditions for Run IB-CL-02

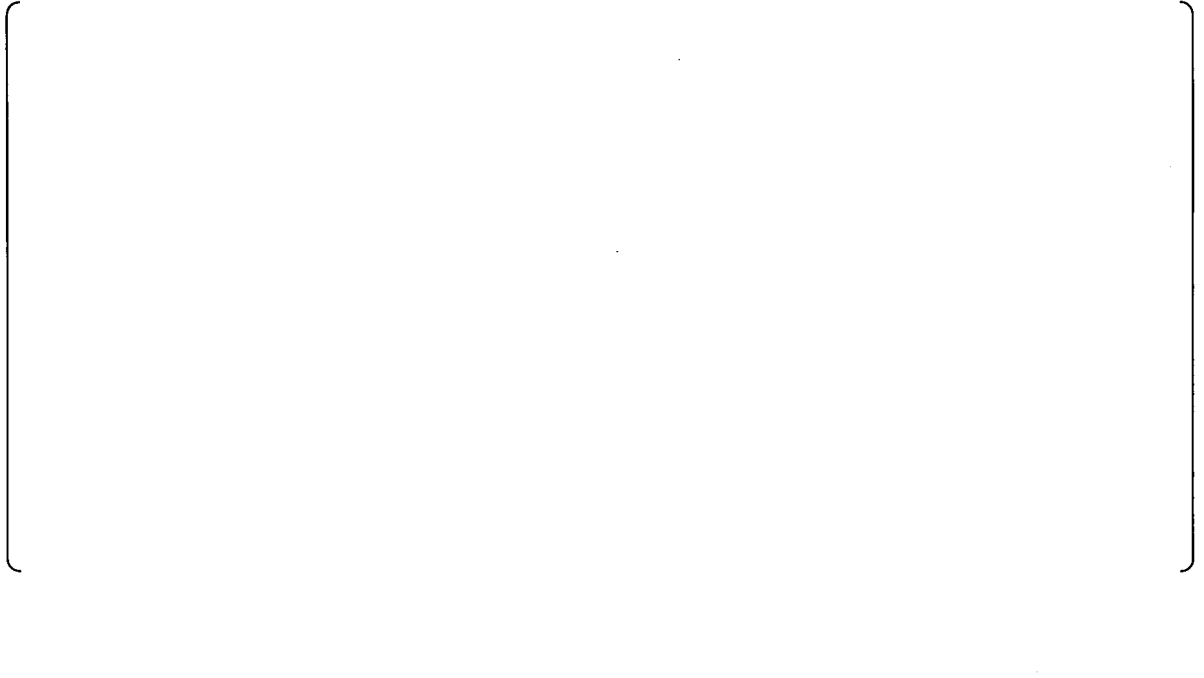


Table 5.2.2.3-4 ECCS Conditions for Run IB-CL-02



5.2.2.4 LOFT small break (2.5%) LOCA test (L3-1)

(1) Facility Design and Scaling Issues/Distortions

(a) Fundamental Design Requirement

The LOFT (Loss-of-Fluid Test) integral test facility (Ref. 5.2.2.4-1) is a scale model of a large 4-loop pressurized water reactor (PWR), which was built at the Idaho National Engineering Laboratory. The intent of the facility is to model the nuclear, thermal-hydraulic phenomena which would take place in a large PWR during a LOCA. A small break (2.5%) LOCA test, L3-1, is selected to assess the M-RELAP5 ability to predict system responses under small break LOCAs.

The general philosophy in scaling coolant volumes and flow areas in LOFT was to use the ratio of the LOFT core (50 MWt) to a large PWR core (3000 MWt). For some components, this factor is not applied; however, it is used as extensively as practical. In general, components used in LOFT are similar in design to those of a large PWR. Because of scaling and component design, the LOFT loss-of-coolant experiment is expected to closely model a large PWR LOCA. Details of the test facility scaling are given in Reference 5.2.2.4-2. In addition, scaling distortions specific to small break LOCAs are addressed in Reference 5.2.2.4-3.

(b) General Functions and Systems

The LOFT, in particular the primary coolant system and reactor core, is a fully operational, scaled representation of a commercial PWR. As such, transients resulting from accident initiating events are representative in complexity and nature of those accidents which may occur in commercial PWRs. The experimental assembly comprises five major subsystems which have been instrumented such that system variables can be measured and recorded during the test. The subsystems include a) the reactor vessel, b) the intact loop, c) the broken loop, d) blowdown suppression system, and e) the emergency core cooling system (ECCS). The LOFT major components are shown in Figure 5.2.2.4-1.

(c) Primary Coolant System

The LOFT reactor vessel, which simulates the reactor vessel of a commercial PWR, has an annular downcomer, a lower plenum, lower core support plates, a nuclear core, and an upper plenum. The downcomer is connected the cold legs of the intact and broken loops and contains two instrument stalks. The upper plenum is connected the hot legs of the intact and broken loops. The core contains 1300 unpressurized nuclear fuel rods arranged in five square (15x15 fuel assemblies) and four triangular fuel modules located in the corners, shown in

Figure 5.2.2.4-2. The fuel rods have an active length of 1.67-m and an outside diameter of 10.72-mm. The fuel consists of UO₂ sintered pellets with an average enrichment of 4.0 st% fissile uranium (U²³⁵) and with a density that is 93% of theoretical density. Fuel pellet diameter and length are 9.29 and 15.24-mm, respectively. Both ends of the pellets are dished with the total dish volume equal to 2% of the pellet volume. Cladding material is Zircaloy-4. Cladding inside and outside diameters are 9.48 and 10.72-mm, respectively. The details are given in Reference 5.2.2.4-4.

The intact loop simulates three loops of a commercial four-loop PWR and contains a steam generator (SG), two primary coolant pumps in parallel, a pressurizer, a venturi flow meter, and connecting piping. The broken loop consists of a hot leg and a cold leg that are connected to the reactor vessel and the blowdown suppression tank (BST) header. Each leg consists of a break plane orifice, a quick-opening blowdown valve (QOBV), a recirculation line, an isolation valve, and connecting piping. The break for Experiment L3-1 is located in the broken loop cold leg. In Experiment L3-1, a single-ended break orifice as shown in Figure 5.2.2.4-3 is adopted to simulate the 4-in small break LOCA. The recirculation lines establish a small flow from the broken loop to the intact loop and are used to warm up the broken loop. The broken loop hot leg also contains a simulated steam generator and simulated pump. These simulators have hydraulic orifice plate assemblies which have similar resistances to flow as an active steam generator and a pump.

The blowdown suppression system is comprised of the BST header, the BST, the nitrogen pressurization system, and the BST spray system. The blowdown header is connected to the suppression tank downcomers which extend inside the tank below the water level. The header is also directly connected to the BST vapor space to allow pressure equilibration. The nitrogen pressurization system is supplied by the LOFT inert gas system and uses a remote controlled pressure regulator to establish and maintain the specified BST initial pressure. The spray system consists of a centrifugal pump that discharges through a heat-up exchanger and any of three spray headers or a pump recirculation line that contains a cool-down heat exchanger. The spray pump suction can be aligned to either the BST or the borated water storage tank. The three spray headers have flowrate capacities of 1.3, 3.8 and 13.9 ℓ/s , respectively, and are located in the BST along the upper centerline.

The LOFT ECCS simulates that of a commercial PWR, which consists of two accumulators, a high-pressure injection system (HPIS), and a low-pressure injection system (LPIS). Each system is arranged to inject scaled flowrates of emergency core coolant directly into the

primary coolant system cold leg. Accumulator ACC-A, HPIS Pump A, and LPIS Pump A were utilized during the L3-1 test. Accumulator ACC-A was preset to inject the ECC at a system pressure of 4.37 MPa. HPIS Pump A was set to initiate injection at a system pressure of 13.16 MPa. The pressure setpoint for automatic LPIS injection was 0.98 MPa. The operational setpoints and conditions, and ECCS conditions are summarized in Tables 5.2.2.4-1 and 5.2.2.4-2, respectively.

(d) Secondary Coolant System

The functions of secondary coolant system (SCS) are: (1) to remove the heat transferred to the SCS in the steam generator to the environment, (2) to control reactor power during power operation and to influence the primary and reactor systems in a manner similar to the SCS of a large PWR, and (3) to remove decay heat under normal conditions. The main loop of the SCS consists of the shell side of the steam generator, the air-cooled condenser, the condensate receiver, the condensate subcooler, the main feed pump, the main steam control and the feed flow regulating valves.

Steam flows from the shell side of the steam generator through the main steam control valve to the air-cooled condenser. The steam control valve controls steam flow from the steam generator and, thus, the reactor power during power range operation. Condensate leaving the condenser passes through a receiver that acts as a surge volume for the system. Condensate leaving the receiver passes through a subcooler and then through the main feed pump. The main feed pump discharge has a recirculation line that allows a small amount of feedwater to return to the subcooler. The feedwater passes through the feedwater regulating valve to the feed ring in the steam generator.

The air-cooled condenser transfers the heat, carried by the secondary coolant, from the steam to the atmosphere. The condenser uses finned tubes with a forced air draft from variable pitch fans. The system is protected from freezing by a forced air propane fixed heater. Air flow can be recirculated through the condenser to maintain the pressure (temperature) of condensing steam at a desired value.

The condensate receiver, an all-welded carbon steel pressure vessel, is a cylindrical vessel mounted horizontally with a bottom tee section containing electric heaters to aid in system purging and provide freeze-up protection. The receiver volume is expected to handle all secondary shrinkage and swelling from normal operation.

The subcooler, an all-welded carbon steel unit, is a vertical shell and tube-type heat exchanger with secondary coolant flow on the shell side. The subcooler would minimize main feed pump cavitation.

The function of the feed pump is to supply the steam generator with high-pressure water from the condensate subcooler. The feed pump is an electrically-driven horizontal split case, multistage centrifugal pump. The feedwater regulating valve is normally an automatically controlled throttle valve used to maintain steam generator water level in a programmed band. It is located in the main feed line downstream of the main feed pump.

(2) Range of Conditions

The LOFT Small Break Experiment Series (Experiment Series L3) was designed to provide large-scale blowdown system data for a PWR small break transient. Parameters varied for Experiment Series L3 include initial power level, break size and location, and primary coolant pump operation.

Experiment L3-1 (Ref. 5.2.2.4-5) was conducted in the LOFT facility at a maximum linear heat generation rate of 51.7 ± 1 kW/m, and a power of 48.9 ± 1 MWt. This power level is about 98% of the LOFT rated thermal power of 50 MWt.

Experiment L3-1 was conducted from initial temperatures in the primary coolant system intact loop of 574 ± 1 and 554 ± 3 K in the hot and cold legs, respectively, and hot leg pressure of 14.85 ± 0.04 MPa. The experiment simulated a break in the cold leg of a four-loop, commercial PWR large enough to cause system depressurization to the LPIS initiation pressure. The reactor was operated sufficiently long to establish a decay heat level corresponding to 40 hours of full power operation. The experimental initial conditions are summarized in Table 5.2.2.4-3.

(3) Data to be compared

As described in Reference 5.2.2.4-1, the following experimental results are available for comparison:

- 1) TE, temperature element,
- 2) PE, pressure element,
- 3) PdE, differential pressure element,
- 4) LE, coolant level element,
- 5) FE, coolant flow element,
- 6) AE, accelerometer.

- 7) RPE, pump speed element,
- 8) DE, densitometer,
- 9) DIE, displacement element,
- 10) ME, momentum flux detector,
- 11) NE, neutron detector.

(4) Data uncertainties

The data presented in Reference 5.2.2.4-5 include selected pertinent thermal-hydraulic and nuclear data from LOFT Experiment L3-1. The data were processed and are presented in graphical form in SI units. Measurements were combined to produce computed variables, and graphs of similar variables at several locations were overlaid to facilitate comparison. The number of data points shown for each instrument has been reduced to 2000 for ease of plotting. To accomplish this reduction, the data were passed through a low-pass filter and then decimated. Computed parameter data from the drag discs, the turbine flowmeters, and the gamma densitometers were filtered with a 4-Hz, low-pass filter prior to presentation.

The 2- σ confidence intervals have been determined from knowledge of the systematic and random errors of the sensors, data system, calibration procedures, and the channel random noise during pretest calibrations. These are presented as functions of output level so that the user may determine the approximate uncertainty over each range of interest for a given variable. Table 7 of Reference 5.2.2.4-5 lists Experiment L3-1 instrumentation and gives the detector location, range, initial condition uncertainty, uncertainty at specific readings, and recording frequency along with the figure numbers. Table 8 of Reference 5.2.2.4-5 lists the variables that were computed from the transducer outputs and other factors, such as geometrical constants. This table also gives the equations used to compute these variables, the figure number, and comments which may reflect on the usefulness of the data.

(5) Distortion

(a) Steam generator leakage

The steam generator leakage is described in Reference 5.2.2.4-6. The main steam control valve does not seat completely after scram, nor does it seat the same each closure. The actual steam leakage from the secondary is not measured directly, but can be calculated from steam generator level when the feedwater is off. The value calculated for Experiment L3-1 is 0.02 kg/s at 3.5 MPa. The steam generator valve leakage determines in part whether the steam control bypass valve opens early in the transient. The effect on primary system pressure is minor.

(b) Environmental heat losses and energy storage

The small break experiments have focused on the need to quantify not only the energy losses from the system to containment but also the energy storage in the facility metal mass. The post-test analysis report (Ref. 5.2.2.4-6) describes that the RELAP5 model includes additional environmental losses and/or metal mass in the pressurizer, steam generator, reactor vessel upper head and primary coolant piping. The environmental heat losses were 250 kW during full power steady state conditions according to Reference 5.2.2.4-6.

(c) Core bypass fraction

In comparison with the US-APWR design, a larger core bypass fraction occurred in the test facility. Reference 5.2.2.4-6 states that the core bypass fractions were 3.6% of primary loop flow for the lower plenum to upper plenum path, 6.6% for the inlet annulus (downcomer) to upper plenum path, and 1.3% for the reflood assist bypass valve at the test initiation. The large core bypass fraction prevented the steam generated in the core from circulating through the primary loop system, resulting in the loop seal uncleared throughout the transient, while the loop seal is expected to be cleared in US-APWR SBLOCAs.

(6) References

- 5.2.2.4-1 D. L. Reeder, "LOFT System and Test Description (5.5-ft Nuclear Core 1 LOCEs)," NUREG/CR-0247, TREE-1208, July 1978.
- 5.2.2.4-2 L. J. Ybarrondo et al., "Examination of LOFT Scaling", ASME 74-WA/HT-53," November, 1974.
- 5.2.2.4-3 N. Zuber, "Problems in Modeling of Small Break LOCA," NUREG-0724, October, 1980.
- 5.2.2.4-4 M. L. Russell, "LOFT Fuel Modules Design, Characterization, and Fabrication Program," TREE-NUREG-1131, June 1977.
- 5.2.2.4-5 P. D. Bayless et al., "Experimental Data Report for LOFT Nuclear Small Break Experiment L3-1," NUREG/CR-1145, EGG-2007, January 1980.
- 5.2.2.4-6 K. G. Condie et al., "Four-Inch Break Loss-of-Coolant Experiments: Posttest Analysis of LOFT Experiment L3-1, L3-5 (Pumps Off), and L3-6 (Pumps On)."

EGG-LOFT-5480, October 1981.

Table 5.2.2.4-1 Operational Setpoints and Conditions for Experiment L3-1

<u>Reactor scram signal</u>	<u>Concurrent with break initiation</u>
<u>Initiation of RC pump coastdown</u>	<u>with reactor scram</u>
<u>High pressure injection</u>	<u>13.16 MPa</u>
<u>Low pressure injection</u>	<u>0.98 MPa</u>
<u>Accumulator injection</u>	<u>4.37 MPa</u>
<u>Main feedwater termination</u>	<u>with reactor scram</u>
<u>Turbine throttle valve closure</u>	<u>with reactor scram</u>
<u>Steam Control Valve on/off</u>	<u>7.13/6.44 MPa</u>

Table 5.2.2.4-2 ECCS Conditions for Experiment L3-1

<u>ECCS</u>	<u>Specification</u>
<u>High pressure injection system</u>	
<u>Pump shut-off head</u>	<u>13.16 MPa</u>
<u>Flowrate</u>	<u>scaled full capacity</u>
<u>Fluid temperature</u>	<u>297 K</u>
<u>Injection location</u>	<u>cold leg</u>
<u>Low pressure injection system</u>	
<u>Pump shut-off head</u>	<u>1.29 MPa</u>
<u>Flowrate</u>	<u>scaled full capacity</u>
<u>Fluid temperature</u>	<u>297 K</u>
<u>Injection location</u>	<u>cold leg</u>
<u>ACC system</u>	
<u>Pressure setpoint</u>	<u>4.37 MPa</u>
<u>Water temperature</u>	<u>305 K</u>
<u>Injection location</u>	<u>cold leg</u>
<u>Initial tank level</u>	<u>1.85 m</u>
<u>Terminal tank level</u>	<u>0.79 m</u>

Table 5.2.2.4-3 Initial Conditions for Experiment L3-1

<u>Parameter</u>	<u>Experiment</u>
<u>Primary system pressure [MPa]</u>	<u>14.81 ± 0.04</u>
<u>Primary system mass flowrate [kg/s]</u>	<u>484.0 ± 6.3</u>
<u>Cold leg temperature [K]</u>	<u>554.0 ± 3</u>
<u>Hot leg temperature [K]</u>	<u>574.0 ± 1</u>
<u>Steam generator pressure [MPa]</u>	<u>5.43 ± 0.11</u>
<u>Steam generator mass flowrate [kg/s]</u>	<u>25.0 ± 0.4</u>
<u>Pressurizer level [m]</u>	<u>1.16⁴⁾ ± 0.01</u>
<u>Core bypass fraction (LP to UP)¹⁾ [%]</u>	<u>3.6</u>
<u>Core bypass fraction (DC to UP)²⁾ [%]</u>	<u>6.6</u>
<u>Core bypass fraction (RABV)³⁾ [%]</u>	<u>1.3</u>
<u>Core power [MW]</u>	<u>48.9 ± 1.0</u>

- 1) Core bypass fraction from lower plenum to upper plenum.
- 2) Core bypass fraction from downcomer to upper plenum.
- 3) Core bypass fraction through the reflood assist bypass valve.
- 4) Including the instrumentation elevation offset

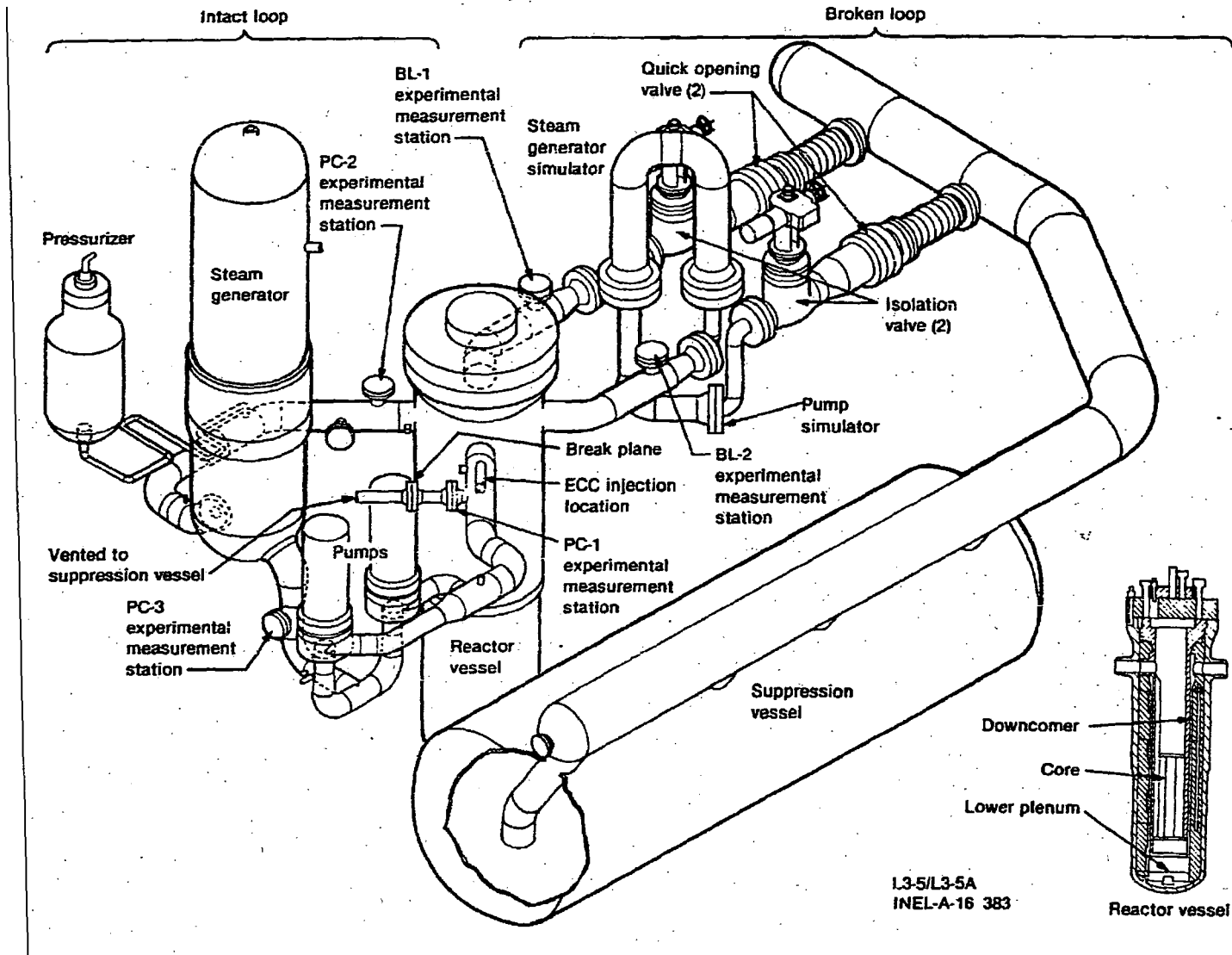


Figure 5.2.2.4-1 Schematic of LOFT Major Components (Ref. 5.2.2.4-1)

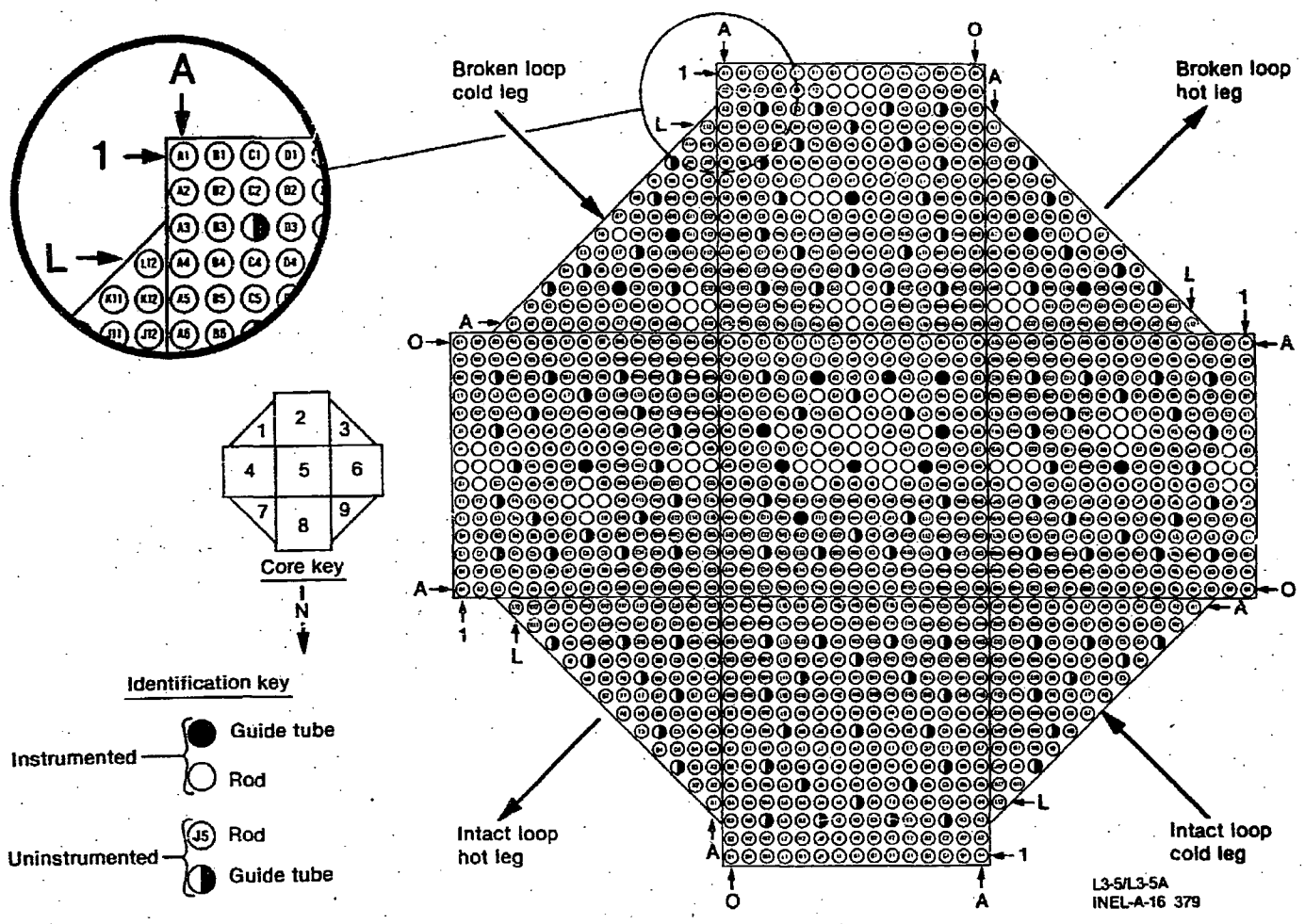


Figure 5.2.2.4-2 LOFT Core Configuration (Ref. 5.2.2.4-1)

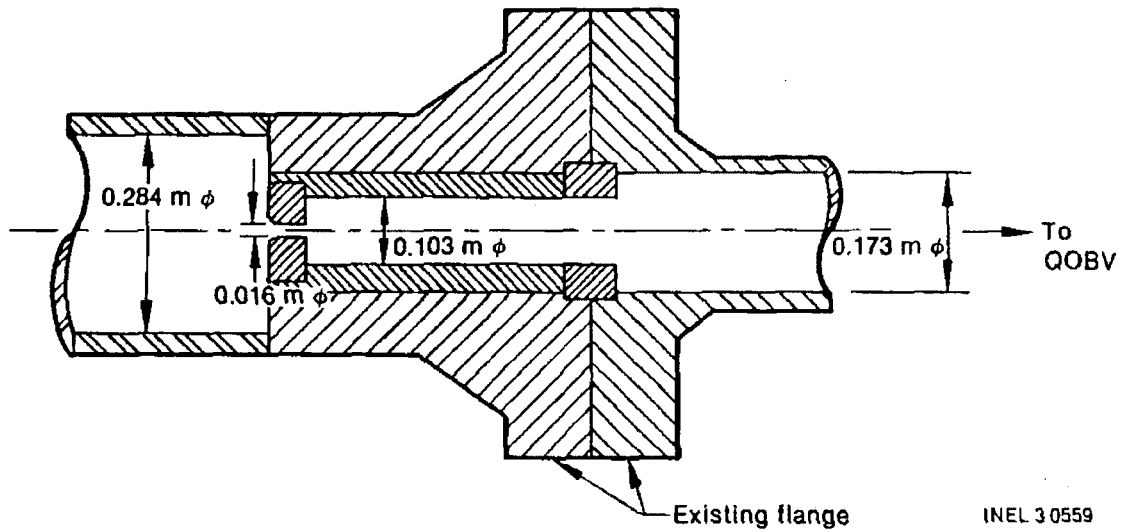


Figure 5.2.2.4-3 Small Break Orifice Configuration for LOFT L3-1 (Ref. 5.2.2.4-5)

5.2.2.5 Semiscale small break (5%) LOCA test (S-LH-1)

(1) Facility Design and Scaling Issues/Distortions

(a) Fundamental Design Requirement

The Semiscale Program was a part of the Water Reactor Research Test Program Division of EG&G Idaho, Inc., which conducted research of the thermal-hydraulic phenomena associated with simulated accident conditions in a PWR. The Semiscale Mod-2C system as structured during the S-LH-1 and S-LH-2 experiments simulated centerline cold leg small break loss-of-coolant accidents (5% SBLOCAs) (Ref. 5.2.2.5-1).

Semiscale Mod-2C is a scaled model representation of a PWR plant, with a fluid volume of about 1/1705 of a Westinghouse 4-loop PWR as shown in Figure 5.2.2.5-1. The modified-volume scaling philosophy followed in the design of the Mod-2C system preserves most of the first-order effects thought important for SBLOCA transients. Most notably, the 1:1 elevation scaling of the Semiscale system is an important criterion for preserving the factors influencing signature response to a SBLOCA. Details are described in Reference 5.2.2.5-2.

(b) General Functions and Systems

Semiscale has provided integral system data for a wide range of transient scenarios. The system was designed to preserve most of the effects thought to be of first-order importance for gravity-dominated, slow, primary transients in SBLOCAs and in transients induced by secondary side accidents. The system simulated the automatically occurring plant protection systems and operator-promoted recovery procedures.

(c) Primary Coolant System

The Mod-2C system consists of a pressure vessel with external downcomer and simulated reactor internals: an "intact loop," with a steam generator (SG), pressurizer, and pump; and a "broken loop," including pump, SG, and associated piping to allow break simulations. The intact loop simulates three "unaffected loops" of a four-loop PWR, and the broken loop simulates an "affected loop" in which the small break is assumed to occur. The break simulates a 5% cold-leg, centerline, communicative break in the loop piping between the pump and vessel, as shown in Figure 5.2.2.5-2. The intact loop SG consists of six inverted U-tubes, and the broken loop SG consists of two inverted U-tubes. Vessel internals include a simulated core, consisting of a 5 x 5 array of internally heated electric rods, of which 23 were powered as shown in Figure 5.2.2.5-3. The rods are geometrically similar to nuclear rods, with a heated length of 3.66 m (12 ft) and an outside diameter of 1.072 cm (0.42 in.). The boundary

conditions for the Semiscale S-LH-1 test are listed in Table 13 of Reference 5.2.2.5-1.

(d) Secondary Coolant System

The secondary system is a once-through system that provides boundary conditions of flow, temperature, and pressure representative of the secondary system of a PWR plant. Normal feedwater is supplied to the steam generator secondary sides, and steam is exhausted to atmosphere via control valves. Feedwater is stored in an 8.5 m³ (300 ft³) feedwater tank and heated by immersion heaters to the required feedwater temperature. Feedwater is provided at temperatures up to 500 K (440 °F) with flow rates adjusted as necessary to provide sufficient heat removal. Steam from the steam generator secondary is vented to atmosphere via a steam header. Although a crossover line exists connecting the intact and broken loop steam generator the crossover block valve is closed for S-LH-1. Secondary pressure relief is provided by atmospheric dump valves located on both the intact and broken loop steam line upstream of the main steam isolation valves which are the main block valves for the secondary system.

(2) Range of Conditions

Table 5.2.2.5-1 summarizes the initial steady state conditions in the experiment. The core power was maintained around 2000 kW and then coasted down according to the preset decay heat curve following the reactor trip signal generated due to the low pressurizer pressure. The specified initial pressurizer pressure was 15.47 MPa (2243.7 psia) and the intact and broken loops for the cold leg temperature was about 562 K (552 °F) and 564 K (556 °F) respectively with 38 K (68 °F) of core ΔT . The nominal primary flow rates through cold legs were 7.13 and 2.35 kg/s between intact and broken loops, in which the loop flow split was 3:1.

(3) Data to be compared

Reference 5.2.2.5-1 lists the measurement Identifiers available to be compared with code calculations. They are as follows:

- 1) pressure,
- 2) fluid temperature,
- 3) heater rod temperature,
- 4) fluid density,
- 5) differential pressure,
- 6) liquid level,
- 7) volumetric flow rate.

(4) Data uncertainties

The Semiscale Mod-2C system is extensively instrumented to provide thermal-hydraulic data necessary for understanding phenomena associated with a SBLOCA. The measurement system consists of primary and secondary system measurement hardware and the software used for measurement recording and subsequent analyses. A block diagram of the data system is illustrated in Figure 4 of Reference 5.2.2.5-2. Information on the anticipated range and required accuracy for each measurement is listed in Table 5 of Reference 5.2.2.5-1.

(5) Distortion

Compensation for environmental heat loss was provided through heat addition with the external heater tape on the exterior of the pressure boundary. The external heaters did not provide enough heat to compensate for all of the environmental heat loss, however, core power was not augmented to make up the difference among the test conducted in the Mod-2C facility. The total environmental heat loss for the mod-2C system excluding the pressurizer as obtained from characterization tests was 61.9 kW (58.76 Btu/s). Table 2.2-2 of Reference 5.2.2.5-3 presents an estimated heat loss for various Semiscale subsystems.

The steam leakage from the steam generator secondary side was recognized during Test S-LH-1. The measured maximum leak rates were 0.006 kg/s (0.013 lbm/s) and 0.0007 kg/s (0.0015 lbm/s) for the primary and broken loops, respectively.

(6) References

5.2.2.5-1 G. G. Loomis, "Experiment Operating Specification for Semiscale Mod-2C 5% Small Break Loss-of-Coolant Experiment S-LH-1," EGG-SEMI-6813, February 1985.

5.2.2.5-2 R. A. Shaw et al., "A Description of the Semiscale Mod-2C Facility, Including Scaling Principle and Current Measurement Capabilities," EGG-M-11485, January 1985.

5.2.2.5-3 R. A. Larson, et al., "The Semiscale Mod-2C Small-Break (5%) Configuration Report for Experiments S-LH-1 and S-LH-2," EGG-RTH-7199, April 1986.

Table 5.2.2.5-1 Initial Conditions for Experiment S-LH-1

<u>Parameter</u>	<u>Experiment</u>
<u>Pressurizer pressure [MPa]</u>	<u>15.47 ± 0.14</u>
<u>Core ΔT</u>	<u>37.65 +1.5/-0.6</u>
<u>Intact loop flow rate [kg/s]</u>	<u>7.13</u>
<u>Broken loop flow rate [kg/s]</u>	<u>2.35</u>
<u>Intact loop cold leg temperature [K]</u>	<u>562.12 ± 2</u>
<u>Broken loop cold temperature [K]</u>	<u>564.05 ± 2</u>
<u>Intact loop Steam generator pressure [MPa]</u>	<u>5.72 ± 0.07</u>
<u>Broken loop Steam generator pressure [MPa]</u>	<u>6.08 ± 0.07</u>
<u>Pressurizer level [cm]</u>	<u>395 ± 14</u>
<u>Core bypass fraction [%]</u>	<u>0.9</u>
<u>Core power [kW]</u>	<u>2014.75 ± 0.15</u>

Table 5.2.2.5-2 Specified Operational Setpoints and Conditions for Experiment S-LH-1

<u>Reactor scram signal</u>	<u>3.4 s after pressurizer pressure reaches 12.6 MPa</u>
<u>Initiation of RC pump coastdown</u>	<u>2.0 s after pressurizer pressure reaches 12.6 MPa</u>
<u>Safety injection (SI) signal</u>	<u>25.0 s after pressurizer pressure reaches 12.6 MPa</u>
<u>High pressure injection</u>	<u>12.16 MPa (1827 psia)</u>
<u>Low pressure injection</u>	<u>not available</u>
<u>Accumulator injection</u>	<u>4.24 MPa (615 psia)</u>
<u>MSIV closure</u>	<u>with reactor scram</u>
<u>Main feedwater termination</u>	<u>0.0 s after pressurizer pressure reaches 12.6 MPa</u>
<u>Pressurizer Relief Valve on/off</u>	<u>not activated</u>
<u>SG Relief Valve on/off</u>	<u>not activated</u>

Table 5.2.2.5-3 ECCS Conditions for Experiment S-LH-1

<u>ECCS</u>	<u>Specification</u>
<u>High Pressure charging system</u>	
<u>Pump shut-off head</u>	<u>12.6 MPa</u>
<u>Delay time from SI signal</u>	<u>25 s</u>
<u>Flowrate</u>	<u>scaled full capacity</u>
<u>Fluid temperature</u>	<u>300 K</u>
<u>Injection location</u>	<u>cold leg</u>
<u>Low pressure injection system</u>	<u>not available</u>
<u>Pump shut-off head</u>	
<u>Delay time from SI signal</u>	
<u>Flowrate</u>	
<u>Fluid temperature</u>	
<u>Injection location</u>	
<u>ACC system</u>	
<u>Pressure setpoint</u>	<u>4.24 MPa</u>
<u>Water temperature</u>	<u>300 K</u>
<u>Injection location</u>	<u>cold leg</u>
<u>Initial liquid volume</u>	
<u>Intact loop</u>	<u>0.048 m³</u>
<u>Broken loop</u>	<u>0.016 m³</u>
<u>Initial nitrogen volume</u>	
<u>Intact loop</u>	<u>0.025 m³</u>
<u>Broken loop</u>	<u>0.0083 m³</u>

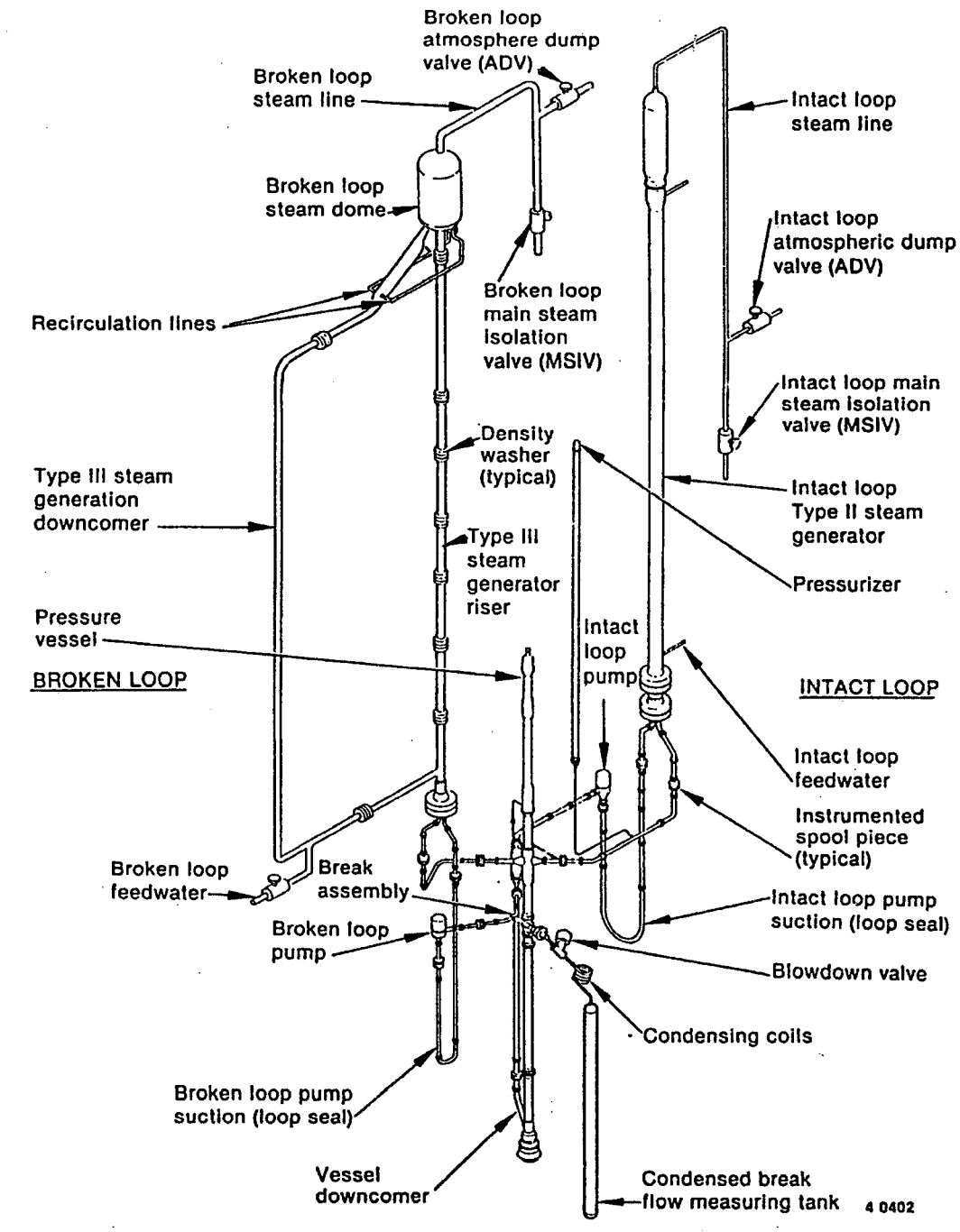


Figure 5.2.2.5-1 Schematic of Semiscale Mod-2C Major Components (Ref. 5.2.2.5-1)

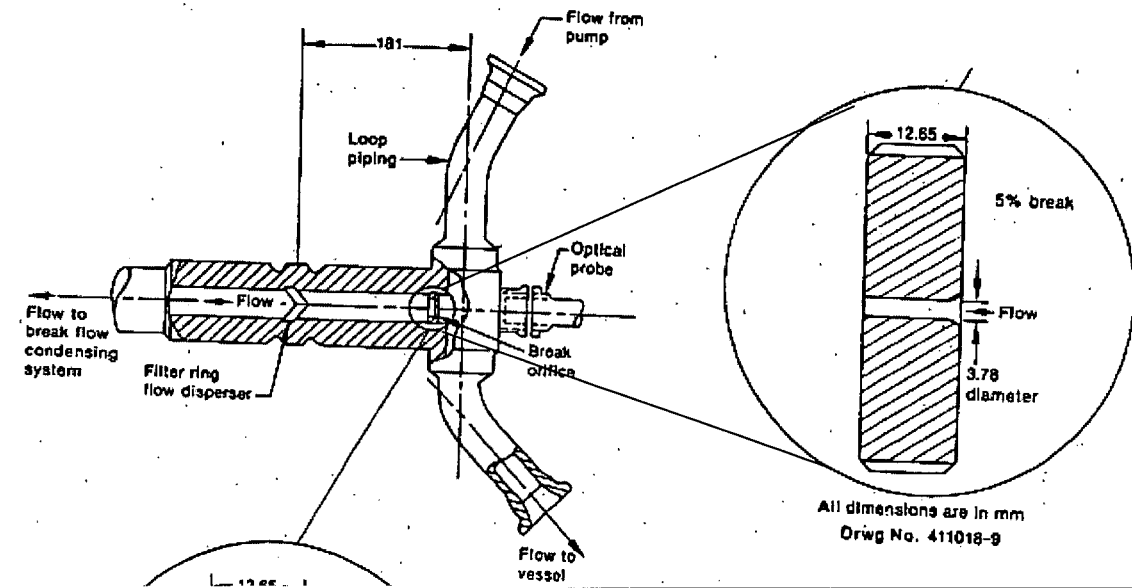
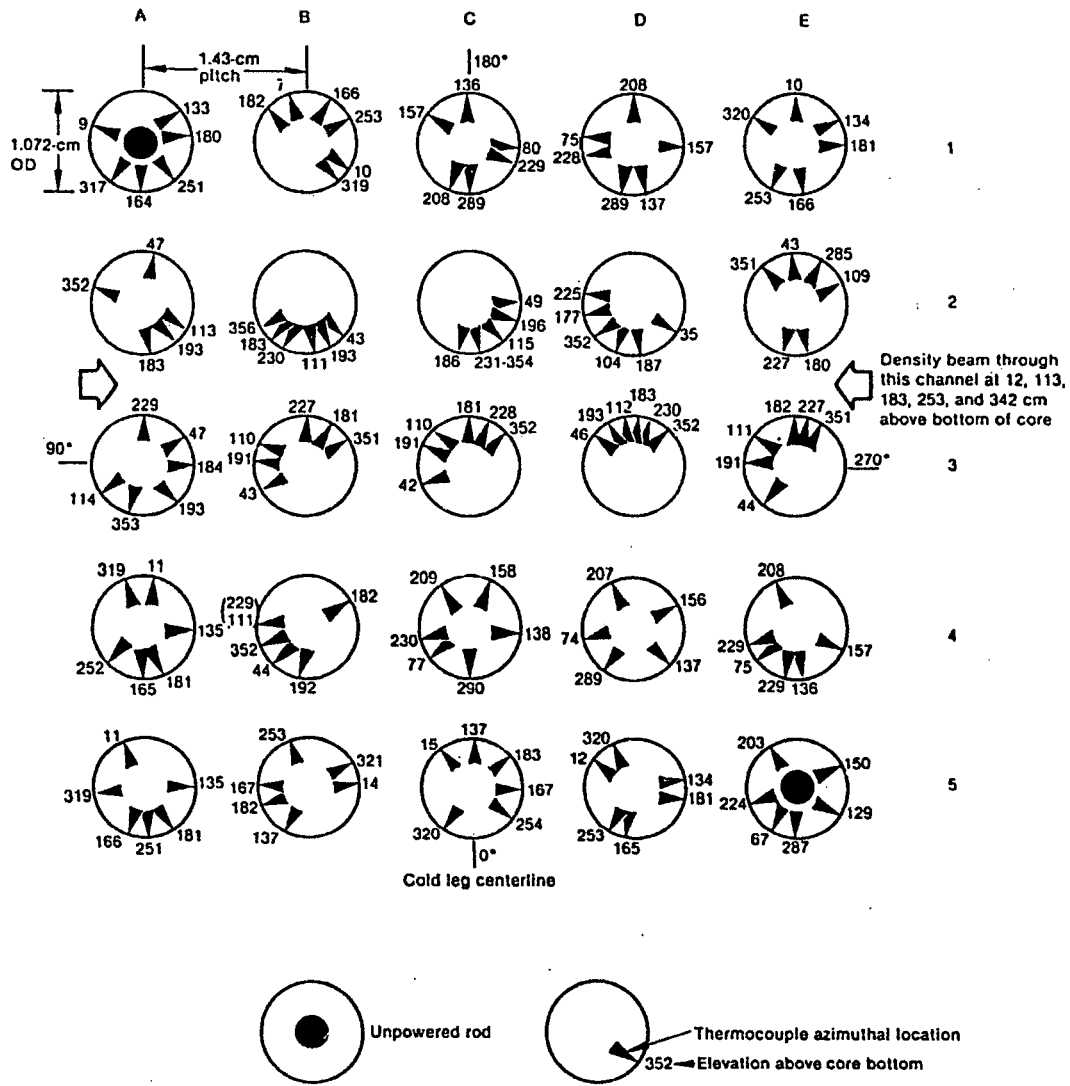


Figure 5.2.2.5-2 Small Break Orifice Configuration for Semiscale S-LH-1 (Ref. 5.2.2.5-1)



4 0403

Figure 5.2.2.5-3 Semiscale Mod-2C Core Heater Rod Configuration (Ref. 5.2.2.5-1)

6.0 DEVELOPMENT AND ASSESSMENT OF THE RELAP5-3D-BASED FRAMEWORK OF THE M-RELAP5 EVALUATION MODEL

As discussed in Section 1.1, the development and assessment of the M-RELAP5 Appendix K Evaluation Model was divided into two parts because the decision made by MHI was to use a RELAP5-based code in conjunction with conservative analysis methods as defined in 10 CFR 50.46, Appendix K. This section describes the development and general assessment of the RELAP5-3D code and models, while Section 7 describes the inclusion and general assessment of the “conservative” Appendix K models. Section 8 then describes the overall assessment of the integrated code M-RELAP5, with particular emphasis on the additional code-to-data comparison that were performed to assess M-RELAP5 as applied to SBLOCA conditions in the US-APWR.

Subsection 6.1 presents the general rationale for the selection of RELAP5-3D with a specific emphasis on the applicability of the Regulatory Guide 1.203 (Ref. 6-1) six principles of evaluation model development. This subsection also includes a brief summary of the relevant features of the code along with appropriate references to specific sections of the detailed RELAP5/MOD3.3 and RELAP5-3D reference manuals. Subsections 6.2 presents the general modeling framework of the code including a discussion of the modeling of different systems and components, constituents and phases, field equations, closure equations, and numerics.

6.1 Selection of a RELAP5-Based Code with Inclusion of Appendix K Conservative Models

The selection of a RELAP5-based code, and specifically the RELAP5-3D version of the code was based on a variety of general criteria as noted below in 6.1.1. However, a more fundamental part of the selection process was the determination that this approach was the most straight forward paths to satisfying the NRC criteria for the analysis of SBLOCAs in the US-APWR. The specific rationale for this determination is given in 6.1.2.

6.1.1 General Selection Process

A RELAP5-based code was selected for the analysis of SBLOCA transients for the US-APWR for various reasons including the following:

1. RELAP5 has been widely applied for best estimate analyses for PWR reactor designs around the world including many safety studies by the NRC and more recently by

- IAEA-sponsored organizations.
2. The code has been widely used to support the analysis of relevant Separate Effects and Integral Effects experiments around the world including the experiments. As a result, the strengths and weaknesses of the code and the latest versions of the models available in the code are widely known and documented in the open literature.
 3. The code has also been specifically used in the analysis of SBLOCAs in representative PWR designs similar to the US-APWR including studies involving estimates of modeling and code uncertainties for best estimate calculations. As a result, representative PWR SBLOCA calculations with, in some cases, estimates of modeling uncertainties have been reported in the open literature.
 4. The code is well documented with peer reviewed reference manuals published as widely reviewed and referenced NUREG reports, References 6.2-6.9, as well as a wide variety of other publicly available reports and technical papers.
 5. Training and technical support providing guidance in the recommended use of the code is also widely available.

The RELAP5-3D was also selected for a variety of reasons. The Idaho National Engineering Laboratory (INL) version of the code has a long pedigree and documentation with many of the current code development and application staff being associated with the code over much of its development history. RELAP5-3D models and correlations are based on the widely accepted and tested RELAP5/MOD3.2, and more recent RELAP5/MOD3.3, models and correlations first released in the NRC versions of RELAP5. Many of the current user guidelines have been prepared by staff members involved in development and validation of the code. The development history and configuration of the code has also been well documented from the original versions of RELAP5. This version of the code is also relatively widely distributed and many of the unique modeling options available in this version have been applied and discussed in the public literature. The RELAP5-3D reference models, largely derived from the original corresponding reference manuals published as NUREG-CR reports, are listed as references (Ref. 6-10 to 14).

RELAP5-3D also offers some advanced modeling options as noted in the following subsections and described in more detail in references (Ref. 6-10 to 14), it was decided to avoid the use of the advanced modeling options in favor of the more widely used and validated RELAP5/MOD3.2 and RELAP5/MOD3.3 modeling options for the analysis of SBLOCA for the US-APWR and the analysis of the representative separate effects experiments and integral tests. Thus, the results from these analyses could be compared to other similar results

published in the open literature.

Although RELAP5-3D are generally considered best estimate codes, it was also decided, as described in Section 7, that the corresponding best estimate modeling options were to be replaced or adjusted using the required Appendix K modeling options to insure the conservatism of the results. Thus, the representative calculations shown in Appendix E is-are based on the selection of the Appendix K models in place of the corresponding best estimate models.

6.1.2 Selection Criteria Based on the Specific NRC Guidelines

An important part of the decision making process in selecting RELAP5-3D as the general framework for M-RELAP5 was the determination that this approach was the most "straight-forward way to satisfy the six basic principles" (Ref. 6-15) for the development and assessment of the over all evaluation model. The rationale for the selection process is outlined below.

Determine requirements for the evaluation model. The two key components of this principle, (a) the identification of mathematical modeling methods...phenomena and (b) phenomena assessment could be clearly identified in the RELAP5 development approach. Over the long history of the development of the code, the code gradually evolved under the guidance of the NRC and others to incorporate the modeling approaches and specific models required to model a wide range of transients in different plant designs. In particular, its ability to model PWRs comparable in design to the US-APWR for SBLOCA conditions was the subject of many studies, resulting in the general framework and modeling approach that exists in the current generation of RELAP5 including RELAP5/MOD3.3 and RELAP5-3D. The identification and international peer review of the modeling approaches and specific modeling features have resulted in detailed theory and models and correlations documents. The assessment of the important phenomena included in the code has been described in the development assessment reports, independent assessment reports, and "publicly available" reports in the open literature.

Develop an assessment base consistent with the determined requirements. The assessment base for RELAP5, TRAC, and other system codes is well known and has been characterized by many international studies. RELAP5 has been directly applied to most if not all of the applicable experiments included in the data base. Many of these experiments and

assessment activities were specifically focused on SBLOCA conditions and phenomena included in many integral experiments designed to represent PWR geometries comparable to the US-APWR.

Develop the evaluation model. RELAP5 has been developed over an extended period of time. RELAP5-3D is the culmination of over 30 years of continuous development and improvement at the Idaho National Laboratory such that an acceptable pedigree exists for the code and it can be used as an evaluation model.

Assess the adequacy of the evaluation model. As noted in the statement of this principle, it is noted that a key feature of the adequacy assessment is the ability to predict appropriate experimental behavior. The ability of RELAP5 to predict the behavior of experiments has been demonstrated. The most recent “publicly available” development assessment report for RELAP5/MOD3.3 (Ref. 6-4) describes the application of code to 13 Separate Effects Experiments and 4 Integral Effects Experiments. The independent assessment performed by the CAMP members (specific to SBLOCAs) covers a large range of facilities and phenomena as shown in Table 6.1-1. Additional examples are available in the public literature.

Follow an appropriate quality assurance protocol during the EMDAP. As noted in the principle statement both quality assurance standards and peer review by independent experiments should be an integral part of the quality assurance process. The development of RELAP5 has followed strict quality assurance standards. Independent peer review has also been a fundamental part of the RELAP5 development history.

Provide comprehensive, accurate, up-to-date documentation. As stated in this principle, this type of documentation “is an obvious requirement for a credible NRC review.... it is most important that documentation of this activity be developed early and kept current.” The RELAP5 documentation covers all fundamental components of this principle as noted below.

- **EM methodology** – The Basis of the systems of equations and the flexibility of the modeling capabilities of the RELAP5 code allows both best-estimate calculations to be performed as well as more conservative Evaluation Model Calculations. To perform evaluation models calculations specific models and correlations need to be modified within the models and correlations logic of RELAP5. The capabilities to make these changes ~~is~~ are straight forward and ~~does~~ do not require significant coding modifications which would invalidate the existing basis for model assessments.

- **Code description** – The RELAP5 code description includes “Code Structure, System Models, and Solution Methods” (Ref. 6-2, 10) and “Models and Correlations” (Ref. 6-6, 13). References 6-2 and 6-6 are the manuals for RELAP5/MOD3.3. References 6-10 and 6-13 are the comparable manuals for RELAP5-3D plus additional manuals describing the code architecture and programming standards (Ref. 6-9) and validation of numerical techniques (Ref. 6-7).
- **User manual and user guidelines** – RELAP5 includes two reference manuals containing the user manual and user guidelines. The combined user guidelines and user manual (Ref. 6-3, 11, 12) are prepared by the code developers. Advanced user guidelines (Ref. 6-8, 14) are prepared by expert RELAP5 users. References 6-3 and 6-8 are the manuals for RELAP5/MOD3.3. References 6-11, 6-12, and 6-14 are the comparable manuals for RELAP5-3D.
- **Scaling and uncertainty analysis** - Several scaling and uncertainty analysis reports have been prepared specifically for RELAP5. In addition, RELAP5 has been compared to several different separate-effects-tests and Integral-effects-tests of different scale which contain the same phenomena. Examples referenced in the Regulatory Guide (Ref. 6-1) include References 6-15 and 6-16.
- **Assessment** – Numerous assessment reports and papers have been published describing the assessment of RELAP5. Two important references are included with the RELAP5/MOD3.3 reference manuals. The first describes the developmental assessment of the latest RELAP5 models and correlations (Ref. 6-4). The second is a summary and review of independent code assessment reports prepared by CAMP members (Ref. 6-8).

6.1.3 Overview of RELAP5 and RELAP5-3D

RELAP5 is based on a non-equilibrium, separated two-phase flow thermal hydraulic approach with additional models to describe the behavior of the components of reactor systems including heat conduction in the core and reactor coolant system, reactor kinetics, control systems and trips. The code also has generic and specialized component models such as pumps and valves. In addition, special process models are included to represent those effects important in a thermal hydraulic system including form loss, flow at an abrupt area change, branching,

choked flow, boron tracking, and non-condensable gas transport.

The RELAP5 modeling approaches, user guidelines, and results of representative assessment calculations are most recently described in an eight volume set of NUREG-CR reports listed as References 6-2 to 6-9, specifically.

- Modeling theory and associated numerical schemes (Ref. 6-2),
- User guidelines and specific instructions for input data preparation (Ref. 6-3),
- Results of developmental assessment cases run with RELAP5/MOD3.3 (Ref. 6-4),
- Detailed discussion of the RELAP5/MOD3.3 models and correlations (Ref. 6-5),
- Additional user guidelines prepared by experienced RELAP5 analysts (Ref. 6-6),
- Numerical scheme (Ref. 6-7),
- Summary of the results of independent assessment activities (Ref. 6-8),
- Programming guidelines (Ref. 6-9).

RELAP5-3D includes several advanced user and modeling options. Although these options are not used in the US-APWR SBLOCA calculations or in the code-to-data comparisons, they are briefly noted in this section for the sake of completeness. The most notable options are (1) the multi-dimensional thermal hydraulic component typically used to model the flow in the lower plenum, core, upper plenum and downcomer regions of an LWR and (2) the multi-dimensional neutron kinetics model based on the NESTLE code. These options can be selected through user input. Other enhancements such as improved numerical solvers are described in more detail in the RELAP5-3D reference manuals included as references (Ref. 6-10 to 14), specifically:

- Modeling theory and associated numerical schemes,
- User guidelines
- Instructions for input data preparation,
- Detailed discussion of the models and correlations used in the code,
- Additional user guidelines prepared by experienced RELAP5 analysts.

Table 6.1-1 RELAP5/MOD3 Code Assessment Matrix for PWR SBLOCAs

MATRIX II Cross-reference matrix for small and intermediate leaks in PWRs Phenomena versus test type ● simulated ○ partially simulated - not simulated Phenomena versus test facility ● suitable for code assessment ○ limited suitability - not simulated Test facility versus test type ● simulated ○ partially simulated - not simulated		Test Type Stationary test addressing energy transportation on primary side Stationary test addressing energy transport on sec. side Small leak w/o HEIS overaccum. secondary side necessary		Test Facility												
				Systems			Sep. effects					Plant Transients				
				1:100 ^a	1:50	1:1600										
Phenomena	Natural circulation in 1-phase flow, primary side	●	●	●	●	●	●	-	-	-	○	-	-	-	●	
	Natural circulation in 2-phase flow, primary side	●	●	●	●	●	●	-	-	-	○	-	-	-	-	
	Reflux condenser mode and CCFL	●	●	●	●	○	-	●	-	-	-	●	-	-	-	-
	Asymmetric loop behavior	-	-	●	-	○	-	-	-	-	-	-	-	-	-	●
	Leak flow	-	-	●	●	●	-	-	●	-	-	●	-	-	-	-
	Phase separation w/o mixture level formation	●	-	●	●	○	-	-	-	-	○	-	-	-	-	-
	Mixture level and entrainment in vert. comp s.g. ^b	●	●	●	●	-	-	-	-	-	-	-	-	-	-	●
	Mixture level and entrainment in the core	●	-	●	○	○	-	-	-	-	-	-	-	-	-	-
	Stratification in horizontal pipes	●	●	●	●	○	○	-	-	-	●	-	-	-	-	-
	ECC-mixing and condensation	-	-	-	-	-	○	-	-	-	-	-	-	-	-	-
	Loop seal clearance	-	-	●	●	●	-	-	-	-	-	-	-	-	-	-
	Pool formation in UP/CCFL (UCSP)	●	●	○	○	○	-	-	-	-	-	-	-	-	-	-
	Core wide void and flow distribution	●	●	○	○	○	-	-	-	-	-	-	-	-	-	-
	Heat transfer in covered core	●	●	○	●	●	-	-	-	-	-	-	-	-	-	●
	Heat transfer partially uncovered core	●	●	○	●	○	-	-	-	-	-	-	-	-	○	-
	Heat transfer in SG primary side	●	●	●	●	○	-	-	-	-	-	-	-	-	-	●
	Heat transfer in SG secondary side	○	●	●	●	○	-	-	-	-	-	-	-	-	-	●
	Pressurizer thermohydraulics	-	-	-	-	-	-	-	-	-	-	-	-	-	-	●
	Surge line hydraulics	-	-	-	-	-	-	-	-	-	-	-	-	-	-	●
	1-and 2-phase pump behavior	-	-	-	-	-	-	-	-	-	-	-	-	-	-	○
Structure heat and losses ^c	●	●	●	○	○	-	-	-	-	-	-	-	-	-	-	
Noncondensable gas effects	-	-	-	-	-	-	-	-	-	-	-	-	-	-	-	
Phase separ. in T-junc. and effect on leak flow	-	-	●	○	○	-	-	-	-	-	-	-	-	-	-	
Test Facility Systems	BETHSY	●	●	●	a. Volumetric											
	LSTF	-	-	●	b. Secondary											
	SEMISCALE	-	-	●	c. Problem for scaled test facilities											

6.2 Evaluation Model Structure

6.2.1 Systems and Components

6.2.1.1 Overview

The code includes many generic component models from which overall systems can be simulated. The thermal hydraulic systems and components can be described by the user using a combination of single thermal hydraulic volumes and junctions, general thermal hydraulic components such as pipes, branches and valves, and more specialized components such as accumulators. (Single thermal-hydraulic volumes and junctions are the basic building blocks used in the code and the solution of the thermal hydraulic field equations can be grouped into thermal hydraulic components such as pipes for the convenience of the user. The thermal-hydraulic volumes describe the physical flow system such as flow area and length while the junctions connect the volumes together.) Time dependent boundary conditions such as pressure and temperature or mass flow rates can be defined through input using time dependent volumes for scalar quantities such as pressure and time dependent junctions for directional quantities such as mass flow rates. The thermal hydraulic system and component models are described in detail in Section 3.5 of Reference 6-10.

The thermal response of the structures in the system is defined using representative heat structures that can be selected and described through user input (Section 4 of Ref. 6-10). The code then uses the models and correlations summarized in Subsection of 6.2.4 of this report to compute the convective and radiation heat transfer associated with each structure described in the system. These models and correlations are also described in more detail in the RELAP5-3D models and correlations manual (Ref. 6-13). Representative heat structures can be used to define the fuel rods with special input options and models such as gap conductance and radiation heat transfer. The heat structure models are also used to describe the thermal response of other system structures, such as pipe walls or the vessel internal structures. The temperature distribution within each representative heat structure is typically computed using a standard 1D finite difference heat conduction model.

RELAP5-3D has the option to describe the reactor kinetics of the core using either (a) point kinetics model that has historically been a part of RELAP5 and a standard feature of most versions of RELAP5 or (b) a multi-dimensional model based on the NESTLE code (Ref. 6-17, 6-18). The reactor kinetics models and detailed references are described in detail in Section

7 of Reference 6-10.

The response of the reactor control systems, special processes not explicitly modeled in the code, and parameters of interest in the analysis can be described using a combination of trips and control system variables as described in Sections 5 and 6 of Reference 6-10. Complex control systems or logic can be described in the code input by integrating together different trip or control variables and operations. Trip logic available to the user includes both variable and logical trips. Control variables and operations include a wide variety of functions including addition, multiplication, and integration. Special steady state controllers such as feedwater controllers can be used to mimic the reactor control systems to establish the correct steady state in the plant.

Other special features of the code such as the time step control logic used to help reduce the effects of numerical roundoff and other errors are described in Section 8 of Reference 6-10. For example, the time step control logic uses the computation of local fluid Courant limits and mass error to minimize the influence of roundoff. A more detailed description of the mathematical basis for such logic is contained in Reference 6-7.

6.2.1.2 Overview of Modeling a Typical PWR with M-RELAP5

The following subsection will briefly describe the basic building blocks used to model a typical PWR. These building blocks include volumes and connecting junctions, pertinent generic hydrodynamic components, special models for hydrodynamic and structural behavior, and the types of trips and control system variables that are used to model a typical PWR. It will also provide examples of the typical applications of some of the representative components. More detailed user guidelines for applying the code to PWRs are included in Section 5 of one of the user guidelines in Reference 6-14.

(1) Volumes and Connecting Junctions

The basic building blocks used to describe the hydrodynamic system of the plant are the volumes and junctions. As shown in Figure 6.2.1-1, the volume component describes the physical characteristics of a specific region of the hydrodynamic system, such as volume, length, and cross sectional area. The user also can select through input, special process models that are to be used in each of these volumes. The junctions connect the volumes together. They can connect to any of the six faces of a volume plus there can be multiple

junctions or connections on one or more faces. Figure 6.2.1-2 shows some examples of the different types of connections. The user can also define the characteristics of the junction such as its cross-sectional area and loss coefficients as well as turn on special process models such as abrupt area change. As described in Section 6.2.4, the volumes and junctions are the basic building block for solving the mass, energy, and momentum conservation equations. The generic component models, discussed in the next subsection, are just input options that allow the user to more readily build the system by combining some of the input quantities of volumes and junctions in a convenient way. For example, a pipe is a convenient way to input the information for a connected set of volumes with similar characteristics.

(2) Generic Hydrodynamic Components Used to Model PWR Systems

Table 6.2.1-1 contains a brief list and description of generic components that are typically used to model PWR systems. The complete list of components, a more detailed description of their features, and guidelines for the recommended use of these components are provided in the References 6-2, 6-11. Note the two specialized components called time dependent volumes and junctions. These components are used to specify transient hydrodynamic boundary conditions. The time dependent volumes are used to specify scalar quantities such as pressure and temperature. The time dependent junctions are used to specify directional quantities such as mass flow or velocity.

As noted in this table there are many kinds of valves that can be used to represent the valves used in a PWR. The types of valves and their characteristics are summarized in Table 6.2.1-2.

(3) Hydrodynamic Component Models

The following figures show examples of these components being used to build a typical PWR plant. The first three figures come from the RELAP5-3D user guidelines (Ref 6-14). The first figure, Figure 6.2.1-3 demonstrates a typical nodalization of the reactor vessel when a hot channel and average channel are used to model the core. Horizontal flows in the core region are not considered in this approach. The vessel nodalization utilizes (a) pipes to model the upper plenum and core, (b) annuli to model the downcomer and core bypass, and (c) branches to model the upper plenum, volumes connecting the cold leg, downcomer and core bypass, and the lower plenum. Figure 6.2.1-4 shows one of the primary system loops and components. The components used to model the primary system loop and components include valves,

pumps, pipes, single volumes, and time dependent volumes and junctions. Figure 6.2.1-5 shows one of the steam generators.

Table 6.2.1-3 contains a brief list and description of the special process models that can be used to model the flow in PWRs. The complete list of these models, a more detailed description of their features, and guidelines for the recommended use of these components are provided in the user guidelines References 6-11, 6-14.

(4) Heat Structure Models

Typical PWR structures that would be described using heat structures would include (a) reactor coolant system piping and component walls, (b) reactor vessel and internal structures, (c) steam generator vessel and tube walls, and (c) fuel rods and other structures. Heat structures are used to describe heat conduction through the wall of the structure, as shown in Figure 6.2.1-6. As shown in this figure, the heat structure can have fluid channels on each side so convective boundary conditions are determined using the heat transfer correlations described in Section 6.2.4. The boundary conditions can also be specified to have a time dependent temperature or flux (typically adiabatic). Heat structures typically only consider heat conduction in 1D so complex 3D structures must be simplified or divided into multiple 1D heat structures to conserve thermal mass and surface area to the extent possible. Internal flow paths, not represented as fluid channels using hydrodynamic components, can only be represented using the appropriate input for effective thermal conductivity and specific heat (the influence of radiation and convection can also be defined if the influence can be determined in terms of the temperature). Any number of heat structures can be connected to a single (or pair of) hydrodynamic volume(s) as shown in Figure 6.2.1-7. However, heat structures representing cylindrical fuel rods or control rods can only be connected to the flow channel surrounding the rod since the inner boundary representing the centerline is adiabatic. The power source can be input from a power vs. time table, reactor kinetics, total reactor power, fission power or a control variable. A user specified scaling factor can be used to input axial and radial power profiles.

(5) Trips and Control Systems

Trips and control variables provide a general capability for modeling interactions among the various types of calculated parameters. Control variables may be used to relate the condition of thermal hydraulic variables (e.g., temperatures, pressures, and flow rates) with the status of the

trip. Control variables also provide a general data manipulation capability. Calculated data may be summed, multiplied, divided, differentiated, integrated, lagged, or raised to a power. Because the responses of the control variables may themselves be interrelated, the response of an actual control system may be simulated. The detailed equations and descriptions of these models are included as Sections 5 and 6 in Reference 6-10, Section 4 in the user guidelines Reference 6-11 and Section 4.4 and 4.10 in the advanced user guidelines Reference 6-14.

This trip system allows the user to specify a group of logical statements. The code then, following the specified order of the statements, will evaluate if each statement is true or false. This evaluation takes place for each time advancement. The results of the evaluation can then be used by other models or variables to perform an action. For example, the trip statement may evaluate whether a set point has been reached. Then a control variable may use the value of that trip to turn off or on a pump.

6.2.1.3 Application to US-APWR

The US-APWR reference input model has been developed following the general user guidelines presented in References 6-11 and 6-14 for the modeling of PWRs. In particular, the model was developed following the approach recommended for PWRs similar to the Westinghouse design, since US-APWR has a very comparable configuration to that of Westinghouse PWRs. This approach is specifically addressed in Section 5.1 of Reference 6-14. The general components, special process models, and special models for heat structures that are used in the model are summarized in Table 6.2.1-4. In some cases, because of the relatively large number of volumes and junctions used in the input model, pipes and branches may be used in combination with single volumes or single junctions for convenience in building the input model. As noted in the preceding section, even though single volumes and junctions can always be used to define the hydrodynamic system since they are the basic components used in the solution of the balance equations, it is also possible to simplify the input by using the corresponding pipes, branches and other components that have been developed for that purpose.

Table 6.2.1-1 Hydrodynamic Components Typically Used for PWR Applications

Component	Description
Single volume	Basic building block for hydrodynamic system
Single junction	Basic connection for hydrodynamic system
Time dependent volume	Defines state variables such as pressures as a function of time or other variables for the hydrodynamic boundary condition
Time dependent junction	Defines directional variables such as mass flow as a function of time or other variables for the hydrodynamic boundary condition
Pipe	String of volumes with interior connecting junctions
Annulus	Pipe with special flow regime considerations
Multiple junction	Enters patterns of junctions. Useful for cross connecting pipes for a multi-dimensional effect.
Branch	One volume and between 0 to 9 connecting junctions
ECC mixer	Branch with special models for entry of ECC water injection into piping.
Separator	Branch plus special models for separation
Valve	Single junction plus models for several valve types
Pump	One volume, two junctions plus pump models
Accumulator	One volume, one junction. Does not use normal two fluid model
Pressurizer	Pipe with pressurizer models

Table 6.2.1-2 Types of Valves

Valve Type	Characteristics
Check Valves <ul style="list-style-type: none"> • Static Pressure Controlled • Dynamic Pressure Controlled • Flow Controlled 	Flow control to prevent backflow when downstream pressure is greater than the upstream pressure. Open and close instantaneously, do not include inertia or momentum effects. Control methods include: <ul style="list-style-type: none"> • Time trip • Pressure trip <ul style="list-style-type: none"> ○ Open and close by a static or dynamic differential pressure ○ Open by a static differential pressure, close by a flow reversal • Flow conditions <ul style="list-style-type: none"> ○ Flow positive (open) ○ Flow negative or reversed (closed, leak possible)
Trip Valves	On/off switch controlled by a trip logic <ul style="list-style-type: none"> • Trip true, valve instantaneously fully open • Trip false, valve instantaneously fully closed
Inertial Swing Check Valves	Simulates dynamic characteristics of a flapper valve including mass and inertia. Flapper angles positive in positive flow direction. Gravity acts in a vertical downward direction. Gravity can open or close a valve depending on junction direction.
Motor Valves	Valve opening controlled by a motor. Position can be stationary or moving at a constant rate. Opening and closing times supplied by user. Motor is controlled by trips. <ul style="list-style-type: none"> • If open and close trips are false, the valve position is stationary. • Open trip true – valve begins opening at rate supplied by the user. • Close trip true – valve begins closing at rate supplied by the user. A table showing normalized stem position or flow area as a function of time may be used.
Servo Valves	Servo valve uses a control variable or table to indicate valve position.
Relief Valves	Simulates dynamic response of spring loaded valves including mass and inertia.

Table 6.2.1-3 List and Description of the Special Process Models

Special Process Models	Description
Choked flow	Used to predict if the flow is choked at a break or nozzle and, if it is, to establish the discharge boundary condition. In addition, the choked-flow model can be used to predict the existence of and calculate choked flow at internal points in the system. Two options available, one developed by Ransom and Trapp, the other, by Henry and Fauske.
Stratification entrainment	Used to predict vapor/gas pull through and liquid entrainment for various conditions for horizontal volumes. Developed by Ardron and Bryce.
Abrupt area change	Used to evaluate the form loss coefficients related to abrupt area changes in single phase and two-phase flow conditions.
User specified form loss	Allows users to specify a form loss in addition to those normally used by the code.
Crossflow junction	Uses a simplified form of the momentum balance equation to represent natural circulation in the core or upper plenum or secondary flows in leakages or tee junctions.
Water packing	Used to minimize spurious pressure spikes sometimes predicted with movement of a liquid front through a vertical volume boundary.
Countercurrent flow limitation	Used to predict countercurrent flows where upward flowing steam can impede the drainage of liquid. The model allows the user to select the Wallis form, the Kutateladze form, or a form in between the Wallis and Kutateladze forms.
Mixture level tracking	Uses special algorithms to identify the mixture level within a vertically aligned flow channel.
Thermal stratification	Used to improve the prediction of the thermal front occurring when there is warm liquid appearing above cold liquid in a vertical stack of cells.
Energy conservation at an abrupt change	Used to improve the prediction of the energy of the fluid moving through abrupt area change. Typically used when modeling the discharge from a break in the piping into the containment vessel.

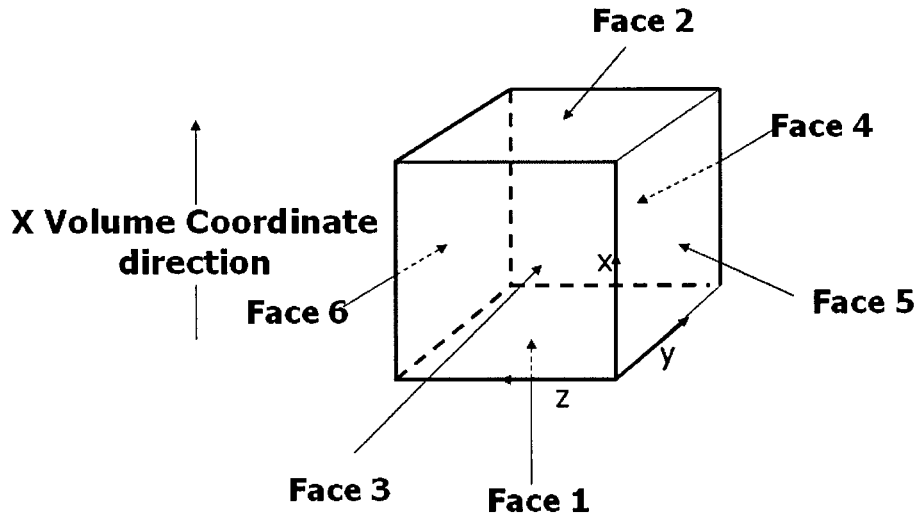


Figure 6.2.1-1 Thermal Hydraulic Volume

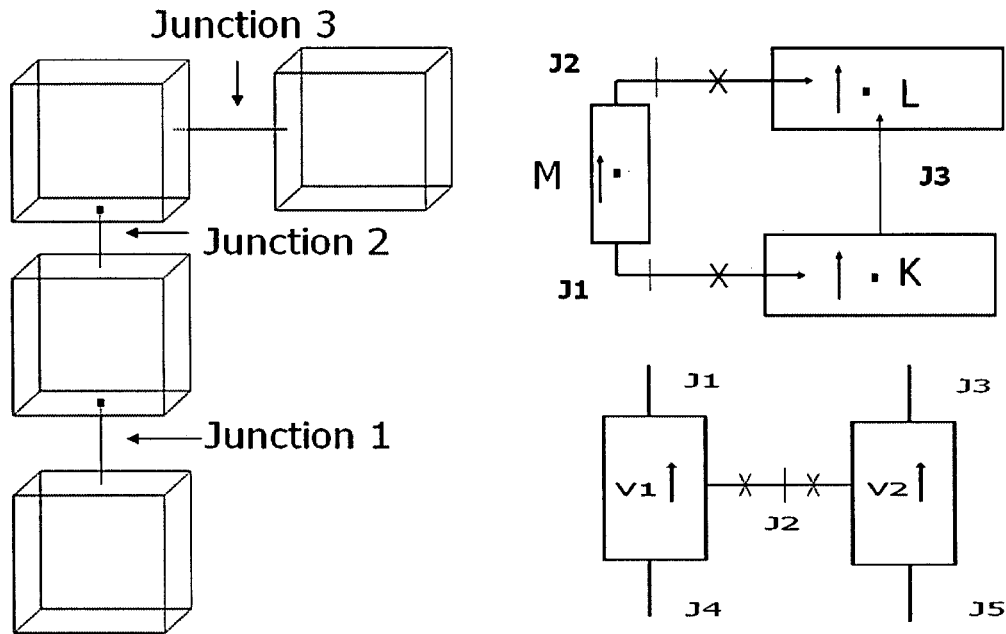


Figure 6.2.1-2 Connecting Volumes with Junctions

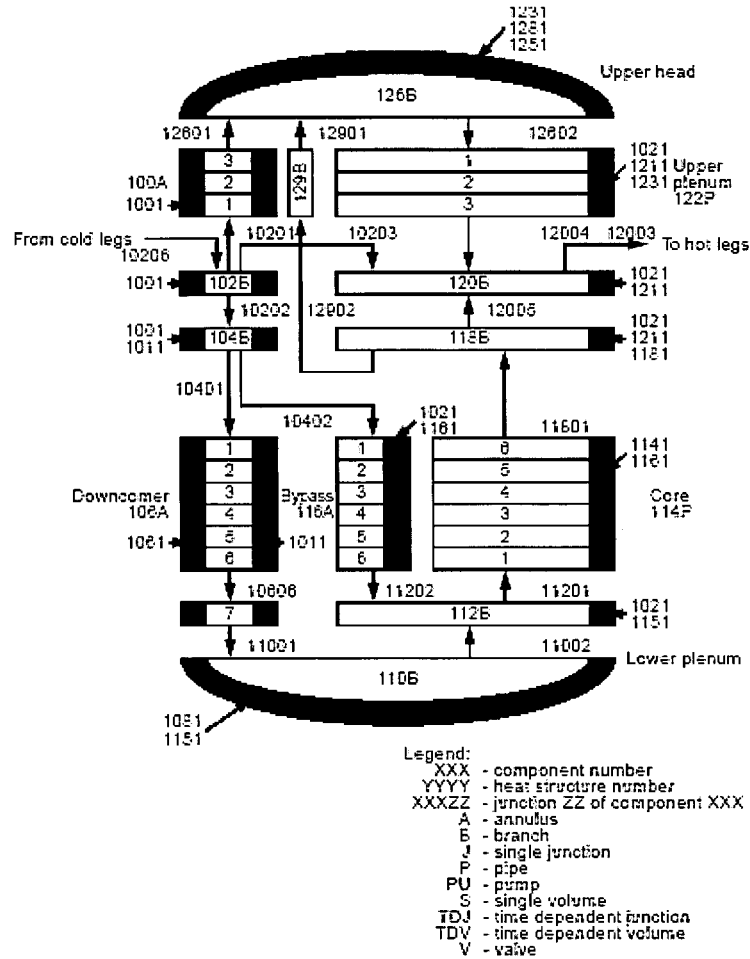


Figure 6.2.1-3 Example of Vessel Nodalization for One Dimensional Flow in the Core
 (From RELAP5-3D[®] CODE MANUAL VOLUME V: USER'S GUIDELINES)

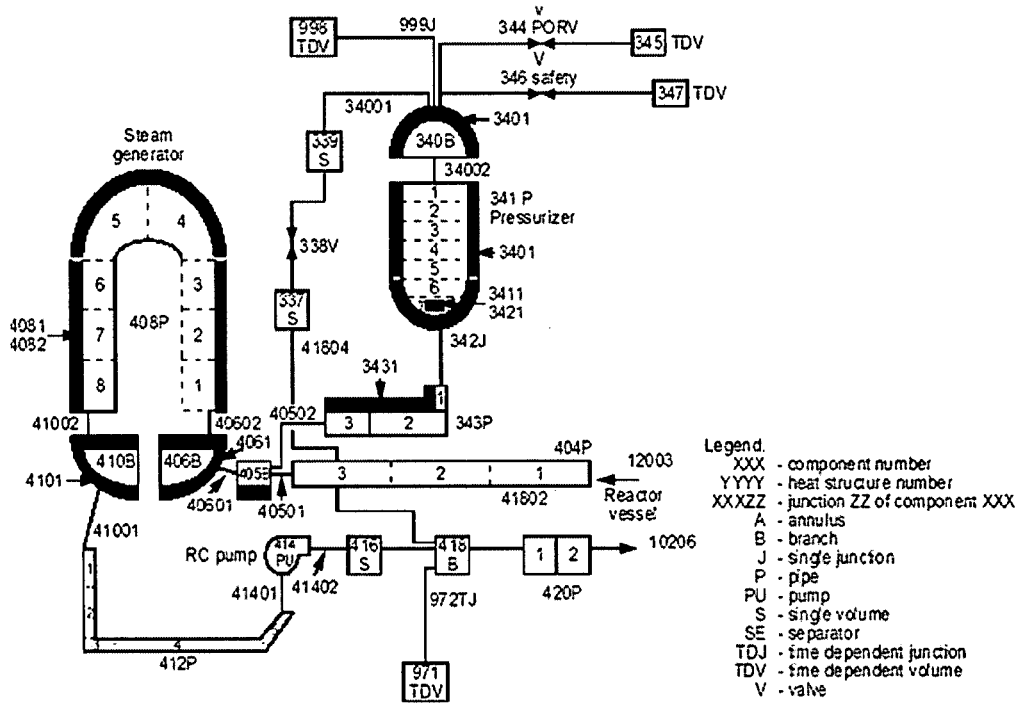


Figure 6.2.1-4 Example of the Nodalization Used for the Primary System Piping and Components

(From RELAP5-3D[®] CODE MANUAL VOLUME V: USER'S GUIDELINES)

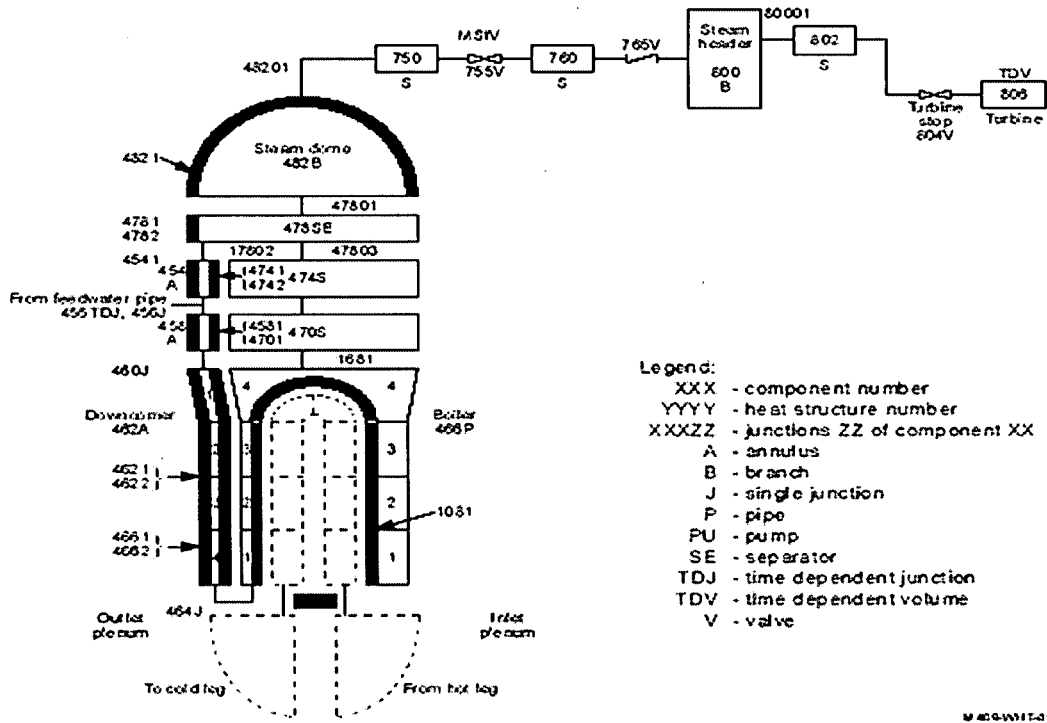


Figure 6.2.1-5 Example of the Nodalization Used for the Steam Generator
 (From RELAP5-3D[®] CODE MANUAL VOLUME V: USER'S GUIDELINES)

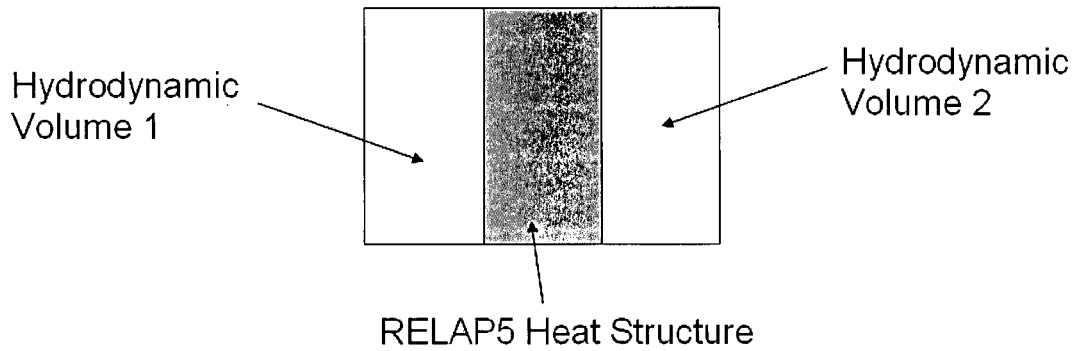


Figure 6.2.1-6 Heat Structure with the Hydrodynamic Volumes Connected to the Two Surfaces

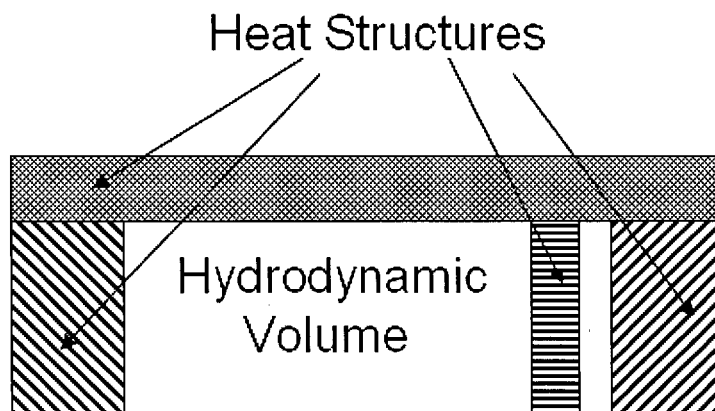


Figure 6.2.1-7 Multiple Heat Structures Connected to a Single Hydrodynamic Volume

6.2.2 Constituents and Phases

6.2.2.1 Overview

M-RELAP5 uses a six equation hydrodynamics model to describe the liquid, vapor, and non-condensable gases in the system. As described in Section 3.2 of Reference 6-10, the six-equation model uses five independent state (thermodynamic fluid) variables with an additional equation for the non-condensable gas component.

6.2.2.2 State Relationships

M-RELAP5 requires thermodynamic properties for single phase liquid, single phase vapor, and the saturated states. The basic thermodynamic quantities needed are temperature, pressure, specific volume/density, internal energy, enthalpy, and entropy. The other derivative quantities either come directly from the equation of state for water or can be computed from properties taken from the equation of state. A hydrodynamic volume can contain liquid, vapor, or a mixture of the two. In addition, the vapor may also be a mixture of steam and non-condensable gases or the liquid may contain dissolved boron. The liquid, vapor and non-condensable gases within a hydrodynamic volume are considered to be at the same pressure but the liquid and vapor/gas mixture may have different temperatures. More detailed explanations and defining equations are described in the Section 3.2 of Reference 6-10.

(1) The Water Property Equations of State

M-RELAP5 uses the 1967 ASME (American Society of Mechanical Engineers)/IFC-67 International Formulation Committee Formulation for Industrial Use to calculate the basic properties for light water (Ref 6-19, 6-20).

(2) State Equations

The basic thermodynamic quantities needed are temperature, pressure, specific volume/density, internal energy, enthalpy, and entropy along with the derivatives of the phasic densities and temperatures as shown below;

$$\left(\frac{\partial \rho_g}{\partial P}\right)_{U_g, X_n}, \left(\frac{\partial \rho_g}{\partial U_g}\right)_{P, X_n}, \left(\frac{\partial \rho_g}{\partial X_n}\right)_{P, U_g}, \left(\frac{\partial \rho_f}{\partial P}\right)_{U_f}, \left(\frac{\partial \rho_f}{\partial U_f}\right)_P$$

$$\left(\frac{\partial T_g}{\partial P}\right)_{U_g, X_g}, \left(\frac{\partial T_g}{\partial U_g}\right)_{P, X_g}, \left(\frac{\partial T_g}{\partial X_g}\right)_{P, U_g}, \left(\frac{\partial T_f}{\partial P}\right)_{U_f}, \left(\frac{\partial T_f}{\partial U_f}\right)_{P, X_f}, \left(\frac{\partial T_f}{\partial P}\right)_{U_f, X_f}, \left(\frac{\partial T_f}{\partial U_f}\right)_{P, X_f}, \left(\frac{\partial T_f}{\partial X_f}\right)_{P, U_f}, \dots \quad (6.2.2-1)$$

where ρ , T , U , X represent the density, temperature, internal energy, and mass fraction. The subscripts f and g represent the liquid and vapor phases, respectively.

The derivatives of the phasic densities and temperatures are not available directly from the water equation of state but must be derived from the isobaric expansion coefficient, β , the isothermal compressibility, κ , and specific heat, C_p .

The interphase mass and heat transfer models use an implicit (linearized) evaluation of the temperature potentials, $T_i - T_f$ and $T_i - T_g$. The quantity T_i is the temperature that exists at the phase interface. For a single-component mixture, T_i is the saturation temperature. When non-condensable gases are present, T_i is the saturation temperature of the partial pressure of steam.

(3) Two Phase Without Non-condensable Gases

The determination of the thermodynamic properties is straightforward in this case. The properties are obtained directly from the thermodynamic tables, given the pressure, P , and phasic internal energy, U . All the desired density and temperature derivatives can then be obtained from the derivatives κ , β , and C_p .

The only complicating factor is the calculation of the ρ , T , κ , β , and C_p derivatives if the vapor is subcooled or the liquid is superheated, i.e., in a metastable state. In these two cases, either an extrapolation of the temperature or specific volume is performed using a Taylor expansion or the metastable properties are looked up directly. The choice depends on the equation of state being used.

(4) Influence of Non-condensable Gases

The gas phase is considered to be a Gibbs-Dalton mixture of gases and steam as shown below, where v the specific volume, and the subscripts s and n refer to steam and each non-condensable gas.

$$P_g = \sum_{i=1}^N P_{ni} \quad \dots\dots\dots (6.2.2-2)$$

$$P = P_g + P_s \quad \dots\dots\dots (6.2.2-3)$$

$$U_g = X_n U_n + (1 - X_n) U_s \quad \dots\dots\dots (6.2.2-4)$$

$$v_g = X_n v_n + (1 - X_n) v_s \quad \dots\dots\dots (6.2.2-5)$$

P_s and P_{ni} are the partial pressures of the vapor and the individual non-condensable components, respectively. The specific internal energies, U , and the specific volumes are evaluated at the vapor/gas temperature and the respective partial pressures. X_n represents the mass fraction of the non-condensable gas in the mixture.

6.2.3 Field Equations

The M-RELAP5 thermal-hydraulic model solves eight field equations for eight primary dependent variables as described in Section 3.1 of Reference 6-10. The primary dependent variables, are pressure, phasic specific internal energies, vapor/gas volume fraction (void fraction), phasic velocities, non-condensable quality, and boron density. The independent variables are time and distance, where distance may be defined by one, two, or three dimensions depending on the nodalization specified by the user. The non-condensable quality is defined as the ratio of the non-condensable gas mass to the total vapor/gas phase mass. The secondary dependent variables used in the equations are phasic densities, phasic temperatures, saturation temperature, and non-condensable mass fraction in the non-condensable gas phase for each non-condensable species represented.

The basic field equations for the two-fluid non-equilibrium model consist of two phasic continuity equations, two phasic momentum equations, and two phasic energy equations. The dependent variables are time (t) and one space dimension (x). The vapor and liquid continuity balance equation has the following form with subscripts g and f corresponding to vapor and liquid, respectively, and Γ representing the generation of vapor or liquid at the interface through mass transfer.

$$\frac{\partial}{\partial t}(\alpha_g \rho_g) + \frac{1}{A} \frac{\partial}{\partial x}(\alpha_g \rho_g v_g A) = \Gamma_g \dots\dots\dots(6.2.3-1)$$

$$\frac{\partial}{\partial t}(\alpha_f \rho_f) + \frac{1}{A} \frac{\partial}{\partial x}(\alpha_f \rho_f v_f A) = \Gamma_f \dots\dots\dots(6.2.3-2)$$

The interface jump condition is

$$\Gamma_f = -\Gamma_g \dots\dots\dots(6.2.3-3)$$

The mass transfer at the interface is further partitioned into the contributions from the bulk fluid (ig) and from the wall (w) in the following form

$$\Gamma_g = \Gamma_{ig} + \Gamma_w \dots\dots\dots(6.2.3-4)$$

The vapor and liquid momentum balance equations are of the form

$$\begin{aligned} \alpha_g \rho_g A \frac{\partial v_g}{\partial t} + \frac{1}{2} \alpha_g \rho_g A \frac{\partial v_g^2}{\partial x} = & -\alpha_g A \frac{\partial P}{\partial x} + \alpha_g \rho_g B_x A - (\alpha_g \rho_g A) FWG(v_g) \\ & + \Gamma_g A (v_{gl} - v_g) - (\alpha_g \rho_g A) FIG(v_g - v_f) \\ & - C \alpha_g \alpha_f \rho_m A \left[\frac{\partial (v_g - v_f)}{\partial t} + v_f \frac{\partial v_g}{\partial x} - v_g \frac{\partial v_f}{\partial x} \right] \dots\dots\dots (6.2.3-5) \end{aligned}$$

$$\begin{aligned} \alpha_f \rho_f A \frac{\partial v_f}{\partial t} + \frac{1}{2} \alpha_f \rho_f A \frac{\partial v_f^2}{\partial x} = & -\alpha_f A \frac{\partial P}{\partial x} + \alpha_f \rho_f B_x A - (\alpha_f \rho_f A) FWF(v_f) \\ & - \Gamma_f A (v_{fl} - v_f) - (\alpha_f \rho_f A) FIF(v_f - v_g) \\ & - C \alpha_f \alpha_g \rho_m A \left[\frac{\partial (v_f - v_g)}{\partial t} + v_g \frac{\partial v_f}{\partial x} - v_f \frac{\partial v_g}{\partial x} \right] \dots\dots\dots (6.2.3-6) \end{aligned}$$

The force terms on the right sides of the equation are, respectively, the pressure gradient, the body force (i.e., gravity and pump head), wall friction, momentum transfer due to interface mass transfer, interface frictional drag, and force due to virtual mass. The terms FWG and FWF are part of the wall frictional drag, are linear in velocity, and are products of the friction coefficient, the frictional reference area per unit volume, and the magnitude of the fluid bulk velocity. The interfacial velocity in the interface momentum transfer term is the unit momentum with which phase appearance or disappearance occurs. The coefficients FIG and FIF are part of the interface frictional drag. The coefficient of virtual mass (C) is based on an approach by Anderson. See Section 3.3 in Reference 6-10 for a more detailed explanation of this coefficient.

The interface jump conditions follow the form, where it is assumed that the mass transfer and interfacial forces sum to zero independently,

$$\begin{aligned} \Gamma_g A v_{gl} - (\alpha_g \rho_g A) FIG(v_g - v_f) - C \alpha_g \alpha_f \rho_m A \left[\frac{\partial (v_g - v_f)}{\partial t} \right] \\ - \Gamma_f A v_{fl} - (\alpha_f \rho_f A) FIF(v_f - v_g) - C \alpha_f \alpha_g \rho_m A \left[\frac{\partial (v_f - v_g)}{\partial t} \right] = 0 \dots\dots\dots (6.2.3-7) \end{aligned}$$

The vapor and liquid energy equation follow the form

$$\frac{\partial}{\partial t}(\alpha_g \rho_g U_g) + \frac{1}{A} \frac{\partial}{\partial x}(\alpha_g \rho_g U_g v_g A) = -P \frac{\partial \alpha_g}{\partial t} - \frac{P}{A} \frac{\partial}{\partial x}(\alpha_g v_g A) + Q_{wg} + Q_{ig} + \Gamma_{ig} h_g + \Gamma_w h_g + DISS_g \dots (6.2.3-8)$$

$$\frac{\partial}{\partial t}(\alpha_f \rho_f U_f) + \frac{1}{A} \frac{\partial}{\partial x}(\alpha_f \rho_f U_f v_f A) = -P \frac{\partial \alpha_f}{\partial t} - \frac{P}{A} \frac{\partial}{\partial x}(\alpha_f v_f A) + Q_{wf} + Q_{if} - \Gamma_{if} h_f - \Gamma_w h_f + DISS_f \dots (6.2.3-9)$$

In the phasic energy equations, Q_{wg} and Q_{wf} are the phasic wall heat transfer rates per unit volume and $DISS_f$ and $DISS_g$ are the phasic dissipation terms. The dissipation terms account for wall friction, pump, and turbine effects. The dissipation effects due to interface mass transfer, interface friction, and virtual mass are neglected.

The total wall heat rate (Q) per unit volume then is the sum of the two phasic wall heat rates as shown below.

$$Q = Q_{wg} + Q_{wf} \dots (6.2.3-10)$$

As in the case of interfacial mass transfer, interfacial heat transfer is also divided into two contributions, heat transfer in the bulk fluid and at the wall. This allows for the treatment of a phase change in the bulk fluid and processes where superheated or subcooled conditions only appear close to the wall, as shown conceptually in Figure 6.2.3-1. The heat and mass transfer, whether in the bulk or at the wall, is strictly linked through vaporization or condensation and the extraction or addition of latent heat.

The conservation equations must also be modified slightly to account for the presence of non-condensable gases. Additional continuity equations are added for each species of gas present plus an additional equation for a mixture as shown below. The equations are for a mixture containing i^{th} species.

$$\frac{\partial}{\partial t}(\alpha_g \rho_g X_{gi}) + \frac{1}{A} \frac{\partial}{\partial x}(\alpha_g \rho_g X_{gi} v_g A) = 0 \dots (6.2.3-11)$$

$$\frac{\partial}{\partial t}(\alpha_g \rho_g X_{gi} X_{ni}) + \frac{1}{A} \frac{\partial}{\partial x}(\alpha_g \rho_g X_{gi} X_{ni} v_g A) = 0 \dots (6.2.3-12)$$

The energy equation is also modified by including an additional interfacial heat transfer term.

For boron transport, M-RELAP5 uses an Eulerian boron tracking model for the transport of boron in the liquid phase. However, it is assumed that the concentration is dilute enough so there is a negligible impact on the liquid. As a result, the presence of boron only requires the addition of another continuity equation like the one above.

The conservation equations are also slightly modified for stratified flow in a horizontal or inclined pipe, or when there is stratified flow in volumes that are vertically oriented but connected by cross-flows. A more detailed explanation of these modifications is included in Section 3.1.1.5 in reference 6-10.

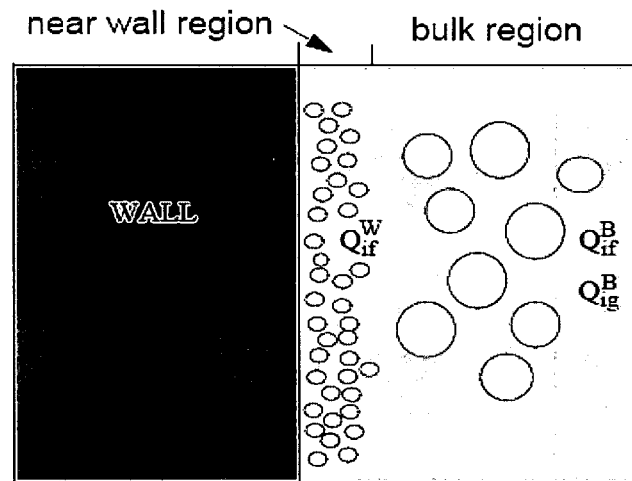


Figure 6.2.3-1 Interface Heat Transfer in the Bulk and Near the Wall for Subcooled Boiling

6.2.4 Closure Relationships

The closure relationships used in the M-RELAP5 computer code are described in detail in the RELAP5-3D Volume I modeling theory and associated numerical schemes reference manual (Ref. 6-10) and the Volume IV models and correlations reference manual (Ref. 6-13). Volume I provides a detailed overview of the closure relationships, while Volume IV provides a detailed description of the technical basis and range of applicability for the specific models and correlations used in the code. In addition, the conservative models described in Section 7 of this report are incorporated to M-RELAP5 to be used for the SBLOCA analysis.

This subsection provides a brief summary and highlights of closure relationships used in M-RELAP5 along with a detailed roadmap identifying the specific sections in the RELAP5 reference manual where the defining equations and discussion of each group of relationships are included.

Volume I (Ref. 6-10) provides a detailed overview, including the defining equations in Sections 3 and 4. These sections include a discussion of the constitutive relationships used for the flow equations, Section 3.3, with a description of the flow regime maps, interface and wall friction, wall heat transfer, and interfacial mass transfer friction. Section 3.4 describes the relationships used in the special process models including choked flow, stratification, countercurrent flow limitations, and mixture level. Section 4.0 describes some of the special relationships used for heat structures including the special models used to describe the behavior of fuel rods. These special fuel rod behavior models and correlations include those for gap conductance, metal water reaction, and cladding deformation.

Specific models and correlations used in the code are also described in detail in the models and correlations reference manual (Ref. 6-13). That document is intended to provide a detailed supplement to the information provided in Reference 6-10. That manual includes (a) a detailed description of the flow regime maps used in the code, Section 3, (b) the models and correlations used for the closure of the energy, mass, and momentum conservation equations, Sections 4 to 5, respectively, (c) the flow process models, such as those for an abrupt area change and critical flow. Section 7, (d) selected component models, specifically, the pump and separator/dryer models, Section 8, (e) the heat structure process models, including the solution of the heat conduction equations and the energy source term model as represented by the reactor kinetics equations, Section 9, (f) closure relations required by extra mass conservation fields for non-condensable gases, Section 10, and (g) the steady-state model, Section 11.

As described in Section 3.3 of Reference 6-10, the hydrodynamic closure relationships include models for defining flow regimes and flow-regime-related models for interfacial friction, the coefficient of virtual mass, wall friction, wall heat transfer, interfacial heat and mass transfer, and direct (sensible) heat transfer. Heat transfer regimes used for wall heat transfer are also defined.

The flow regime maps are based on the work of Taitel and Dukler and Ishii with detailed references provided in Section 3.1.12 in Reference 6-10. The flow regime maps for volumes and junctions are described in Sections 3.3.1 to 3.3.5 in Reference 6-10.

6.2.4.1 Vertical Volume Flow Regime Map

As shown schematically in Figure 6.2.4-1, the vertical flow-regime map describes nine regimes, four for pre-CHF heat transfer, four for post-CHF heat transfer, and one for vertical stratification. This map applies to upward and downward flows in volumes with a vertical inclination angle between 60 to 90 degrees. The vertical inclination angle is measured from the horizontal. The pre-CHF regimes modeled are bubbly, slug, annular mist, and pre-CHF mist. The post-CHF regimes for heat transfer are inverted bubbly, slug, and annular mist plus a mist post-CHF regime that was added for symmetry. The flow regime transitions are functions of void fraction, α_g , average mixture velocity, v_m , and boiling regime (pre-CHF, transition, and post-dryout).

6.2.4.2 Horizontal Volume Flow Regime Map

As shown schematically in Figure 6.2.4-2, the horizontal flow regime map is a function of relative velocity, mass flux, and void fraction. This map is applied to volumes whose inclination vertical angles are less than or equal to 30 degrees. An interpolation region between the vertical and horizontal flow regimes is used for volumes whose absolute value of inclination is between 30 and 60 degrees. The map is similar to the vertical flow regime map except that the post CHF regimes are not included. A horizontally stratified regime replaces the vertically stratified regime. The horizontal flow regime map therefore consists of the horizontally stratified bubbly, slug, annular-mist and mist pre-CHF regimes.

6.2.4.3 High Mixing Region

The high mixing flow regime map (used in pumps and compressors), as shown in Figure 6.2.4-3, is based on the vapor/gas void fraction α_g and consists of a bubbly regime for $\alpha \leq 0.5$, a mist regime for $\alpha \geq 0.95$, and a transition regime for $0.5 < \alpha < 0.95$. The transition regime is modeled as a mixture of bubbles dispersed in liquid and droplets dispersed in vapor. The upper limit for bubbly flow of $\alpha_g = 0.5$ is based on Taitel, Bornea, and Dukler (Ref. 6-21, 6-22).

6.2.4.4 Junction Flow Regime

The junction flow regime maps use both volume and junction volume quantities. For the volumes, four junction flow regime maps are used. They are a horizontal map for flow in pipes; a vertical map for flow in pipes, annuli, and bundles; a high mixing map for flow in pumps; and an ECC mixer map for flow in a horizontal pipe near the ECC injection port. These maps are used for the interfacial drag and shear, as well as the coefficient of virtual mass. The junction map regimes are functions of junction phasic velocities, donored (based on phasic velocities), phasic densities, and donored (based on mixture superficial velocity) surface tension.

6.2.4.5 Interfacial Friction

The interfacial friction models are described in Section 3.3.6 of Reference 6-10 and in more detail in Section 6.1.3 of Reference 6-13. Two models are used with the selection depending on the flow regime. The drift flux model is used in the bubbly and slug flow regimes for vertical flow. This model was not used in early versions of RELAP5 but is used in RELAP5/MOD3.3, RELAP5-3D and M-RELAP5. The drag coefficient method is used in all of the other flow regions. The drag coefficient method was used in earlier versions of RELAP5 as well as in RELAP5/MOD3.3 and RELAP5-3D for all interfacial friction calculations as well as in M-RELAP5.

The computation of the interfacial friction expressed in terms of F_i , the interfacial friction per unit volume, comes from the following expressions:

$$F_i = C_i |C_1 v_g - C_0 v_f| (C_1 v_g - C_0 v_f) \quad \dots\dots\dots (6.2.4-1)$$

$$C_i = \frac{\alpha_g \alpha_f^3 (\rho_f - \rho_g) g}{V_{gj}^2} \quad \dots\dots\dots (6.2.4-2)$$

$$C_1 = \frac{1 - \alpha_g C_0}{1 - \alpha_g} \dots\dots\dots (6.2.4-3)$$

The coefficients, C_0 , and vapor/gas drift velocity, v_{gj} , come from the drift flux correlations summarized below. The derivation of these expressions and the definition of the correlation parameters are provided in Section 3.3.6 of Reference 6-10.

The application of the various void fraction correlations used in the drift flux model to calculate the interfacial friction for vertical bubbly-slug flow is summarized in Table 6.2.4-1. The general expressions describing the correlations are provided in Table 6.2.4-2. Specific references for the correlations are provided in Sections 3.3.6 and 3.3.13 in Reference 6-10 with a more detailed discussion of the correlations and their range of validity in the models and correlation manual, Section 6.1.3 (Ref. 6-13). In the table, the term transition means interpolation and is applied between different flow rates in pipes.

As discussed in the models and correlations manual Section 6.1.3 of Reference 6-13, the selection of these correlations is based on a literature search and comparisons with experiments as initially reported by Putney. It should be noted that, in the reference manuals (Ref. 6-10, 6-13), the modified Chexal and Lellouche correlations are often referred to as the EPRI correlations. (Ref. 6-23, 6-24, 6-25) There is also some difference in the implementation of this correlation depending on whether the flow is in a bundle or in a pipe. These differences are discussed in Reference 6-13. (As noted in Section 6.1 of Reference 6-13, the modified Chexal and Lellouche correction was selected for co-current upflow in rod bundles based on its wider range of validation, better accuracy when compared to ORNL THTF tests, and better performance against FROJA, FRIGG, and CISE high-pressure, high-flow tests.)

The drag coefficient method is used in all other flow regimes. The derivation and definition of the correlation parameters are also provided in Section 3.3.6 of Reference 6-10. This method uses correlations for drag coefficients and interfacial area density and is based on the calculation of the frictional force on a body moving relative to a fluid. The drag coefficient model calculates the interfacial friction factor using the concept of a continuous fluid density, drag coefficient, interfacial area density, and shape factor for the different flow regimes. Specific references for the different correlations used are provided in Section 3.3.6 of reference 6-10.

For dispersed flow, which includes the bubbly, mist, mist pre-CHF, and mist post-CHF flow regimes, the dispersed bubbles or droplets are assumed to be spherical particles with a size

distribution of the Nukiyama-Tanasawa form (Ref.6-26). This form is then converted into an interfacial area per unit volume, a_{gf} , using a critical Weber number, We , which varies as a function of the flow regime. The drag coefficients, C_D , for non-vertical bubbly flow and all droplet flow situations are given by correlations developed by Ishii and Chawla (Ref.6-27). The continuous phase density is either the density of the liquid for bubbles or of the vapor for drops. The choice of the appropriate viscosity, which is used in drag coefficient formulation, is also dependent on the flow regions.

The computation of the interfacial friction using the drag coefficient method comes from the following relations.

$$F_i = \frac{1}{8} \rho_c |v_g - v_f| (v_g - v_f) C_D S_F a_{gf} \quad \dots\dots\dots (6.2.4-4)$$

$$C_D = \frac{24(1.0 + 0.1 Re_p^{0.75})}{Re_p} \quad \dots\dots\dots (6.2.4-5)$$

$$a_{gf} = \frac{3.6 \bar{\alpha}}{d_o} \quad \dots\dots\dots (6.2.4-6)$$

$$d_o = (1/2) d_{max} \quad \dots\dots\dots (6.2.4-7)$$

$$We = \frac{d_{max} \rho_c (v_g - v_f)^2}{\sigma} \quad \dots\dots\dots (6.2.4-8)$$

The values for critical Weber number, We , are 10.0 for bubbly flow, 3.0 for mist-pre-CHF flow, and 12.0 for mist and mist-post-CHF flow. The shape factor, S_F , is taken as 1.0.

For non-vertical slug flow, the drag coefficient model solves for the interfacial friction based on the concept of a series of Taylor bubbles separated by liquid slugs containing small bubbles. The Taylor bubble has a diameter nearly equal to the pipe diameter and a length varying from 1 to 100 pipe diameters.

The interfacial area per unit volume can be determined from geometric considerations as shown in the following relationship where α_b/L is the Taylor bubble frontal area per unit volume and L is the cell length.

$$a_{gf} = \frac{\alpha_b}{L} + \left(\frac{3.6 \alpha_{gs}}{d_o} \right) (1 - \alpha_b) \quad \dots\dots\dots (6.2.4-9)$$

The drag coefficients for the Taylor bubble and the small bubbles are given by correlations

developed by Ishii and Chawla, where D' is the Taylor bubble diameter and D is the pipe diameter.

$$C_D = 10.9 \left(\frac{D'}{D} \right) (1 - \alpha_b)^3 \dots\dots\dots (6.2.4-10)$$

For annular mist flow, characterized by a liquid film along the wall with a vapor gas core containing entrained liquid droplets, the interfacial area per unit area can be determined from geometric considerations and expressed by the following relationship, where α_{ff} is the average liquid volume fraction of the liquid film along the wall:

$$a_{gf} = \left(\frac{4C_{ann}}{D} \right) (1 - \alpha_{ff})^{1/2} + \left(\frac{3.6\alpha_{fd}}{d_o} \right) (1 - \alpha_{ff}) \dots\dots\dots (6.2.4-11)$$

For vertical flow regimes,

$$\alpha_{ff} = \alpha_f C_f \exp \left[-7.5 \times 10^{-5} \left(\frac{\alpha_g V_g}{u_c} \right)^6 \right] \dots\dots\dots (6.2.4-12)$$

For horizontal flow regimes,

$$\alpha_{ff} = \alpha_f C_f \exp \left[-4.0 \times 10^{-5} \left(\frac{|V_g - V_f|}{V_{gL}} \right)^6 \right] \dots\dots\dots (6.2.4-13)$$

For flow in an annular region such as a downcomer, it is assumed that all of the liquid is film and that there are no entrained liquid droplets. This assumption, discussed in Section 6.3.1 in Reference 6-13, was found to be necessary to get downcomer penetration following a cold leg break. The interfacial friction factor for the liquid film is a standard Reynolds number dependent correlation in the laminar region and is a modified Wallis correlation in the turbulent region. (Ref. 6-26)

$$C_D = \begin{cases} \frac{64}{Re_g} & : Re_g \leq 500 \\ \left(\frac{1,500 - Re_g}{1,000} \right) \frac{64}{Re_g} + \left(\frac{Re_g - 500}{1,000} \right) 0.02 \{ 1 + 150 [1 - (1 - \alpha_{ff})^{1/2}] \} & \dots\dots\dots (6.2.4-14) \\ 500 < Re_g < 1,500 \\ 0.02 \{ 1 + 150 [1 - (1 - \alpha_{ff})^{1/2}] \} & Re_g \geq 1,500. \end{cases}$$

The drag coefficient for the entrained droplets is given by a correlation developed by Ishii and Chawla for dispersed flow. For bundles in vertical annular-mist flow, the maximum of the interfacial drag coefficient from the modified Chexal and Lellouche drift flux correlation for bubbly-slug flow and the interfacial drag coefficient for the annular mist flow is used to improve void predictions in rod bundles as discussed in Section 6.3.1 in Reference 6-13.

For vertically stratified flow, the interfacial drag above and below the stratified region is based on a weighted function of the void fraction above and below the stratified region using the logic described in Section 3.3.6.8 of Reference 6-10.

For horizontally stratified flow, the interfacial area per unit volume is determined from geometrical considerations and the interfacial friction factors are computed from typical Reynolds number dependent relationships. The corresponding expressions for the interfacial surface area and drag coefficient are

$$a_{gf} = 4C_{st} \frac{\sin \theta}{\pi D} \quad \dots\dots\dots (6.2.4-15)$$

$$C_D = \max\left(\frac{64}{Re_i}, \frac{0.3164}{Re_i^{0.25}}\right) \quad \dots\dots\dots (6.2.4-16)$$

The constant C_{st} is 1.

Inverted flow regimes arise when there is hot vapor/gas in the volume and either hot walls or the reflood model is on. The interfacial drag relationships for post-CHF inverted and corresponding pre-CHF flow regimes are used, except that the roles of vapor/gas and liquid are interchanged. An inverted annular flow regime may occur immediately downstream of a quench front or CHF position, if the combination of liquid flow and subcooling are high enough. The concepts used to determine the interfacial friction factors are the same as those for the annular-mist flow regime.

$$\alpha_{gf} = \frac{3.6\alpha_{gb}(1 - \alpha_B)}{d_o} \quad \dots\dots\dots (6.2.4-17)$$

In this case, d_o is the bubble diameter and α_B is the fraction of the total area occupied by the vapor/gas annulus. The drag coefficient for the vapor/gas bubbles in the liquid core is given by a correlation developed by Ishii and Chawla for dispersed flow. The Weber number used to solve for the bubble diameter is 10.

6.2.4.6 Wall Friction

The wall friction is determined based on the volume flow regime map. The wall friction force terms include only wall shear effects. Losses due to abrupt area change are calculated using mechanistic form-loss models. Other losses due to elbows or complicated flow passage

geometry are modeled using energy-loss coefficients that must be entered as inputs by the user.

The wall friction model is based on a two-phase multiplier approach in which the two-phase multiplier is calculated using a modified Baroczy correlation. (Ref. 6-28) The individual phasic wall friction components are calculated by apportioning the two-phase friction between the phases using a technique derived by Chisholm (Ref. 6-29) from the Lockhart-Martinelli model. (Ref. 6-30) The partitioning model is based on the assumption that the frictional pressure drop may be calculated using a quasi-steady form of the momentum equation. This wall friction partitioning model is used with the drag coefficient method of the interfacial friction model. This model is derived in Section 3.3.8 of Reference 6-10. However, the relevant expressions are shown below. The first two expressions show the wall friction factors which can be expressed in terms of the two phase friction pressure drop, $dP/dx|_{2\phi}$ and, Z^2 , the ratio of the phasic wall friction gradients. The third expression gives the two phase friction pressure drop in terms of the Darcy-Weisbach friction factor, λ , and Z^2 .

$$FWF(\alpha_f \rho_f v_f) = \alpha_f \left(\frac{dP}{dx} \right)_{2\phi} \left(\frac{Z^2}{\alpha_g + \alpha_f Z^2} \right) \dots\dots\dots (6.2.4-18)$$

$$FWG(\alpha_g \rho_g v_g) = \alpha_g \left(\frac{dP}{dx} \right)_{2\phi} \left(\frac{1}{\alpha_g + \alpha_f Z^2} \right) \dots\dots\dots (6.2.4-19)$$

$$\left(\frac{dP}{dx} \right)_{2\phi} = \frac{1}{2D} \{ \lambda'_f \rho_f (\alpha_f v_f)^2 + C [\lambda'_f \rho_f (\alpha_f v_f)^2 \lambda'_g \rho_g (\alpha_g v_g)^2]^{1/2} + \lambda'_g \rho_g (\alpha_g v_g)^2 \} \dots\dots\dots (6.2.4-20)$$

$$Z^2 = \frac{\lambda_f (Re_f) \rho_f v_f^2 \frac{\alpha_{fw}}{\alpha_f}}{\lambda_g (Re_g) \rho_g v_g^2 \frac{\alpha_{gw}}{\alpha_g}} \dots\dots\dots (6.2.4-21)$$

The Darcy-Weisbach friction factor is computed from correlations for laminar and turbulent flows with interpolation in the transition regime. The friction factor model is simply an interpolation scheme linking the laminar, laminar-turbulent transition, and turbulent flow regimes. The laminar friction factor, given by Eq. (6.2.4-22), is calculated using a standard Reynolds number relationship with a user-input shape factor for noncircular flow channels. The friction factor in the transition region between laminar and turbulent flows is computed by reciprocal interpolation using Eq (6.2.4-23). The turbulent friction factor is given by the Zigrang-Sylvester (Ref. 6-31) approximation to the Colebrook-White correlation (Ref. 6-32)

using Eq. (6.2.4-24).

$$\lambda_L = \frac{64}{Re\Phi_s} \quad 0 \leq Re \leq 2,200 \quad \dots\dots\dots (6.2.4-22)$$

$$\lambda_{L,T} = \left(3.75 - \frac{8,250}{Re}\right)(\lambda_{T,3000} - \lambda_{L,2200}) + \lambda_{L,2200} \quad 2,200 < Re < 3,000 \quad \dots\dots\dots (6.2.4-23)$$

$$\frac{1}{\sqrt{\lambda_T}} = -2\log_{10}\left\{\frac{\epsilon}{3.7D} + \frac{2.51}{Re}\left[1.14 - 2\log_{10}\left(\frac{\epsilon}{D} + \frac{21.25}{Re^{0.9}}\right)\right]\right\} \quad 3,000 \leq Re \quad \dots\dots\dots (6.2.4-24)$$

The preceding turbulence friction factor can also be replaced using an exponential function with user input coefficients.

While this model applies to unheated surfaces, the user may select an option to apply a heat wall correction term to account for the variation in the fluid viscosity near the heated surface. The heat wall correction and other references for the wall friction models are provided in Section 3.3.8 of Reference 6-10.

6.2.4.7 Wall Heat Transfer Models

The total wall heat flux is the sum of the heat fluxes to the vapor/gas and liquid and also considers the presence of non-condensable gases present in the vapor. This heat flux is a function of the vapor/gas and liquid heat transfer coefficients, and the vapor/gas, liquid, and saturation temperatures. The saturation temperatures used are determined by either the total or partial pressure of the vapor in the vapor/gas mixture. A detailed discussion of these models is provided in Section 3.3.9 of Reference 6-10. The expression for the heat flux is

$$q''_{total} = h_{wgg}(T_w - T_g) + h_{wgspt}(T_w - T_{spt}) + h_{wgspp}(T_w - T_{spp}) + h_{wff}(T_w - T_f) + h_{wfspt}(T_w - T_{spt}) \quad \dots\dots\dots (6.2.4-25)$$

where, **q'' total** is the heat flux, **h** is the heat transfer coefficient, and **T** is the temperature. The subscripts refer to the wall, **w**, vapor/gas, **g**, liquid, **f**, and **spt** and **spp** refer to the saturation temperature based on the total pressure and saturation temperature based on the partial pressure of vapor.

A boiling curve is used to govern the selection of the wall heat transfer correlations when the wall surface temperature is above the saturation temperature (superheated relative to the saturation temperature based on total pressure). When a hydraulic volume is voided and the adjacent surface temperature is subcooled, vapor condensation on the surface is predicted. If

non-condensable gases are present, the phenomena are more complex because, while boiling is a function of the wall superheat based on the total pressure, condensation is based on the partial pressure of vapor. When the wall temperature is less than the saturation temperature based on total pressure, but greater than the saturation temperature based on vapor partial pressure, a convection condition exists. Figure 6.2.4-4 shows the regions considered.

6.2.4.8 Wall Heat Transfer Correlations

The M-RELAP5 wall heat transfer correlations are based mainly on the internal flow in pipes and the correlations developed for RELAP-3D. Additional geometries considered in the logic are vertical parallel plates, vertical and horizontal tube bundles, and horizontal flat plates. The correlations and references for the individual correlations are provided in Section 3.3.10 of Reference 6-10. Additional material is included in the models and correlations reference manual (Ref. 6-13) including a table of the correlations used as a function of the type of heat transfer, Section 4.2.1. For convenience, a condensed version of this table is provided below as Table 6.2.4-3. Table 6.2.4-4 provides a brief summary of the correlation form for representative correlations. The expressions for the correlations for vertical parallel plates and flat plates are specifically excluded from the summary since they would not be used for PWR designs.

The boiling curve uses the Chen boiling correlation up to the critical heat flux point (Ref. 6-33). A table lookup method developed by Groeneveld, Cheng, and Doan (Ref. 6-34) is used for the prediction of the critical heat flux. When the wall superheat exceeds the critical value, the heat flux for both the transition boiling and the film boiling regimes are calculated and the maximum value is used. This eliminates the need for a prediction of a minimum film boiling temperature. The Chen-Sundaram-Ozkaynak correlation (Ref. 6-35) is used for transition boiling and a modified Bromley correlation (Ref. 6-36) is used for film boiling. To obtain the fraction of the boiling heat flux which causes vapor generation near a superheated wall, the Lahey method (Ref. 6-37) is used.

Convection mode calculations rely on evaluating forced turbulent convection, forced laminar convection, and natural convection and the selection of the maximum of these three. The correlations are by Dittus-Boelter, Kays, and Churchill-Chu, respectively (McAdams is used for natural convection when connecting volumes are horizontal.) (Ref. 6-38, 6-39, 6-40). The heat transfer coefficients are also modified in vertical bundles relative to the coefficients used in pipes.

Except for the feed water heater component, the heat transfer coefficient in the condensation mode uses the maximum of the Nusselt (laminar) and Shah (turbulent) correlations for vertical or inclined surfaces and the maximum of the Chato (laminar) and Shah (turbulent) correlations for horizontal surfaces. (Ref. 6-41, 6-42) When non-condensable gases are present, the Colburn-Hougen iteration method (Ref. 6-43) is used to solve for the interface temperature between the vapor/gas and liquid and this value is then used in the heat flux calculation.

For the right side (outside diameter) of heat slabs associated with a feedwater heater component, the condensation heat transfer coefficient is that from Chen (Ref. 6-44), and is applied to that fraction of the heat slab above the water level. For the fraction of the heat slab below the water level, the heat transfer is based on the maximum of liquid forced turbulent convection, forced laminar convection, and natural convection in a horizontal bundle.

6.2.4.11 Bulk Interfacial Heat Transfer

The interfacial mass transfer is modeled according to the volume flow regime discussed previously. It is used to determine the phasic interfacial area and to select the interfacial heat transfer correlation for superheated liquid (SHL), subcooled liquid (SCL), superheated vapor/gas (SHG), and subcooled vapor/gas (SCG). The mass transfer model is formulated so that the net interfacial mass transfer rate is composed of two components; the mass transfer rate in the bulk fluid, and the mass transfer rate near the wall. The bulk interfacial heat transfer modeling is described briefly in Section 3.3.10 of Reference 6-10 with a more detailed description presented Reference 6-13. Detailed references for the different correlations are provided in both reference documents.

For components not modeling wall heat transfer and for the general bulk mass transfer processes, the interfacial mass transfer model in the bulk fluid depends on the volume flow regime. In the bubbly flow regime for a condition of superheated liquid, interfacial mass transfer is the larger of either the model for bubble growth developed by Plesset and Zwick (Ref. 6-45) or the model for convective heat transfer for a spherical bubble (modified Lee and Ryley) (Ref. 6-46). For the bubbly flow regime with a condition of superheated vapor/gas, an interfacial heat transfer coefficient is assumed that is high enough that the vapor/gas temperature will relax toward the equilibrium (saturation) condition. Analogously, in the mist flow regime for the condition of superheated vapor/gas, a convective heat transfer model for a spherical droplet is used for the interfacial heat transfer coefficient. For mist flow with superheated liquid, an

interfacial heat transfer coefficient is assumed that is high enough so that the liquid temperature will relax toward the equilibrium (saturation) condition. In the bubbly flow regime for the subcooled liquid condition, the interfacial mass transfer is calculated by the modified Unal bubble collapse model (Ref. 6-47, 6-48) and the Lahey model (Ref. 6-37). In the annular-mist flow regime for the subcooled liquid conditions, the interfacial mass transfer is calculated by the modified Brown droplet model (Ref. 6-49) or the drops and the modified Theofanous interfacial condensation model (Ref. 6-50) or the film. Correlations used to calculate the coefficients for the interfacial mass transfer in the bulk fluid are described in detail in the models and correlations manual Reference 6-13. A few representative examples of the expressions used for bubbly and dispersed flows are shown in Table 6.2.4-5.

Table 6.2.4-1 Drift Flux Correlations Used for Vertical Bubbly-Slug Flow

Flow rates	Rod bundles	Narrow rectangular channels	Small pipes	Intermediate pipes	Large pipes
High upflow rates	Chexal and Lellouche. (modified)	Griffith	Chexal and Lellouche. (modified)	Chexal and Lellouche. (modified)	Churn-turbulent bubbly flow Zuber-Findlay Transition Kataoka-Ishii
Medium upflow rates			Transition	Transition	
Low upflow, downflow, and countercurrent flow rates			Zuber-Findlay slug flow	Churn-turbulent bubbly flow Zuber-Findlay Transition Kataoka-Ishii	
Medium downflow rates			Transition	Transition	
High downflow rates			Chexal and Lellouche. (modified)	Chexal and Lellouche. (modified)	

Table 6.2.4-2 Drift Flux Correlation Used for Vertical Bubbly-Slug Flow

Correlation	Defining Expression
Chexal and Lellouche. (modified) (Ref. 6-23, 6-24, 6-25)	$C_0 = \frac{L(\alpha_g, P)}{K_0 + (1 - K_0)\alpha_g^r}$ $v_{gj} = 1.41 \left[\frac{(\rho_f - \rho_g)\sigma g}{\rho_f^2} \right]^{1/4} f(p, Re, \dots)$
Griffith (Ref. 6-51)	$C_0 = 1.35 - 0.35 \sqrt{\frac{\rho_g}{\rho_f}}$ $v_{gj} = \left(0.23 + 0.13 \frac{W}{S} \right) \left(\frac{(\rho_f - \rho_g)gS}{\rho_f} \right)^{1/2}$
Zuber-Findlay slug flow (Ref. 6-52, 6-53)	$C_0 = 1.2$ $v_{gj} = 0.35 \left[\frac{(\rho_f - \rho_g)gD}{\rho_f} \right]^{1/2}$
Transition Kataoka-Ishii (Ref. 6-54)	$C_0 = C_\infty - (C_\infty - 1) \left(\frac{\rho_g}{\rho_f} \right)^{1/2}$ $C_\infty = 1 + 0.2 \left[\frac{\rho_f (gD)^{1/2}}{ G + 0.001} \right]^{1/2}$ $v_{gj} = 0.0019 (D^*)^{0.809} \left(\frac{\rho_g}{\rho_f} \right)^{-0.157} N_{\mu f}^{-0.562} \left[\frac{\sigma g (\rho_f - \rho_g)}{\rho_f^2} \right]^{1/4} \text{ for } D^* \leq 30$ $v_{gj} = 0.030 \left(\frac{\rho_g}{\rho_f} \right)^{-0.157} N_{\mu f}^{-0.562} \left[\frac{\sigma g (\rho_f - \rho_g)}{\rho_f^2} \right]^{1/4} \text{ for } D^* > 30$ $N_{\mu f} = \frac{\mu_f}{\left\{ \rho_f \sigma \left[\frac{\sigma}{g(\rho_f - \rho_g)} \right]^{1/2} \right\}^{1/2}}$
Churn turbulent bubbly flow Zuber-Findlay. (Ref. 6-52, 6-53)	$C_0 = C_\infty - (C_\infty - 1) \left(\frac{\rho_g}{\rho_f} \right)^{1/2}$ $C_\infty = 1 + 0.2 \left[\frac{\rho_f (gD)^{1/2}}{ G + 0.001} \right]^{1/2}$ $v_{gj} = 1.41 \left[\frac{\sigma g (\rho_f - \rho_g)}{\rho_f^2} \right]^{1/4}$

Table 6.2.4-3 Wall Heat Transfer Correlations

Geometry	Laminar	Natural	Turbulent	Condensation	Nucleate boiling	Transition boiling	Film boiling	CHF
Vertical <ul style="list-style-type: none"> • single wall • annuli with this wall unheated • annuli with this outer wall heated • annuli with this inner wall heated • single rod • single rod with crossflow 	Sellars Nu=4.36	Churchill- Chu	Dittus- Boelter	Nusselt/ Chato- Shah- Colburn- Hougen	Chen	Chen	Bromley	Table
Vertical <ul style="list-style-type: none"> • bundle with in-line rods, parallel-flow only 	Sellars Nu=4.36	Churchill- Chu or McAdams	Dittus- Boelter- Inayatov	Nusselt/ Chato- Shah- Colburn- Hougen	Chen- Inayatov	Chen	Bromley	Table
Vertical <ul style="list-style-type: none"> • bundle with in-line rods, parallel-flow and crossflow 	Sellars Nu=4.36	Churchill- Chu or McAdams	Dittus- Boelter Inayatov- Shah	Nusselt/ Chato- Shah- Colburn- Hougen	Chen	Chen	Bromley	Table
Horizontal <ul style="list-style-type: none"> • plate above fluid 	Sellars Nu=4.36	McAdams	Dittus- Boelter	Nusselt/ Chato- Shah- Colburn- Hougen	Chen	Chen	Bromley	Table

Table 6.2.4-4 Expressions Used in Correlations

Correlation	Expression
Sellers (Ref. 6-55)	$Nu = 4.36$
Dittus-Boelter (Ref. 6-38)	$Nu = CRe^{0.8}Pr^n$
Churchill-Chu natural convection (Ref. 6-40)	$Nu_L = \left\{ 0.825 + \frac{0.387(Ra_L)^{\frac{1}{4}}}{\left[1 + \left(\frac{0.492}{Pr} \right)^{\frac{9}{16}} \right]^{\frac{8}{27}}} \right\}^2$
McAdams (Ref. 6-55)	$Nu_L = 0.27Ra_L^{0.25}$
Chen (Nucleate Boiling) (Ref. 6-33)	$q'' = h_{mac}(T_w - T_{spt})F + h_{mic}(T_w - T_{spt})S$ $h_{mic} = 0.00122 \left(\frac{k_f^{0.79} C_{pf}^{0.45} \rho_f^{0.49}}{\sigma^{0.5} \mu_f^{0.29} h_{fg}^{0.24} \rho_g^{0.24}} \right) \Delta T_w^{0.24} \Delta P^{0.75}$ $S = \begin{cases} (1 + 0.12Re_{tp}^{1.14})^{-1} & Re_{tp} < 32.5 \\ (1 + 0.42Re_{tp}^{0.78})^{-1} & 32.5 \leq Re_{tp} < 70 \\ 0.0797 & Re_{tp} \geq 70 \end{cases}$ $F = 2.35 \left(\frac{1}{\chi_{tt}} + 0.213 \right)^{0.736} \quad \chi_{tt}^{-1} = \left(\frac{G_g}{G_f} \right)^{0.9} \left(\frac{\rho_f}{\rho_g} \right)^{0.5} \left(\frac{\mu_g}{\mu_f} \right)^{0.1}$
Chen (Transition) (Ref. 6-35)	$q_{tb} = q_{CHF} A_f M_f + h_{wgg} (T_w - T_g) (1 - A_f M_f)$
Bromley (Ref. 6-36)	$h = C \left[\frac{g \rho_g k_g^2 (\rho_f - \rho_g) h'_{fg} C_{pg}}{L (T_w - T_{spt}) Pr_g} \right]^{0.25}$
Nusselt (Ref. 6-57)	$h_{Nusselt} = \frac{k_f}{\delta} \left 0.9086 \left[\frac{\mu_f^2 Re_f}{g \rho_f (\rho_f - \rho_g)} \right]^{\frac{1}{3}} \right $
Shah (Ref. 6-42)	$h_{Shah} = h_{sf} \left(1 + \frac{3.8}{Z^{0.95}} \right) \quad Z = \left(\frac{1}{X} - 1 \right)^{0.8} P_{red}^{0.4}$ $P_{red} = \frac{P}{P_{critical}} \quad h_{sf} = h_1 (1 - X)^{0.8} \quad h_1 = 0.023 \left(\frac{k_1}{D_h} \right) Re_1^{0.8} Pr_1^{0.4}$

Table 6.2.4-5 Examples of the Expressions Used for Bubbly and Dispersed Flows

Condition	Expression
<p>Bubbly Flow (superheated liquid)</p>	$H_{if} = \max \left[\begin{array}{l} -\frac{k_f 12}{d_b \pi} \Delta T_{sf} \frac{\rho_f C_{pf} \beta}{\rho_g h_{fg}} \quad \text{(Plesset-Zwick)} \\ \frac{k_f}{d_b} (2.0 + 0.74 Re_b^{0.5}) \quad \text{(modified Lee-Ryley)} \end{array} \right] a_{gf}$ $Re_b = \frac{We \cdot \sigma (1 - \alpha_{bub})}{\mu_f (v_{fg}^2)^{1/2}} \quad \beta = 1.0$ $d_b = \frac{We \cdot \sigma}{\rho_f v_{fg}^2}, \quad We = 5, \quad We \cdot \sigma = \max(We \cdot \sigma, 10^{-10})$
<p>Bubbly Flow (subcooled liquid)</p>	$H_{if} = \frac{F_5 h_{fg} \rho_g \rho_f \alpha_g}{\rho_f - \rho_g} \quad \text{(modified Unal, Lahey)} \quad \alpha_g > 0.0$ $= 0.0 \quad \alpha_g = 0.0$ $F_5 = 0.075 \quad \alpha_{bub} \geq 0.25$ $= 1.8 \phi C \exp(-45 \alpha_{bub}) + 0.075 \quad \alpha_{bub} < 0.25$
<p>Bubbly Flow (superheated vapor/gas) (subcooled vapor/gas)</p>	$H_{ig} = 10^4 \cdot a_{gf}$
<p>Dispersed Flow (superheated liquid)</p>	$H_{if} = \frac{k_f F_{13} a_{gf}}{d_d}$ <p>where</p> $a_{gf} = \frac{3.6 \alpha_g}{d_d}$ $d_d = \frac{We \sigma}{\rho_g v_{fg}^2}, \quad \text{where } We = 1.5 \text{ for pre-CHF and } 6.0 \text{ for post-CHF}$ $v_{fg} = v_g - v_f$ $F_{13} = 2.0 + 7.0 \min \left[1.0 + \frac{C_{FF} \max(0.0, \Delta T_{if})}{h_{fg}}, 8.0 \right]$
<p>Dispersed Flow (superheated vapor/gas)</p>	$H_{ig} = \frac{k_g}{d_d} (2.0 + 0.5 Re_{d,fp}^{0.5}) a_{gf} \quad \alpha_f > 0.0$ $Re_{d,fp} = \frac{(1 - \alpha_f)^{2.5} \rho_g v_{fg} d_d}{\mu_g} = \frac{We \cdot \sigma (1 - \alpha_f)^{2.5}}{\mu_g v_{fg}} \quad \text{pre-CHF and post-CHF.}$

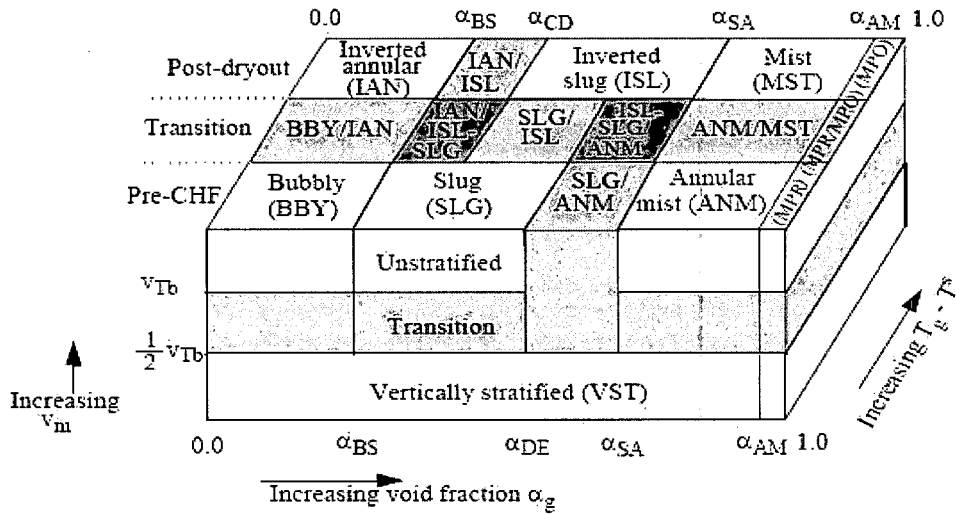


Figure 6.2.4-1 Schematic of the Vertical Flow Regime Map

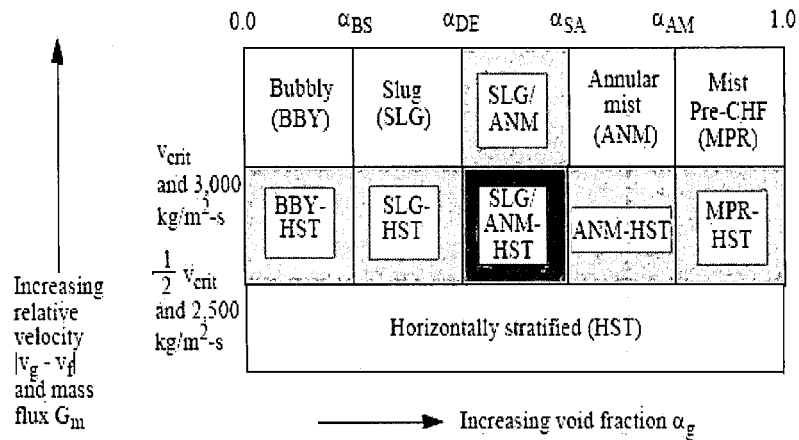


Figure 6.2.4-2 Schematic of the Horizontal Flow Regime Map

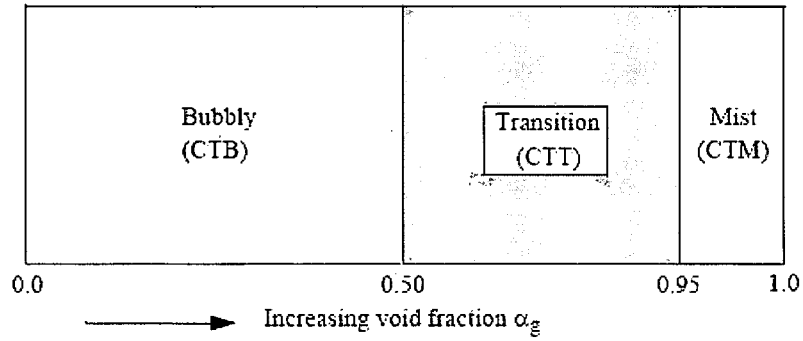


Figure 6.2.4-3 Schematic of the Flow Regime Map Using in a High Mixing Region

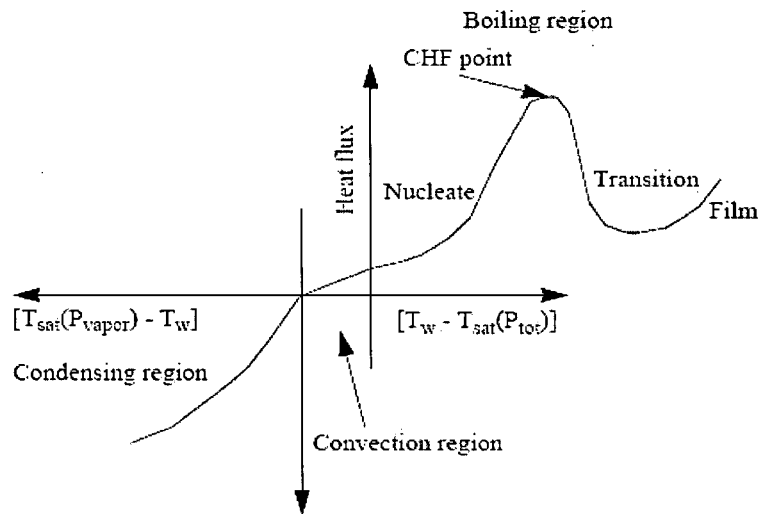


Figure 6.2.4-4 Boiling and Condensation Curve Regions

6.2.5 Numerics

The basic numerical approaches to solution the hydrodynamic and other equations for M-RELPA5 are described in Reference 6-10 with some additional detail added in the models and correlations Reference 6-13. However, the fundamental mathematical basis for the hydrodynamic equations is provided in the numerics reference manual (Ref. 6-7).

As discussed in more detail in Sections 8.1 and 8.2 of Reference 6-10, two important numerical approaches are used in the hydrodynamic solution to insure the accuracy of the time advancement, time step control and mass/energy error mitigation.

Other numeric techniques as well as a discussion of the mathematical basis for the hydrodynamic partial differential equations, not discussed in this section, are provided in Reference 6-7. The topics included in Reference 6-7 that are not discussed in this report are (a) the characteristics of the two flow equations, (b) a detailed discussion of the semi-implicit and nearly implicit time advancement schemes including a discussion of the regions of stability, accuracy and convergence, (c) truncation and linearization errors, (d) time smoothing and (e) single to two-phase transitions.

The time steps are controlled to insure the accuracy and stability of the calculations. Several factors are used including:

- Fluid Courant limit,
- Mass error,
- Limit on the extrapolation of state (thermodynamic fluid) properties in metastable regimes,
- Phase appearance/disappearance checks,
- Limit on the pressure change in a volume where a non-condensable appears.

The comparison of the requested time step to the fluid Courant limit is made before the time advancement is made. The requested time step is then reduced depending on the time step algorithm being used. In the case of the semi-implicit algorithm described in a preceding section, the requested time step is reduced by a factor of 2 until it is less than the Courant limit. For the nearly implicit algorithm, the requested time step is reduced until the requested time step is less than the Courant limit times a factor set in the code, typically a factor of 20 to 40. All of the other factors result in the total or part of the time advancement to be repeated at a smaller requested time step.

The fluid Courant limit used to control the time advancement is based on the minimum Courant limit for all hydrodynamic volumes for phasic velocities, v , and volume fraction, α . The fluid Courant limit is expressed in the following form

$$\Delta t = C \cdot \text{Min}(\Delta x_i(\alpha_{ij}/v_{ij})) \text{ for all volumes } i \text{ and phases } j. \quad (6.2.5-1)$$

For the semi-implicit scheme the constant, C , is 1. For the nearly implicit scheme, C is 20 for the transient option and 40 for the steady-state option.

A mass error check is made when the time step solution is nearly complete. If excessive mass error is detected, the time step is repeated at a reduced time interval. Two types of mass error measures are computed. The first one is designed to check the validity of the density linearization and is expressed in the form

$$\epsilon_m = \max \left(\frac{|\rho_{mi} - \rho_i|}{\rho_i} \right) \quad (6.2.5-2)$$

where ρ_{mi} is the total density of the i^{th} volume obtained from the mass continuity equation, and ρ_i is the total density of the i^{th} volume computed from the state relationship. The second one is a measure of overall system mass error and is expressed in the form

$$\epsilon_{\text{rms}} = \frac{2 \sum_{i=1}^N [V_i(\rho_i - \rho_{mi})]^2}{\sum_{i=1}^N (V_i \rho_i)^2} \quad (6.2.5-3)$$

where V is the volume and N is the total number of volumes. If either term exceeds the limit for this value, a new time advancement is requested and then repeated as $1/2$ of the previously requested time step. If the time advancement is accepted, the succeeding requested time step either remains the same or is doubled depending on the value of the two mass error limits. The succeeding requested time step is then subject to the same checks as the next advancement proceeds.

The checks on the other limits also control the time advancement in a similar fashion. The tolerances for the other limits are discussed in Section 8.1 of Reference 6-10.

6.2.6 Additional Features

The US-APWR design includes both new features as well as improved components which will enhance the safety, operation and performance of the reactor system. The new design features and improved components include:

- Direct Vessel Injection (DVI) for Safety Injection Pumped safety injection flow
- Neutron Reflector (NR) to reduce the neutron damage to the reactor pressure vessel
- Refueling Water Storage Pit (RWSP) located in Containment to eliminate sump switchover
- Model 100A Reactor Coolant Pump (RCP) for increased reactor flow
- Advanced Accumulator for improved accumulator flow delivery

The DVI safety injection system is designed such that four trains construction inject coolant directly into the reactor vessel. To simulate the DVI performance, it is necessary to model the initiation of injection by an SI signal, the injection characteristics of an SI pump, the enthalpy of injected coolant, and the location of injection. M-RELAP5 provides flexible modeling functions allowing the DVI to be simulated:

- Initiation of injection
The safety injection into the reactor vessel can be initiated using the signal logic given in M-RELAP5. The thermal hydraulic component simulating an SI pump can be turned ON/OFF depending on a specified set-point based on the plant technical specifications. For the US-APWR, the Safety injection is initiated by the “pressurizer low-low pressure” set point as specified in the US-APWR design. If this pressure would be reached, the safety injection would automatically begin just as in the plant.
- Injection characteristics of an SI pump, and enthalpy of injected coolant
The SI is simulated by a combination of a time-dependent junction component and a time-dependent volume component. The injection characteristics of an SI pump can be simulated by a flow rate table for a time-dependent junction as a function of the pressure in downstream side of the injection location. The enthalpy of injected coolant is simulated by a time-dependent volume component as a function of time or a function of the integrated injection flow rate.
- Location of injection
The location of injection can be specified arbitrary by a junction component. The

location of injection is specified by using a time-dependent junction simulating the injection characteristics of an SI pump. For the US-APWR, the junction component is connected to the reactor vessel downcomer.

The modeling scheme mentioned above is equivalent to that for existing PWR designs using a cold-leg injection, except for the location of injection.

The Neutron Reflector is a stainless steel component of a ring block construction that replaces a baffle plate surrounding the reactor core in existing PWRs and is installed between the reactor core and a core barrel of the US-APWR. The component reduces the number of parts significantly and realizes enhanced reliability. The installation of the Neutron Reflector reduces neutron leakage from the core, alleviates neutron irradiation damage to the inner wall of RV, and hence can lower the fuel cycle cost by more effective neutron utilization. The Neutron Reflector may have an effect on a transient behavior during a small-break LOCA event through an increase in the enthalpy of the coolant due to an increase in heat capacity of the stainless steel structure surrounding the core since the structure can be a heat source for core coolant. M-RELAP5 can model the Neutron Reflector structure's thermal response and its effects on the heat transfer to the reactor coolant. M-RELAP5 models the flow holes through the reflector as well as the coolant flowing in the holes.

The In-containment RWSP is a design that provides a water source to the core within the reactor containment. The In-containment RWSP removes a requirement for the changeover from an injection mode to a recirculation mode for the SI system, and thereby enhances reliability of core cooling following a postulated accident. The In-containment RWSP may have an effect on a transient behavior during a small-break LOCA event because of an increase in the enthalpy of the coolant injected by the SI pumps. M-RELAP5 has the capability to simulate the enthalpy of the injected flow as a function of time or a function of integrated injection flow rate by a time-dependent volume similar to the simulation method used for the injection enthalpy in existing PWR designs.

The Model 100A Reactor Coolant Pump is the primary coolant pump for the US-APWR. The Model 100A Reactor Coolant Pump achieves high capacity and enhanced efficiency through a redesign of the impeller / diffuser configuration. The primary coolant pump may have an effect on a transient behavior during a small-break LOCA event during the coast down period as well as later in the transient as a flow resistance. M-RELAP5 incorporates the same pump model

that has been developed for the RELAP3, RELAP4, RELAP5/MOD1 and RELAP5/MOD2. The pump characteristics in a transient are simulated by a homologous curve. The pump coast-down is calculated using the angular momentum equation with the torque and the momentum of inertia as input data for the calculations. The flow resistance after the shutdown can be simulated through the input because it is determined by the characteristics of homologous curve corresponding to the condition during shutdown. Therefore, M-RELAP5 code has the capability to simulate a Model 100A Reactor Coolant Pump as well as a conventional primary coolant pump.

In the Advanced Accumulator, injection flow rate is controlled by a variable resistance damper. The Advanced Accumulator is designed to provide initially a high injection flow rate, which compensates for the coolant lost in a LOCA event and allows refilling. After the initial high flow rate period, the advanced accumulator provides longer term cooling at a lower flow rate after the vessel is refilled. The injection characteristics of the Advanced Accumulator have been determined by a full height, one-half scale experimental facility. The injection characteristics of the Advanced Accumulator have been developed using correlations which relate a cavitation factor and a flow rate coefficient. The existing accumulator model in RELAP5-3D can not simulate these injection flow rate characteristics. Therefore, it is necessary to incorporate specific advanced accumulator model into M-RELAP5 for the US-PWR as discussed in Section 7.

6.3 References

- 6-1. Regulatory Guide 1.203, "Transient and Accident Analysis Methods," December 2005.
- 6-2. RELAP5/MOD3.3 CODE MANUAL VOLUME I: CODE STRUCTURE, SYSTEM MODELS, AND SOLUTION METHODS, NUREG/CR-5535/Rev 1, December 2001.
- 6-3. RELAP5/MOD3.3 CODE MANUAL VOLUME II: USER'S GUIDE AND INPUT REQUIREMENTS, NUREG/CR-5535/Rev 1, December 2001.
- 6-4. RELAP5/MOD3.3 CODE MANUAL VOLUME III: DEVELOPMENTAL ASSESSMENT PROBLEMS, NUREG/CR-5535/Rev 1, December 2001.
- 6-5. RELAP5/MOD3.3 CODE MANUAL VOLUME IV: MODELS AND CORRELATIONS, NUREG/CR-5535/Rev 1, December 2001.
- 6-6. RELAP5/MOD3.3 CODE MANUAL VOLUME V USER'S GUIDELINES, NUREG/CR-5535/Rev 1, December 2001.
- 6-7. RELAP5/MOD3 CODE MANUAL VOLUME 6: VALIDATION OF NUMERICAL TECHNIQUES IN RELAP5/MOD3.0, A. S. Shieh, V. H. Ransom, R. Krishnamurthy, NUREG/CR-5535/Rev 1, October 1994 [Issued with minor revisions December 2001].
- 6-8. RELAP5/MOD3.3 CODE MANUAL VOLUME VII: SUMMARIES AND REVIEWS OF INDEPENDENT CODE ASSESSMENT REPORTS, NUREG/CR-5535/Rev 1, December 2001.
- 6-9. RELAP5/MOD3.3 CODE MANUAL VOLUME VIII: PROGRAMMERS MANUAL, NUREG/CR-5535/Rev 1, December 2001.
- 6-10. RELAP5-3D[©] CODE MANUAL VOLUME I: CODE STRUCTURE, SYSTEM MODELS, AND SOLUTION METHODS, INEEL-EXT-98-00834, Revision 2.4, June 2005.
- 6-11. RELAP5-3D[©] CODE MANUAL VOLUME II: USER'S GUIDE AND INPUT REQUIREMENTS, INEEL-EXT-98-00834, Revision 2.4, June 2005.
- 6-12. RELAP5-3D[©] CODE MANUAL VOLUME II: APPENDIX A - INPUT REQUIREMENTS, INEEL-EXT-98-00834, Revision 2.4, June 2005.
- 6-13. RELAP5-3D[©] CODE MANUAL VOLUME IV: MODELS AND CORRELATIONS, INEEL-EXT-98-00834, Revision 2.4, June 2005.
- 6-14. RELAP5-3D[©] CODE MANUAL VOLUME V: USER'S GUIDELINES, INEEL-EXT-98-00834, Revision 2.4, June 2005.
- 6-15. M.G. Ortiz and L.S. Ghan, "Uncertainty Analysis of Minimum Vessel Liquid Inventory During a Small Break LOCA in a Babcock and Wilcox Plant," NUREG/CR-5818, USNRC, December 1992.

- 6-16. C.D. Fletcher et al., "Adequacy Evaluation of RELAP5/MOD3, Version 3.2.1.2 for Simulating AP600 Small-Break Loss-of-Coolant Accidents," INEL-96/0400 (Nonproprietary version), April 1997.
- 6-17. R. J. Wagner, IREKIN -- Program for the Numerical Solution of the Reactor Kinetics Equations, IDO-17114, National Reactor Testing Station, January 1966.
- 6-18. P. J. Turinsky et al., NESTLE: A Few-Group Neutron Diffusion Equation Solver Utilizing the Nodal Expansion Method for Eigenvalue, Adjoint, Fixed-Source Steady State and Transient Problems, EGG-NRE-11406, Idaho National Engineering Laboratory, June 1994.
- 6-19. C. A. Meyer, R. G. McClintock, G. J. Silvestri, and R. C. Spencer, Jr., 1967 ASME Steam Tables--Thermodynamic and Transport Properties of Steam, New York: The American Society of Mechanical Engineers, 1967.
- 6-20. 3.2-4. K. V. Moore, ASTEM--A Collection of FORTRAN Subroutines to Evaluate the 1967 ASME Equations of State for Water/Steam and Derivatives of These Equations, ANCR-1026, Aerojet Nuclear Company, National Reactor Testing Station, October 1971.
- 6-21. Y. Taitel and A. E. Dukler, "A Model of Predicting Flow Regime Transitions in Horizontal and Near Horizontal Gas-Liquid Flow," AIChE Journal, 22, 1976, pp. 47-55.
- 6-22. Y. Taitel, D. Bornea, and A. E. Dukler, "Modeling Flow Pattern Transitions for Steady Upward Gas-Liquid Flow in Vertical Tubes," AIChE Journal, 26, 1980, pp. 345-354.
- 6-23. B. Chexal and G. Lellouche, A Full-Range Drift-Flux Correlation for Vertical Flows (Revision 1), EPRI NP-3989-SR, September 1986.
- 6-24. B. Chexal et al., The Chexal-Lellouche Void Fraction Correlation for Generalized Applications, Electric Power Research Institute, NSAC-139, April 1991.
- 6-25. B. Chexal et al., Void Fraction Technology for Design and Analysis, Electric Power Research Institute, TR-106326, March 1997.
- 6-26. G. B. Wallis, One-dimensional Two-phase Flow, New York: McGraw-Hill, 1969.
- 6-27. M. Ishii and T. C. Chawla, Local Drag Laws in Dispersed Two-Phase Flow, NUREG/CR-1230, ANL-79-105, Argonne National Laboratory, December 1979.
- 6-28. K. T. Claxton, J. G. Collier, and J. A. Ward, H.T.F.S. Correlation for Two-Phase Pressure Drop and Void Fraction in Tubes, HTFS Proprietary Report HTFS-DR-28, AERE-R7162, November 1972.
- 6-29. D. Chisholm, "A Theoretical Basis for the Lockhart-Martinelli Correlation for Two-Phase Flow," International Journal of Heat and Mass Transfer, 10, 1967, pp. 1767-1778.

- 6-30. R. W. Lockhart and R. C. Martinelli, "Proposed Correlation of Data for Isothermal Two-Phase, Two-Component Flow in Pipes," *Chemical Engineering Progress*, 45, 1, 1949, pp. 39-48.
- 6-31. D. J. Zigrang and N. D. Sylvester, "A Review of Explicit Friction Factor Equations," *Transactions of ASME, Journal of Energy Resources Technology*, 107, 1985, pp. 280-283.
- 6-32. C. F. Colebrook, "Turbulent Flow in Pipes with Particular Reference to the Transition Region Between Smooth and Rough Pipe Laws," *Journal of Institute of Civil Engineers*, 11, 1939, pp. 133-156.
- 6-33. J. C. Chen, "A Correlation for Boiling Heat Transfer to Saturated Fluids in Convective Flow," *Process Design and Development*, 5, 1966, pp. 322-327.
- 6-34. D. C. Groeneveld, S. C. Cheng, and T. Doan, "1986 AECL-UO Critical Heat Flux Lookup Table," *Heat Transfer Engineering*, 7, 1-2, 1986, pp. 46-62.
- 6-35. J. C. Chen, R. K. Sundaram, and F. T. Ozkaynak, "A Phenomenological Correlation for Post-CHF Heat Transfer," *NUREG-0237*, June 1977.
- 6-36. L. A. Bromley, "Heat Transfer in Stable Film Boiling," *Chemical Engineering Progress*, 46, 1950, pp. 221-227.
- 6-37. R. T. Lahey, "A Mechanistic Subcooled Boiling Model," *Proceedings Sixth International Heat Transfer Conference, Toronto, Canada, August 7-11, 1978, Volume 1*, pp. 293-297.
- 6-38. F. W. Dittus and L. M. K. Boelter, "Heat Transfer in Automobile Radiators of the Tubular Type," *Publications in Engineering*, 2, University of California, Berkeley, 1930, pp. 443-461.
- 6-39. W. M. Kays, "Numerical Solution for Laminar Flow Heat Transfer in Circular Tubes," *Transactions of the ASME*, 77, 1955, pp. 1265-1274.
- 6-40. S. W. Churchill and H. H. S. Chu, "Correlating Equations for Laminar and Turbulent Free Convection from a Vertical Plate," *International Journal of Heat and Mass Transfer*, 18, 1975, pp. 1323-1329.
- 6-41. J. C. Chato, "Laminar Condensation Inside Horizontal and Inclined Tubes," *American Society of Heating, Refrigeration, and Air Conditioning Journal*, 4, 1962, pp. 52-60.
- 6-42. M. M. Shah, "A General Correlation for Heat Transfer during Film Condensation Inside Pipes," *International Journal of Heat and Mass Transfer*, 22, 1979, pp. 547-556.
- 6-43. A. P. Colburn and O. A. Hougen, "Design of Cooler Condensers for Mixtures of Vapors with Non-Condensing Gases," *Industrial and Engineering Chemistry*, 26, 1934, pp. 1178-1182.

- 6-44. M. M. Chen, "An Analytical Study of Laminar Film Condensation: Part 2 - Single and Multiple Horizontal Tubes," Transactions of the ASME, Journal of Heat Transfer, 83, 1961, pp. 55-60. 6-59
- 6-45. M. S. Plesset and S. A. Zwick, "Growth of Vapor Bubbles in Superheated Liquids," Journal of Applied Physics, 25, 4, 1954, pp. 493-500.
- 6-46. K. Lee and D. J. Ryley, "The Evaporation of Water Droplets in Superheated Steam," Transactions of the ASME, Journal of Heat Transfer, November 1968, pp. 445-456.
- 6-47. H. C. Unal, "Maximum Bubble Diameter, Maximum Bubble-Growth Time and Bubble-Growth Rate During the Subcooled Nucleate Flow Boiling of Water up to 17.7 MN/m²," International Journal of Heat and Mass Transfer, 19, 1976, pp. 643-649.
- 6-48. R. A. Riemke, "Modification to Unal's Subcooled Flow Boiling Bubble Model," Nuclear Technology, 102, 1993, pp. 416-417.
- 6-49. G. Brown, "Heat Transmission by Condensation of Steam on a Spray of Water Drops," Institute of Mechanical Engineers, 1951, pp. 49-52.
- 6-50. T. G. Theofanous, "Modeling of Basic Condensation Processes," The Water Reactor Safety Research Workshop on Condensation, Silver Springs, MD, May 24-25, 1979.
- 6-51. P. Griffith, "The Prediction of Low-Quality Boiling Voids," Transactions of the ASME, Journal of Heat Transfer, 86, 1964, pp. 327-333.
- 6-52. N. Zuber and J. A. Findlay, "Average Volumetric Concentrations in Two-Phase Flow Systems," Transactions of the ASME, Journal of Heat Transfer, 87, 1965, pp. 453-568.
- 6-53. N. Zuber et al., Steady-State and Transient Void Fraction in Two-Phase Flow Systems, General Electric Company, GEAP-5417, 1967.
- 6-54. I. Kataoka and M. Ishii, "Drift Flux Model for Large Diameter Pipe and New Correlation for Pool Void Fraction," International Journal of Heat and Mass Transfer, 30, 1987, pp. 1927-1939.
- 6-55. J. R. Sellars, M. Tribus, and J. S. Klein, "Heat Transfer to Laminar Flows in a Round Tube or Flat Conduit: The Graetz Problem Extended," Transactions of the ASME, 78, 1956, p. 441.
- 6-56. W. H. McAdams, Heat Transmission, 3rd Edition, New York: McGraw-Hill, 1954.
- 6-57. W. Nusselt, "Die Oberflächenkondensation des Wasserdampfes," Zeitschrift Ver. Deutsch. Ing., 60, 1916, pp. 541-546 and 569-575.

7.0 DEVELOP OR INCORPORATE CLOSURE MODELS

7.1 Appendix-K compliant models

7.1.1 Selection for Appendix-K requirements

The required and acceptable features of the evaluation models (EM) are specified in Section I of Appendix K to Part 50 of Title 10 of the Code of Federal Regulations. Section I of Appendix K (Ref. 7-1) is divided into four subsections: A. Sources of Heat During LOCA; B. Swelling and Rupture of the Cladding and Fuel Rod Thermal Parameters; C. Blowdown Phenomena; and D. Post-Blowdown Phenomena; Heat Removal by the ECCS.

The evaluation models and analysis requirements stemming from these subsections are summarized in Table 7.1.1-1. The table shows each Appendix K requirement, the location of the requirement in the Appendix K, the acceptance limits of the Appendix K requirement, and the approach for meeting the requirement. Altogether the Appendix K requirements are listed as twenty-nine separate items in Table 7.1.1-1.

The appendix K evaluation models were defined in 1974. Since then, the evaluation models have been added to a number of thermal-hydraulic codes, and the thermal-hydraulic codes became more advanced. Hence an implicit assumption is that it is advantageous to perform Appendix K EM calculations using the most advanced thermal-hydraulic code. RELAP5-3D is the most advanced and thoroughly checked version of RELAP5 produced to date.

RELAP5-3D, in its current state, has a number of models that enable it to meet many of the Appendix K requirements with no modification. Thus many of the Appendix K requirements can be achieved by simply providing the appropriate input in the plant model. This includes the appropriate plant nodalization together with appropriate initial conditions, boundary conditions, and the proper code options and also performing sensitivity calculations if necessary. However, some Appendix K requirements can only be achieved through the implementation of new models or the modification of existing RELAP5-3D models. A few models must be also be validated by the additional comparison with appropriate experimental data to confirm the applicability of the models to Small Break LOCA EM calculations.

Actions to conform to Appendix K requirements fall within three categories:

Category 1: required models are missing and need to be added to RELAP5-3D,

Category 2: additional validation needs to be performed to be able to use the model presented in RELAP5-3D,

Category 3: appropriate inputs or sensitivity studies are needed to be able to use already presented in RELAP5-3D

As noted in column 4 of Table 7.1.1-1, seven requirements, 4, 7, 9, 12, 14, 20, and 22, belong to Category 1. ~~Two~~Four requirements, ~~19 and 24~~, 21, 27 and 29 belong to Category 2. Eighteen requirements, 1 through 3, ~~5, 6~~, 8, 10, 11, 13, 16 through 18, and 23 through ~~28~~26, and 28, belong to Category 3. Requirements 15, ECC water bypass, ~~and 29, refill/reflood heat transfer~~, ~~are~~ is for LBLOCA calculations and ~~are~~ is not applicable to SBLOCA calculations.

Subsections 7.1.2 to 7.1.7 describe the M-RELAP5 modeling approaches to meet Appendix K requirements of Category 1 and 2.

Table 7.1.1-1(1/4) Appendix K Required and Acceptable Features of Evaluation Models and Approach for Acceptance

Appendix K Requirement	Ref. (*1)	Acceptable Limits	Approach for Acceptance
1. Steady state power level	I. A	Power level shall be at least 1.02 times the licensed power level.	- Provide appropriate input.
2. Maximum peaking factor	I. A	Maximum peaking factor shall be that allowed by the technical specification.	- Provide appropriate input.
3. Power distribution shape	I. A	Power distribution shape and peaking factor combination giving highest PCT shall be considered.	- Provide appropriate input.
4. Initial stored energy in fuel	I. A. 1	Steady state temperature distribution and stored energy in the fuel shall be calculated for the burn-up that yield highest PCT.	- Provide appropriate input. - Gap conductance model consistent with fuel design code is installed. (*2)
5. Fission heat	I. A. 2	Fission heat shall be calculated using reactivity and reactor kinetics. Shutdown reactivity from temperature and voids shall be given their minimum plausible values.	- Provide appropriate input.
6. Actinide decay heat	I. A. 3	The heat from actinide decay shall be calculated.	- Provide appropriate input.
7. Fission Product decay heat	I. A. 4	Fission product decay heat shall be 1.2 times the values for infinite operating time in the ANS standard 1971.	- ANS standard 1971 is installed. (*2)
8. Gamma energy redistribution	I. A. 4	The fraction of the gamma energy deposited in the fuel shall be justified by a suitable calculation.	- Provide appropriate input.
9. Metal water reaction rate	I. A. 5	Influence of the metal/water reaction shall be calculated using the Baker-Just equation. The reaction shall be assumed not to be steam limited. The inside of the cladding shall be assumed to react after the rupture.	- Baker-Just equation is installed. (*2)

(*1) 10 CFR Part 50, Appendix K, "ECCS Evaluation Models."

(*2) New function of M-RELAP5

Table 7.1.1-1(2/4) Appendix K Required and Acceptable Features of Evaluation Models and Approach for Acceptance

Appendix K Requirement	Ref.(*1)	Acceptable Limits	Approach for Acceptance
10. Reactor internal heat transfer	I. A. 6	Heat transfer from piping, vessel walls, and non-fuel internal hardware shall be taken into account.	- Provide appropriate input.
11. SG heat transfer	I. A. 7	Heat transferred between primary and secondary systems through heat exchangers shall be taken into account.	- Provide appropriate input.
12. Cladding swelling & rupture	I. B	Cladding swelling and rupture calculations shall be based on applicable data in such a way that the degree of swelling and incidence of rupture are not underestimated. The gap conductance shall be varied in accordance with changes in gap dimensions and any other applicable variables.	- Cladding swelling and rupture model for ZIRLO™ alloy is installed. (*2) - Gap conductance calculation for rupture node is installed. (*2)
13. Break characteristics	I. C. 1a	A spectrum of possible break shall be considered.	- Perform sensitivity study.
14. Discharge model	I. C. 1b	Two-phase discharge rate shall be calculated using the Moody model with at least three values of a discharge coefficient. Discharge coefficient will span 0.6 to 1.0 or even a lower value If a maximum PCT may be calculated at such values.	- The Moody model is installed. (*2) - Perform sensitivity study.
15. ECC water bypass	I. C. 1c	ECC water shall be subtracted from the reactor vessel inventory during the bypass period. The end-of-bypass definition shall be justified by a suitable combination of analysis and experimental data.	- This requirement is for LBLOCA, and is not for SBLOCA.
16. Noding near break and ECC water injection points	I. C. 1d	Noding near break and ECC water injection point shall be chosen to permit a reliable analysis of the thermodynamic history in these regions.	- Provide appropriate input. - Perform sensitivity study.

(*1) 10 CFR Part 50, Appendix K, "ECCS Evaluation Models."

(*2) New function of M-RELAP5

Table 7.1.1-1(3/4) Appendix K Required and Acceptable Features of Evaluation Models and Approach for Acceptance

Appendix K Requirement	Ref.(*1)	Acceptable Limits	Approach for Acceptance
17. Frictional pressure drop	I. C. 2	The frictional losses shall be calculated using models that include Reynolds number dependency, and realistic two-phase friction multipliers that have been adequately verified.	- Provide appropriate input.
18. Momentum equation	I. C. 3	Momentum equation shall include temporal change of momentum; momentum convection; area change of momentum flux; momentum change due to compressibility; pressure losses due to wall friction, and area change; and gravitational acceleration.	- Provide appropriate input.
19. Critical heat flux	I. C. 4	Correlations developed from appropriate steady state and transient-state experimental data are acceptable. The computer programs shall contain suitable checks to assure that the physical parameters are within the range of parameters specified for use of the correlations.	- CHF correlation incorporated in RELAP5-3D satisfies this requirement. Additional validation is performed.
20. Return to nucleate boiling	I. C. 4e	After CHF is predicted during blowdown, the calculation shall not use nucleate boiling heat transfer correlations subsequently during the blowdown.	- The logic to prevent return to nucleate boiling during blowdown is installed. (*2)
21. Post-CHF heat transfer correlation	I. C. 5	Transition and film boiling correlation, compared to applicable steady-state and transient-state data, shall be shown to predict values of heat transfer coefficient equal to or less than the mean value of data throughout the range of parameters for which the correlations are to be used. The Dougall-Rohsenow correlation under conditions where nonconservative predictions of heat transfer result will no longer be acceptable.	- Post-CHF heat transfer correlation incorporated in RELAP5-3D satisfies this requirement. Additional validation is performed.

(*1) 10 CFR Part 50, Appendix K, "ECCS Evaluation Models."

(*2) New function of M-RELAP5

Table 7.1.1-1(4/4) Appendix K Required and Acceptable Features of Evaluation Models and Approach for Acceptance

Appendix K Requirement	Ref.(*1)	Acceptable Limits	Approach for Acceptance
22. Return to transition boiling	I. C. 5b	Transition boiling heat transfer shall not be used during the blowdown after the temperature difference between the clad and the saturated fluid first exceeds 300°F.	- The logic to prevent return to transition boiling during blowdown is installed. (*2)
23. Pump modeling	I. C. 6	The pump model for the two-phase region shall be verified by applicable two-phase pump performance data.	- Provide appropriate input.
24. Core flow distribution	I. C. 7	The flow rate through the hot region of the core during blowdown shall be calculated as a function of time considering cross flow between regions and any flow blockage due to cladding swelling or rupture.	- Provide appropriate input.
25. Single failure criterion	I. D. 1	The most damaging single failure of ECCS equipment shall be considered.	- Perform sensitivity study.
26. Containment pressure	I. D. 2	The containment pressure used during reflood shall not exceed a pressure calculated conservatively for this purpose.	- Containment back pressure is modeled.
27. Reflood rate	I. D. 3	The rate of reflooding of core shall be calculated by an acceptable model that takes into consideration the thermal and hydraulic characteristics of the core and of reactor systems.	- Small break core recovery due to accumulator injection is modeled. <u>Additional validation is performed.</u>
28. ECC water/steam interaction	I. D. 4	The thermal-hydraulic interaction between steam and all emergency core cooling water shall be taken into account in calculating the core reflooding rate.	- Provide appropriate input.
29. Refill/Reflood heat transfer	I. D. 6	For reflooding rates of 1 in/s or higher, heat transfer shall be used based on applicable experimental data. When For reflooding rates are 1 in/s, heat transfer calculation shall be based on the assumption that cooling is only by steam.	- <u>Small break core recovery due to accumulator injection is modeled. Additional validation is performed.</u> —

(*1) 10 CFR Part 50, Appendix K, "ECCS Evaluation Models."

(*2) New function of M-RELAP5

This requirement is for LBLOCA, and is not for SBLOCA.			
--	--	--	--

7.1.2 Gap Conductance Model

The fuel-to-cladding gap heat transfer is provided to calculate initial stored energy and transient heat transfer across the gap.

One of the Appendix K requirements related to the fuel-to-cladding gap heat transfer is that “the steady state temperature distribution and stored energy in the fuel before the hypothetical accident shall be calculated for the burn-up that yields the highest calculated cladding temperature.” The initial fuel temperature is adjusted to that calculated by the fuel design code, FINE (Ref. 7-2), which is a detailed fuel rod design computer code that considers various burn-up effects on fuel temperature.

FINE’s gap heat transfer model is based on the pellet concentric annular gap model. The following concentric annular gap model is implemented in M-RELAP5 to maintain consistency with the FINE fuel design code as:

$$h_g = \frac{k_g}{g + 3.2(R_F + R_C) + (g_1 + g_2)} \quad (7.1.2-1)$$

where h_g is gap conductance through the gas in the gap, k_g is thermal conductivity of gas, g is fuel-cladding gap width, R_F is are surface roughness of the fuel, R_C is surface roughness of the cladding and g_1 , g_2 are temperature jump distance terms for fuel and cladding respectively.

RELAP5-3D takes into account the gap heat transfer term by thermal radiation across the gap. This term is retained in M-RELAP5.

7.1.3 Fission Product Decay

7.1.3.1 Fission product decay heat

10CFR50 Appendix K specifies that for the evaluation of the decay heat from fission products, the ANS decay heat model of 1971 version (Ref. 7-3) multiplied by 1.2 should be applied assuming that the reactor has been operating at a constant total power for an infinite period of time. Therefore, the existing RELAP-3D decay model was modified as described below to apply the 1971 ANS standard model when evaluating the decay heat in a small-break LOCA event.

The 1971 ANS standard model is expressed by the following equation.

$$\frac{P}{P_0}(\infty, t_s) = A \cdot t_s^{-a} \quad (7.1.3-1)$$

Where,

Time interval (s)	<i>A</i>	<i>a</i>
$10^{-1} \leq t_s \leq 10^1$	0.0603	0.0639
$10^1 \leq t_s \leq 1.5 \times 10^2$	0.0766	0.181
$1.5 \times 10^2 \leq t_s \leq 4 \times 10^6$	0.130	0.283
$4 \times 10^6 \leq t_s \leq 2 \times 10^8$	0.266	0.335

The point kinetics model in the RELAP5-3D incorporates the 1973 ANS standards, the 1979 ANSI/ANS standards, and the 1994 ANSI/ANS standards as a decay heat model. Among them, the 1973 ANS standard model has the greatest similarity with the 1971 ANS standard model and provides the energy yields and the decay constants of 11 groups. These energy yields and decay constants are compiled in Section 9.2.5 Ultimate Heat Sink (Rev.2) of NUREG-0800 (Ref. 7-4). The 1973 ANS standards in the RELAP5-3D are calculated by the following equations with the energy yields and the decay constants.

$$\frac{d\gamma_j(t)}{dt} = F_\gamma E_j \psi(t) - \lambda_j \gamma_j(t) \quad j = 1, \dots, J \quad (7.1.3-2)$$

$$P_\gamma(t) = \sum_{j=1}^J \lambda_j \gamma_j(t) \quad (7.1.3-3)$$

Where,

- $\psi(t)$: Fission rate;
 γ_j : Nuclide concentration for j th group;
 F_γ : Input factor to allow specification of conservative calculation
 E_j : Energy yield for j th group;
 λ_j : Decay constant for j th group
 $P_\gamma(t)$: Decay power; and
 J : Number of groups.

The data of E_j and λ_j for 11 groups are provided as built-in tables.

The existing RELAP5-3D decay heat model was modified using built in tables to obtain the 1971 ANS standard model energy yields and decay constants. The following process was used. First the decay heat curve from the equation of the 1971 ANS standard model was calculated. Energy yields and the decay constants, as shown in Table 7.1.3-1, were obtained by fitting the 1971 ANS standard curve with 11 groups. The resulting energy yields and decay constants for the 11 groups were then built into RELAP5-3D as tables. The modified decay heat model was then validated by running a sample problem and comparing the results to the 1971 ANS standard model. Figure 7.1.3-1 shows a comparison of the 1971 ANS standard model with the resulting M-RELAP5 decay heat model. Figure 7.1.3-2 compares the integral decay heat power from the M-RELAP5 model to the 1971 ANS standard equation.

7.1.3.2 Actinide decay heat

10CFR50 Appendix K specifies that the heat from the decay of actinides shall be calculated in accordance with fuel cycle calculations and known radioactive properties and shall be that appropriate for the time in the fuel cycle that yields the highest calculated fuel temperature during the LOCA.

The point kinetics model in the RELAP5-3D includes the ANSI/ANS 5.1-1979 standard decay heat model from actinide series, which is accepted in Section 9.2.5 Ultimate Heat Sink (Rev.3) of NUREG-0800 (Ref. 7-30). The default values of the ANSI/ANS 5.1-1979 standard are as follows:

The yield of ^{239}U produced per a nuclear fission 1.0

The released energy from the decay of an actinide nucleus

^{239}U 0.474 (MeV)

^{239}Np 0.419 (MeV)

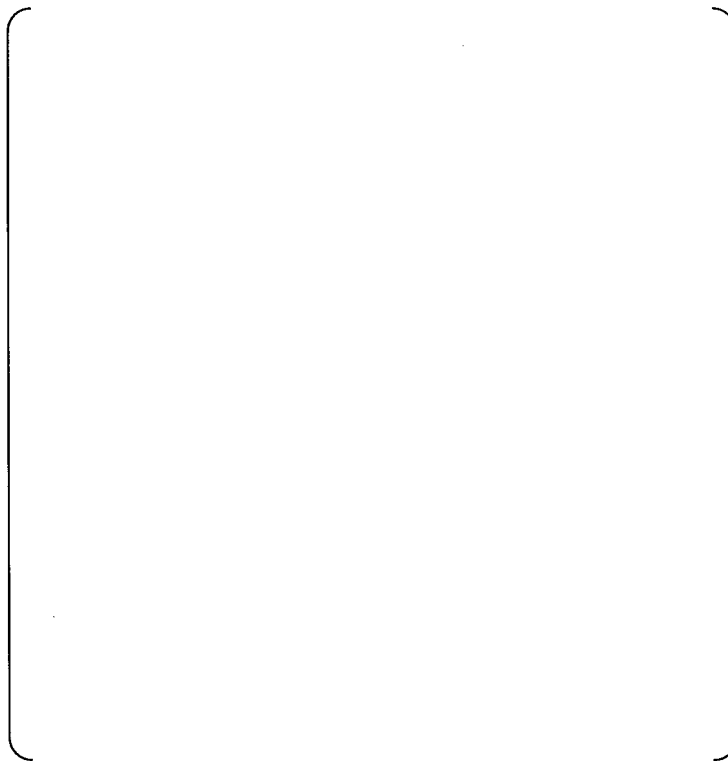
The decay constant

$$^{239}\text{U} \quad 4.91 \times 10^{-4} \text{ (sec}^{-1}\text{)}$$

$$^{239}\text{Np} \quad 3.41 \times 10^{-6} \text{ (sec}^{-1}\text{)}$$

Fuel cycle calculations for the US-APWR have confirmed that the above model is appropriate to yield the highest decay heat from actinide series. Therefore, these default values is used to evaluate the decay heat from actinide series.

Table 7.1.3-1 Energy yields and decay constants for ANS 1971



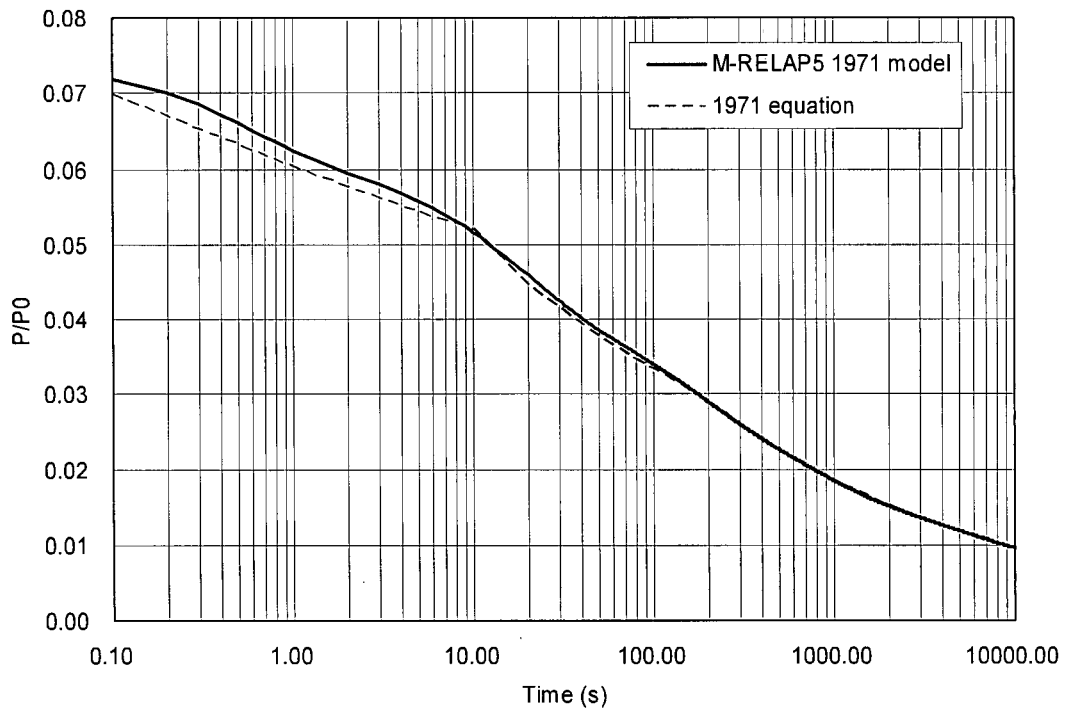


Figure 7.1.3-1 Decay heat power obtained by applying the ANS 1971 decay heat model

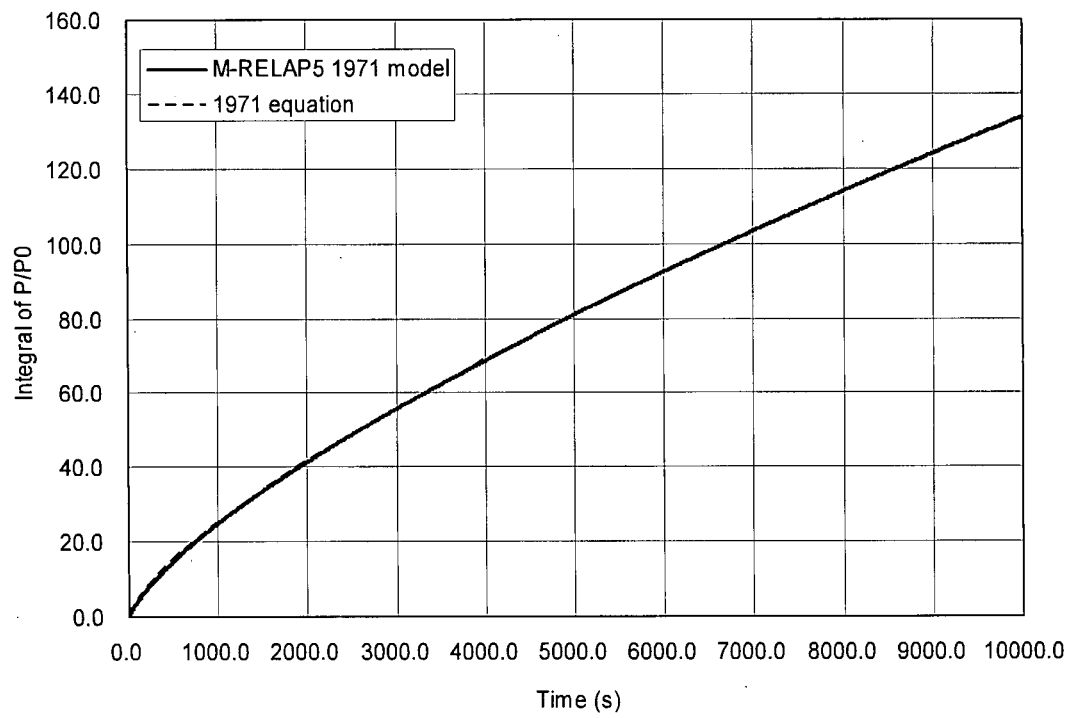


Figure 7.1.3-2 Integral decay heat power

7.1.4 Metal Water Reaction Model

The Appendix K requirement is: "The rate of energy release, hydrogen generation, and cladding oxidation from the metal/water reaction shall be calculated using the Baker-Just equation." The metal-water reaction model included in RELAP5-3D is based on the Cathcart model (Ref. 7-6), and this model does not meet the Appendix K requirement. The Baker-Just equation (Ref. 7-7) is therefore incorporated in M-RELAP5. Applying Baker-Just equation will bound the estimated oxidation for advanced zirconium alloy material cladding: ZIRLO™ used in the US-APWR.

7.1.4.1 Metal Water Reaction Rate Model

The Baker-Just equation is:

$$w^2 = 33.3 \times 10^6 t \exp\left[-\frac{45,500}{RT}\right] \quad (7.1.4-1)$$

where w is the weight of zirconium reacted per unit surface area (mg/cm^2), t is the reaction time (s), R is the universal gas constant, 1.987 (cal/mol-K), and T is the oxide surface temperature (K).

Differentiating Equation 7.1.4-1 with t gives the reaction rate equation:

$$\frac{dw}{dt} = \frac{33.3 \times 10^6 \exp\left[-\frac{45,500}{RT}\right]}{2w} \quad (7.1.4-2)$$

When the density of zirconium, ρ , is set to 6500 (kg/m^3), which is a preset value of RELAP5-3D, and the thickness of the zirconium reacted is denoted by dr (m), the following equation holds:

$$w = \rho dr \times 10^2 = 6.5 \times 10^5 dr \quad (7.1.4-3)$$

Substituting this relationship into Equation 7.1.4-2, it can be expressed as the amount of zirconium reacted in terms of the thickness of the zirconium for convenience:

$$\frac{d(dr)}{dt} = \frac{7.882 \times 10^{-5} \exp\left[-\frac{45,500}{RT}\right]}{2dr} = \frac{K \exp\left[-\frac{A}{RT}\right]}{2dr} \quad (7.1.4-4)$$

where $K=7.882 \times 10^{-5}$ and $A/R=22899$.

Finally, the thickness of zirconium reacted until the time point n is

$$dr_n = \left[dr_{n-1}^2 + K\Delta t \exp\left(-\frac{A}{RT}\right) \right]^{1/2} \quad (7.1.4-5)$$

where dr_{n-1} is the thickness of zirconium reacted at the time point n-1, and Δt is time step size.

The amount of heat added to the cladding outer surface between time point n-1 and n is given by multiplying the volume of cladding undergoing reaction by the density of zirconium, 6500 (kg/m³):

$$Q = \rho\pi \left[2r_o(dr_n - dr_{n-1}) + dr_{n-1}^2 - dr_n^2 \right] \frac{H}{W} \quad (7.1.4-6)$$

where Q is heat addition per unit length, r_o is cladding outer radius (m), H is reaction heat release, 5.94×10^8 (J/(kg-mol)), and W is molecular weight of zirconium, 91.22 (kg/(kg-mol)). If cladding rupture occurs, the reaction is assumed to take place on the inner surface as well. The metal-water reaction heat calculated with Equation 7.1.4-6 is transferred to heat conduction calculations in M-RELAP5.

The thermal properties of cladding change when the oxide layer is produced by metal-water reaction. However, as the oxide layer formed in the SBLOCA is considered to be small, the thermal properties change by the oxide layer is to be neglected as the original RELAP5-3D.

7.1.4.2 Cladding Swelling and Rupture Effect on Metal-Water Reaction

The cladding geometry change caused by plastic strain before rupture or rupture leads to the thinning of the oxide layer and the increase of the reaction surface area. These changes increase the heat generation by metal-water reaction. Therefore, it is necessary to consider the effect of the cladding deformation caused by the plastic strain or rupture.

When the cladding geometry change caused by plastic strain or rupture cannot be neglected, the cladding outer radius and the thickness of the zirconium reacted change between time point n-1 and n. When the cladding outer radius changes from r_o^{n-1} at time point n-1 to r_o^n at time point n, and oxide layer of thickness dr_{n-1} produced until time point n-1 is assumed to become uniformly thinner in the circumference direction by the cladding strain, the oxide layer

thickness $d\tilde{r}_{n-1}$ is calculated by:

$$d\tilde{r}_{n-1} = \hat{r}_o^n - \sqrt{\hat{r}_o^{n^2} - 2\hat{r}_o^{n-1}dr_{n-1} + dr_{n-1}^2} \quad (7.1.4-7)$$

Consequently, the outer surface oxide thickness dr_n at time point n, and the reaction heat release between time point n-1 and n are evaluated as follows:

$$dr_n = \left[(d\tilde{r}_{n-1})^2 + K\Delta t e^{-\frac{A}{RT}} \right]^{1/2} \quad (7.1.4-8)$$

$$Q = \rho\pi \left[2\hat{r}_o^n (dr_n - d\tilde{r}_{n-1}) - dr_n^2 + d\tilde{r}_{n-1}^2 \right] \frac{H}{W} \quad (7.1.4-9)$$

New oxide layer is the initial condition of next time step calculation. After a rupture occurs, it is not necessary to consider the thinning of the reacted oxide layer any longer. It is necessary to consider metal-water reaction on the inside surface at the rupture node as mentioned above and the energy source of the cladding oxidation will be added to the temperature calculation.

7.1.5 Cladding Swelling and Rupture Model

7.1.5.1 Cladding Swelling and Rupture Model

The empirical correlations of Powers and Meyer (Ref. 7-8) are implemented in RELAP5-3D for predicting the cladding rupture, the cladding strain at rupture and resulting flow blockage for Zircaloy-4. These correlations are based on applicable data in such a way that the incidence of rupture and the degree of swelling and flow blockage are not underestimated. As the cladding rupture temperature is a function of the cladding hoop stress and cladding heat-up rate, and the cladding strain at rupture and flow blockage are also function of rupture temperature and cladding heat-up rate in the Powers and Meyer model, the cladding heat-up rate is necessary to predict the cladding rupture, strain at rupture, and flow blockage. If the cladding temperature transient is not continuous, the definition of the cladding heat-up rate is not simple. However, as the cladding temperature transient during SBLOCA is considered to be relatively continuous, the instantaneous temperature change already incorporated in RELAP5-3D is to be used for the cladding temperature heat-up rate.

These models have been used successfully to calculate cladding swelling and rupture in RELAP4/MOD5 (Ref. 7-9) used by NRC for auditing purposes.

[

]

In RELAP5-3D, the cladding plastic hoop strain before rupture is calculated using the FRAP-T6 (Ref. 7-11) high temperature creep model:

$$\varepsilon = 0.25 \times \varepsilon_{rup} \exp[-0.0153(T_{rup} - T_c)] \quad (7.1.5-1)$$

where ε is the plastic hoop strain before rupture, T_c is the current cladding temperature, T_{rup} is the cladding rupture temperature calculated from the current hoop stress and heat-up rate, and ε_{rup} is the strain at rupture calculated from the rupture temperature and heat-up rate. This correlation is to be applied not only to Zircaloy-4 cladding but also to ZIRLO™ cladding

but with ZIRLO™ properties.

When the hot assembly average rod ruptures, additional form loss coefficients, which cause the flow diversion from the cladding rupture region through the momentum calculations, are applied to the junctions just below and just above the rupture location. Extensive experimental studies have shown that the effect of flow diversion due to blockage is offset by heat transfer enhancement due to flow blockage. The model, which addresses only the negative aspects of flow blockage and does not take credit for the heat transfer enhancement due to flow blockage, is a conservative representation of these phenomena.

The temperature of heat structure is calculated at the fixed mesh points by the heat conduction equation in RELAP5-3D. If the cladding geometry is greatly changed by the plastic hoop strain or rupture, its effect on the heat conduction calculation should be taken into account. The methodology to account the effect of the cladding geometry change is introduced in M-RELAP5. It is shown in Appendix B.

7.1.5.2 Cladding Rupture Effect on Gap Conductance

One of the other Appendix K requirements related to the fuel-to-cladding gap heat transfer is that “the gap conductance shall be varied in accordance with changes in gap dimensions and any other applicable variables.” As the fuel-cladding gap dimension at any time is calculated considering not only the pellet/cladding thermal expansion and the cladding elastic deformation but also the cladding swelling and rupture to obtain the gap conductance, the Appendix K requirement is satisfied. The gap conductance at the rupture node is to be calculated using the thermal conductivity of steam after cladding rupture is calculated in M-RELAP5. As the gap width is usually large at the rupture node, the effects of temperature jump distance and fuel/cladding surface roughness is considered to be small. Thus, these effects are to be neglected for the rupture node in M-RELAP5.



Figure 7.1.5-1 Burst Temperature of ZIRLO™



Figure 7.1.5-2 Burst Strain of ZIRLO™

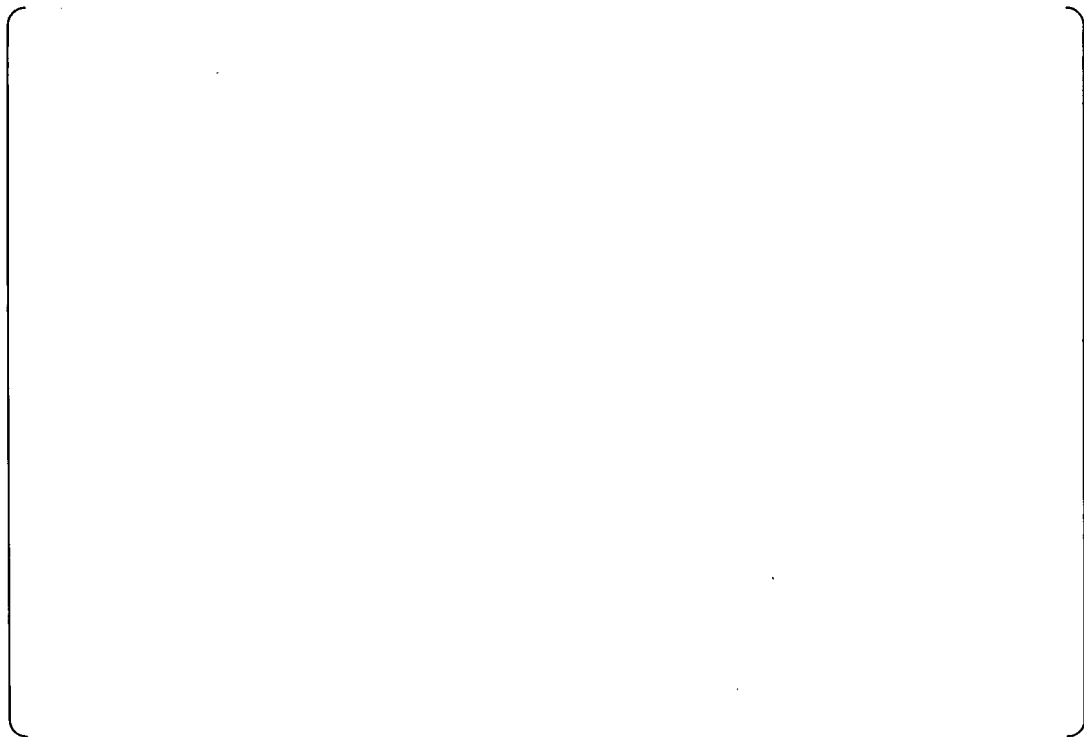


Figure 7.1.5-3 Assembly Blockage of ZIRLO™

7.1.6 Discharge Model

7.1.6.1 Implementation of Moody's critical flow model

Appendix K specifies that Moody's critical flow model (Ref. 7-12) should be applied for the evaluation of a discharge under a two phase flow conditions at a break location. Therefore, the Moody's critical flow model must be incorporated into M-RELAP5 when evaluating the discharge flow in a small break LOCA event.

Moody's critical flow model was derived using the following assumptions.

- Each steam and liquid phase is in an equilibrium condition at same static pressure.
- The flow scheme is annular flow without entrainment.
- The discharge velocity for each steam and liquid phase is uniform.
- The slip ratio at the exit is treated as an independent variable.
- The quantity of a saturation state is a function of pressure alone.

Based on the above assumptions, the equation for the flow rate, G , was derived from the mass and energy conservation laws for a two phase flow, mixture as:

$$G = \sqrt{\frac{2 \left[h_0 - h_f - \frac{h_{fg}}{s_{fg}} (s_0 - s_f) \right]}{\left[\frac{K(s_g - s_0)v_f}{s_{fg}} + \frac{(s_0 - s_f)v_g}{s_{fg}} \right]^2 \left[\frac{s_0 - s_f}{s_{fg}} + \frac{s_g - s_0}{K^2 s_{fg}} \right]}} \quad \dots \dots \dots (7.1.6-1)$$

where,

- h = Specific enthalpy;
- s = Specific entropy;
- v = Specific volume;
- K = Slip ratio;

Suffix 0 = Quantity of state at stagnation point (if without suffix 0, it denotes the quantity of state at an exit.);

Suffix f = Liquid phase; and,

Suffix g = Steam phase.

Equation (7.1.6-1) shows that the flow rate G is a function of the slip ratio K and the pressure P .

Therefore, assuming that the slip ratio K and the pressure P are independent, the conditions for the flow rate G to attain its maximum value are as follows:

$$\left(\frac{\partial G}{\partial K}\right)_P = 0 \dots\dots\dots (7.1.6-2)$$

$$\left(\frac{\partial G}{\partial P}\right)_K = 0 \dots\dots\dots (7.1.6-3)$$

From Equation (7.1.6-2), the slip ratio K at the maximum flow rate is given as:

$$K = K_M = \left(\frac{v_g}{v_f}\right)^{1/3} \dots\dots\dots (7.1.6-4)$$

Equation (7.1.6-4) shows that the slip ratio K depends only on pressure P at the maximum flow rate. Therefore, by combining Equations (7.1.6-1) and (7.1.6-4), the maximum flow rate will satisfy the following condition:

$$\frac{dG}{dP} = 0 \dots\dots\dots (7.1.6-5)$$

When using the quantity at a stagnation point, in addition to Equations (7.1.6-1) and (7.1.6-4), the system equation can be formulated using the following state equation.

$$h_0 = h_{f0} + \frac{h_{fg0}}{s_{fg0}}(s_0 - s_{f0}) \dots\dots\dots (7.1.6-6)$$

Moody prepared figures using Equations (7.1.6-1), (7.1.6-4) and (7.1.6-6) based on the quantity of saturation state, and calculated the pressure, P_M , for the maximum flow rate under the conditions of the pressure, P_0 , and the enthalpy, h_0 , as the input values. The calculation results show that the maximum flow rate G is attained at a single point in the range of the given pressure P_0 and the enthalpy h_0 . Therefore, the maximum flow rate G_M could be determined. The calculation results from Moody's paper are shown in Figures 7.1.6-1 and 7.1.6-2.

The pressure ranges used for the calculations described in his paper and shown in the figures were 25–3000 psia (0.172–20.684 MPa) for the pressure P and 0.01–1.0 for the equilibrium quality χ .

Currently, RELAP5-3D selects either Ransom-Trapp (Ref. 7-13, 14, 15) or Henry-Fauske (Ref. 7-16) for a critical calculation. To comply with Appendix K requirement for break flow calculations, it was decided to use Moody's critical flow model combined with the Henry-Fauske's critical flow model to cover the expected range of conditions. In the

subroutine jchoke, which selects the critical flow model to be adopted for the given hydrodynamic condition, the quality range from 0.01 to 1.0 was set so that the Moody critical flow model is selected.

7.1.6.2 Incorporation of Moody's critical flow model

[

]

7.1.6.3 Applicable Condition for each Discharge Model

The critical flow model for single phase liquid, two-phase flow or single phase vapor is selected in the subroutine jchoke by the given hydrodynamic condition. In the original RELAP5-3D code, the applicable condition for each critical flow model is

- Subcooled single phase flow : equilibrium quality $< 10^{-6}$
Henry-Fauske
- Two phase flow : equilibrium quality < 0.998
Extended Henry-Fauske
- Steam single phase flow : equilibrium quality ≥ 0.998 .

With incorporating Moody critical flow model, the applicable condition is modified as

- Subcooled single phase flow : equilibrium quality $< 10^{-6}$
Henry-Fauske
- Two phase flow : equilibrium quality < 0.998
✓ Noncondensable gas quality $< 10^{-8}$

- Equilibrium quality > 0.01
Moody
- Equilibrium quality ≤ 0.01
Extended Henry-Fauske
- ✓ Noncondensable gas quality $\geq 10^{-8}$
Extended Henry-Fauske
- Steam single phase flow : equilibrium quality ≥ 0.998 .

[

]

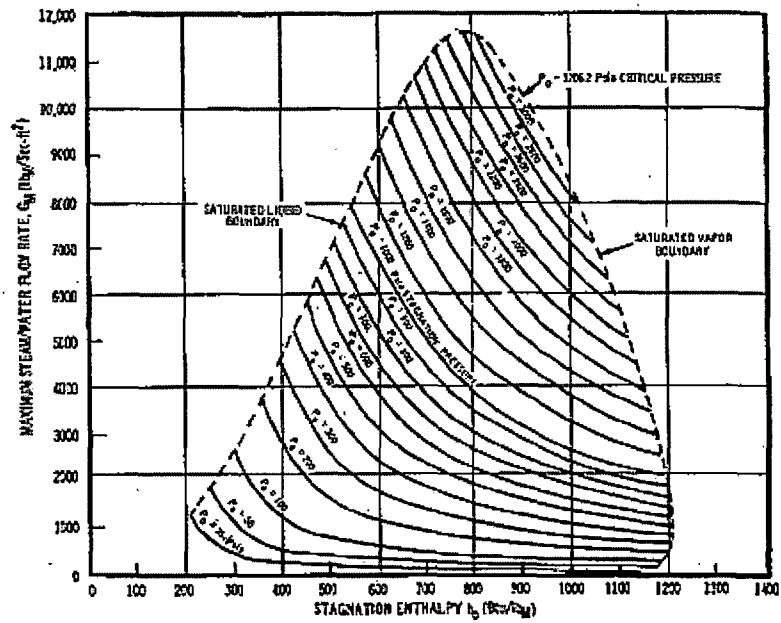


Figure 7.1.6-1 Maximum steam/water flow rate and local stagnation properties

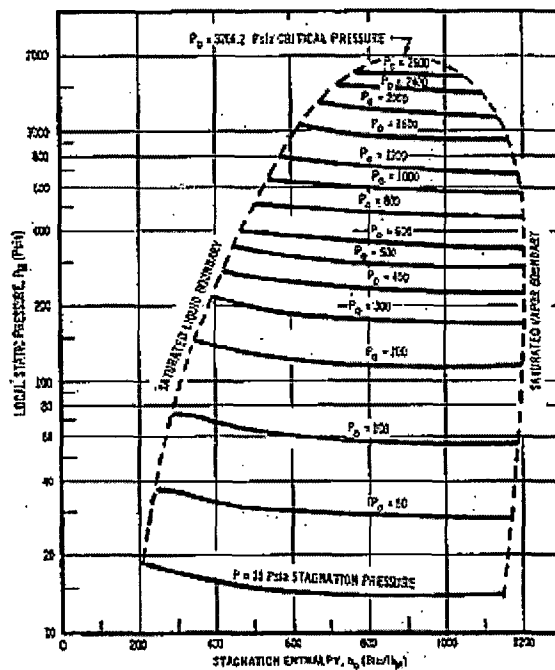


Figure 7.1.6-2 Local static pressure and stagnation properties at maximum steam/water flow rate

7.1.7 Critical Heat Flux and Post-CHF Heat Transfer Model

7.1.7.1 Feature of SBLOCA Rod Heat Transfer

If the core is uncovered during the loop seal clearance period or the core boil-off period in a SBLOCA transient, a core heat-up will occur. Therefore, the calculation of critical heat flux (CHF) and post-CHF heat transfer are important for predict the resulting cladding temperature history. As the two-phase mixture level decreases and uncovers a portion of the fuel rod, the heat transfer changes from nucleate boiling to post-CHF heat transfer. At the top of the mixture region, a dryout occurs which is the interface between the good cooling region and the fuel rod heat-up region. The fuel rod cladding temperature rise above the mixture level depends on the local power, the integral of power below the mixture height (integrated steam flow), the distance from the mixture level and the Post-CHF heat transfer coefficient. Especially, the post-CHF heat transfer by vapor convection in two-phase flow or in single-phase vapor flow is important for the evaluation of the peak cladding temperature in SBLOCA analysis.

The cladding temperature decreases gradually and finally quenches as the core mixture level and two-phase mixture height is recovered. The heat transfer in this recovery period depends on film boiling and transition boiling heat transfer to evaluate the cladding temperature during this period.

Appendix K requires that post-CHF heat transfer correlations “predict values of heat transfer coefficient equal to or less than the mean values of applicable experimental heat transfer data throughout the range of parameters for which the correlations are to be used.” Appendix K also requires for CHF correlations that “the computer programs in which these correlations are used shall contain suitable checks to assure that the physical parameters are within the range of parameters specified for use of the correlations by their representative authors.”

MHI intends to use the existing RELAP5-3D wall heat transfer correlations, in M-REALP5, for standard geometry for SBLOCA analysis. The correlations for CHF, transition boiling, film boiling and vapor convection heat transfer, which are important for SBLOCA analysis, are discussed in the following sections along with applicable range of physical parameters and predictability of applicable experimental data.

7.1.7.2 Critical Heat Flux

The CHF correlation is used not only to predict CHF occurrence, but also to determine when transition boiling heat transfer occurs and the magnitude of the transition boiling heat transfer coefficient.

The Biasi correlation had been incorporated in RELAP5/MOD2. The 1986 AECL-UO Critical Heat Flux Lookup Table (Ref. 7-17) replaced the Biasi correlation in the process of developing RELAP5-3D, because the comparison with the CHF data indicates that the AECL-UO lookup table was found to be more accurate than the Biasi correlation.

The AECL-UO lookup table was developed from more than 15,000 CHF data points, and the parameter ranges are given as follows:

Tube diameter	0.001 - 0.0924 m
System Pressure	0.1 - 196.2 MPa
Mass Flux	6 - 15,700 kg/(m ² -s)
Equilibrium Quality	-0.98 - 1.58
Heat Flux	0.13 - 21.4 MW/m ²

The AECL-UO lookup table was compared with the tube CHF data in INEL bank under "Critical Heat Flux" (Ref. 7-18). There were 9687 CHF data points but as some data showed energy balance problems, and those data were removed. The remaining 9353 CHF data were compared with the AECL-UO lookup table. The average error of (predicted value – measured value)/ (predicted value) was -0.049 and root mean square error was 0.39. And the ranges of CHF data were as follows:

Tube diameter	0.001 - 0.0375 m
System Pressure	0.1 - 20.0 MPa
Mass Flux	10.0 - 18600 kg/(m ² -s)
Equilibrium Quality	-0.097 - 0.988
Heat Flux	0.1 - 21.4 MW/m ²

The physical parameters expected in a SBLOCA analysis are within the range of the above CHF data.

CHF at the low mass flux region is reset to the value evaluated by the Zuber pool-boiling CHF correlation, and is multiplied by the vertical flow factor k_7 to account for the effect of void

fraction:

$$\begin{aligned} k7 &= (1.0 - \alpha) && \text{for } \alpha < 0.8 \\ k7 &= (1.0 - \alpha) \frac{0.8 + 0.2(\rho_f / \rho_g)}{\alpha + (1.0 - \alpha)(\rho_f / \rho_g)} && \text{for } \alpha \geq 0.8 \end{aligned} \quad (7.1.7-1)$$

where α is void fraction, ρ_f is liquid density and ρ_g is vapor density.



The applicability of the AECL-UO lookup table to CHF predictions was also verified by the comparison with ORNL Uncovered Bundle Heat Transfer Test data. The results are shown in Section 8.1.2.



7.1.7.3 Transition Boiling Heat Transfer

The transition boiling incorporated in RELAP5-3D and used in M-RELAP5 is based on the Chen transition boiling model (Ref. 7-19). This model considers the total transition boiling heat transfer to be the sum of individual components, one describing wall heat transfer to the liquid (boiling term) and a second describing the wall heat transfer to the vapor (convective term).

The model is expressed as:

$$q_{TB} = q_{wf} A_f + h_{wg}(T_w - T_g)(1 - A_f) \quad (7.1.7-3)$$

where q_{TB} is transition boiling heat flux, q_{wf} is heat flux by contact between the liquid and wall evaluated by a complex three step model, h_{wg} is heat transfer coefficient to vapor, and A_f is fractional wall wetted area. A_f is dependent on wall super-heat degree, void fraction, and mass flux.

The Chen transition boiling model was compared to 4167 data from eight sources for water flowing in tubes. A mean deviation of measured heat flux to predicted heat flux is 16.0%.

The parameter ranges of the test data are as follows:

Tube diameter	0.00488 – 0.02 m
System Pressure	0.42 - 19.5 MPa
Mass Flux	16.3 – 5,235 kg/(m ² -s)
Equilibrium Quality	0.151 - 1.728
Heat Flux	0.034 - 2.05 MW/m ²

The physical parameters expected in a SBLOCA analysis are within the range of the above test data.

In RELAP5-3D and also in M-RELAP5, the q_{wf} term is replaced by the critical heat flux

calculated with the AECL-UO lookup table for the current local conditions to simplify the computational process. The results of Elias et al. (Ref. 7-20) indicate that the same transition boiling heat transfer model as implemented in RELAP5/MOD3 predicts reasonably well the high quality data in which the vapor convection term is dominant, but under-predicts a large fraction of the transition boiling data, especially the low quality data in which the boiling term is dominant. It is explained that the introduction of the critical heat flux instead of the heat flux function suggested by Chen strongly reduces the contribution of the boiling term in the transition boiling heat transfer. The transition boiling heat transfer model implemented in RELAP5-3D and M-RELAP5 could be applied reasonably to high quality transition boiling region, and could be applied conservatively to low quality transition boiling region.

The applicability of the transition boiling heat transfer model was verified by the comparison with ORNL High-Pressure Reflood Test data. The results are shown in Section 8.1.3.

7.1.7.4 Film Boiling Heat Transfer

Film boiling heat transfer consists of conduction across vapor film blanket next to a heated wall, convection to flowing vapor and radiation across the film to a continuous liquid blanket or dispersed mixture of liquid droplet and vapor.

The conduction heat transfer coefficient through vapor film is obtained by the Bromley correlation (Ref. 7-21) as:

$$h_f = 0.62 \left[\frac{g \rho_g k_g^2 (\rho_f - \rho_g) h'_{fg} C p_g}{L (T_w - T_s) Pr_g} \right] M_a \quad (7.1.7-4)$$

where h'_{fg} is a correction to the heat of vaporization, h'_{fg} , which includes the energy absorbed by the vapor surrounding the tube, and tube diameter L is replaced with the minimum critical wave length (Ref. 7-22) as:

$$L = 2\pi \left[\frac{\sigma}{g(\rho_f - \rho_g)} \right]^{0.5} \quad (7.1.7-5)$$

M_a is void fraction factor, which smooth h_f over the range of the void fraction from an inverted annular flow to a dispersed flow. A spline fit is used between 0.2 and 0.999 in RELAP5-3D. M_a is one below $\alpha = 0.2$, and is zero at $\alpha = 0.999$.

The convection heat transfer to vapor is obtained by the modified Dougall-Rohsenow correlation in M-RELAP5, described in the next section.

In RELAP-3D, the radiation heat transfer to drops and vapor is based on Sun, Gonzalez-Santalo, and Tien (Ref. 7-23) with some modifications to the droplet diameter model and to the mean path length. The same model is used in M-RELAP5.

The film boiling and transition boiling heat transfer models are used to predict the cladding temperature behavior during the core mixture level recover period. Applicability of these models for the heat transfer during the core mixture level recovery period have been verified with the ORNL High-Pressure core mixture level recovery Reflood Test data analyses presented in Section 8.1.2. Combination of the film boiling and transition boiling heat transfer models incorporated in M-RELAP5 predict the experimental data in a reasonable manner.

7.1.7.5 Vapor Convection Heat Transfer

The rod wall heat transfer above the two-phase mixture level is most important to evaluate the peak cladding temperature in SBLOCA analysis. The heat transfer just above the two-phase mixture level depends on film boiling at high quality condition in which vapor convection term is dominant. And the heat transfer depends on single vapor convection above two-phase flow region. Then, the vapor forced convection heat transfer in two-phase flow and in single-phase vapor flow is most important for SBLOCA analysis.

For heat transfer from a heated wall to single-phase vapor during turbulent forced convection, the Dittus-Boelter correlation (Ref. 7-24) used is:

$$Nu = h \frac{D}{k_g} = 0.023 Re_g^{0.8} Pr_g^{0.4} \quad (7.1.7-6)$$

In two-phase flow, the liquid mass flux times the vapor-to-liquid density ratio is added to the vapor mass flux. This effectively converts the Dittus-Boelter correlation for two-phase vapor convection heat transfer and the smooth transition from two-phase flow to single-phase vapor flow is made:

$$Nu = h \frac{D}{k_g} = 0.023 \left[Re_g \left\{ x + \frac{\rho_g}{\rho_f} (1-x) \right\} \right]^{0.8} Pr_g^{0.4} \quad (7.1.7-7)$$

This converted correlation for two-phase vapor convection heat transfer implemented in M-RELAP5 is the Dougall-Rohsenow correlation (Ref. 7-25) except that the physical properties of vapor: thermal conductivity, viscosity and specific heat in Equation 7.1.7-7 are evaluated at the film temperature. On the other hand, the saturation temperature is used to evaluate the physical properties of vapor in the original Dougall-Rohsenow correlation. The modified correlation using the vapor properties at the film temperature gives smaller heat transfer coefficient than the original one.

The revised Appendix K states that: "At that time continued use of the Dougall-Rohsenow correlation under conditions where non-conservative predictions of heat transfer result will no longer be acceptable." ORNL rod bundle data show that the original Dougall-Rohsenow correlation overpredicts heat transfer for high quality conditions. This result was obtained using the fluid saturation temperature rather than the actual vapor temperature for the vapor temperature. M-RELAP5 is capable of calculating the actual vapor temperature with non-equilibrium model. Therefore, it is expected that M-RELAP5 can adequately calculate rod heat transfer by two-phase vapor convection with the modified Dougall-Rohsenow correlation.

Applicability of the Dittus-Boelter correlation and the modified Dougall-Rohsenow correlation to SBLOCA analysis can be verified by experimental data, which simulate the core uncover phase during SBLOCA. The results of the comparison with ORNL Steady-State Uncovered Bundle Heat Transfer Test data are presented in Section 8.1.2. The vapor convection heat transfer model implemented in M-RELAP5 code predicts reasonably the experimental data.

7.1.7.6 Prevent Return to Nucleate Boiling and Transition Boiling

Appendix K requires that the return to nucleate boiling be prevented during the blowdown phase, once CHF has been predicted. The original RELAP5-3D did not contain any logic to prevent return to nucleate boiling once CHF has occurred. A new heat transfer control parameter to prevent the return to nucleate boiling during the blowdown after first CHF occurrence has been added in M-RELAP5 to satisfy the Appendix K requirement.

Appendix K also requires that the returns to transition boiling be prevented during the blowdown after the cladding surface superheat exceeds 300 R. The original RELAP5-3D did not contain any logic to prevent return to transition boiling. The new added heat transfer control parameter mentioned above will be also used to prevent the return to transition boiling once the cladding superheat has exceeded 300 R.

Applicability of the transition boiling and nucleate boiling models incorporated in M-RELAP5 for the heat transfer and rewet phenomena during the core mixture level recovery phase was confirmed by the comparison with ORNL High-Pressure Reflood Test data as shown in Section 8.1.3. As the Appendix K requirements indicate, the requirements are necessary only during blowdown phase, and are not necessary during the core mixture level recovery period.

7.2 Advanced Accumulator

An advanced accumulator design (Ref. 7-29) is used in the US-APWR. The unique feature of the advanced accumulator design is to be able to control the injection flow rate using a flow damper. The advanced accumulator is designed to initially inject a large amount of coolant just after activation that compensates for the loss of coolant from the LOCA. After the initial high flow period, the advanced accumulator will inject water at a small flow rate for longer-term cooling after the initial high flow injection.

7.2.1 Advanced Accumulator Model

The total resistance coefficient K_D , is determined from the accumulator flow coefficient C_V and the resistance coefficient from the injection piping. The flow coefficient is a function of the cavitation factor σ_V , and the water level in the accumulator. The total resistance coefficient is calculated as follows:

(1) σ_V is calculated from the flow condition at flow damper

$$\sigma_V = \frac{P_D + P_{at} - P_v}{(P_A + \rho g H) - \left(P_D + \frac{\rho_f V_D^2}{2} + \rho g H' \right)} \dots\dots\dots (7.2-1)$$

Where

- σ_V : Cavitation factor
- P_{at} : Atmospheric pressure [abs]
- P_D : Flow damper outlet pressure [gage]
- P_A : Gas pressure in accumulator [gage]
- P_v : Vapor pressure [abs]
- ρ_f : Density of water
- g : Acceleration of gravity
- H : Distance between accumulator water level and vortex chamber
- H' : Distance between outlet pipe and vortex chamber
- V_D : Velocity of injection pipe.

(2) The flow rate coefficient C_V is calculated using the following correlations obtained from test data which cover the range of applicability for the US-APWR design. The empirical correlations of C_V are derived separately for large and small flow rate injections as a function

of cavitation factor of σ_v as shown in Figure 7.2-1.

$$\text{For large flow rate: } C_v = 0.7787 - 0.6889 \exp(-0.5238\sigma_v) \dots\dots\dots (7.2-2)$$

$$\text{For small flow rate: } C_v = 0.07197 - 0.01904 \exp(-6.818\sigma_v) \dots\dots\dots (7.2-3)$$

(3) C_v is converted to K_D

$$K_D = \frac{1}{C_v^2} \dots\dots\dots (7.2-4)$$

(4) Total resistance coefficient is calculated by

$$K_{ACC} = K_D + K_{pipe} \dots\dots\dots (7.2-5)$$

Where

K_{ACC} : Total resistance coefficient of the flow damper and injection piping

K_{pipe} : Total resistance coefficient of injection piping.

Since subroutine accum calculates flow resistance and residual water volume, this subroutine was revised to incorporate these correlations. The advanced accumulator model as coded is detailed in Appendix D.

7.2.2 Model Validation

The advanced accumulator model has been incorporated into the RELAP5-3D code according to the method described above. The prediction accuracy of the injection characteristic was validated by the analysis of full height 1/2-scale injection experiments.

(1) Test cases and test conditions

Full height 1/2 scale test cases selected for validation analysis simulate ECCS performance during a large LOCA and are shown in Table 7.2-1. The following four cases were tested on initial tank pressure that reflects the Accumulator operating conditions during a large LOCA. The pressure of the exhaust tank corresponds to RCS pressure.

- Case 1: The initial test tank pressure was 586 psig (4.04 MPa [gage]) simulating the condition for ECCS performance during a large LOCA.

- Case 2: The initial test tank pressure was 657 psig (4.53 MPa [gage]) to obtain data for high pressure design.

- Case 3: The initial tank pressure was 758 psig (5.23 MPa [gage]) to obtain data for high pressure design.

- The pressure in the exhaust tank was 14 psig (0.098 MPa [gage]) for Case 1, 2, and 3. Since the pressure of the exhaust tank becomes the same as the pressure of the containment vessel (C/V) after the blowdown phase during a large LOCA, and ECCS performance analysis uses approximately 14 psig (0.098 MPa [gage]), the backpressure was set at 14 psig (0.098 MPa [gage]).

- Case 4: The initial tank pressure was the same as Case 1. However, the pressure in the exhaust tank was maintained at 71 psig (0.49 MPa [gage]) to obtain data for high backpressure.

(2) Analytical model and boundary conditions for test analyses

The noding diagram is shown in Figure 7.2-2. [

]

(3) Initial conditions

Pressure, water level, temperature, etc. were supplied by input data as the initial conditions of the accumulator tank, based on the test data. However, because gas and liquid phase were assumed to be in equilibrium in RELAP5, the gas temperature was set to the same value as that of the coolant.

(4) Wall heat transfer

The heat transfer between the accumulator tank wall and nitrogen gas was simulated here because this is a test analysis.

(5) Analysis results and comparison with test data

After input data describing the test system were prepared, the analysis carried out until 170 seconds.

Figure 7.2-3 through Figure 7.2-14 show the analysis results of the injection volumetric flow

rate, the tank pressure and the tank water level for four cases in comparison with the test results. In each case the analysis results are in good agreement with the test results, and it is shown that the injection characteristic is well simulated by the advanced accumulator model. In particular, the analysis results reproduce the test results very well with regard to the tank water level, which is the integration value of the injection volumetric flow rate.

The total uncertainty concerning the flow damper is addressed in Appendix D, including discussion about the uncertainty of the flow resistance and the water level that switches flow resistance. The uncertainties are quantified based on the full height 1/2 scale test data.

The uncertainties of the flow damper resistance and the flow switching level is considered deterministically for the US-APWR SBLOCA analysis.

Table 7.2-1 Test Conditions of Full Height 1/2 Scale Test

	Test Tank Pressure	Exhaust Tank Pressure	Initial Gas Volume	Injection Water Volume		Objective
				Large Flow	Small Flow	
	psig [MPa [gage]]	psig [MPa [gage]]		ft ³ [m ³]	ft ³ [m ³]	
Case 1	586 (4.04)	14 (0.098)				Obtain flow characteristics for ECCS performance evaluation during a large LOCA
Case 2	657 (4.53)	14 (0.098)				Obtain flow characteristics for high pressure design
Case 3	758 (5.23)	14 (0.098)				Obtain flow characteristics for large differential pressure
Case 4	586 (4.04)	71 (0.49)				Obtain flow characteristics for small differential pressure



Figure 7.2-1 The Flow Characteristics of the Flow Damper



Figure 7.2-2 Noding diagram



Figure 7.2-3 Injection volumetric flow rate (analysis result of 1/2-scale test: case 1)



Figure 7.2-4 Tank pressure (analysis result of 1/2-scale test: case 1)



Figure 7.2-5 Tank water level (analysis result of 1/2-scale test: case 1)



Figure 7.2-6 Injection volumetric flow rate (analysis result of 1/2-scale test: case 2)



Figure 7.2-7 Tank pressure (analysis result of 1/2-scale test: case 2)

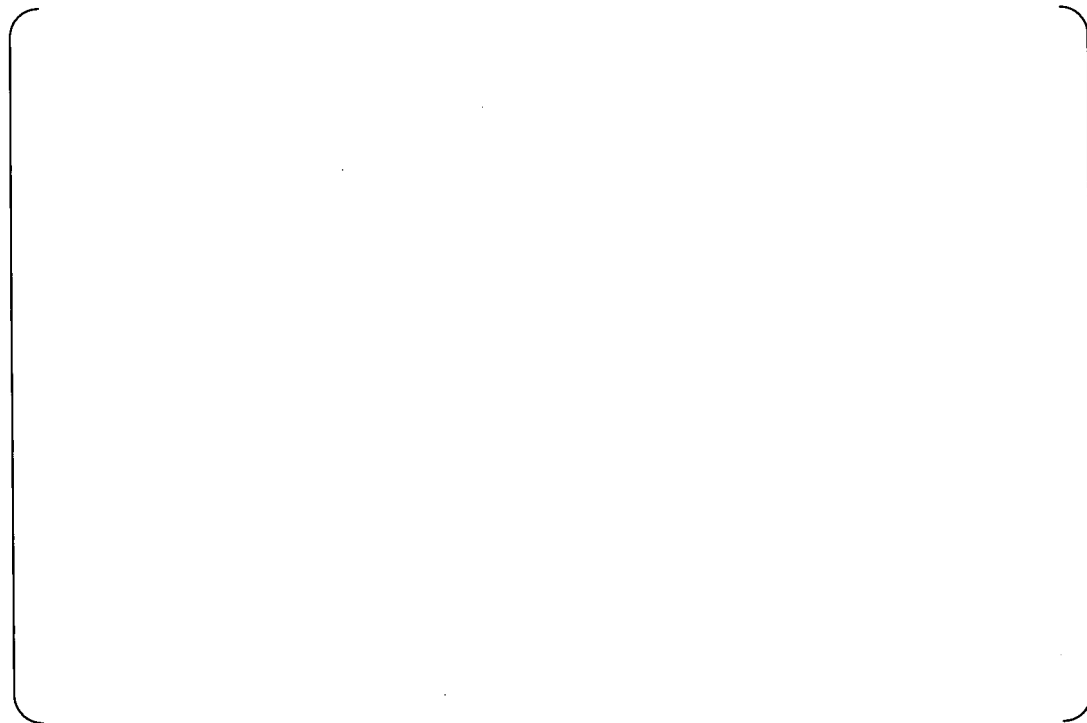


Figure 7.2-8 Tank water level (analysis result of 1/2-scale test: case 2)



Figure 7.2-9 Injection volumetric flow rate (analysis result of 1/2-scale test: case 3)



Figure 7.2-10 Tank pressure (analysis result of 1/2-scale test: case 3)



Figure 7.2-11 Tank water level (analysis result of 1/2-scale test: case 3)



Figure 7.2-12 Injection volumetric flow rate (analysis result of 1/2-scale test: case 4)



Figure 7.2-13 Tank pressure (analysis result of 1/2-scale test: case 4)



Figure 7.2-14 Tank water level (analysis result of 1/2-scale test: case 4)

7.3 References

- 7-1. 10 CFR 50 Part 50, Appendix K, "ECCS Evaluation Models."
- 7-2. T. Shimomura, et al., Fuel System Design Criteria and Methodology, MUAP-07008-P, Mitsubishi Heavy Industries, 2007.
- 7-3. AMERICAN NUCLEAR SOCIETY PROPOSED ANS STANDARD "Decay Energy Release Rates Following Shutdown of Uranium-Fueled Thermal Reactors." Approved by Subcommittee ANS-5, ANS Standards Committee, October 1971
- 7-4. NUREG-0800 : STANDARD REVIEW PLAN "9.2.5 ULTIMATE HEAT SINK" Revision 2, July 1981.
- 7-5. ANS-5.1-1979, "American National Standard for Decay Heat Power in Light-Water Reactors," August 1979.
- 7-6. Cathcart, J. V. et al., Reaction Rate Studies, IV, Zirconium Metal-Water Oxidation Kinetics, ORNL/NUREG-17, August 1977.
- 7-7. Baker, L., and Just, L. C., Studies of Metal Water Reactions at High Temperatures, III. Experimental and Theoretical Studies of Zirconium-Water Reaction, NL-6548, May 1962.
- 7-8. Powers, D. A. and Meyer, R. O., Cladding Swelling and Rupture Models for LOCA Analysis, NUREG-0630, April 1980.
- 7-9. RELAP4/MOD5-A Computer Program for Transient Thermal-Hydraulic Analysis of Nuclear Reactors and Related Systems User's Manual, Volume 1, RELAP4/MOD5 Description, ANCR-NUREG-1335, September, 1976. ~~Bruch, C. G., RELAP4/MOD5-A Computer Program for Transient Thermal-Hydraulic Analysis of Nuclear Reactors and Related Systems User's Manual, Volume 1, RELAP4/MOD5 Description, SRD 113-76, June 1990.~~
- 7-10. Davidson, S. L. and Ryan, T. L., VANTAGE+ Fuel Assembly Reference Core Report,

WCAP-12610-P-A, April 1995.

- 7-11. Resch, S. C. et al., FRAP-T6: The Transient Fuel Rod Behavior Code, NUREG/CR-2950, September 1982.
- 7-12. Moody, F. J., "Maximum Flow Rate of a Single Component, Two-Phase Mixture," J. of Heat Transfer, Trans. ASME, Series C, Vol. 87, No. 1, February 1965, PP. 134–142.
- 7-13. RELAP5-3D© Code Manual VOLUME I: CODE STRUCTURE, SYSTEM MODELS, AND SOLUTION METHODS, INEEL-EXT-98-00834 Revision 2.4, June 2005
- 7-14. V. H. Ransom and J. A. Trapp, "The RELAP5 Choked Flow Model and Application to a Large Scale Flow Test," Proceedings of the ANS/ASME/NRC International Topical Meeting on Nuclear Reactor Thermal-Hydraulics, Saratoga Springs, New York, October 5-8, 1980, pp. 799-819.
- 7-15. J. A. Trapp and V. H. Ransom, "A Choked-Flow Calculation Criterion for Nonhomogeneous, Nonequilibrium, Two-Phase Flows," International Journal of Multiphase Flow, 8, 6, 1982, pp. 669-681.
- 7-16. R. E. Henry and H. K. Fauske, "The Two-Phase Critical Flow of One-Component Mixtures in Nozzles, Orifices, and Short Tubes," J. of Heat Transfer, Trans. ASME, Vol. 93, May 1971, pp. 179-187.
- 7-17. Groenveld, D. C., Cheng, S. C., and Doan, T., 1986 AECL-UO Critical Heat Flux Lookup Table, Heat Transfer Engineering, 7, 1-2, 1986, pp.46-62.
- 7-18. Shumway, R., New Critical Heat Flux Method for RELAP5/MOD3 Completion Report, EGG-EAST-8443, January 1989.
- 7-19. Chen, J. C., Sundaram, R. K., and Ozkaynak, F. T., A Phenomenological Correlation for Post-CHF Heat Transfer, NUREG-0237, June 1977.
- 7-20. Elias, E., Sanchez, V., and Hering, W., Development and Validation of a Transition

Boiling Model for RELAP5/MOD3 Reflood Simulation, N.E.D. 183, 1998, pp.269-286.

- 7-21. Bromley, L. A., Heat Transfer in Stable Film Boiling, Chemical Engineering Progress, 46, 1950, pp.221-227.
- 7-22. Berenson, P. J., Film Boiling Heat Transfer from a Horizontal Surface, J. of Heat Transfer, 1961, pp.351-358.
- 7-23. Sun, K. H., Gonzalez-Santolo, J. M., and Tien, C. L., Calculations of Combined Radiation and Convection Heat Transfer in Rod Bundles Under Emergency Cooling Conditions, Transactions of ASME, J. of Heat Transfer, 98, 1976, pp.414-420.
- 7-24. Dittus, F. W., and Boelter, M. K., Heat Transfer in Automobile Radiators of the Tubular Type, Publications in Engineering, 2, University of California, Berkeley, 1930, pp.443-461.
- 7-25. Dougall, M. S., and Rohsenow, W. M., Film Boiling on the Inside of Vertical Tubes with Upward Flow of a Fluid at Low Qualities, MIT-ME 9079-26, 1963.
- 7-26. Groeneveld, D. C. and Snoek, C. W., A Comprehensive Examination of Heat Transfer Correlations Suitable for Reactor Safety Analysis, Multiphase Science and Technology, Vol.2, pp.181-274, Hemisphere, Washington D. C., 1986.
- 7-27. Makino, Y., et al., Thermal Design Methodology, MUAP-07009-P, May 2007.
- 7-28. Davidson, S. L. and Kramer, W. R. (Ed.), Reference Core Report VANTAGE 5 Fuel Assembly, WCAP-10444-P-A, September 1985.
- 7-29. T. Ogino, et al., THE ADVANCED ACCUMULATOR, MUAP-07001-P(R1), Mitsubishi Heavy Industries, 2007.
- 7-30. NUREG-0800 : STANDARD REVIEW PLAN "9.2.5 ULTIMATE HEAT SINK" Revision 3, March 2007.

8.0 ASSESSMENT OF EM ADEQUACY

8.1 Prepare Input and Perform Calculations To Assess Model Fidelity or Accuracy

The Phenomena Identification and Ranking Table (PIRT) for small break LOCA of the US-APWR is developed as described in Section 4.3. The phenomena that are ranked High in the PIRT and also confirmed by the test calculations are the following: CHF/core dryout, uncovered core heat transfer, rewet, core mixture level, water hold up in SG primary side, SG primary and secondary heat transfer, water level in the SG outlet piping, loop seal formation and clearance, downcomer mixture level/downcomer void distribution.

To validate M-RELAP5 for the high-ranking phenomena, the following six Separate Effect Tests (SETs) and one Integral Effects Test (IET) were analyzed with M-RELAP5:

- ROSA/LSTF Void Profile test
- ORNL/THTF Void Profile test
- ORNL/THTF Uncovered heat transfer test
- ORNL/THTF Reflood test
- UPTF SG plenum CCFL test
- Dukler Air-Water Flooding test
- ROSA/LSTF small break (5%) LOCA test (SB-CL-18)

8.1.1 ROSA/LSTF Void Profile Test

8.1.1.1 Introduction

During a small break LOCA, voiding occurs due to flashing and boiling in the core, and a two-phase mixture level is formed. Prediction and tracking of the two-phase mixture level in the core is important for evaluation of peak clad temperature (PCT) through the periods of loop seal clearance, boil-off and recovery since the mixture level can eventually drop into the core in these periods and core cooling capability is degraded.

A series of experiments (Ref. 8.1.1-1) have been performed at the ROSA-IV Large Scale Test Facility (LSTF) (Ref. 8.1.1-2 and 8.1.1-3) to measure the void fraction distribution in the simulated reactor core rod bundle under high-pressure low-flow conditions. In this section, the simulation for ROSA-IV/ LSTF void profile tests using M-RELAP5 is described.

8.1.1.2 ROSA/LSTF Description and Experimental Procedures

The ROSA-IV LSTF is a volumetrically-scaled (1:48) full-height model of a Westinghouse designed 4-loop PWR. The facility includes a pressure vessel and two symmetric loops, which consist of steam generators, coolant pumps and loop piping.

The pressure vessel contains a full-length (3.66 m) bundle composed of 1104 rods (1008 electrically heated and 96 unheated). Table 8.1.1-1 summarizes rod bundle characteristics. Rod diameter and pitch are of typical 17 X 17 fuel assembly. The heated rods are supported at ten different elevations by grid spacers. The radial power distribution of the bundle is uniform while the axial power profile is chopped-cosine with a peaking factor 1.495. Locations of differential pressure measurements and spacers are shown with the axial power profile in Figure 8.1.1-2.

A series of experiments was performed at the ROSA-IV LSTF to measure the void fraction distribution in the simulator reactor core rod bundle under high-pressure low-flow conditions. The test cases and conditions are summarized in Table 8.1.1-2. The tests were conducted in the pressure range of 1.0 to 17.2 MPa and the rod bundle power range of 0.5 to 7.2 MW corresponding to the average heat flux range 4.5 to 62 kW/m². For lower pressures than 8 MPa and lower powers than 4 MW, the void fraction distributions were measured under steady-state reflux condensation conditions. The mixture level was kept constant at slightly below the hot leg bottom, i.e. 2 m above the top of bundle. For the higher pressures than 8 MPa or the higher powers than 4 MW, the data were obtained from the quasi-steady conditions. In both conditions, the low inlet flow conditions into the bundle were used such that the rod bundle entirely covered by a two-phase mixture.

The void fraction data was derived from the differential pressures along the rod bundle, assuming negligible friction and form-loss pressure drop. The bundle-averaged void fraction was obtained from the overall bundle differential pressure (DP1 in Figure 8.1.1-2).

8.1.1.3 Simulation of ROSA/LSTF Void Profile Test

(1) Modeling Regions

Figure 8.1.1-3 illustrates a schematic of M-RELAP5 modeling regions. Water is supplied through the inlet (cold leg) nozzle of the pressure vessel as a boundary condition. The flow

path regions within the pressure vessel consist of the downcomer, the lower plenum, the core channel, the upper plenum, the upper head and the control rod guide tube. These regions are modeled with hydrodynamic volumes. The exit pressure at the hot legs is also specified as a boundary condition for the modeling of the experiments. The rod bundle and the metal structures, which contact the above mentioned flow path regions, are represented with heat structure modeling.

(2) Nodalization

The nodalization of M-RELAP5 of the pressure vessel and internals is shown in Figure 8.1.1-4 and is similar as that used in the US-APWR M-RELAP5 small break LOCA plant model. The cells enclosed with real lines represent hydrodynamic volumes while the one with hatched lines represent heat structure segments.

[

]

[

]

(3) Analysis cases and results

The following 11 test cases for different three pressures are shown in the Reference 8.1.1-1.

- ST-VF-01A, ST-VF-01B, ST-VF-01C, ST-VF-01D: 1.0 MPa
- ST-NC-01, ST-NC-06E, SB-CL-16L: 7.3 MPa
- ST-VF-01E, ST-VF-01F, ST-VF-01G, ST-VF-01H: 15.0 MPa

Among these tests, the tests at 7.3 MPa were selected for analysis with M-RELAP5, because the pressure during the loop seal and core uncover periods is around this pressure so that the void prediction at this pressure is important.

The transient calculation for each case was performed over a 5,000 s period and the quasi-steady state was achieved within 2,000 s. The typical transient results for void fraction of the test ST-NC-06E is shown in Figure 8.1.1-5 over a 3,000 s period.

Figure 8.1.1-6 shows the calculation results for axial void profile of the test ST-NC-06E comparing with for each test data. The calculation result of the test ST-NC-06E (7.3 MPa) shows a good agreement with the test data over the full-length.

Figure 8.1.1-7 shows the calculation results for over-all bundle void fraction of the test cases

with the pressure 7.3 MPa and for different bundle powers. The calculation result of the test cases with 7.3 MPa shows a good agreement with the test data, although the test cases are limited to higher bundle powers.

8.1.1.4 Summary

The ROSA/LSTF void profile test for the rod bundle region was simulated using M-RELAP5. The calculation result for the pressure 7.3 MPa test cases show good agreement with the test data for both the axial void fraction profile and the averaged void fraction.

8.1.1.5 References

- 8.1.1-1. Y. Anoda, Y. Kukita and K. Tasaka, "Void fraction distribution in rod bundle under high pressure conditions," HTD-Vol.155, Am. Soc. Mech. Eng., Winter Annual Meeting, Dallas, Nov. 25-30, 1990.
- 8.1.1-2. ROSA-IV Large Scale Test Facility(LSTF) System Description, JAERI-M 84-237.
- 8.1.1-3. ROSA-IV Large Scale Test Facility(LSTF) System Description For Second Simulated Fuel Assembly, JAERI-M 90-176.

Table 8.1.1-1 Characteristics of LSTF rod bundle

Parameter	Value/Property
Number of heated rods	1008*
Number of unheated rods	96*
Heated length (m)	3.66
Diameter of heated rod (mm)	9.5
Diameter of unheated rod (mm)	12.24
Lattice	Square
Pitch (mm)	12.6
Maximum power (MW)	10.0
Axial peaking factor	1.495
Number of grid spacers (m)	9
Inner diameter of shroud (m)	0.514
Flow area (m ²)	0.1134

*In First Simulated Fuel Assembly, LSTF has 1064 heater rods and 104 unheated rods.

Table 8.1.1-2 Summary of test conditions

Test	Pressure (MPa)	Power (MW)	Heat flux (kW/m ²)	Exit Velocity Jg (m/s)
ST-VF-01A	1.0	0.5	4.5	0.425
ST-VF-01B	1.0	1.0	9.1	0.851
ST-VF-01C	1.0	2.0	18.2	1.702
ST-VF-01D	1.0	3.5	31.8	2.978
ST-NC-08E	2.4	1.426	13.0	0.566
ST-NC-01	7.3	3.57	30.7	0.553
ST-NC-06E	7.3	3.95	34.0	0.612
SB-CL-16L	7.3	5.0	43.0	0.774
ST-SG-04	7.35	7.17	61.7	1.104
ST-VF-01E	15.0	1.0	9.1	0.091
ST-VF-01F	15.0	0.5	4.5	0.045
ST-VF-01G	15.0	2.0	18.2	0.182
ST-VF-01H	15.0	4.0	36.3	0.363
TR-LF-03	17.2	0.94	7.2	0.080

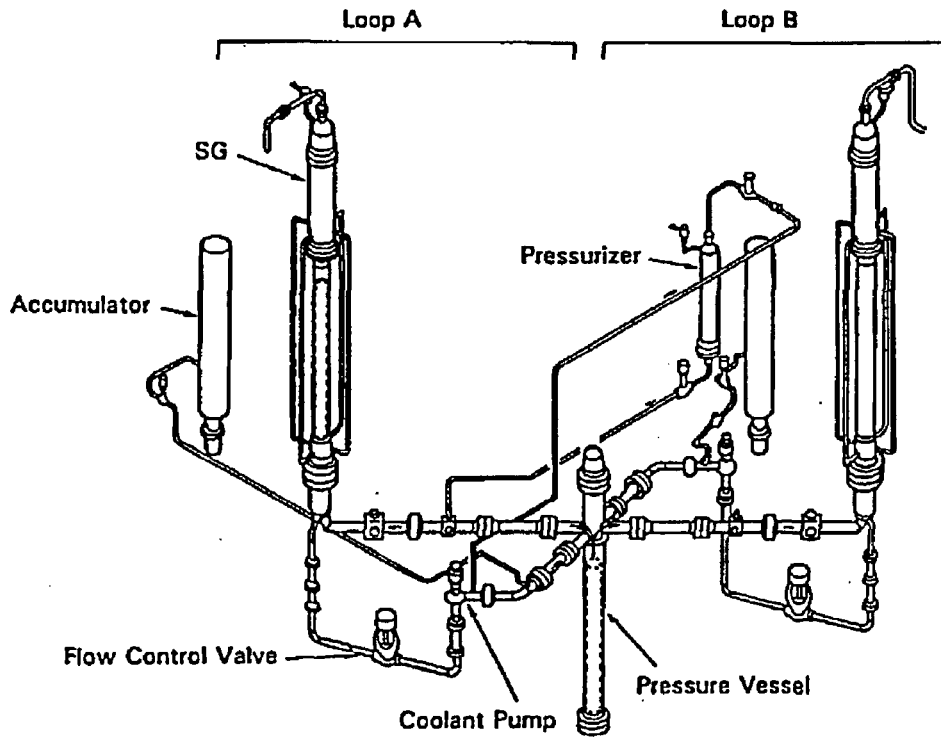


Figure 8.1.1-1 Schematic of ROSA-IV Large Scale Test Facility (LSTF)
(From JAERI-M 84-237)

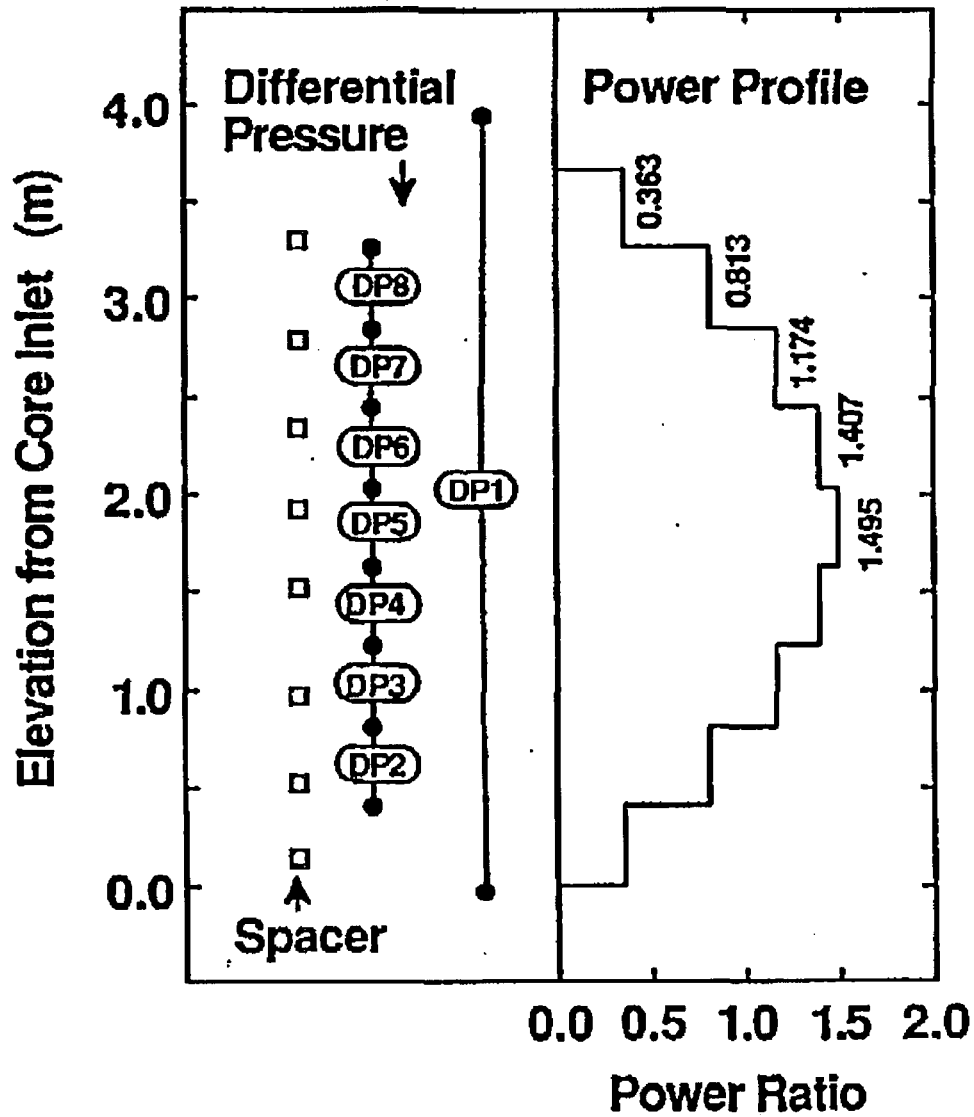


Figure 8.1.1-2 Axial power profile and locations of differential pressure Measurements and grid spacers

(From Ref. 8.1.1-1 "Void Fraction Distribution in Rod Bundle under High Pressure Conditions")

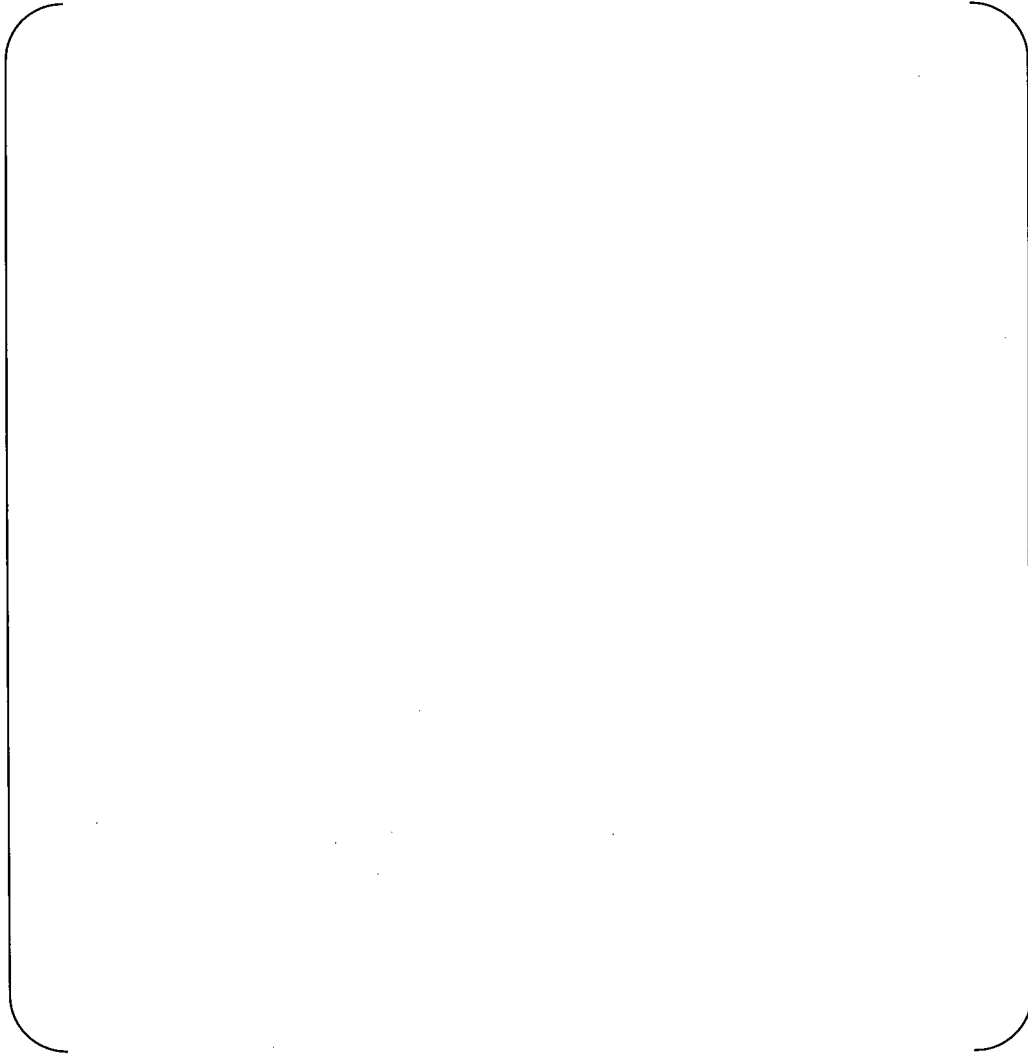


Figure 8.1.1-3 Schematic of M-RELAP5 modeling regions

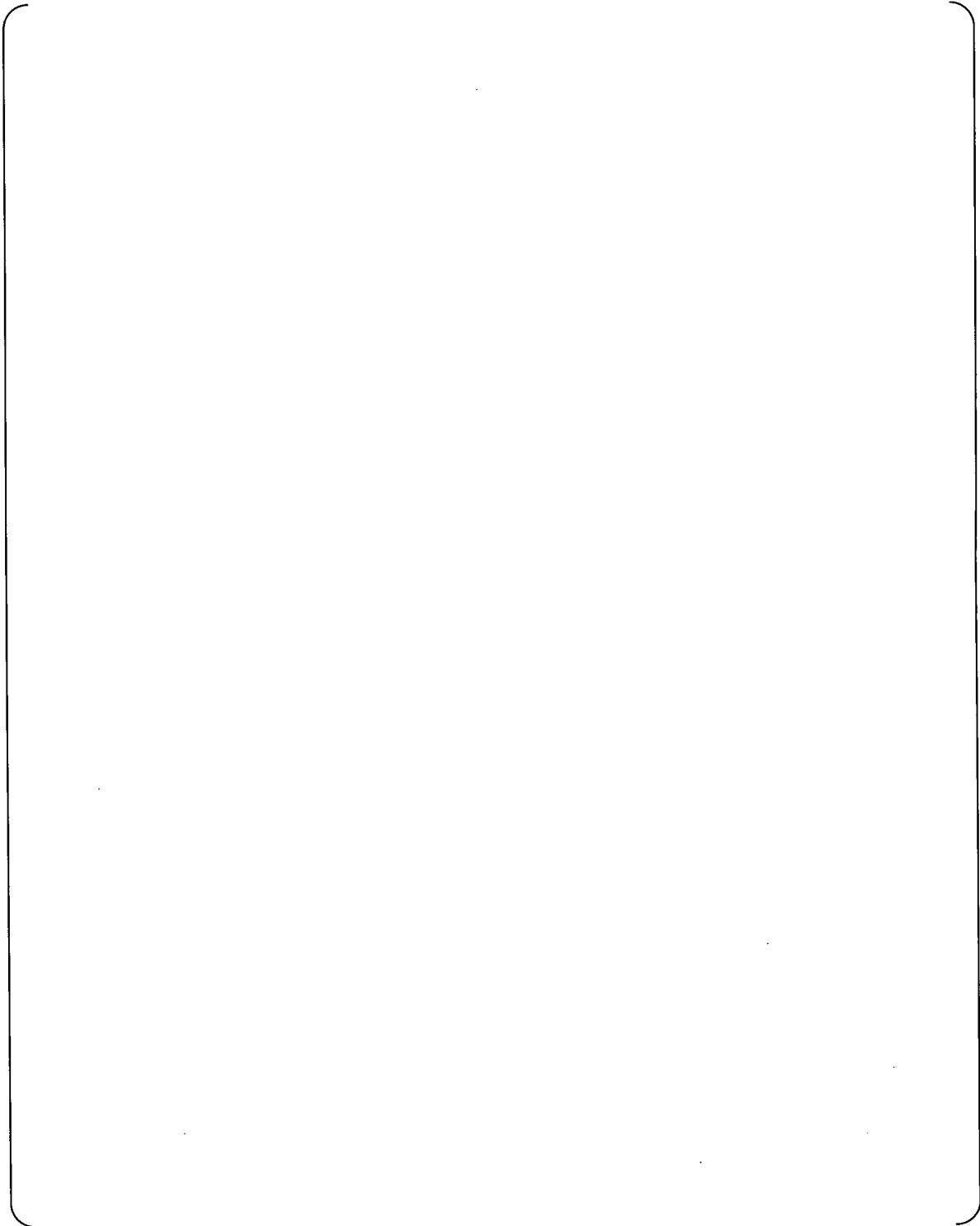


Figure 8.1.1-4 Nodalization of M-RELAP5 model

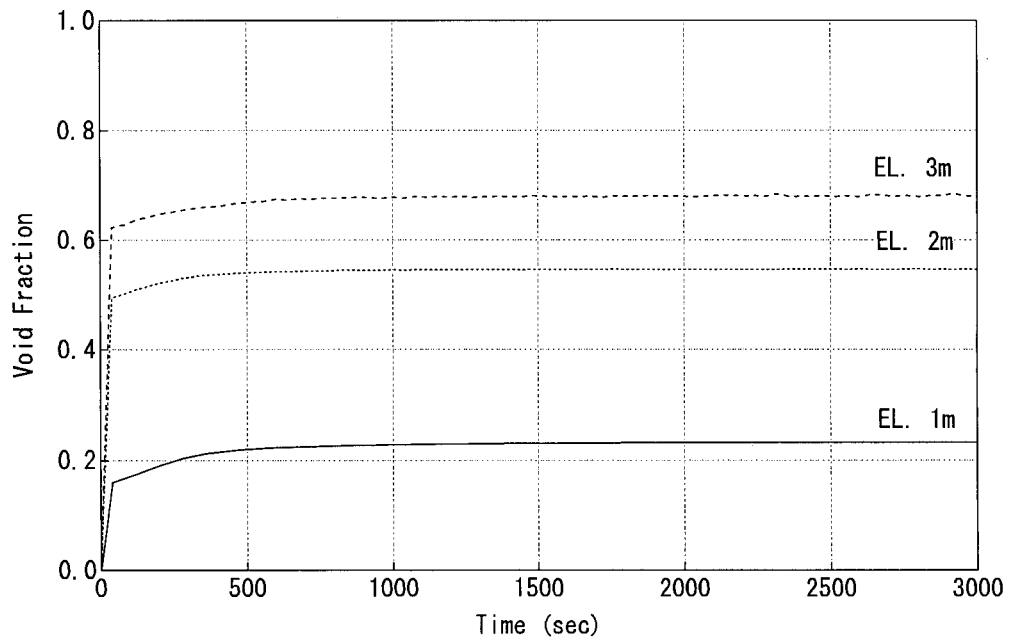


Figure 8.1.1-5 Simulated void fraction transient for test ST-NC-06E

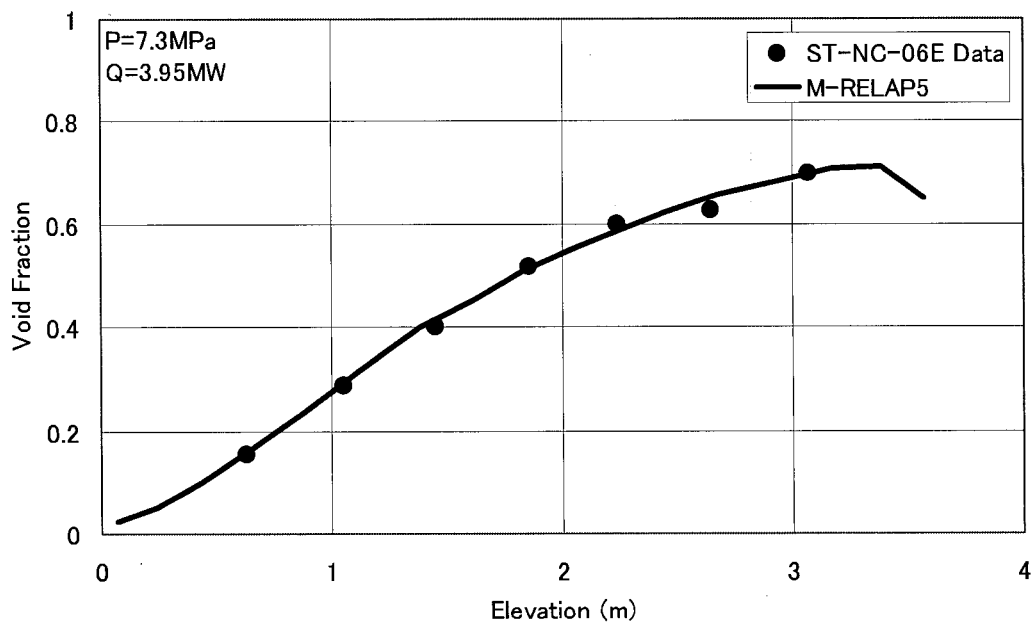


Figure 8.1.1-6 Simulated void fraction profile for test ST-NC-06E

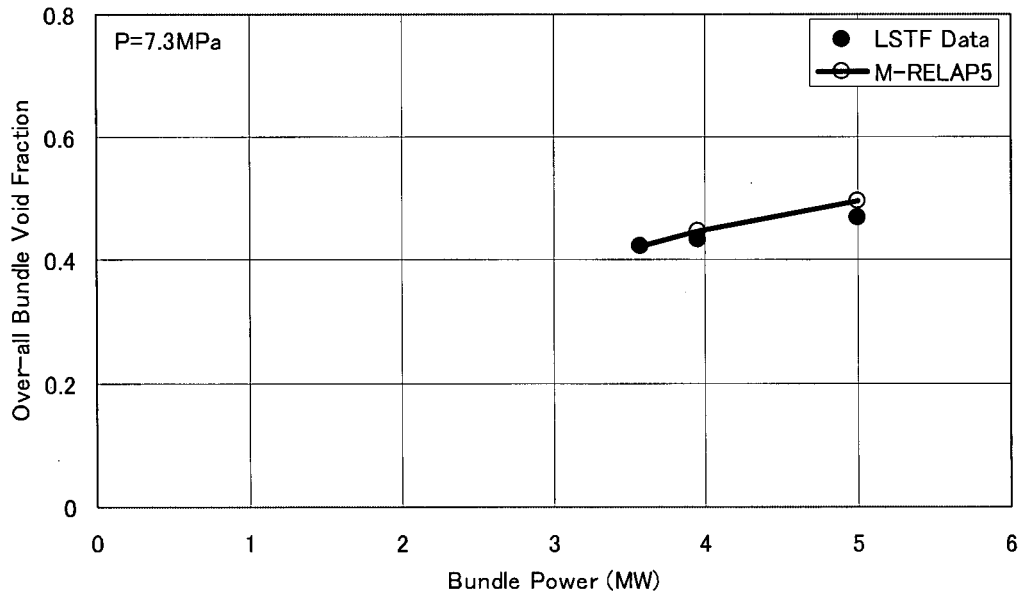


Figure 8.1.1-7 Simulated averaged void fraction profile for 7.3 MPa tests

8.1.2 ORNL/THTF Void Profile and Uncovered-Bundle Heat Transfer Tests

8.1.2.1 Introduction

Prediction of two-phase mixture level or void fraction profile in the core is important during the loop seal, boil-off, and recovery periods of a small break LOCA (SBLOCA). In these periods the two-phase mixture level can eventually drop into the core. The fuel rod is covered by high void fraction two-phase flow at the two-phase mixture level, and is essentially covered by single-phase vapor above the two-phase mixture level, and the fuel rod heat transfer becomes poor beyond the two-phase mixture level. As a result, the cladding temperature increases rapidly above the two-phase mixture level. On the other hand, good rod heat transfer can be maintained below the two-phase mixture level. Thus, prediction of the two-phase mixture level and void fraction profile near and below the two-phase mixture level is vital to accurate prediction of the peak cladding temperature (PCT) in a SBLOCA.

A series of small break experiments have been conducted in the Thermal Hydraulic Test Facility (THTF) at Oak Ridge National Laboratory (ORNL). These experiments include the two-phase mixture level swell tests and the uncovered-bundle heat transfer tests that were performed under quasi-steady state conditions. The axial void fraction profile was obtained from differential pressure measurements in the two-phase mixture level swell test, and the fuel rod simulator (FRS) temperatures and vapor temperatures above the mixture level were measured in the uncovered-bundle heat transfer test. These tests were used to assess the M-RELAP5 code applicability to the prediction of SBLOCA mixture levels, void fraction distributions and rod heat transfer.

The details of the test facility and test procedure are presented in References 8.1.2-1 and 8.1.2-2, which are summarized in the sections below.

8.1.2.2 Test Facility and Test Section

The THTF is a high-pressure-bundle thermal-hydraulics test loop. System configuration was designed to produce thermal-hydraulic conditions similar to those expected in a SBLOCA. It contained a 64-rod electrically heated bundle with identical dimensions typical of 17 x 17 PWR fuel assembly.

Figure 8.1.2-1 is an illustration of the THTF for a small-break test configuration. Flow leaves the

main coolant pump and passes directly into the lower plenum. Flow proceeds upward through the heated bundle and exits through the bundle outlet spool piece. Spool piece measurements include pressure, temperature, density, volumetric flow, and momentum flux. On leaving the orifice manifold, flow passes through a heat exchanger and returns to the pump inlet. System pressure is controlled via the loop pressurizer.

The THTF test section contains a 64-rod electrically heated bundle. Figure 8.1.2-2 is a cross section of the test section. The test bundle is placed in the shroud box. Rod diameter and pitch are typical of a 17 x 17 fuel assembly. The four unheated rods are designed to represent control-rod guide tubes in a nuclear fuel assembly. Figure 8.1.2-3 is a cross section of a typical FRS. The FRS has stainless steel cladding and an Inconel heating element and the FRS is filled with boron nitride as a high temperature insulating material.

Figure 8.1.2-4 is an axial profile of the THTF bundle that illustrates the positions of spacer grids and FRS thermocouples. The heated length is 3.66 m (12 ft), and a total of 25 FRS thermocouple levels are distributed over that length. The upper third of the bundle is more heavily instrumented than the lower portion, since for most tests the two-phase mixture level was in the top 1/3 of the heated length. In addition to the FRS thermocouples, fluid temperatures are measured at a number of locations. Two-phase mixture level and void fraction profile were obtained through the use of thermocouple and differential pressure cell measurements. Figure 8.1.2-5 illustrates the differential pressure measurement locations.

8.1.2.3 Test Procedure and Test Matrix

After the desired loop temperature and pressure had been established by accumulating pump heat in the primary flow circuit, the test section flow was reduced to a predetermined level, and bundle power was applied. The two-phase mixture level swell tests or the uncovered-bundle heat transfer tests were started by boiling off water from the bundle, which was originally filled with water. Excess volume was accumulated in the pressurizer, and nitrogen was vented from the pressurizer to maintain constant pressure. Eventually, the THTF settled into a quasi-steady state with the bundle partially uncovered and inlet flow just sufficient to make up for the liquid being vaporized. Measurements were made at this steady state condition. The bundle power was adjusted to produce peak FRS temperatures of about 1033 K, imposed by safety limits.

The test conditions of the two-phase mixture level swell tests are listed in Table 8.1.2-1. The test bundle was uncovered for the first six tests 3.09.10I-N. Three experiments were run at

roughly 4MPa, and three experiments at roughly 7MPa. The three experiments at each pressure level were designed to span a range of linear heat powers. The two-phase mixture level was not established in the bundle and the bundle was covered with two-phase water for the remaining six tests 3.09.10AA-FF. The pressure conditions of these tests were same as the first six tests.

In SBLOCA transients, the first core uncover during the loop seal period is expected to occur when the RCS pressure is relatively high, and the second core uncover during the boil-off period is expected to occur when the RCS pressure is relatively low, which is about the accumulator pressure. The THTF two-phase mixture level swell tests cover the expected range of pressure conditions in the US-APWR SBLOCAs.

The uncovered-bundle heat transfer tests were conducted at the same time under the same condition as the two-phase mixture level tests for the six uncovered-bundle tests 3.09.10I to N.

8.1.2.4 M-RELAP5 Model for THTF Void Profile and Uncovered-Bundle Heat Transfer Tests

Figure 8.1.2-6 shows the M-RELAP5 noding diagram for the ORNL/THTF. [

]

Of the uncovered-bundle tests 3.09.10I to N, tests 3.09.10I and L are not adopted as validation

tests because they have a higher liner power/rod compared with that of the US-APWR SBLOCA transient.

For cases with low linear power, the heat loss to the environment from the rod bundle and housing was significant and could affect the experimental results. [

]

8.1.2.5 M-RELAP5 Results for THTF Void Profile Tests

The void profiles based on readings of the differential pressure cells and those calculated using M-RELAP5 are compared in Figures 8.1.2-7, 11, 15 and 19 for tests 3.09.10J, K, M and N, and in Figures 8.1.2-23 to 28 for tests 3.09.10AA to FF, respectively. The M-RELAP5 calculated void fraction profiles, in general, agree well with the experimental data, and in most cases the calculated void fractions are slightly larger than the experimental values. For the small liner power case 3.09.10 K, M-RELAP5 calculated void fraction is smaller than that of experimental data below the mixture level and rises sharply to 1.0 to catch up with the experimental data above the mixture level. This behavior is caused by the effect of heat loss boundary condition for the shroud box outer surface modeled as described in section 8.1.2.4. Although Reference 8.1.2-2 says that heat loss in the upper portion of the steam-cooling region were greater than in the lower portion and that as a result the rate of vapor temperature rise with elevation decrease in the upper portion of the steam-cooling region, [

] and

thus, the rate of void fraction increase is smaller below the mixture level and greater above the mixture level in the M-RELAP5 calculation than that of experimental data.

The comparison of the bundle collapsed levels is shown in Figure 8.1.2-29. The calculated bundle collapsed levels agree well with the experimental data. This means that the interfacial momentum exchange model incorporated in the M-RELAP5 code is adequate to predict

SBLOCA core behaviors.

8.1.2.6 M-RELAP5 Results for THTF Uncovered-Bundle Heat Transfer Tests

Comparison of void fraction, FRS surface temperature, vapor temperature and heat transfer coefficient between measurement and M-RELAP5 calculation for tests 3.09.10J, K, M and N is presented in Figures 8.1.2-7 to 22

As indicated in the previous section, calculated void profiles reasonably agree with measured values. The post-CHF FRS surface heat transfer coefficient and temperature also, in general, reasonably agree with measured values and show slightly conservative results for tests 3.09.10J and M. The vapor temperature in the experiment was calculated from an energy balance and the measured bundle exit steam temperature. The predicted steam temperature by the M-RELAP5 code reasonably agrees with the experimental data. This means that the rod heat transfer model by vapor convection incorporated in the M-RELAP5 is adequate to predict SBLOCA core behaviors.

There are dips in rod surface temperature and leaps in heat transfer coefficient downstream of a grid spacer for the experiments. M-RELAP5 has no mechanism to increase the heat transfer coefficients downstream of grids, and the calculated rod surface temperatures show no dips.

Figures 8.1.2-11, 19 and 28 show a small dip in the calculated void profile. As described in reference 8.1.2-3, this inversion occurs when the flow regime changes from bubbly/slug flow to mist flow and thereby interfacial drag coefficient becomes small. Although this phenomenon stems from a short cell length and an increase in the vapor velocity, the calculated rod surface temperatures show no dip and reasonably reproduce the experimental results.

The two-phase mixture levels defined in Reference 8.1.2-2, indicated in Figures 8.1.2-8, 12, 16 and 20, were identified by observing the average temperature at the FRS thermocouple levels and were assumed to be midway between the highest level where the average temperature indicated nucleate boiling and the lowest level where the average temperature indicated CHF. The two-phase mixture level was defined from the experimental data such that nucleate boiling is maintained and rod surface temperatures are close to the saturation temperature below this level and CHF occurs then the temperature excursion occurs above this level. As shown in Figures 8.1.2-8, 12, 16, and 20, the rod surface temperature distributions predicted by the M-RELAP5 code match well this description.

The accurate prediction of the two-phase mixture level is also essential for a SBLOCA analysis. The comparison of the predicted and measured two-phase mixture level is made in Figure 8.1.2-30, and it is noted from this comparison that the M-RELAP5 code reasonably predicts the two-phase mixture level beyond which the rod temperature start to increase.

Figures 8.1.2-31 and 32 show a sensitivity study (sensitivity 1) in which the rod power is raised to 1.2 times the nominal power, assuming application of Appendix K in the SBLOCA analysis for the US-APWR. The results show large conservativeness in the mixture level and rod surface temperature predictions.

8.1.2.7 Conclusion

The accurate prediction of the two-phase mixture level is important to predict the PCT in a SBLOCA. The M-RELAP5 code was assessed by the comparison with the ORNL/THTF the two-phase mixture level swell test and the uncovered-bundle heat transfer test. The assessment showed that the M-RELAP5 code reasonably predicts these parameters.

The accurate prediction of the rod heat transfer above the two-phase mixture level is also important to predict the PCT in a SBLOCA. The M-RELAP5 code was assessed by the comparison with the ORNL/THTF uncover-bundle heat transfer test. The assessment showed that the M-RELAP5 code reasonably predicts the rod heat transfer above the two-phase mixture level.

8.1.2.8 References

- 8.1.2-1 D. K. Felde et al., "Facility Description – THTF MOD 3 ORNL PWR BDHT Separate-Effects Program," NUREG/CR-2640, ORNL/TM-7842, September 1982.
- 8.1.2-2 T. M. Anklam, R. J. Miller, and M. D. White, "Experimental Investigations of Uncovered-Bundle Heat Transfer and Two-Phase Mixture Level Swell Under

High-Pressure Low Heat-Flux Conditions," NUREG/CR-2456, ORNL-5848, March 1982.

8.1.2-3 D. G. Morris, C. B. Mullins, and G. L. Yoder, "An Analysis of Transient Film Boiling Of High-Pressure Water In A Rod Bundle," NUREG/CR-2469, ORNL/NUREG-85 Rev.2, March 1982.

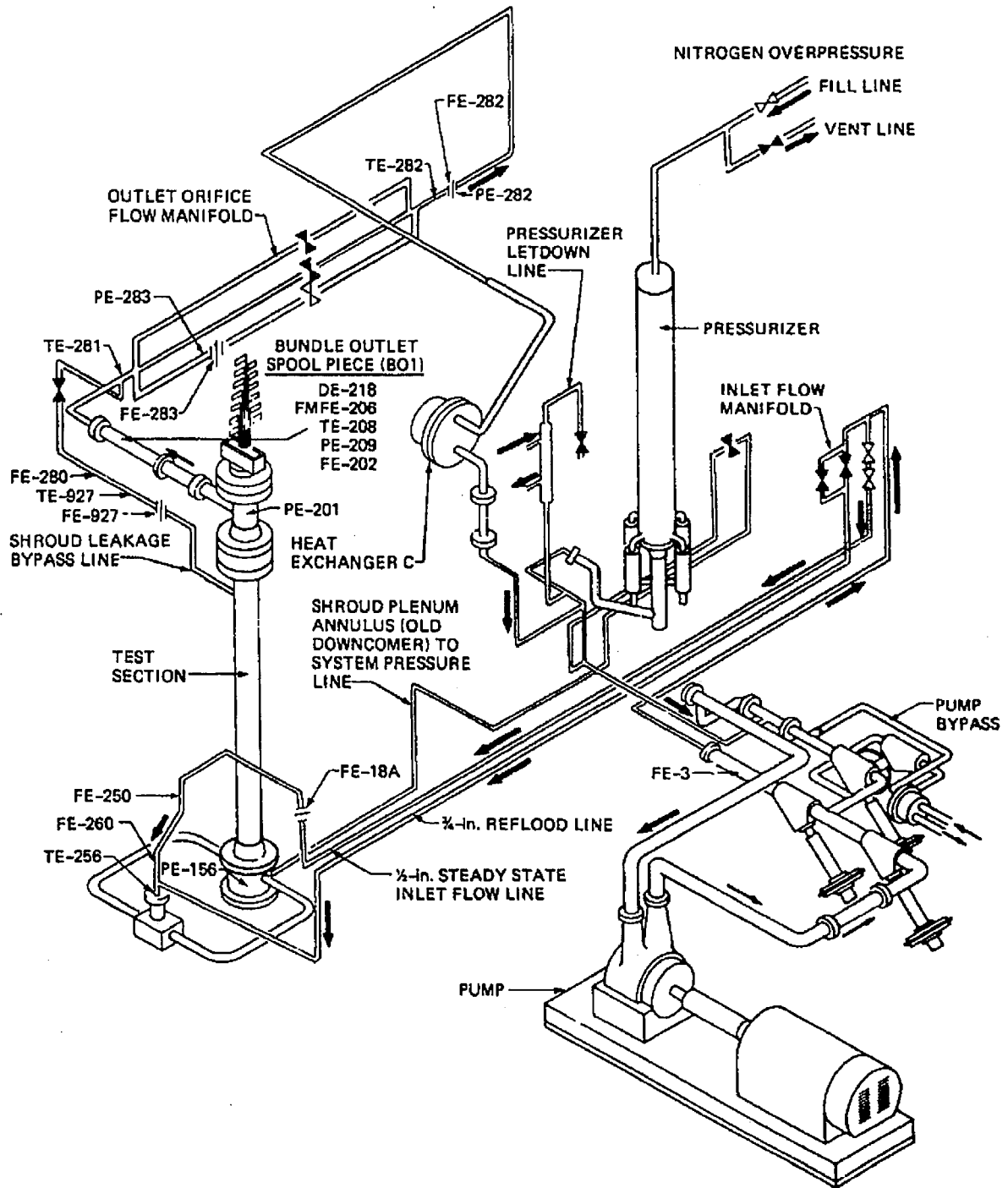
8.1.2-4 A S. Shieh, V. H. Ransom, and R. Krishnamurthy, "RELAP5/MOD3 Code Manual Volume 6:Validation of Numerical Techniques in RELAP5/MOD3.0," NUREG/CR-5535 Rev.1-Vol.VI, December 2001.

**Table 8.1.2-1 ORNL/THTF 3.09.10 Series ;
Void Profile and Uncovered-Bundle Heat Transfer Test Conditions**

Reference 8.1.2-2

Test	Pressure (MPa)	Mass flux (kg/s·m ²)	Inlet temperature (Subcooling) (K)		Liner heat power (kW/m)	Fractional heat loss
I	4.50	29.76	473.0	(57.6)	2.22	0.018
J	4.20	12.93	480.3	(46.1)	1.07	0.052
K	4.01	2.22	466.5	(57.2)	0.32	0.176
L	7.52	29.11	461.3	(102.6)	2.17	0.017
M	6.96	13.38	474.4	(84.2)	1.02	0.042
N	7.08	4.33	473.1	(86.7)	0.47	0.162
AA	4.04	21.15	450.9	(73.2)	1.27	0.020
BB	3.86	9.44	458.2	(63.2)	0.64	0.034
CC	3.59	7.22	467.6	(49.6)	0.33	0.035
DD	8.09	19.82	453.4	(115.5)	1.29	0.030
EE	7.71	11.00	455.9	(109.7)	0.64	0.039
FF	7.53	4.83	451.4	(112.6)	0.32	0.092

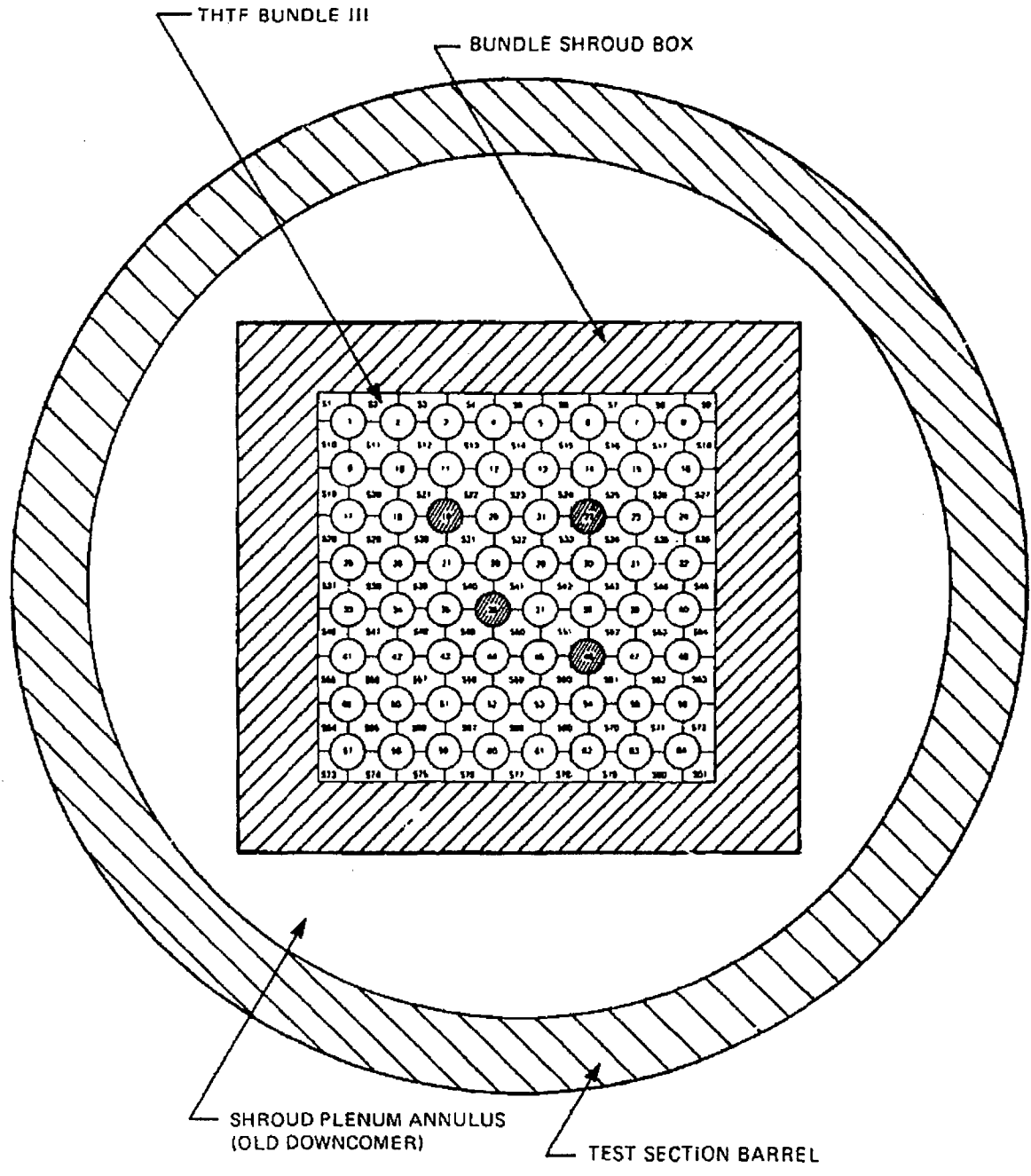
ORNL -DWG B1-7837R ETD



Reference 8.1.2-2

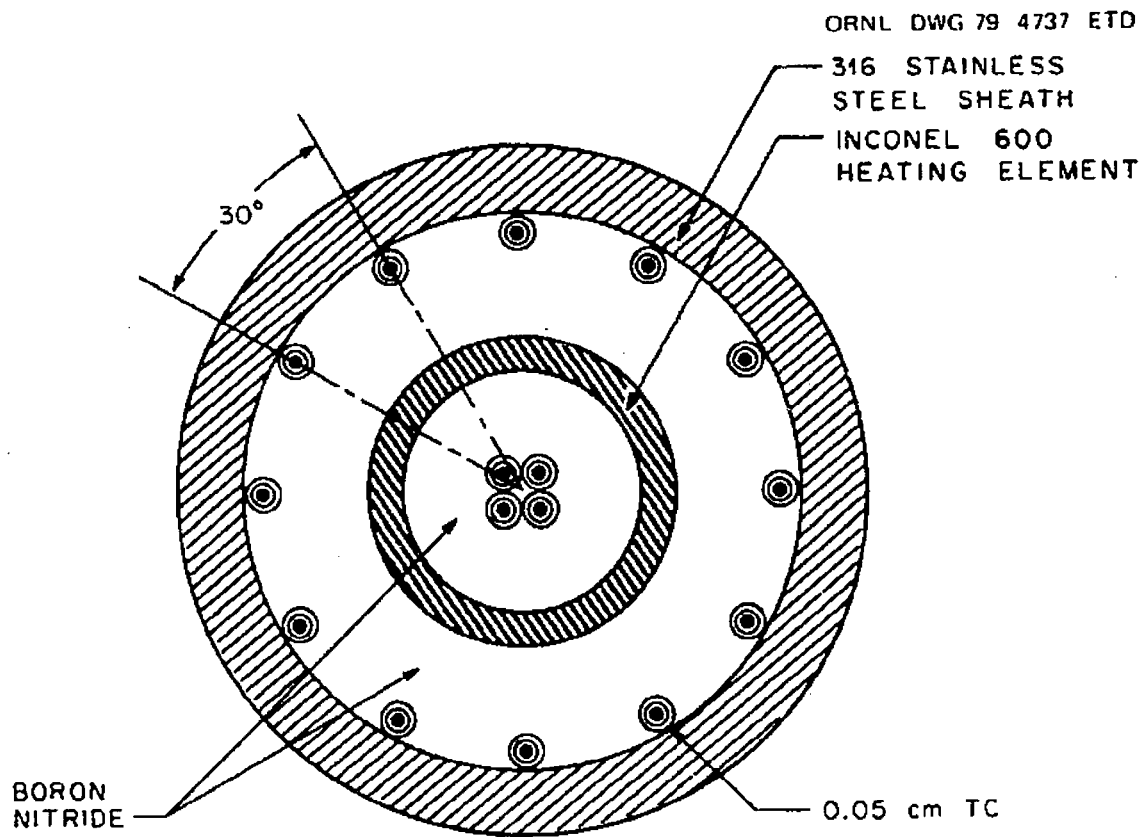
Figure 8.1.2-1 THTF in Small-Break Test Configuration

ORNL-DWG 82-4875 ETD



Reference 8.1.2-2

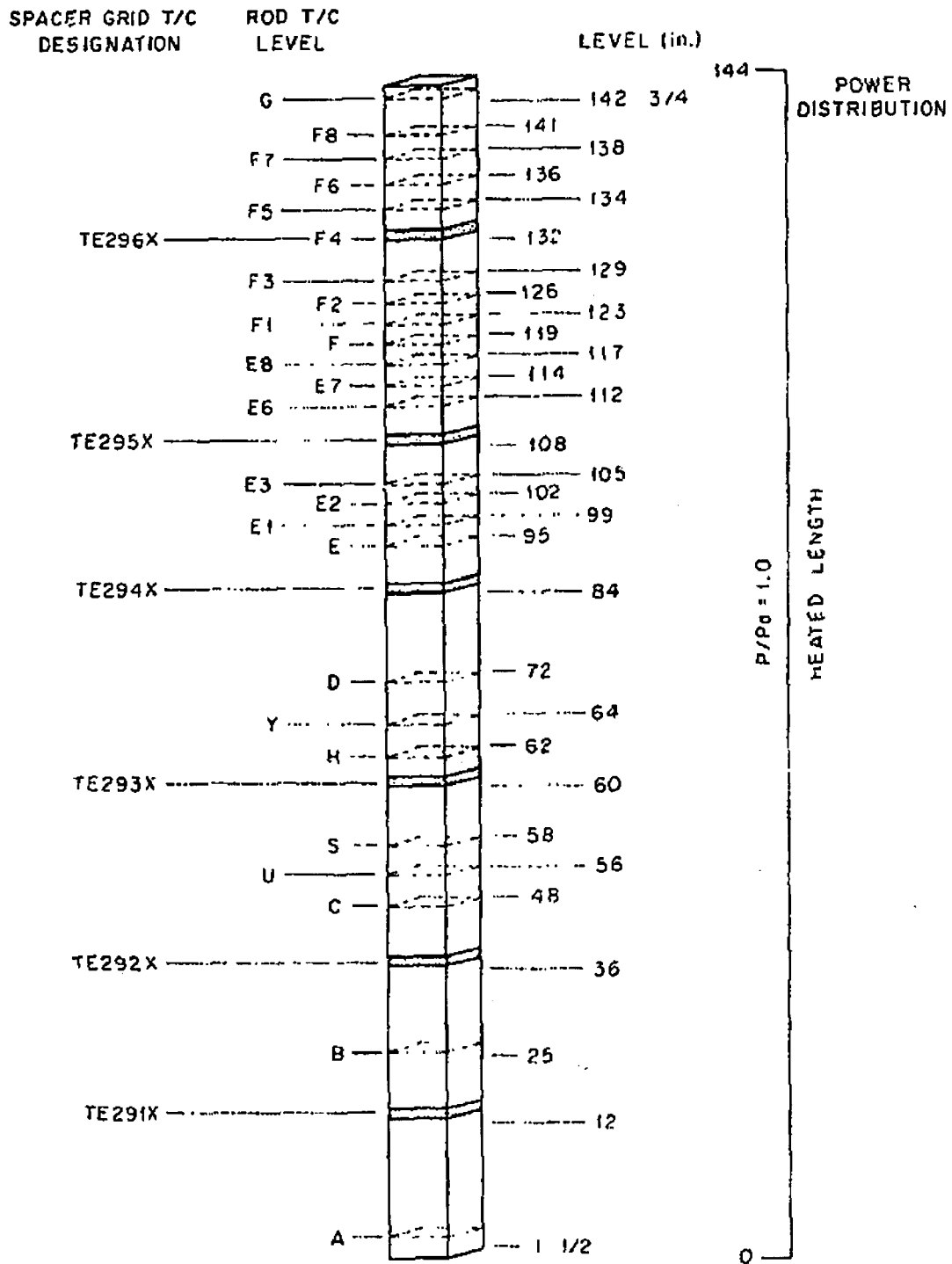
Figure 8.1.2-2 Cross Section of THTF Test Section



Reference 8.1.2-2

Figure 8.1.2-3 Cross Section of a typical Fuel Rod Simulator

ORNL-DWG 81-20288 ETD



Reference 8.1.2-2

Figure 8.1.2-4 Axial Location of Spacer Grids and FRS Thermocouples

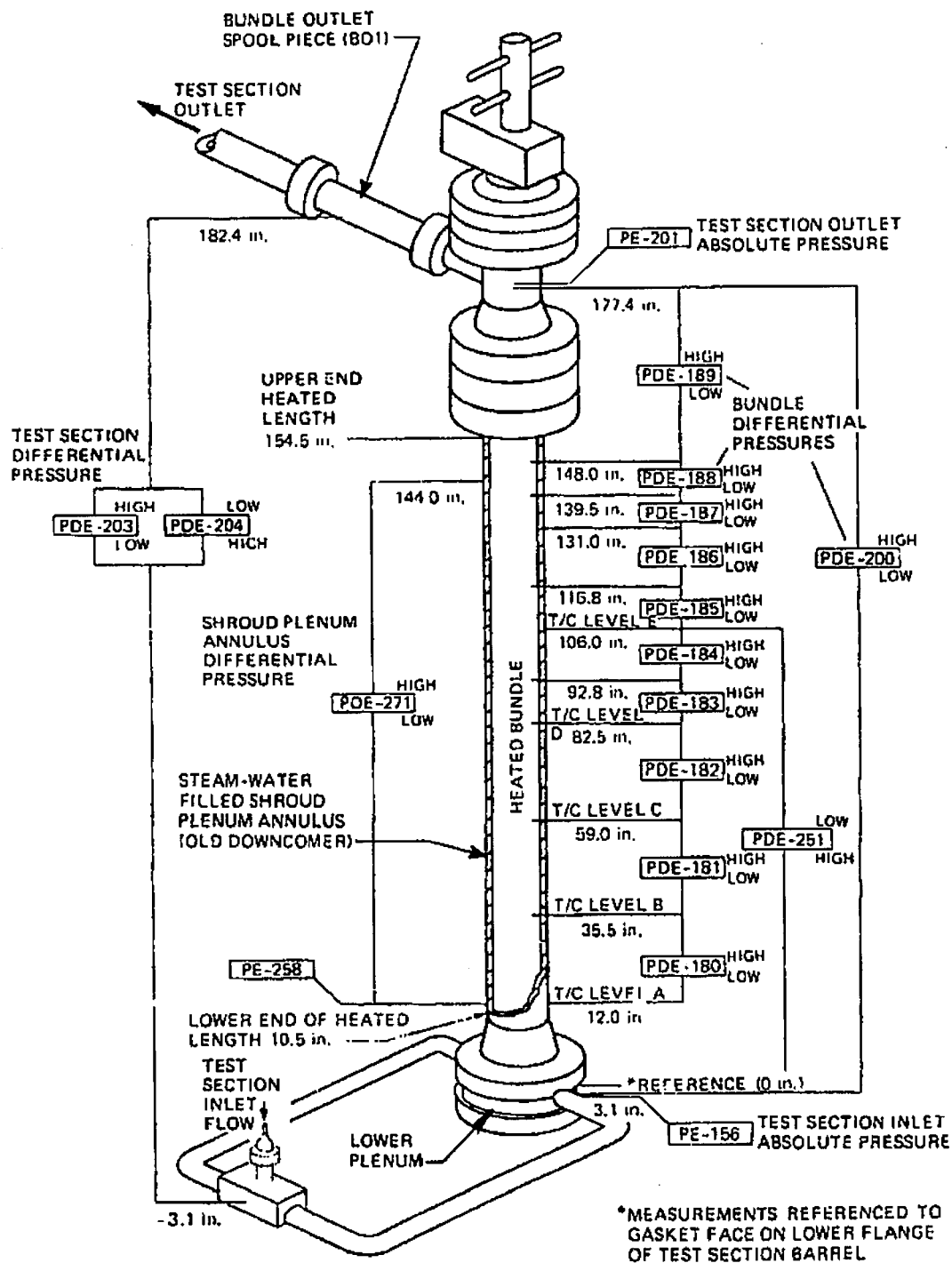


Figure 8.1.2-5 THTF In-Bundle Pressure Instrumentation

Reference 8.1.2-2

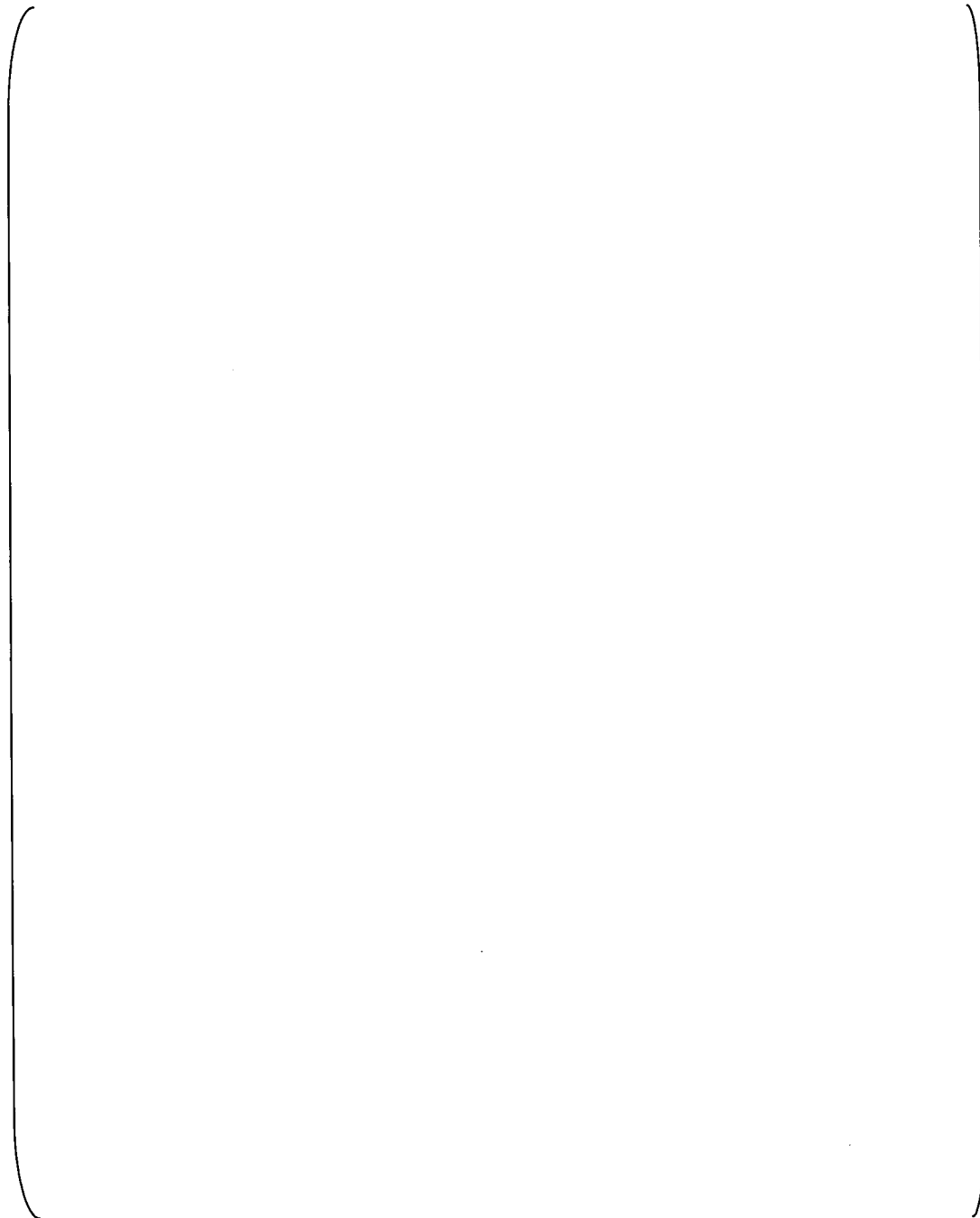


Figure 8.1.2-6 M-RELAP5 Noding Scheme for ORNL/THTF Tests

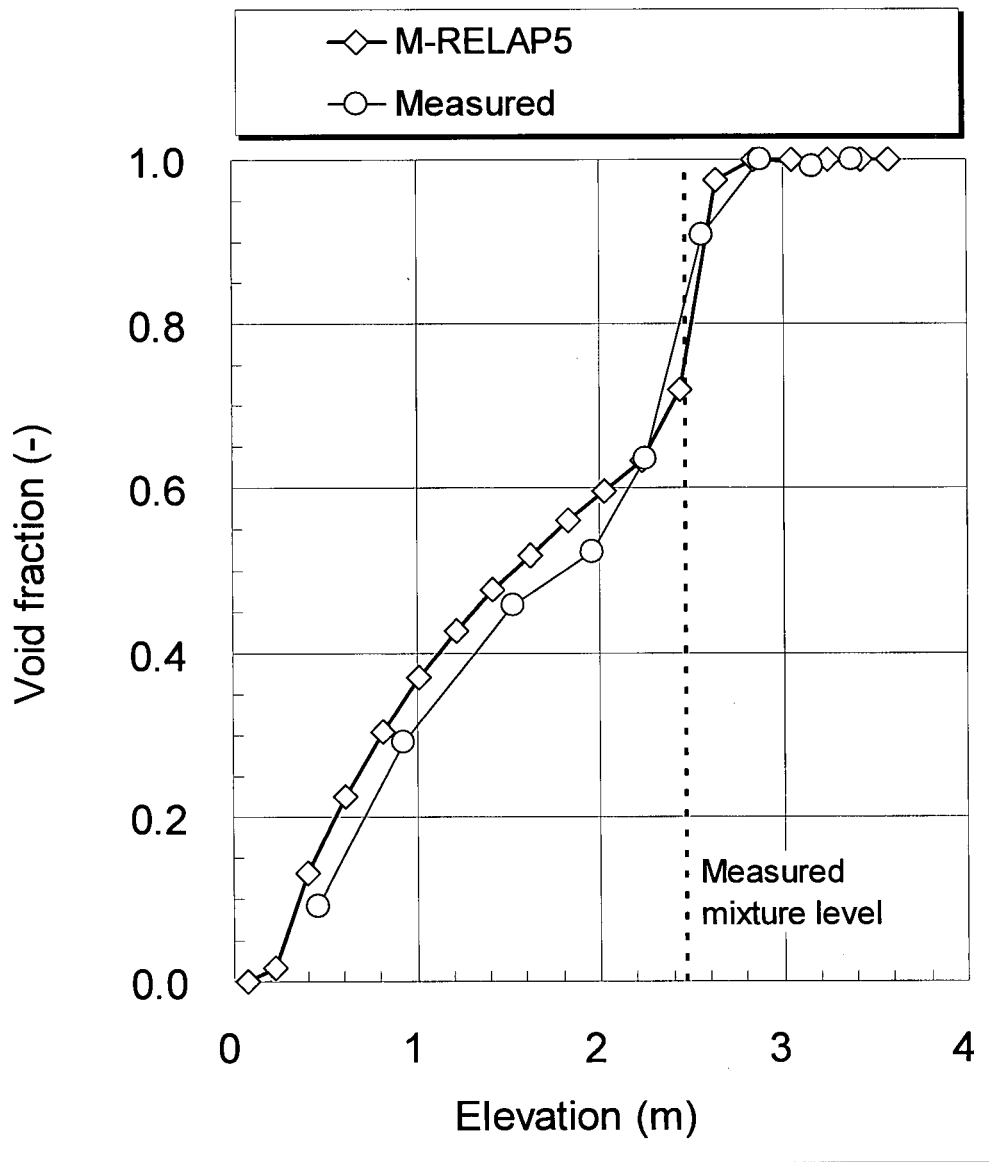


Figure 8.1.2-7 Comparison of Predicted and Measured Void Fraction Profiles for ORNL/THTF Test 3.09.10J

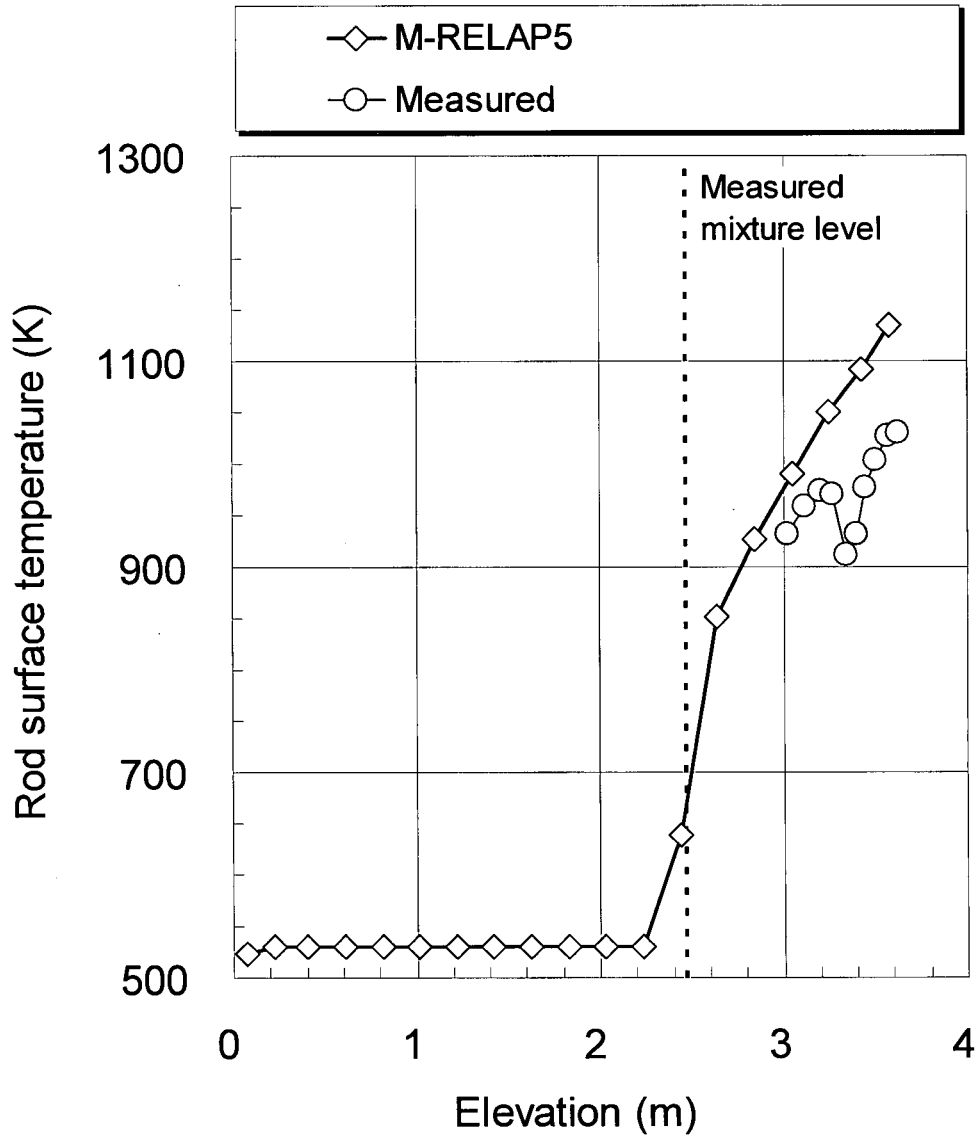


Figure 8.1.2-8 Comparison of Predicted and Measured FRS Surface Temperature Profiles for ORNL/THTF Test 3.09.10J

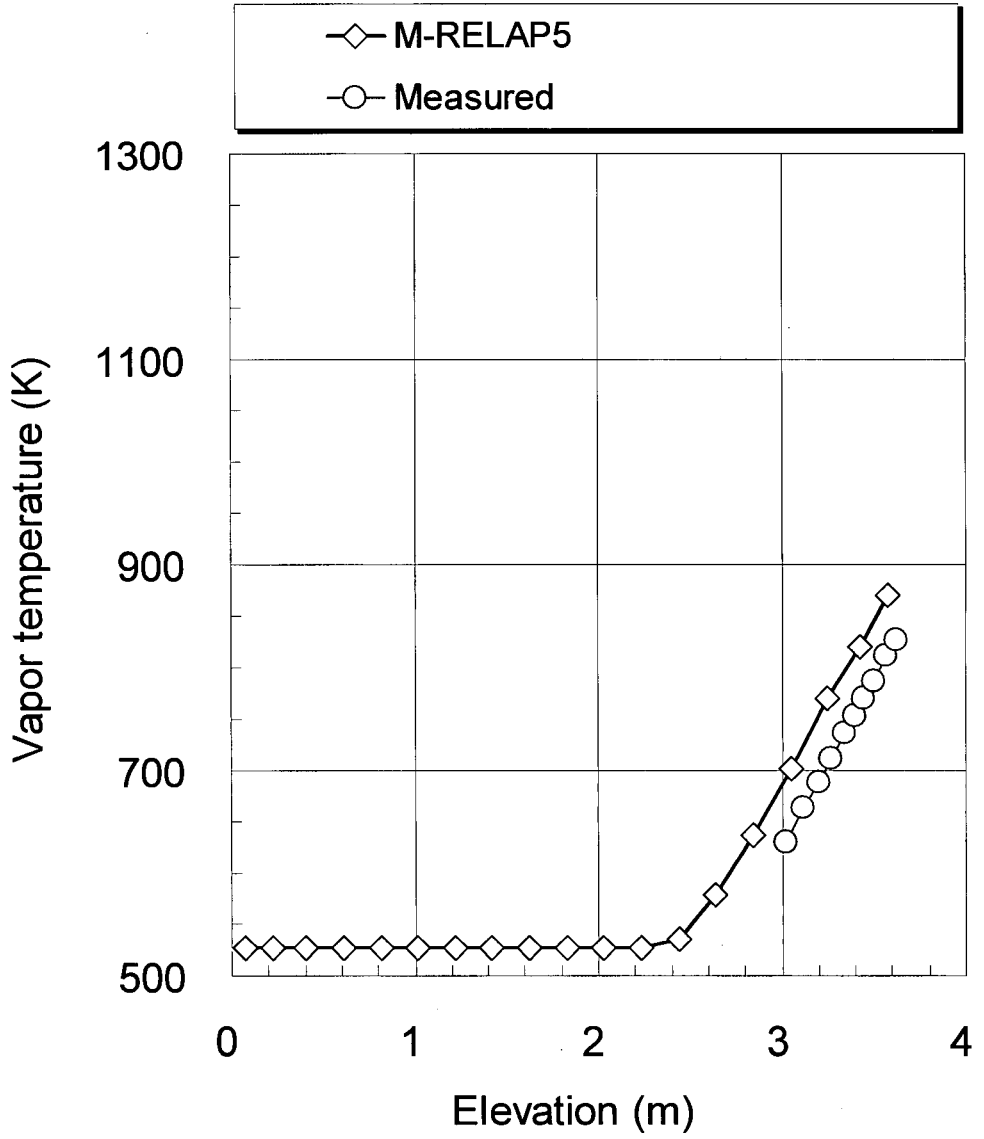


Figure 8.1.2-9 Comparison of Predicted and Measured Vapor Temperature Profiles for ORNL/THTF Test 3.09.10J

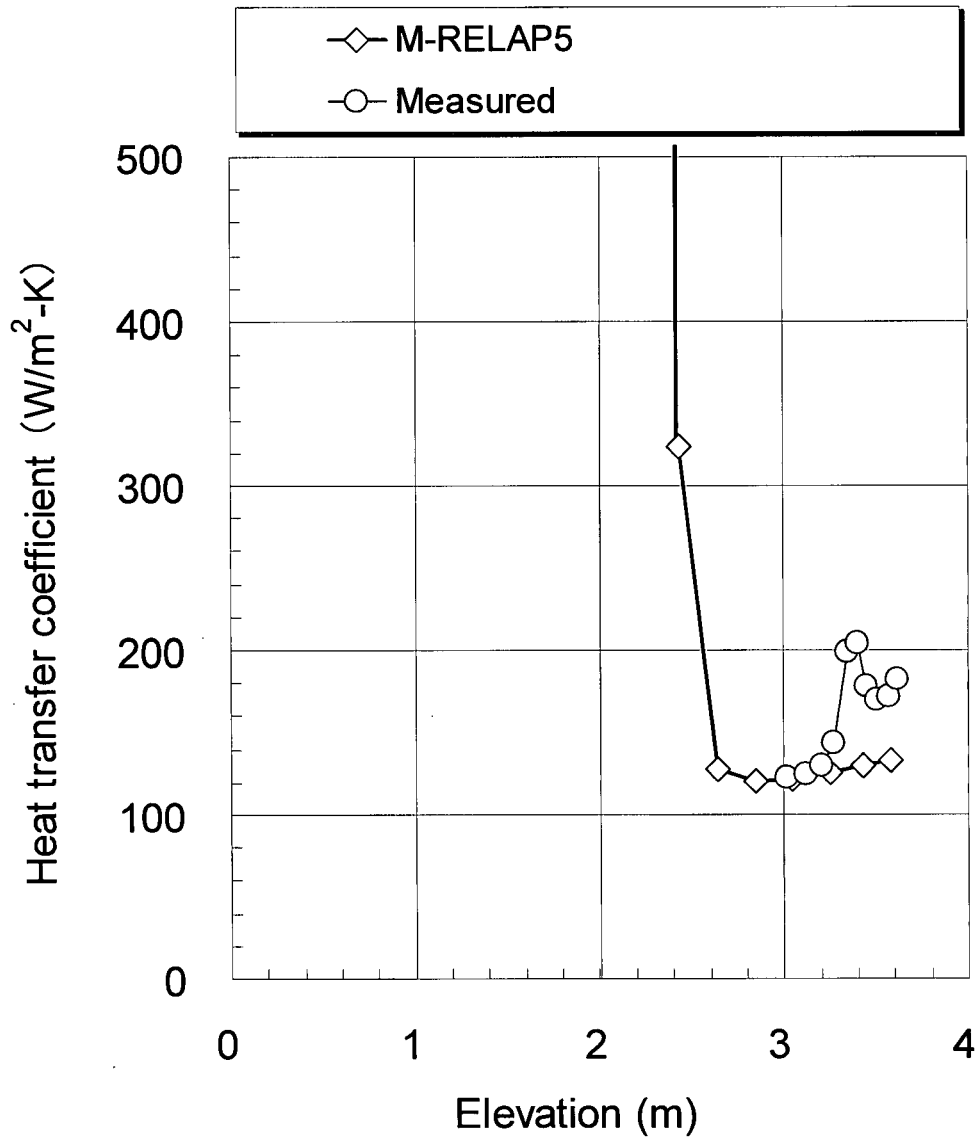


Figure 8.1.2-10 Comparison of Predicted and Measured Heat Transfer Coefficient Profiles for ORNL/THTF Test 3.09.10J

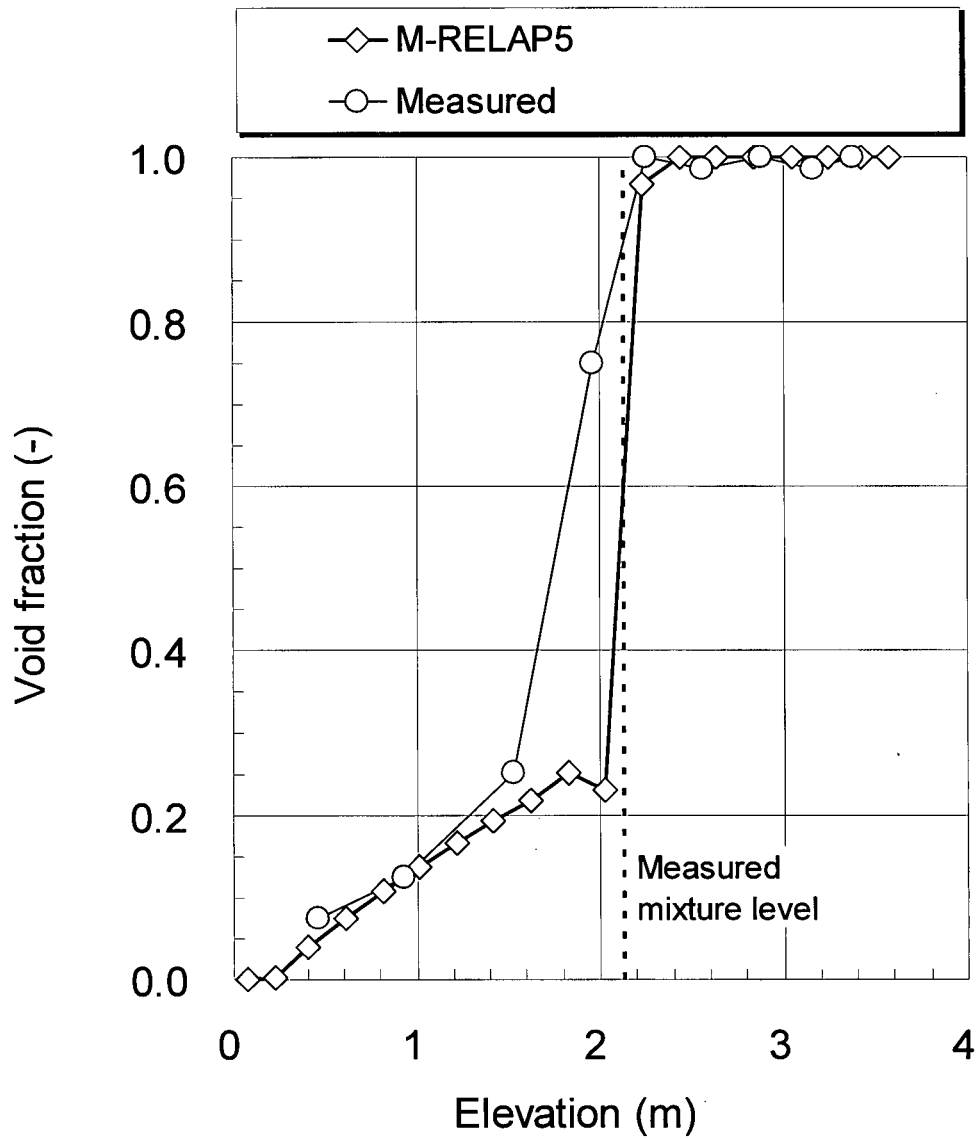


Figure 8.1.2-11 Comparison of Predicted and Measured Void Fraction Profiles for ORNL/THTF Test 3.09.10K

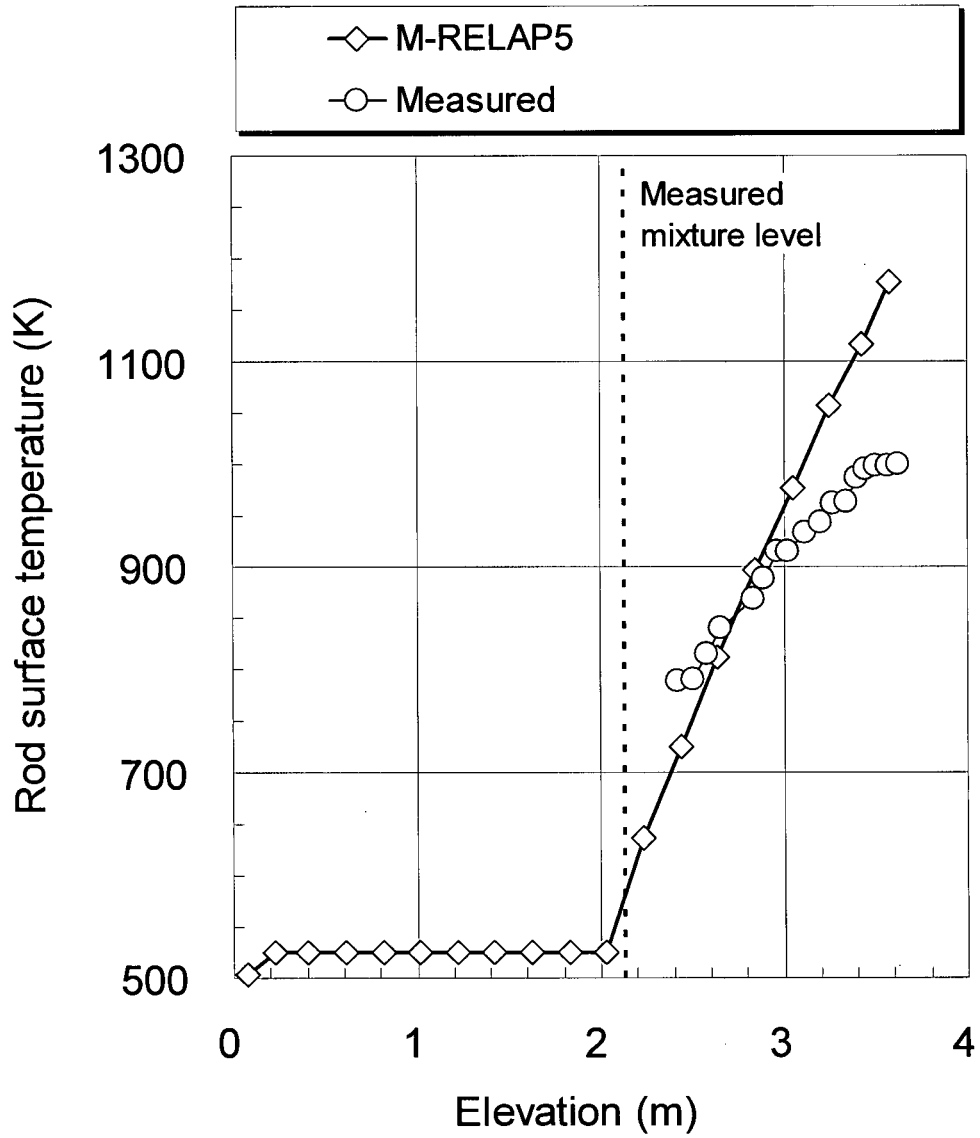


Figure 8.1.2-12 Comparison of Predicted and Measured FRS Surface Temperature Profiles for ORNL/THTF Test 3.09.10K

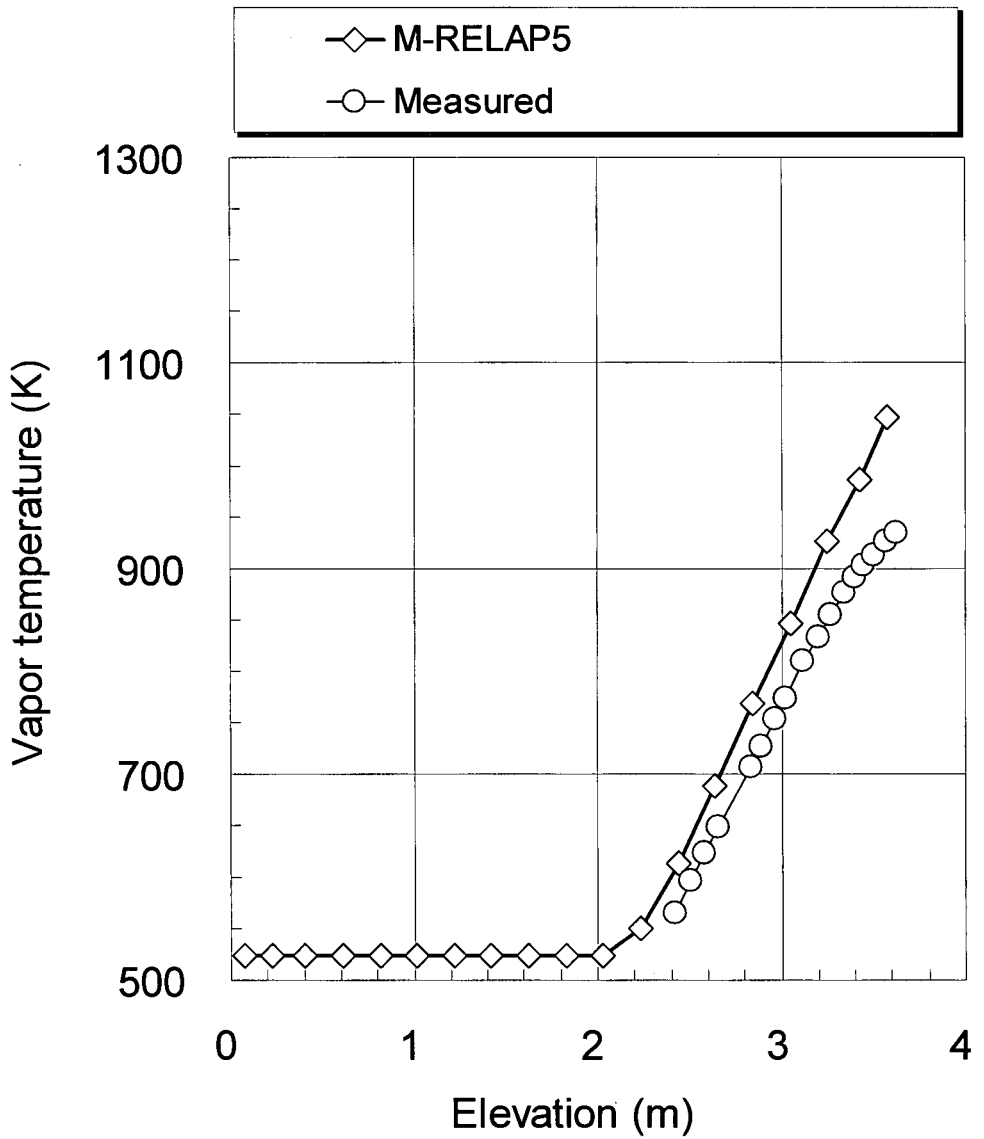


Figure 8.1.2-13 Comparison of Predicted and Measured Vapor Temperature Profiles for ORNL/THTF Test 3.09.10K

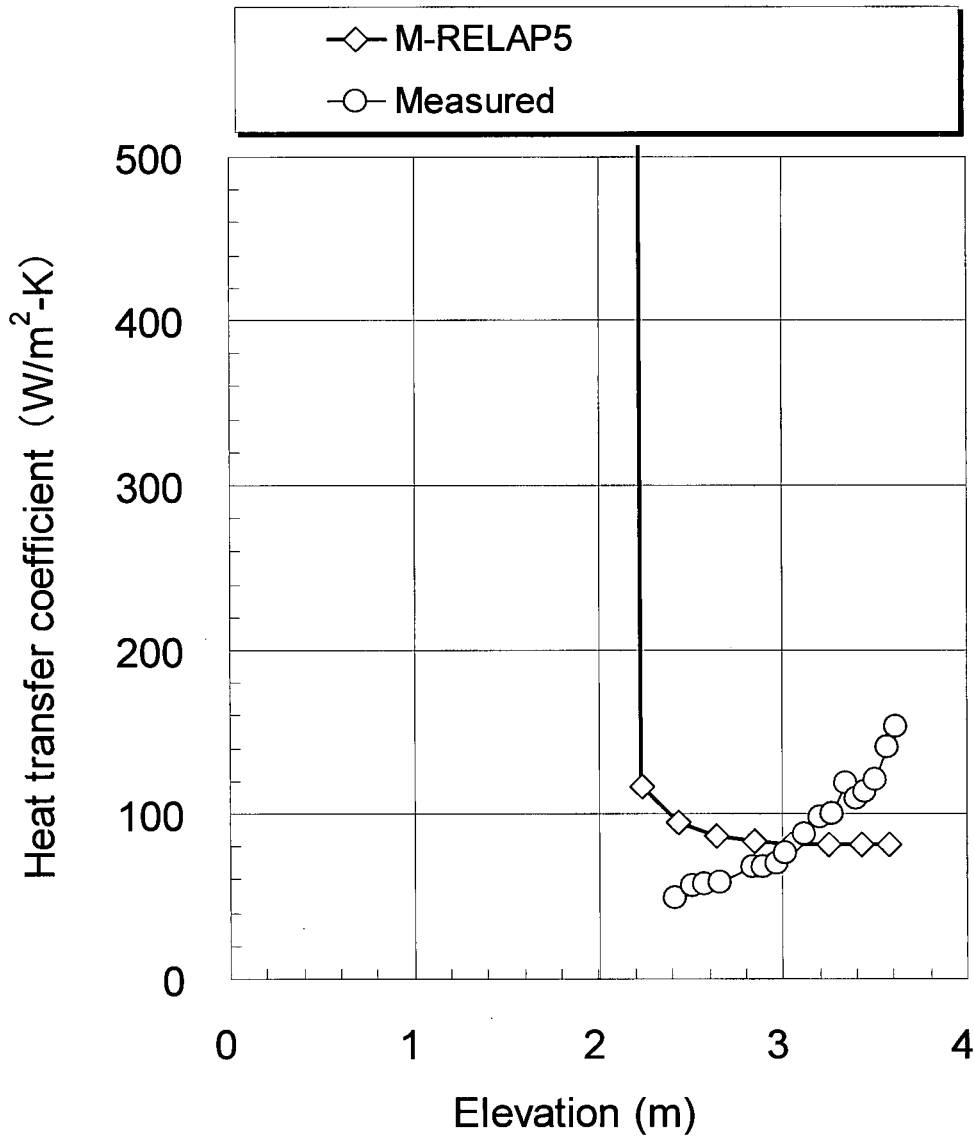


Figure 8.1.2-14 Comparison of Predicted and Measured Heat Transfer Coefficient Profiles for ORNL/THTF Test 3.09.10K

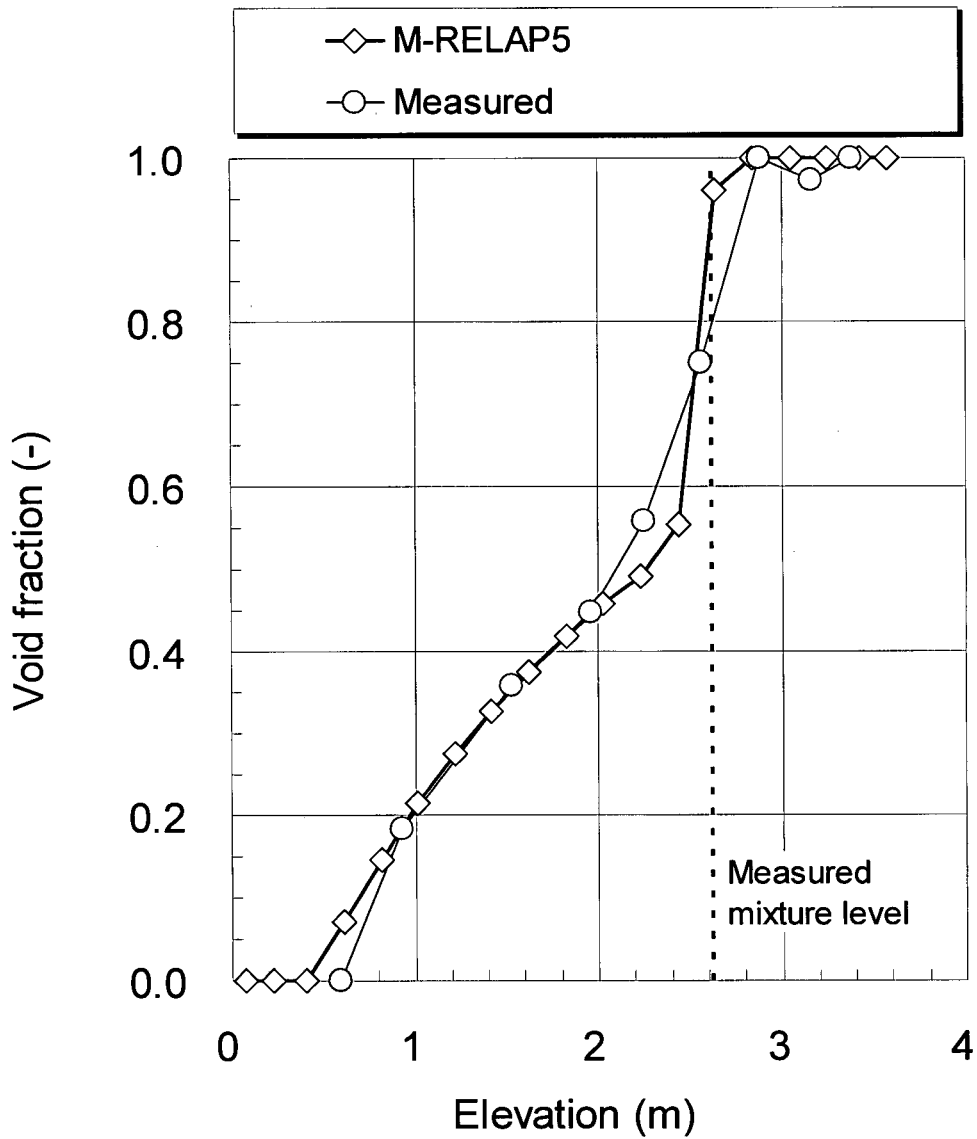


Figure 8.1.2-15 Comparison of Predicted and Measured Void Fraction Profiles for ORNL/THTF Test 3.09.10M

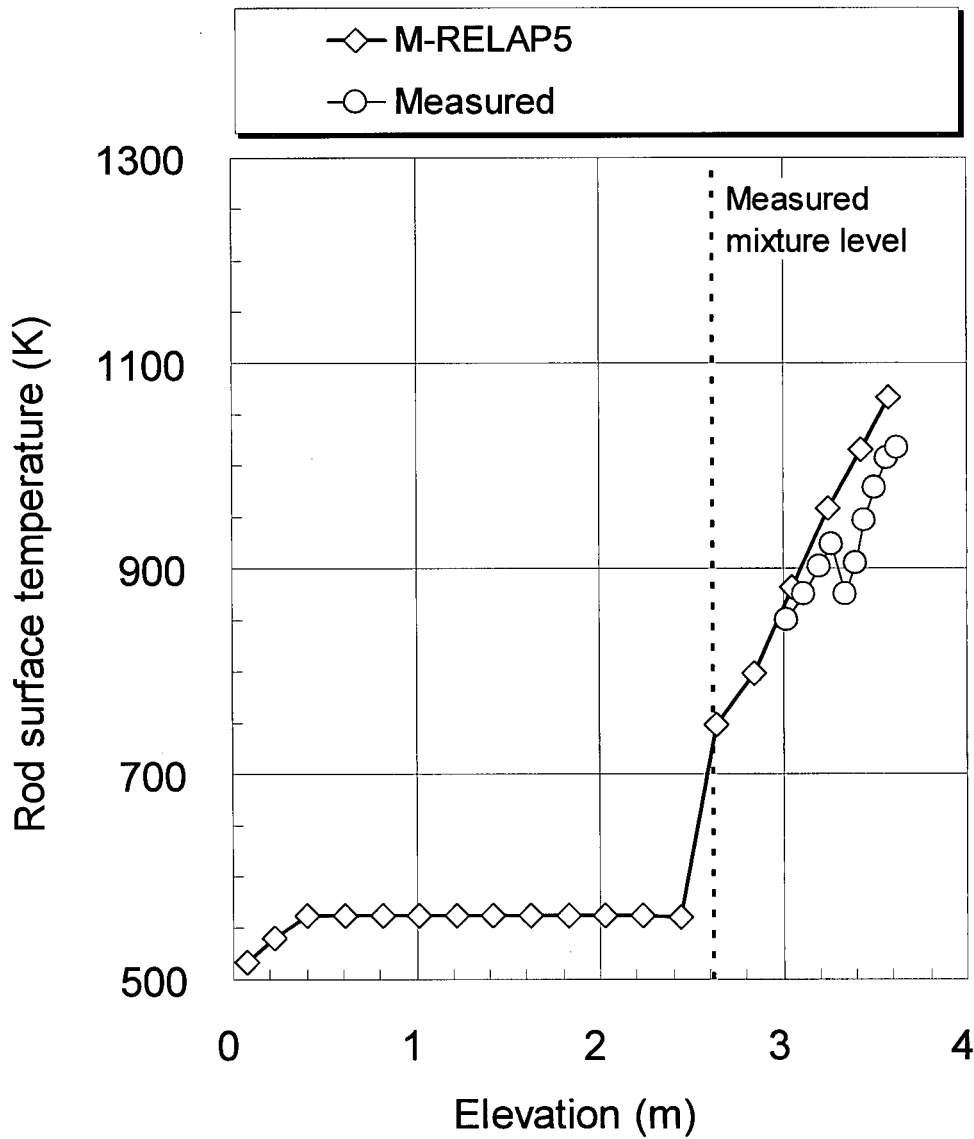


Figure 8.1.2-16 Comparison of Predicted and Measured FRS Surface Temperature Profiles for ORNL/THTF Test 3.09.10M

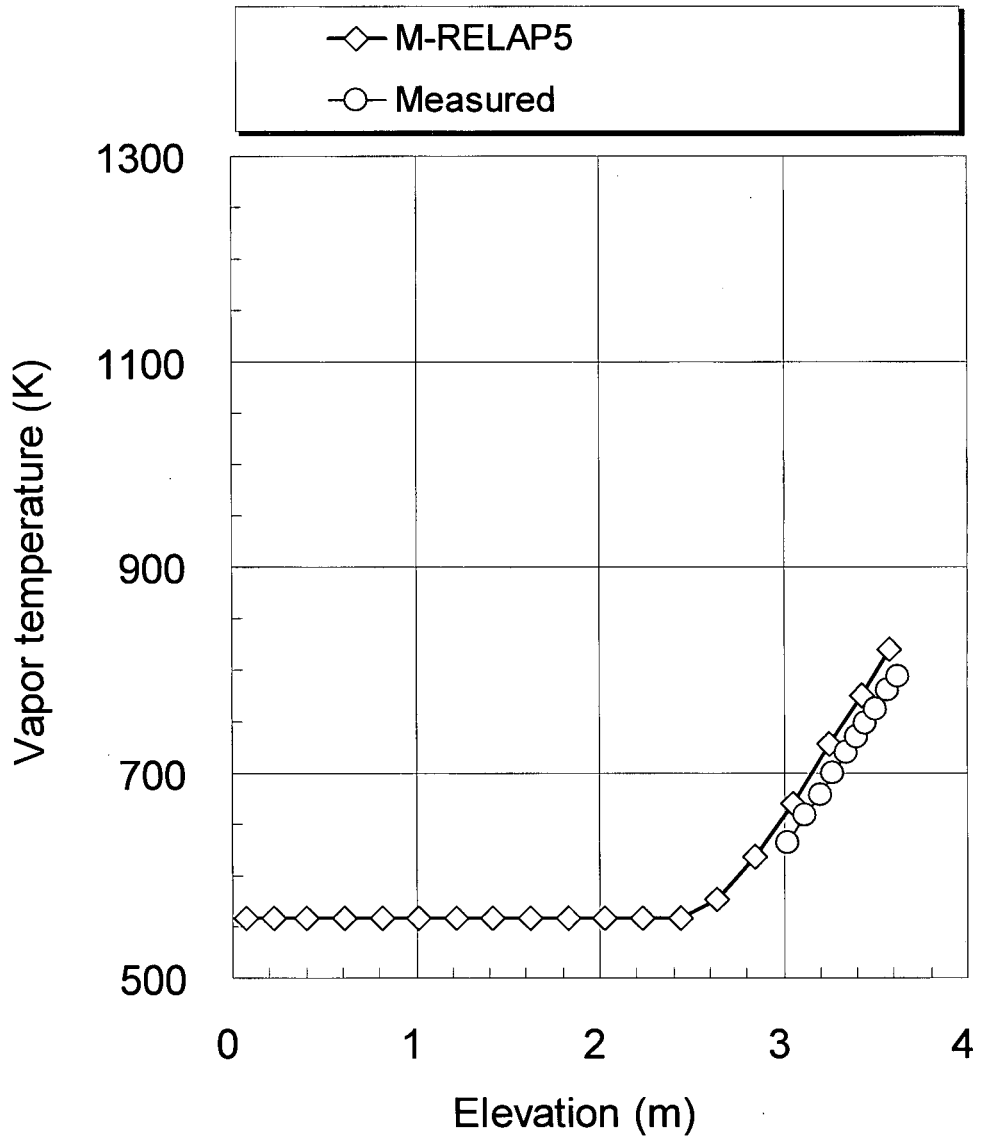


Figure 8.1.2-17 Comparison of Predicted and Measured Vapor Temperature Profiles for ORNL/THTF Test 3.09.10M

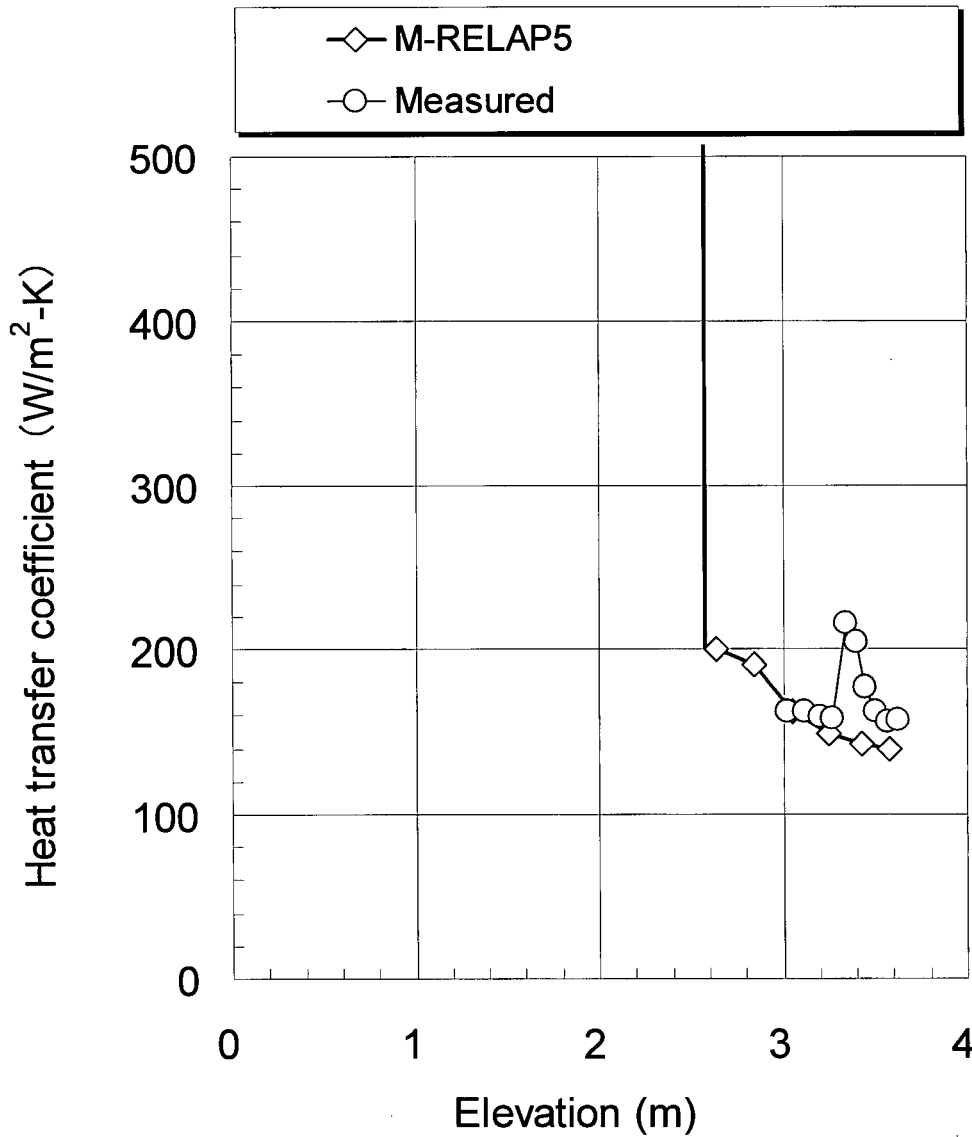


Figure 8.1.2-18 Comparison of Predicted and Measured Heat Transfer Coefficient Profiles for ORNL/THTF Test 3.09.10M

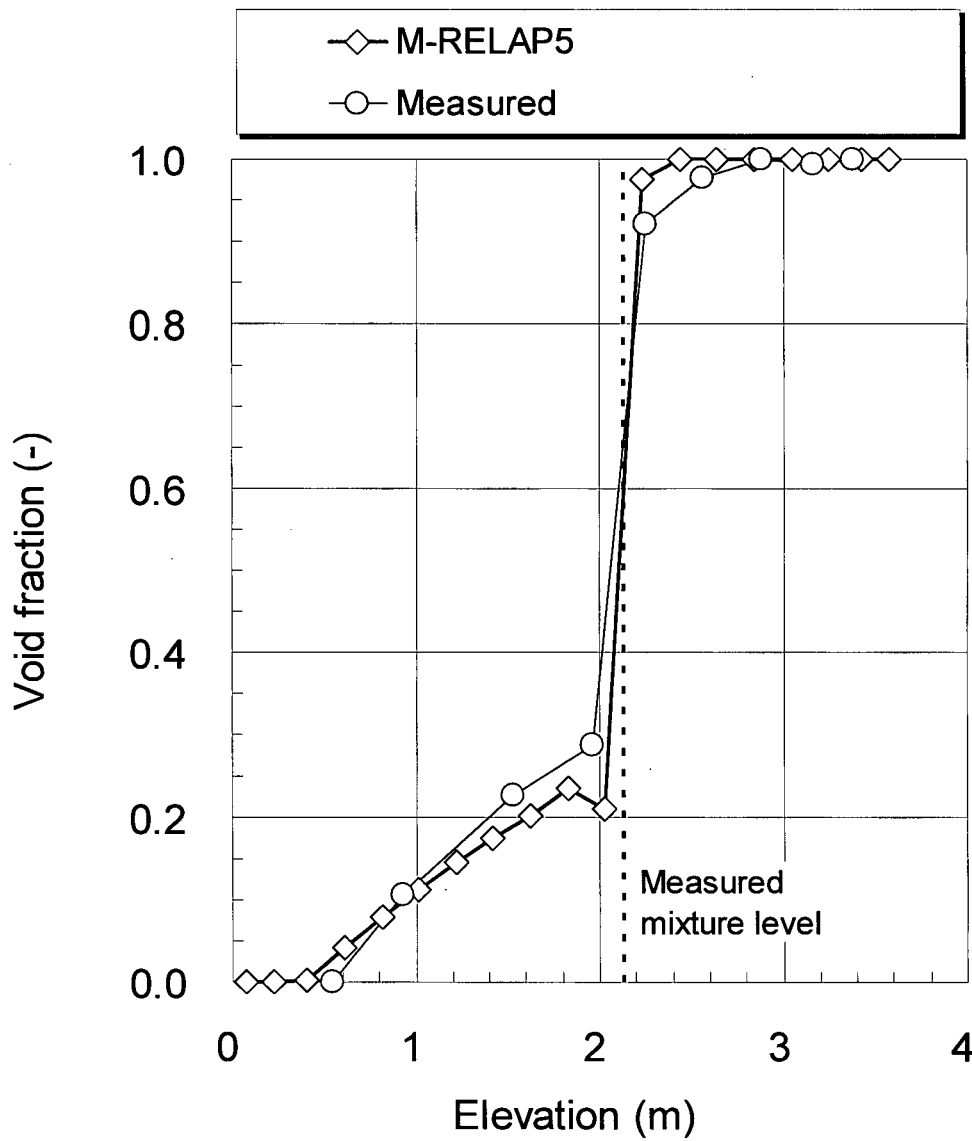


Figure 8.1.2-19 Comparison of Predicted and Measured Void Fraction Profiles for ORNL/THTF Test 3.09.10N

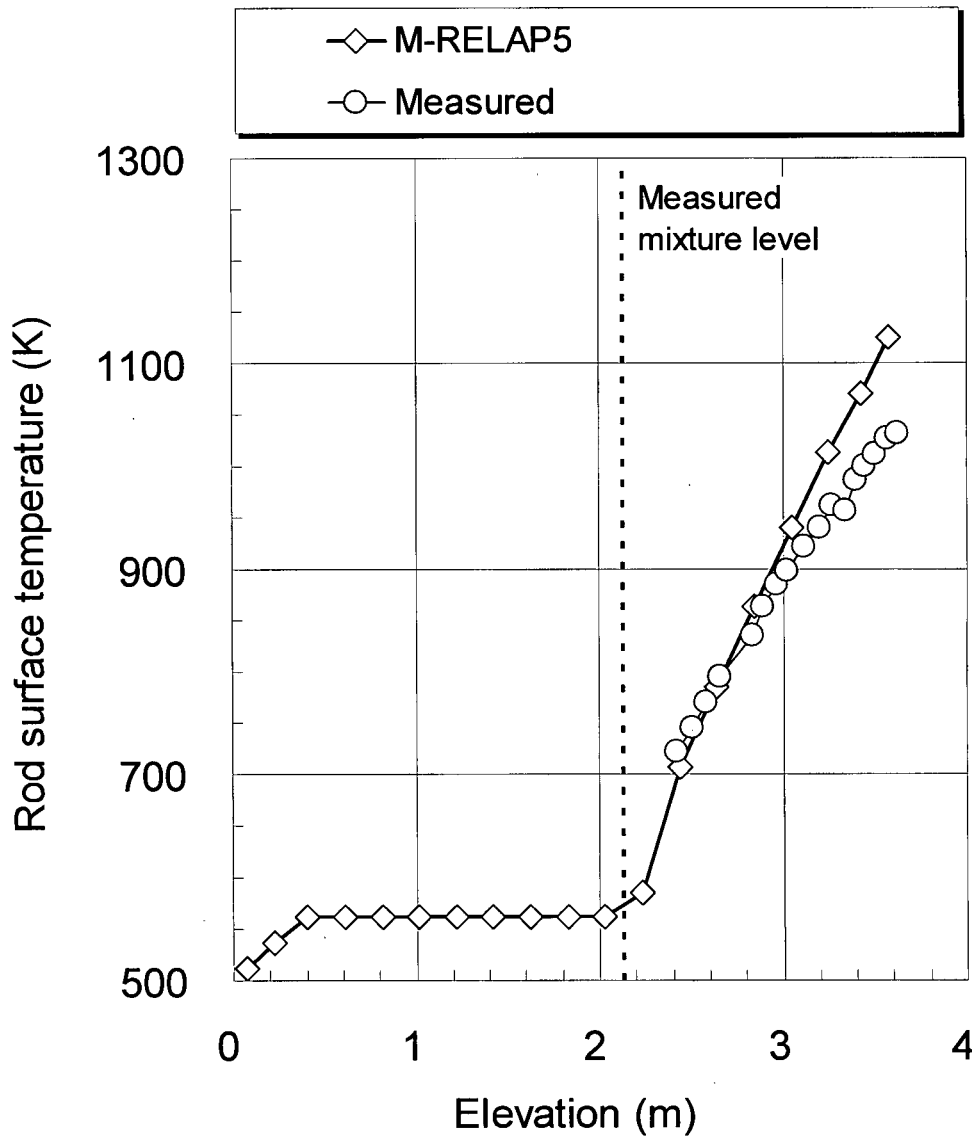


Figure 8.1.2-20 Comparison of Predicted and Measured FRS Surface Temperature Profiles for ORNL/THTF Test 3.09.10N

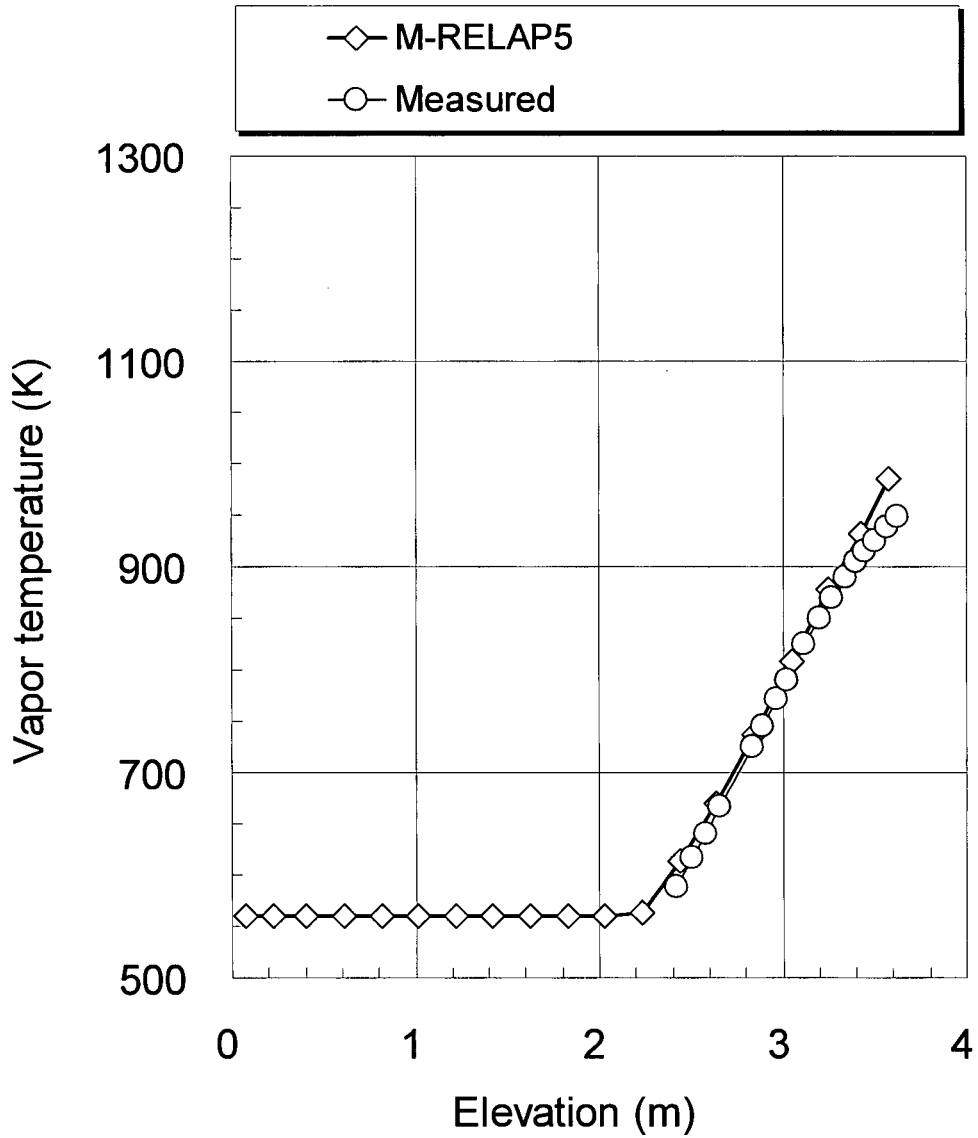


Figure 8.1.2-21 Comparison of Predicted and Measured Vapor Temperature Profiles for ORNL/THTF Test 3.09.10N

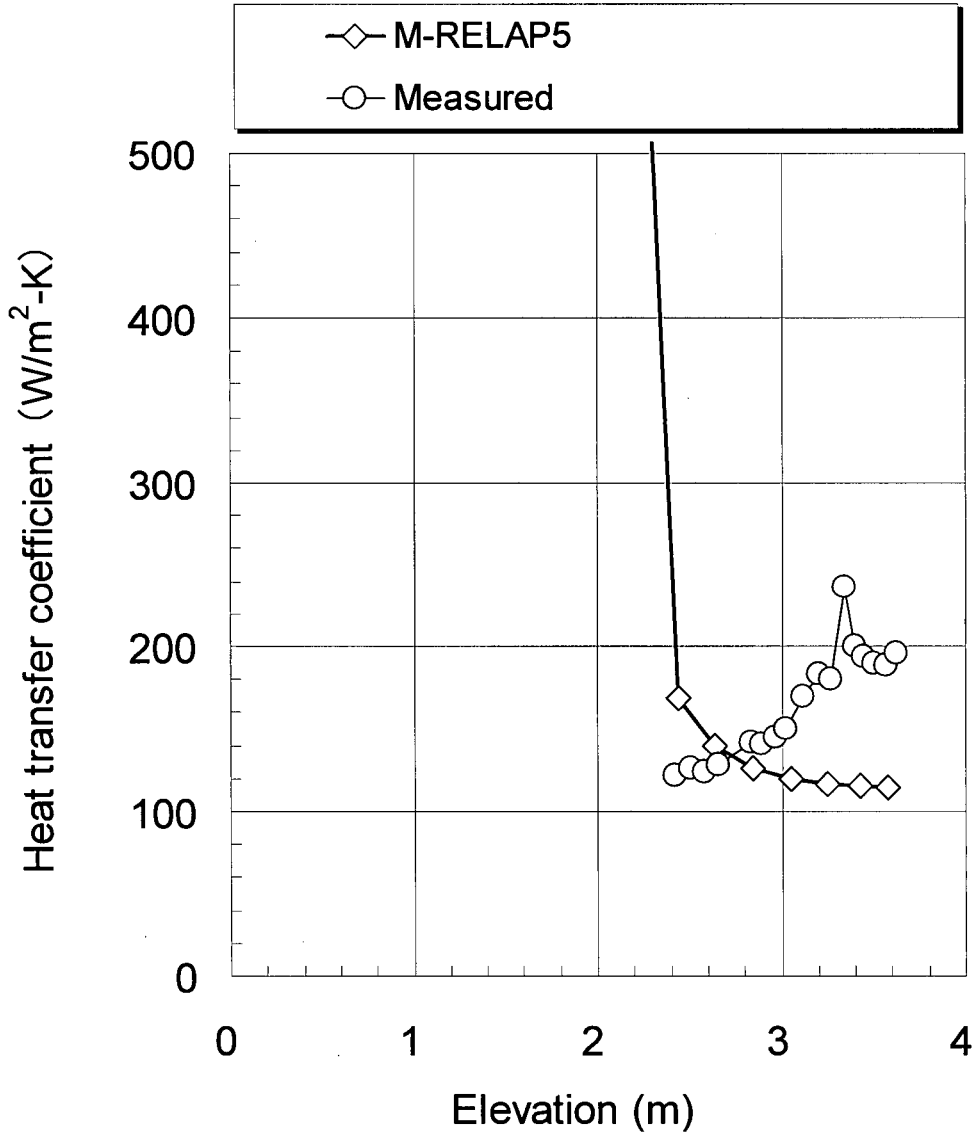


Figure 8.1.2-22 Comparison of Predicted and Measured Heat Transfer Coefficient Profiles for ORNL/THTF Test 3.09.10N

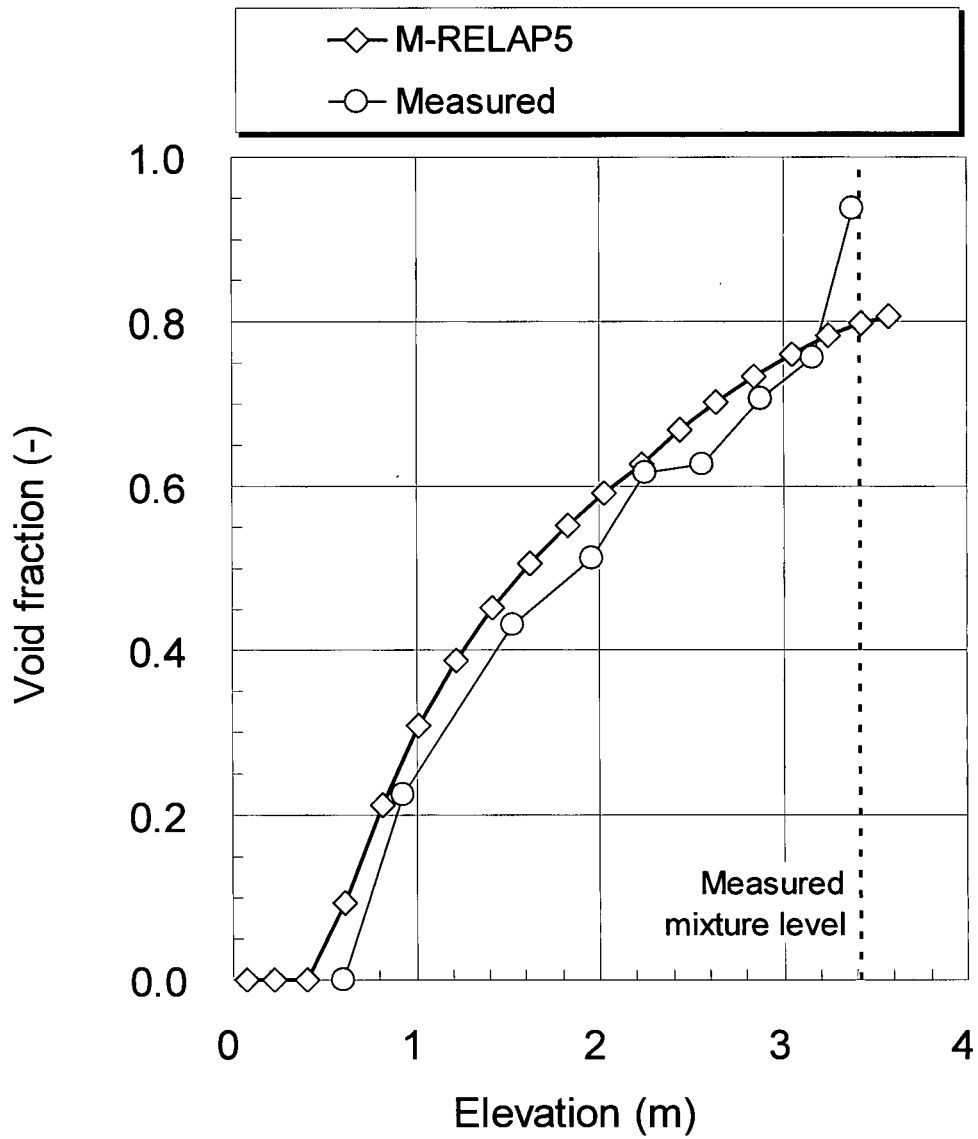


Figure 8.1.2-23 Comparison of Predicted and Measured Void Fraction Profiles for ORNL/THTF Test 3.09.10AA

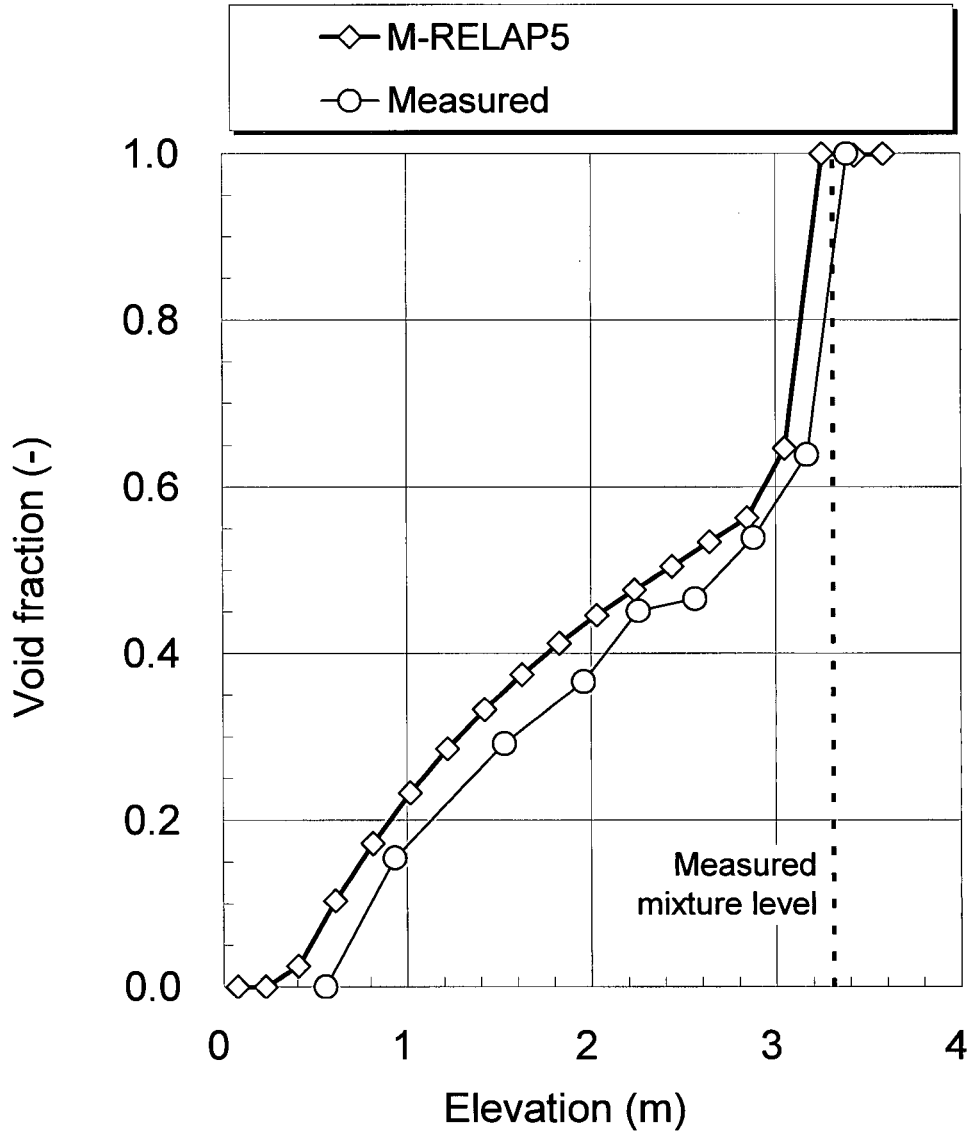


Figure 8.1.2-24 Comparison of Predicted and Measured Void Fraction Profiles for ORNL/THTF Test 3.09.10BB

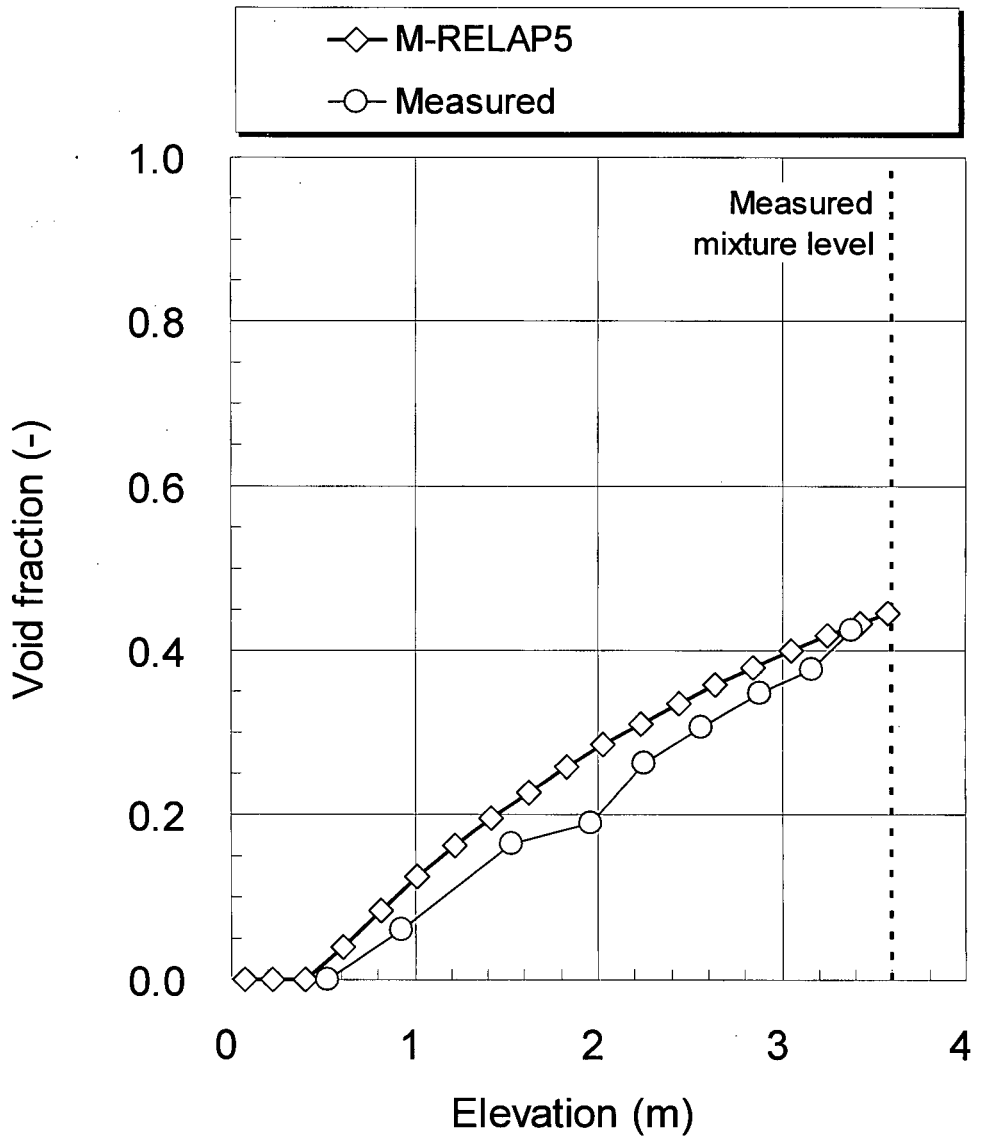


Figure 8.1.2-25 Comparison of Predicted and Measured Void Fraction Profiles for ORNL/THTF Test 3.09.10CC

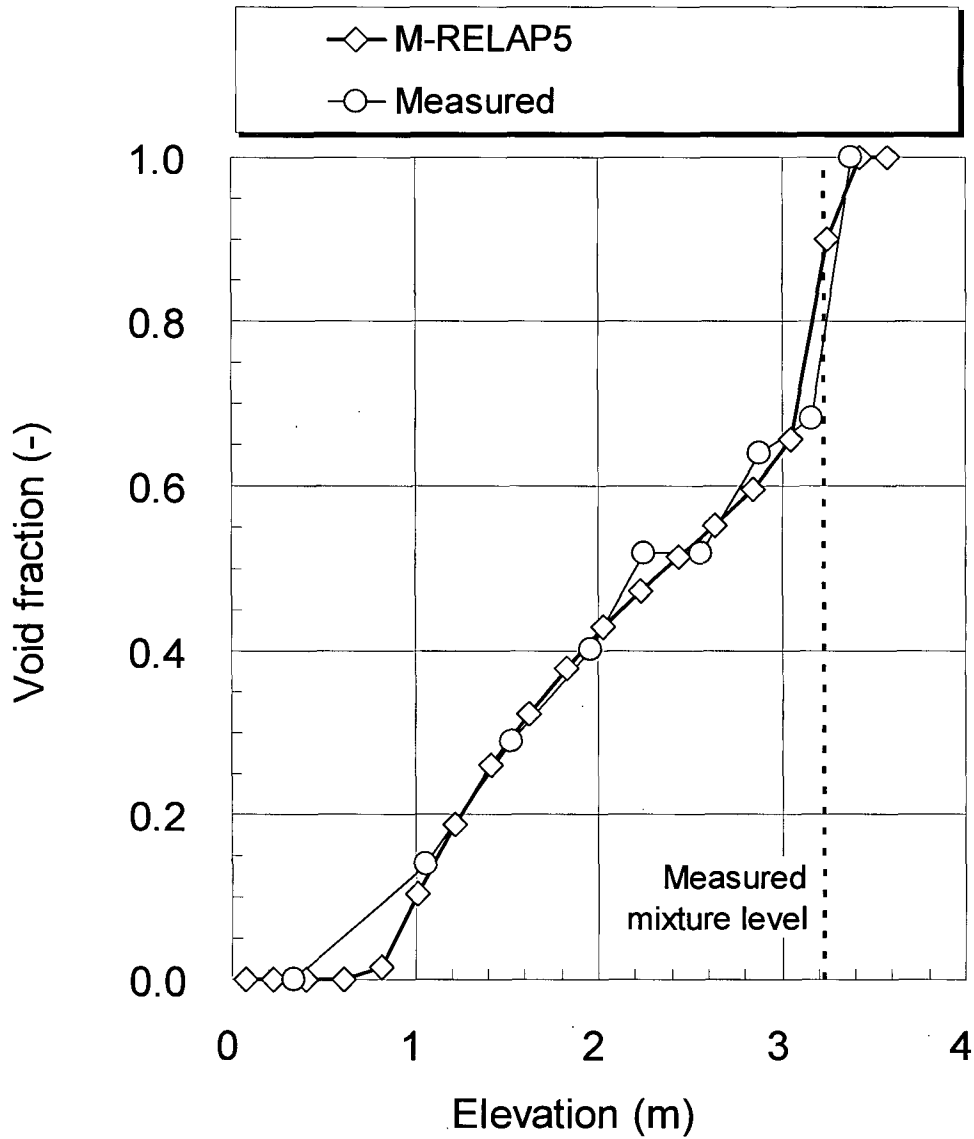


Figure 8.1.2-26 Comparison of Predicted and Measured Void Fraction Profiles for ORNL/THTF Test 3.09.10DD

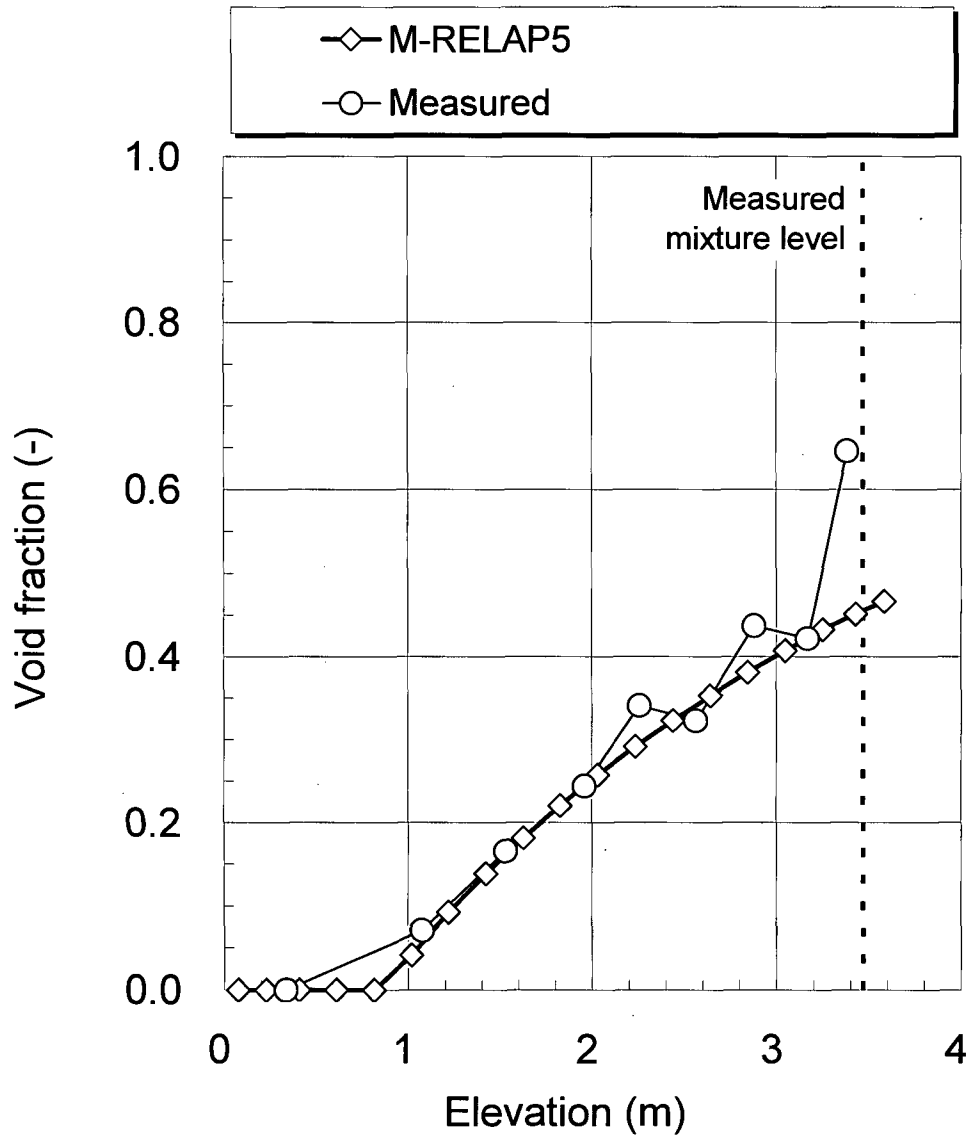


Figure 8.1.2-27 Comparison of Predicted and Measured Void Fraction Profiles for ORNL/THTF Test 3.09.10EE

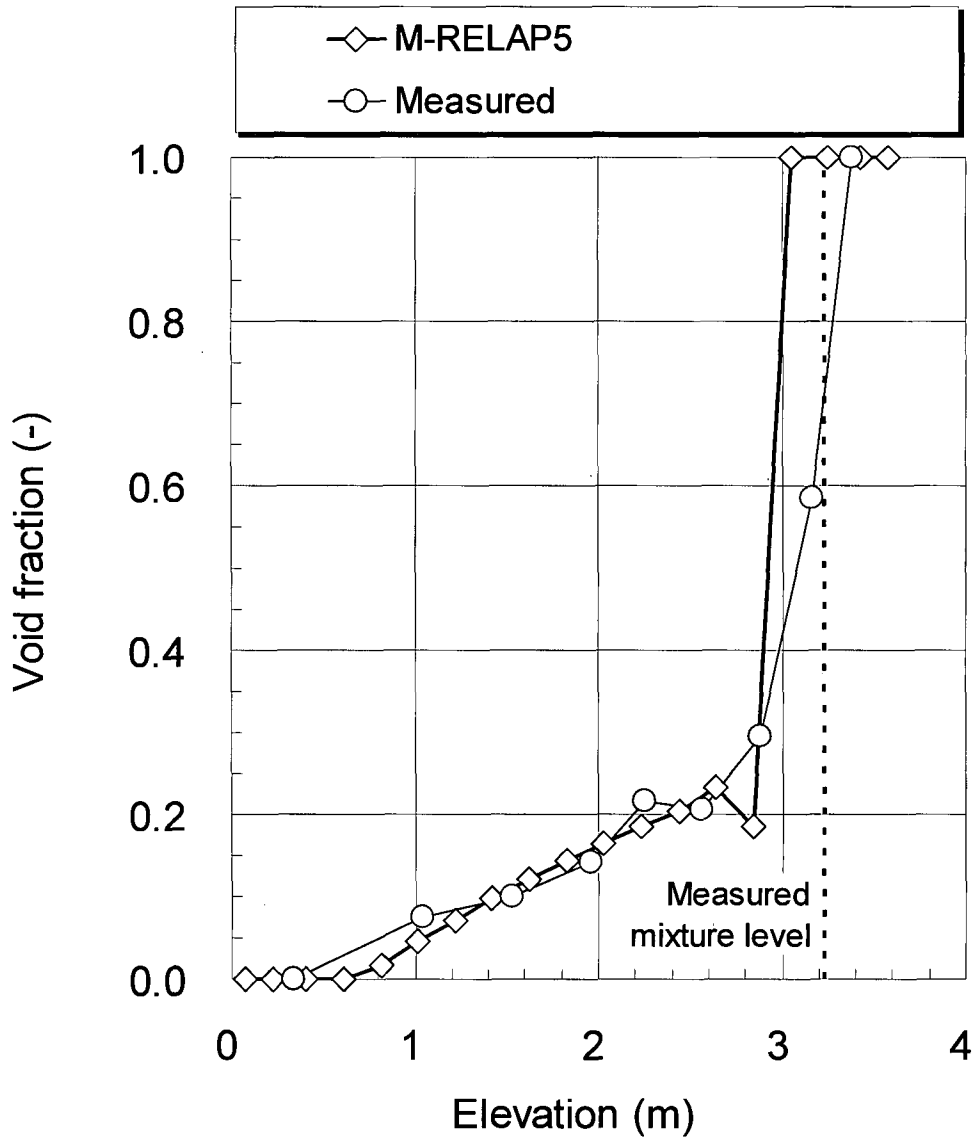


Figure 8.1.2-28 Comparison of Predicted and Measured Void Fraction Profiles for ORNL/THTF Test 3.09.10FF

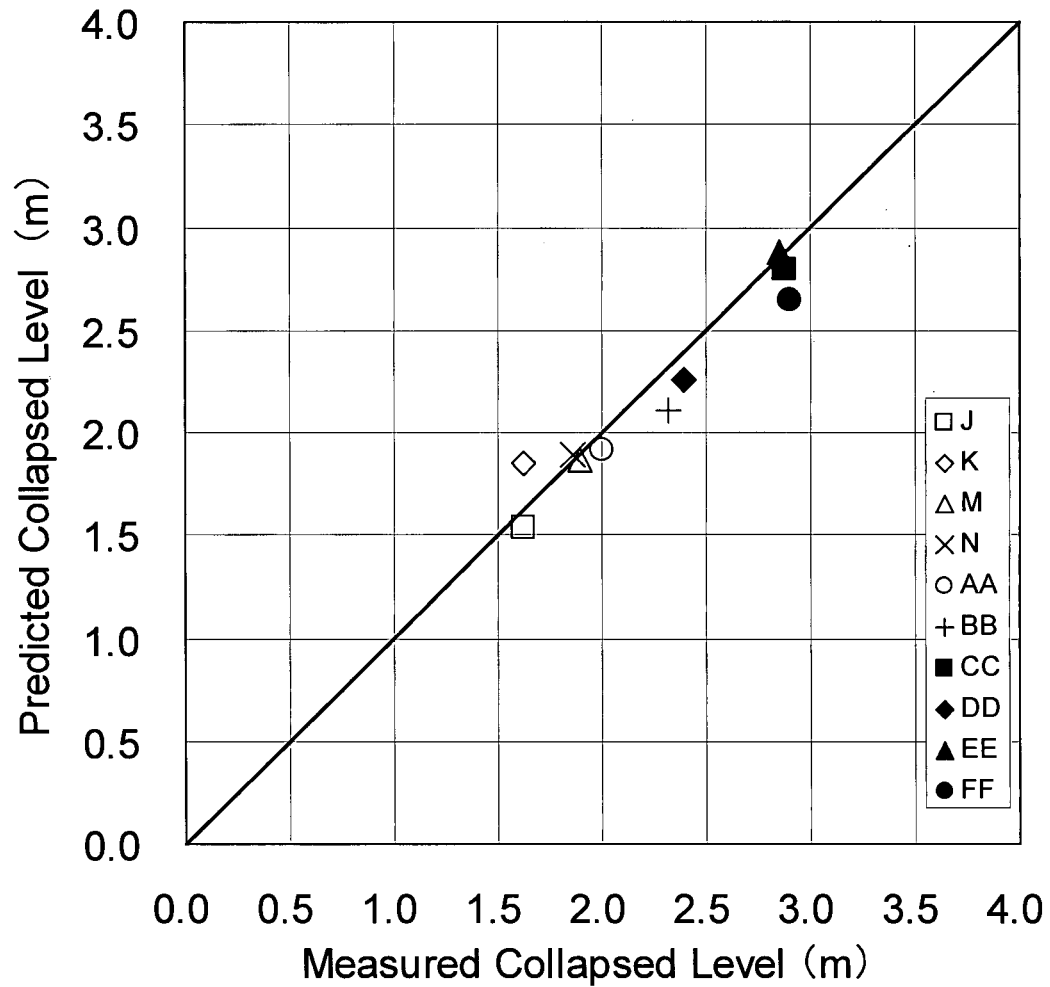


Figure 8.1.2-29 Comparison of Predicted and Measured Collapsed Liquid Levels for ORNL/THTF Tests

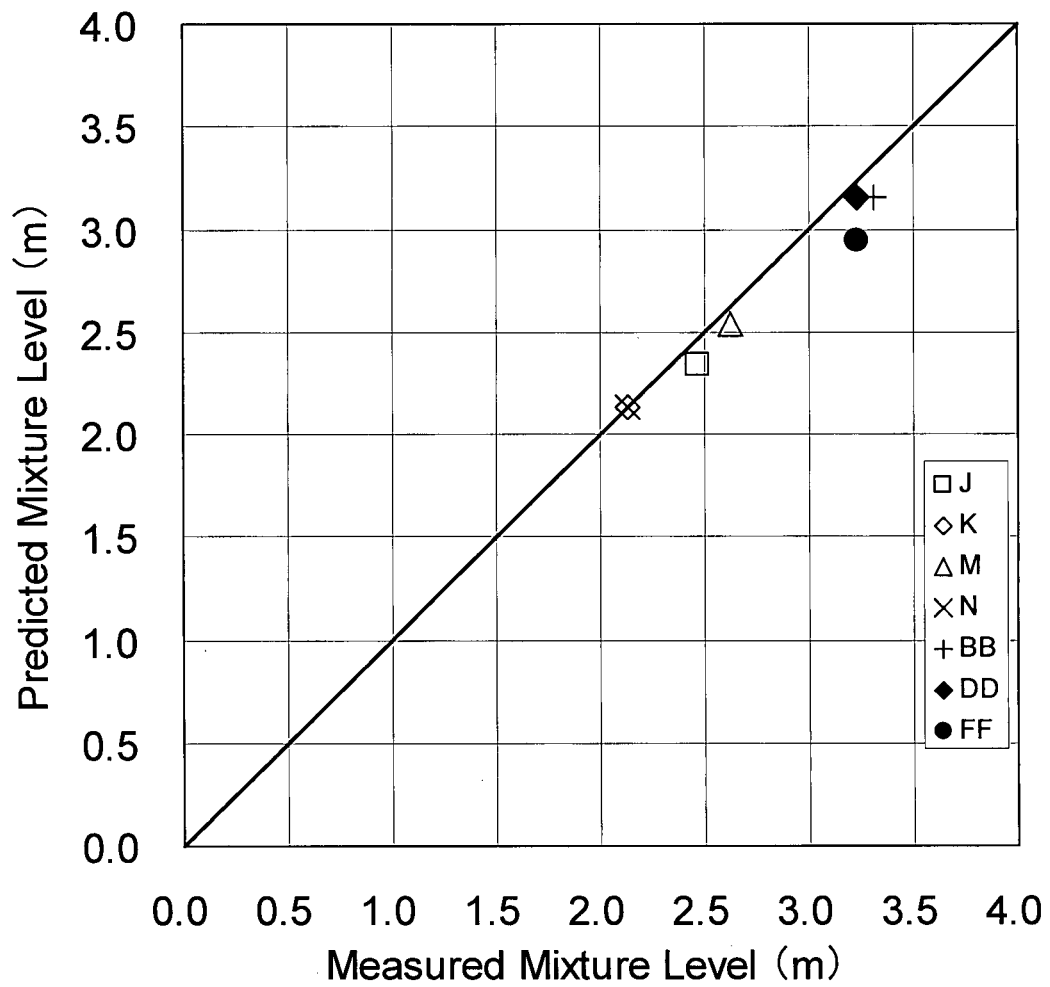


Figure 8.1.2-30 Comparison of Predicted and Measured Mixture Levels for ORNL/THTF Tests

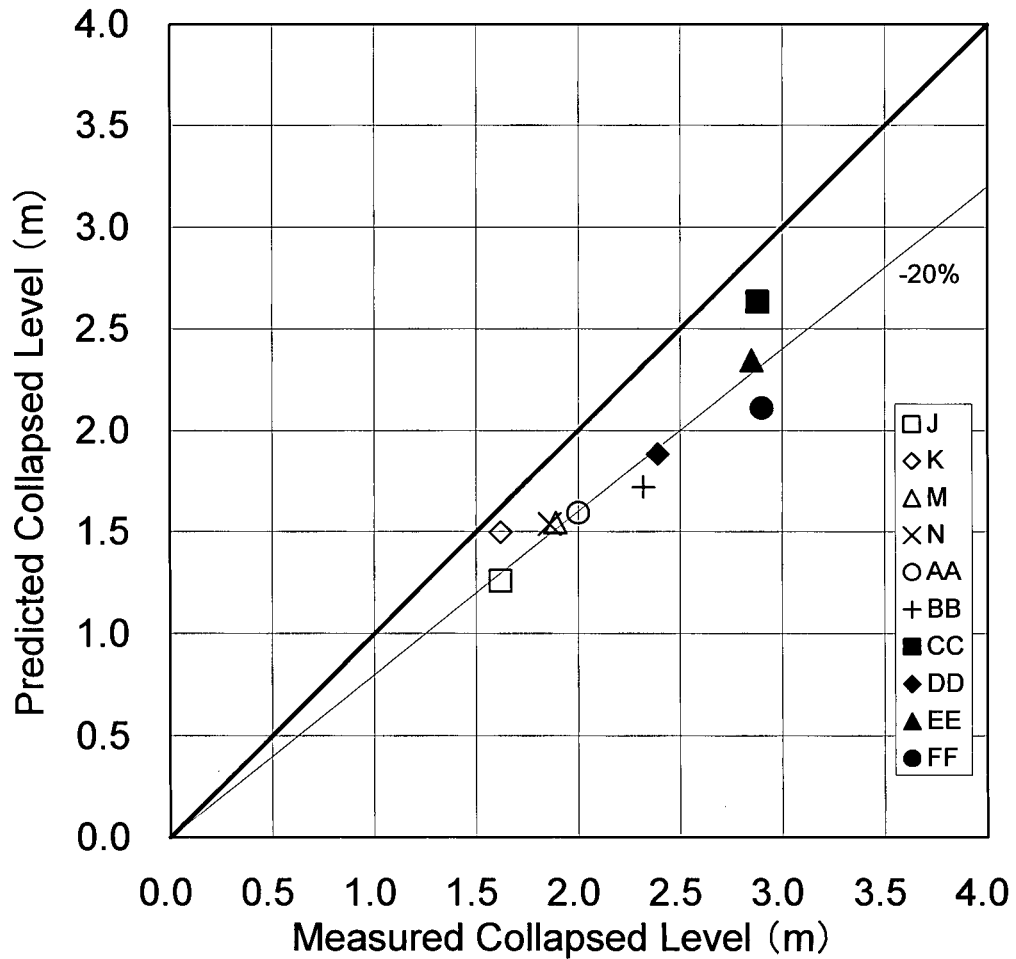


Figure 8.1.2-31 Sensitivity 1 : Comparison of Predicted and Measured Collapsed Liquid Levels for ORNL/THTF Tests (1.2 X nominal power cases)

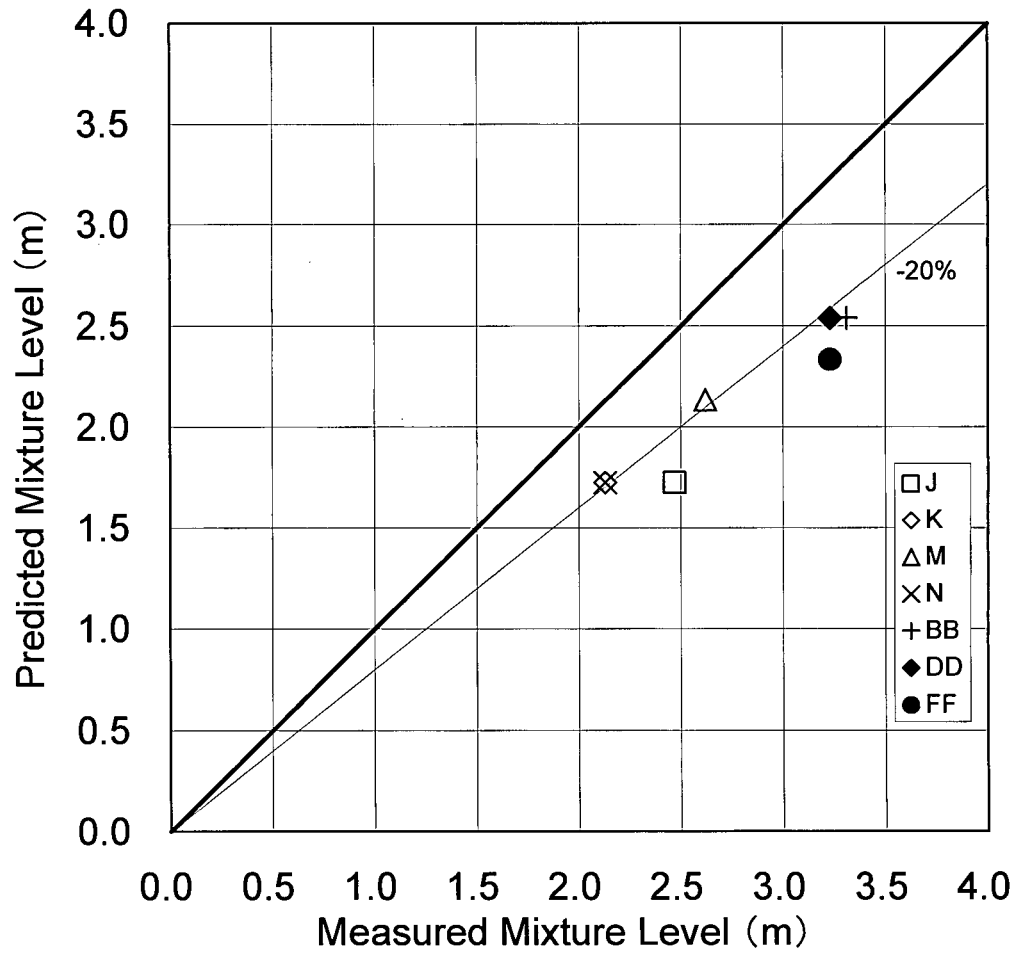


Figure 8.1.2-32 Sensitivity 1 : Comparison of Predicted and Measured Mixture Levels for ORNL/THTF Tests (1.2 X nominal power cases)

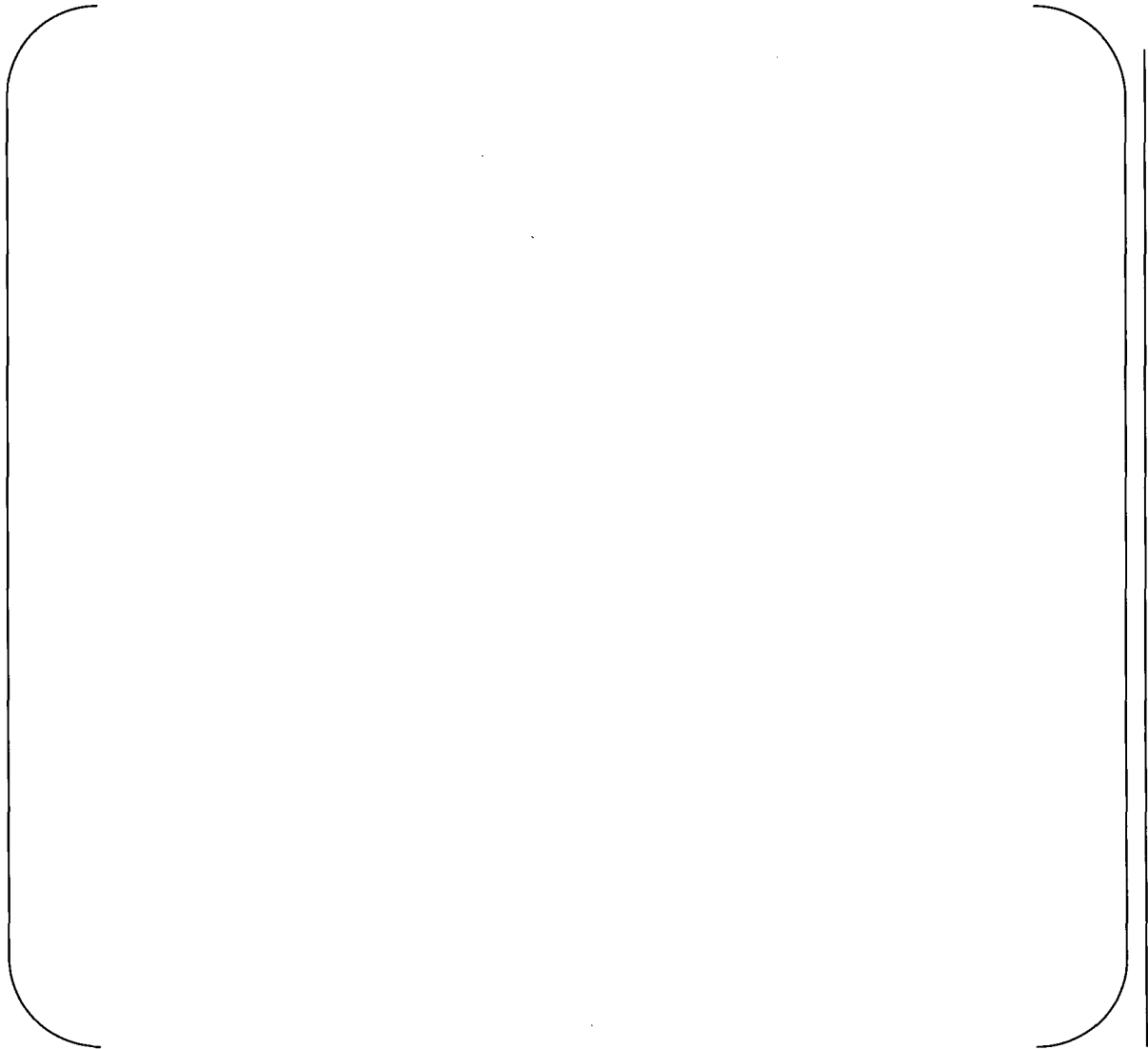


Figure 8.1.2-33 Sensitivity 2 : Comparison of Predicted and Measured Mixture Levels for ORNL/THTF Tests

8.1.3 ORNL/THTF High-Pressure Reflood test

8.1.3.1 Introduction

Following loop seal clearance, the two-phase core mixture level in the core is recovered. Following the loop seal recovery, coolant boil-off in the core may occur due to the greater coolant loss through the break, such that the two-phase core mixture level may decrease again. The core mixture level is recovered when the safety injection rate exceeds the coolant loss through the break. When the reactor system pressure drops below the accumulator set-point the accumulators begin to inject into the cold legs and refill both the downcomer and the core. Along with the core mixture level recovery in the core (core reflood), fuel cladding temperature decreases due to precursory cooling and finally drops to just above the saturation temperature due to rewet. Accurate predictions of the precursory cooling and rewet during the reflood phase are important to confirm the core coolability during a SBLOCA.

A series of the high-pressure reflood tests were performed under conditions similar to those expected in a SBLOCA in THTF at ORNL. The objective of the reflood tests was to study bundle-rewetting (or quenching) behavior under conditions of varying system pressure, linear power, and flooding rate. These tests were used to assess the M-RELAP5 code applicability to the prediction of the core reflood behavior in a SBLOCA.

8.1.3.2 Test Facility and Test Section

The high-pressure reflood test was conducted using the same test facility and test section as the uncovered-bundle heat transfer and two-phase mixture level swell test, which are already described in Section 8.1.2.2.

8.1.3.3 Test Procedure and Test Matrix

Initial conditions for the high-pressure reflood test were established in a manner identical to that used in the uncovered bundle heat transfer and two-phase mixture swell test. Reflood was initiated from a configuration in which the bundle was partially uncovered and peak cladding temperature was on the order of 1033K (1400F). Flow-power matching was such that 22 to 34% of the bundle heated length was initially uncovered.

To initiate reflood, the inlet flooding valve was opened to a predetermined setting. This caused

the test section inlet flow to increase, thus commencing bundle recovery. Bundle power remained constant until completion of core recovery. Data were also taken until core recovery was complete.

The test conditions of the high-pressure reflood test are shown in Table 8.1.3-1. Parametric variations include pressure, flooding rate, and linear heat rate. The initial system pressure ranged from 3.9 to 7.5MPa. Average inlet flooding velocities ranged from 5.9 to 12.2cm/s. Linear heat rate ranged from 1.00 to 2.16kW/m. These test conditions cover the possible range of conditions for the reflood recovery during SBLOCAs. Among these tests, 3.09.10P and Q were used as validation tests because they have suitable liner power/rod for the US-APWR SBLOCA transient.

8.1.3.4 M-RELAP5 Model of THTF of High-Pressure Reflood Test

Figure 8.1.3-1 shows the M-RELAP5 noding diagram for the ORNL/THTF high-pressure reflood test. Since a simulation of the high-pressure reflood tests is a transient calculation, the fuel rod simulator (FRS) is divided into a number of nodes in the radial direction, and reliable values of the thermal properties are produced from Reference 8.1.3-3 and ASME Physical Properties Tables (2001) for stainless steel cladding, inconel heating element, and filled boron nitride. The transients of reflood rate, inlet temperature, and pressure were supplied as boundary conditions, which are presented in Figure 8.1.3-2 through 8.1.3-7. These boundary conditions were imposed by time-dependent volume components and a time-dependent junction component identical to those of the uncovered-bundle heat transfer and two-phase mixture level swell test.

There are no data reported regarding heat loss in Reference 8.1.3-2. The effect of heat loss was considered insignificant and therefore not modeled in the simulation because expected heat loss from a two-phase mixture-level swell test 3.09.10J, performed under a similar pressure and power condition to 3.09.10P and Q, is small, about 5%.

Prior to the initiation of reflood analysis, adequate agreement of the initial FRS surface temperature was established between experimental and analysis values. To do this, initial values of inlet flow and subcooling were adjusted in the steady state calculation prior to the transient calculation by using values slightly shifted from those reported in Reference 8.1.3-2 such that the initial conditions for the simulation best matched the experimental data. In this fashion, the uncertainty in the M-RELAP5 model initial conditions was minimized so a more

accurate assessment of the M-RELAP5 high pressure reflood behavior and models could be assessed.

The reflood test calculation was started at a condition where the test bundle partially uncovered by imposing the boundary conditions shown in Figures 8.1.3-2 through 8.1.3-7.

8.1.3.5 Results

Figures 8.1.3-8 through 15 show comparison of FRS surface temperature, fluid temperature, collapsed liquid level, and quench level between the M-RELAP5 calculated results and the experimental data for tests 3.09.10P and Q.

The collapsed liquid levels are presented in Figures 8.1.3-10 and 14. The rate of rise in collapsed levels is large in the early time and becomes gradually small at a later time. This is because the axial power distributions for the tests are flat over the heated length; thus in the beginning of reflooding the FRS superheat is small near the two-phase mixture level and grows larger with distance from the mixture level. Consequently initial stored energy in the FRS is small near the mixture level and increases as the distance from the mixture level increases. As a result, the evaporation rate is small in the beginning of the reflooding and larger at later time when more stored energy is removed by quenching of the FRS. Since the inlet flow for test 3.09.10 Q (Figure 8.1.3-5) is smaller than test 3.09.10 P (Figure 8.1.3-2), the rate of rise in collapsed level for test 3.09.10 Q is smaller than that for test 3.09.10 P. M-RELAP5 predicts this tendency well.

Figures 8.1.3-10 and 14 indicate good agreement between the calculated results and the experimental data. Although the oscillation of the collapsed liquid level for test 3.09.10 Q results from rewetting at elevations representing discretized bundle volumes, the average behavior of the collapsed liquid level seems well simulated.

The variation of the collapsed liquid level with time relates to vapor generation under the two-phase mixture level and entrainment from the liquid-vapor interface. The comparisons indicate that M-RELAP5 adequately simulates these phenomena.

The FRS surface temperatures at levels F and G (see Figure 8.1.2-4) for both tests are presented in Figures 8.1.3-8, 9, 12 and 13. In the experiments the FRS surface temperature decreased gradually before the quench occurred and dropped to the saturation temperature in

a short time once the quench conditions were met. M-RELAP5 predicted this precursory cooling together with changes in heat transfer mode from single-phase vapor convection to saturated film boiling. In the later time, however, the M-RELAP5-predicted FRS surface temperature did not show clear-cut quench but gradually decreased and finally reached the saturation temperature when the superheat dropped below 100K and thereby the heat transfer mode changed from transition boiling to nucleate boiling. This conservative evaluation showing a delay in quench time, resulted from the facts that the M-RELAP5 predicted heat transfer for film boiling and transition boiling, which are dominant in the pre-quench cooling is conservatively modeled and that axial heat conduction in the heated rod surface at the quench front, also dominant effect in the quench, is not considered in the simulation.

Figures 8.1.3-11 and 15 show comparisons of the quench level variation with time between experimental data and M-RELAP5 result for tests 3.09.10 P and Q, respectively. The quench times resulted from the M-RELAP5 calculation were identified by heat transfer mode change from transition boiling to nucleate boiling that occurred just before the FRS surface temperature reduced to the saturation temperature. These figures indicate that the M-RELAP5 calculated quench velocities, which can be obtained by differentiating the quench level with respect to time, are much smaller than the experimental results.

It is noted from the above that the M-RELAP5 heat transfer model for the reflooding phase calculates a longer quench time than the experiment, and thus evaluates the FRS surface temperature conservatively.

8.1.3.6 Conclusion

M-RELAP5's reflood modeling was assessed against the ORNL/THTF high-pressure reflood tests. It was concluded that M-RELAP5 adequately predicts fluid conditions such as fluid collapsed level during reflood and higher FRS surface temperature, and thus M-RELAP5 conservatively predicts the rod heat transfer behavior during reflood. In conclusion, it is reasonable to apply M-RELAP5 to simulation of reflooding phase of US-APWR SBLOCA EM analysis.

8.1.3.7 References

- 8.1.3-1 D. K. Felde et al., "Facility Description – THTF MOD 3 ORNL PWR BDHT Separate-Effects Program," NUREG/CR-2640, ORNL/TM-7842, September 1982.
- 8.1.3-2 C. R. Hyman, T. M. Anklam, and M. D. White, "Experimental Investigations of Bundle Boiloff and Reflood Under High-Pressure Low Heat-Flux Conditions," NUREG/CR-2455, ORNL-5846, April 1982.
- 8.1.3-3 D. G. Morris, C. B. Mullins, and G. L. Yoder, "An Analysis of Transient Film Boiling Of High-Pressure Water In A Rod Bundle," NUREG/CR-2469, ORNL/NUREG-85 Rev.2, March 1982.
- 8.1.3-4 The RELAP5-3D Code Development Team, "RELAP5-3D Code Manual Volume IV: Models and Correlations," INEEL-EXT-98-00834 Revision 2.4, June 2005.
- 8.1.3-5 T. M. Anklam, R. J. Miller, and M. D. White, "Experimental Investigations of Uncovered-Bundle Heat Transfer and Two-Phase Mixture Level Swell Under High-Pressure Low Heat-Flux Conditions," NUREG-2456, ORNL-5848, March 1982.

Reference 8.1.3-2

Table 8.1.3-1 ORNL/THTF High-Pressure Reflood Test Conditions

Test	Pressure	Inlet mass flux	<u>Flooding velocity</u>	Inlet temperature		Linear heat
	(MPa)	(kg/s·m ²)	(<u>cm/s</u>)	(Subcooling)	(K)	power
O	3.88	25.36	<u>12.2</u>	447.7	(74)	2.03
P	4.28	12.19	<u>9.2</u>	462.6	(65)	0.997
Q	3.95	12.68	<u>5.9</u>	456.8	(66)	1.02
R	7.34	27.64	<u>11.7</u>	449.2	(113)	2.16
S	7.53	13.82	<u>10.2</u>	459.0	(105)	1.38

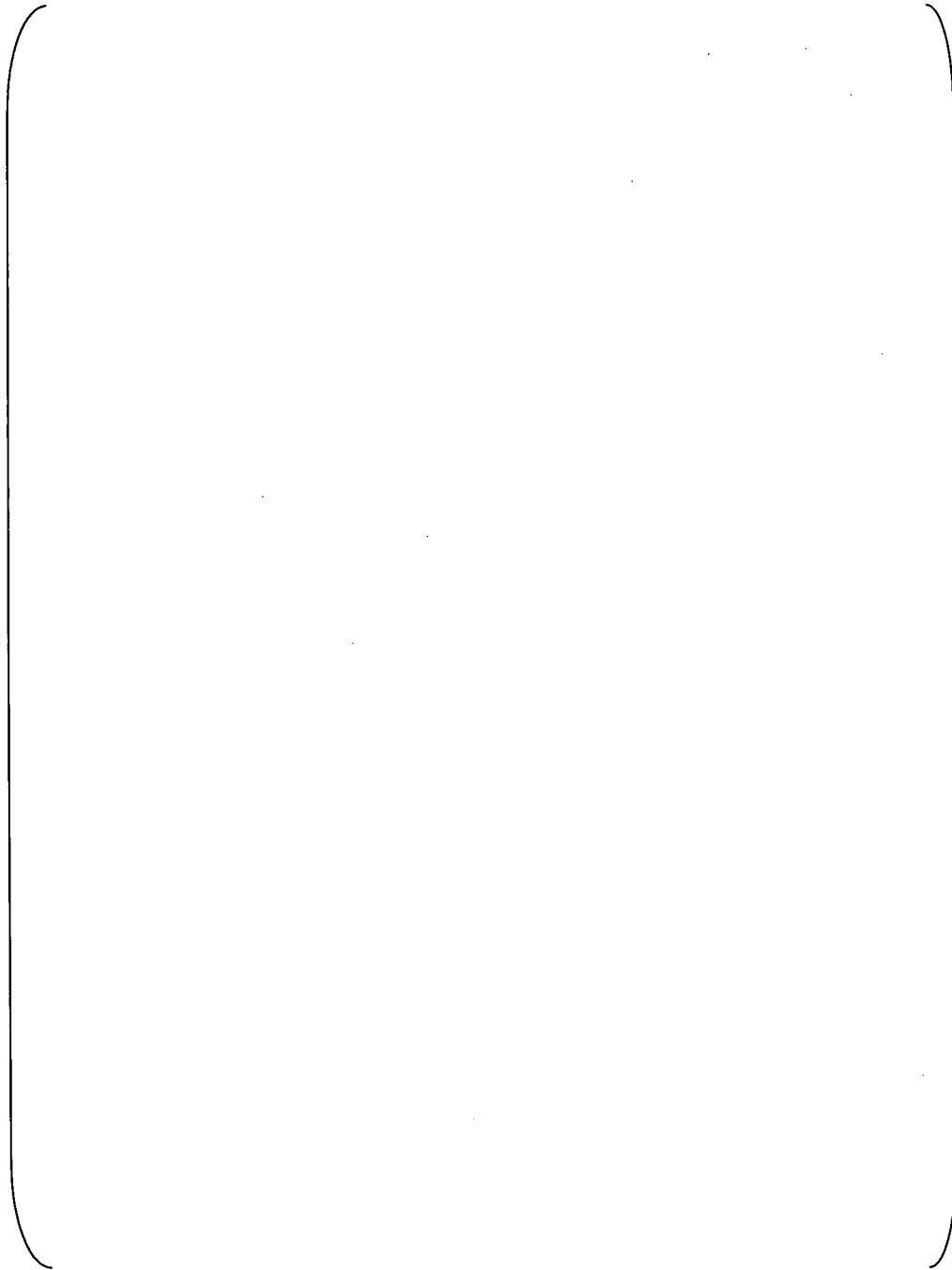


Figure 8.1.3-1 M-RELAP5 Noding Diagram for ORNL/THTF High-Pressure Reflood Test

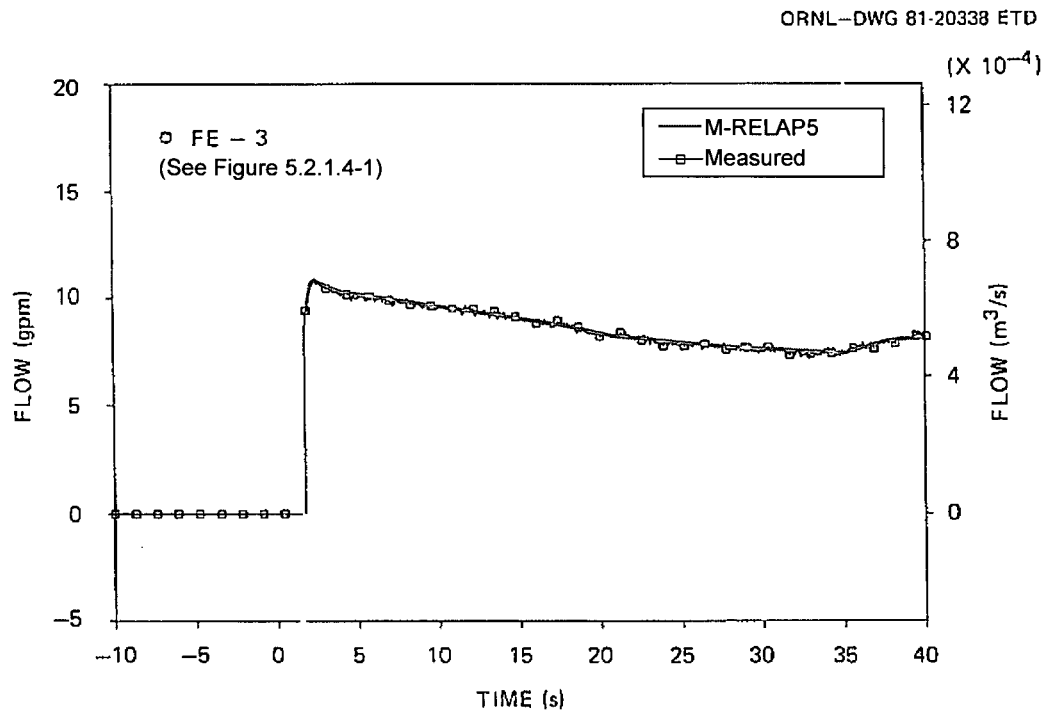


Figure 8.1.3-2 Comparison of Inputted and Measured Test Section Inlet Flows for ORNL/THTF Test 3.09.10P

Reference 8.1.3-2

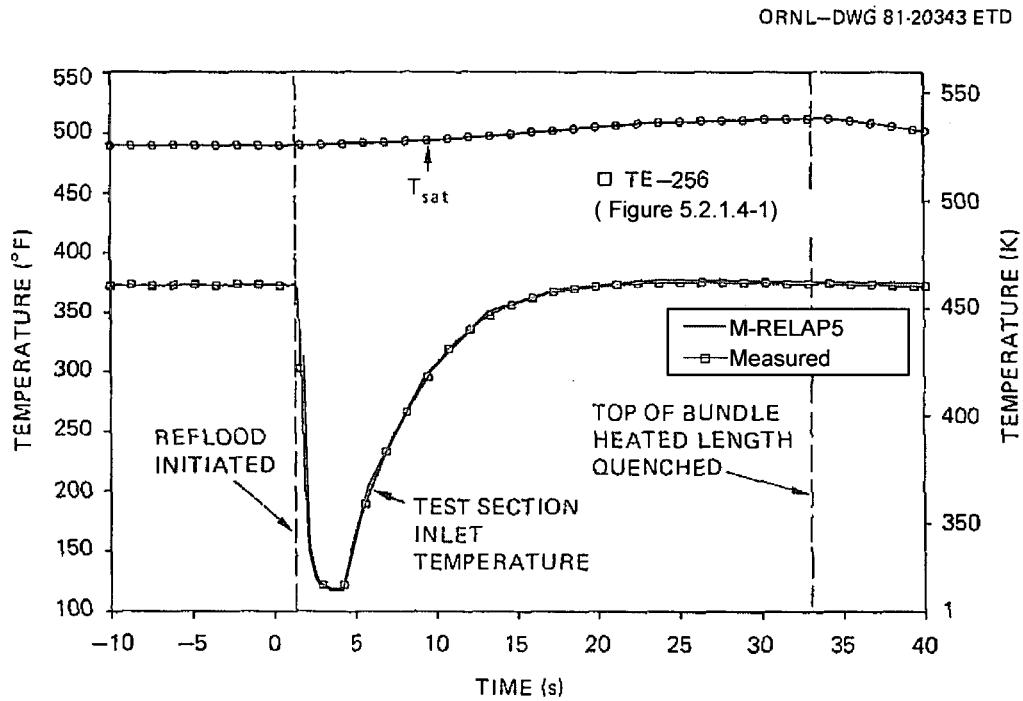


Figure 8.1.3-3 Comparison of Inputted and Measured Test Section Inlet Temperatures for ORNL/THTF Test 3.09.10P

Reference 8.1.3-2

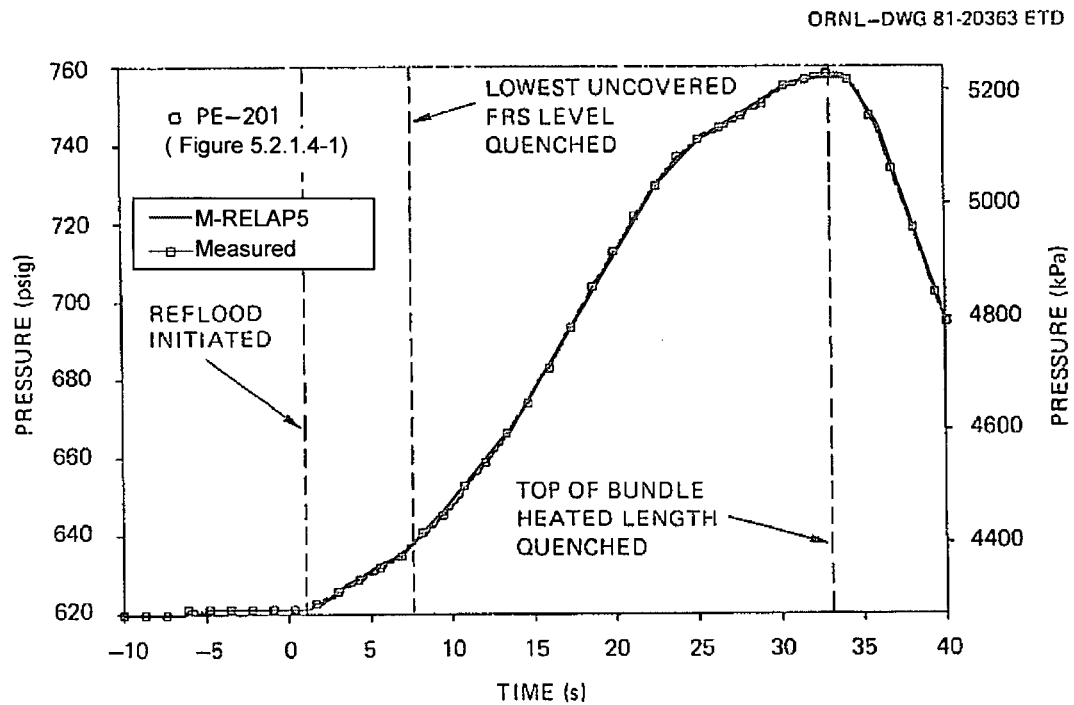


Figure 8.1.3-4 Comparison of Inputted and Measured Test Section Outlet Pressures for ORNL/THTF Test 3.09.10P

Reference 8.1.3-2

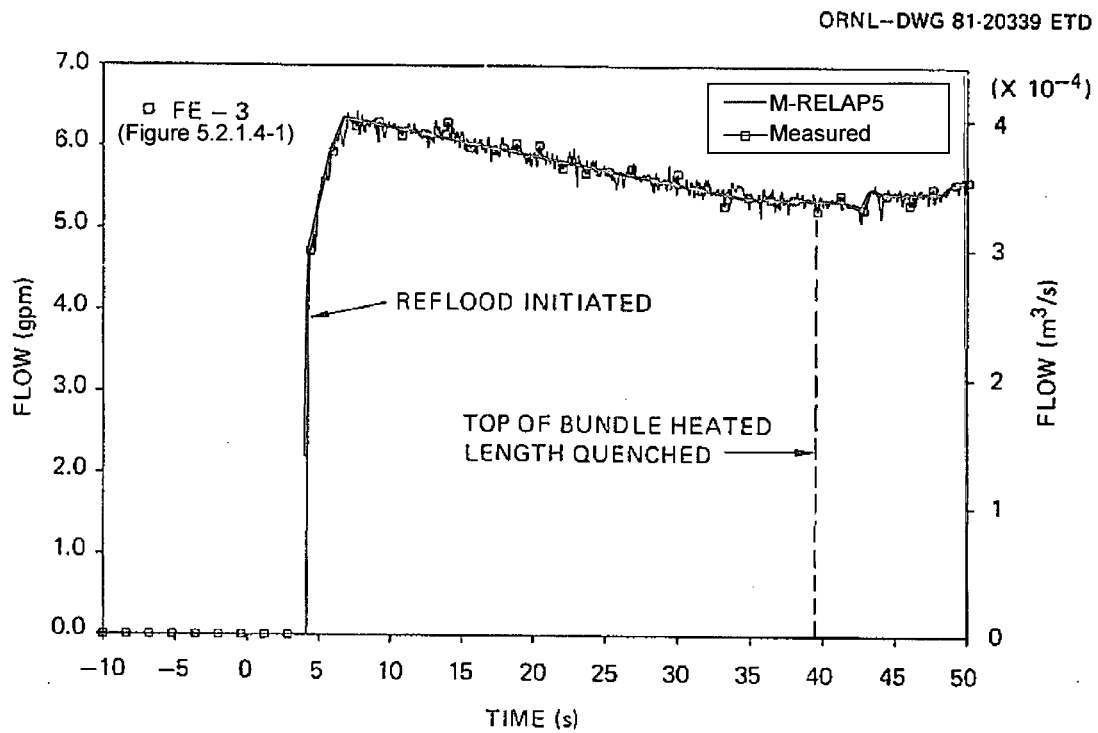


Figure 8.1.3-5 Comparison of Inputted and Measured Test Section Inlet Flows for ORNL/THTF Test 3.09.10Q

Reference 8.1.3-2

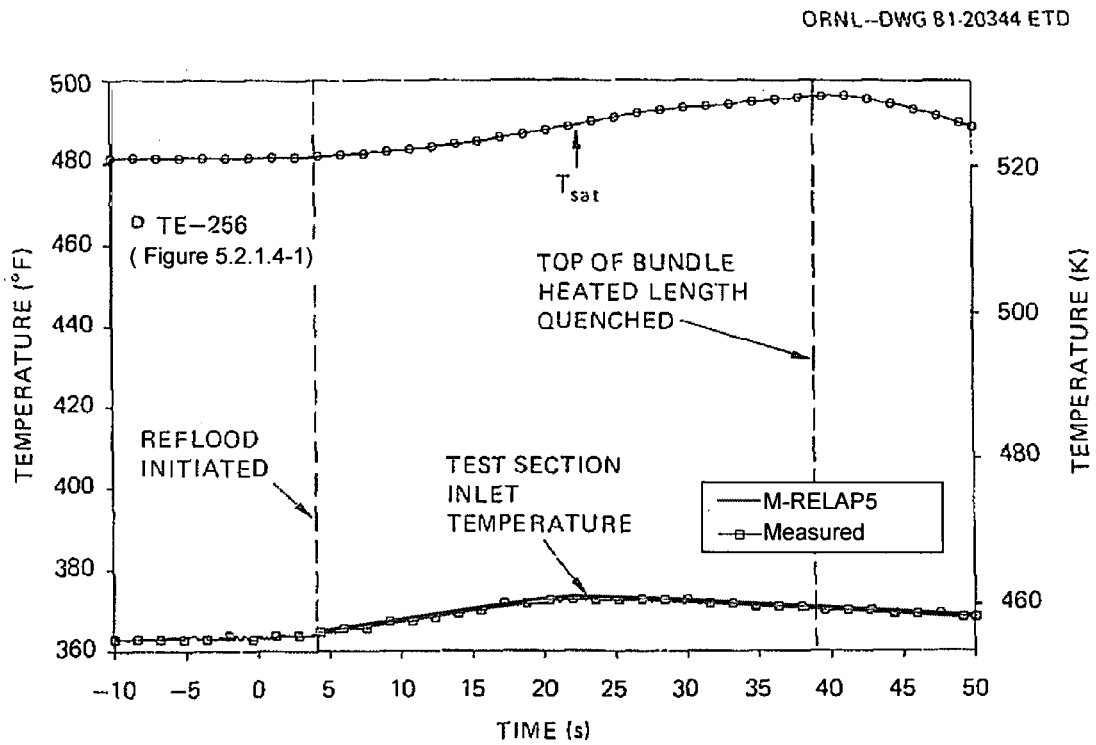


Figure 8.1.3-6 Comparison of Inputted and Measured Test Section Inlet Temperatures for ORNL/THTF Test 3.09.10Q

Reference 8.1.3-2

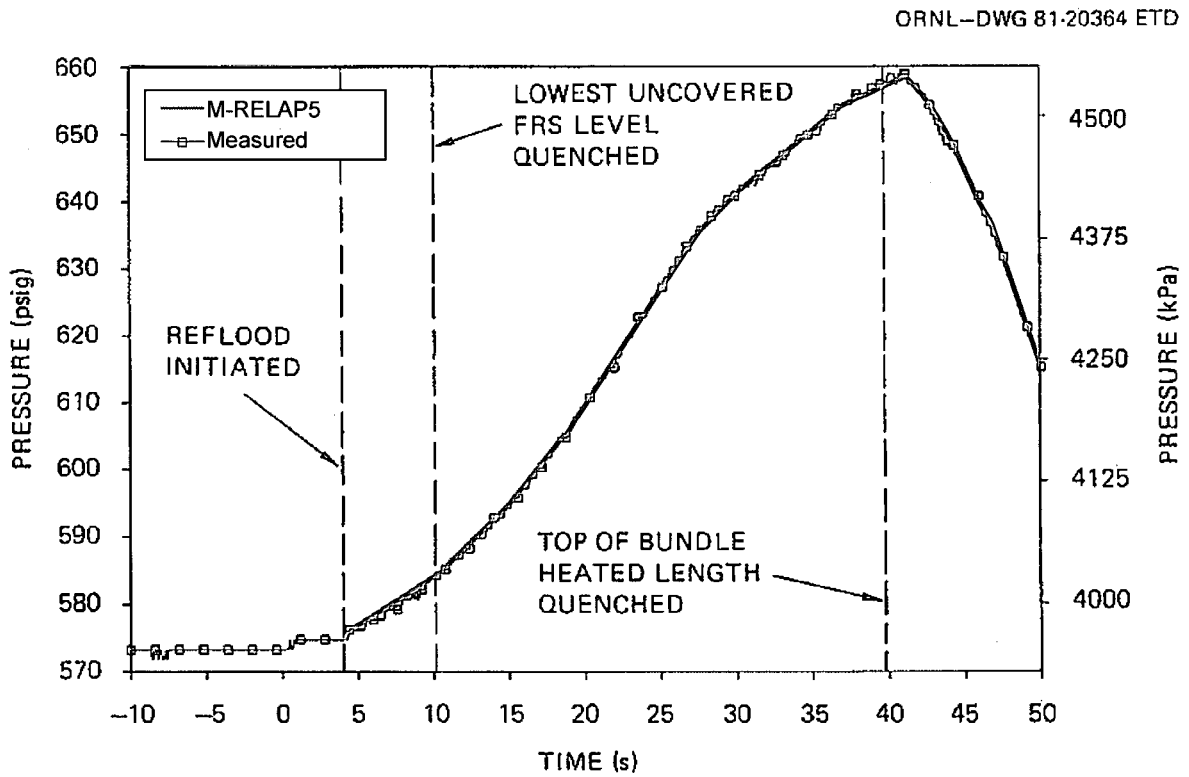


Figure 8.1.3-7 Comparison of Inputted and Measured Test Section Outlet Pressures for ORNL/THTF Test 3.09.10Q

Reference 8.1.3-2

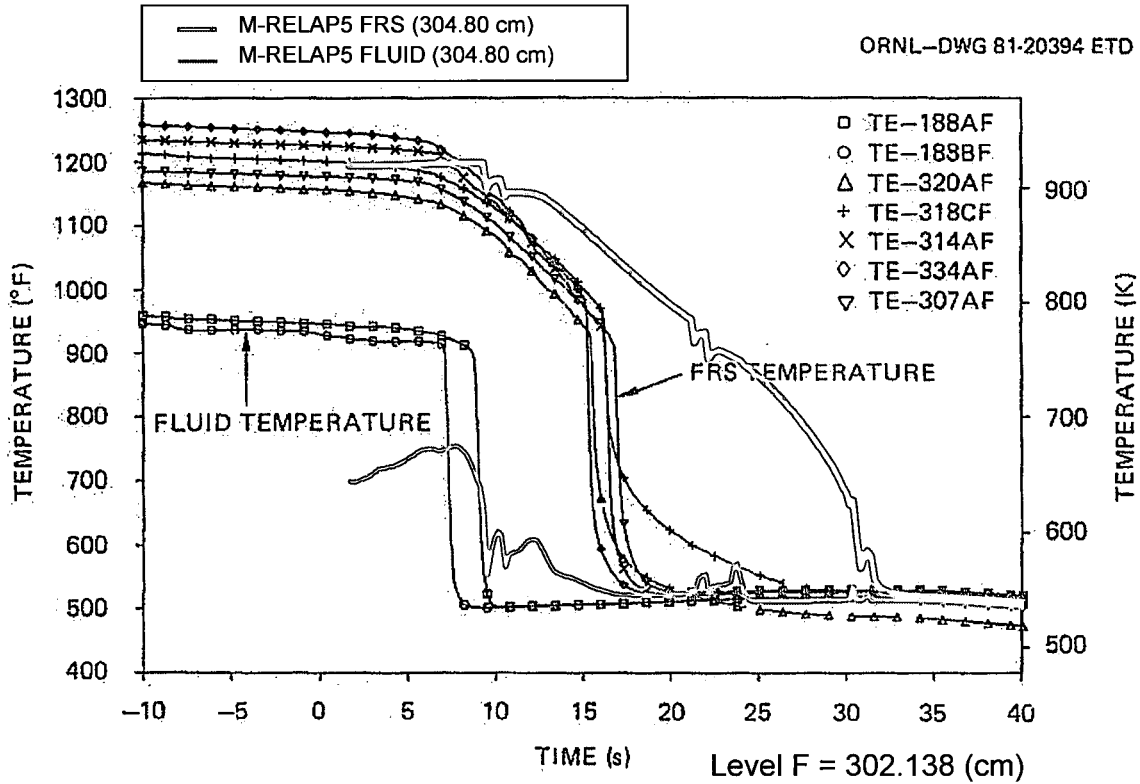


Figure 8.1.3-8 Comparison of Predicted and Measured FRS and Fluid Temperatures at Level F for ORNL/THTF Test 3.09.10P

Reference 8.1.3-2

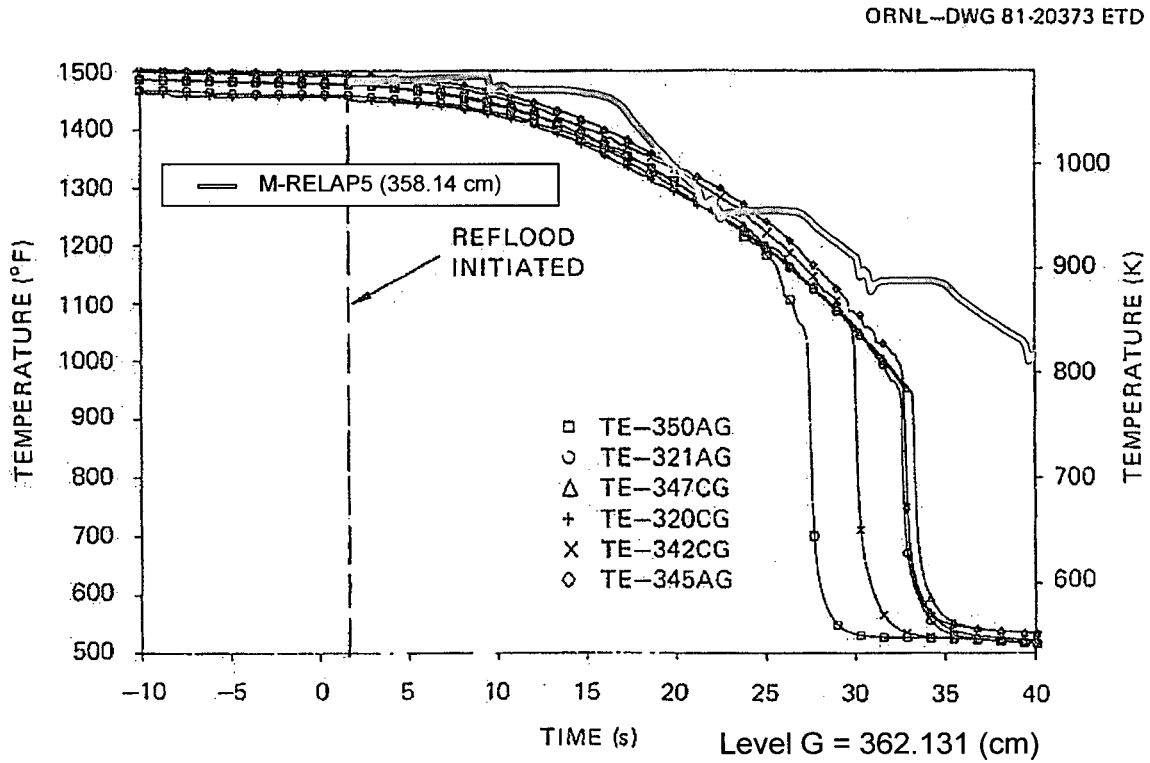


Figure 8.1.3-9 Comparison of Predicted and Measured FRS Temperatures at Level G for ORNL/THTF Test 3.09.10P

Reference 8.1.3-2

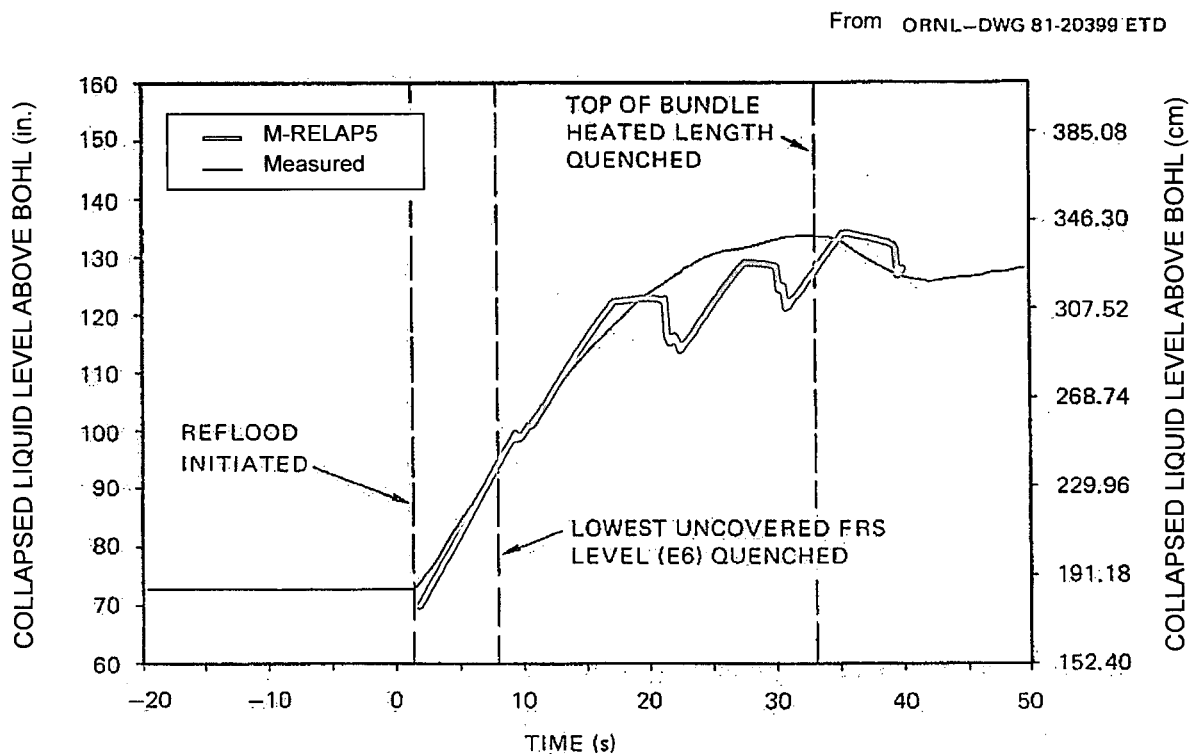
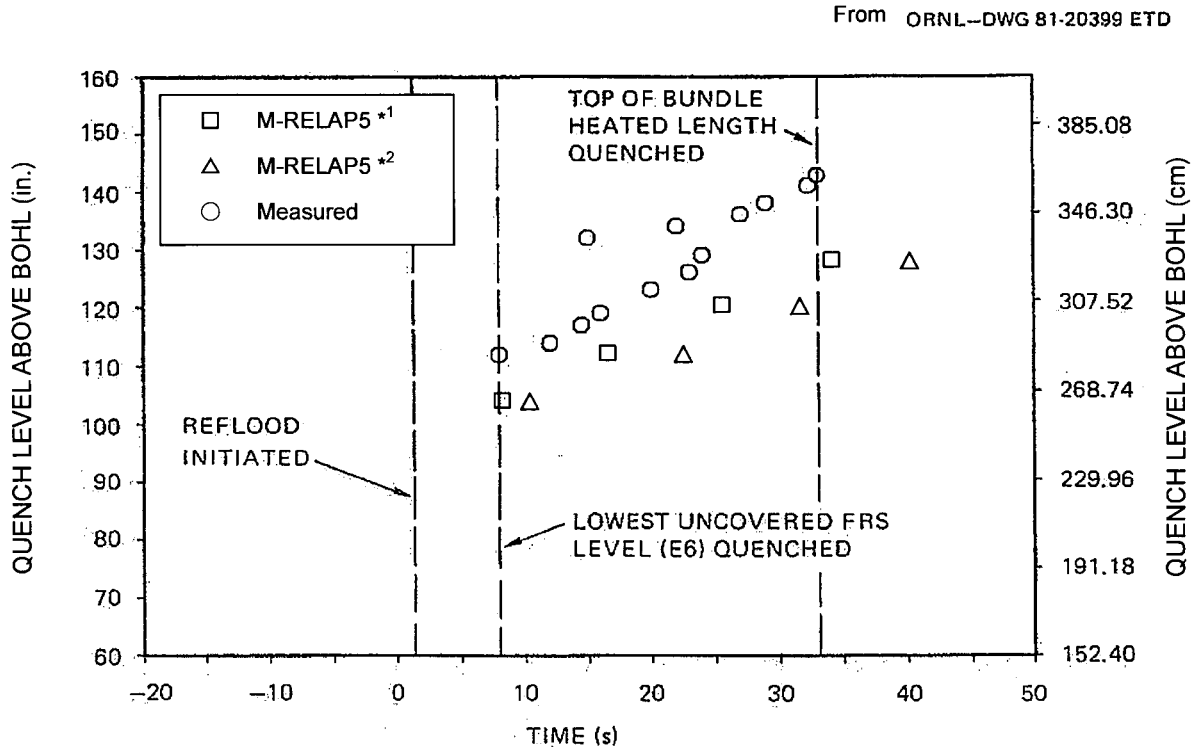


Figure 8.1.3-10 Comparison of Predicted and Measured Collapsed Liquid Level for ORNL/THTF Test 3.09.10P

Reference 8.1.3-2



*1 The time when the heat transfer mode switches from film boiling to transition boiling.
 *2 The time when the heat transfer mode switches from transition boiling to nucleate boiling.

Figure 8.1.3-11 Comparison of Predicted and Measured Quench Level for ORNL/THTF Test 3.09.10P

Reference 8.1.3-2

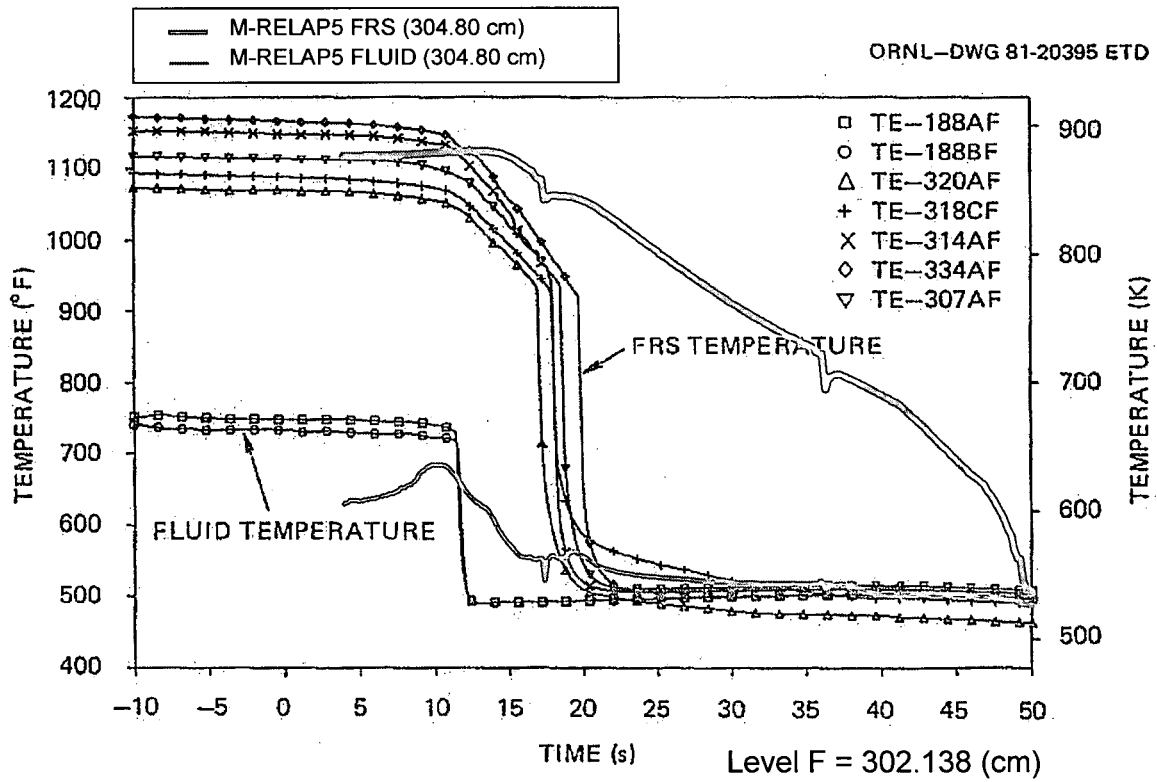


Figure 8.1.3-12 Comparison of Predicted and Measured FRS and Fluid Temperatures at Level F for ORNL/THTF Test 3.09.10Q

Reference 8.1.3-2

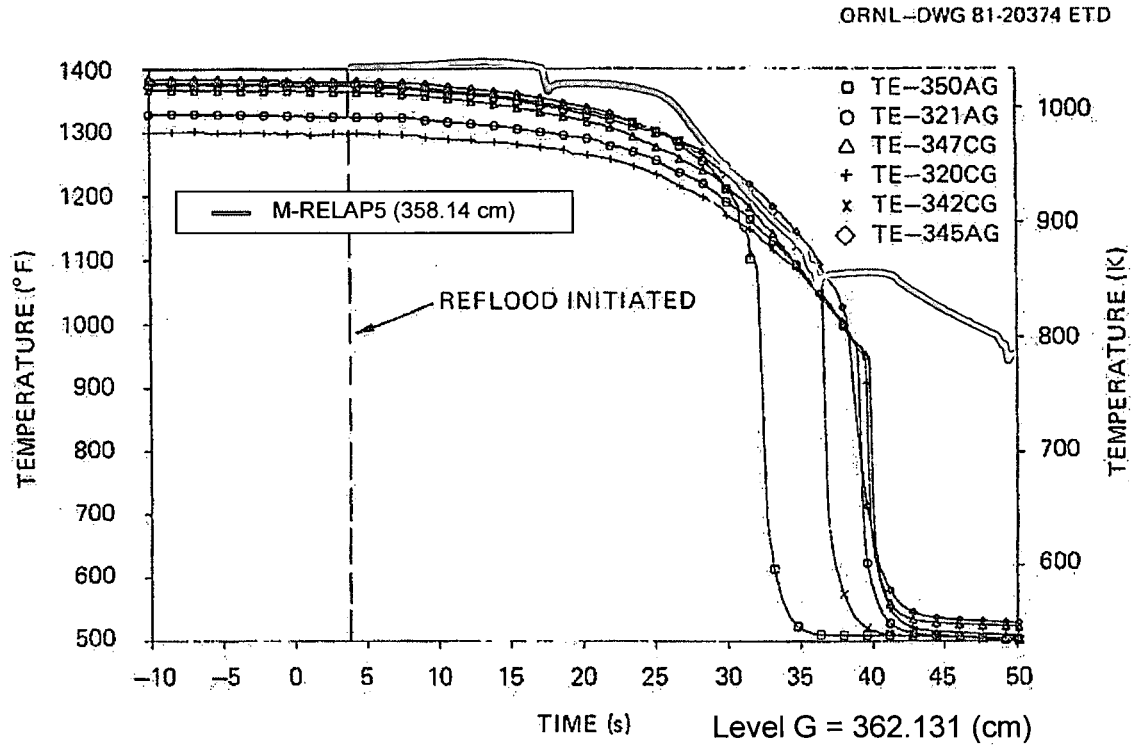


Figure 8.1.3-13 Comparison of Predicted and Measured FRS Temperatures at Level G for ORNL/THTF Test 3.09.10Q

Reference 8.1.3-2

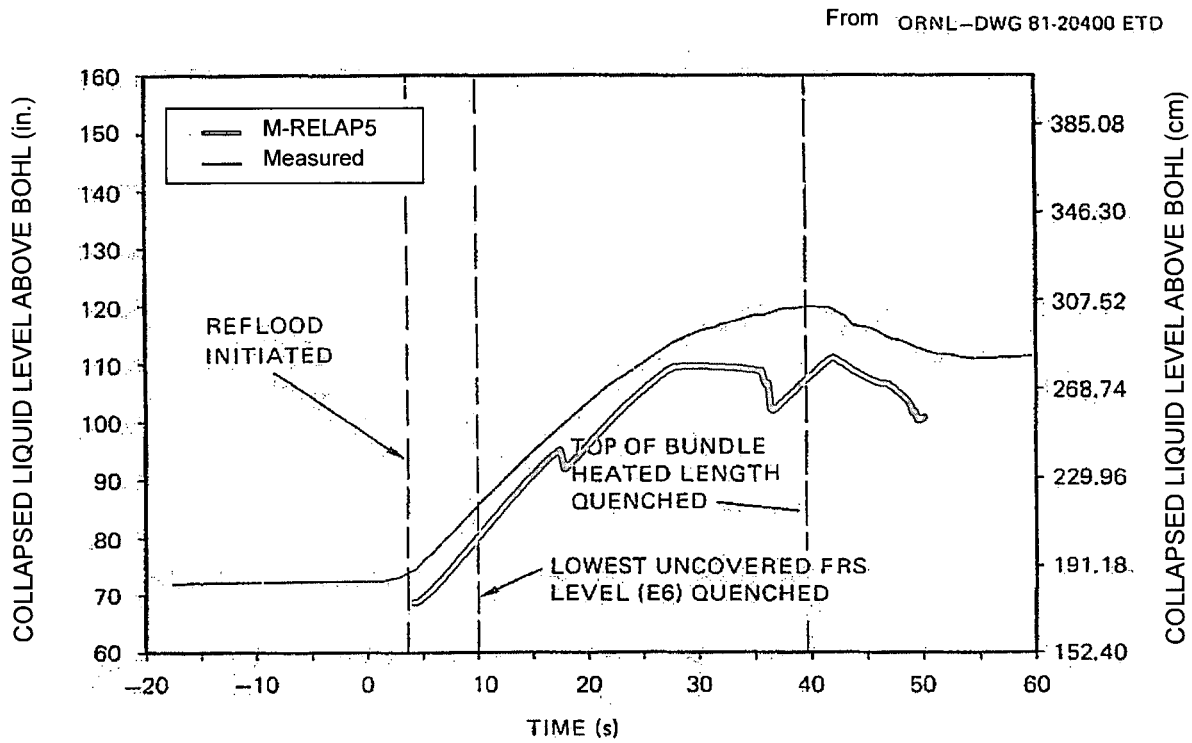
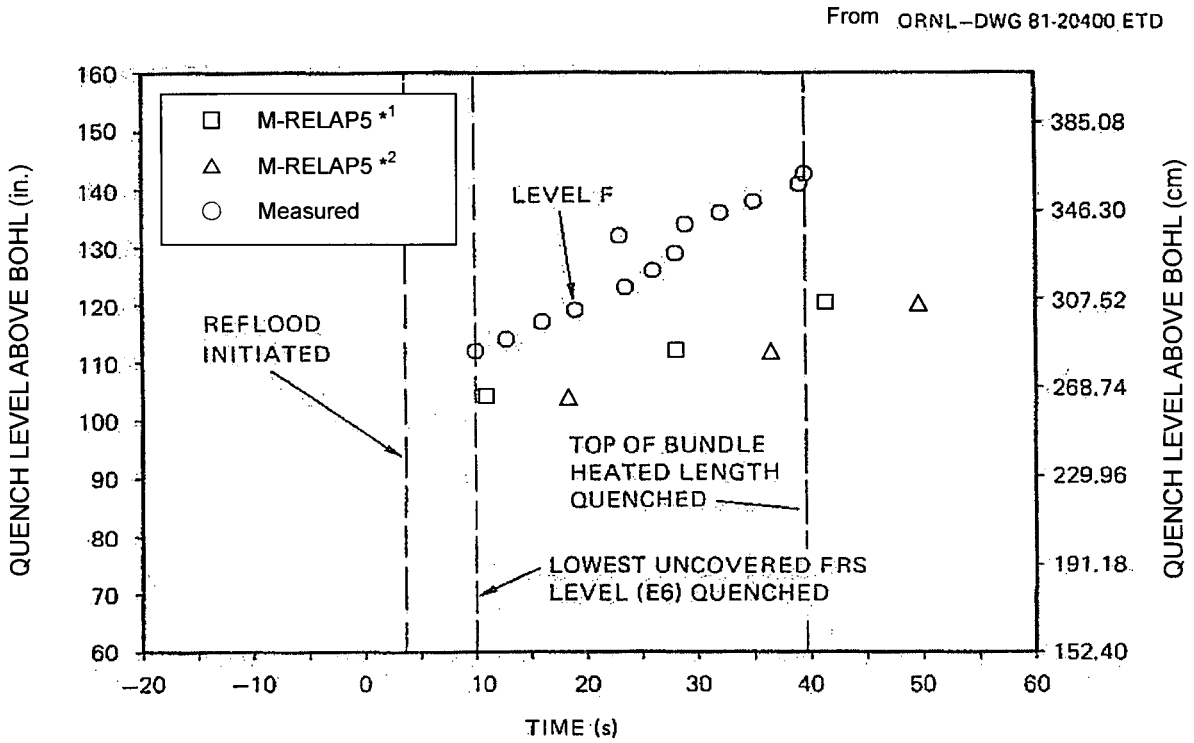


Figure 8.1.3-14 Comparison of Predicted and Measured Collapsed Liquid Level for ORNL/THTF Test 3.09.10Q

Reference 8.1.3-2



*1 The time when the heat transfer mode switches from film boiling to transition boiling.
 *2 The time when the heat transfer mode switches from transition boiling to nucleate boiling.

Figure 8.1.3-15 Comparison of Predicted and Measured Quench Level for ORNL/THTF Test 3.09.10Q

Reference 8.1.3-2

8.1.4 UPTF CCFL

8.1.4.1 Introduction

Heat removal by the steam generator plays important role in the small break LOCA when break flow rate is small and primary pressure remains higher than secondary side pressure. In this situation condensed water in the SG U-tube either accumulates in the SG U-tube and SG inlet plenum or flows back to the reactor vessel against steam flow. Counter-Current Flow Limitation (CCFL) characteristics in the SG U-tube and the hot leg will affect core cooling through behavior of the condensed water in the SG U-tube.

Verification of CCFL modeling in the hot leg region by the M-RELAP5 is conducted against the UPTF hot leg CCFL experiment (Ref. 8.1.4-1).

8.1.4.2 Test Facility and Test Conditions

Geometry of the test region in the UPTF facility is shown on Figure 8.1.4-1. The hot leg diameter is 0.75 m which is the same order of the US-APWR. In this separate effect test one of the four hot legs was used. Other loops are isolated from the test region. In the test facility, an ECCS line was connected to the hot leg location and the area of water drainage reduced by about 10% in a region called as "HUTZE" near the connection location. The ECCS injection to the hot leg is unique design to German type PWR which the UPTF facility simulates.

CCFL condition in the hot leg region is realized by injecting water into SG inlet plenum and steam injection into reactor vessel. Injected air is exhausted through the SG simulator and some of water is going down to the reactor vessel with remaining water flowing up with steam. System pressure and flow conditions of the test are as follows:

System pressure: 3 bar , 15 bar

Water flow rate: 30 kg/s

Steam flow rate: 12 kg/s to 20 kg/s six(6) conditions for 3bar

24 kg/s to 40 kg/s ten(10) conditions for 15 bar

One flow condition in 3 bar test and three flow conditions in 15 bar test do not show CCFL and all injected water goes down because of small steam flow.

8.1.4.3 Analysis Conditions

a. Derivation of CCFL parameters correlation

Parameters of CCFL correlation were derived from the test data for the analysis. The CCFL correlation used in the M-RELAP5 has the following general form (Ref. 8.1.4-2).

$$H_g^{1/2} + mH_f^{1/2} = c$$

$$H_i = j_i \left[\frac{\rho_i}{gw(\rho_f - \rho_g)} \right]^{1/2}$$

$$w = D_j^{1-\beta} L^\beta$$

$$L = \left[\frac{\sigma}{g(\rho_f - \rho_g)} \right]^{1/2}$$

where j is superficial velocity, ρ is density of fluid, g is gravity constant, D_j is junction hydraulic diameter, L is the Laplace capillary constant and σ is surface tension. m, c, β are used as input data. Suffix g and f represent gas and liquid respectively. Generally hydraulic diameter dependency disappears for large diameter pipe and β is assumed one (1.0). m and c are calculated by linear regression analysis of the experimental data. Figure 8.1.4-2 shows results of linear regression analysis and [] are obtained.

b. M-RELAP5 analysis with the CCFL correlation

To confirm validity of the derived CCFL correlation with M-RELAP5, analysis of the CCFL test data is performed using the CCFL correlation. The flow conditions applied to the analyses are shown in Table 8.1.4-1. The nodalization applied for the analysis is shown on Figure 8.1.4-3.

[

]

8.1.4.4 Analysis Results

Results of M-RELAP5 analysis with the CCFL correlation are shown on Table 8.1.4-2, Table 8.1.4-3, and Figure 8.1.4-4. In the tables, positive water flow means downflow to the reactor vessel and negative flow means almost complete flooding condition and unstable flow occurs. The characteristics of water downflow rate against steam upflow rate is well reproduced by the analysis for both 3 bar and 15 bar conditions.

8.1.4.5 Conclusion

CCFL parameters were derived for large diameter pipe from the UPTF CCFL test data. The M-RELAP5 analysis with the derived CCFL parameters well reproduced the test data. It is confirmed that M-RELAP5 with the CCFL parameters is applicable to CCFL behavior of the hot leg and the SG plenum in the US-APWR.

8.1.4.6 References

8.1.4-1. P. S. Damerell, N. E. Ehrich, K. A. Wolfe, "Use of Full-Scale UPTF Data to Evaluate Scaling of Downcomer (ECC Bypass) and Hot Leg Two-Phase Flow Phenomena," NUREG-CP-0091 vol4

8.1.4-2. "RELAP5-3D Code Manual (Volume II: User's Guide and Input Requirements)," INEEL-EXT-98-00834, Revision 2.3, April 2005

Table 8.1.4-1 Flow Rate Conditions for UPTF CCFL Test Analysis

System pressure	Flow rate of injected steam (kg/s)
15bar	24, 25, 28, 30, 31, 32, 33, 34, 35, 37, 39, 40
3bar	12, 13, 14, 15, 16, 17, 18, 20

Table 8.1.4-2 Results of UPTF CCFL Test Analysis (15bar)

Steam mass flow [kg/s]	24	25	28	30	31	32	33	34	35	37	39	40
Water mass flow [kg/s]	20.4	17.2	9.6	5.8	4.3	3.0	2.0	1.3	0.7	0.1	0.0	0.0

Table 8.1.4-3 Results of UPTF CCFL Test Analysis (3 bar)

Steam mass flow [kg/s]	12	13	14	15	16	17	18	20
Water mass flow [kg/s]	25.9	25.2	13.8	12.3	7.7	-0.9	-1.1	-1.4

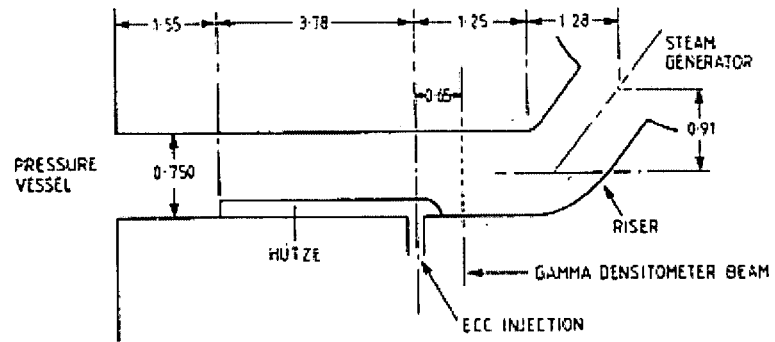


Figure 8.1.4-1 UPTF CCFL Test Analysis, Geometry of a Broken Loop Hot Leg



**Figure 8.1.4-2 Regression Analysis Results of the UPTF CCFL
Parameters β , c and m for M-RELAP5**

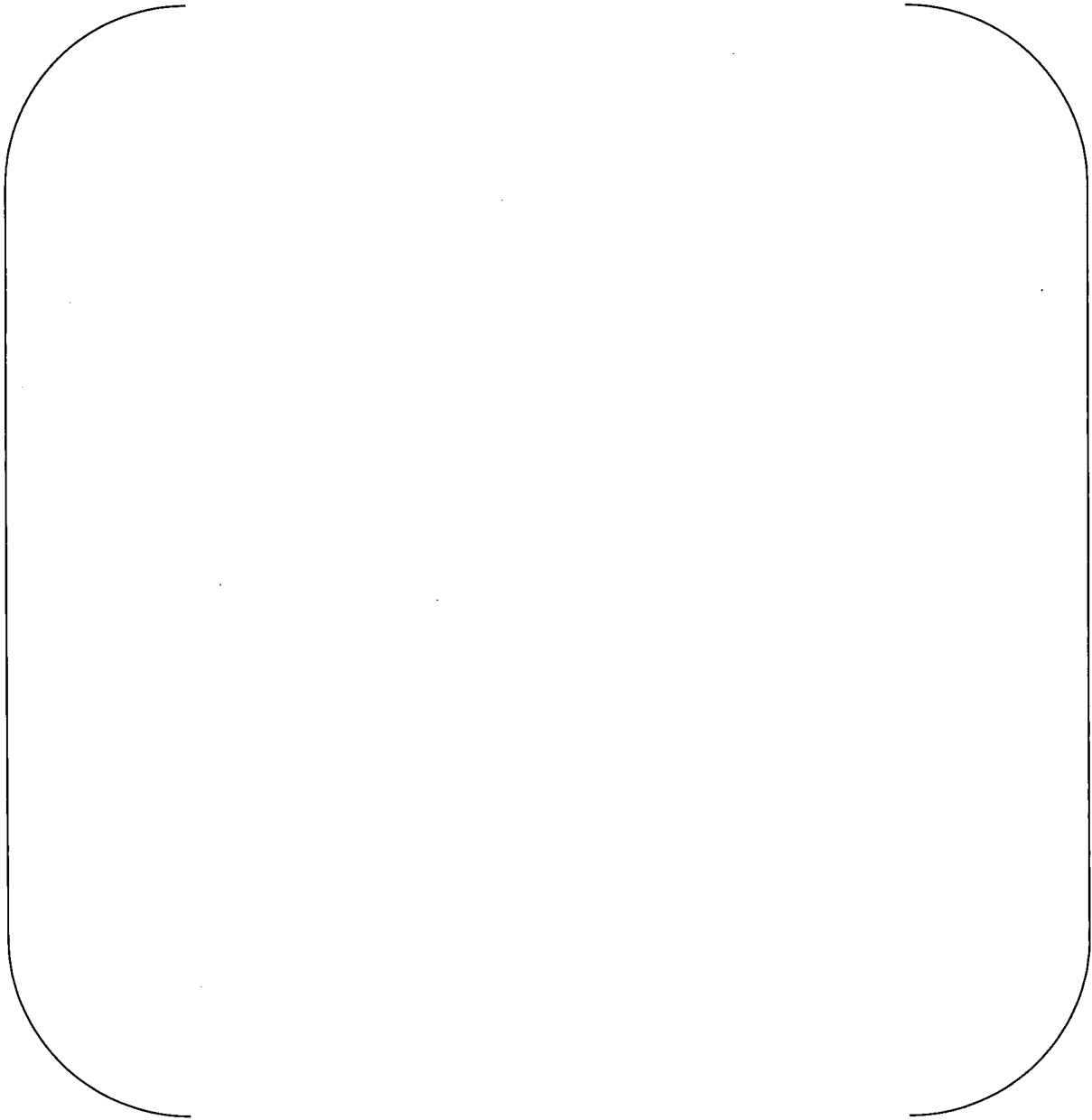


Figure 8.1.4-3 Nodalization Diagram Used for the UPTF CCFL Test Analysis

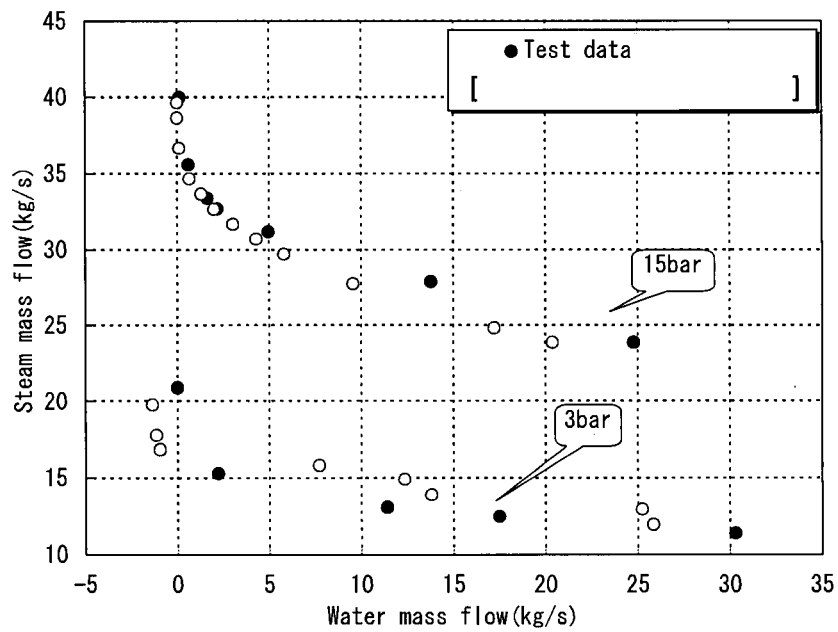


Figure 8.1.4-4 UPTF CCFL Test Analysis, Comparison of the Flooding Curves of Analysis Results and Test Results

8.1.5 Dukler Air-Water Flooding Test

8.1.5.1 Introduction

Heat removal by the steam generator plays important role in the small break LOCA when break flow rate is small and primary pressure remains higher than secondary side pressure. In this situation condensed water in the SG U-tube either accumulates in the SG U-tube and SG inlet plenum or flows back to the reactor vessel against steam flow. Counter-Current Flow Limitation (CCFL) characteristics in the SG U-tube and the hot leg will affect core cooling through behavior of the condensed water in the SG U-tube.

Verification of CCFL modeling in relatively small diameter pipe like a SG U-tube by the M-RELAP5 is conducted against the Dukler Air-Water Flooding Test (Ref. 8.1.5-1).

8.1.5.2 Test facility and test conditions

Figure 8.1.5-1 shows schematic of the facility of Dukler air-water flooding test. The test facility consists of a CALMING section which separates the falling liquid film and guides air into the test section (flow length:1.524m, ID= 0.0508m), a Test section (flow length:3.96 m, ID=0.0508 m), an AIR INLET section and a EXIT section which separates upflow water film and air. Entrained water is separated in the separator further in the downstream before air exhaust. The flow rate, pressure and liquid film thickness were measured during the test. The thickness of liquid film and the flow rate of entrainment were decided by weight change of a collection tank.

The tests were carried out at the four liquid flow conditions of 100, 250, 500, and 1000 lbm/hr at low pressure and atmospheric temperature. Air flow rate was varied at each liquid flow rate condition and steady condition was established. Water downflow rate was measured at each air flow rate. Table 8.1.5-1 shows water and air flow rate conditions of the test selected for the verification analysis and also resultant water downflow rate in comparison to analysis result.

8.1.5.3 Analysis conditions

a. Nodalization diagram

Figure 8.1.5-2 shows the nodalization diagram used for this analytical study. The model is

summarized as follows: [

]

b. CCFL option

The parameters of CCFL correlation proposed by Hewit & Wallis (Ref. 8.1.5-2) are used for this analysis.

$$\beta = 0.0$$

$$c = 0.88$$

$$m = 1.0$$

$$J_g^{*0.5} + J_f^{*0.5} = 0.88$$

$$J_g^* = j_g \left[\frac{\rho_g}{gD(\rho_f - \rho_g)} \right]^{1/2}$$

$$J_f^* = j_f \left[\frac{\rho_f}{gD(\rho_f - \rho_g)} \right]^{1/2}$$

where j_g is the vapor/gas superficial velocity, j_f is the liquid superficial velocity, ρ_g is the vapor/gas density, ρ_f is the liquid density, g is the gravitational acceleration, and D is the hydraulic diameter

8.1.5.4 Analysis results

Figure 8.1.5-3 shows characteristics of water downflow rate against air upflow rate in comparison to the test data. The liquid downflow rate is slightly underestimated but agreement with the test data is good. The calculated water downflow rate is 30% smaller than the test data on the average. Figure 98.1.5-4 shows the same characteristics with non-dimensional form.

8.1.5.5 Conclusion

Analysis of the Dukler Air-Water Flooding Test was conducted using M-RELAP5 with CCFL parameters proposed by Hewit & Wallis. The analysis results show good agreement with the test data. This verification analysis demonstrates that M-RELAP5 with the CCFL parameters proposed by Hewit & Wallis is applicable to simulation of CCFL behavior of small diameter pipe such as SG U-tube in the US-APWR.

8.1.5.6 Reference

- 8.1.5-1. A. E. Dukler, and L. Smith , " Two Phase Interactions in Counter-Current Flow : Studies of the Flooding Mechanism, Annual Report November 1975 – October 1977," NUREG/CR-0617, January 1979
- 8.1.5-2. Graham B. Wallis , "One dimensional Two Phase Flow," McGraw-Hill, 1969

Table 8.1.5-1 Experimental results

Point	Input Liquid Flow Rate (lb _m /hr)	Experimental Results	
		Input Gas Flow Rate (lb _m /hr)	Liquid Flow Down (lb _m /hr)
1	100	250	100
2	100	265	50
3	100	277	10
4	250	218	250
5	250	232	180
6	250	247	105
7	250	262	55
8	250	278	10
9	250	292	0
10	500	192	490
11	500	214	310
12	500	231	200
13	500	251	105
14	500	269	45
15	1000	133	1000
16	1000	159	720
17	1000	185	525
18	1000	210	370
19	1000	229	205
20	1000	262	60

(From NUREG/CR-0617)

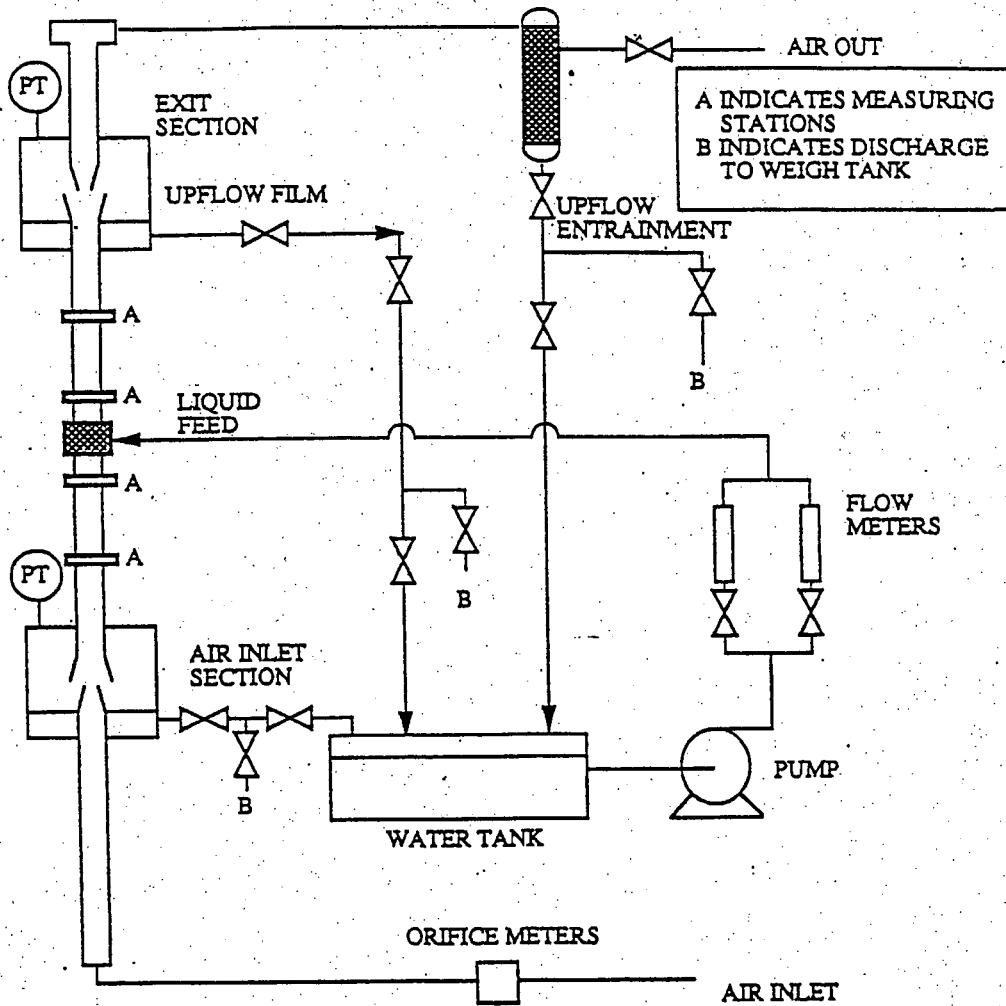


Figure 8.1.5-1 Schematic of the Dukler Air/Water Test Facility
(From NUREG/CR-0617)

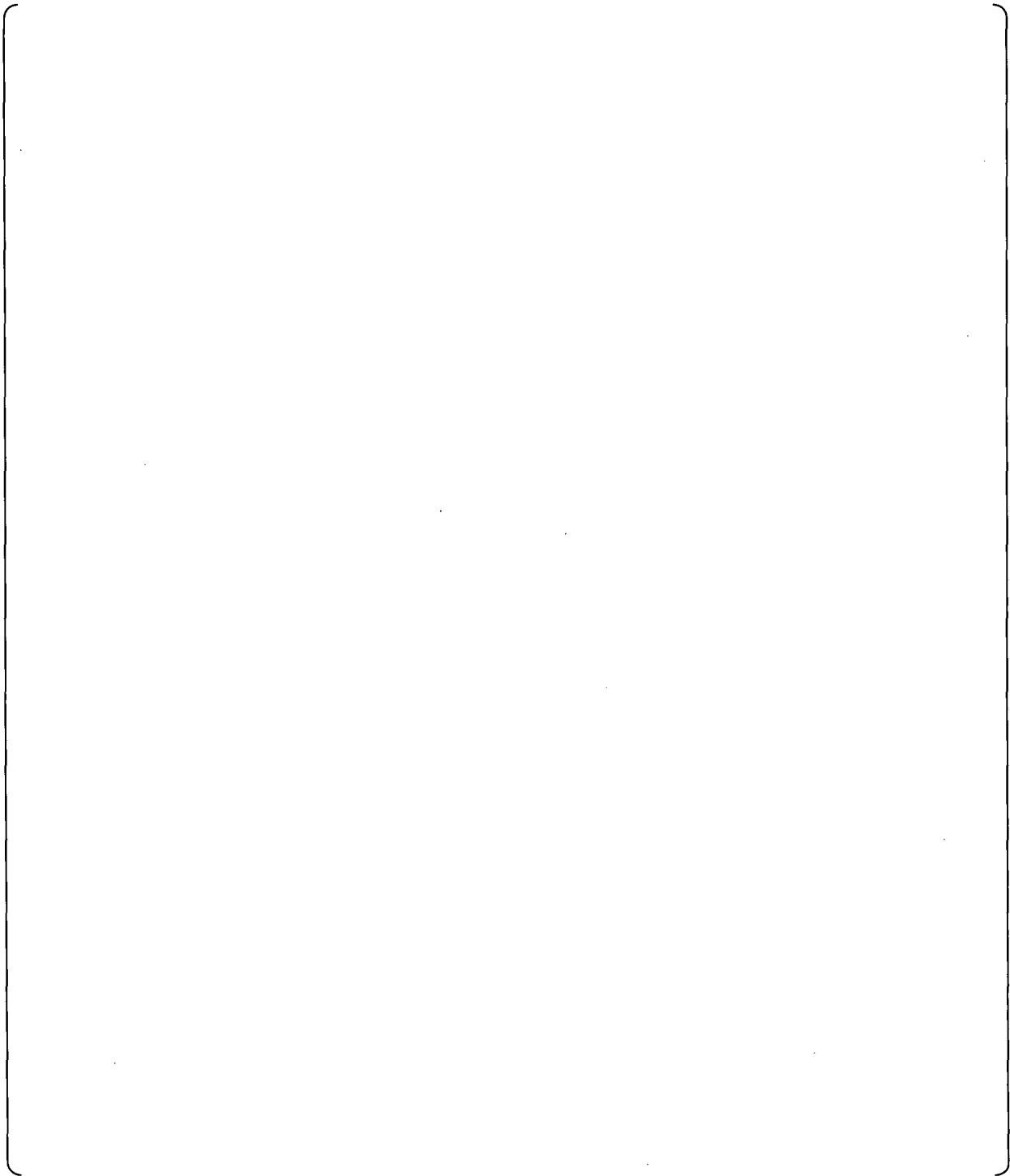


Figure 8.1.5-2 Nodalization Diagram of the Dukler Air/Water Flooding Experiment

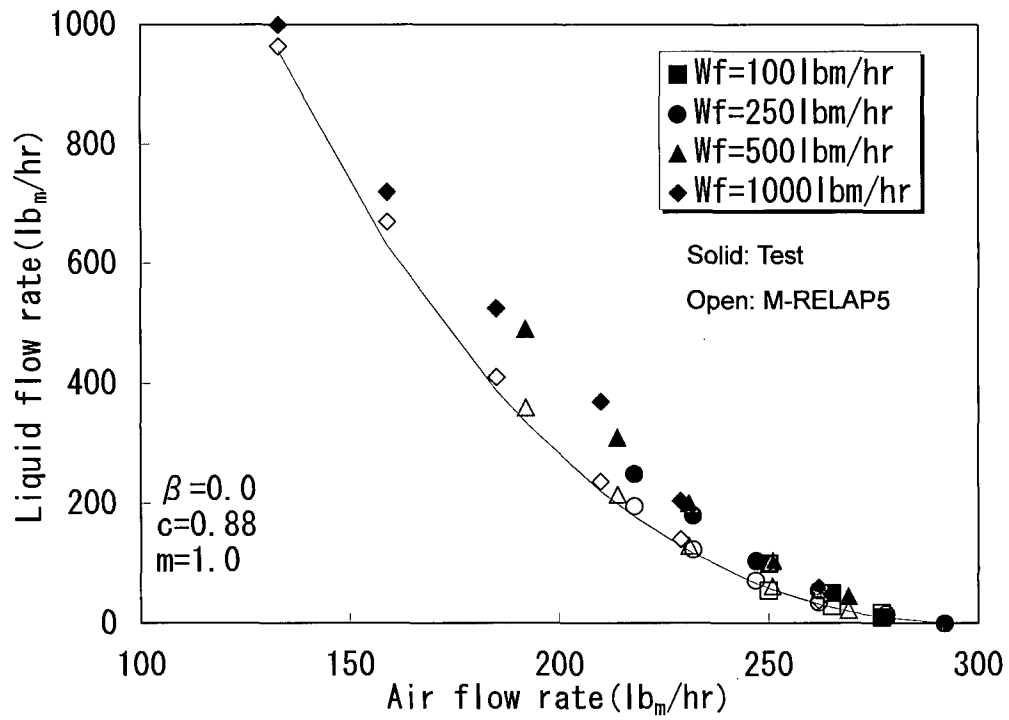


Figure 8.1.5-3 Comparison of Calculated and Measured Results Using the Wallis Flooding Correlation Constants($c=0.88$, $m=1.0$)

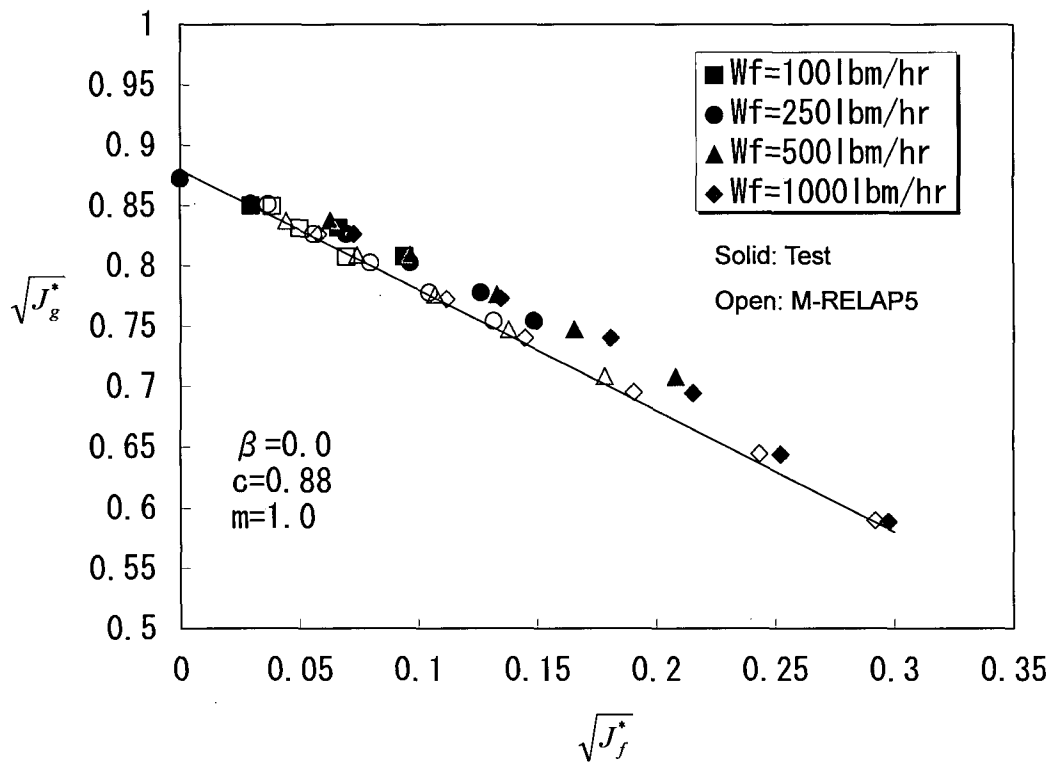


Figure 8.1.5-4 Comparison of Calculated and Measured Results Using the Wallis Flooding Correlation Constants($c=0.88$, $m=1.0$)

8.2 Prepare Input and Perform Calculations To Assess System Interaction and Global Capability

8.2.1 ROSA/LSTF small break (5%) LOCA test (SB-CL-18)

8.2.1.1 Introduction

The purpose of ROSA-IV/LSTF calculation is validation of M-RELAP5 code performance to predict following phenomena ranked high importance in PIRT for Small Break LOCA. : core dryout, Post-CHF heat transfer, rewet, core mixture level, water hold up in SG primary side, condensation drainage to inlet plenum, SG primary and secondary heat transfer, water level in SG outlet piping, loop seal formation and clearance, downcomer mixture level.

In the present calculation, the break flow and the SG secondary system pressure behaviors are specified as boundary conditions based on the measured data so as to validate M-RELAP5 ability to predict the reactor primary system responses in particular for the loop seal behavior. A sensitivity calculation is also performed to validate [

] is validated using the present SB-CL-18 test data. In addition, a sensitivity calculation, where the core decay heat curved is increased by 20% as same as is done for plant calculations by M-RELAP5, is performed to quantify its impact on PCTs for the present experimental analysis.

The base calculation, however, is difficult to validate the SG primary to secondary heat transfer [] since the primary and secondary system pressures are regulated by the given boundary conditions for the break flow and the SG secondary system, respectively. In addition, it is important to assess the integral code capability to predict the overall plant response, and to comprehend safety conservatism expected by using the code, by a manner applied to actual plant calculations. Therefore, an additional calculation is conducted so as to confirm that M-RELAP5 conservatively predicts the PCTs when the analysis scheme applied to US-APWR SBLOCAs concerning the break and secondary system is employed for the code assessment using the ROSA experimental data.

8.2.1.2 Selection of SB-CL-18

There are 5% break tests, 10% break test, 0.5% break tests, 2.5% break tests, and so on in all ROSA-IV/LSTF SBLOCA tests.

For ROSA-IV/LSTF calculation, the case SB-CL-18 (5% break) was selected. 5% break is equivalent to 6 in. break SBLOCA of reference 4-loop PWR (Ref. 8.2.1-3). The reason why SB-CL-18 is selected for M-RELAP5 calculation is that both loop seal phenomena and boil off phenomena considered important for SBLOCA were observed in the experiment. In addition, SB-CL-18 is selected as international standard problem No.26 (ISP-26) (Ref. 8.2.1-4).

8.2.1.3 Test Condition

(a) Test Facility (Ref. 8.2.1-1 and Ref. 8.2.1-2)

The LSTF is a 1/48 volumetrically scaled model of a Westinghouse-type 3423MWt four loop PWR. The LSTF has the same major component elevations as the reference PWR to simulate the natural circulation phenomena, and large loop pipes (hot and cold legs of 207mm in diameter) to simulate the two-phase flow regimes and phenomena of significance in an actual plant. The LSTF equipment can be controlled in the same way as that of the reference PWR to simulate long term operational transients. Furthermore, the LSTF is designed to be operated at the same high pressures and temperatures as the reference PWR.

Figure 8.2.1-1 and Table 8.2.1-1 show the structure and major dimensions of the LSTF, respectively. Figure 8.2.1-2 shows the pressure vessel assembly. The four primary loops of the reference PWR are represented by two equal-volume loops. The overall facility scaling factor is 1/48. The hot and cold legs were sized to conserve the volume scaling and ratio of the length to the square root of pipe diameter, L/\sqrt{D} , for the reference PWR in expectation that the flow regime transitions in the primary loops can be simulated appropriately by taking this scaling approach.

(b) Test Procedure

The major initial conditions of the LSTF 5% cold leg break test, Run SB-CL-18, are shown in Table 8.2.1-2. Both the initial steady state conditions and the test procedures were designed to minimize the effects of LSTF scaling compromises on the transients during the test.

The most important design scaling compromise is the 10MW maximum core power limitation, 14% of the scaled reference PWR rated power. The steady-state condition is restricted to a core mass flow rate that is 14% of the scaled value to simulate the reference PWR temperature

distribution in the primary loop. The desired primary coolant flow rate was established by reducing the pump speed with the flow control valves (FCVs) in the cross-over legs fully open. The primary loop flow rate was then increased at the time of break to improve the similarity of the LSTF to the reference PWR by increasing the pump speed.

The primary-to secondary heat transfer must also be maintained at 10MW, i.e., 14% of the scaled value. Since the LSTF steam generators (SGs) are geometrically scaled to the reference PWR, the 14% primary-to-secondary heat transfer rate is established by raising the secondary temperature such that the primary pressure and temperature are representative of the reference PWR.

Major operational setpoints and conditions including emergency core cooling system (ECCS) actuation logic for this test are summarized in Table 8.2.1-3. After the break occurred at time zero, the primary system depressurizes quickly. At a pressurizer pressure of 12.97MPa, the reactor scrams. Loss of offsite power concurrent with the reactor scram is assumed and the primary coolant pumps are tripped to begin coastdown and the core power begins to decrease along the pre-programmed decay curve. The power decay curve used in the test takes into account the fission products and actinides decay powers, and delayed neutron fission power, and gives a slower decrease than the ANS standard. The core power decay curve used in the test is tabulated in Table 8.2.1-4. The SG auxiliary feed water is assumed to fail to simplify the transient.

At a pressurizer pressure of 12.27 MPa, the safety injection signal is sent that trips ECCS to be actuated at respective pressure setpoints. However, the high pressure charging system and high pressure injection system (HPIS) are assumed to fail in the test. The ECCS conditions are summarized in Table 8.2.1-5. The accumulator (ACC) system and the low pressure injection system (LPIS) are specified to initiate coolant injection into the primary system at pressures of 4.51 and 1.29 MPa, respectively. The accumulator-cold (ACC-Cold) system simulates ACC injection flow to the cold leg A and the accumulator-hot (ACC-Hot) system simulates ACC injection flow to the cold leg B. The water temperature of ACC-Cold and ACC-Hot tanks are the same and the ratio of ACC injection flow rate to cold leg A and cold leg B is 3:1. This injection method is adopted for good simulation of ACC injection flow rate to each ~~cold~~-cold leg in the LSTF.

The break point was located in the B-loop (loop without a pressurizer) cold leg between the reactor coolant pump and the reactor pressure vessel. The break orientation was horizontal.

The break assembly and break orifice are shown schematically in Figure 8.2.1-3 and 8.2.1-4, respectively.

(c) Test Results

The chronology of events for Run SB-CL-18 is shown in Table 8.2.1-6.

The experiment was initiated by opening the break valve at time zero. The reactor scram signal was sent at a pressurizer pressure of 12.97 MPa, 10 s after break, and this signal closed the turbine throttle valve. The turbine bypass system was inactive due to the assumption of loss-of-offsite power occurring concurrently with scram. The loss of offsite power terminated the main feedwater, and also tripped the reactor coolant pumps to initiate coastdown. The reactor coolant pumps completely stopped at about 265 s after break.

The safety injection signal was sent at a pressurizer pressure of 12.27 MPa, about 12 s after break. However, the high pressure charging and high pressure safety injection systems were not activated because of the failure assumptions. The secondary pressure increased after the closure of the turbine throttle valve, but was maintained at approximately 8 MPa due to the SG relief valve operation.

The core was temporarily uncovered between about 120 s and 155 s after break, and the heater rods in most of the core experienced superheating of up to about 190 K. This temporary core uncover occurred during loop seal clearing. The core liquid level was depressed concurrently with the level drop in the cross-over leg downflow sides. The core level drop was amplified by the manometric effect caused by an asymmetric coolant holdup in the SG upflow and downflow sides. At about 140 s after the break, loop seal clearing occurred in both loops and the core liquid level recovered rapidly. After the loop seals cleared, the break flow changed from low quality to high quality two-phase flow, and the depressurization of the primary loop was accelerated. By about 180 s after the break, the primary loop pressure decreased below the SG secondary side pressure. Thereafter, the steam generators no longer served as heat sinks and the energy removal from the primary system was through the discharge of coolant from the break. It is noted that the loop seal clearing occurred before the reversal in primary and secondary pressures.

The core was uncovered again after about 420 s due to vessel coolant boil-off, and the heater rods in the upper part of the core showed superheating of up to about 80 K. Due to

depressurization of the primary system, the accumulators were automatically actuated at 455 s to fill the system with the emergency core cooling (ECC) water. The core was covered with two-phase mixture again after about 540 s by the ACC water injection.

The peak cladding temperature in the test was approximately 740 K, observed during the temporary core uncovering just before the loop seal clearing.

8.2.1.4 M-RELAP5 Calculation Procedure

M-RELAP5 capability to predict the integral effects occurring under SBLOCAs is validated using the SB-CL-18 test data obtained in ROSA-IV/LSTF. SBLOCAs contain several complicated phenomena and processes occurring in the primary system, which are significantly affected by the break flow and/or the secondary system behavior, such as the loop seal behavior. On the other hand, the SBLOCA analysis based on M-RELAP5 employs the Appendix K methodology, where several models and correlations are specified to use for plant safety calculations so as to ensure sufficient conservatism. Use of these conservative models and correlations tends to deviate validations for a code from investigating its precise ability to predict important phenomena and processes.

Therefore, the break flow and the SG secondary system pressure responses are given as boundary conditions for Base Case calculation in order to reasonably evaluate code ability to predict thermal-hydraulic responses occurring in the primary system. Based upon this calculation, [] is assessed, which is provided as Sensitivity-1 in Section 8.2.1.6. Since the core power decay is conservatively treated for plant safety calculations, Sensitivity-2 calculation provides impacts of the conservative assumption, particularly on cladding heat-up behaviors, in Section 8.2.1.7.

As discussed in Base Case, early core liquid level depression is observed in M-RELAP5 prediction. The additional sensitivity calculations (Sensitivity-3, -4, and -5) are performed in order to examine the possible causes. The results are reported in Section 8.2.1.8.

Finally, the over all code ability to predict the experimental test is assessed by a calculation where the break flow and the SG secondary system pressure are explicitly simulated using code models as same as is done for plant safety calculations. It is noted that the safety assumption with respect to the core power decay is not taken into account for this calculation. The results are described in Section 8.2.1.9 of the present material.

The followings describe the M-RELAP5 model applied in the ROSA-IV/LSTF SBLOCA experimental test analysis primarily for Base Case calculation. Changes of the applied model for each sensitivity calculation are given in each of the corresponding sections.

(a) M-RELAP5 Model of the LSTF

The M-RELAP5 noding diagrams for the LSTF uses a similar amount of detail in the vessel, steam generators, and loops as used in the actual PWR plant model. Figure 8.2.1-5 shows the M-RELAP5 noding diagram of a cold leg break LOCA for the LSTF. Figure 8.2.1-6, Figure 8.2.1-7, Figure 8.2.1-8, and Figure 8.2.1-9 show the M-RELAP5 noding diagrams of the LSTF pressure vessel, hot leg, steam generator (SG), cross-over leg and cold leg, respectively.

[

.]

[

.]

[

.]

SG noding is shown in Figure 8.2.1-8. [

]

[

]

[

]

[

]

[

]

(b) Calculation Conditions

Initial conditions:

Table 8.2.1-2 summarizes initial conditions before break. 2000-second steady-state simulation was performed. At the end of this 2000-second simulation, predicted and measured flow parameters were compared to ensure reasonably good agreement by the model.

Boundary conditions:

Core power curve (Figure 8.2.1-10), pump coastdown data (Figure 8.2.1-11 and 8.2.1-12), SG secondary pressure (Figure 8.2.1-13 and 8.2.1-14), feed water stop timing, and main steam line valve close timing uses time table boundary condition data made from experimental data.

To ensure the calculated break flowrate equal to test data, critical flow model was not used and velocity boundary condition was used. [

] Break flow velocity is calculated from break mass flowrate and M-RELAP5 calculation result of two-phase mixture density at break nozzle. The comparison of break flow in test data and M-RELAP5 calculation is shown in Figure 8.2.1-15.

Assumptions for analysis:

[

]

8.2.1.5 M-RELAP5 Calculation Result (Base Case)

The comparisons between test data and M-RELAP5 result (base case) are shown in Figure 8.2.1-16 through 44.

(a) Discussion of Blowdown Period (0 - 50 sec)

Primary pressure drop behavior of M-RELAP5 agrees with that of test data (Figure 8.2.1-16). And loop flowrate drop of M-RELAP5 agrees with that of test data (Figure 8.2.1-18 and 19). ~~So, M-RELAP5 capability to predict blowdown phase is excellent.~~]

Therefore, it is judged that M-RELAP5 well predicts the blowdown phase. It is noted that an additional calculation is performed to validate the M-RELAP5 predictability in Section 8.2.1.9, where the break flow and the SG secondary system behaviors are explicitly simulated using the code models.

(b) Discussion of Natural Circulation Period (50 - 95 sec)

After blowdown period, the core heat was removed by the natural circulation flow, which is driven by the heat transfer between SG primary and secondary side. The liquid velocity at the top of SG U-tube stopped at about 95 sec, and then the liquid condensed in the U-tubes is

accumulated in the SG inlet plenum and SG U-tube uphill side because of the CCFL phenomena.

Both loops flowrate at cross-over leg of M-RELAP5 calculation agree with these of the test data during natural circulation period (Figure 8.2.1-18 and 19). [

] Hence, it is judged that ~~As a result, M-RELAP5 capability to predict SG primary and secondary heat transfer is good.~~

(c) Discussion of Loop Seal Period (95 - 160 sec)

(1) Hydraulic Result

Break flowrate of M-RELAP5 calculation is adjusted to test data (Figure 8.2.1-15), as a result, primary pressure drop behavior agrees with test data excellently (Figure 8.2.1-16). Signal timings agree with test data (Table 8.2.1-6). Secondary pressures are also adjusted to test data (Figure 8.2.1-13 and 8.2.1-14). Primary pressure and secondary pressures of M-RELAP5 calculation agree with test data, as a result, M-RELAP5 capability to predict SG primary and secondary heat transfer is good. Therefore, M-RELAP5 ability to predict the SG primary and secondary heat transfer is addressed in Section 8.2.1.9, where the break flow and the SG secondary system behaviors are explicitly simulated using the code models.

The timing and depth of core level drop caused by loop seal of M-RELAP5 result agree with test data (Figure 8.2.1-17). The timing of loop seal clearing of M-RELAP5 result also agrees with test data excellently. After loop seal clearing, core water level recovered to 15kPa, equivalent to test data.

As a result, M-RELAP5 can predict the phenomena of core mixture level and loop seal formation and clearance.

Downcomer water level of M-RELAP5 result agrees with that of test data at about 150 sec (Figure 8.2.1-34). As a result, M-RELAP5 capability to predict downcomer mixture level is good during loop seal period. Downcomer water level of M-RELAP5 result tends to agree with that of test data. However, the downcomer water level drop timing is earlier in the M-RELAP5 calculation similarly to the core liquid level depression. Possible causes of the early liquid level depression by M-RELAP5 are investigated in Section 8.2.1.8.

SG U-tube downhill side and cross-over leg downhill side water level drop of M-RELAP5 result agree with these of test data (Figure 8.2.1-28 through 31). ~~As a result, M-RELAP5 capability to predict water level in SG outlet piping is excellent.~~

The timing when cross-over leg downhill side water level dropped to bottom (Figure 8.2.1-30 and 31), core water level began to recover (Figure 8.2.1-17), and break flow switched from two-phase mixture flow to single phase vapor flow (Figure 8.2.1-15). As a result, M-RELAP5 can predict loop seal formation and clearance phenomena.

Differential pressure from hot leg to SG U-tube top of M-RELAP5 calculation result agrees with that of test data (Figure 8.2.1-20 and 21). As a result M-RELAP5 can predict important phenomena during loop seal period.

To check further details about water held up in hot leg, SG inlet plenum and SG U-tube uphill side, their differential pressures of M-RELAP5 calculation are shown in Figures 8.2.1-22 through 27, respectively. These figures present that water was held up in both SG U-tube uphill side and SG inlet plenum. In the test, the amount of water held up in 141 SG U-tubes were different each other because of multi-dimensional effect (Figures 8.2.1-26 and 27). In M-RELAP5, water is easily held up in SG U-tube, because SG U-tube is modeled with one pipe. As a result, M-RELAP5 capability to predict water hold up in SG primary side and condensation drainage to inlet plenum is good.

(2) Heat-up

Core collapsed water level drop agree with test data at the timing of loop seal ~~formation~~ formation (Figure 8.2.1-17). The comparison of heater rod temperature that heated up highest in test data in hot assembly is shown following paragraph.

In the test data, the surface temperature of high-power rod heated up at 124 sec after break (Figure 8.2.1-37). In the M-RELAP5 result, heater surface temperature heated up at 134 sec after break (Figure 8.2.1-38). As a result, M-RELAP5 capability to predict core dryout phenomenon is a little conservative in hot assembly.

In the test data, heater surface temperature reached 739 K at 147 sec and then cooled down (Figure 8.2.1-37 and 42), so that this is the maximum rod surface temperature during loop seal

period. In the M-RELAP5 result, heater surface temperature reached 730 K at 158 sec and then cooled down (Figure 8.2.1-38 and 41), so that this is the maximum rod surface temperature during loop seal period. As a result, M-RELAP5 capability to predict Post-CHF heat transfer is good in hot assembly.

In the test data, heater surface temperature reached saturated temperature and then all of rods were rewetted before 155 sec (Figure 8.2.1-37). In the M-RELAP5 result, heater surface temperature reached saturated temperature and then rewetted at 212 sec after break (Figure 8.2.1-38). As a result, M-RELAP5 capability to predict rewet is conservative.

As a result, M-RELAP5 can predict core dryout, Post-CHF heat transfer, and rewet during loop seal ~~formation~~ formation and clearing period.

(d) Discussion of Boil Off Period

(1) Hydraulic Result

Pressure drop to equal to data of test data, break flowrate is adjusted when the break flow become to single-phase vapor flow (Figure 8.2.1-15 and 16).

Core water level was dropping at about 300 sec in M-RELAP5, while core water level did not drop until 400sec in test data (Figure 8.2.1-17). Downcomer water level drop timing is also earlier than the test data (Figure 8.2.1-34). As a result, the water mass inventory in the vessel of M-RELAP5 was smaller than that of the test data. Details are investigated in Section 8.2.1.8.

Loop seal clearing was occurred in both loops in M-RELAP5 calculation (Figure 8.2.1-18 and 8.2.1-19). But much liquid remain in the cross-over leg uphill side (Figure 8.2.1-32 and 8.2.1-33). It is insufficient to predict the liquid distribution after loop seal clearing and the core liquid level of M-RELAP5 is conservative.

(2) Heat-up

Heater rod surface temperature heat up timing is earlier than test data (Figure 8.2.1-37 and 38) because onset of core collapsed liquid level depression is earlier than test data (Figure 8.2.1-17). In M-RELAP5, heater rod surface temperature heated up when core collapsed liquid level was about 15kPa, while in test data, heater rod surface temperature heated up when core collapsed liquid level was about 16kPa, equivalent to M-RELAP5. This difference in pressure

drop is negligibly small, after converting to the collapsed liquid level and comparing with the node height employed for the core nodalization. As a result, M-PRELAP5 capability to predict core dryout in boil off transient is good.

In the test data, the surface temperature of high-power rod reached 620 K at 497 sec and then cooled down, so that this is the maximum rod surface temperature during boil off period (Figure 8.2.1-37). In the M-RELAP5 result, heater surface temperature reached 761 K at 472 sec and then cooled down (Figure 8.2.1-38). In M-RELAP5, peak temperature was higher because core collapsed water level was lower (Figure 8.2.1-17). It indicates M-RELAP5 results are conservative enough.

Heat-up rate in M-RELAP5 was greater than that in test data (Figure 8.2.1-37 and 38). The reason is that core power was higher because of the early core water level drop timing. M-RELAP5 capability to predict Post-CHF heat transfer is good.

(e) Discussion of Recovery Period

ACC flow was initiated at 455 sec (test data) or 480445 sec (M-RELAP5), and then core water level started to recover (Figure 8.2.1-35 and 36). And downcomer water level also started to recover. In test data, heater rod surface temperature reached saturated temperature and then rewetted at 538 sec (Figure 8.2.1-37). In M-RELAP5 result, heater rod surface temperature reached saturated temperature and then rewetted at 554 sec (Figure 8.2.1-38). The difference of core collapsed liquid level between M-RELAP5 and test data is very small (Figure 8.2.1-17), so that the final rewet time of M-RELAP5 agrees with test data.

The temperature behavior of heater rod depends on the core liquid level profile. M-RELAP5 can validly predict these phenomena as shown above. It is concluded that M-RELAP5 predict the rewet phenomena conservatively.

8.2.1.6 M-RELAP5 Calculation Result (Sensitivity-1 Calculation)

In the base case, it is insufficient to predict the dryout phenomena at the upper portion (above about 2.45m) of the heater rod during loop seal period. This discrepancy is due to the nominal analysis condition of M-RELAP5 which purpose is to estimate the average thermal hydraulic behavior.

There are some heater rods heated up at such a upper portion in the experimental data. It indicates that the accumulated water on the upper plenum region partly flow down to the core region. This is consistent with the view that a spatially non-uniform liquid distribution exists in the core region. Such liquid distribution effects are already modeled as CHF multiplier in M-RELAP5. But ~~this~~ these base case results indicate that this CHF multiplier is not enough for ROSA-IV/LSTF SBLOCA analysis.

[

]

Figure 8.2.1-45 and Figure 8.2.1-46 show the void fraction in the upper part (about 3.57m and 3.17m) of the core. It is seen that the void fraction of both cases are high and greater than [] during loop seal period. Subsequently, the dryout phenomena at the upper portion (about 3.57m and 3.17m) are now calculated to occur in this sensitivity-1 calculation, as illustrated in Figure 8.2.1-47 and Figure 8.2.1-48.

It is concluded that M-RELAP5 under the nominal conditions can simulate the overall hydraulic behavior during the loop seal period very well and can predict the heat-up behavior of the average heater rod due to core uncover, and M-RELAP5 under the conservative conditions for dryout can also predict the heat-up behavior at the upper portion.

8.2.1.7 M-RELAP5 Calculation Result (Sensitivity-2 Calculation)

As described above sections, the validity of M-RELAP5 capability to predict the SBLOCA scenario, typically loop seal formation and clearance, is confirmed by both base case and the sensitivity-1 calculation.

For the safety analysis of the US-APWR, the ANS (1971) decay heat multiplied by 1.2 should be applied for the conservativeness. Therefore, to try to evaluate this conservativeness of decay heat, the sensitivity analysis with 1.2 times core power was executed (hereafter sensitivity-2) (Figure 8.2.1-53).

The core differential pressure is shown in Figure 8.2.1-54. The rod surface temperatures are also shown in Figures 8.2.1-55 through 7060. Figure 8.2.1-54 shows that the core collapsed

liquid level of this sensitivity calculation is equivalent to that of the base case (Figure 8.2.1-17) until loop seal clearing. It indicates that the effect of core power uprate is small and there is no impact against the thermal hydraulic behavior before loop seal clearing. And then, because of the excess core power, the amount of vapor generation is too much and the core liquid level did not completely recover after loop seal clearing. As results, the onset of the heat-up during boil off period became too early and very conservative rod temperatures were obtained.

8.2.1.8 Sensitivity Calculations for Core Water Level Depression (Sensitivity-3, 4, 5)

Three additional sensitivity analyses have been performed to investigate the difference in core water level between the Base Case and test data described in section 8.2.1.5. [

[

]

[

]

[

]

8.2.1.9 Sensitivity Calculation with Simulated Secondary System and Break Flow Behaviors

An additional assessment with the simulated secondary system and the break behavior in the same manner as the US-APWR analysis is performed. [

]

The M-RELAP5 nodding diagram near the break is shown in Figure 8.2.1-81. The nodding diagrams for the remainder of the system are same as shown in Figures 8.2.1-5 to 8.2.1-9. The critical flow model is applied to VALVE 915 and the stratification entrainment/pullthrough model for a side located junction is specified at SNGLJUN 917. The main steam isolation valve is modeled at VALVE 529(329) and is assumed to close at 14.0 seconds as measured. The steam line relief valve is modeled at VALVE 569(369) between steam dome BRANCH 518(318) and the atmosphere in TMDPVOL 570(370). Steam line relief valve is assumed to be opened at 8.20MPa and closed at 7.90MPa. Flowrate through steam line relief valve is calculated using the Ransom-Trapp critical flow model in M-RELAP5. Main feed water is modeled with TMDPJUN 561(361) and is tripped at 16.0 seconds as measured. Auxiliary feed water is modeled with TMDPJUN 551(351), but no auxiliary feed water injection occurs in the calculation because auxiliary feed water failure was assumed in this experiment.

The comparison of the sequence of events is shown in Table 8.2.1-7. The comparisons of main parameters between test data and M-RELAP5 predictions are shown in Figures 8.2.1-82 to 8.2.1-99.

The primary system depressurizes after the break initiation until the pressure is equalized at the level slightly above the secondary system pressure, through the natural circulation phase to the loop seal clearance. The primary and secondary pressure responses agree well with the measured values from the break initiation through the loop seal clearance shown in Figures 8.2.1-82 to 84. Almost all of the heat transferred from the primary side to the secondary side through the SG is used to generate vapor in the SG and most of the generated vapor is released through the main steam line or the steam line relief valves. The comparison of the integral of vapor mass released from the SG from the break initiation to the loop seal clearing is shown in Figure 8.2.1-99. The difference between the calculation and measurement is less

than 8%. These agreements of the primary/secondary pressure and the integrated vapor mass release from the SG indicate that M-RELAP5 is able to predict the SG primary to secondary heat transfer [

1.

Figures 8.2.1-88 and 89 show that the loop seal was formed around 100 seconds and was cleared around 160 seconds after the break initiation in the experiment. M-RELAP5 accurately simulates the loop seal behavior both for the intact and broken loops, although the water retention in the intact loop is slightly overestimated in the M-RELAP5 calculation as shown in Figure 8.2.1-90. This overestimated water remained in the intact loop leads to under-prediction in the coolant provided toward the reactor vessel after the loop seal clearance as shown in Figure 8.2.1-92, resulting in PCTs higher than the measurements.

Break flowrate during the two-phase or single vapor phase conditions is over-predicted compared with that specified as the boundary condition in the base case as shown in Figure 8.2.1-85. This causes the faster depressurization of the predicted primary system pressure after the loop seal clearing and the faster accumulator actuation than in the experiment as shown in Figure 8.2.1-82, Figure 8.2.1-86 and Figure 8.2.1-87. Although the accumulators initiate earlier than in the experiment, the predicted heater rod surface temperatures are over-predicted even for the second core heat-up as mentioned previously.

The predicted PCTs are higher than the measured ones as shown in Figures 8.2.1-93 through 8.2.1-98. The predicted and measured PCTs during both the loop seal clearance and boil-off periods are compared in Table 8.2.1-8. It is confirmed from this calculation that M-RELAP5 conservatively predicts the PCTs when the analysis scheme applied to US-APWR SBLOCAs concerning the break and secondary system is employed for the code assessment using the ROSA experimental data. It must be emphasized that any conservatism for the decay heat is not taken into account in the present calculation, although the decay heat is increased by 20% from the ANS 1971 decay curve for the plant calculations to attain sufficient conservatism.

8.2.1.108 Conclusions

~~M-RELAP5 predicted 5 period phenomena specific to SBLOCA. In addition, M-RELAP5 predicted excellently the following important parameters: water hold up in SG primary side, condensation drainage to inlet plenum, SG primary and secondary heat transfer, water level in SG outlet piping, and loop seal formation and clearance. And M-RELAP5 predicted the~~

following important parameters excellently in loop seal period and conservatively in boil-off period: core dryout, Post CHF heat transfer, rewet, core mixture level, and downcomer mixture level. Particularly, the loop seal in both loops are gradually cleared in M-RELAP5. It makes the results conservative. In the base calculation, the break flow and the SG secondary system pressure behaviors are specified as boundary conditions based on the measured data so as to validate M-RELAP5 ability to predict the important phenomena in the primary system in SBLOCA analysis. It is confirmed that M-RELAP5 predicts excellently the following phenomena and their interactions in the loop seal clearance phase: water hold up in SG primary side, condensation drainage to SG inlet plenum, water level in SG outlet piping, loop seal formation and clearing. And it is confirmed that M-RELAP5 predicts adequately or conservatively the following phenomena and their interactions in the loop seal clearance, boil-off and core recovery phases: core dryout, post-CHF heat transfer, rewet, core mixture level.

In the Sensitivity-1 calculation, the additional multiplier to CHF for low flowrate and high void fraction conditions described in Section 7.1.7.2 is validated. In the Sensitivity-2 calculation, the conservativeness of the decay heat model used in the plant calculation is confirmed.

The three sensitivity calculations (Sensitivity-3, 4, 5) are performed to investigate the difference in core water level during the boil-off period between the prediction and test data. Although it is found that the various mechanisms affect the prediction of the core water level, any sensitivity calculation can't reproduce the experimental results. The Sensitivity-1 calculation which is consistent with the US-APWR calculation gives most conservative results compared with these sensitivity calculations.

Finally, the conservatism of M-RELAP5 for US-APWR SBLOCA analysis is confirmed by the calculation performed in the same manner as the plant analysis which includes the calculations of the break flow and secondary system behaviors. And also, it is confirmed that M-RELAP5 predicts adequately the SG primary to secondary heat transfer in this calculation.

Consequently, it is concluded that M-RELAP5 predicts conservatively SBLOCA from the result of ROSA-IV SB-CL-18 simulation.

8.2.1.911 References

8.2.1-1. The ROSA-IV Group, 1985, "ROSA-IV Large Scale Test Facility (LSTF) System Description," JAERI-M 84-237.

- 8.2.1-2. The ROSA-IV Group, 1989, "Supplemental Description of ROSA-IV/LSTF with No. 1 Simulated Fuel-Rod Assembly," JAERI-M 89-113.
- 8.2.1-3. Kumamaru, H., et al., 1989, "ROSA-IV/LSTF 5% Cold Leg Break LOCA Experiment RUN SB-CL-18 Data Report," JAERI-M 89-027.
- 8.2.1-4. Kukita, Y., et al., 1992, "OECD/NEA/CSNI International Standard Problem No.26 (ISP-26) ROSA-IV LSTF Cold-Leg Small-Break LOCA Experiment Comparison Report," NEA/CSNI/R(91)13.

Table 8.2.1-1 Major Design Characteristics of LSTF and PWR

Characteristic	LSTF	PWR	PWR/LSTF
Pressure (MPa)	15.5	15.5	1
Temperature (K)	598	598	1
Number of fuel rods	1064	50,952	48
Core height (m)	3.66	3.66	1
Fluid volume (m ³)	7.23	347	48
Core power (MW)	10	3423(t)	342
Power density (MW/m ³)	1.4	9.9	7.1
Core inlet flow (ton/s)	0.0488	16.7	342
Downcomer gap (m)	0.053	0.260	4.91
Hot leg			
Diameter (D) (m)	0.207	0.737	3.56
Length (L) (m)	3.69	6.99	1.89
L/\sqrt{D} (m ^{1/2})	8.15	8.15	1.0
$\frac{\pi}{4}D^2L$ (m ³)	0.124	2.98	24.0
Number of loops	2	4	2
Number of tubes in steam generator	141	3382	24.0
Length of steam generator tube (average) (m)	20.2	20.2	1.0

Table 8.2.1-2 Steady-State Parameter Checklist

Parameter	Target	Predicted
Pressurizer pressure (MPa)	15.5	15.48
Hot leg fluid temperature (K)	599 / 599	599.2 / 599.2
Cold leg fluid temperature (K)	563 / 564	563.7 / 563.7
Core power (MW)	10.0	10.0
Core inlet flowrate (kg/s)	48.7	48.7
Pressurizer water level (m)	2.7	2.74
Pump speed (rpm)	769 / 796	769 / 796
Steam generator secondary pressure (MPa)	7.3 / 7.4	7.31 / 7.31
Steam generator secondary level (m)	10.8 / 10.6	10.6 / 10.6
Steam generator feedwater temperature (K)	494	494
Steam generator feedwater flowrate (kg/s)	2.6~2.8	2.7 / 2.8
Steam generator steam flowrate (kg/s)	2.6~2.8	2.7 / 2.8

Table 8.2.1-3 Operational Setpoints for Run SB-CL-18

Event	Setpoint
Reactor scram signal (MPa)	12.97
Initiation of RCP coastdown	With reactor scram
Safety injection signal (MPa)	12.27
High pressure charging	not actuated
Safety injection	not actuated
Accumulator injection (MPa)	4.51
Low pressure injection (MPa)	1.29
Main feedwater termination	With reactor scram
Turbine throttle valve closure	With reactor scram
Auxiliary feedwater initiation	not actuated

Table 8.2.1-4 Core Power Decay Curve

Time s	Power MW	Time s	Power MW
0.000	10.000	100.000	5.200
1.000	10.000	150.000	3.632
2.000	10.000	200.000	2.848
3.000	10.000	400.000	1.776
4.000	10.000	600.000	1.568
5.000	10.000	800.000	1.488
6.000	10.000	1000.000	1.424
7.000	10.000	1500.000	1.280
8.000	10.000	2000.000	1.200
10.000	10.000	4000.000	.992
15.000	10.000	6000.000	.848
20.000	10.000	7980.000	.784
29.000	10.000	10020.000	.784
40.000	8.912	19980.000	.592
60.000	7.344	60000.000	.464
80.000	6.128	100020.000	.368

Table 8.2.1-5 ECCS Conditions for Run SB-CL-18

ECCS	Specification
High pressure charging system Pump shut-off head Delay time from SI signal Flowrate Fluid temperature Injection location (ratio)	not actuated
High pressure injection system Pump shut-off head Delay time from SI signal Flowrate Fluid temperature Injection location (ratio)	not actuated
Low pressure injection system Pump shut-off head Delay time from SI signal Flowrate Fluid temperature Injection location (ratio)	1.29MPa 17 s scaled full capacity 310 K CLA, CLB (3:1)
Acc system Pressure setpoint Water temperature Injection location (ratio) Initial tank level to loop-A : ACC-Cold to loop-B : ACC-Hot Terminal tank level to loop-A : ACC-Cold to loop-B : ACC-Hot	4.51 MPa 320 K CLA, CLB (3:1) 5.76 m 6.43 m 3.38 m 5.64 m

Table 8.2.1-6 Transient Results Summary for 5-Percent Cold Leg Side Break

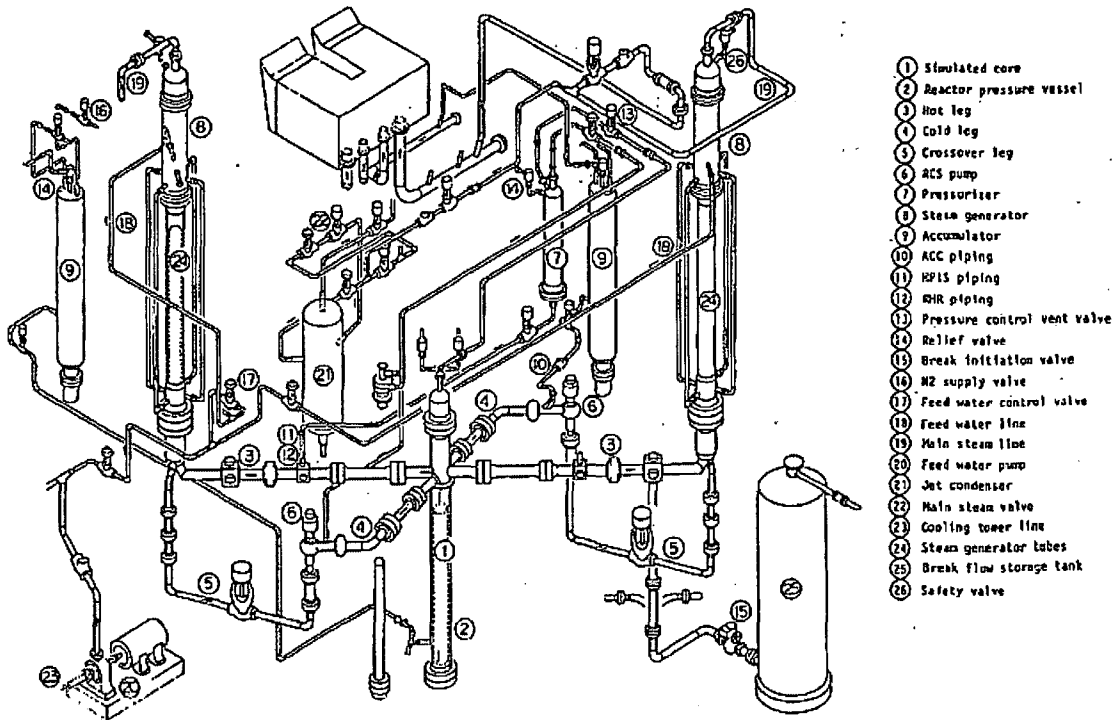
Event	Data	Prediction
Break (s)	0	0
Reactor trip (s)	~10	13.0
Safety injection signal (s)	~12	16.3
Main steam line valve close (s)	14	14
SG feedwater stop (s)	16	16
High pressure charging injection (s)	-	-
High pressure safety injection (s)	-	-
Auxiliary Feedwater ON (s)	-	-
First Core Uncovery (s)	120 - 155	95 - 175
Loop Seal Clearing (Loop A/B) (s)	~140	130
Primary / Secondary Pressure Reversal (s)	~180	172
Reactor Coolant Pumps (PC-A/B) stop (s)	265	265
Second Core Uncovery (s)	420 - 540	300 - 540
Accumulator Injection ON (s)	455	480

**Table 8.2.1-7 Transient Results Summary for 5-Percent Cold Leg Side Break
(Calculation with Simulated Secondary System and Break Flow
Behavior)**

	<u>Data</u>	<u>Prediction</u>
<u>Break Occurrence (s)</u>	<u>0</u>	<u>0</u>
<u>Reactor Trip (s)</u>	<u>~10</u>	<u>10.5</u>
<u>Safety Injection Signal (s)</u>	<u>~12</u>	<u>14.4</u>
<u>Main Steamline Valve Close (s)</u>	<u>14</u>	<u>14</u>
<u>SG Feedwater Stop (s)</u>	<u>16</u>	<u>16</u>
<u>High Pressure Charging Injection (s)</u>	<u>-</u>	<u>-</u>
<u>High Pressure Safety Injection (s)</u>	<u>-</u>	<u>-</u>
<u>Auxiliary Feedwater On (s)</u>	<u>-</u>	<u>-</u>
<u>First Core Uncovery (s)</u>	<u>120 – 156</u>	<u>130 – 205</u>
<u>Loop Seal Clearing (s)</u>	<u>~140</u>	<u>~160</u>
<u>Primary/Secondary Pressure Reversal (s)</u>	<u>~180</u>	<u>~180</u>
<u>Reactor Coolant Pumps (PC-A/B) Stop (s)</u>	<u>265</u>	<u>268</u>
<u>Secondary Core Uncovery (s)</u>	<u>420 – 540</u>	<u>260 – 440</u>
<u>Accumulator Injection ON (s)</u>	<u>455</u>	<u>366</u>

**Table 8.2.1-8 Comparison of PCT (Calculation with Simulated Secondary System and
Break Flow Behavior)**

	<u>Measured PCT (K)</u>	<u>Predicted PCT (K)</u>
<u>Loop Seal Clearance Period</u>	<u>738</u>	<u>775</u>
<u>Boil-off /Core Recovery Period</u>	<u>620</u>	<u>727</u>



- ① Simulated core
- ② Reactor pressure vessel
- ③ Hot leg
- ④ Cold leg
- ⑤ Crossover leg
- ⑥ RCS pump
- ⑦ Pressurizer
- ⑧ Steam generator
- ⑨ Accumulator
- ⑩ ACC piping
- ⑪ HPIS piping
- ⑫ RHR piping
- ⑬ Pressure control vent valve
- ⑭ Relief valve
- ⑮ Break initiation valve
- ⑯ N2 supply valve
- ⑰ Feed water control valve
- ⑱ Feed water line
- ⑲ Main steam line
- ⑳ Feed water pump
- ㉑ Jet condenser
- ㉒ Main steam valve
- ㉓ Cooling tower line
- ㉔ Steam generator tubes
- ㉕ Break flow storage tank
- ㉖ Safety valve

**Figure 8.2.1-1 General Structure of Large Scale Test Facility (LSTF)
(From JAERI-M 84-237)**

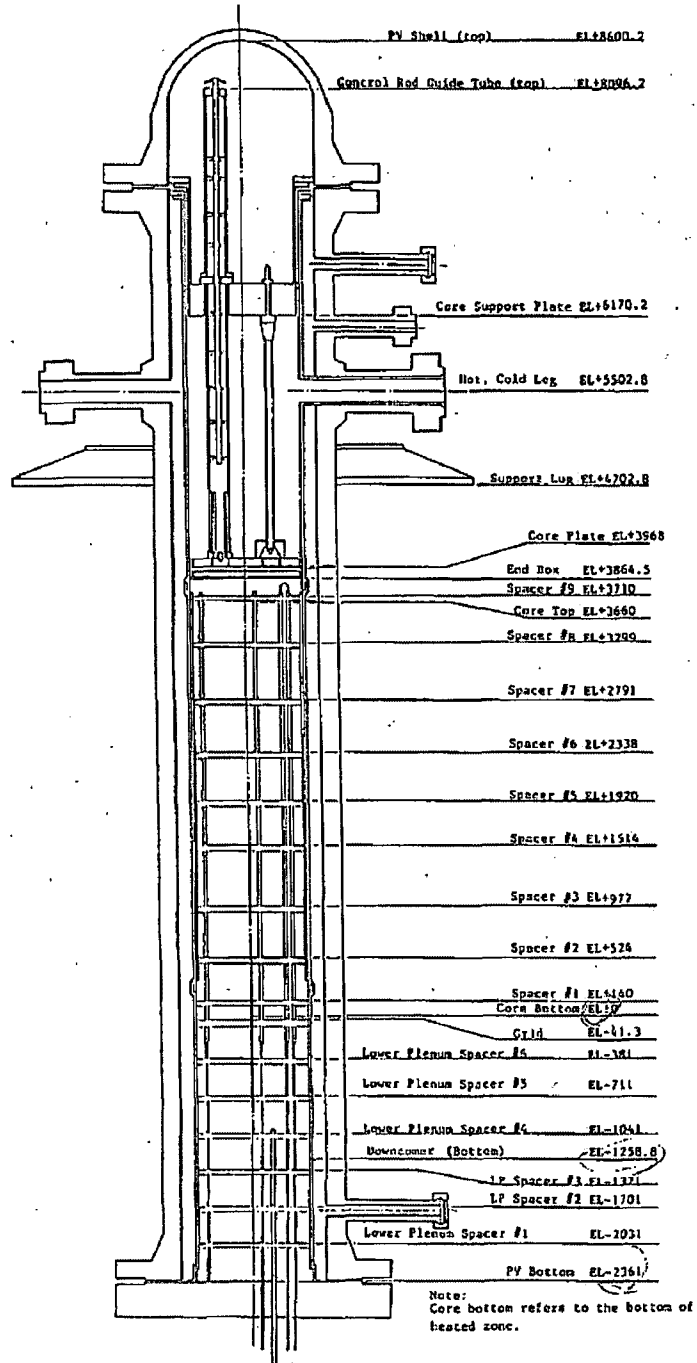
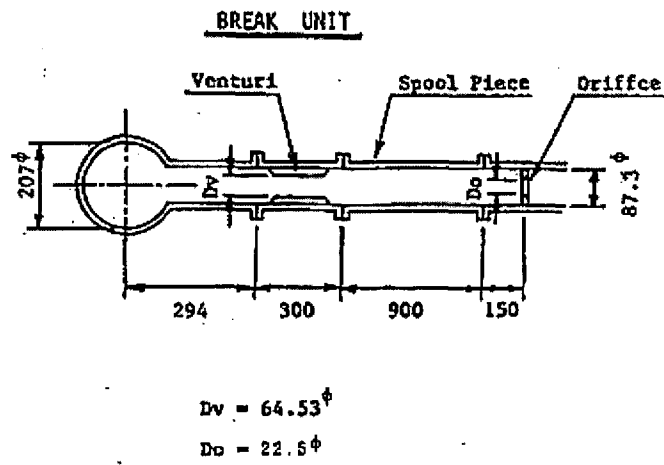


Figure 8.2.1-2 Pressure Vessel Assembly
(From JAERI-M 84-237)



**Figure 8.2.1-3 Break Assembly
(From JAERI-M 89-027)**



Figure 8.2.1-5 M-RELAP5 Noding Diagram of a Cold Leg Break LOCA for the LSTF

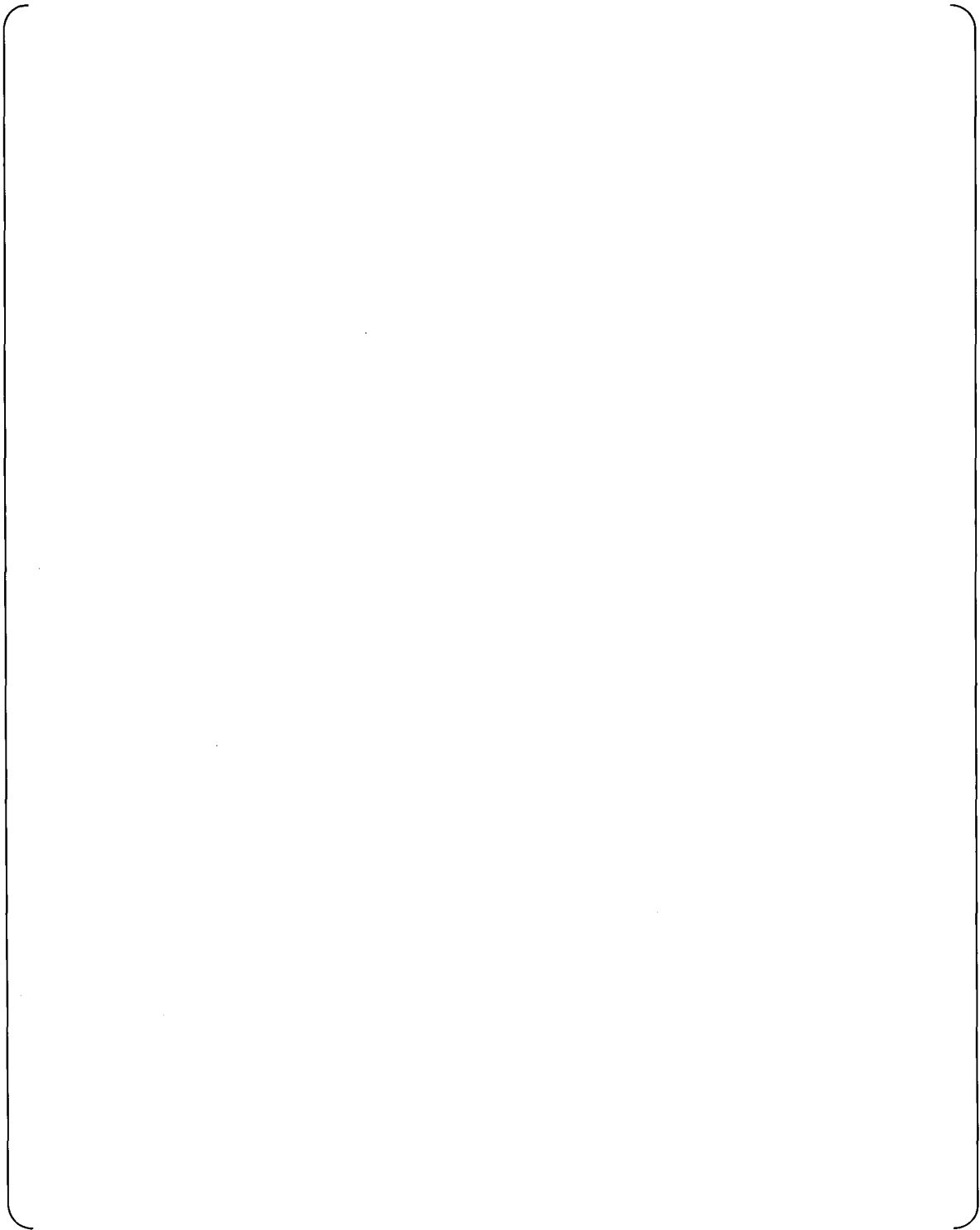


Figure 8.2.1-6 Vessel Noding

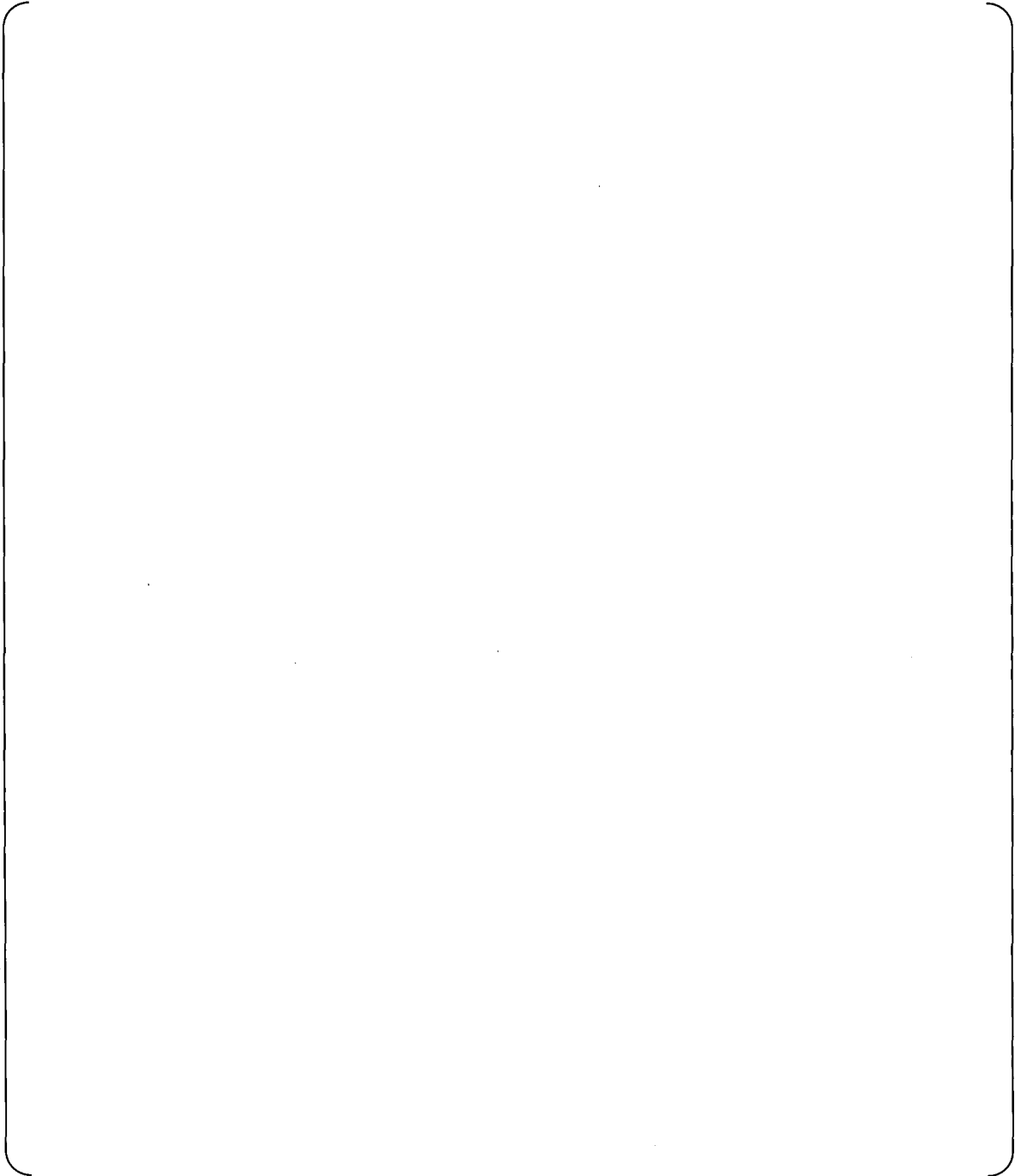


Figure 8.2.1-7 Hot Leg Noding

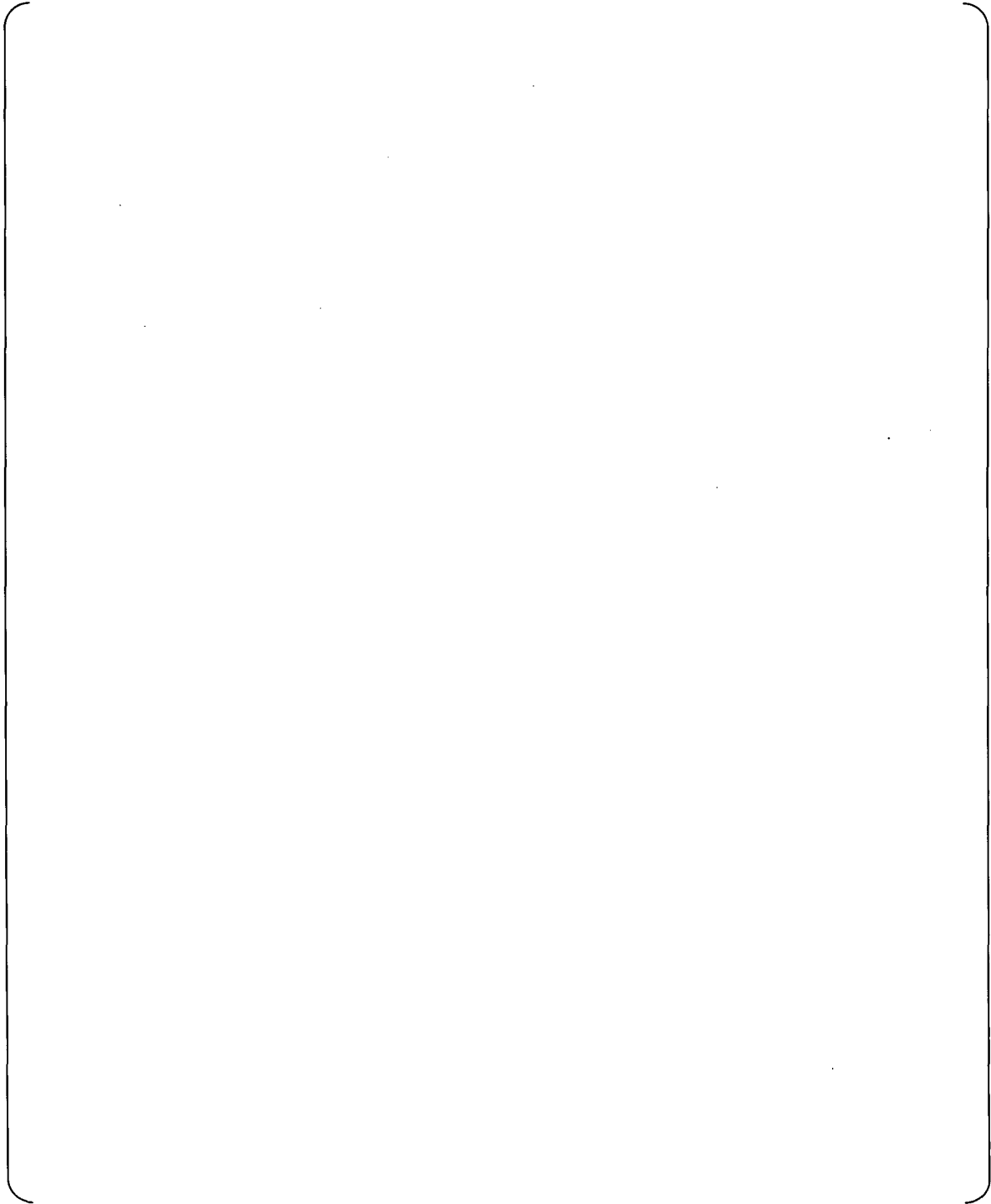


Figure 8.2.1-8 SG Primary and Secondary Side Noding

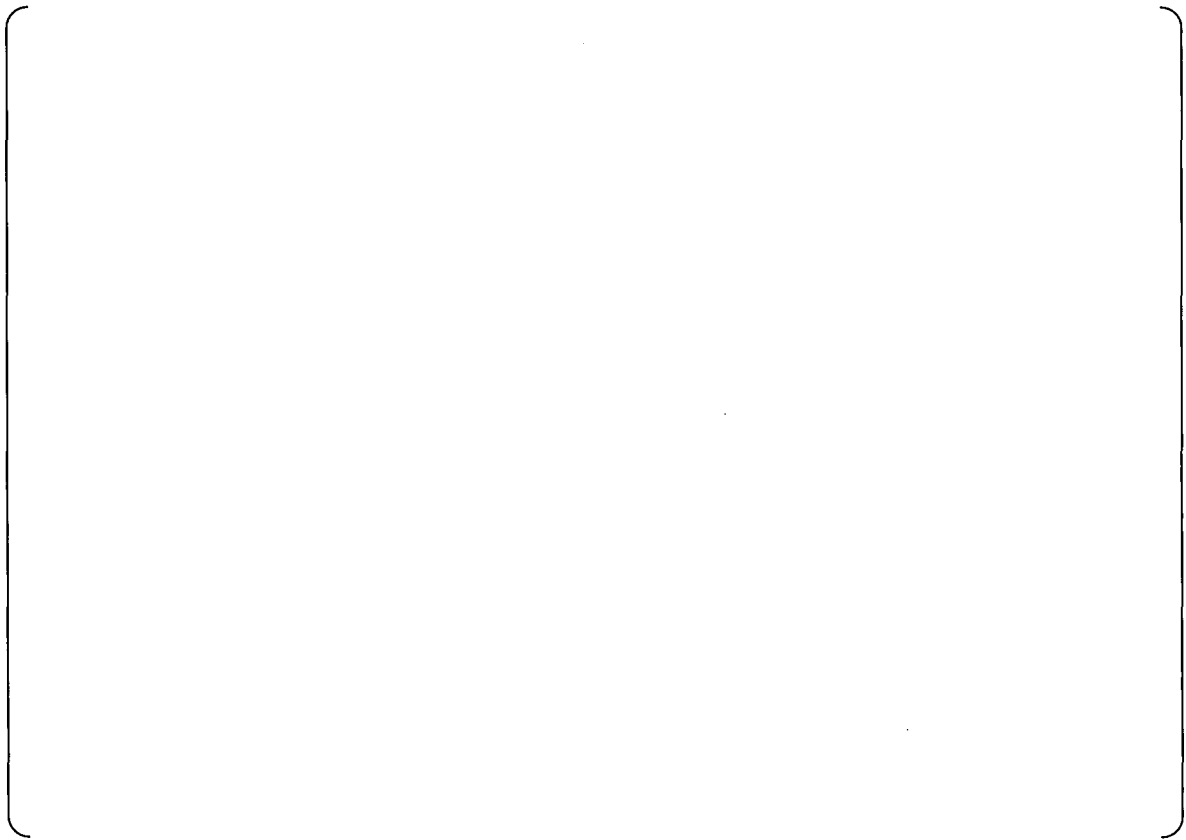


Figure 8.2.1-9 Cross-Over Leg Noding

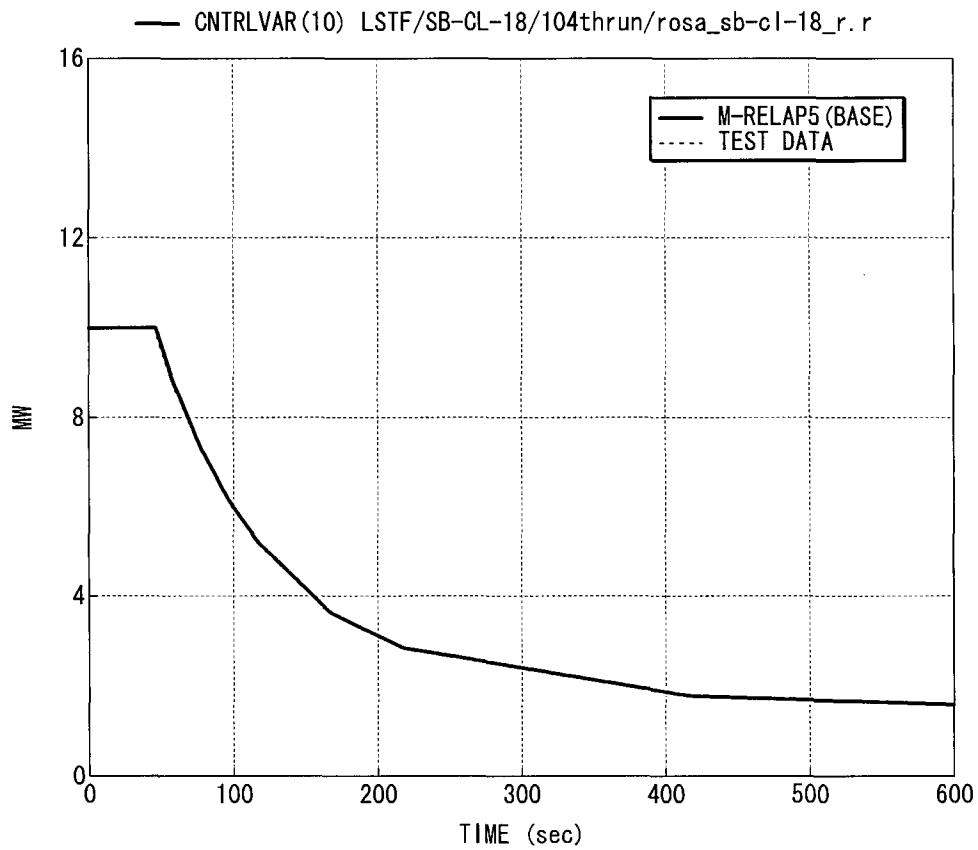


Figure 8.2.1-10 Total Core Power (Base Case)

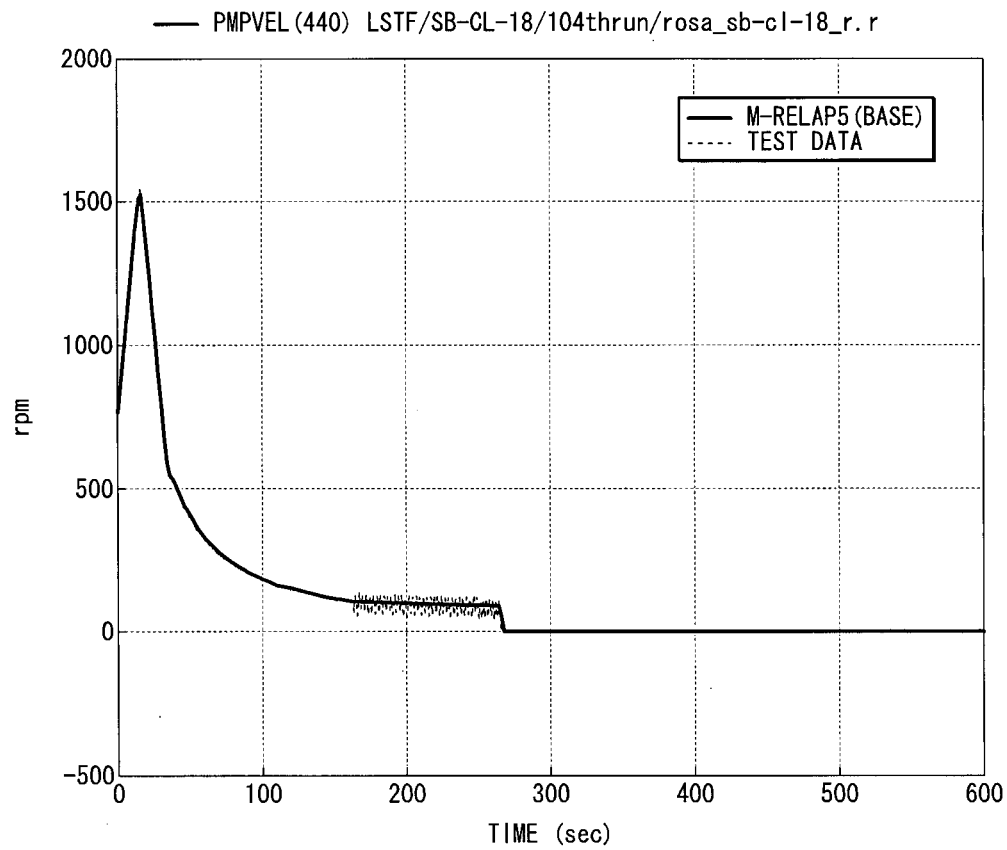


Figure 8.2.1-11 Reactor Coolant Pump in Primary Loop-A Rotation Speed

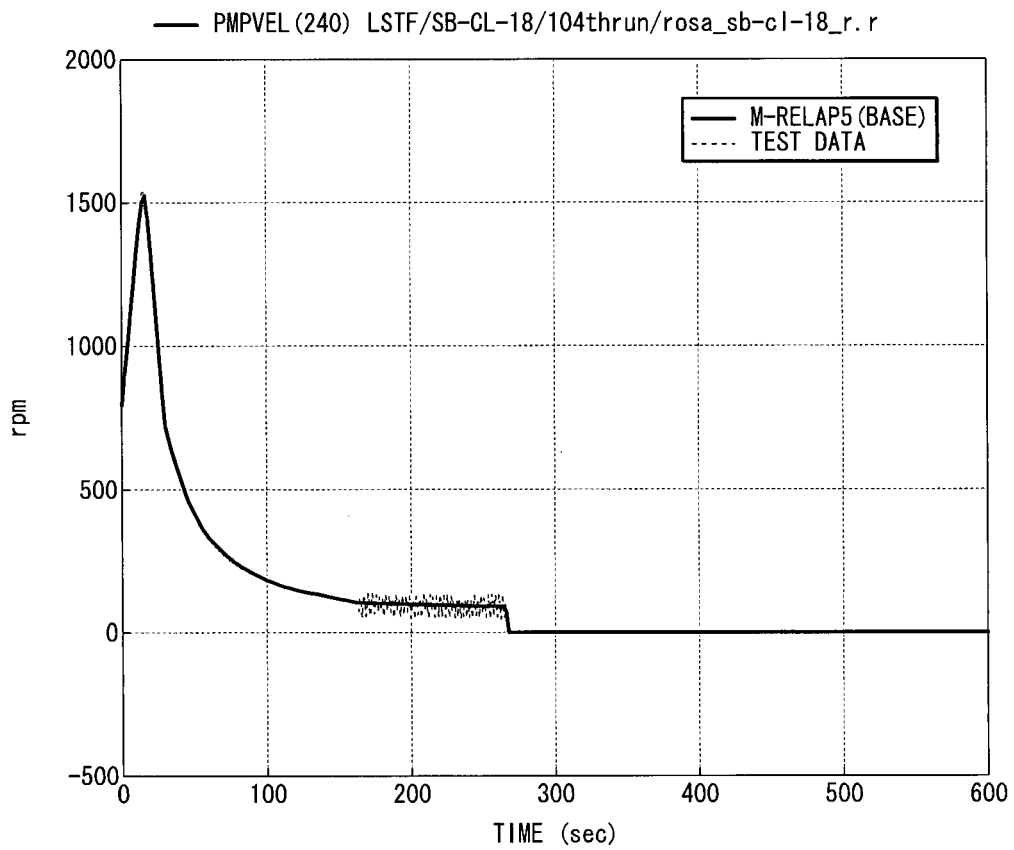


Figure 8.2.1-12 Reactor Coolant Pump in Primary Loop-B Rotation Speed

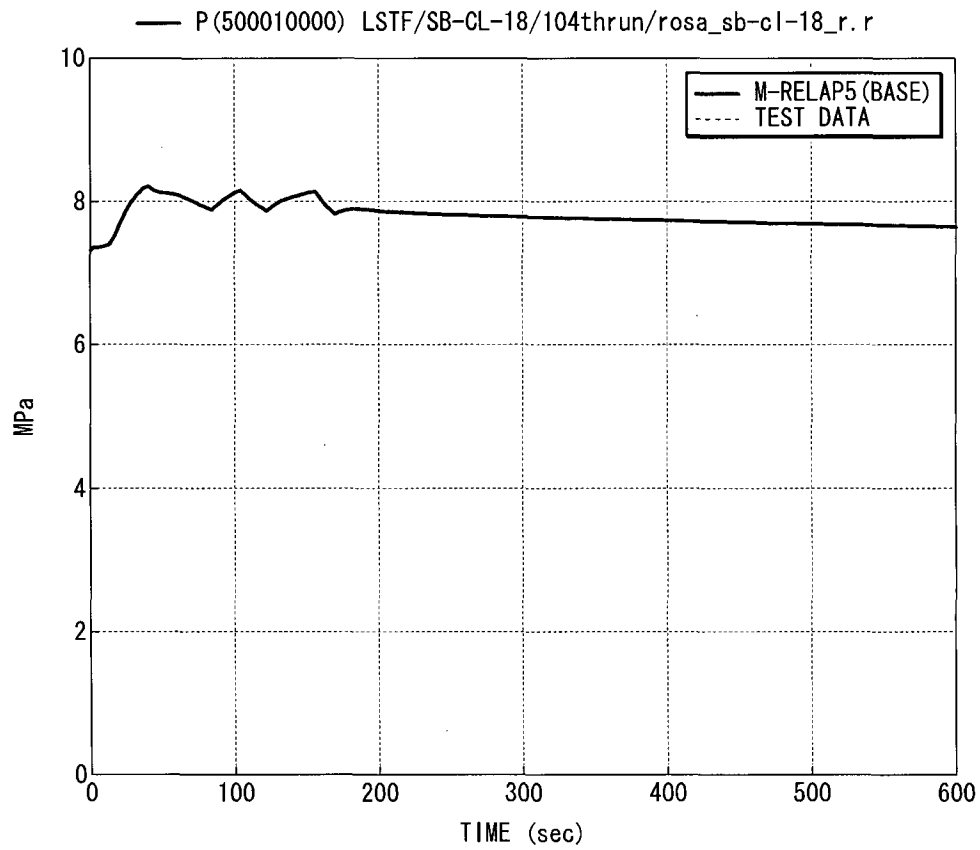


Figure 8.2.1-13 SGA Steam Dome Pressure

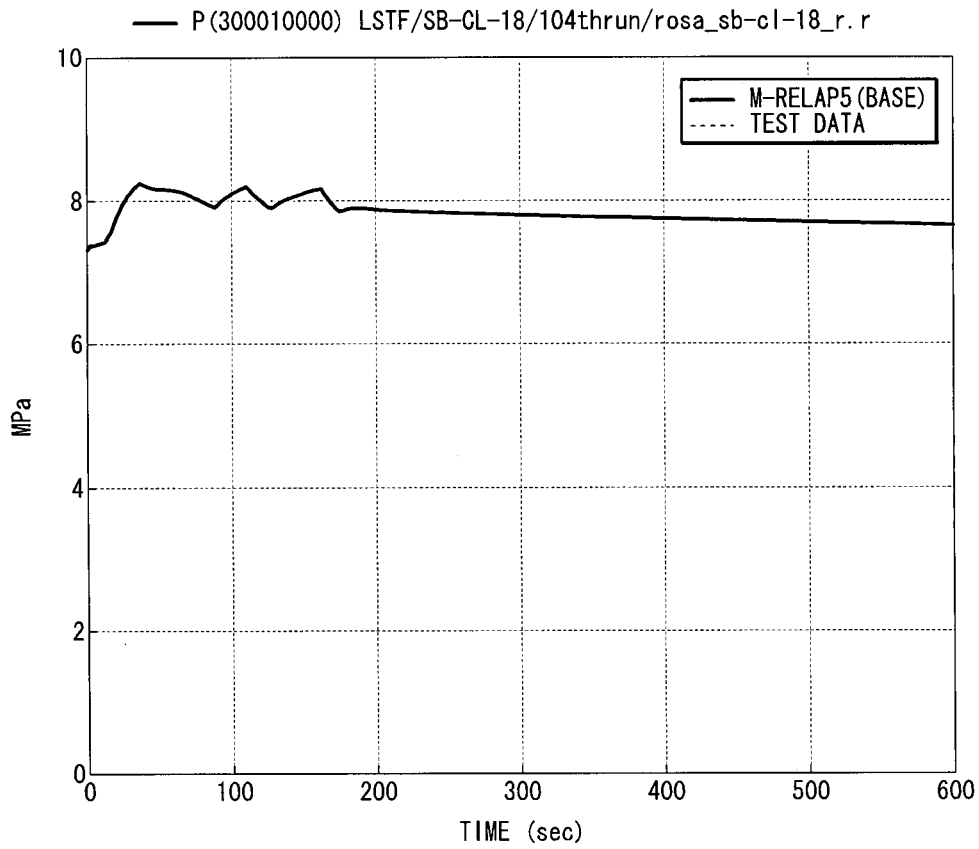


Figure 8.2.1-14 SGB Steam Dome Pressure

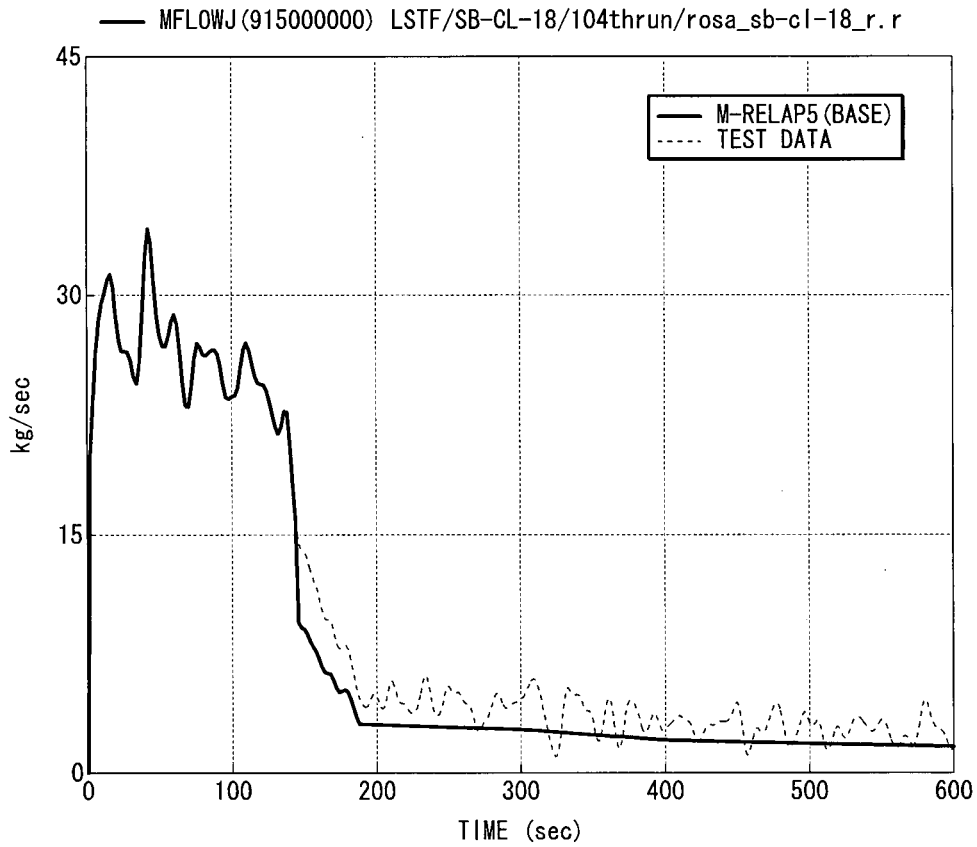


Figure 8.2.1-15 Break Flowrate

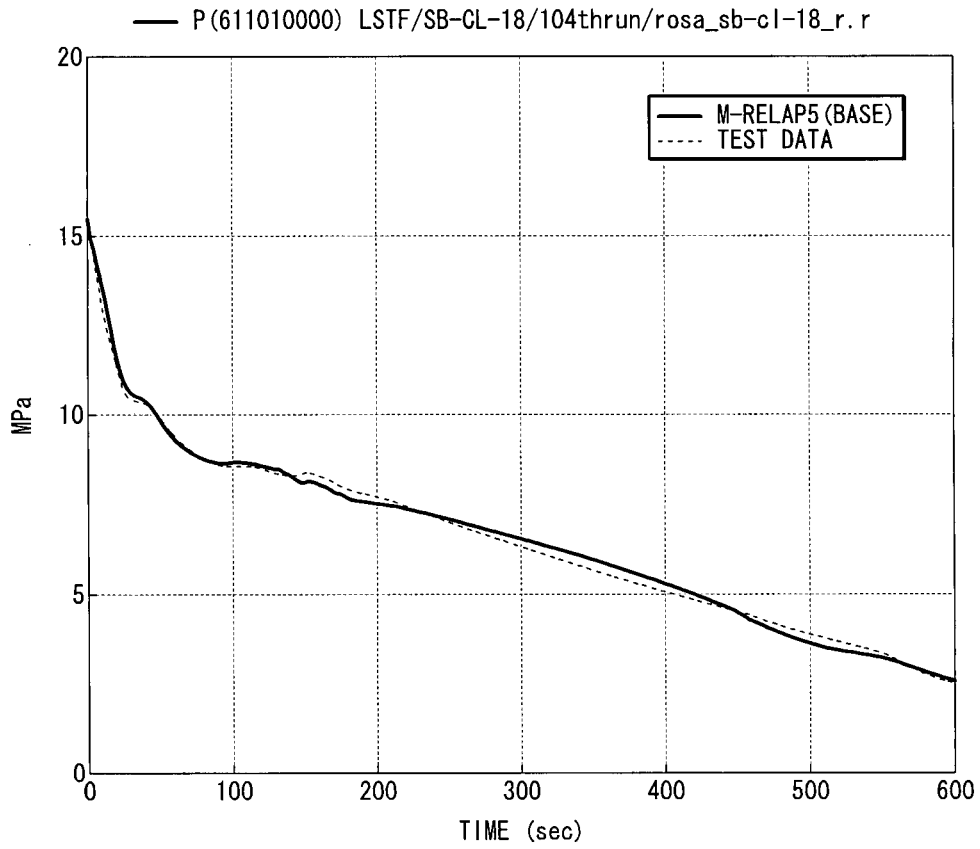


Figure 8.2.1-16 Pressurizer Pressure

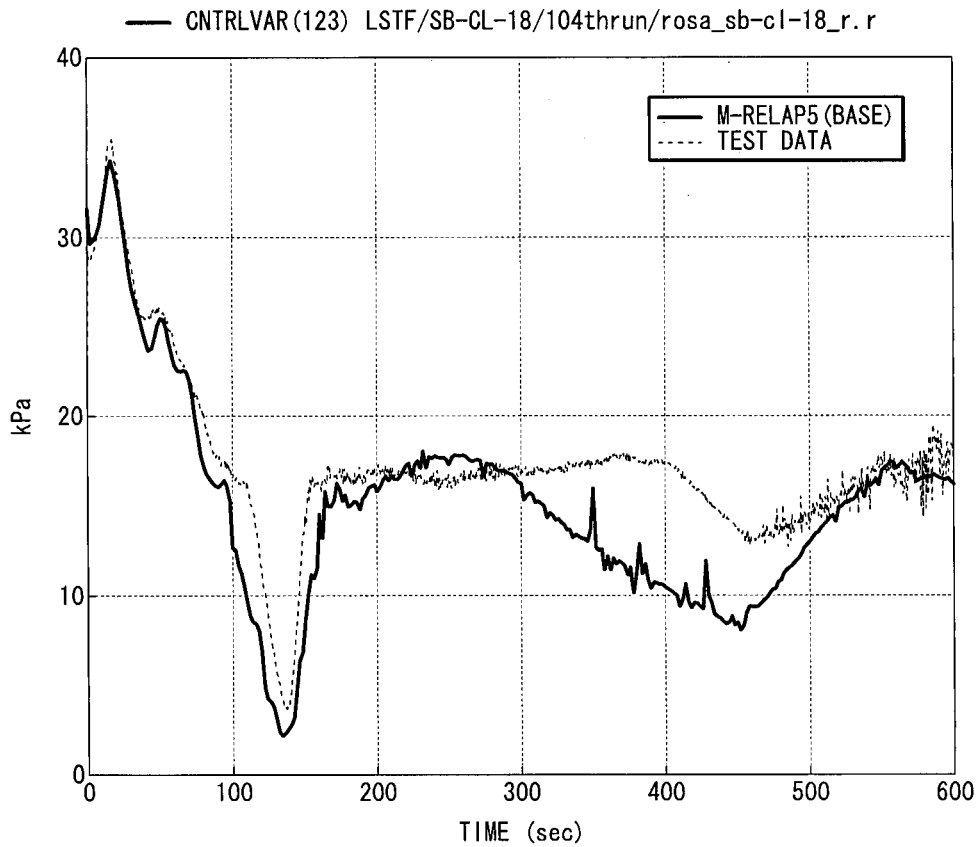


Figure 8.2.1-17 Core Differential Pressure (Base Case)

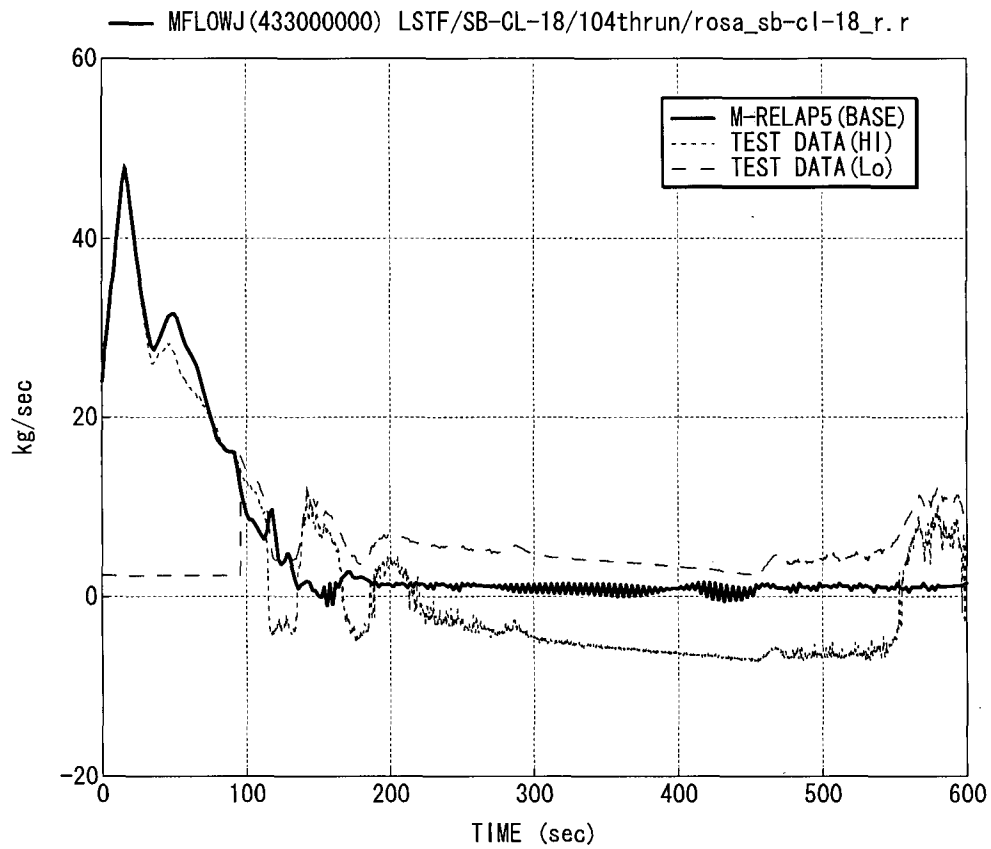


Figure 8.2.1-18 Loop-A Cross-Over Leg Flowrate

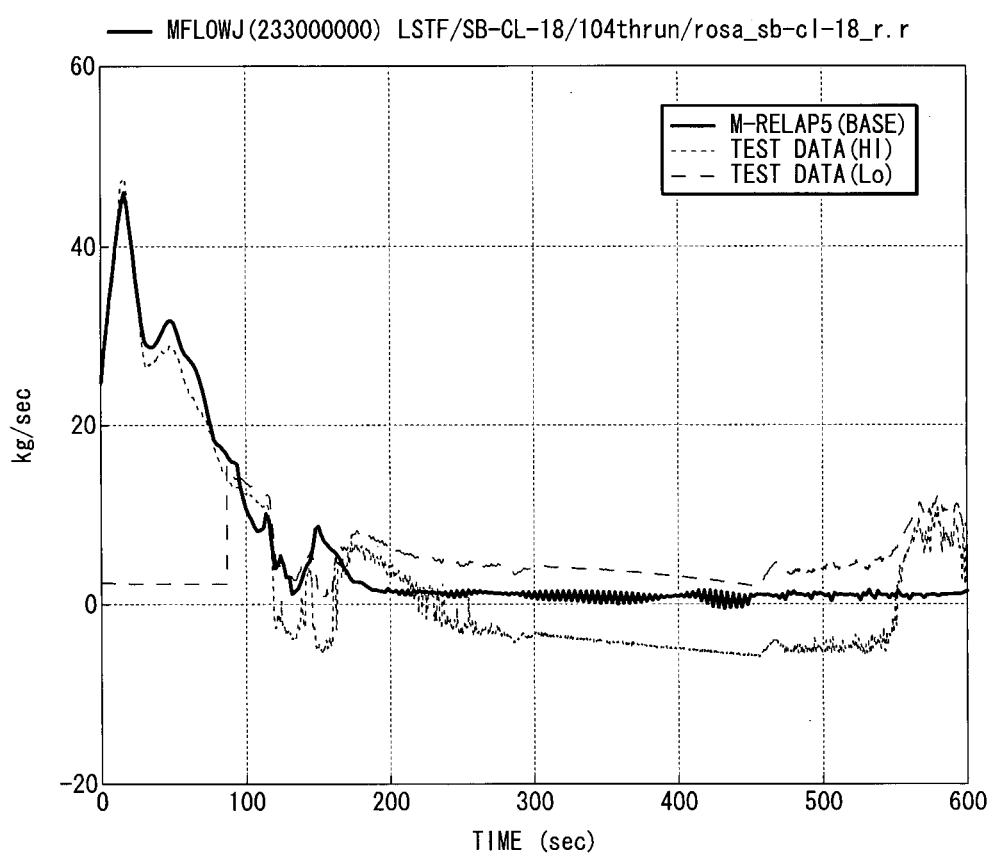


Figure 8.2.1-19 Loop-B Cross-Over Leg Flowrate

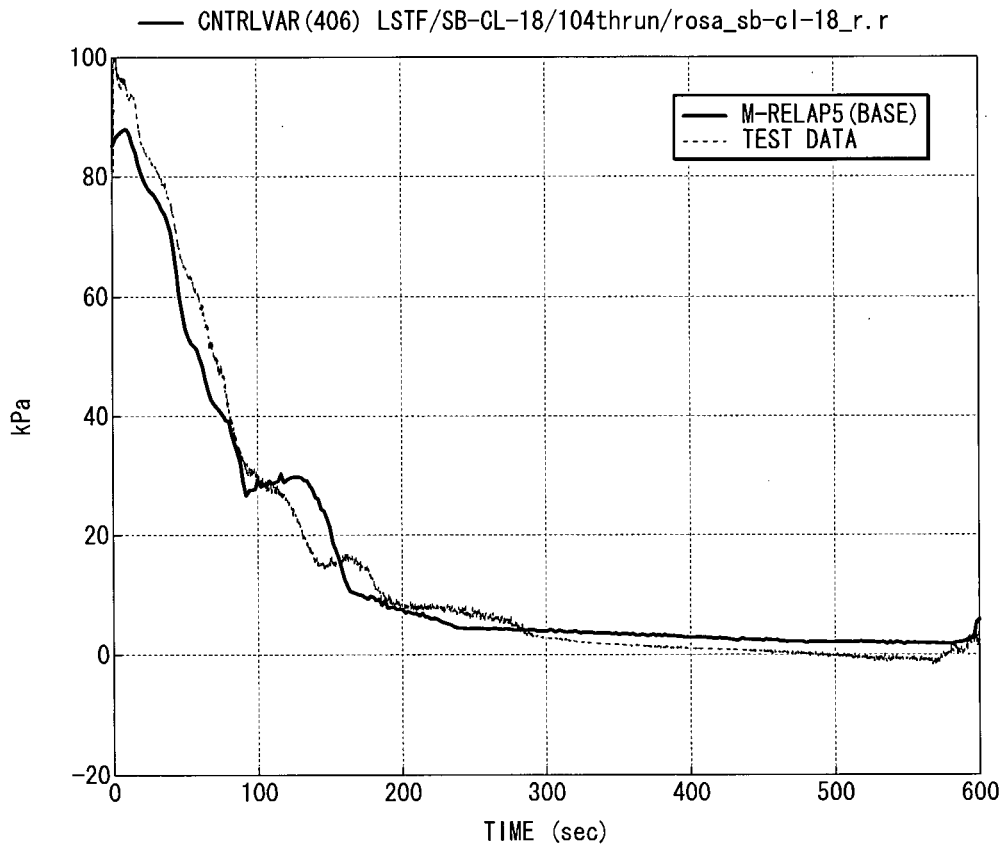


Figure 8.2.1-20 Loop-A Hot Leg to U-Tube Top Differential Pressure

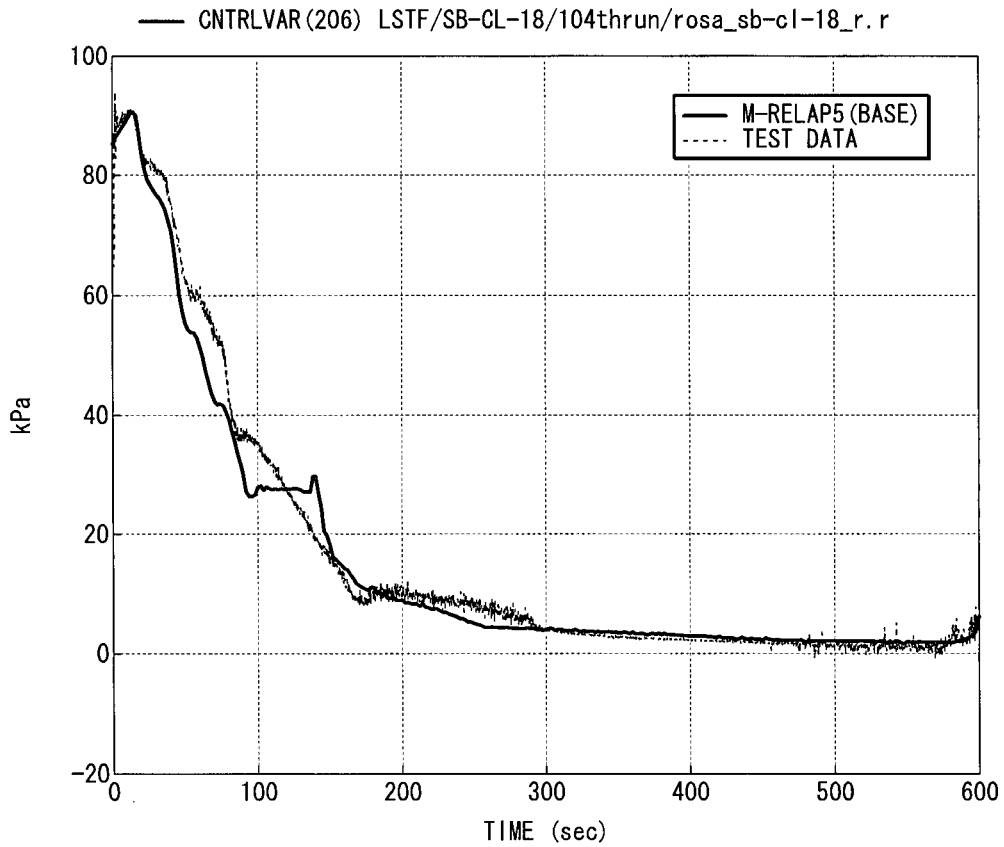


Figure 8.2.1-21 Loop-B Hot Leg to U-Tube Top Differential Pressure

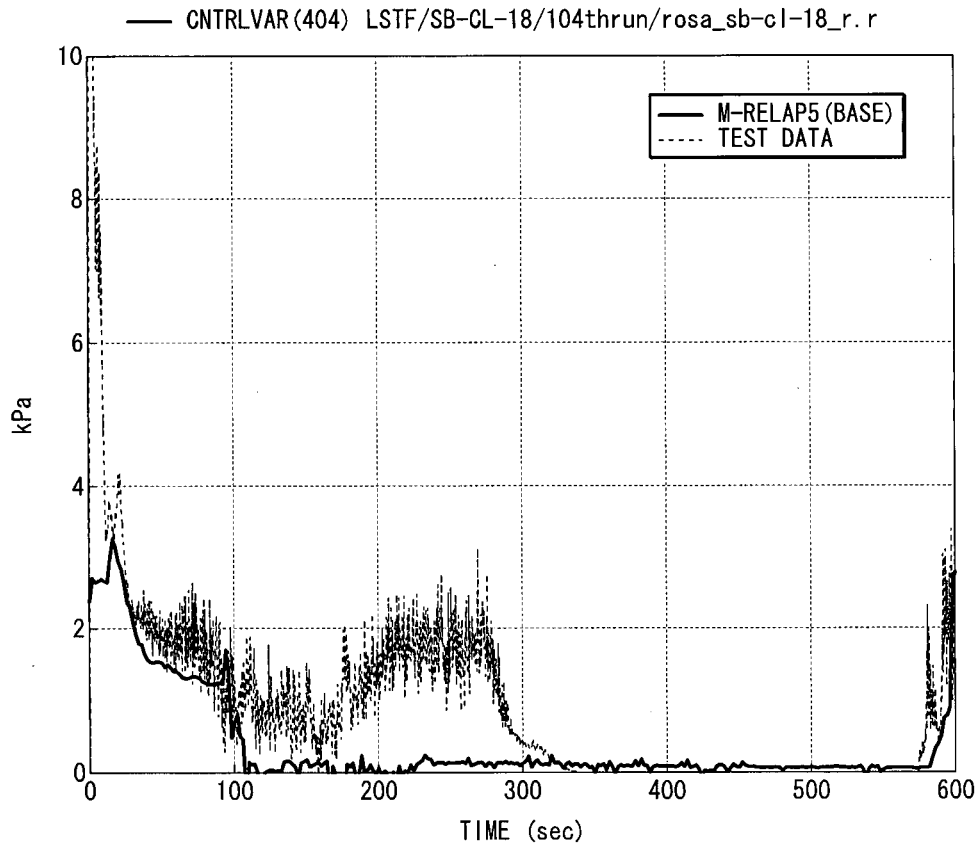


Figure 8.2.1-22 Loop-A Hot Leg to SG Inlet Plenum Bottom Differential Pressure

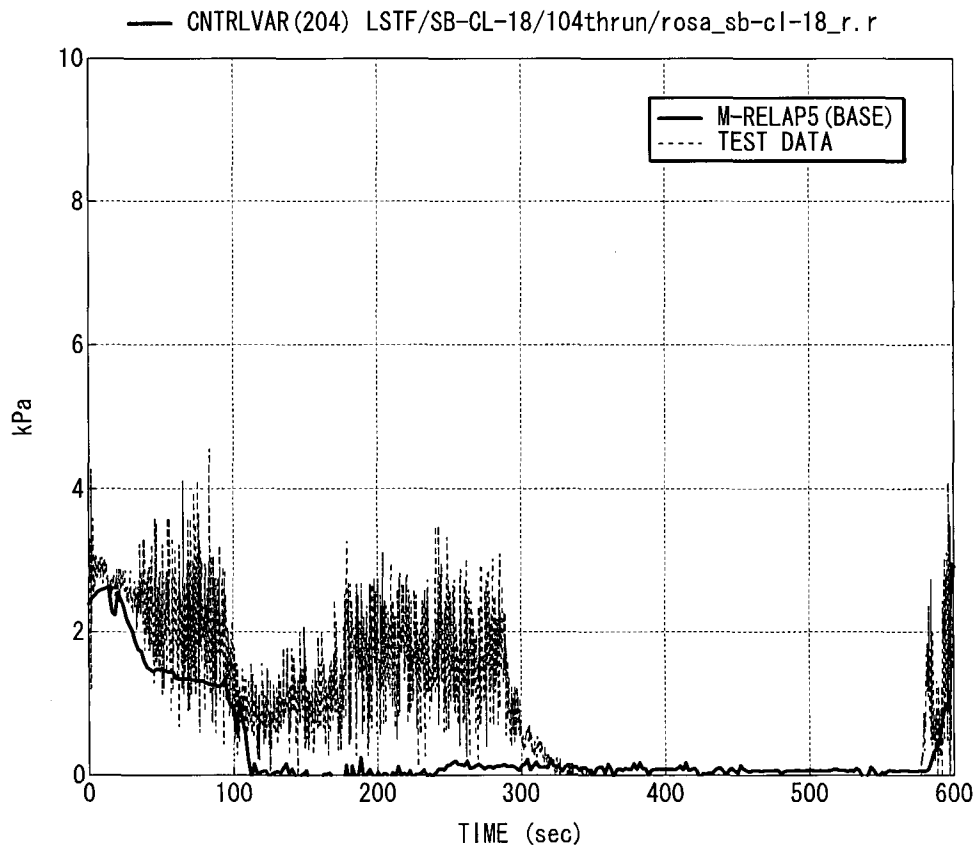


Figure 8.2.1-23 Loop-B Hot Leg to SG Inlet Plenum Bottom Differential Pressure

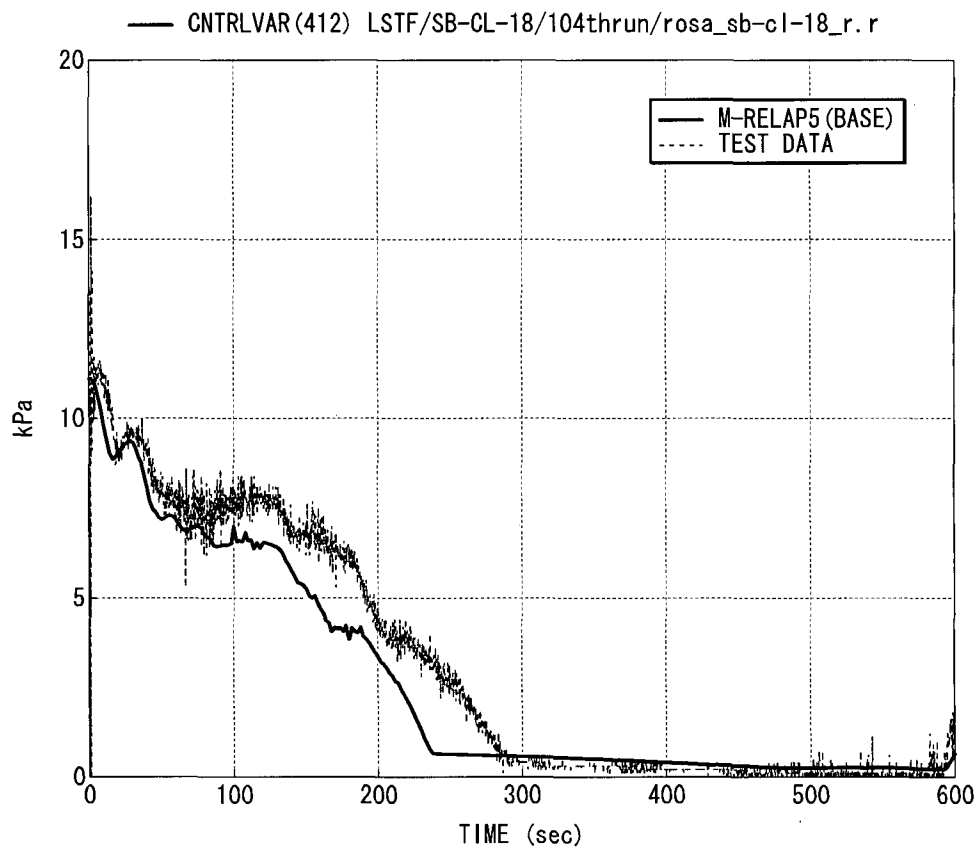


Figure 8.2.1-24 Loop-A SG Inlet Plenum Differential Pressure

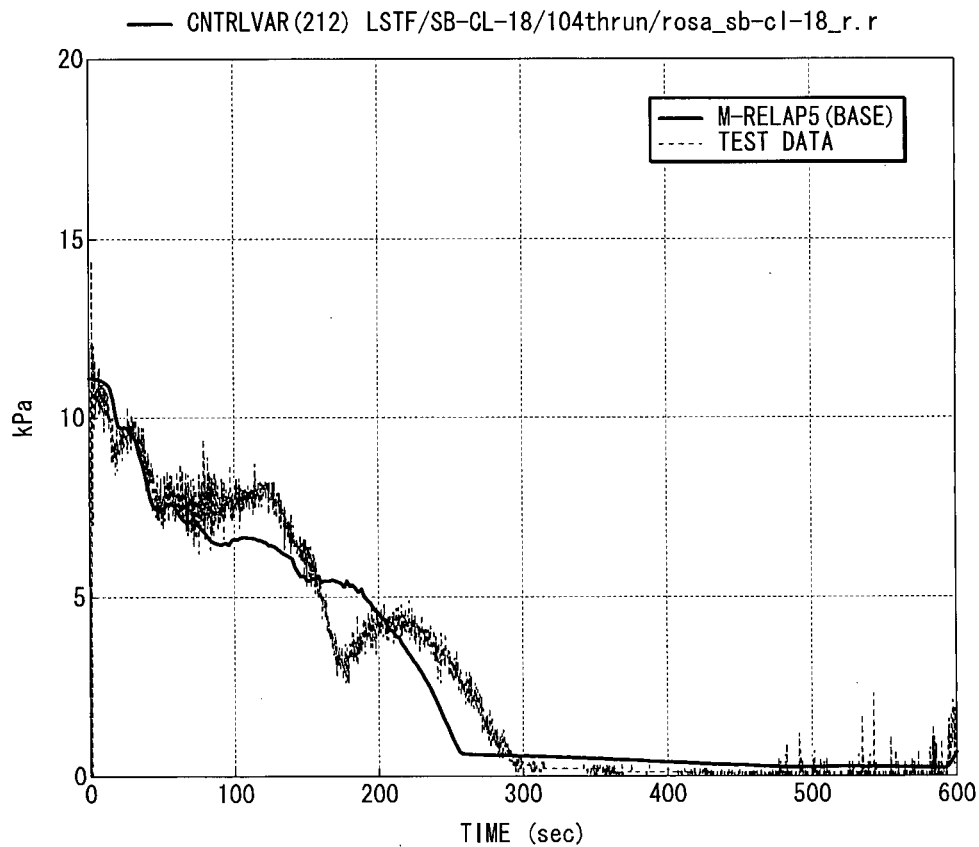


Figure 8.2.1-25 Loop-B SG Inlet Plenum Differential Pressure

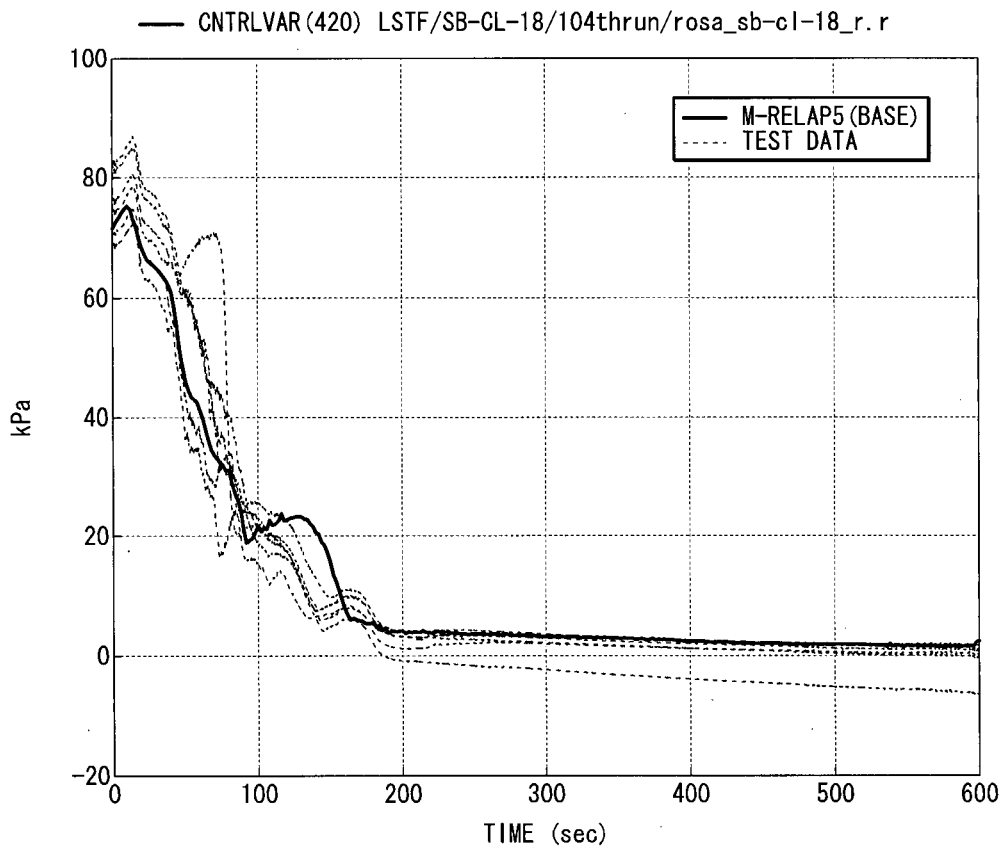


Figure 8.2.1-26 Loop-A SG U-tube Uphill Side Differential Pressure

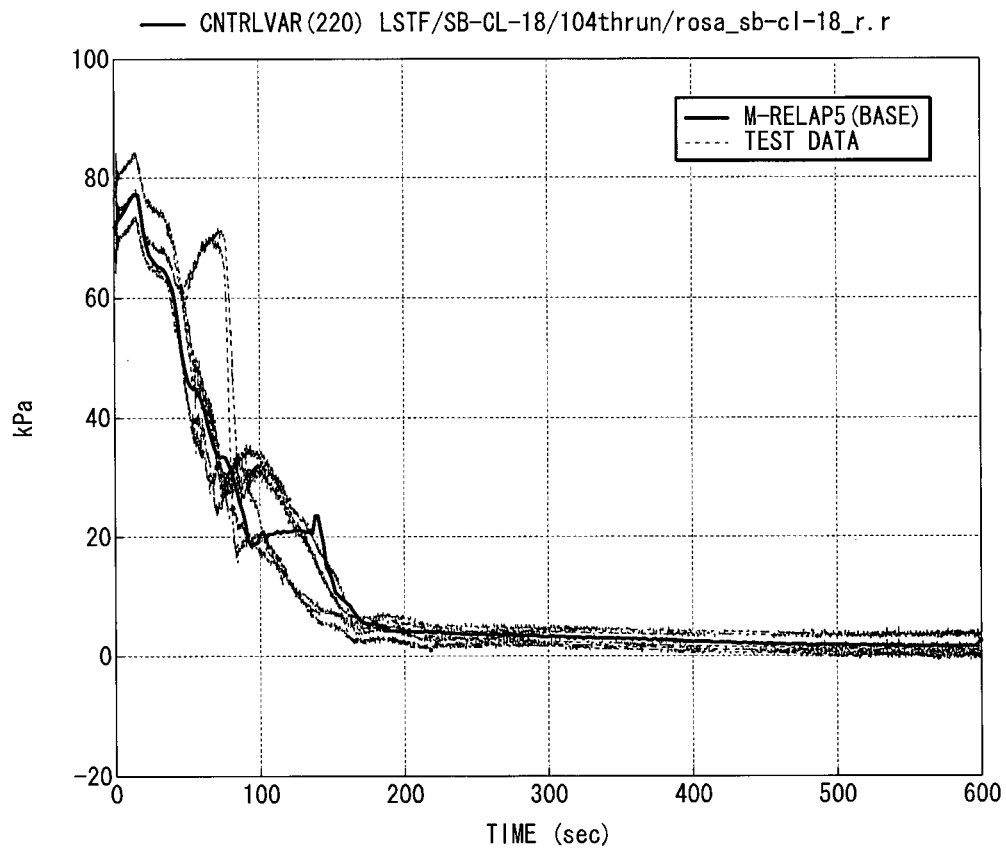


Figure 8.2.1-27 Loop-B SG U-tube Uphill Side Differential Pressure

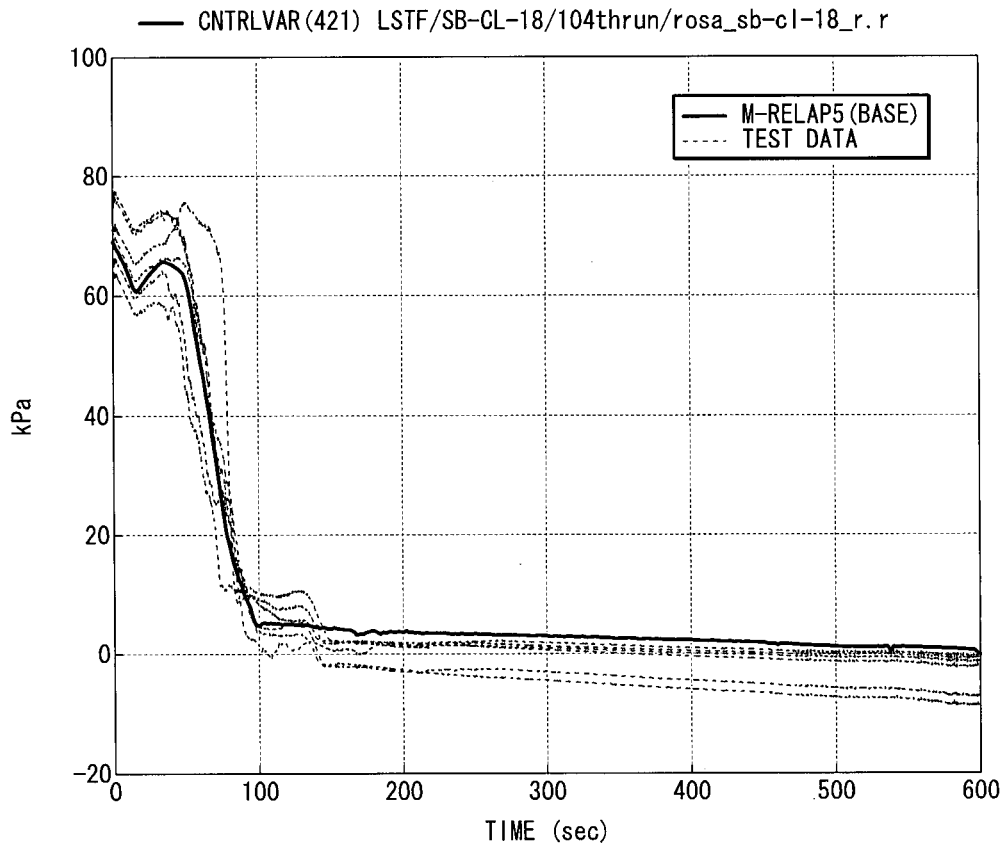


Figure 8.2.1-28 Loop-A SG U-tube Downhill Side Differential Pressure

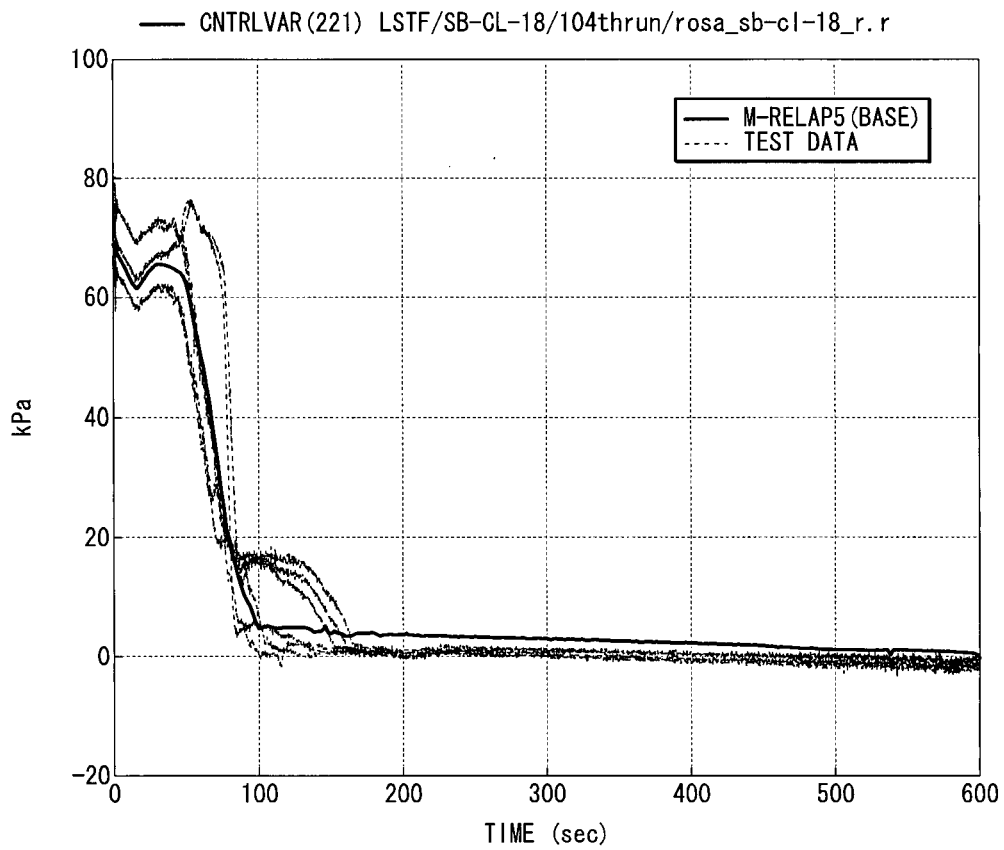


Figure 8.2.1-29 Loop-B SG U-tube Downhill Side Differential Pressure

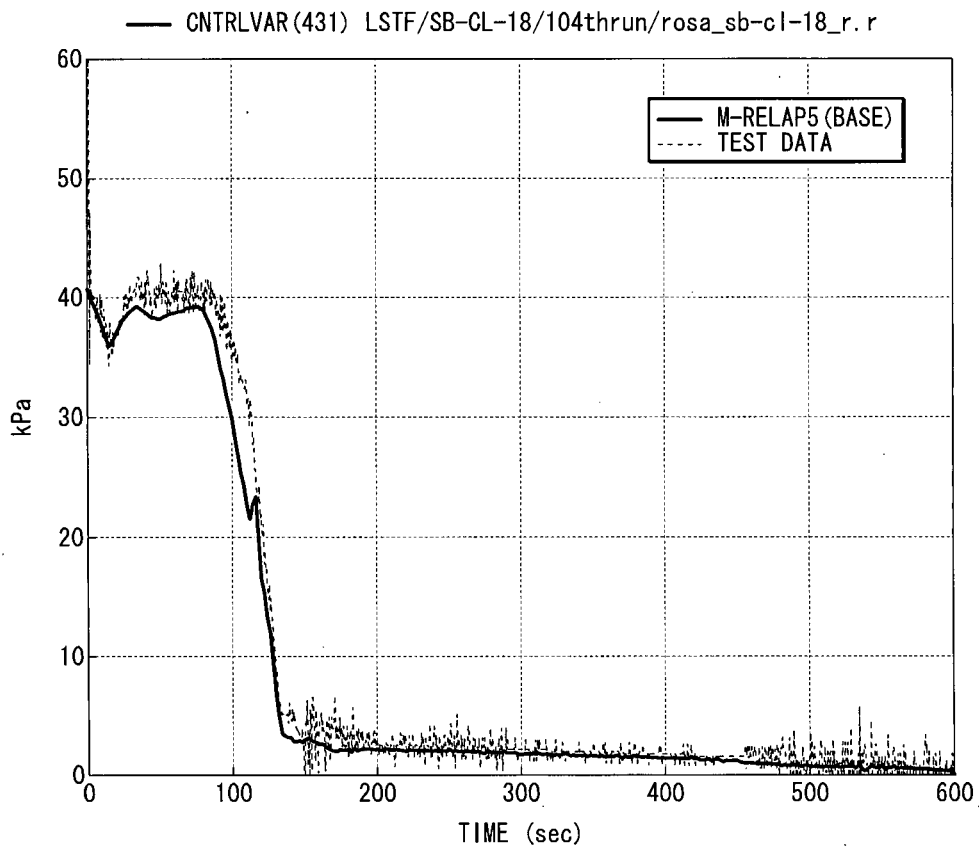


Figure 8.2.1-30 Loop-A Cross-over Leg Downhill Side Differential Pressure

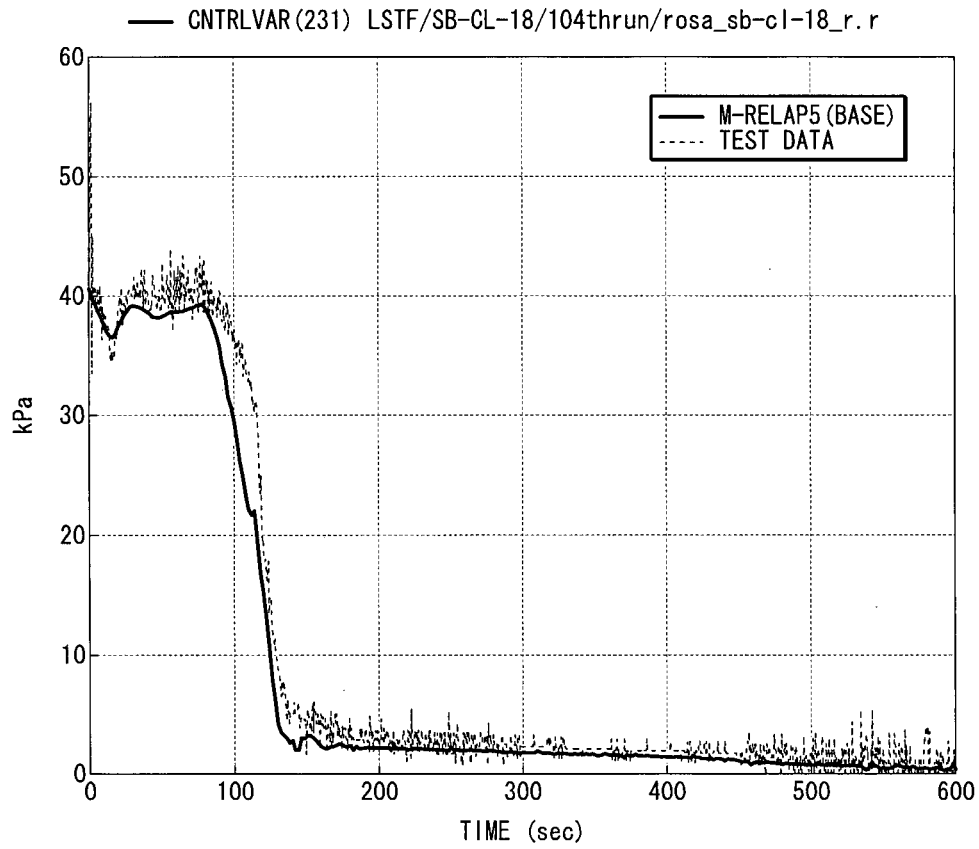


Figure 8.2.1-31 Loop-B Cross-over Leg Downhill Side Differential Pressure

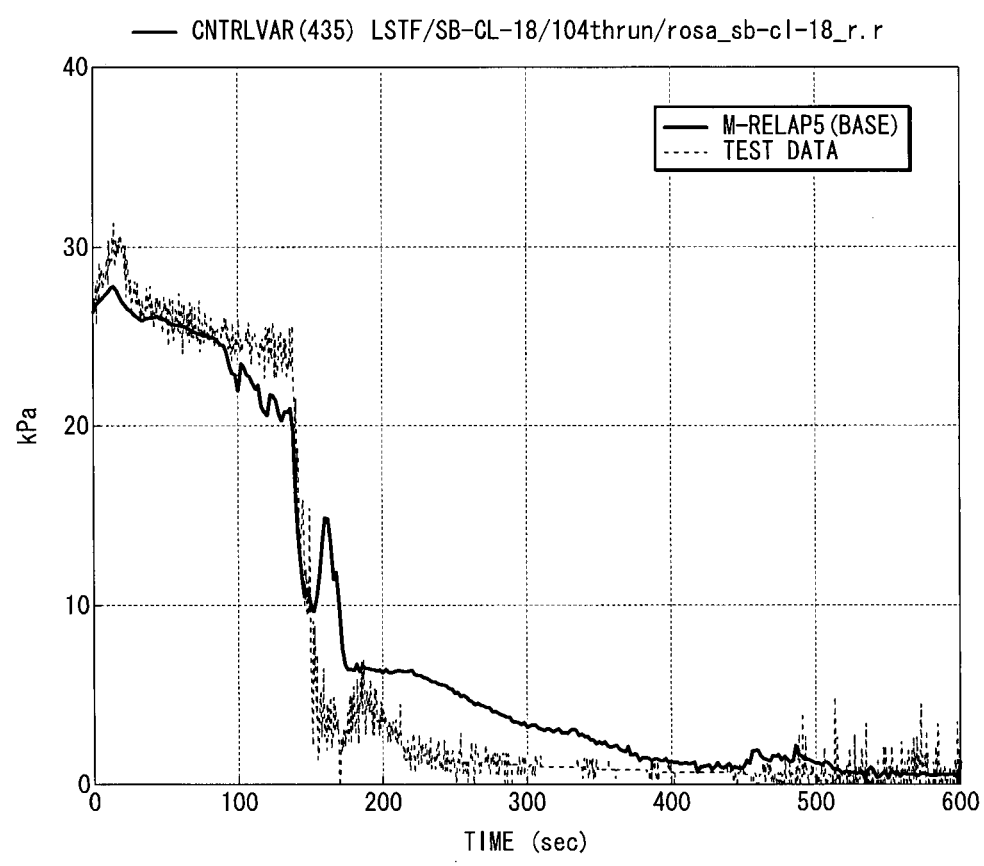


Figure 8.2.1-32 Loop-A Cross-over Leg Uphill Side Differential Pressure

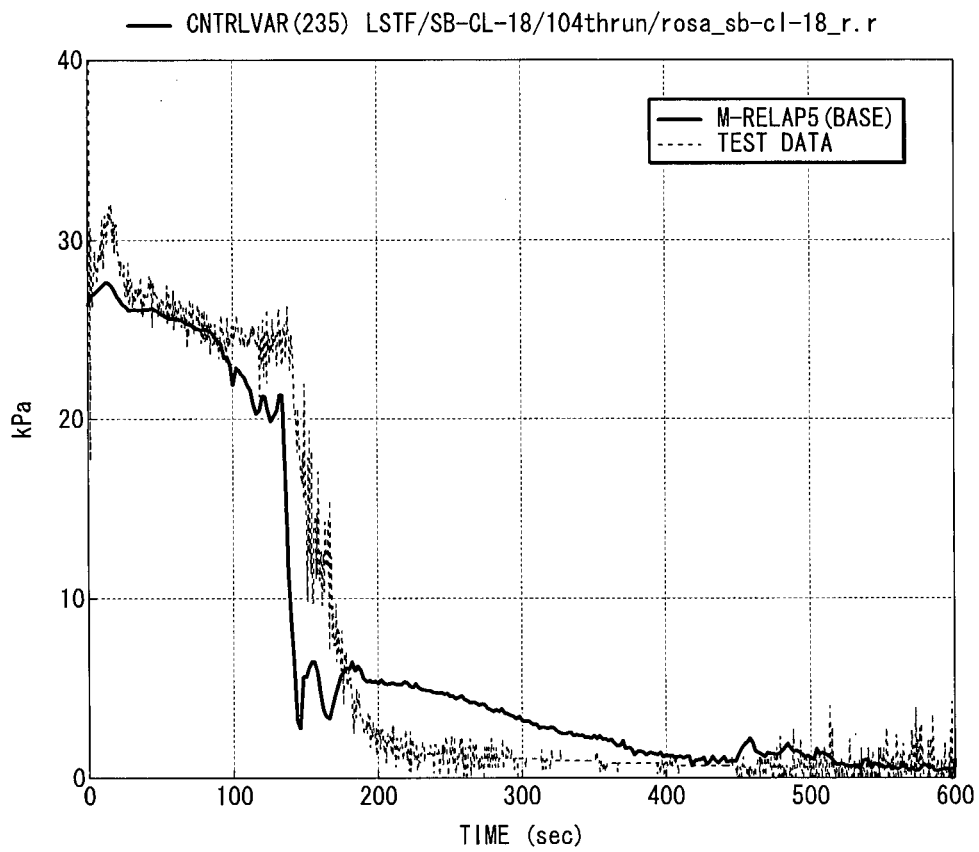


Figure 8.2.1-33 Loop-B Cross-over Leg Uphill Side Differential Pressure

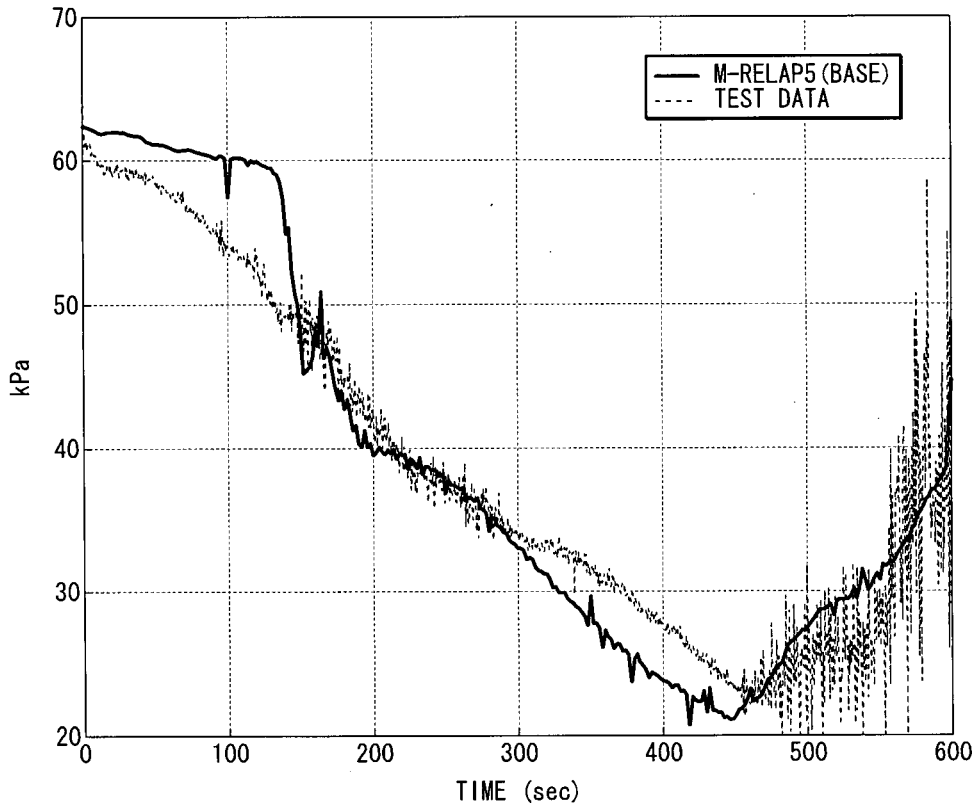


Figure 8.2.1-34 Downcomer Differential Pressure

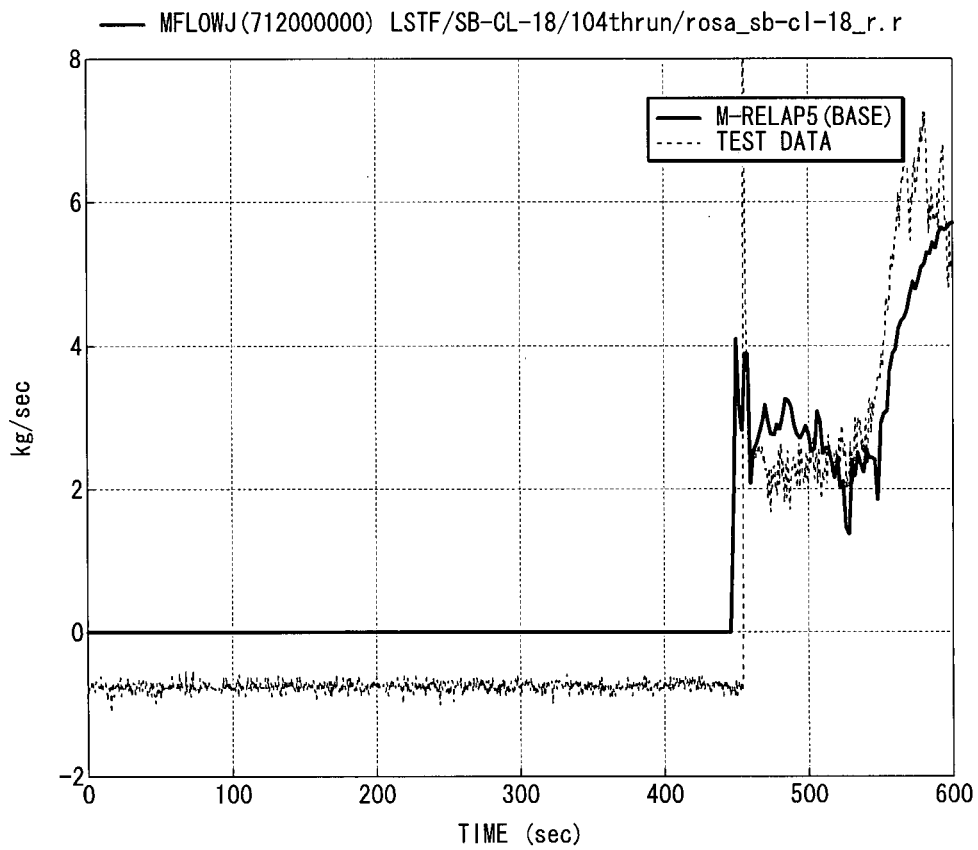


Figure 8.2.1-35 Loop-A Accumulator Injection Flowrate

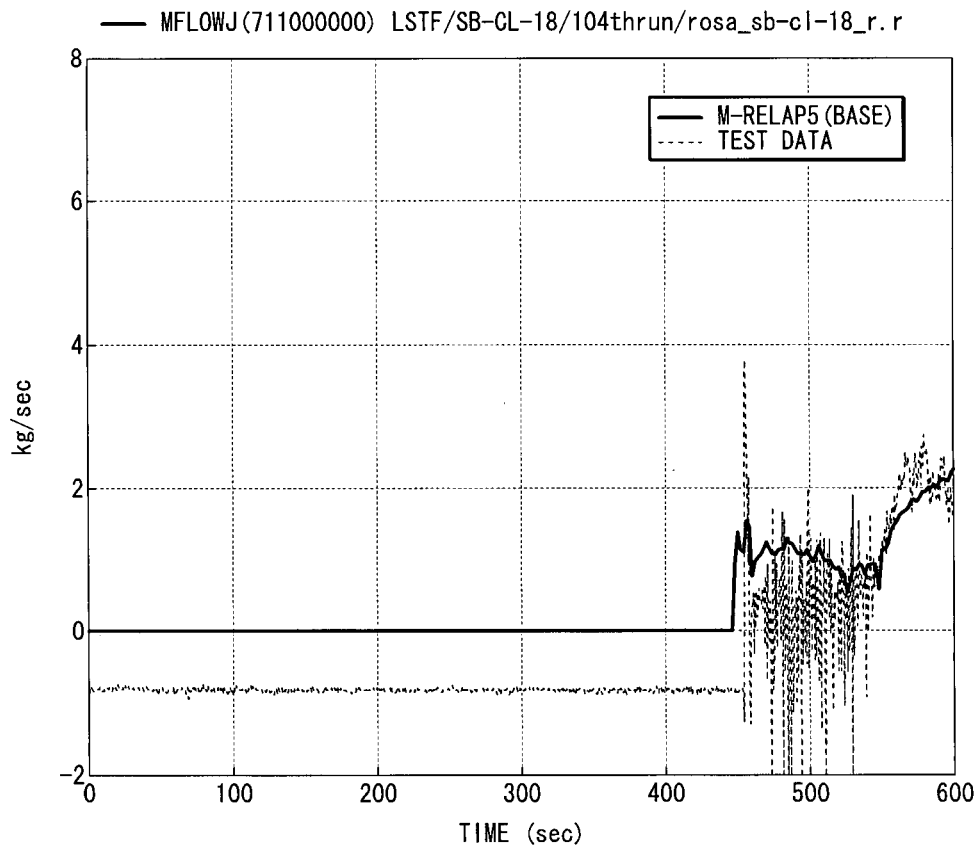


Figure 8.2.1-36 Loop-B Accumulator Injection Flowrate

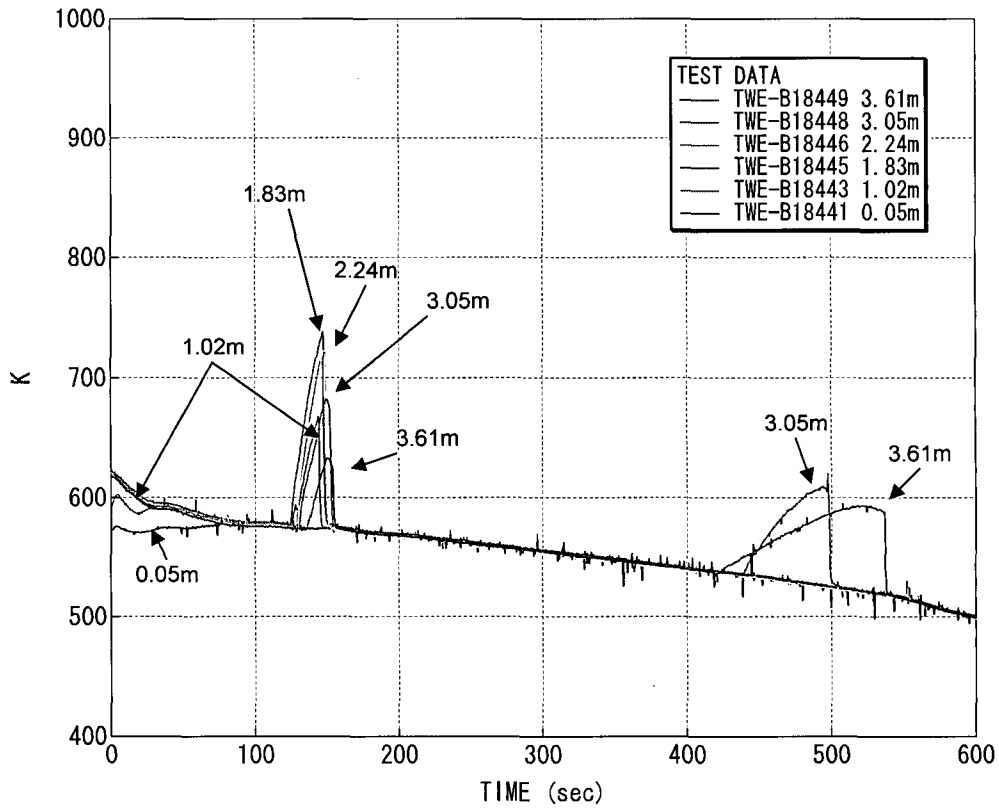


Figure 8.2.1-37 Heater Rod Surface Temperature (Test Data)

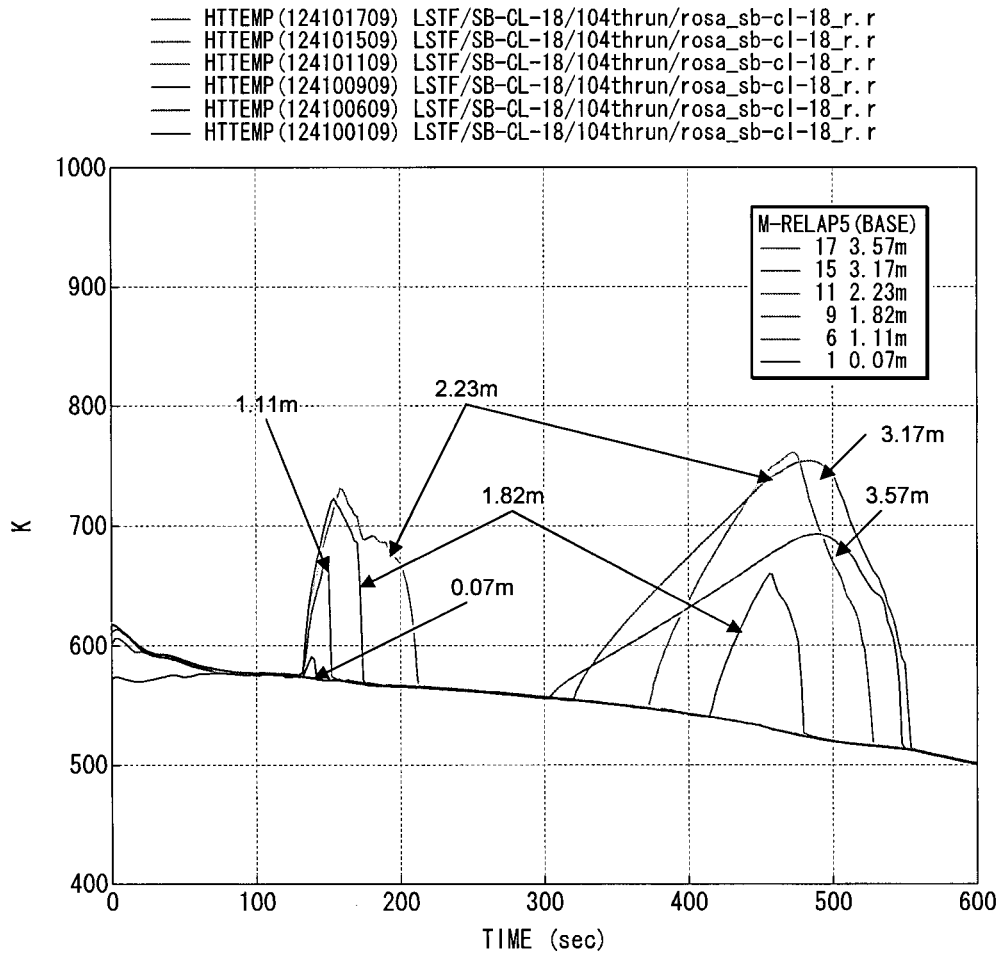


Figure 8.2.1-38 Heater Rod Surface Temperature (M-RELAP5, Base Case)

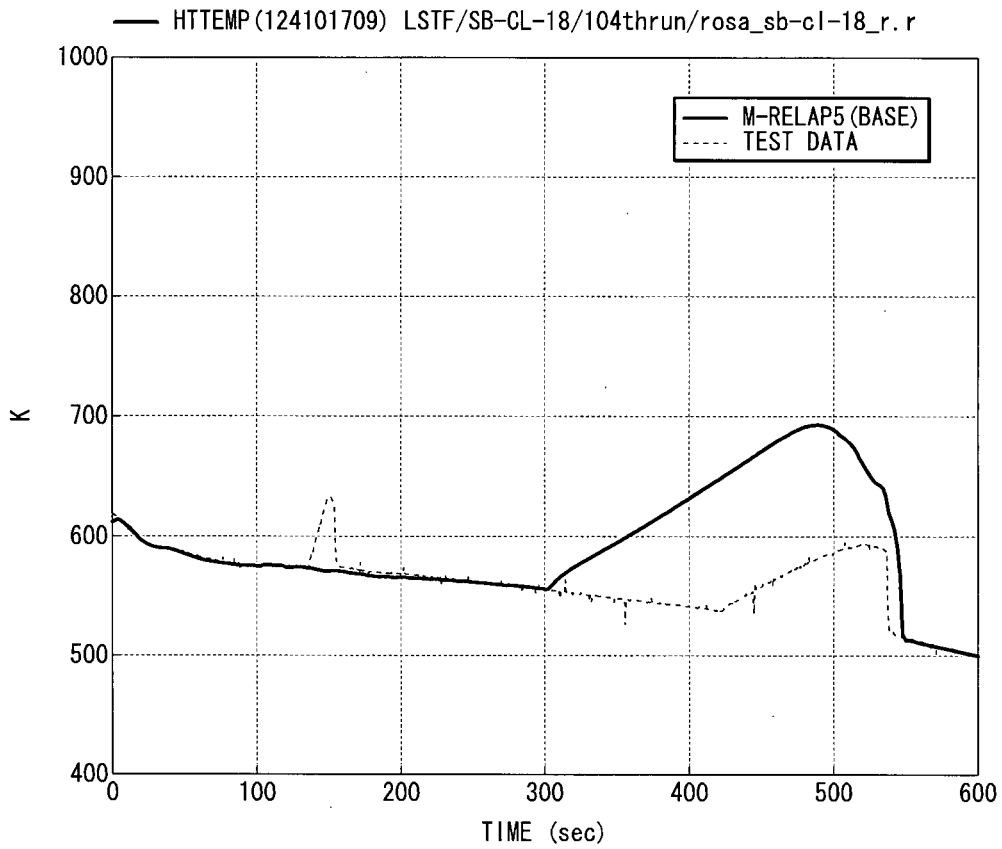


Figure 8.2.1-39 Heater Rod Surface Temperature at 3.61m (Test Data) and at 3.57m (M-RELAP5, Base Case)

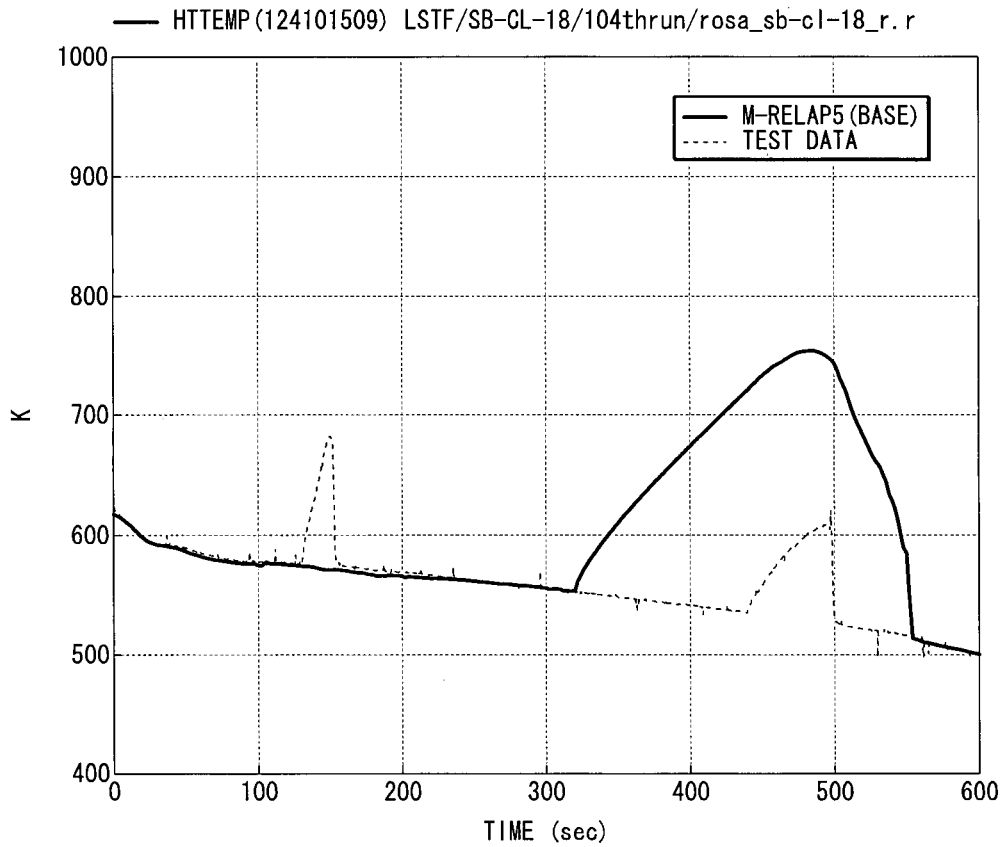


Figure 8.2.1-40 Heater Rod Surface Temperature at 3.05m (Test Data) and at 3.17m (M-RELAP5, Base Case)

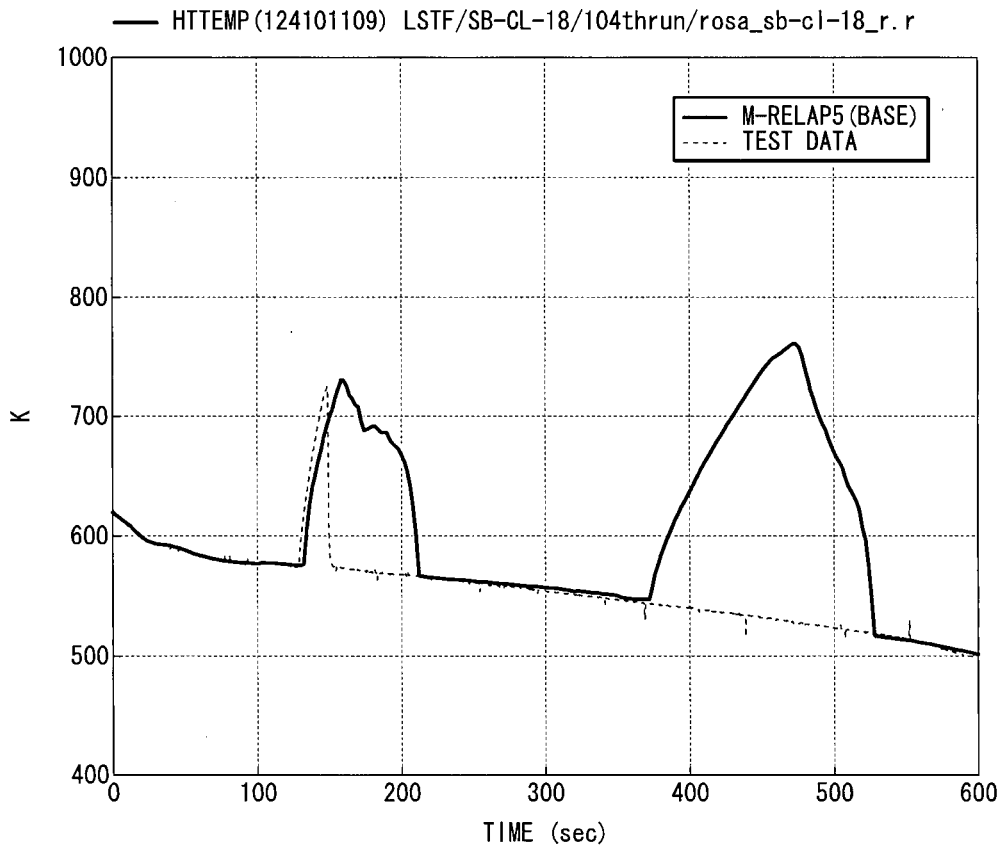


Figure 8.2.1-41 Heater Rod Surface Temperature at 2.24m (Test Data) and at 2.23m (M-RELAP5, Base Case)

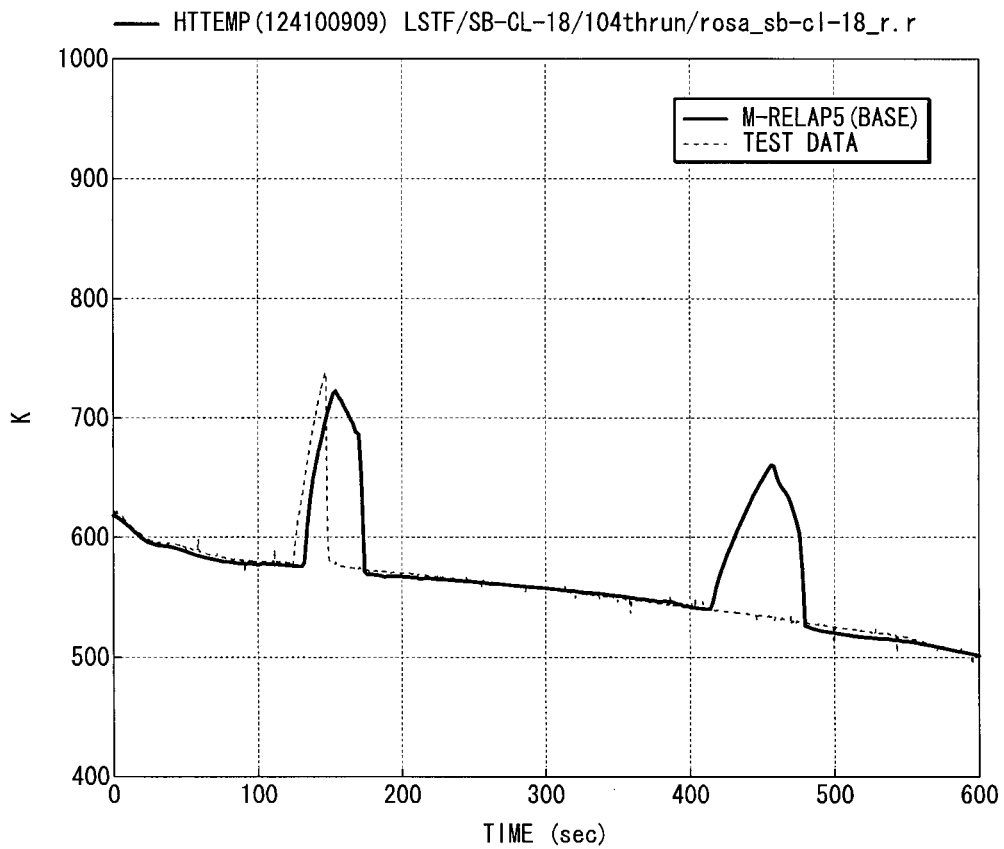


Figure 8.2.1-42 Heater Rod Surface Temperature at 1.83m (Test Data) and at 1.82m (M-RELAP5, Base Case)

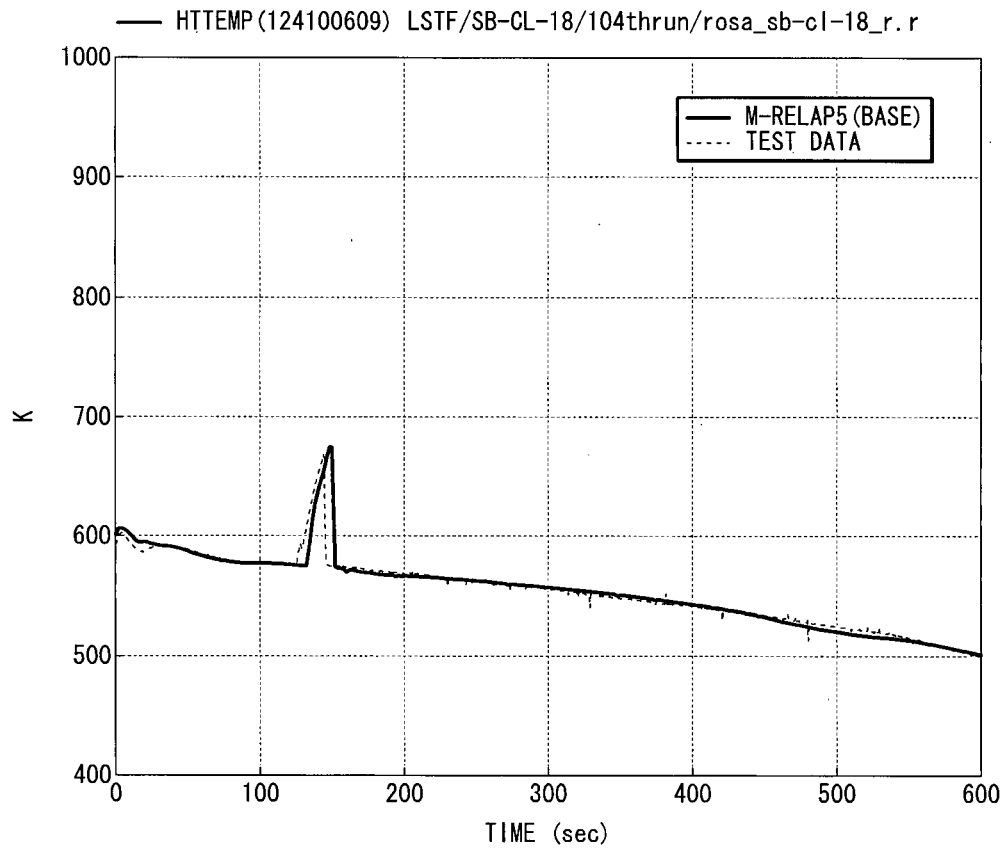


Figure 8.2.1-43 Heater Rod Surface Temperature at 1.02m (Test Data) and at 1.11m (M-RELAP5, Base Case)

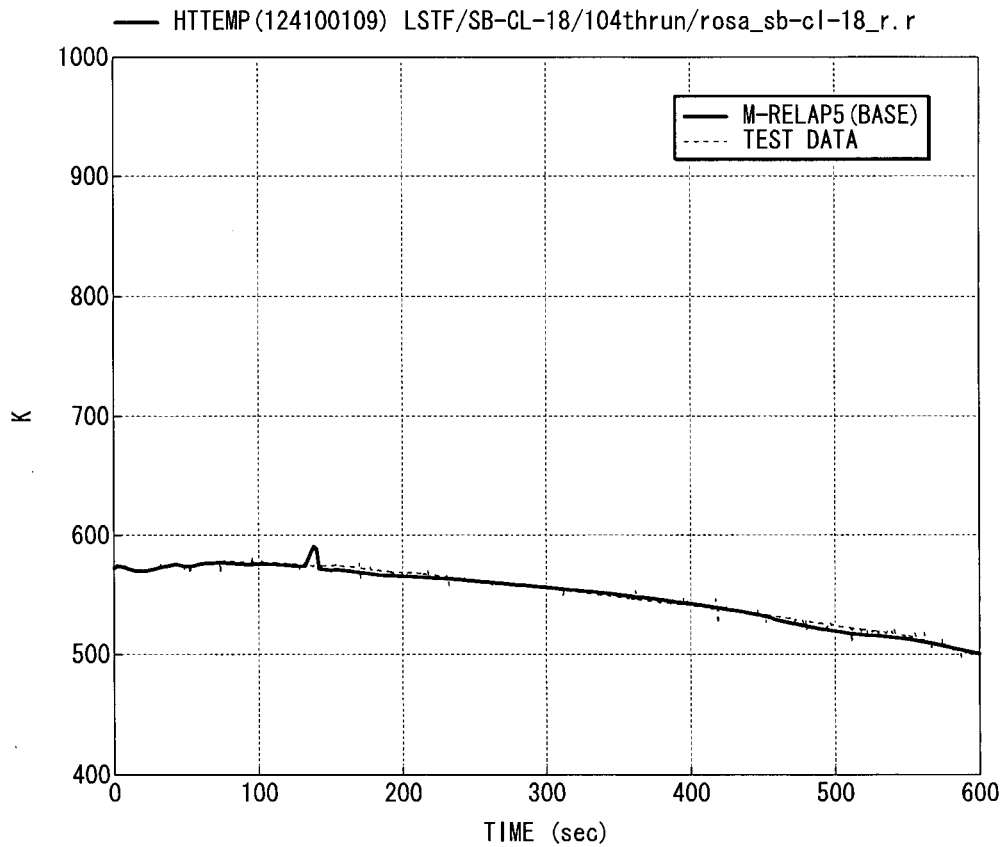


Figure 8.2.1-44 Heater Rod Surface Temperature at 0.05m (Test Data) and at 0.07m (M-RELAP5, Base Case)



Figure 8.2.1-45 Void Fraction at 3.57m (High Power Channel)



Figure 8.2.1-46 Void Fraction at 3.17m (High Power Channel)



Figure 8.2.1-47 Heater Rod Surface Temperature at 3.61m (Test Data) and at 3.57m (M-RELAP5, Sensitivity-1)



Figure 8.2.1-48 Heater Rod Surface Temperature at 3.05m (Test Data) and at 3.17m (M-RELAP5, Sensitivity-1)



Figure 8.2.1-49 Heater Rod Surface Temperature at 2.24m (Test Data) and at 2.23m (M-RELAP5, Sensitivity-1)



Figure 8.2.1-50 Heater Rod Surface Temperature at 1.83m (Test Data) and at 1.82m (M-RELAP5, Sensitivity-1)



Figure 8.2.1-51 Heater Rod Surface Temperature at 1.02m (Test Data) and at 1.11m (M-RELAP5, Sensitivity-1)



Figure 8.2.1-52 Heater Rod Surface Temperature at 0.05m (Test Data) and at 0.07m (M-RELAP5, Sensitivity-1)

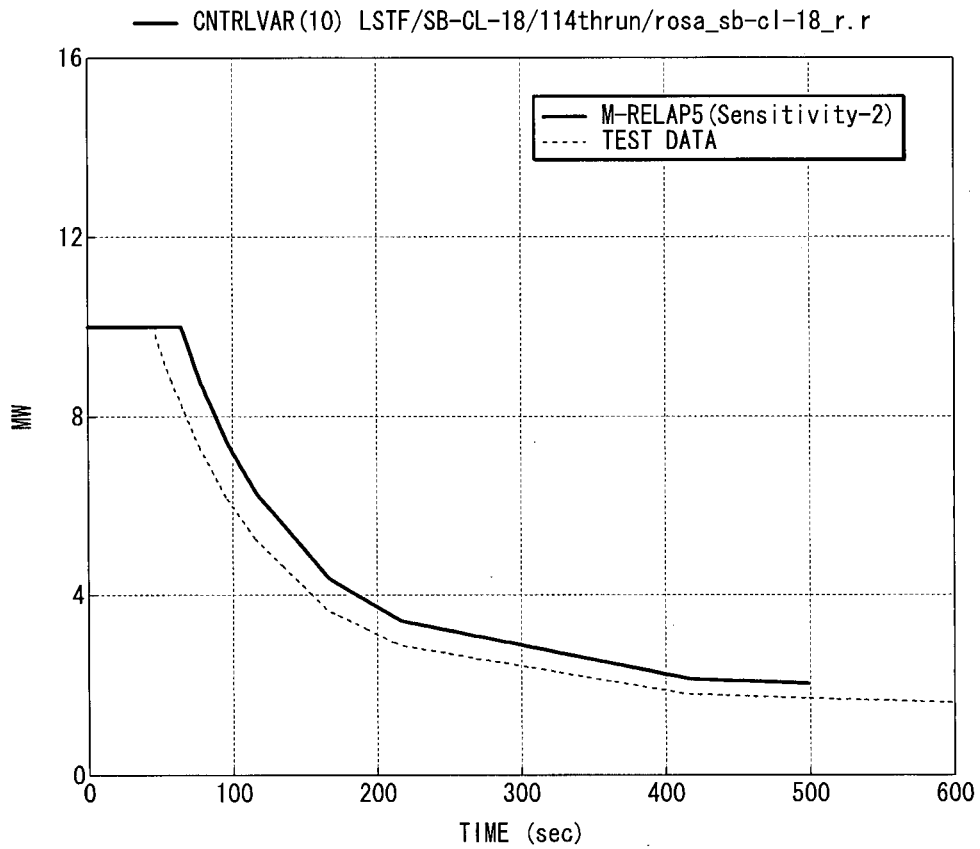


Figure 8.2.1-53 Total Core Power (Sensitivity-2)

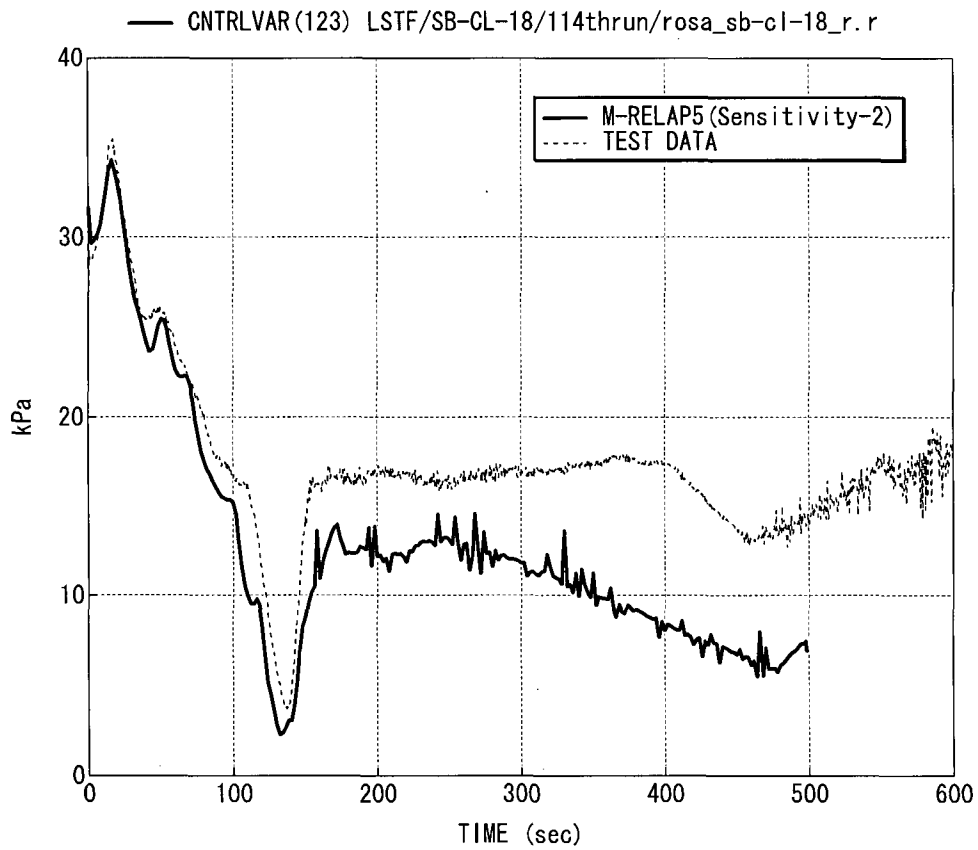


Figure 8.2.1-54 Core Differential Pressure (Sensitivity-2)

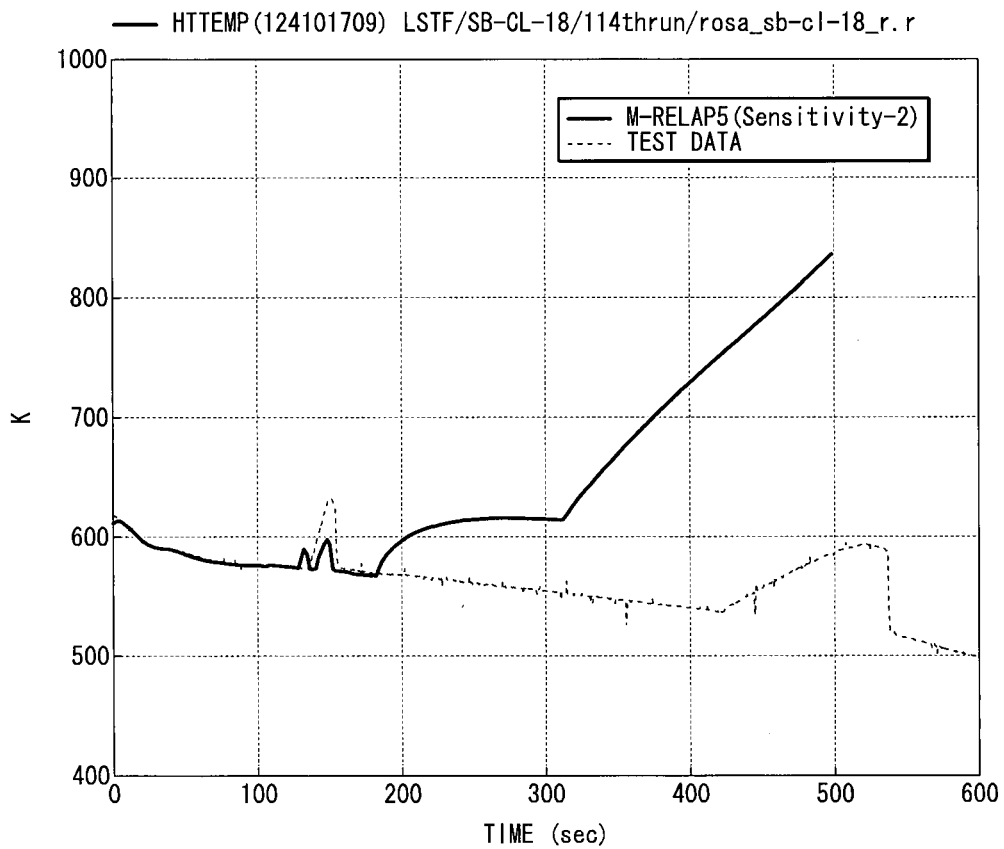


Figure 8.2.1-55 Heater Rod Surface Temperature at 3.61m (Test Data) and at 3.57m (M-RELAP5, Sensitivity-2)

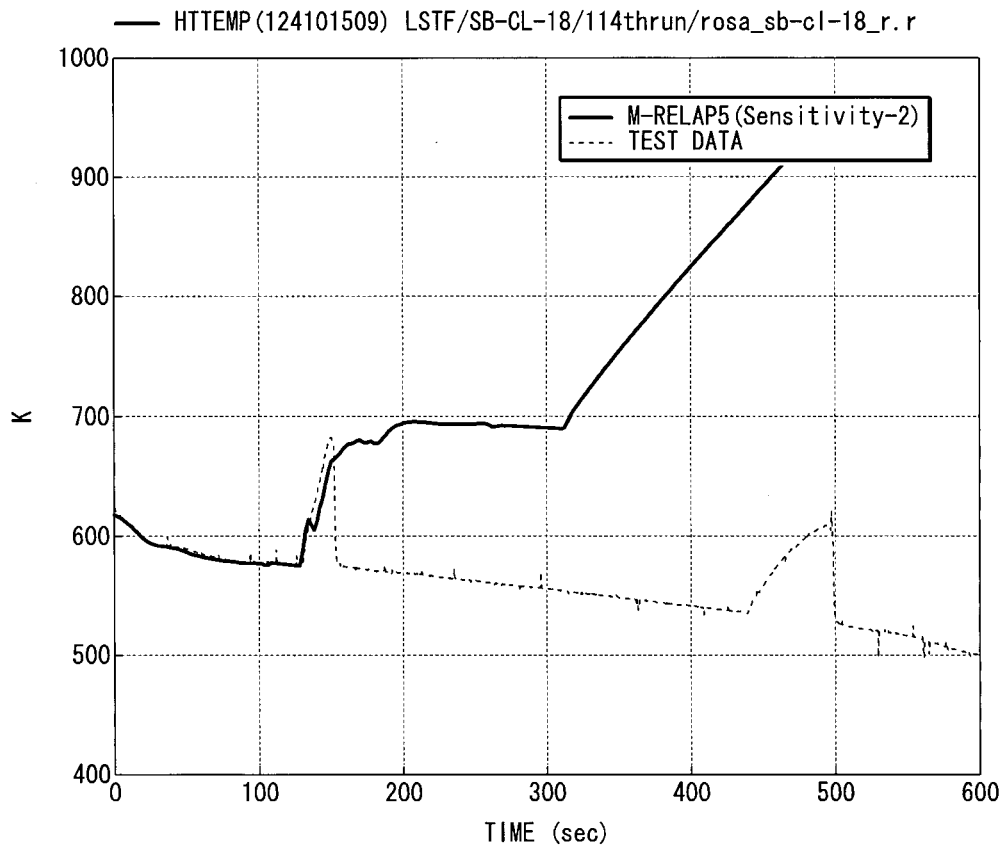


Figure 8.2.1-56 Heater Rod Surface Temperature at 3.05m (Test Data) and at 3.17m (M-RELAP5, Sensitivity-2)

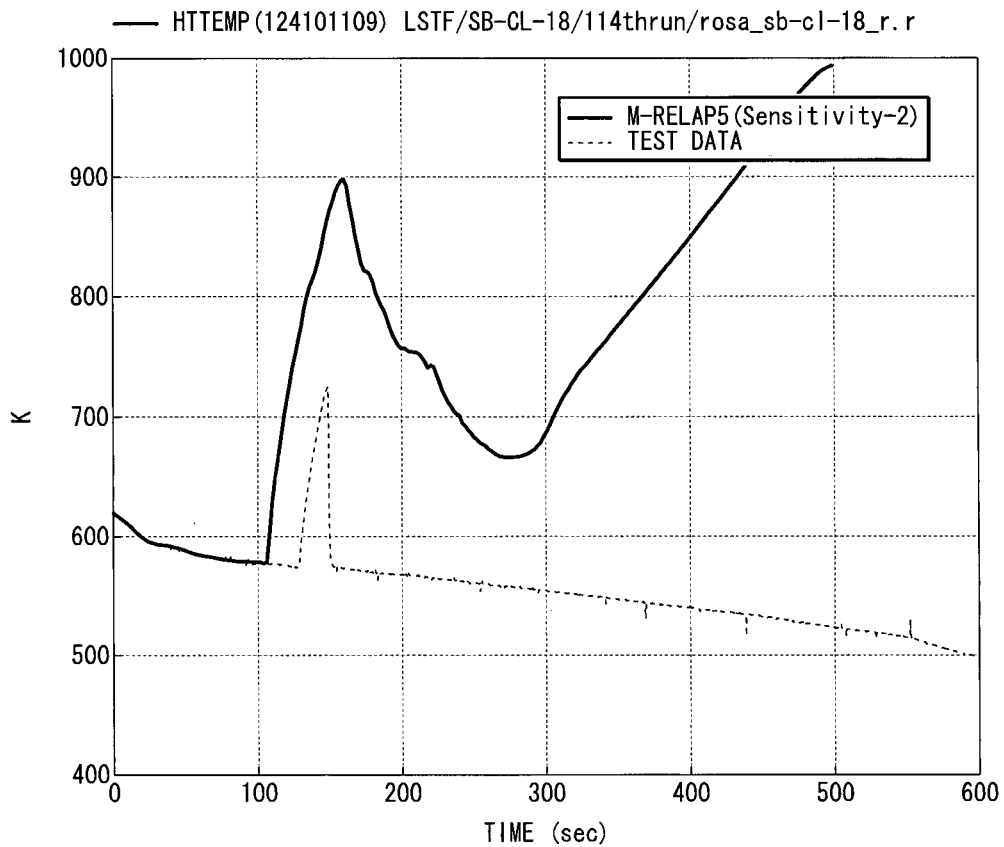


Figure 8.2.1-57 Heater Rod Surface Temperature at 2.24m (Test Data) and at 2.23m (M-RELAP5, Sensitivity-2)

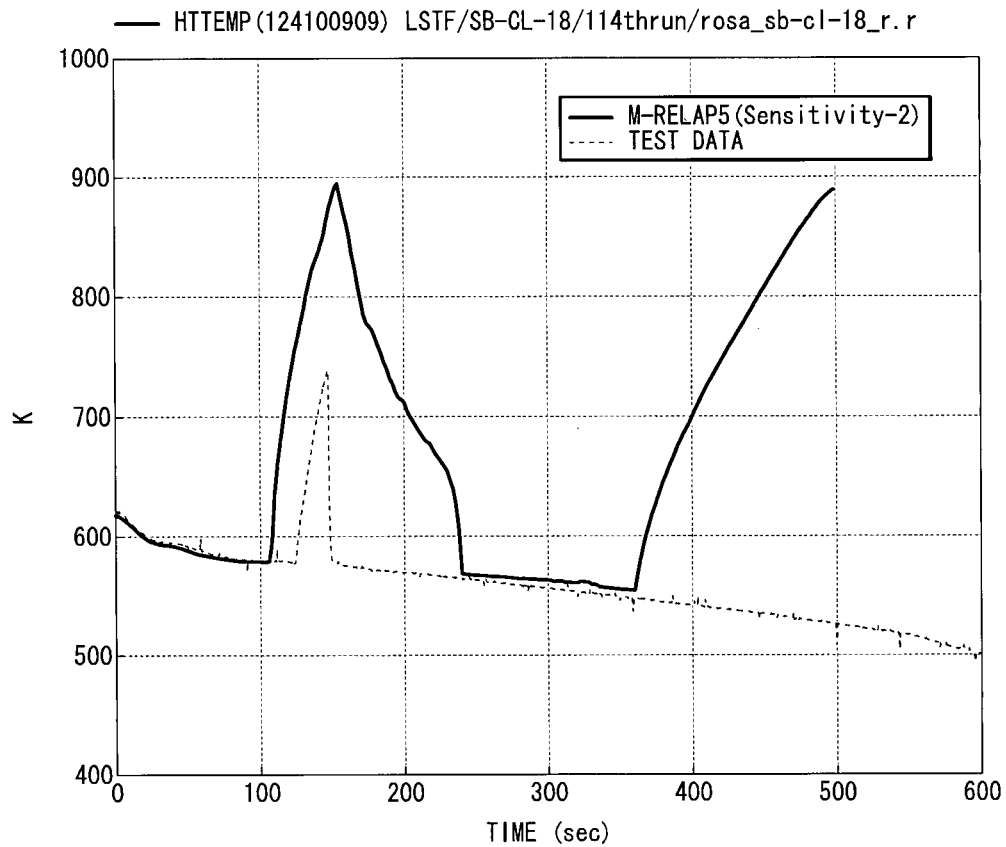


Figure 8.2.1-58 Heater Rod Surface Temperature at 1.83m (Test Data) and at 1.82m (M-RELAP5, Sensitivity-2)

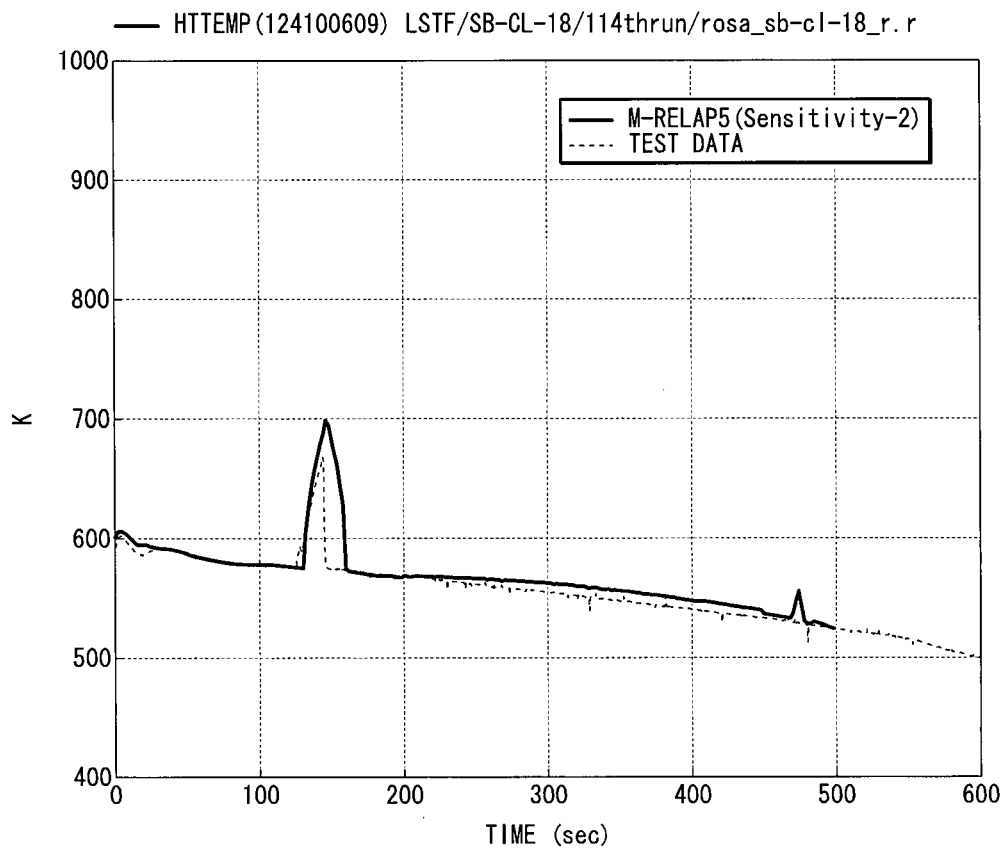


Figure 8.2.1-59 Heater Rod Surface Temperature at 1.02m (Test Data) and at 1.11m (M-RELAP5, Sensitivity-2)

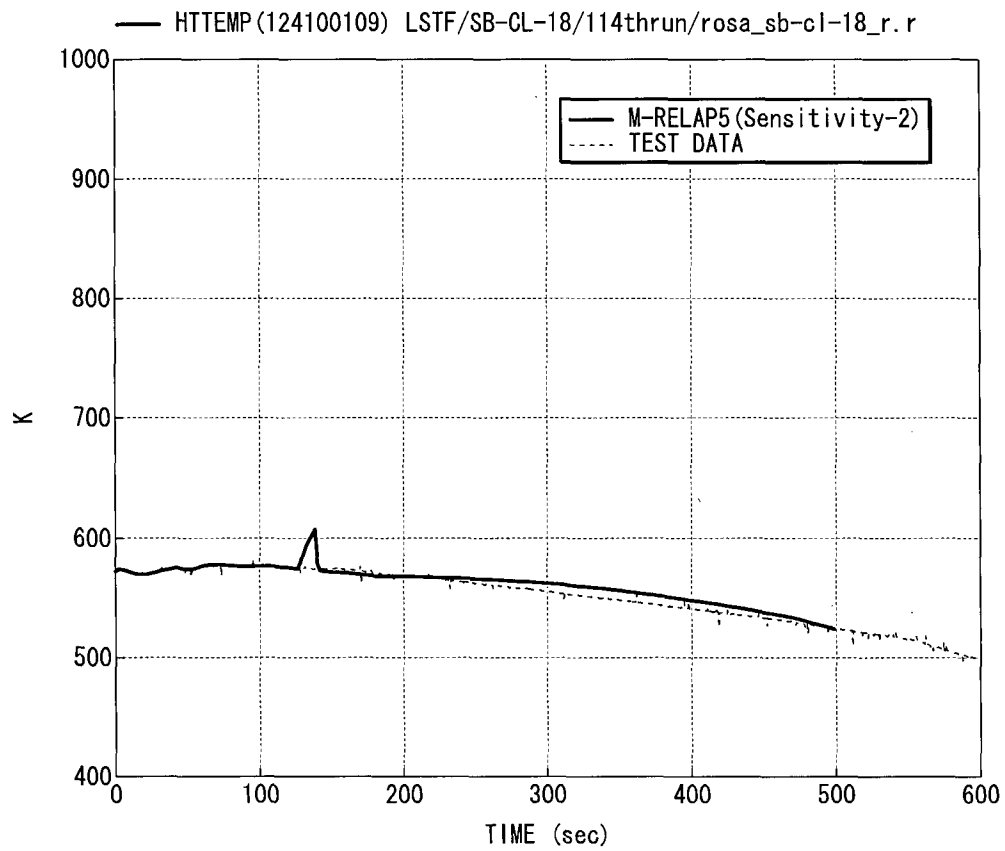


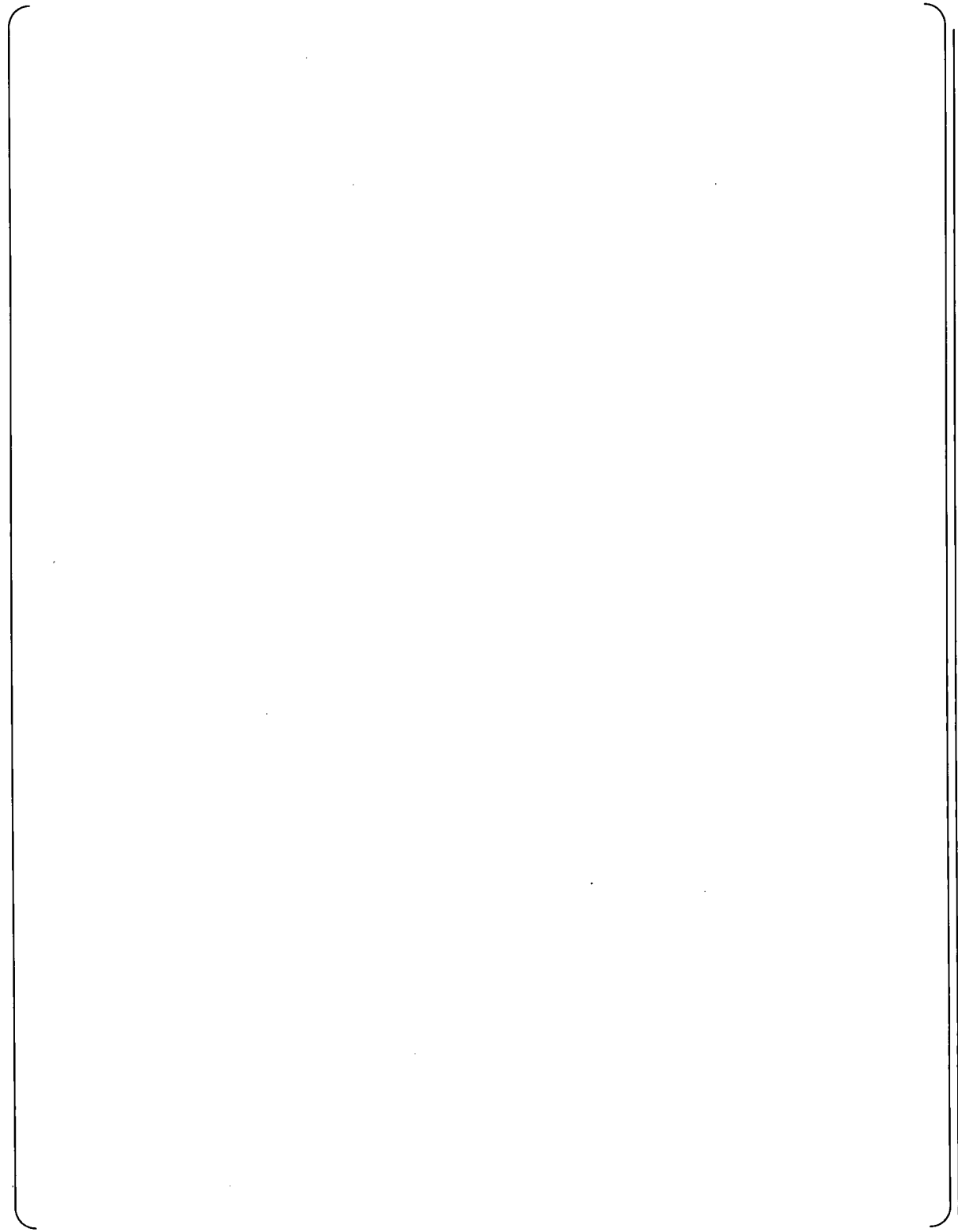
Figure 8.2.1-60 Heater Rod Surface Temperature at 0.05m (Test Data) and at 0.07m (M-RELAP5, Sensitivity-2)



Figure 8.2.1-61 Upper Plenum Differential Pressure



Figure 8.2.1-62 Upper Head Liquid Level



**Figure 8.2.1-63 ROSA/LSTF Noding Diagram
(Sensitivity-3 Upper Head Nodalization Sensitivity Study)**



Figure 8.2.1-64 Upper Head Liquid Level (Sensitivity-3)



Figure 8.2.1-65 Core Differential Pressure (Sensitivity-3)



Figure 8.2.1-66 Downcomer Differential Pressure (Sensitivity-3)



Figure 8.2.1-67 Upper Plenum Differential Pressure (Sensitivity-3)



Figure 8.2.1-68 Loop-A Cross-Over Leg Uphill Side Differential Pressure (Sensitivity-4)



Figure 8.2.1-69 Loop-B Cross-Over Leg Uphill Side Differential Pressure (Sensitivity-4)



Figure 8.2.1-70 Core Differential Pressure (Sensitivity-4)



Figure 8.2.1-71 Upper Plenum Collapsed Liquid Level (Sensitivity-4)



Figure 8.2.1-72 Break Flowrate (Sensitivity-5)



Figure 8.2.1-73 Pressurizer Pressure (Sensitivity-5)



Figure 8.2.1-74 Loop-A Hot Leg to SG Inlet Plenum Bottom Differential Pressure (Sensitivity-5)



**Figure 8.2.1-75 Loop-B Hot Leg to SG Inlet Plenum Bottom Differential Pressure
(Sensitivity-5)**



Figure 8.2.1-76 Core Differential Pressure (Sensitivity-5)



Figure 8.2.1-77 Upper Plenum Collapsed Liquid Level (Sensitivity-5)



Figure 8.2.1-78 Heater Rod Surface Temperature (Sensitivity-3)



Figure 8.2.1-79 Heater Rod Surface Temperature (Sensitivity-4)



Figure 8.2.1-80 Heater Rod Surface Temperature (Sensitivity-5)



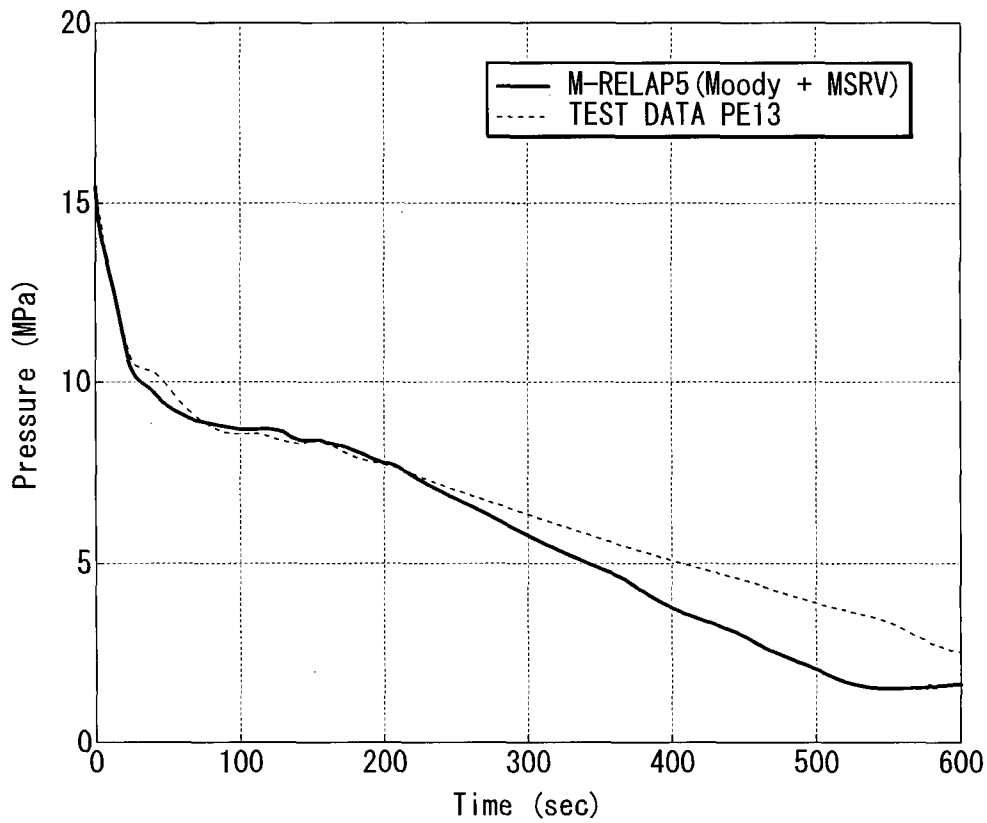


Figure 8.2.1-82 Pressurizer Pressure (Calculation with Simulated Secondary System and Break Flow Behavior)

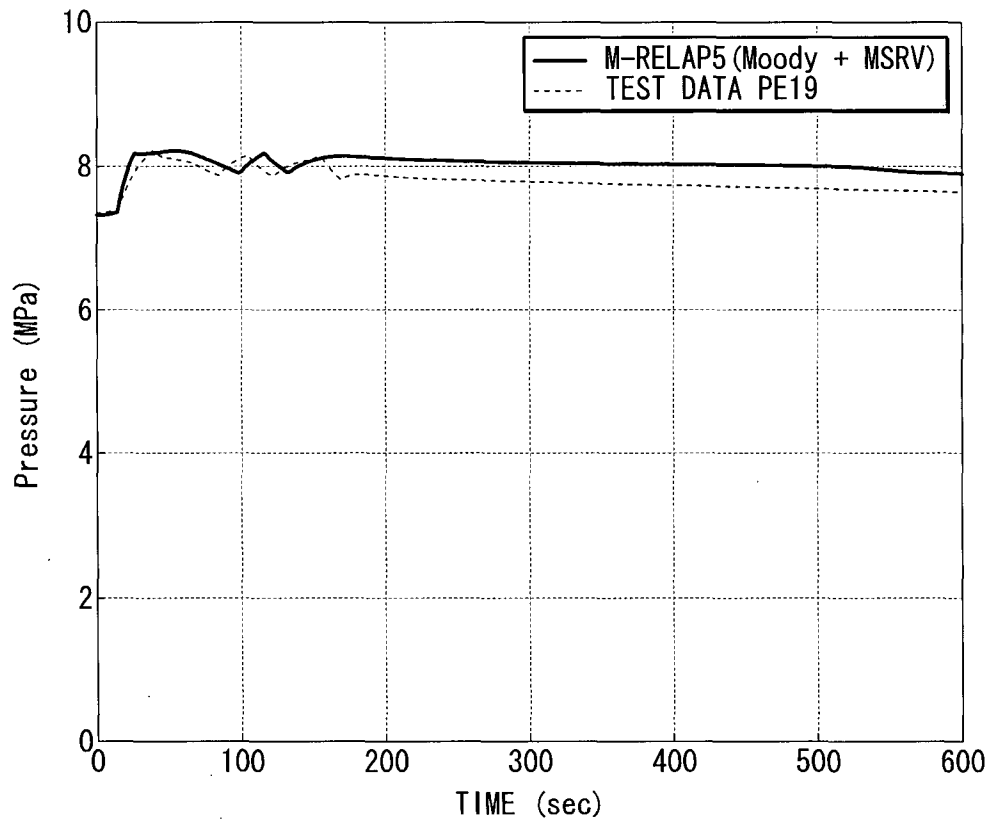


Figure 8.2.1-83 SG-A Steam Dome Pressure (Calculation with Simulated Secondary System and Break Flow Behavior)

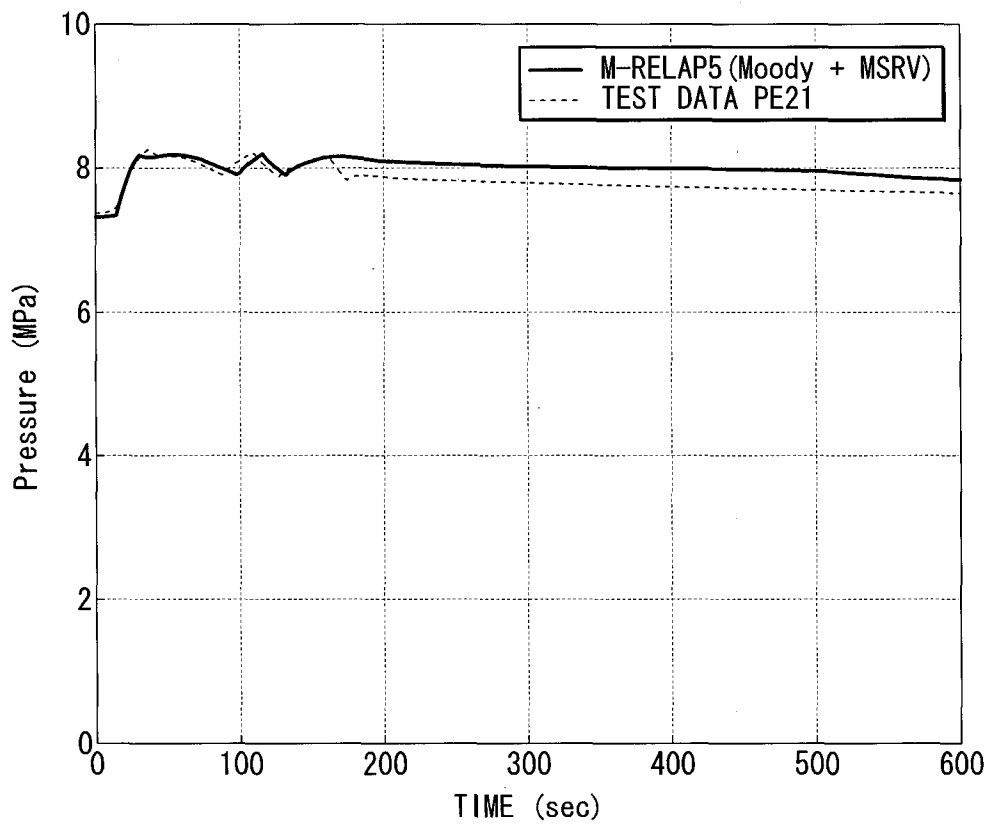


Figure 8.2.1-84 SG-B Steam Dome Pressure (Calculation with Simulated Secondary System and Break Flow Behavior)

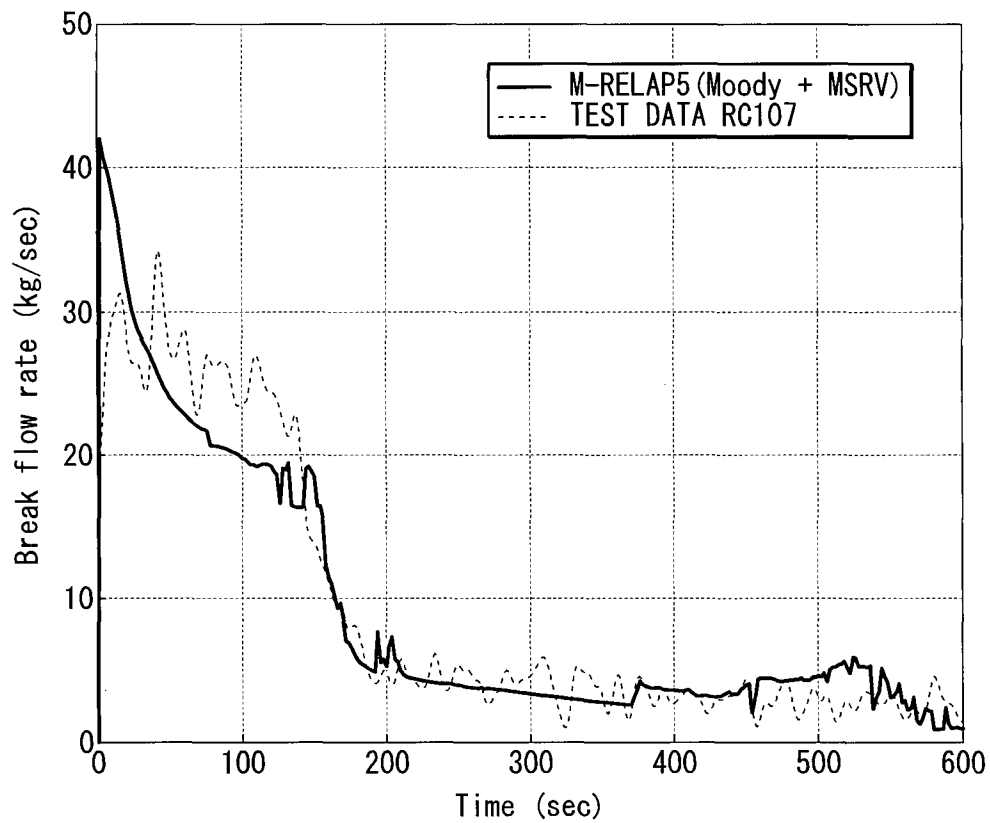


Figure 8.2.1-85 Break Flowrate (Calculation with Simulated Secondary System and Break Flow Behavior)

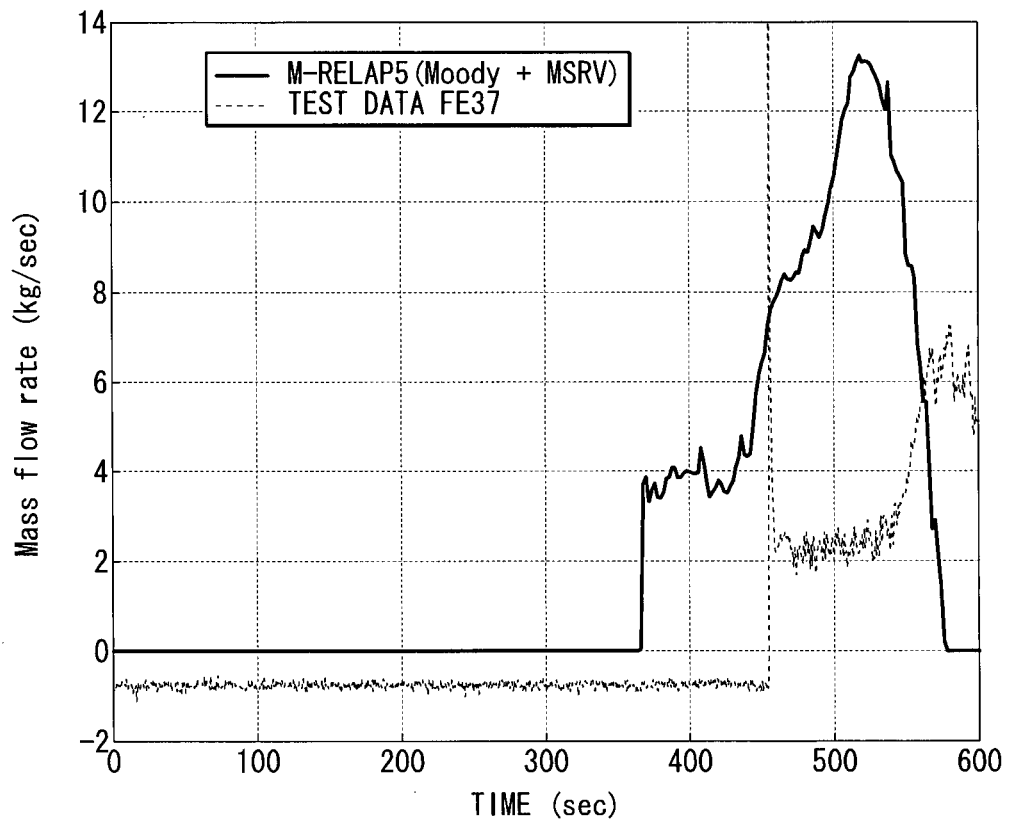


Figure 8.2.1-86 Loop-A Accumulator Injection Flowrate (Calculation with Simulated Secondary System and Break Flow Behavior)

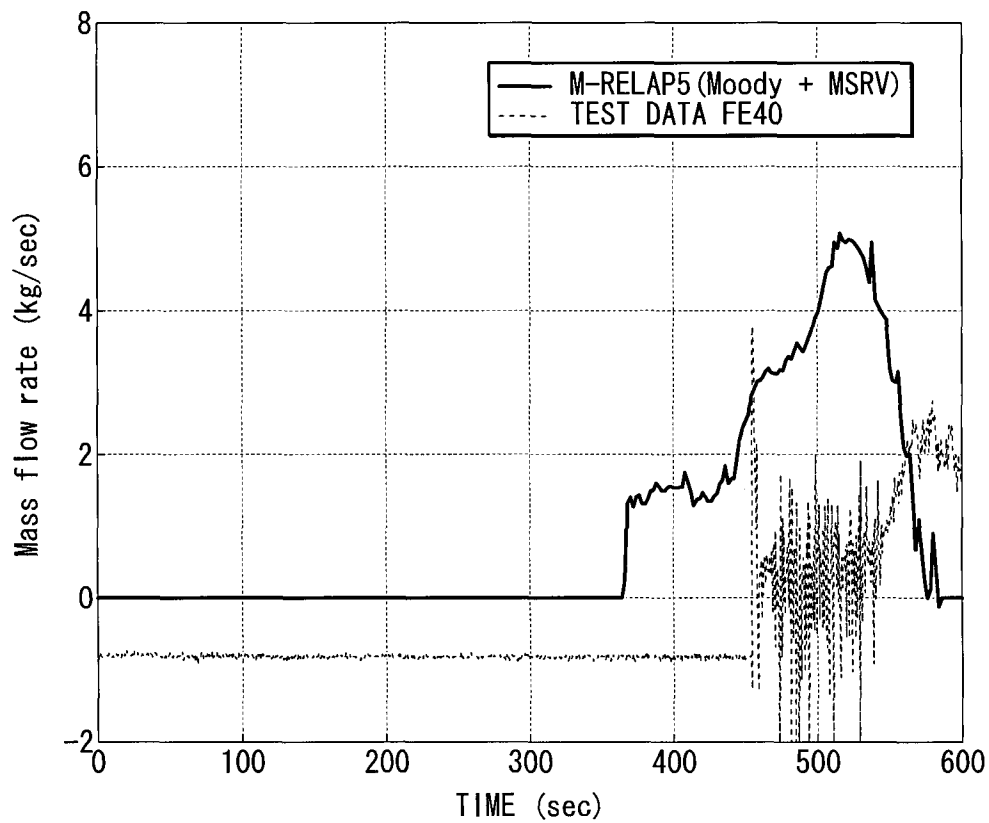


Figure 8.2.1-87 Loop-B Accumulator Injection Flowrate (Calculation with Simulated Secondary System and Break Flow Behavior)

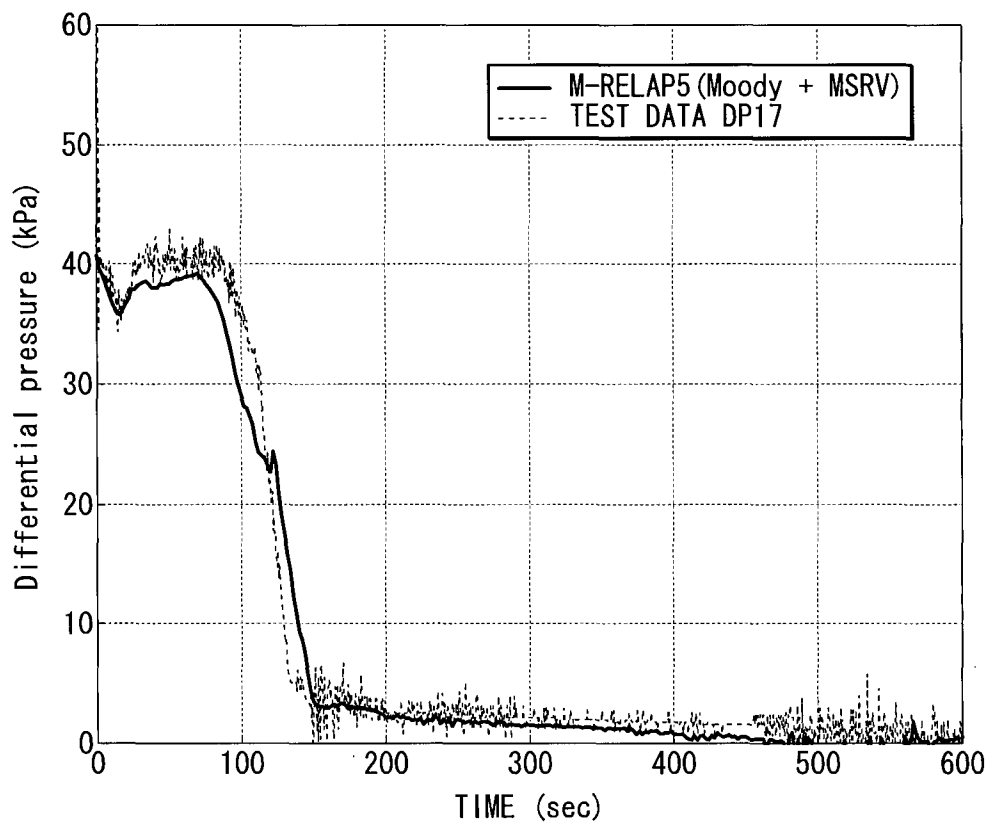


Figure 8.2.1-88 Loop-A Cross-over Leg Downhill Side Differential Pressure (Calculation with Simulated Secondary System and Break Flow Behavior)

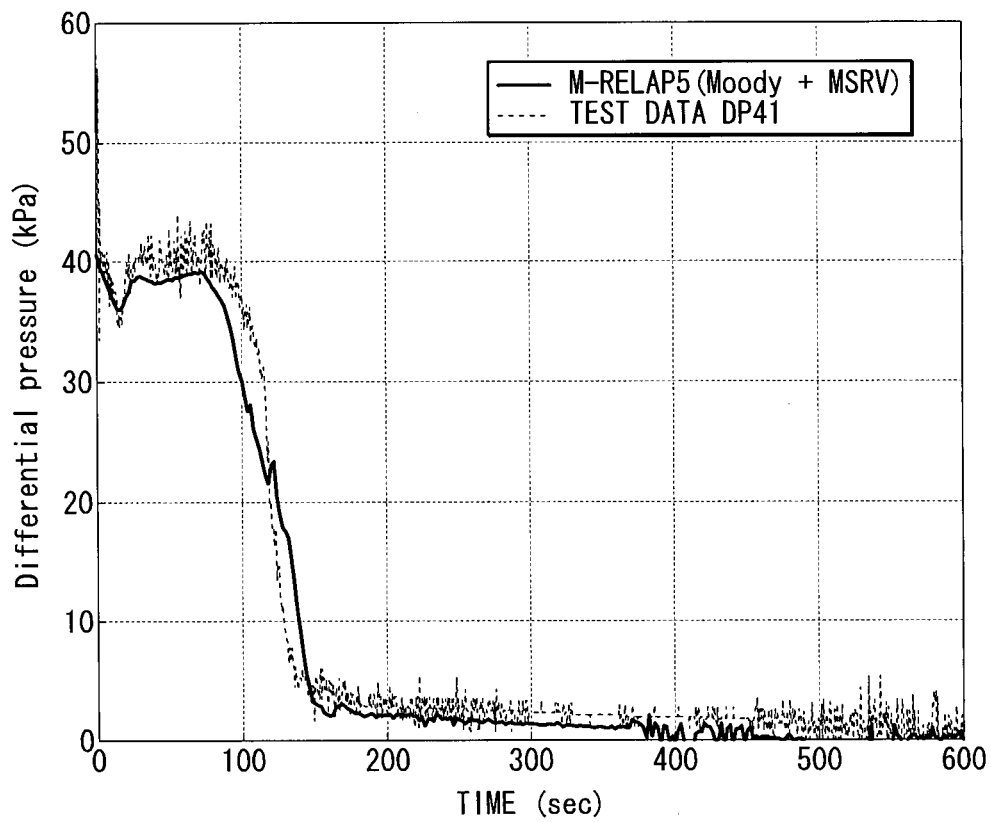


Figure 8.2.1-89 Loop-B Cross-over Leg Downhill Side Differential Pressure (Calculation with Simulated Secondary System and Break Flow Behavior)

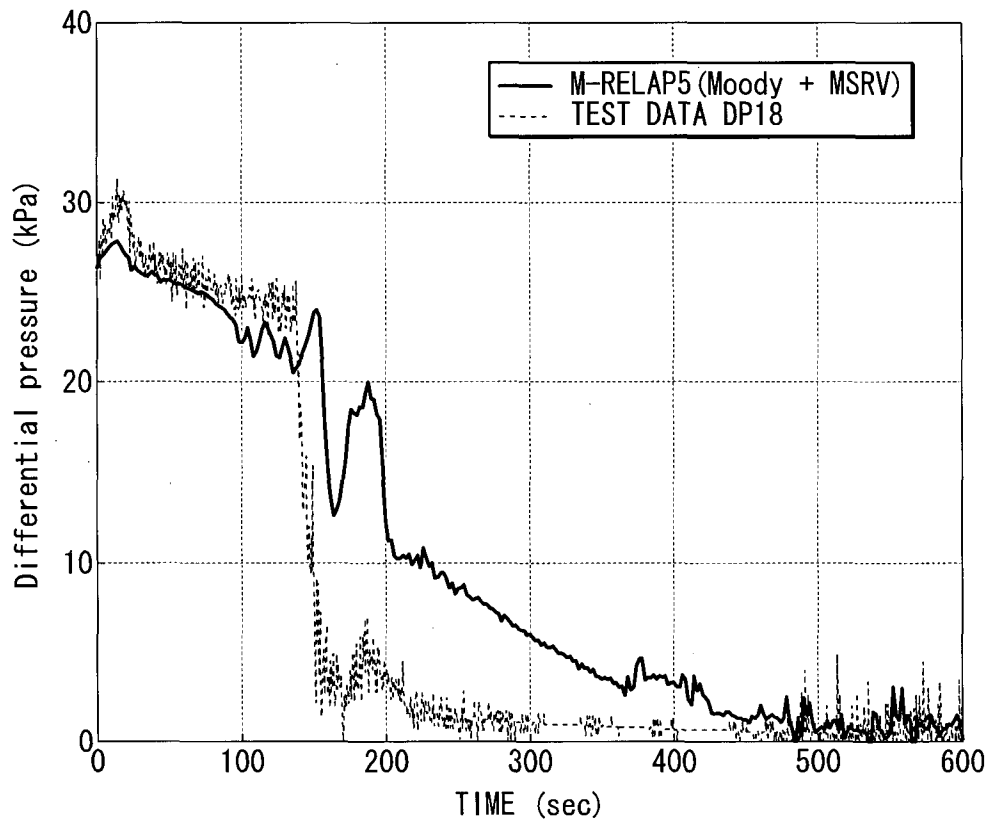


Figure 8.2.1-90 Loop-A Cross-over Leg Uphill Side Differential Pressure (Calculation with Simulated Secondary System and Break Flow Behavior)

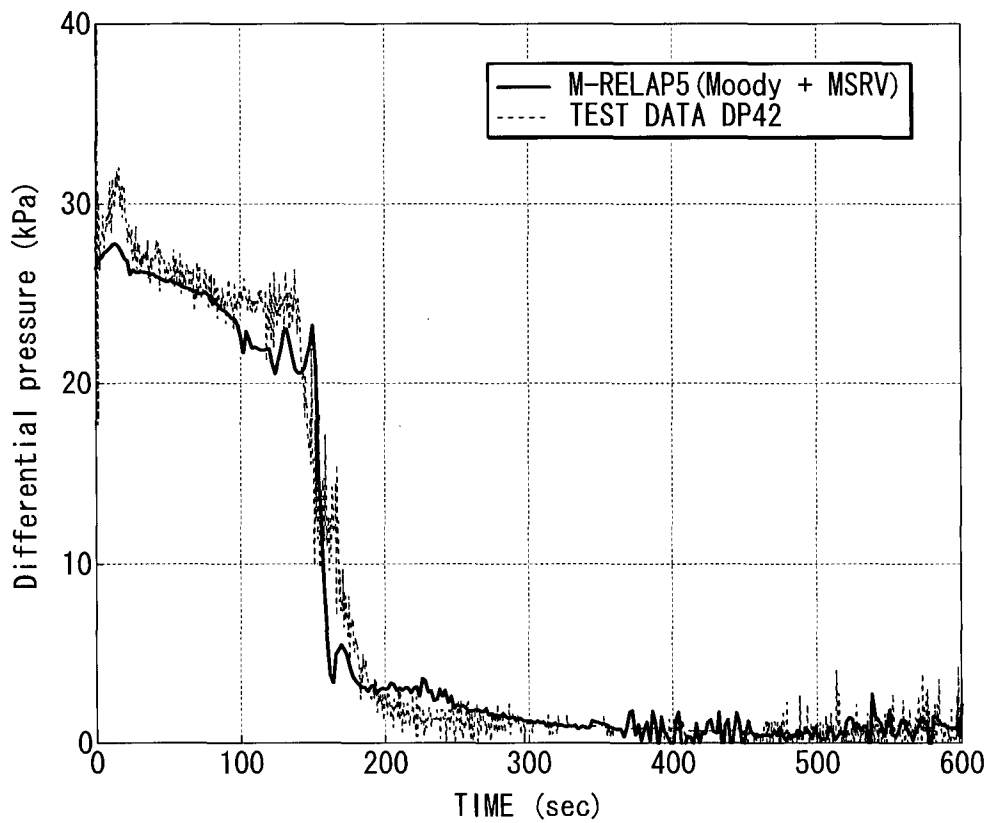


Figure 8.2.1-91 Loop-B Cross-over Leg Uphill Side Differential Pressure (Calculation with Simulated Secondary System and Break Flow Behavior)

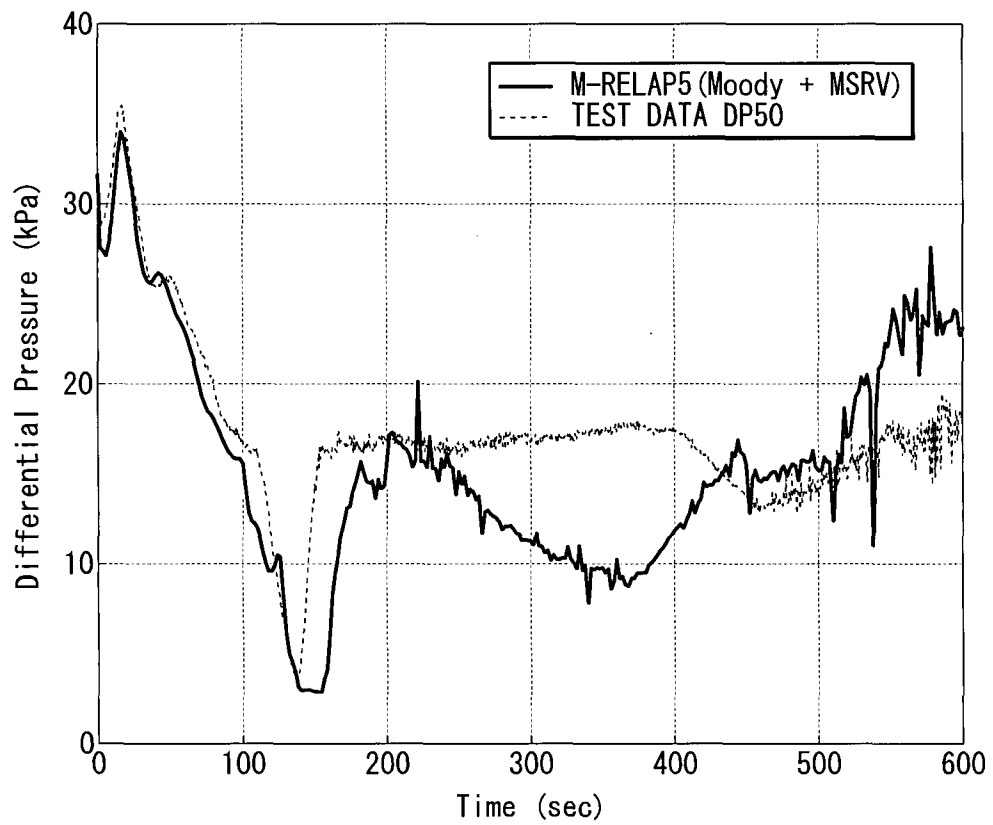


Figure 8.2.1-92 Core Differential Pressure (Calculation with Simulated Secondary System and Break Flow Behavior)

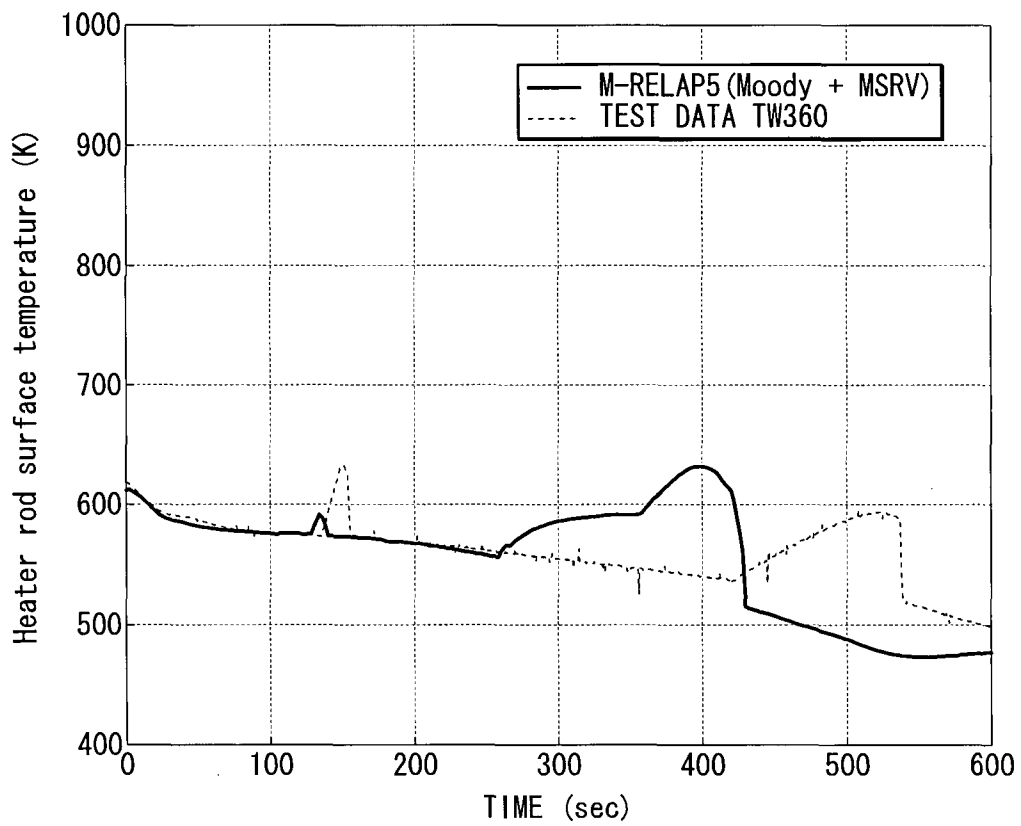


Figure 8.2.1-93 Heater Rod Surface Temperature at 3.61m (M) and 3.57m (P) (Calculation with Simulated Secondary System and Break Flow Behavior)

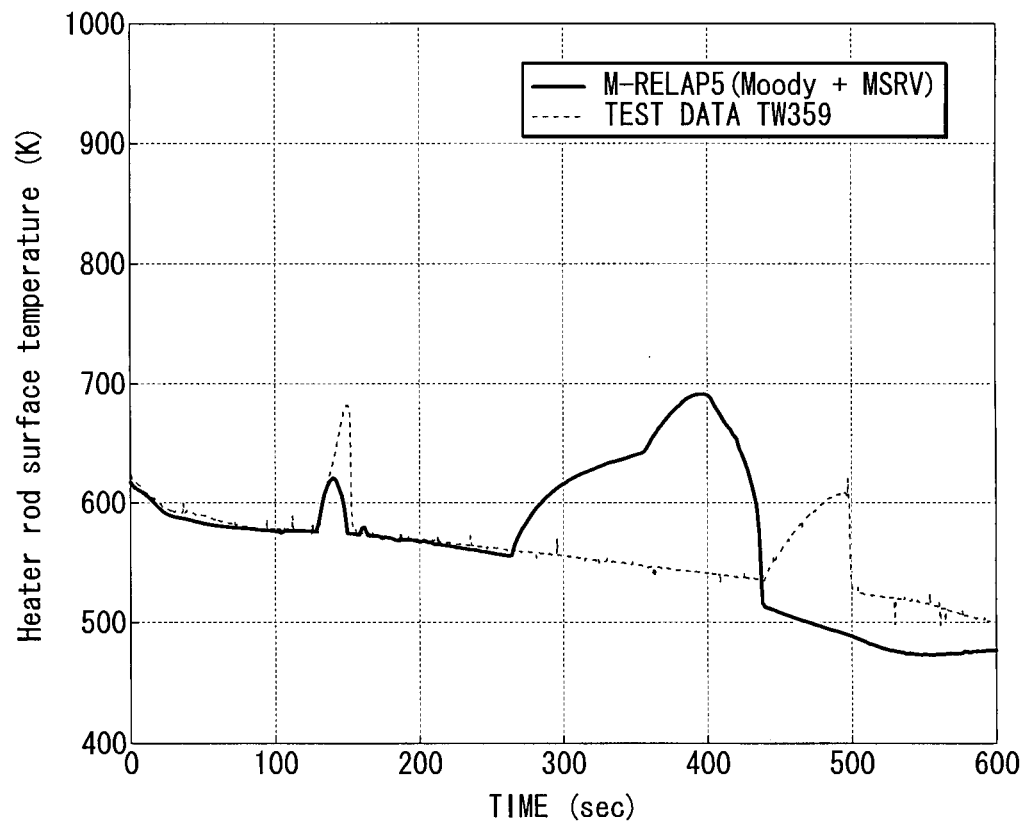


Figure 8.2.1-94 Heater Rod Surface Temperature at 3.05m (M) and 3.17m (P) (Calculation with Simulated Secondary System and Break Flow Behavior)

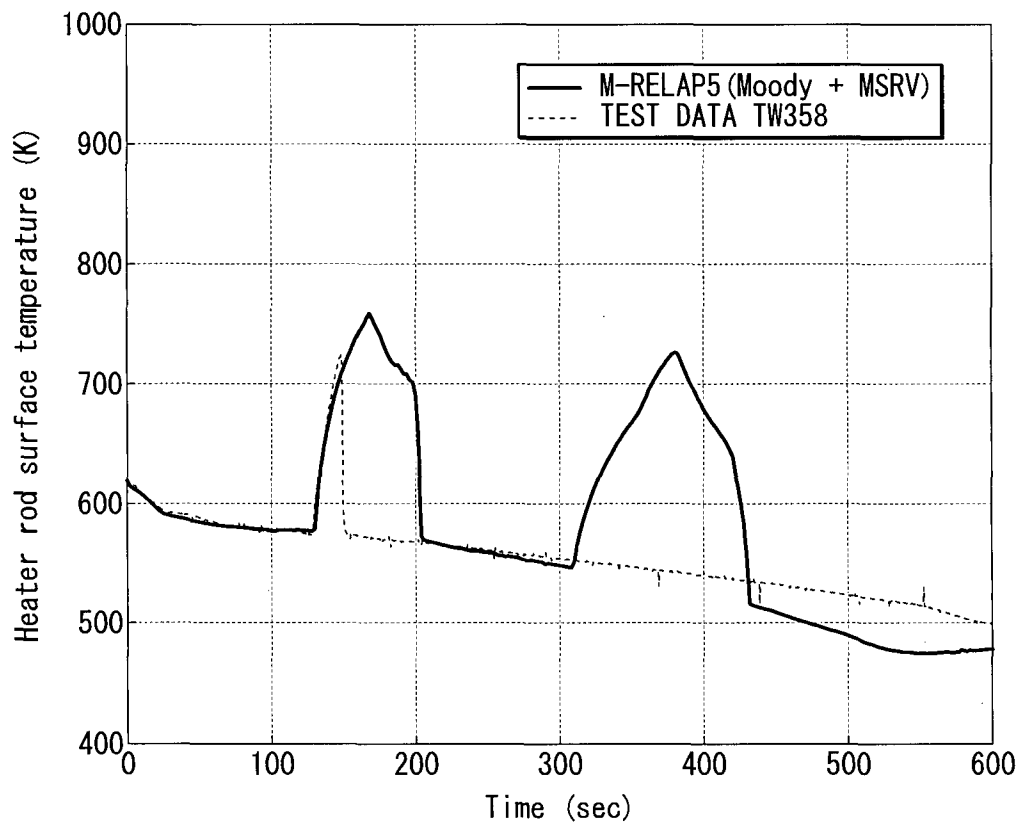


Figure 8.2.1-95 Heater Rod Surface Temperature at 2.24m (M) and 2.23m (P) (Calculation with Simulated Secondary System and Break Flow Behavior)

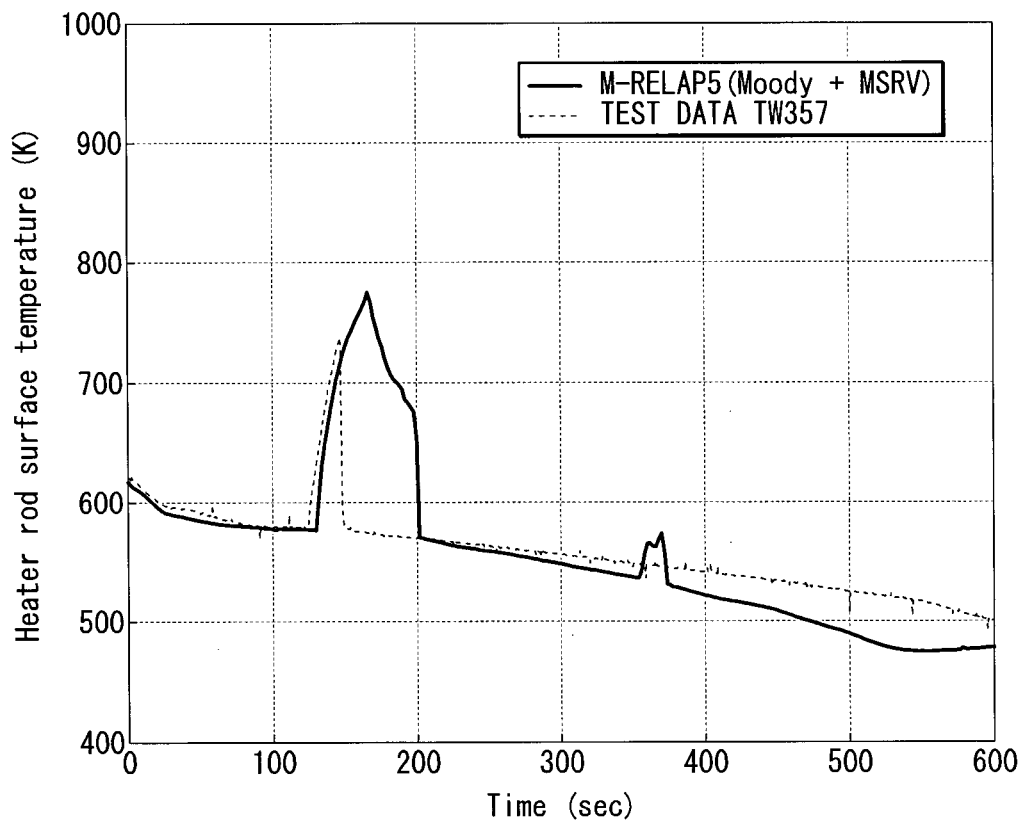


Figure 8.2.1-96 Heater Rod Surface Temperature at 1.83m (M) and 1.82m (P) (Calculation with Simulated Secondary System and Break Flow Behavior)

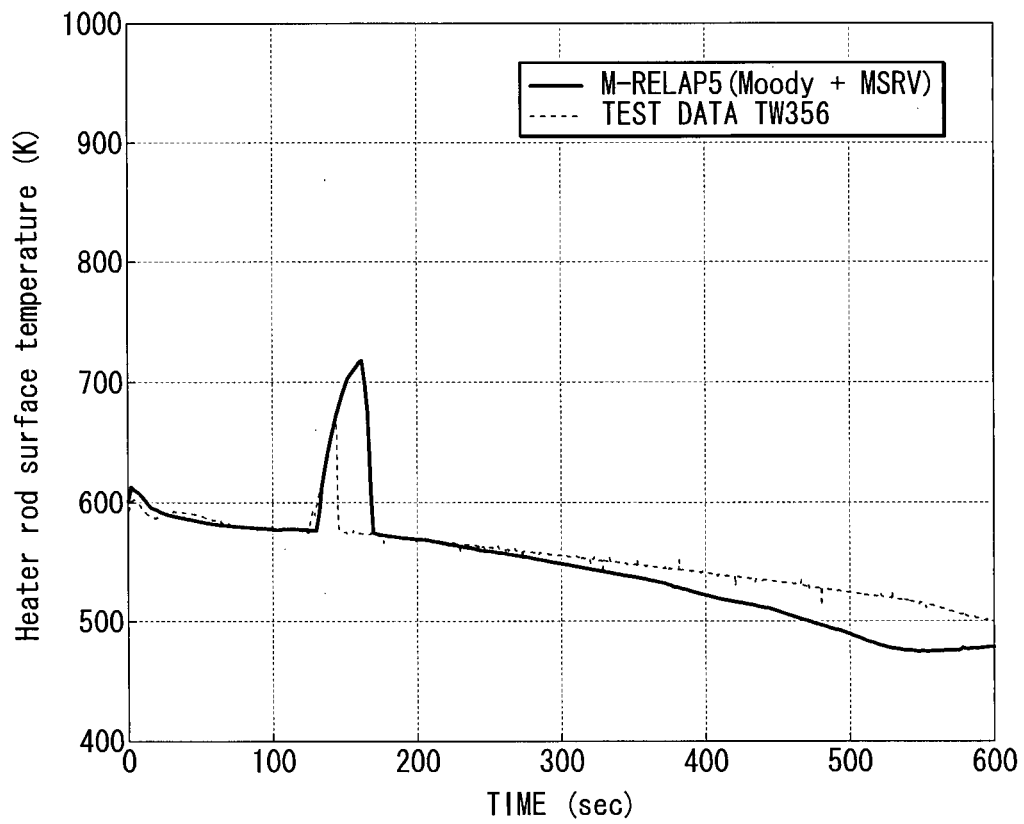


Figure 8.2.1-97 Heater Rod Surface Temperature at 1.02m (M) and 1.11m (P) (Calculation with Simulated Secondary System and Break Flow Behavior)

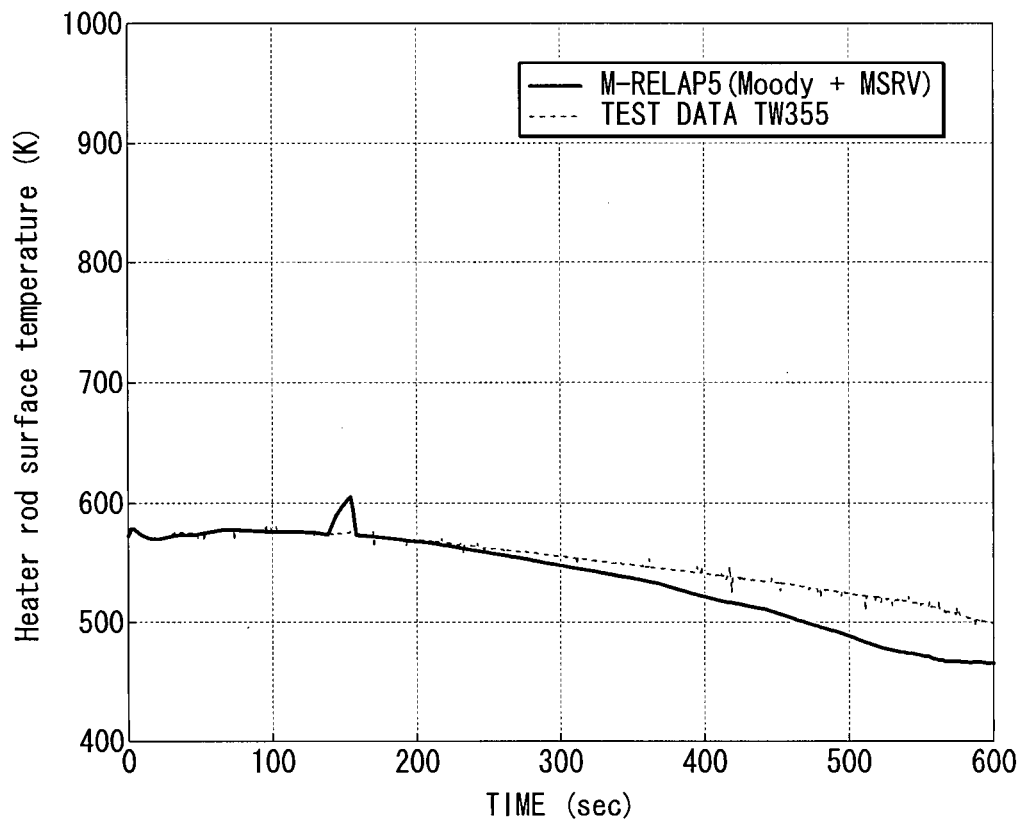


Figure 8.2.1-98 Heater Rod Surface Temperature at 0.05m (M) and 0.07m (P) (Calculation with Simulated Secondary System and Break Flow Behavior)

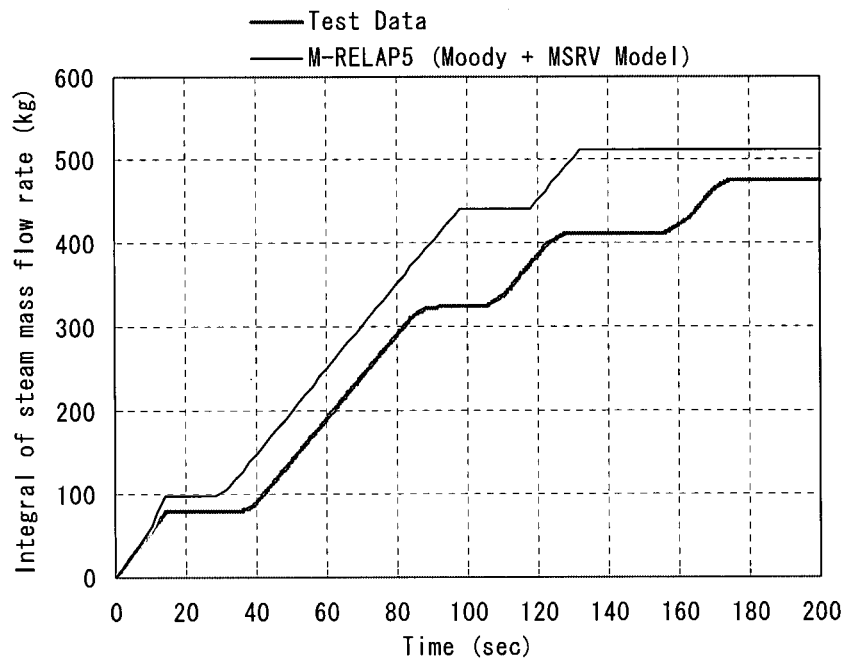


Figure 8.2.1-99 Integral of Vapor Mass Released from SGs (Calculation with Simulated Secondary System and Break Flow Behavior)

8.2.2 ROSA/LSTF small break (10%) LOCA test (SB-CL-09)

8.2.2.1 Introduction

The purpose of the calculation of ROSA-IV/LSTF test SB-CL-09 is to validate the ability of the M-RELAP5 code to predict the following phenomena ranked of high importance in the small break LOCA PIRT: core dryout, post-CHF heat transfer, rewet, core mixture level, water hold up in SG primary side, condensation drainage to inlet plenum, SG primary and secondary heat transfer, water level in SG outlet piping, loop seal formation and clearance, and downcomer mixture level. A primary difference from test SB-CL-18 is that the postulated break size is larger in the present test.

8.2.2.2 Selection of SB-CL-09

The ROSA-IV/LSTF SBLOCA tests simulated breaks between 0.5% and 10% in size. Test SB-CL-09 (10% break) was selected for analysis because it is the largest break size in the ROSA SB test series. A 10% break in ROSA-IV/LSTF is equivalent to about a 10.5 inch break in the US-APWR.

8.2.2.3 Test Condition

(a) Test Facility

The description of the test facility is provided in section 8.2.1.3(a).

(b) Test Procedure

The major initial conditions of the LSTF 10% cold leg break test, Run SB-CL-09, are shown in Table 8.2.2-1. Both the initial steady state conditions and the test procedures were designed to minimize the effects of LSTF scaling compromises on the transients during the test.

The most important design scaling compromise is the 10MW maximum core power limitation, 14% of the scaled reference PWR rated power. The steady-state condition is restricted to a core mass flow rate that is 14% of the scaled value to simulate the reference PWR temperature distribution in the primary loop. The desired primary coolant flow rate was established by reducing the pump speed with the flow control valves (FCVs) in the cross-over legs fully open.

The primary loop flow rate was then increased at the time of break to improve the similarity of the LSTF to the reference PWR by increasing the pump speed.

The initial primary-to-secondary heat transfer must also be maintained at 10MW, i.e., 14% of the scaled value. Since the LSTF steam generators (SGs) are geometrically scaled to the reference PWR, the 14% primary-to-secondary heat transfer rate is established by raising the secondary temperature such that the primary pressure and temperature are representative of the reference PWR.

Major operational setpoints and conditions, including emergency core cooling system (ECCS) actuation logic, for this test are summarized in Table 8.2.2-2. After the break occurred at time zero, the primary system depressurizes quickly. At a pressurizer pressure of 12.97MPa, the reactor scrams. Loss of offsite power concurrent with the reactor scram is assumed and the primary coolant pumps are tripped to begin coastdown and the core power begins to decrease along the pre-programmed decay curve. The power decay curve used in the test takes into account the fission products and actinides decay powers and delayed neutron fission power, and gives a slower decrease than the ANS standard. The core power decay curve used in the test is tabulated in Table 8.2.2-3. The SG auxiliary feed water is assumed to fail to simplify the transient.

At a pressurizer pressure of 12.27 MPa, the safety injection signal is sent that trips ECCS to be actuated at respective pressure setpoints. However, the high pressure charging system and high pressure injection system (HPIS) are assumed to fail in the test. The ECCS conditions are summarized in Table 8.2.2-4. The accumulator (ACC) system and the low pressure injection system (LPIS) are specified to initiate coolant injection into the primary system at pressures of 4.51 and 1.29 MPa, respectively. The accumulator-cold (ACC-Cold) system simulates ACC injection flow to the cold leg A and the accumulator-hot (ACC-Hot) system simulates ACC injection flow to the cold leg B. The water temperatures of ACC-Cold and ACC-Hot tanks are the same and the ratio of ACC injection flow rate to cold leg A and cold leg B is 3:1. This injection method is adopted for good simulation of ACC injection flow rate to each cold leg in the LSTF.

The break point was located in the B-loop (loop without a pressurizer) cold leg between the reactor coolant pump and the reactor pressure vessel. The break orientation was horizontal. The break assembly and break orifice are shown schematically in Figure 8.2.2-1 and 8.2.2-2, respectively.

(c) Test Results

The chronology of events for Run SB-CL-09 is shown in Table 8.2.2-5.

The experiment was initiated by opening the break valve at time zero. The reactor scram signal was sent at a pressurizer pressure of 12.97 MPa and this signal closed the turbine throttle valve. The turbine bypass system was inactive due to the assumption of loss-of-offsite power occurring concurrently with scram. The loss of offsite power terminated the main feedwater, and also tripped the reactor coolant pumps to initiate coastdown.

The safety injection signal was sent at a pressurizer pressure of 12.27 MPa. However, the high pressure charging and high pressure safety injection systems were not activated because of the failure assumptions.

The secondary pressure increased after the closure of the turbine throttle valve, but was maintained at approximately 8 MPa due to the SG relief valve operation. Auxiliary feedwater was not supplied to either steam generator as specified. Both hot legs saturated shortly after the break and the two-phase circulation started. After the termination of the two-phase circulation, the upflow-side and downflow-side SG U-tubes started to drain. Thereafter, the downflow side of the crossover leg emptied and the loop seal clearing occurred in both loops. After the loop seal clearing, steam generated in the core reached the cold leg via the SG U-tubes and exited through the break. Between the onset of U-tube draining and loop seal clearing, the upflow-side of the SG U-tubes drained slower than the downflow-side of the SG U-tubes, which elevated the hot-leg pressure compared to the cold leg pressure. Thus, the elevated pressure in the hot leg depressed the core liquid level lower than the elevation of the bottom of the loop seal. This core liquid level depression caused an excursion of heater rod temperatures. After the loop seal clearing, the core liquid level recovered, however it was not complete and the core was still partially uncovered since some liquid remained in the upflow-side SG U-tubes, the SG inlet plenum, and the bending portion between the SG inlet plenum and the hot leg. Therefore, the heater rod temperature continued to increase. Finally, the system to protect the heater rods from physical damage automatically tripped off the power supply for the heater rods. After the power trip-off, the core liquid level increased and the heater rods were rewetted.

8.2.2.4 M-RELAP5 Calculation Procedure

(a) M-RELAP5 Model of the LSTF

The M-RELAP5 model of the LSTF is described in the section 8.2.1.4. The break flow and the main steam isolation valve are explicitly simulated in this calculation. The modifications described in section 8.2.1.9 are adopted. [

]

(b) Calculation ConditionsInitial conditions:

Table 8.2.2-1 summarizes initial conditions before the break opens. A 2000-second steady-state simulation was performed. At the end of this 2000-second simulation, predicted and measured flow parameters were compared. These comparisons show reasonably good agreement.

Boundary conditions:

Time-dependent tables, which were constructed from experimental data, were used to represent the core power (Figure 8.2.2-3) and pump coastdown (Figure 8.2.2-4 and 8.2.2-5) curves.

The break flow is explicitly simulated by using the Moody critical flow model with the atmospheric outer boundary condition. [

]

The secondary system pressure behavior is also explicitly simulated by modeling the main steam isolation and steam relief valves with the imposed boundary condition for the feedwater flow following the reactor trip.

Assumptions for analysis:

[

1

8.2.2.5 M-RELAP5 Calculation Result

The comparisons between test data and M-RELAP5 results are shown in Figure 8.2.2-6 through 33.

Figure 8.2.2-6 shows the primary pressure transient. The M-RELAP5 prediction agrees with test data until 75 seconds, and after 75 seconds, the depressurization is faster in the M-RELAP5 prediction.

Figures 8.2.2-7 and 8 show the secondary pressure transients of A-loop and B-loop, respectively. The M-RELAP5 prediction agrees reasonably well with the test data.

Figure 8.2.2-9 shows the break flow rate. The break flow is calculated by the same critical flow model used in the US-APWR licensing calculation, which is described in the section 7.1.6. Overall, M-RELAP5 provides a reasonable prediction of the break flow rate until the initiation of the accumulator flow at 160 seconds. Taking account of the faster depressurization in the M-RELAP5 calculation after 75 seconds, the calculated mass flow is expected to be higher than the actual value. Based on the adjustments to the measured break flow in the Base Case for test SB-CL-18 (5% break), the mass actually discharged from the RCS during the two-phase or single-phase vapor regimes is also considered to be less than the measured break flow rate. M-RELAP5 over-predicts the break flow rate after 160 seconds, since the accumulators start injecting safety coolant earlier in the calculation.

Figure 8.2.2-10 shows the core differential pressure transient. M-RELAP5 underestimates the core differential pressure except for a brief part of the loop seal phase. M-RELAP5 does not calculate the rapid core recovery after the trip-off of core power at 111 s because the M-RELAP5 heat transfer model is conservative in evaluating the quench behavior and vaporization of liquid in the core continues for more than 100 seconds after the trip in the M-RELAP5 calculation. On the other hand, heater rods rewet and quench before the core power trip at lower elevations and within about 40 seconds after the core power trip at higher elevations in the test (See Figures 8.2.2-25 to 33). The predictability of the residual liquid in the loops or the upper head described in Section 8.2.1.8 also may affect the prediction of the core differential pressure during this phase.

Figures 8.2.2-11 and 12 show the SG inlet plenum differential pressure transients of loop-A and loop-B, respectively. M-RELAP5 predicts the SG inlet plenum differential pressure reasonably well until 150 seconds.

Figures 8.2.2-13 and 14 show the SG U-tube uphill side differential pressure transients of loop-A and loop-B, respectively. M-RELAP5 predicts the SG U-tube uphill side differential pressure reasonably well.

Figures 8.2.2-15 and 16 show the SG U-tube downhill side differential pressure transients of loop-A and loop-B, respectively. M-RELAP5 calculates earlier decrease comparison with the test data.

Figures 8.2.2-17 and 18 show the crossover leg downhill side differential pressure transients of loop-A and loop-B, respectively, and Figures 8.2.2-19 and 20 show the crossover leg uphill side differential pressure transients of loop-A and loop-B, respectively. The loop seal clearance is a little earlier in the M-RELAP5 prediction than in the test data. The residual amount of liquid is larger than the test data in the uphill side of the intact loop (loop-A) after loop seal clearance. However, M-RELAP5 excellently predicts the overall behavior of loop seal clearance in this experiment.

Figure 8.2.2-21 shows the downcomer differential pressure. M-RELAP5 overestimates until 100 seconds, and then slightly under-predicts until 160 seconds. After 160 seconds, accumulator injection starts in the prediction, and M-RELAP5 again over-predicts. However,

the overall response in the downcomer liquid level predicted by M-RELAP5 agrees reasonably well with the measurement.

Figure 8.2.2-22 shows the upper plenum differential pressure. The differential pressure increases after the core is completely quenched in both the test and the calculation. This increase occurs at about 160 s in the test and at about 215 s in the calculation. As will be shown later, M-RELAP5 predicts that the core quenches more slowly than in the test.

Figures 8.2.2-23 and 24 show the accumulator injection flowrate transients. The start of accumulator injection is earlier in the M-RELAP5 because the RCS depressurization after 75 seconds is faster in the M-RELAP5 calculation.

Figures 8.2.2-25 to 33 show the transients of heater rod surface temperature. At the upper elevation of the heater rod, the initiation of heat up is slightly later in the prediction. But, at the other elevations, the initiation of heat-up is conservatively or adequately predicted. The rewet is later at all elevations of the heater rod in the prediction. Except for the upper elevations of the heater rod, the predicted heater rod surface temperatures are much higher than the measured ones because the post-CHF heat transfer model in M-RELAP5 is conservative and the predicted mixture level is lower than the measured one. The predicted and measured peak heater rod surface temperatures are 1423 F and 1215 F, respectively. The predicted peak heater rod surface temperature is much higher than the measured one.

8.2.2.6 Conclusions

M-RELAP5 well predicts the 10% cold leg break transient. The results are similar to those obtained previously for the 5% cold leg break test. The calculated heater rod temperatures are higher than the measurements, demonstrating the ability of M-RELAP5 to predict the PCT conservatively for small break LOCAs with larger break sizes.

8.2.2.7 References

8.2.1-1. Suzuki, M., et al., 2008, "A Study on ROSA/LSTF SB-CL-09 Test Simulating PWR 10% Cold Leg Break LOCA," JAEA-Research 2008-087.

Table 8.2.2-1 Steady-State Parameter Checklist

<u>Parameter</u>	<u>Target</u>	<u>Predicted</u>
Pressurizer pressure (MPa)	15.45	15.48
Hot leg fluid temperature (K)	601 / 600	601 / 601
Cold leg fluid temperature (K)	566 / 565	565 / 565
Core power (MW)	10.0	10.0
Pressurizer water level (m)	2.67	2.67
Primary coolant pump speed (rpm)	769 / 792	769 / 792
SG secondary pressure (MPa)	7.45 / 7.48	7.47 / 7.49
SG secondary liquid level (m)	10.7 / 10.6	10.7 / 10.6
SG feedwater temperature (K)	495.2	495.2
SG feedwater and steam flowrate (kg/s)	2.60 / 2.95	2.73 / 2.79

Table 8.2.2-2 Operational Setpoints for Run SB-CL-09

<u>Event</u>	<u>Setpoint</u>
<u>Reactor scram signal (MPa)</u>	<u>12.97</u>
<u>Initiation of RCP coastdown</u>	<u>With reactor scram</u>
<u>Safety injection signal (MPa)</u>	<u>12.27</u>
<u>High pressure charging</u>	<u>not actuated</u>
<u>Safety injection</u>	<u>not actuated</u>
<u>Accumulator injection (MPa)</u>	<u>4.51</u>
<u>Low pressure injection (MPa)</u>	<u>1.29</u>
<u>Main feedwater termination</u>	<u>With reactor scram</u>
<u>Turbine throttle valve closure</u>	<u>With reactor scram</u>
<u>Auxiliary feedwater initiation</u>	<u>not actuated</u>

Table 8.2.2-3 Core Power Decay Curve

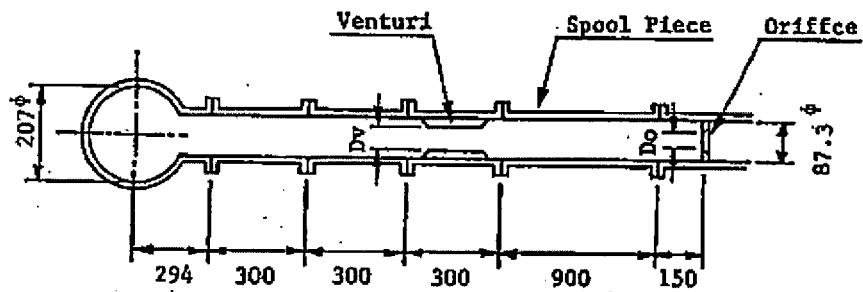
<u>Time</u> <u>s</u>	<u>Power</u> <u>MW</u>	<u>Time</u> <u>s</u>	<u>Power</u> <u>MW</u>
<u>0.000</u>	<u>10.000</u>	<u>100.000</u>	<u>5.200</u>
<u>1.000</u>	<u>10.000</u>	<u>150.000</u>	<u>3.632</u>
<u>2.000</u>	<u>10.000</u>	<u>200.000</u>	<u>2.848</u>
<u>3.000</u>	<u>10.000</u>	<u>400.000</u>	<u>1.776</u>
<u>4.000</u>	<u>10.000</u>	<u>600.000</u>	<u>1.568</u>
<u>5.000</u>	<u>10.000</u>	<u>800.000</u>	<u>1.488</u>
<u>6.000</u>	<u>10.000</u>	<u>1000.000</u>	<u>1.424</u>
<u>7.000</u>	<u>10.000</u>	<u>1500.000</u>	<u>1.280</u>
<u>8.000</u>	<u>10.000</u>	<u>2000.000</u>	<u>1.200</u>
<u>10.000</u>	<u>10.000</u>	<u>4000.000</u>	<u>.992</u>
<u>15.000</u>	<u>10.000</u>	<u>6000.000</u>	<u>.848</u>
<u>20.000</u>	<u>10.000</u>	<u>7980.000</u>	<u>.784</u>
<u>29.000</u>	<u>10.000</u>	<u>10020.000</u>	<u>.784</u>
<u>40.000</u>	<u>8.912</u>	<u>19980.000</u>	<u>.592</u>
<u>60.000</u>	<u>7.344</u>	<u>60000.000</u>	<u>.464</u>
<u>80.000</u>	<u>6.128</u>	<u>100020.000</u>	<u>.368</u>

Table 8.2.2-4 ECCS Conditions for Run SB-CL-09

<u>ECCS</u>	<u>Specification</u>
<u>High pressure charging system</u>	<u>not actuated</u>
<u>Pump shut-off head</u>	
<u>Delay time from SI signal</u>	
<u>Flowrate</u>	
<u>Fluid temperature</u>	
<u>Injection location (ratio)</u>	
<u>High pressure injection system</u>	<u>not actuated</u>
<u>Pump shut-off head</u>	
<u>Delay time from SI signal</u>	
<u>Flowrate</u>	
<u>Fluid temperature</u>	
<u>Injection location (ratio)</u>	
<u>Low pressure injection system</u>	<u>1.29MPa</u> <u>17 s</u> <u>scaled full capacity</u> <u>310 K</u> <u>CLA, CLB (3:1)</u>
<u>Pump shut-off head</u>	
<u>Delay time from SI signal</u>	
<u>Flowrate</u>	
<u>Fluid temperature</u>	
<u>Injection location (ratio)</u>	
<u>Acc system</u>	<u>4.51 MPa</u> <u>320 K</u> <u>CLA, CLB (3:1)</u> <u>5.76 m</u> <u>6.43 m</u> <u>3.38 m</u> <u>5.64 m</u>
<u>Pressure setpoint</u>	
<u>Water temperature</u>	
<u>Injection location (ratio)</u>	
<u>Initial tank level</u>	
<u>to loop-A : ACC-Cold</u>	
<u>to loop-B : ACC-Hot</u>	
<u>Terminal tank level</u>	
<u>to loop-A : ACC-Cold</u>	
<u>to loop-B : ACC-Hot</u>	

Table 8.2.2-5 Transient Results Summary for 10-Percent Cold Leg Side Break

<u>Event</u>	<u>Data</u>	<u>Prediction</u>
<u>Break (s)</u>	<u>0</u>	<u>0</u>
<u>Reactor trip (s)</u>	<u>11</u>	<u>7</u>
<u>Main steam line valve close (s)</u>	<u>11</u>	<u>11</u>
<u>Safety injection signal (s)</u>	<u>11</u>	<u>12</u>
<u>Start of pumps coast down (s)</u>	<u>12</u>	<u>12</u>
<u>SG feedwater stop (s)</u>	<u>15</u>	<u>15</u>
<u>Core power decreased from 10 MW (s)</u>	<u>42</u>	<u>42</u>
<u>Core heat-up started (s)</u>	<u>62</u>	<u>48</u>
<u>Loop-seal clearing (s)</u>	<u>74</u>	<u>72</u>
<u>Core power supply terminated (s)</u>	<u>111</u>	<u>111</u>
<u>Core finally quenched (s)</u>	<u>153</u>	<u>212</u>
<u>Accumulator injection system started (s)</u>	<u>195</u>	<u>158</u>



$$D_v = 64.53\phi$$

$$D_o = 31.9\phi$$

Figure 8.2.2-1 Break Assembly
(From JAEA Research 2008-087)

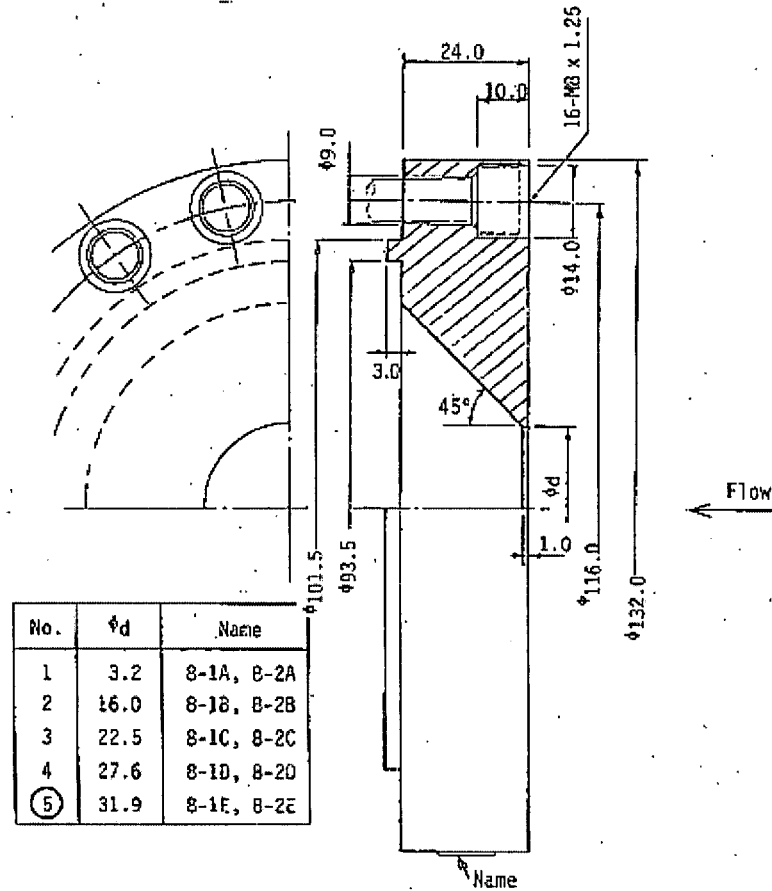


Figure 8.2.2-2 Break Orifice
(From JAEA Research 2008-087)

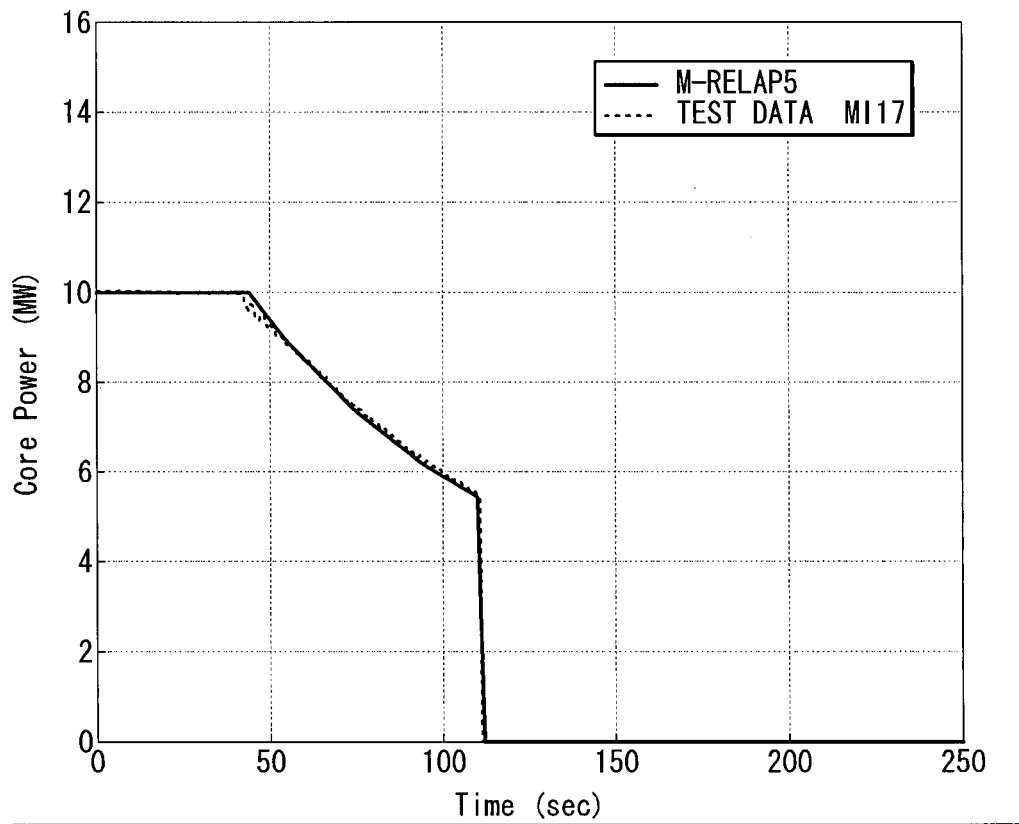


Figure 8.2.2-3 Total Core Power

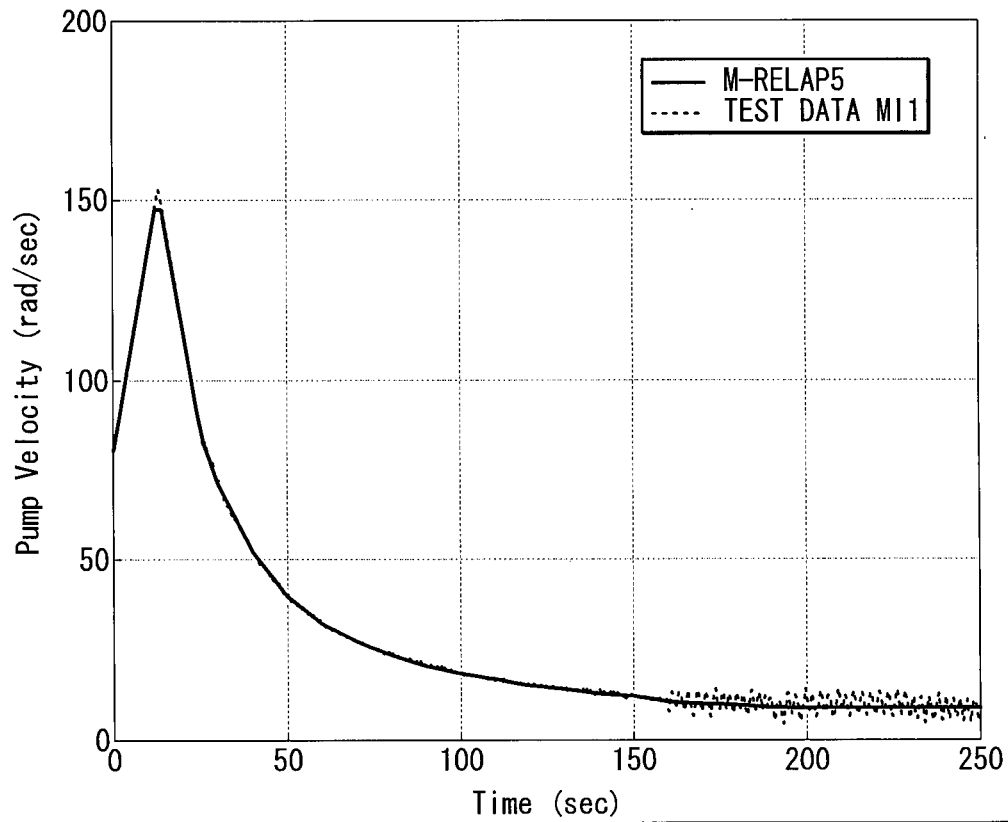


Figure 8.2.2-4 Reactor Coolant Pump in Primary Loop-A Rotation Speed

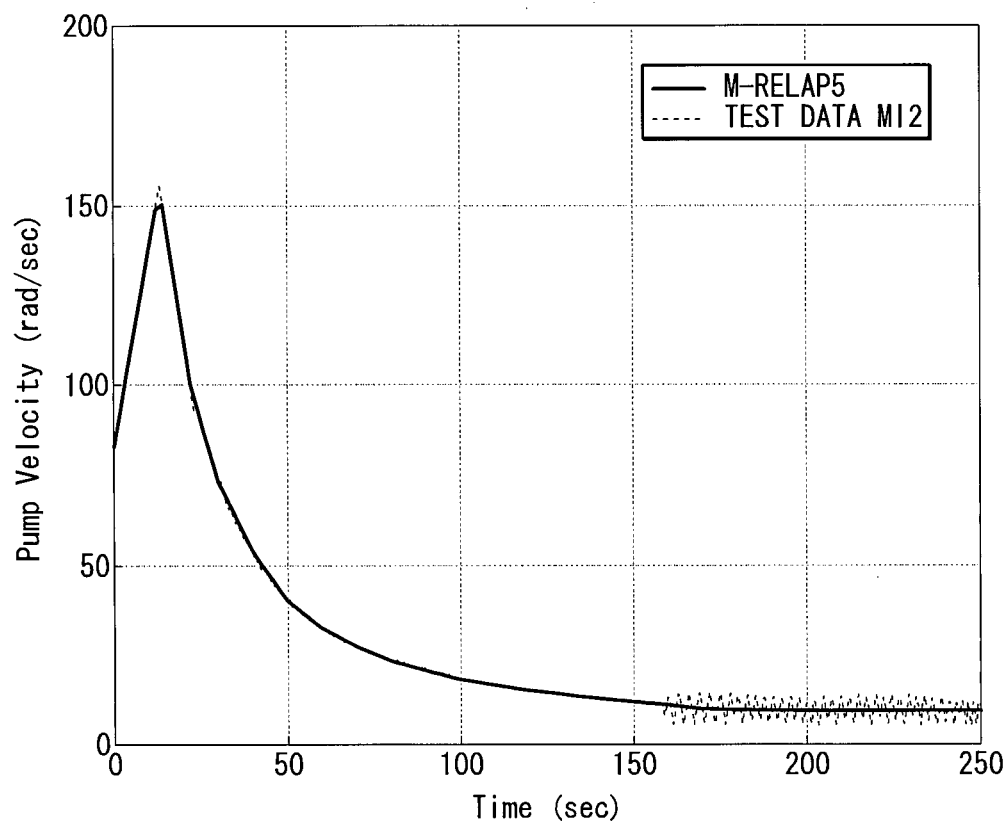


Figure 8.2.2-5 Reactor Coolant Pump in Primary Loop-B Rotation Speed

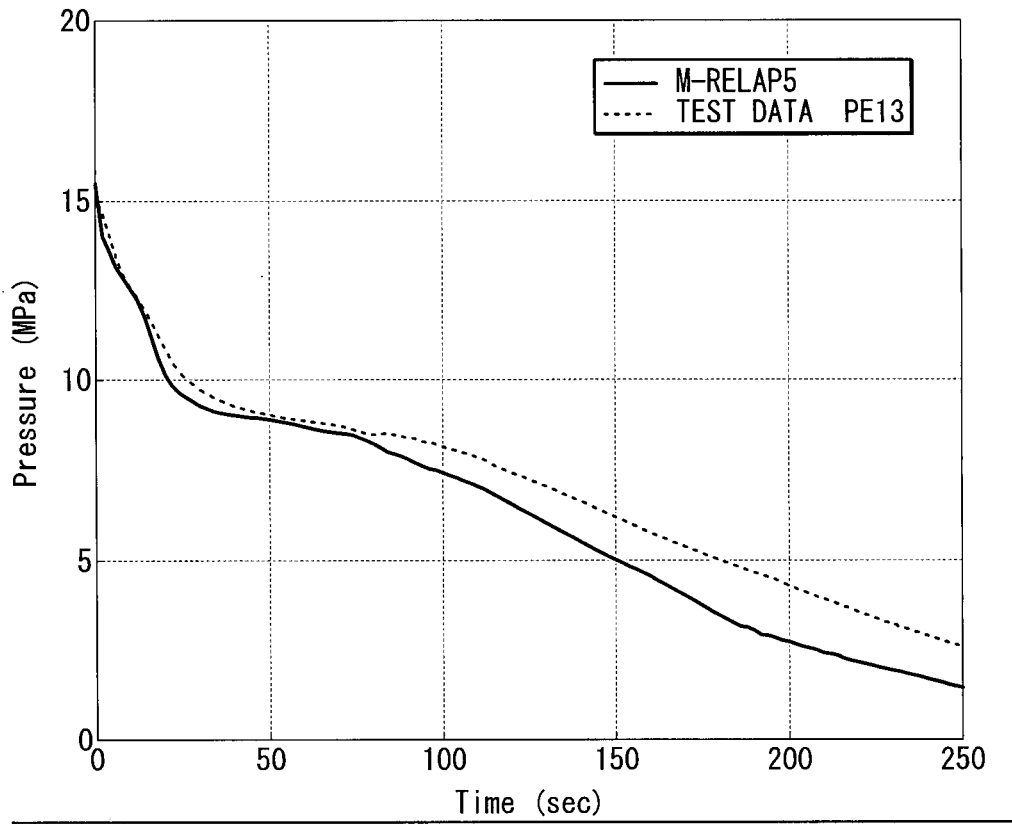


Figure 8.2.2-6 Pressurizer Pressure

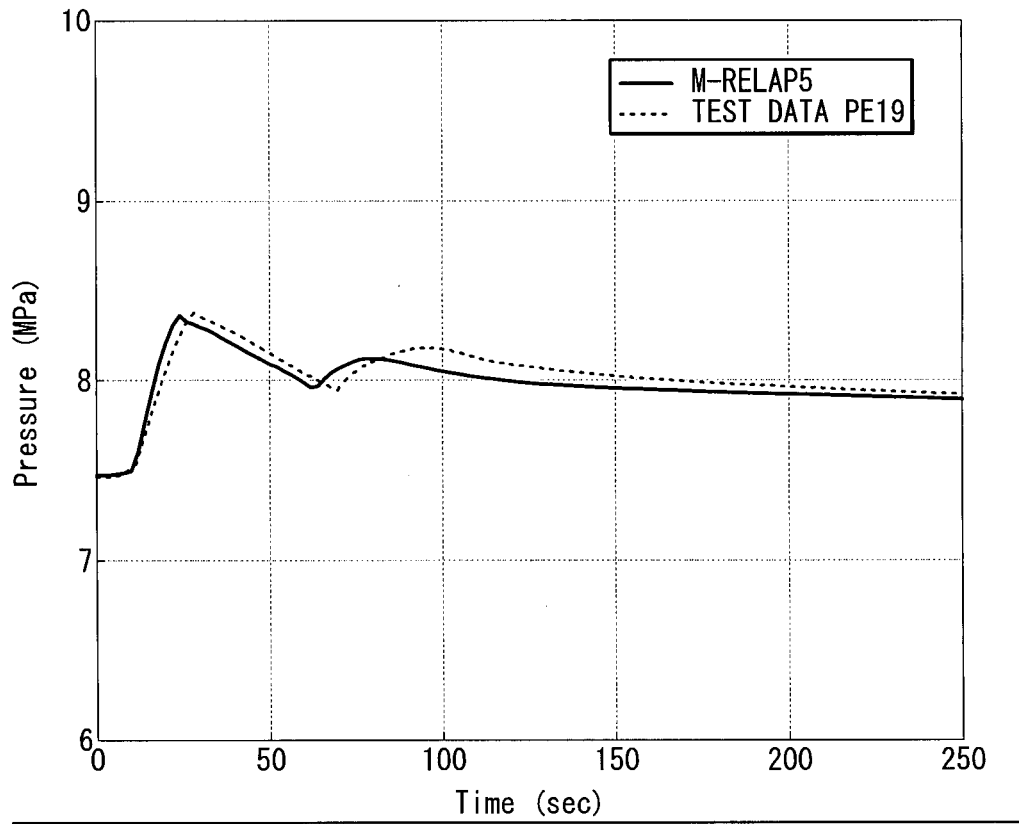


Figure 8.2.2-7 SGA Steam Dome Pressure

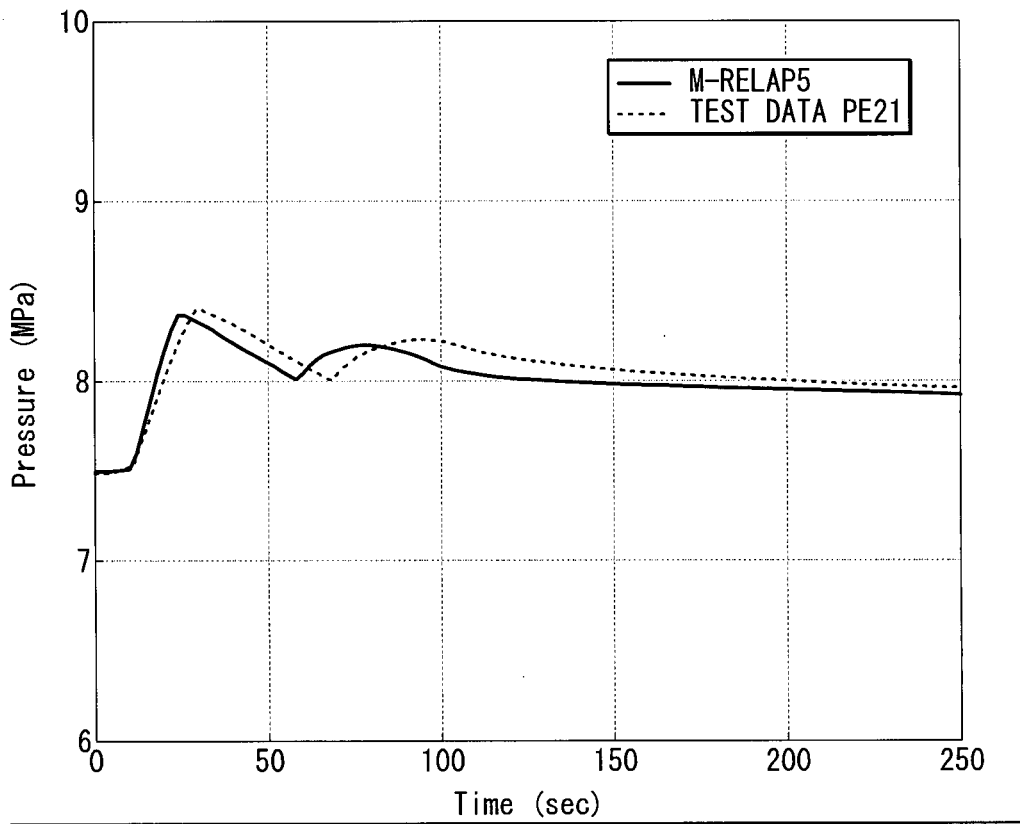


Figure 8.2.2-8 SGB Steam Dome Pressure

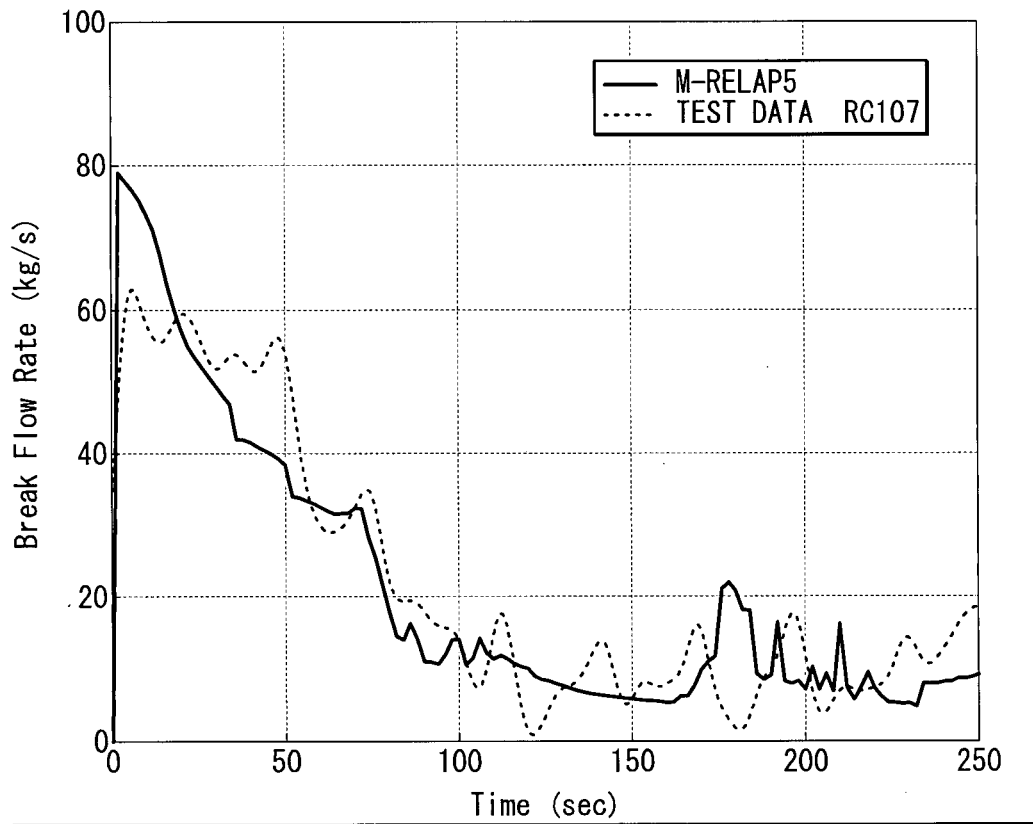


Figure 8.2.2-9 Break Flowrate

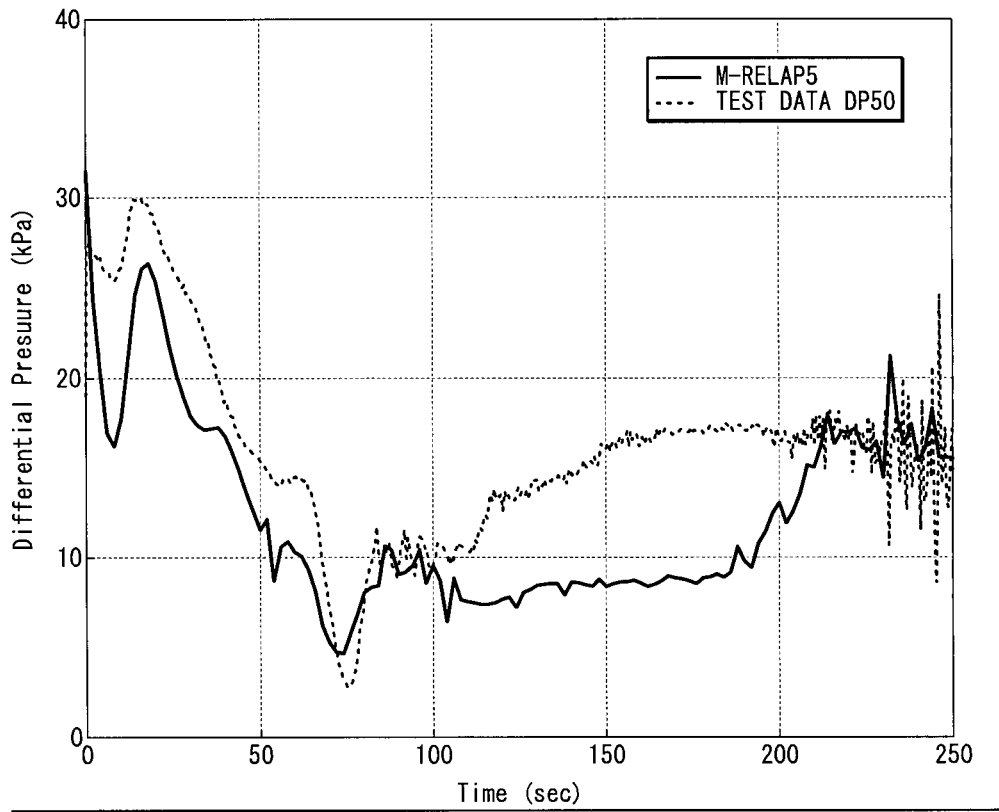


Figure 8.2.2-10 Core Differential Pressure

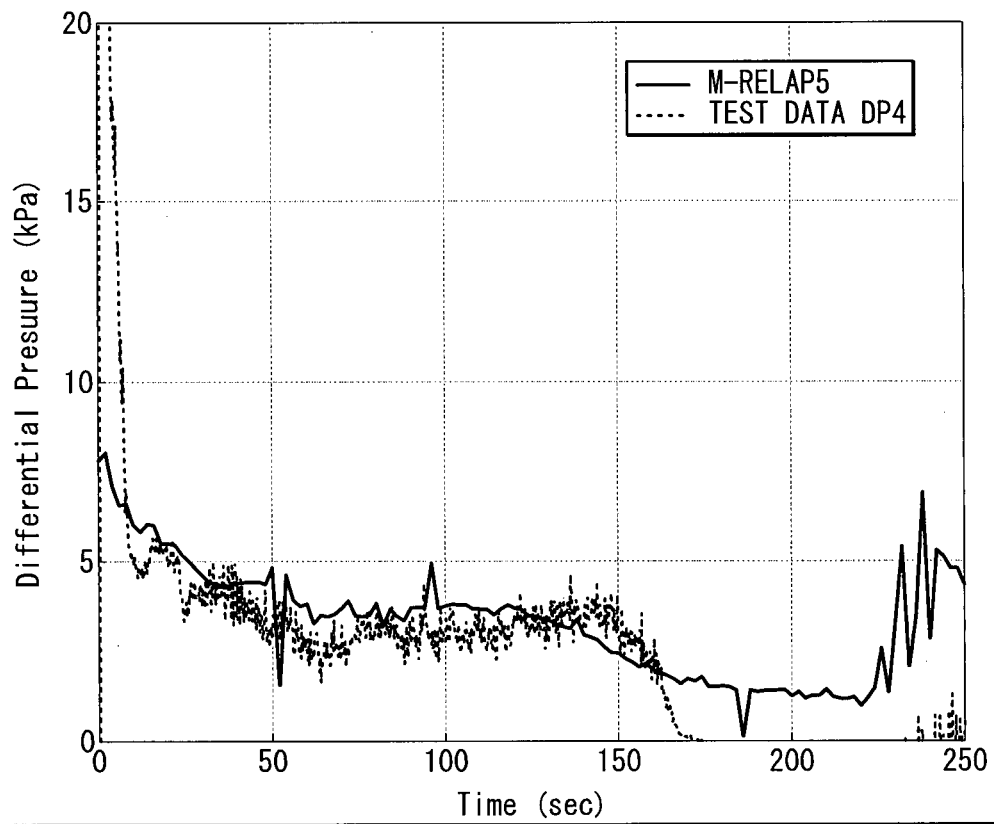


Figure 8.2.2-11 Loop-A SG Inlet Plenum Differential Pressure

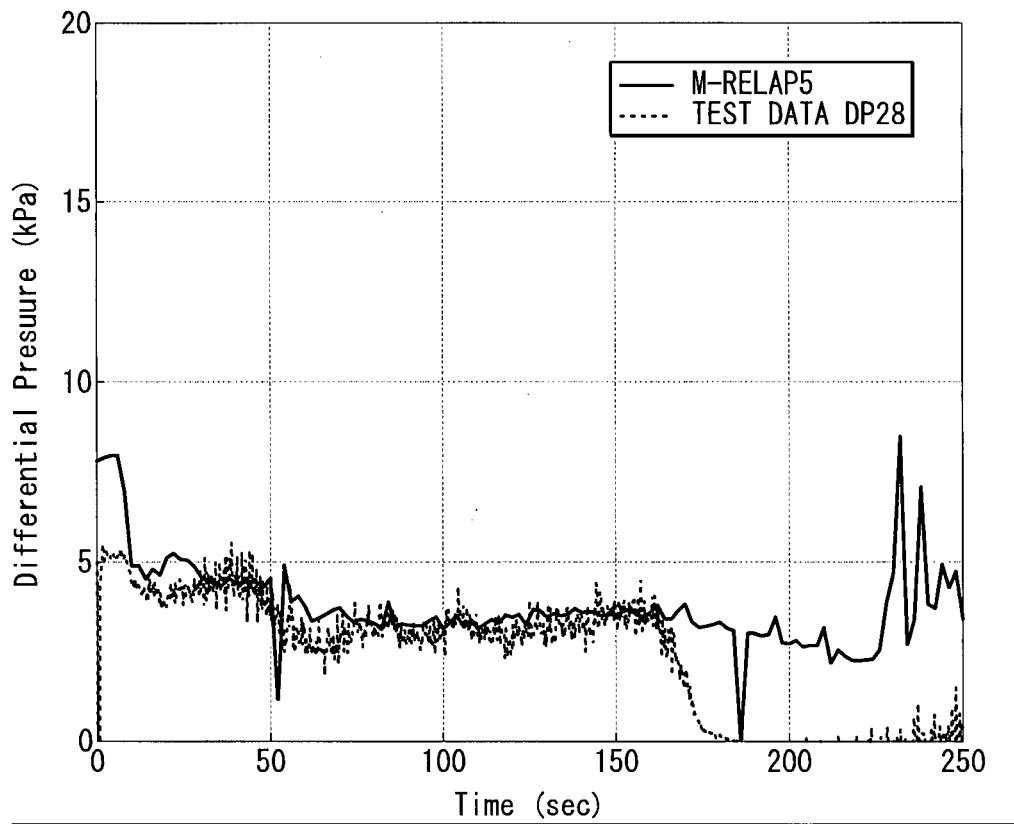


Figure 8.2.2-12 Loop-B SG Inlet Plenum Differential Pressure

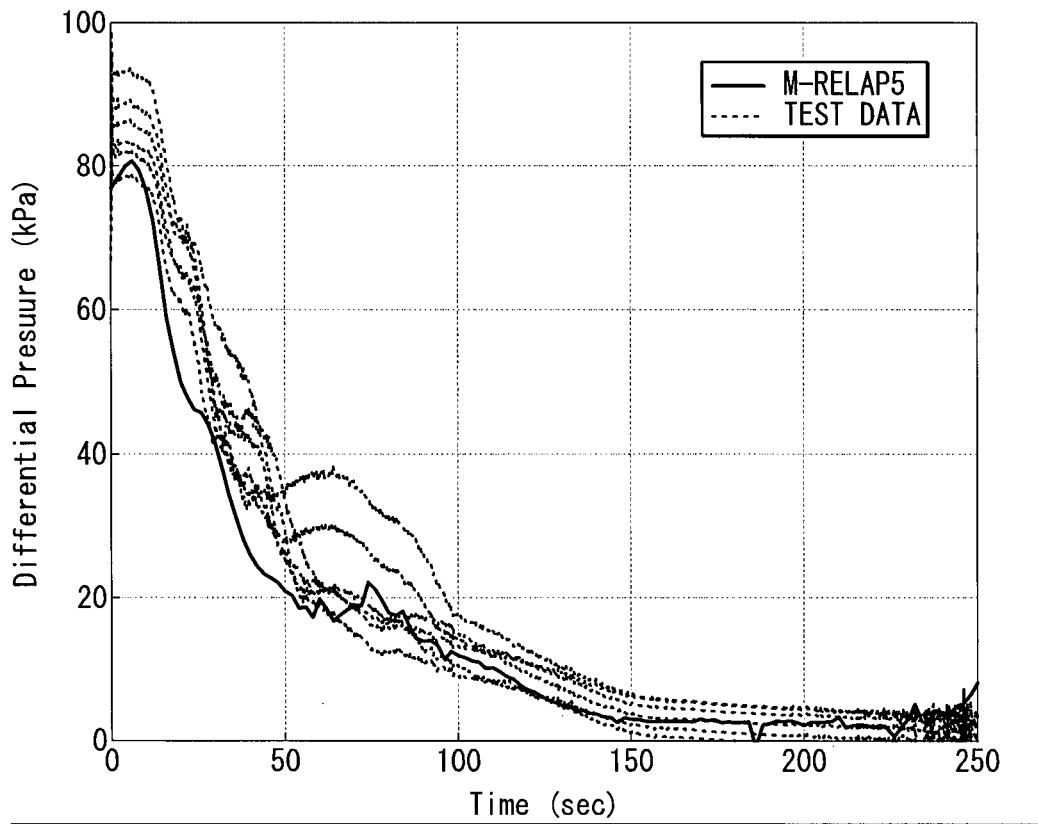


Figure 8.2.2-13 Loop-A SG U-tube Uphill Side Differential Pressure

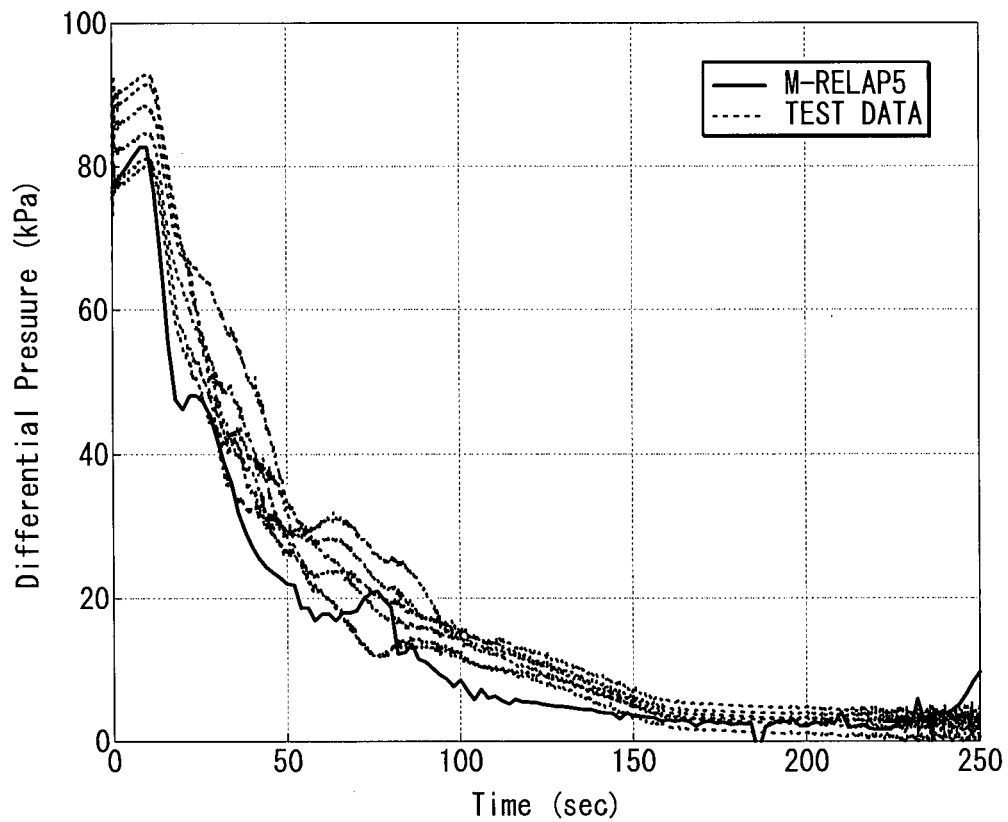


Figure 8.2.2-14 Loop-B SG U-tube Uphill Side Differential Pressure

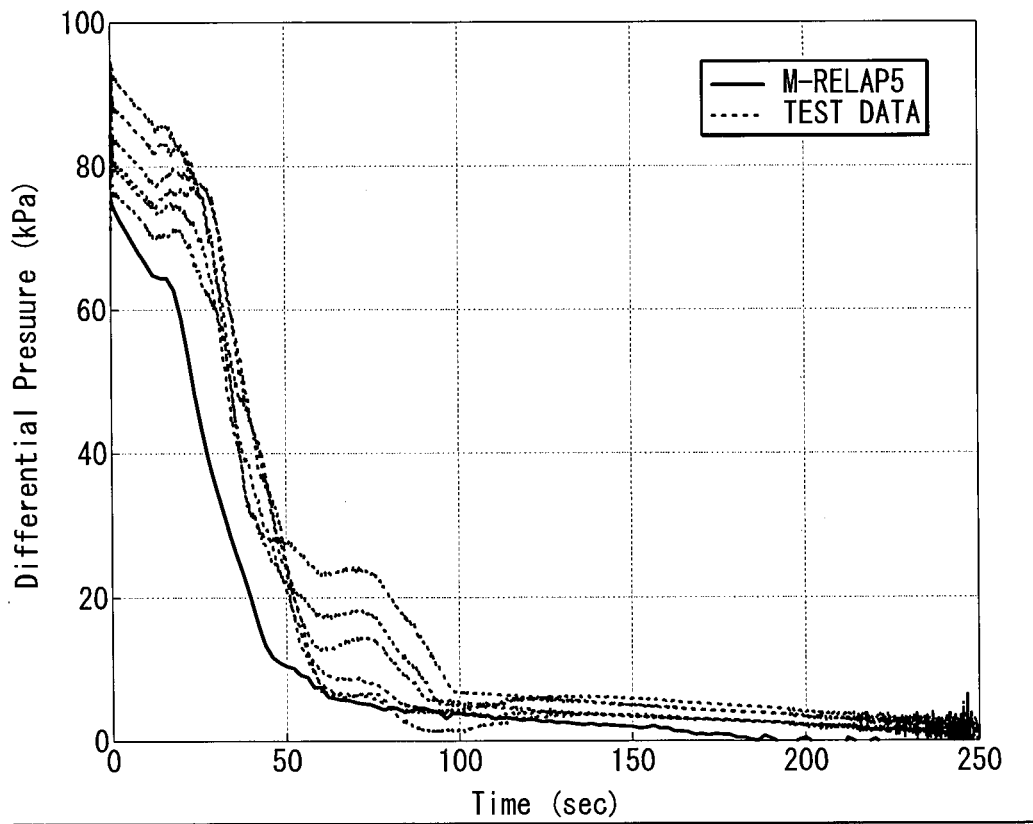


Figure 8.2.2-15 Loop-A SG U-tube Downhill Side Differential Pressure

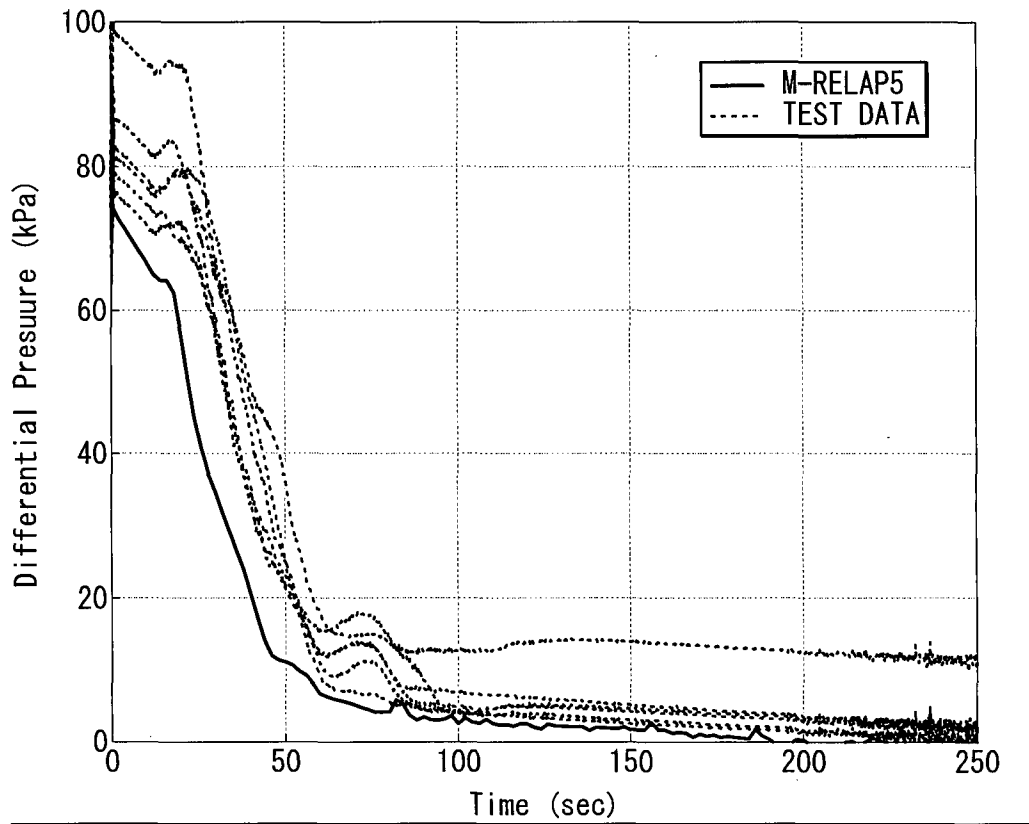


Figure 8.2.2-16 Loop-B SG U-tube Downhill Side Differential Pressure

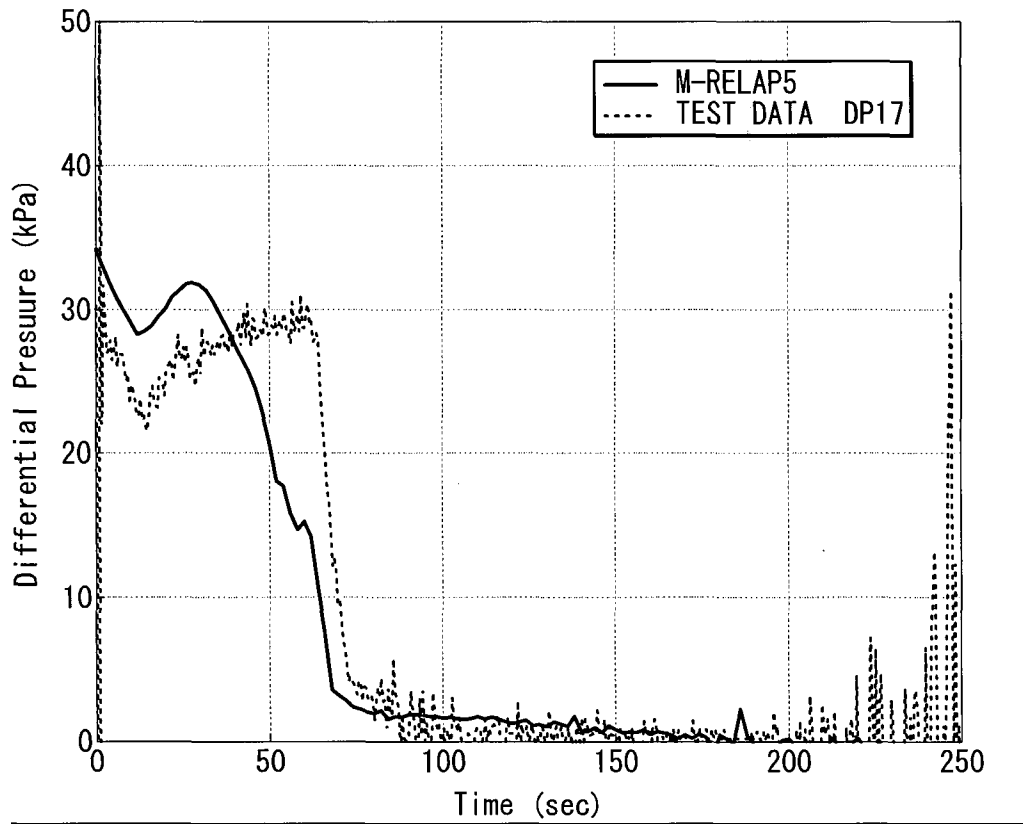


Figure 8.2.2-17 Loop-A Cross-over Leg Downhill Side Differential Pressure

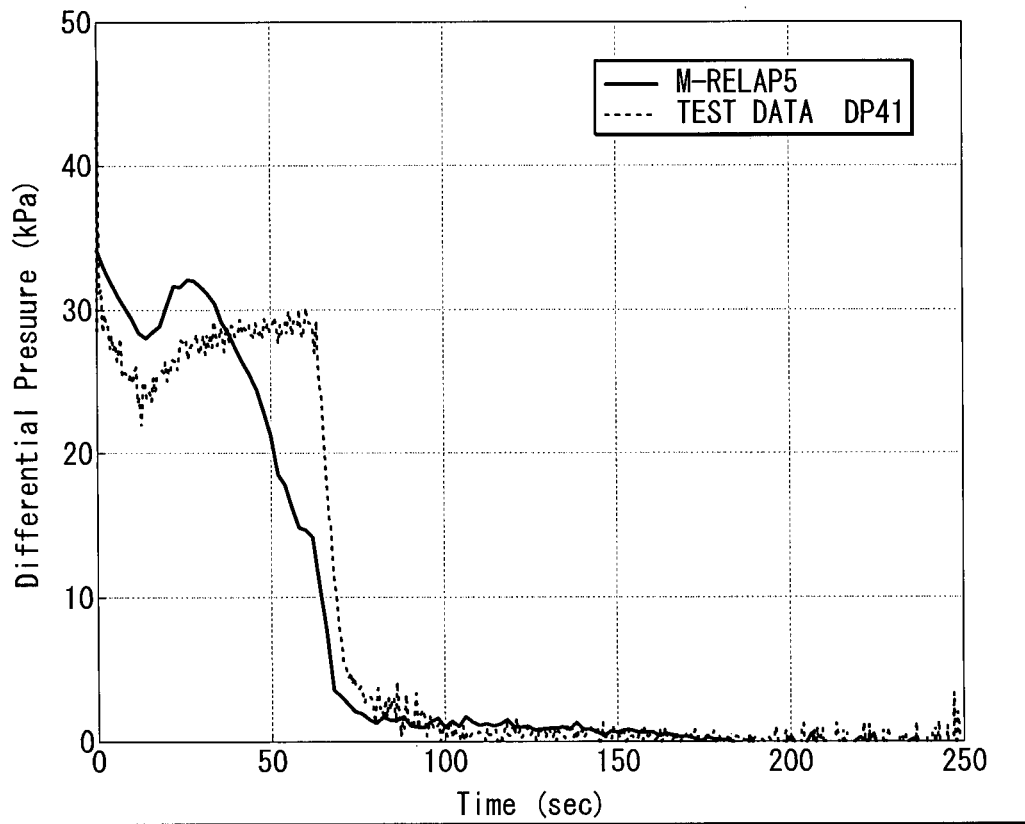


Figure 8.2.2-18 Loop-B Cross-over Leg Downhill Side Differential Pressure

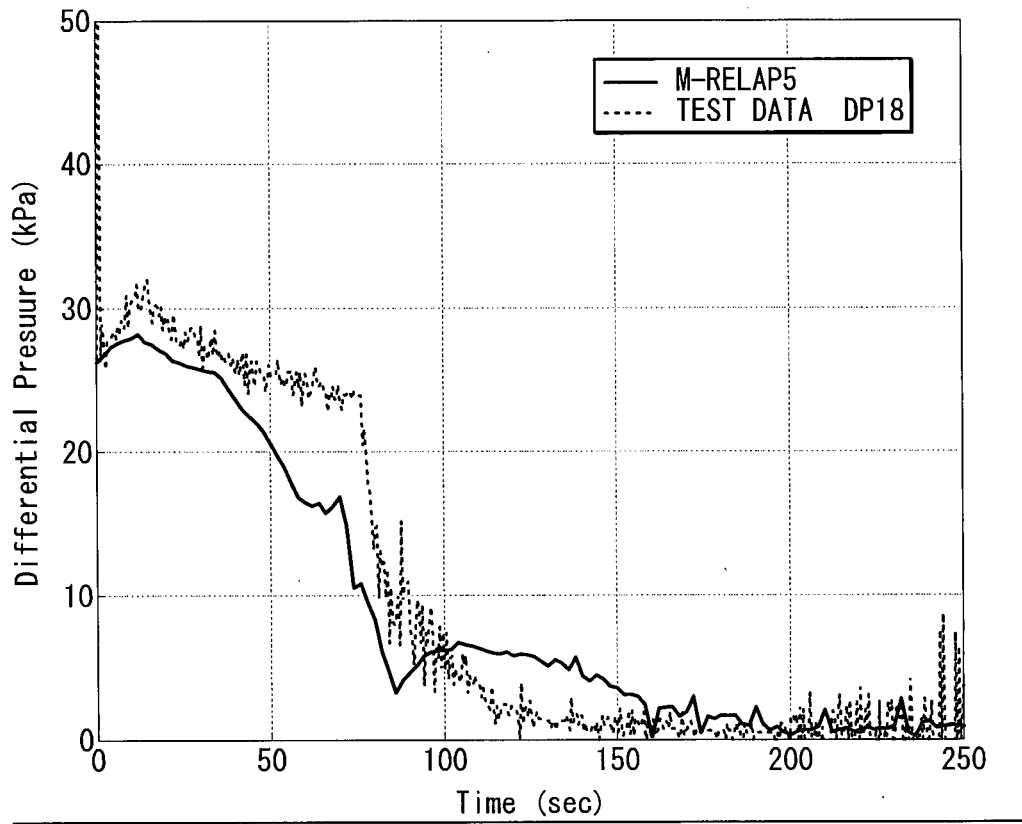


Figure 8.2.2-19 Loop-A Cross-over Leg Uphill Side Differential Pressure

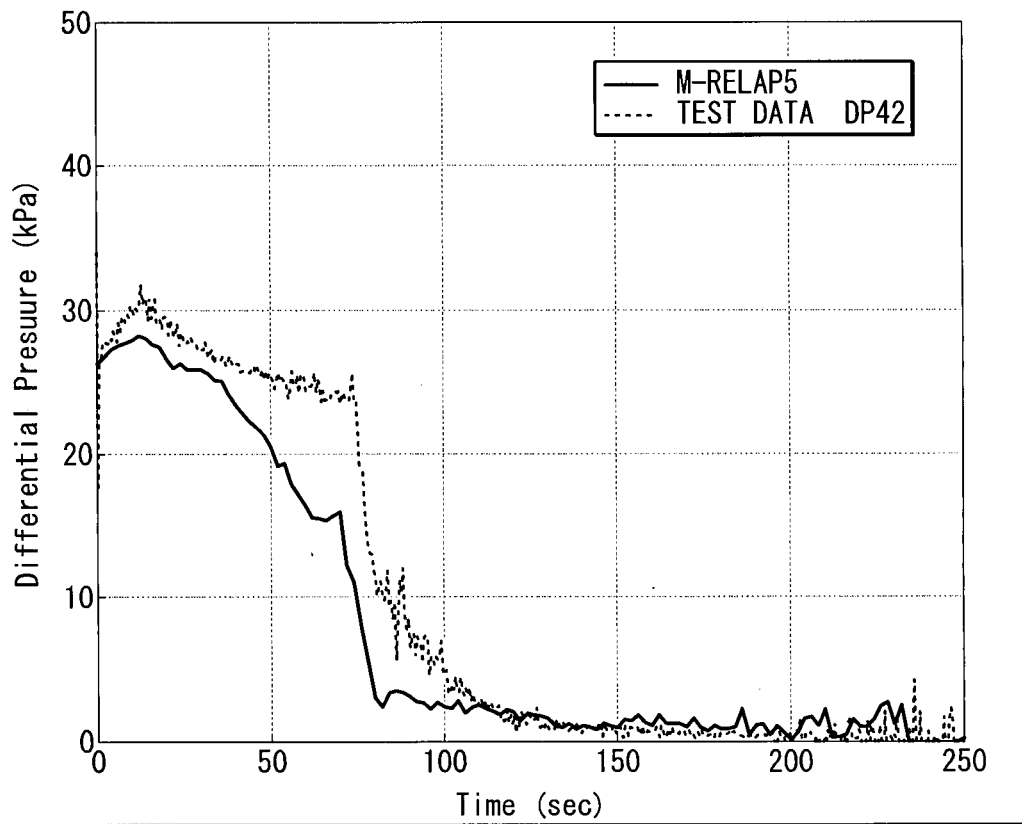


Figure 8.2.2-20 Loop-B Cross-over Leg Uphill Side Differential Pressure

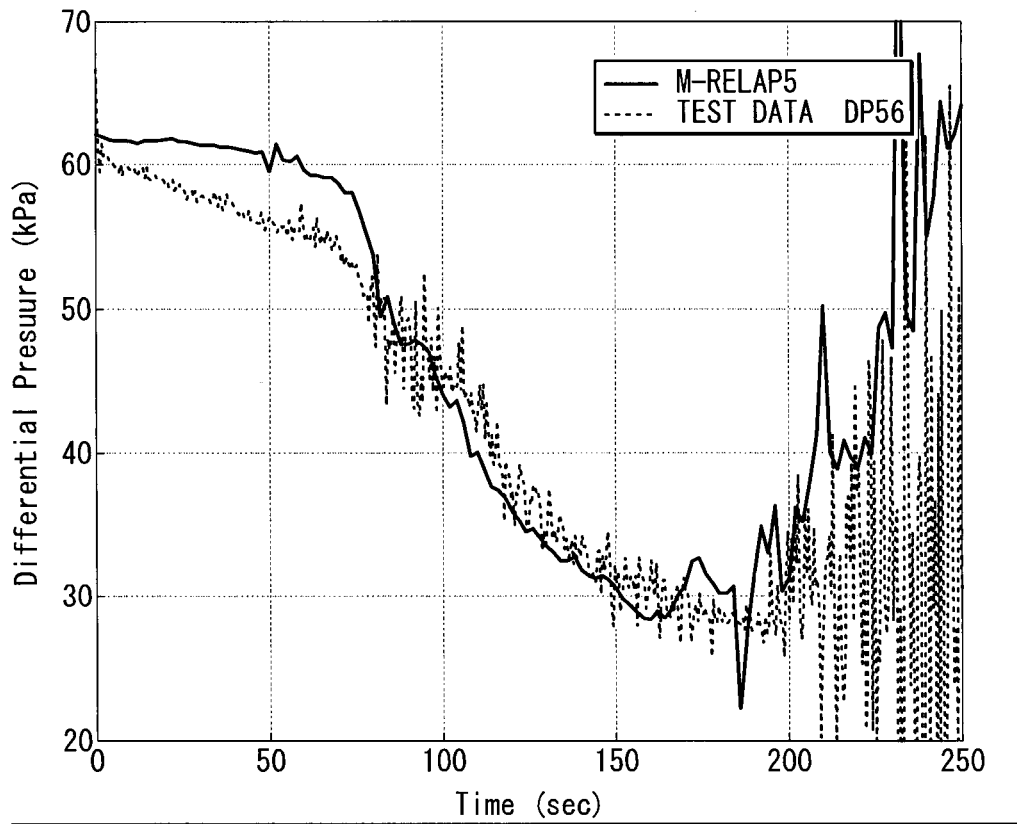


Figure 8.2.2-21 Downcomer Differential Pressure

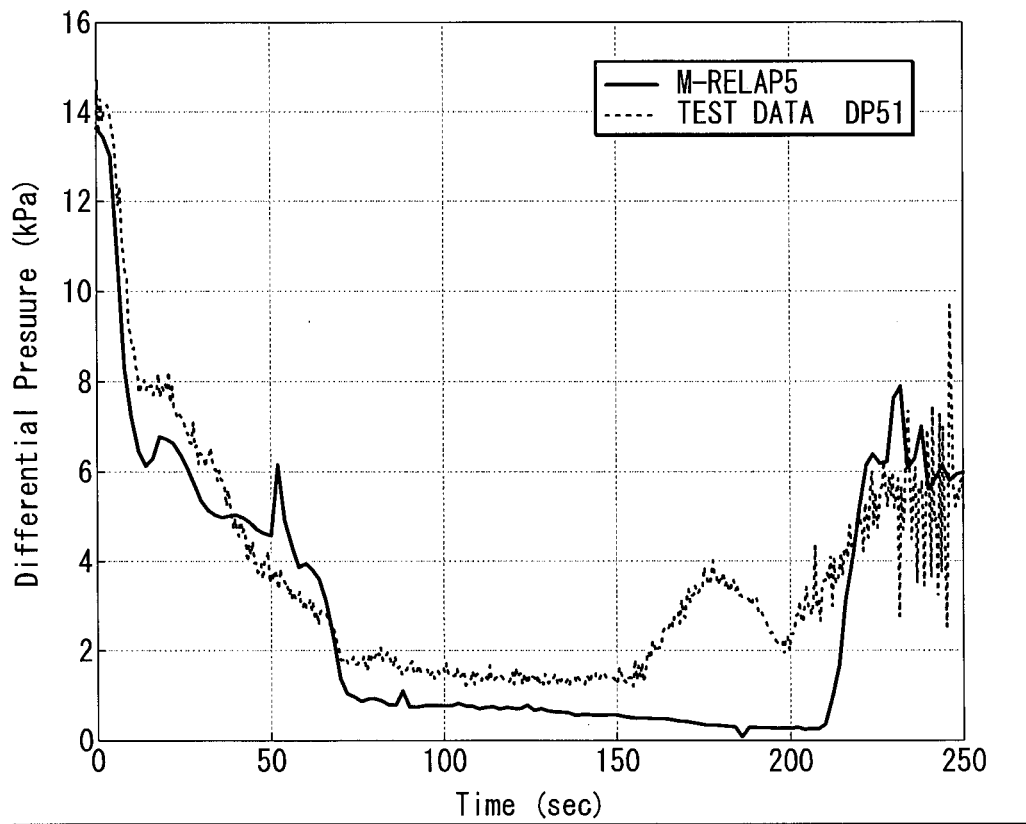


Figure 8.2.2-22 Upper Plenum Differential Pressure

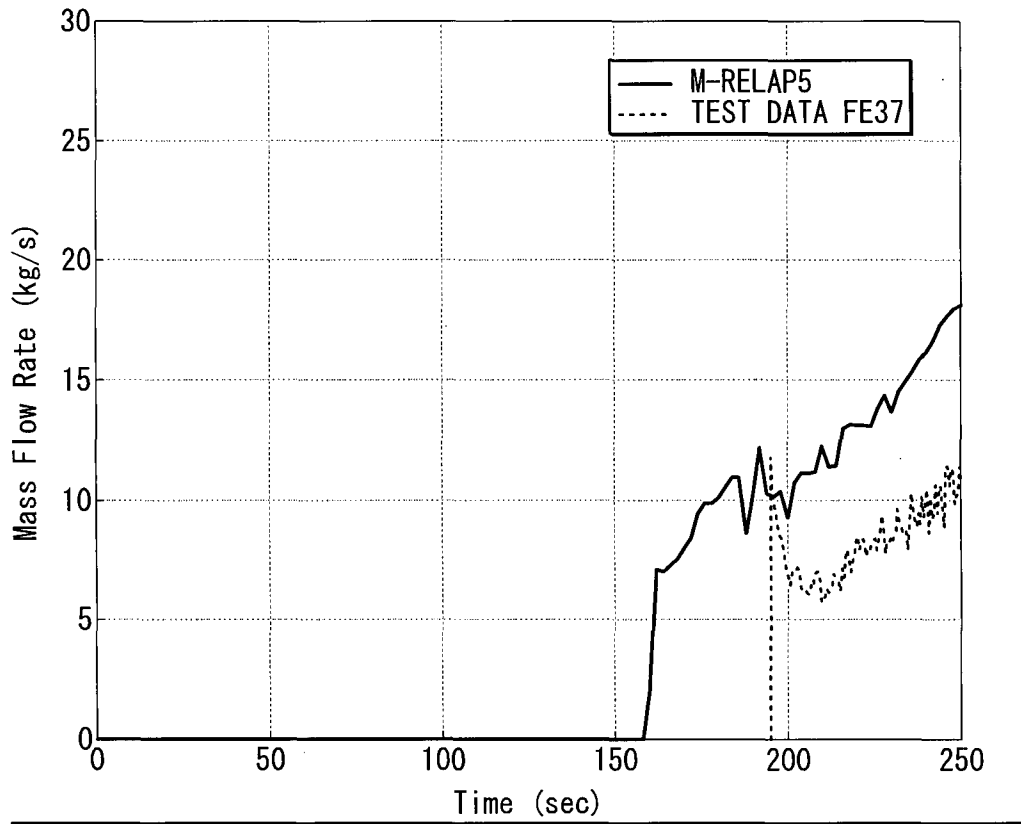


Figure 8.2.2-23 Loop-A Accumulator Injection Flowrate

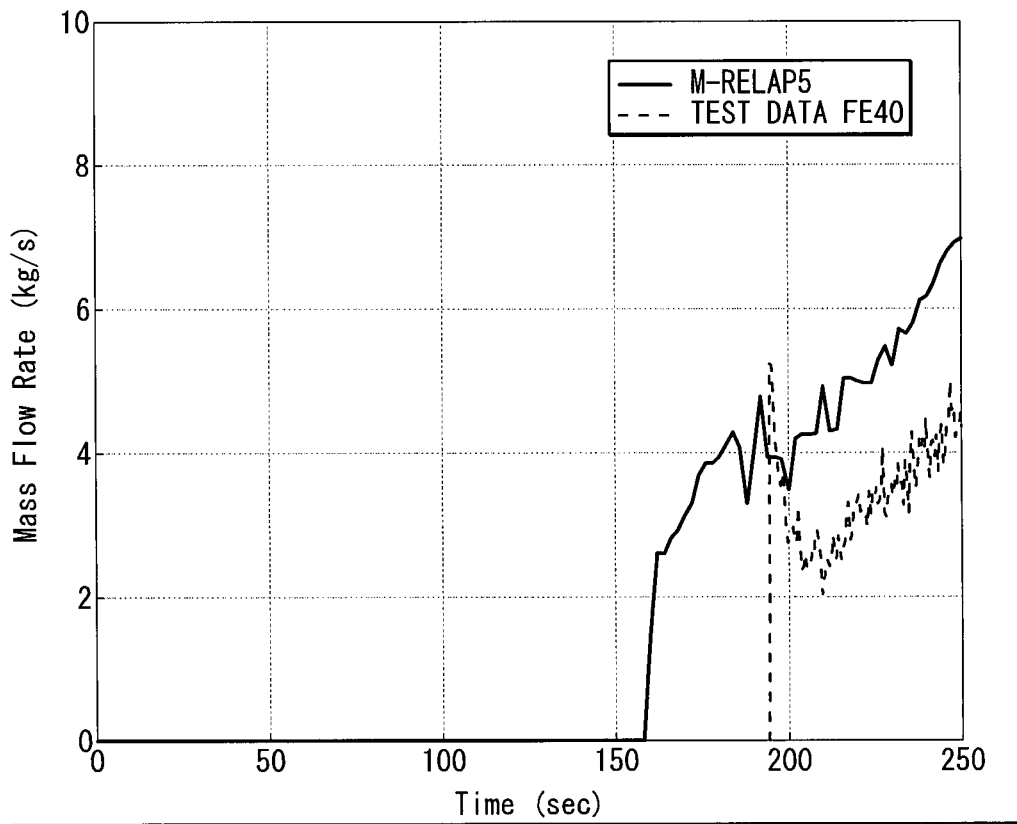


Figure 8.2.2-24 Loop-B Accumulator Injection Flowrate

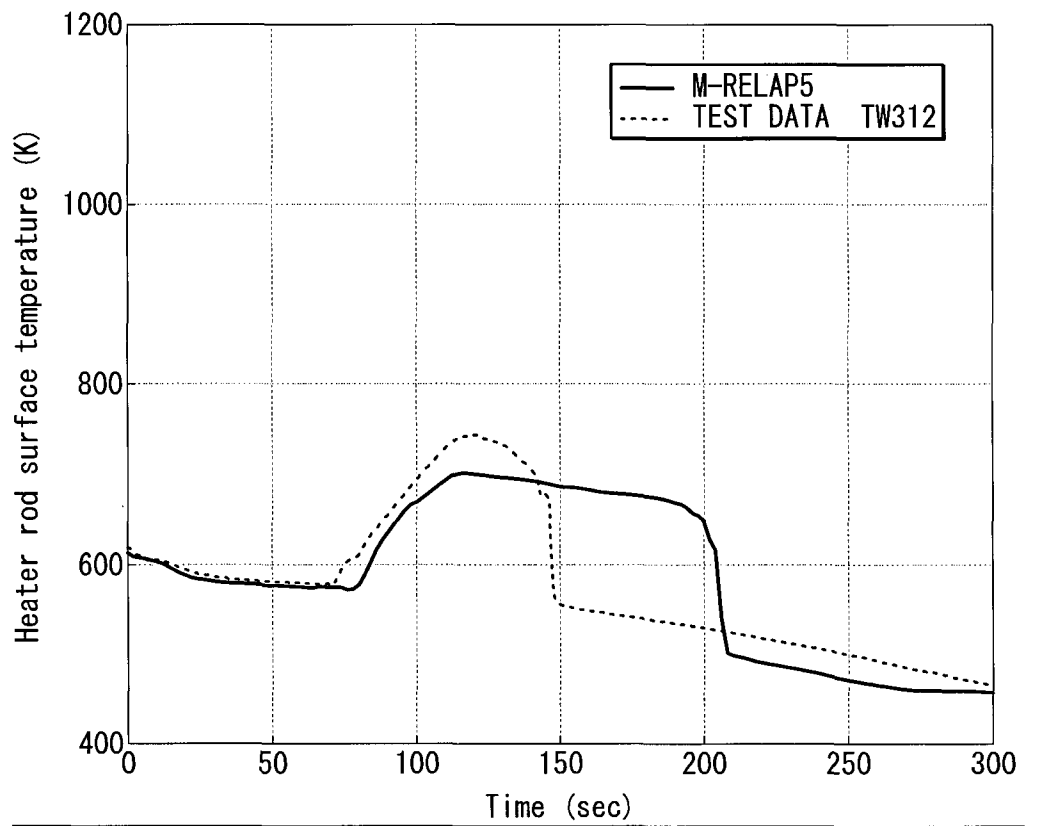


Figure 8.2.2-25 Heater Rod Surface Temperature at 3.61m (M) and at 3.57m (P)

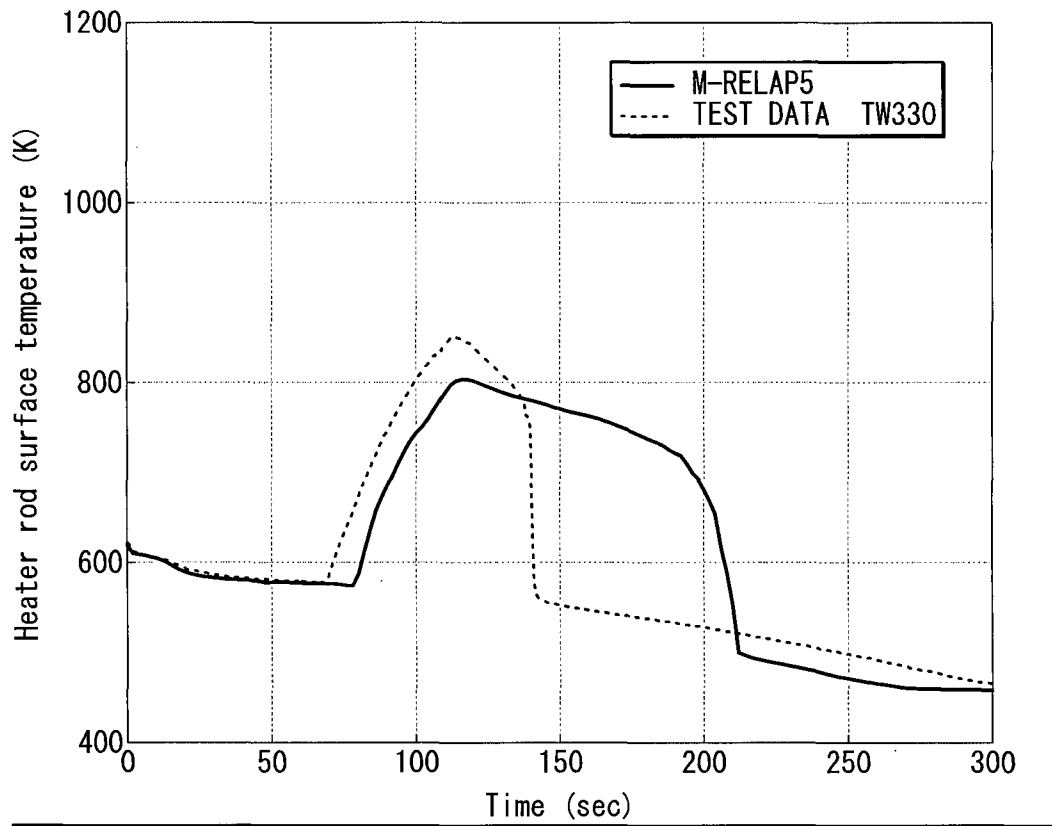


Figure 8.2.2-26 Heater Rod Surface Temperature at 3.05m (M) and at 3.17m (P)

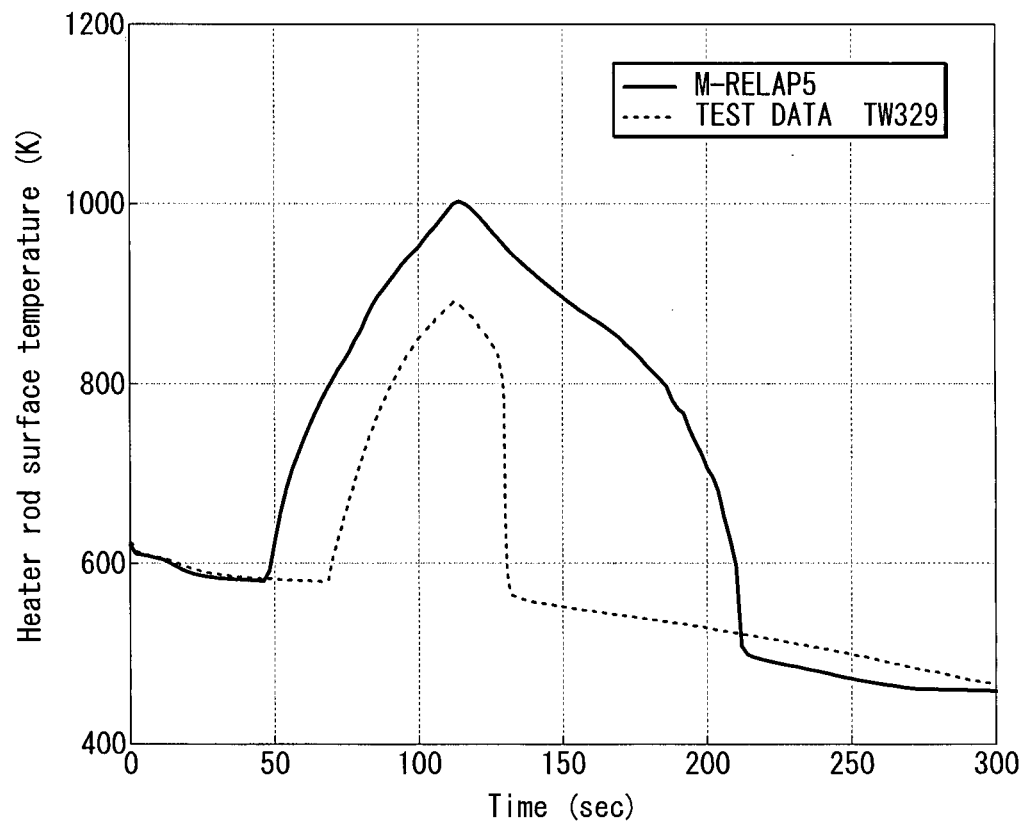


Figure 8.2.2-27 Heater Rod Surface Temperature at 2.64m (M) and at 2.68m (P)

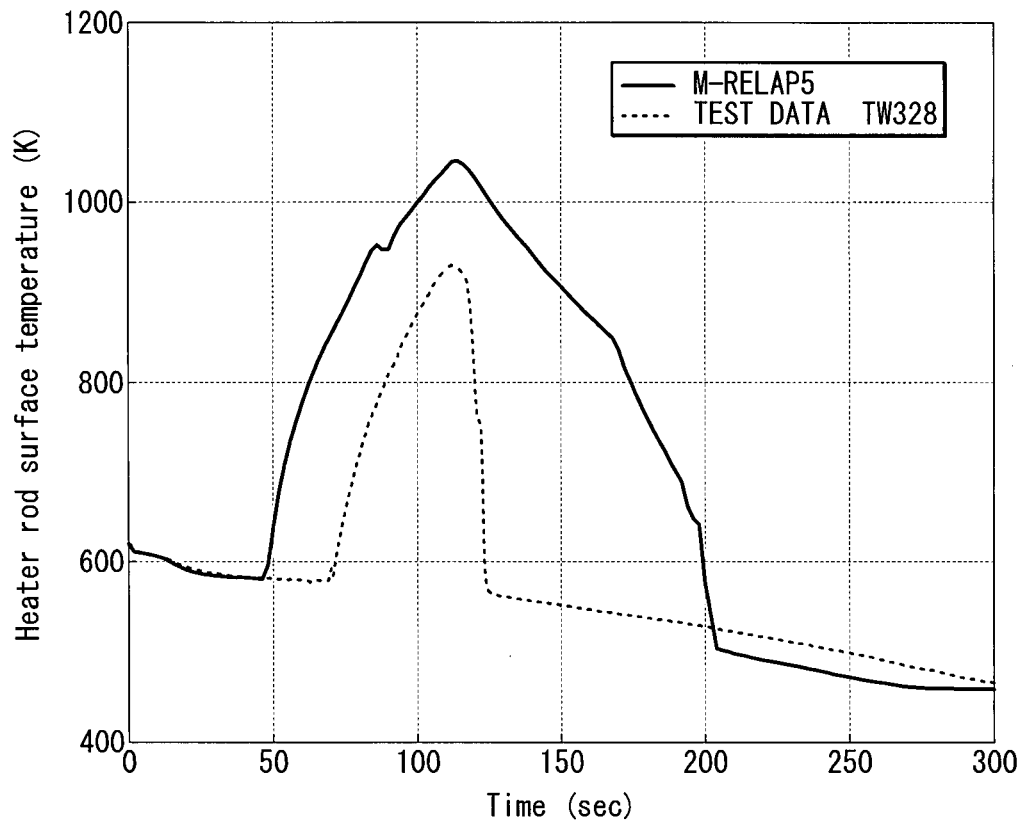


Figure 8.2.2-28 Heater Rod Surface Temperature at 2.24m (M) and at 2.23m (P)

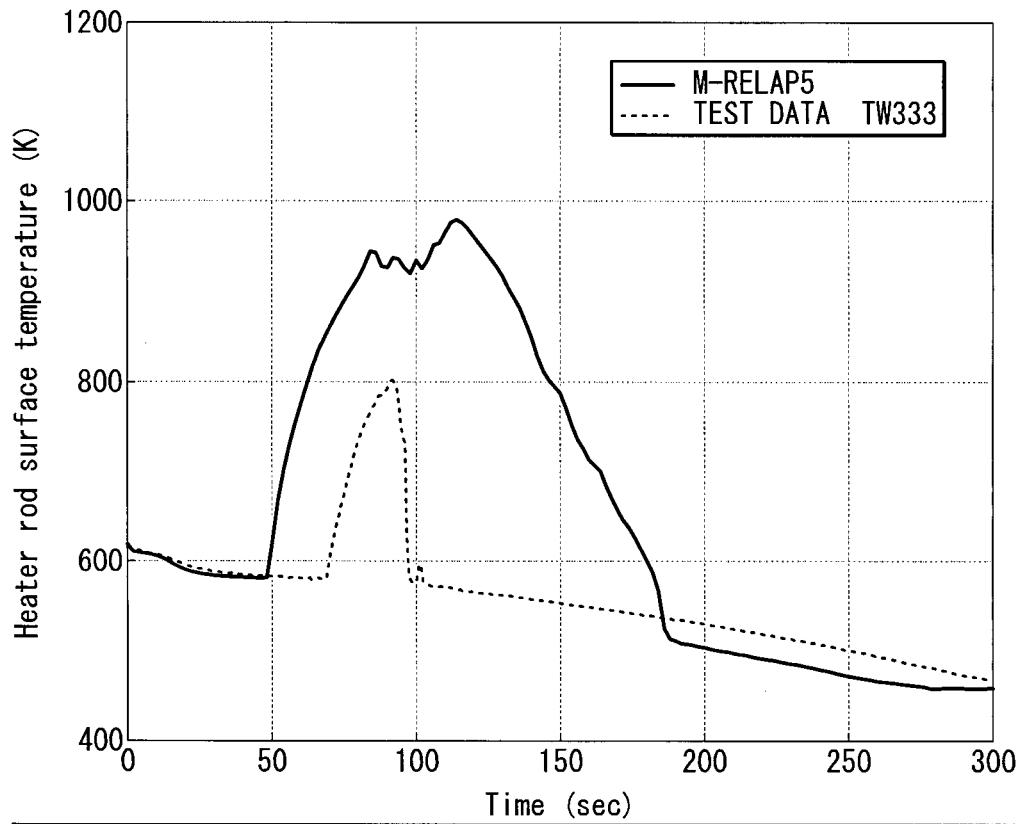


Figure 8.2.2-29 Heater Rod Surface Temperature at 1.83m (M) and at 1.82m (P)

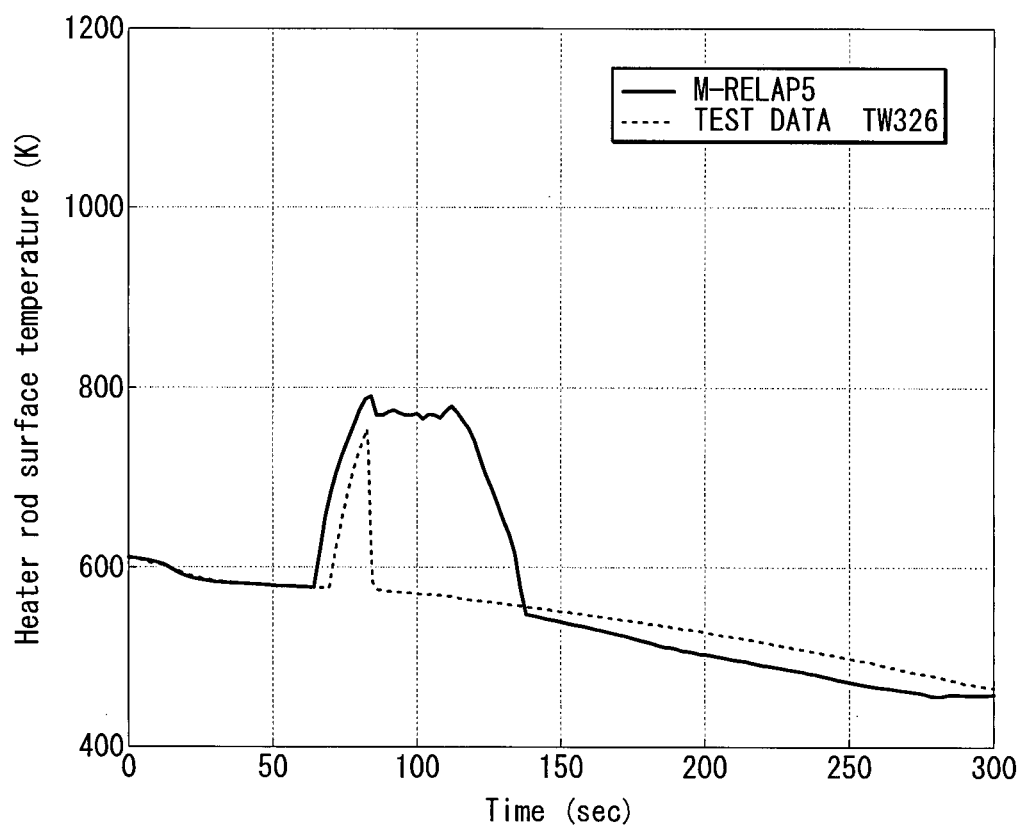


Figure 8.2.2-30 Heater Rod Surface Temperature at 1.42m (M) and at 1.37m (P)

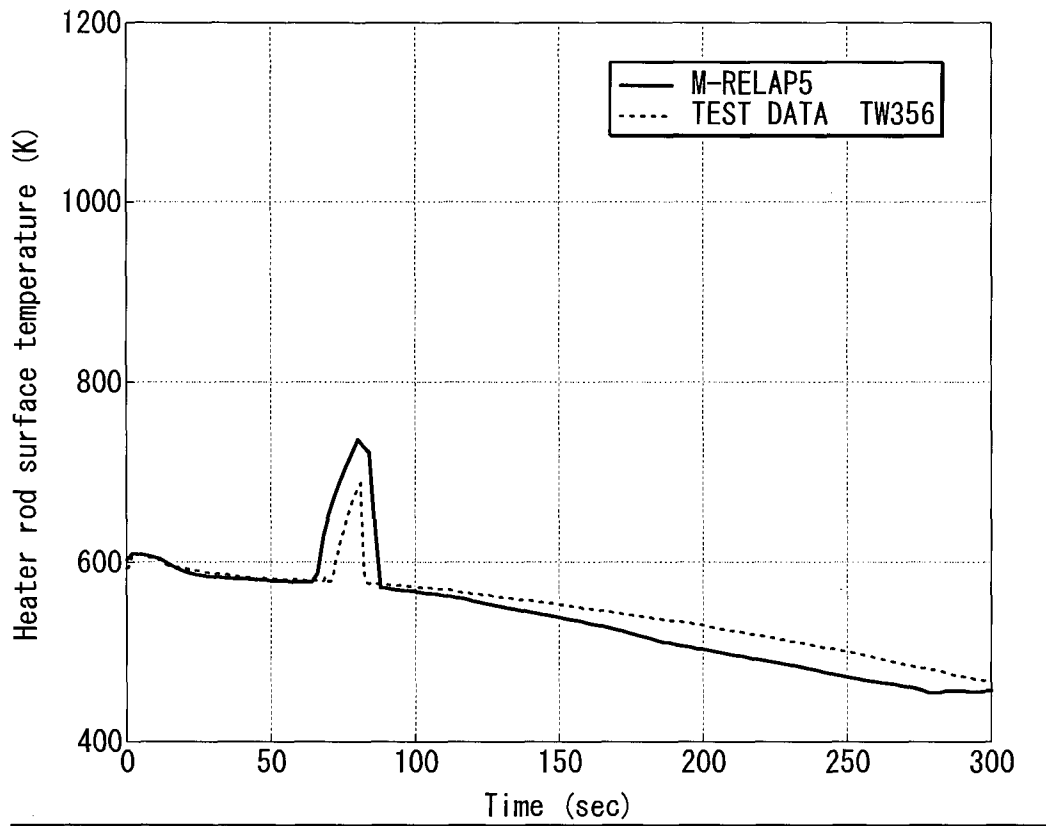


Figure 8.2.2-31 Heater Rod Surface Temperature at 1.02m (M) and at 1.11m (P)

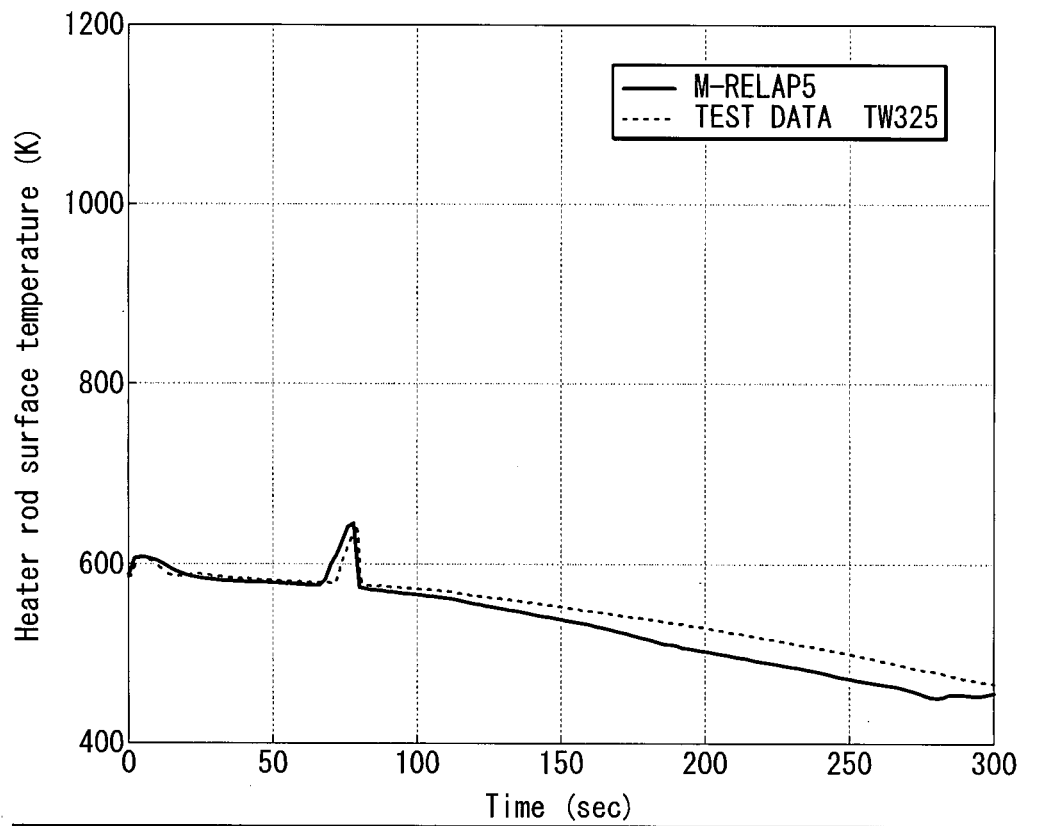


Figure 8.2.2-32 Heater Rod Surface Temperature at 0.61m (M) and at 0.64m (P)

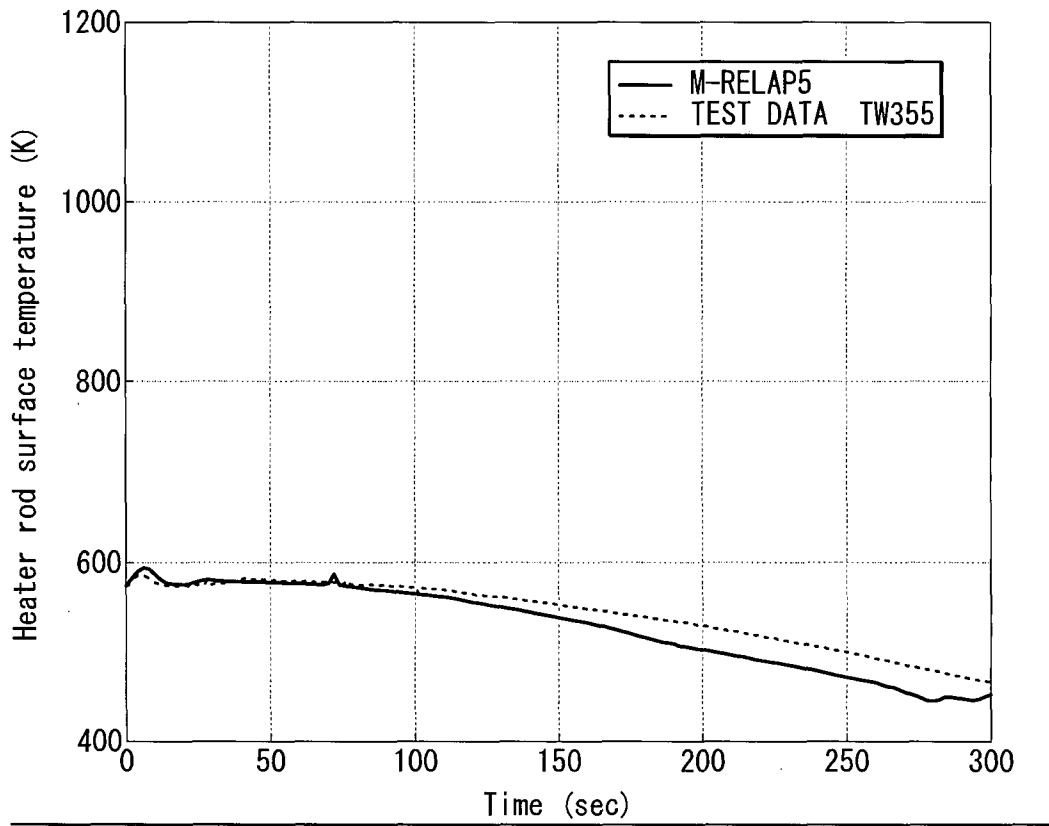


Figure 8.2.2-33 Heater Rod Surface Temperature at 0.05m (M) and at 0.07m (P)

8.2.3 ROSA/LSTF small break (17%) LOCA test (IB-CL-02)

8.2.3.1 Introduction

The purpose of the calculation of ROSA/LSTF test IB-CL-02 (Ref. 8.2.3-1) is to validate the ability of the M-RELAP5 code to predict the following phenomena ranked of high importance in the small break LOCA PIRT: core dryout, post-CHF heat transfer, rewet, core mixture level, and downcomer mixture level. A primary difference from test SB-CL-18 is that the postulated break size is larger in the present test, which is corresponding to the 1-ft² break in the US-APWR.

8.2.3.2 Selection of IB-CL-02

Test IB-CL-02 (17% break) was selected for analysis because the break size is the equivalent to the 1ft² break in the US-APWR. Therefore, a rapid depression in the primary system, and important phenomena occurring in the boil-off and core recovery phases in US-APWR SBLOCAs could be identified in the experiment.

8.2.3.3 Test Condition

(a) Test Facility

The description of the test facility is provided in section 8.2.1.3(a).

(b) Test Procedure

[

I

I

I

1

(c) Test Results

I

1

8.2.3.4 M-RELAP5 Calculation Procedure**(a) M-RELAP5 Model of IB-CL-02**

The M-RELAP5 model of the IB-CL-02 is the same as described in the section 8.2.1.4, except for the break modeling and main steam relief valve. The break modeling for Run IB-CL-02 is shown in Figure 8.2.3-3. The break flow and the main steam relief valve are explicitly simulated in this calculation. The modifications described in section 8.2.1.9 are adopted. [

1

(b) Calculation ConditionsInitial conditions:

Table 8.2.3-1 summarizes the initial conditions before the break opens. A 2000-second steady-state simulation was performed. At the end of this 2000-second simulation, predicted and measured flow parameters are compared. These comparisons show reasonably good agreements.

Boundary conditions:

Time-dependent tables, which were constructed from the experimental data, are used to represent the core power (Figure 8.2.3-4) and pump coastdown (Figure 8.2.3-5 and 8.2.3-6) curves.

The break flow is explicitly simulated by using the Moody critical flow model with the atmospheric outer boundary condition. [

1

The secondary system pressure behavior is also explicitly simulated by modeling the main steam isolation and steam relief valves with the imposed boundary condition for the feedwater flow following the reactor trip.

Assumptions for analysis:

[

1

I

1

8.2.3.5 M-RELAP5 Calculation Result

The comparisons of test and M-RELAP5 chronology are summarized in Table 8.2.3-4. The comparisons between test data and M-RELAP5 results are shown in Figure 8.2.3-7 through 35.

I

1

I

1

8.2.3.6 Conclusions

M-RELAP5 well predicts the 17% cold leg break transient. M-REAP5 demonstrates the ability to predict the PCT for small break LOCA with larger break size equivalent to 1ft².]

]]

8.2.3.9 References

8.2.3-1. JAEA, Experimental Report on Simulated Intermediate Break Loss-of-Coolant Accident using ROSA/LSTF, March 2010 (in Japanese, proprietary).

Table 8.2.3-1 Steady-State Parameter Checklist



Table 8.2.3-2 Core Power Decay Curve



Table 8.2.3-3 Pump Coastdown Curve



Table 8.2.3-4 Transient Results Summary for 17-Percent Cold Leg Side Break





Figure 8.2.3-1 Break Assembly
(From JAEA Research 2008-087)



Figure 8.2.3-2 Break Orifice
(From JAEA Research 2008-087)



Figure 8.2.3-3 Break Modeling of IB-CL-02



Figure 8.2.3-4 Total Core Power



Figure 8.2.3-5 Reactor Coolant Pump in Primary Loop-A Rotation Speed



Figure 8.2.3-6 Reactor Coolant Pump in Primary Loop-B Rotation Speed



Figure 8.2.3-7 Pressurizer Pressure



Figure 8.2.3-8 SGA Steam Dome Pressure



Figure 8.2.3-9 SGB Steam Dome Pressure



Figure 8.2.3-10 Break Flowrate



Figure 8.2.3-11 Integral of Break Flow



Figure 8.2.3-12 Core Differential Pressure



Figure 8.2.3-13 Loop-A SG Inlet Plenum Differential Pressure



Figure 8.2.3-14 Loop-B SG Inlet Plenum Differential Pressure



Figure 8.2.3-15 Loop-A SG U-tube Uphill Side Differential Pressure



Figure 8.2.3-16 Loop-B SG U-tube Uphill Side Differential Pressure



Figure 8.2.3-17 Loop-A SG U-tube Downhill Side Differential Pressure



Figure 8.2.3-18 Loop-B SG U-tube Downhill Side Differential Pressure



Figure 8.2.3-19 Downcomer Differential Pressure



Figure 8.2.3-20 Upper Plenum Differential Pressure



Figure 8.2.3-21 Accumulator Injection Flowrate



Figure 8.2.3-22 Safety Injection Flowrate



Figure 8.2.3-23 Heater Rod Surface Temperature at 3.61m (M) and at 3.57m (P)



Figure 8.2.3-24 Heater Rod Surface Temperature at 3.05m (M) and at 3.17m (P)



Figure 8.2.3-25 Heater Rod Surface Temperature at 2.64m (M) and at 2.68m (P)



Figure 8.2.3-26 Heater Rod Surface Temperature at 2.24m (M) and at 2.23m (P)



Figure 8.2.3-27 Heater Rod Surface Temperature at 1.83m (M) and at 1.82m (P)



Figure 8.2.3-28 Heater Rod Surface Temperature at 1.42m (M) and at 1.37m (P)



Figure 8.2.3-29 Heater Rod Surface Temperature at 1.02m (M) and at 1.11m (P)



Figure 8.2.3-30 Heater Rod Surface Temperature at 0.61m (M) and at 0.64m (P)



Figure 8.2.3-31 Heater Rod Surface Temperature at 0.05m (M) and at 0.07m (P)

8.2.4 LOFT small break (2.5%) LOCA test (L3-1)

8.2.4.1 Introduction

LOFT (Loss-of-Fluid Test) L3-1 (Ref. 8.2.4-1) was the first nuclear powered SBLOCA experiment. The test was designed to simulate a 4-in diameter equivalent single-ended break in the cold leg of a large 4-loop PWR. The primary purpose of code validation using the LOFT L3-1 data is to assess the code ability to predict the primary plant responses following the small break.

8.2.4.2 Selection of L3-1

Parameters that were varied for Experiment Series L3 include initial power level, break size and location (orientation), primary coolant pump operation, and the time and manner of ECCS injection. Test L3-1, a baseline test, simulated a 2.5% break in the cold leg of a 4-loop PWR primary coolant pipe. The test provided information on system responses for a small break where break flow always exceeds HPIS flow. In addition, the TMI action plan requires assessing a computer code's ability to predict several important phenomena and processes specific to small break LOCAs such as a natural circulation, using experimental test data obtained in LOFT L3-1.

8.2.4.3 Test Condition

(a) Test Facility

A summary description of the LOFT facility is given in Section 5.2.2.4 of the present report.

(b) Test Procedure

After reactor criticality was achieved, reactor power was increased to 48.9 ± 1.0 MWt, and maintained at that level until experiment initiation. The conditions in the intact loop were established to provide a mass flow of 484.0 ± 6.3 kg/s. The primary coolant system boron concentration was adjusted to establish a reactor vessel inlet temperature of 554.0 ± 3 K at a hot leg pressure of 14.85 ± 0.04 MPa.

The DAVDS (Data Acquisition and Visual Display System) was activated and data recording was started 7 min prior to the blowdown. The experiment was initiated by opening the broken loop cold leg QOBV (Quick Opening Blowdown Valve).

Electrical power to the PSMG (Primary System Motor Generator) sets was terminated at blowdown initiation, and the primary coolant pumps began to coast down under the influence of a flywheel system. At 17.6 seconds, the primary coolant pump speed had decreased to 12.5 Hz and the PSMG set field breakers tripped open to disconnect the PSMG sets from the pumps. The pumps had coasted down and stopped at 19 seconds.

(c) Test Results

The reactor was scrammed manually at 2 seconds prior to the break initiation (defined to occur at time zero) when the cold leg blowdown valve was opened. The pumps were tripped at the break initiation and coasted down in about 19 seconds. The HPIS flow initiated automatically at about 5 seconds. The pressurizer was empty by 17 seconds and the upper plenum fluid was saturated by 25 seconds.

Natural circulation began as the pumps completed their coastdown and continued until 390 seconds when the primary system pressure dropped below the secondary pressure and the steam generator was no longer a heat sink. The break flow was sufficient, however, to remove the decay heat and to continue system depressurization.

ECC injection was directed to the intact loop cold leg during blowdown. The HPIS flow was initiated automatically 4.6 seconds after blowdown initiation. The injection flow rate was held constant until the pressure reached 8.36 MPa, at which point the HPIS flow was increased with decreasing system pressure by operator action. At about 630 seconds the accumulator started injecting the ECC. The accumulator emptied of water and nitrogen entered the system at about 1750 seconds. No effects of the nitrogen on the RCS response were observed in the measurements. The LPIS setpoint was purposely lowered from a normal pressure of 2.12 MPa to 0.98 MPa to assure nitrogen injection from the accumulator to the RCS.

The pump inlet loop seal did not clear during the transient as expected because of the large core bypass paths from the upper plenum to the cold leg which allowed pressure equalization between the hot and cold legs.

At about 3600 seconds, secondary bleed and feed was initiated by the operator action, which imposed a 38.8 to 50 K/hr cool-down rate on the secondary system. This procedure had no effect on the primary system pressure because the primary and secondary systems were thermally decoupled.

The mass inventory in the reactor vessel was sufficient at all times to keep the core completely covered, consequently the core remained cooled with the clad temperatures following the coolant saturation temperature.

8.2.4.4 M-RELAP5 Calculation Procedure

(a) M-RELAP5 Model of the LOFT

The LOFT L3-1 test was simulated by M-RELAP5 such that the code ability to predict the SBLOCA test was examined as was done for the other IET analyses, including ROSA/LSTF SB-CL-18 and Semiscale S-LH-1. The M-RELAP5 LOFT model used here is based on the input model developed by INL (Ref. 8.2.4-2). However, the noding scheme and the thermal-hydraulic model options have been modified so as to conform to the models applied to the US-APWR SBLOCA analysis. The noding diagram is shown in Figure 8.2.4-1.

The M-RELAP5 LOFT model primarily consists of the a) reactor vessel, b) pressurizer, c) steam generator, d) intact loop, e) broken loop, f) ECCS, and g) break assembly. [

1

Heat conduction in the nuclear core fuel rods and the reactor component structures are taken into account.]

1

HPIS, LPIS and accumulator injections are explicitly simulated in the present model. Although Reference 8.2.4-1 mentions that no significant effects of noncondensable gas from the accumulator were observed after the accumulator emptied, the noncondensable gas model simulating the nitrogen entering the RCS was applied in the present calculation.

The M-RELAP5 transient calculation simulated the experiment from the break initiation until shortly before the operators manually initiated the steam bleed of the secondary coolant system. The latter portion of the experiment was not simulated because the behavior of the LOFT facility after the onset of the steam bleed is not relevant to the behavior of the US-APWR.

(b) Calculation Conditions

Initial conditions:

Table 8.2.4-1 summarizes initial conditions prior to the blowdown, where the M-RELAP5 results are compared with the measurements. The comparisons demonstrate that the model is capable of reproducing the experimental steady state.

Boundary conditions:

The core fission power and decay power history are given through the input data table for the present calculation.

The break flow is explicitly simulated by using the Moody critical flow model with the offtake/pullthrough model. The LOFT L3-1 test employed the single-ended break unit with a centered orifice (Figure 5.2.2.4-3), and the quick opening blowdown valve was attached in the downstream of the break orifice.]

1

Regarding the secondary system model, the post-test analysis report (Ref. 8.2.4-2) states that the steam control valve of the SG secondary system did not seat 100% nor did it seat the same each closure. The value calculated for Experiment L3-1 is 0.02 kg/s at 3.5 MPa, which is assumed for the present M-RELAP5 calculation.

Assumptions for analysis:

The counter-current flow limitation (CCFL) occurring in the piping with a smaller diameter is taken into account for the calculation. The CCFL in the SG U-tubes is modeled using the Wallis correlation (Ref. 8.2.4-3), where $\beta=0.0$, $c=0.88$, and $m=1.0$ are applied. This modeling

is identical to that for the US-APWR plant calculation, because the geometric scaling of the SG U-tubes is almost identical between the LOFT and US-APWR. [

]

8.2.4.5 M-RELAP5 Calculation Result

The chronology during the LOFT L3-1 test is listed in Table 8.2.4-2, where the experimental and calculated results are compared.

Following the break initiation, the RCS rapidly decreases to the secondary system pressure during the blowdown phase. Figure 8.2.4-2 compares the calculated break flow rate with the measurement. The Moody critical flow model tends to overestimate the two-phase break flow rate. Around 1500 seconds after the break initiation, M-RELAP5 suddenly underestimates the break flow rate because the accumulator injection stops and void fraction at the break location increases. It is noted that the experimental test report (Ref. 8.2.4-1) mentions that the uncertainty for the measured break flow rate was $\pm 15\%$.

The primary and secondary system pressures are compared with the measurements in Figures 8.2.4-3 and 8.2.4-4, respectively. Similarly, pressurizer liquid level is shown in Figure 8.2.4-5. The temporal changes of these parameters are well reproduced by M-RELAP5. The natural circulation begins as the pumps complete their coastdown, and then the primary and secondary pressures equivalently decrease. Around 400 seconds after the break initiation, the primary system pressure falls below the secondary system pressure, which is the end of the natural circulation phase. After that, the SG no longer behaves as a heat sink.

Calculated differential pressures in terms of the intact loop crossover leg downhill-side and uphill-side are compared with the measurements in Figures 8.2.4-6 and 8.2.4-7, respectively. The differential pressure is essentially due to the liquid level after the natural circulation period ends. In the experiment, the loop seal formed in the intact loop crossover leg was not cleared because the steam generated in the core was able to be vented through the bypass paths. Reference 8.2.4-2 describes that the initial core bypass fractions were 3.6% of primary

loop flow for the lower plenum to upper plenum path, 6.6% for the inlet annulus (downcomer) to upper plenum path, and 1.3% for the reflood assist bypass valve at the test initiation. This large core bypass flow fraction prevented the coolant in the crossover leg from clearing. Similar to the measurement, the M-RELAP5 calculation predicts that the loop seal in the intact loop crossover leg does not clear throughout the transient as shown in Figures 8.2.4-6 and 8.2.4-7.

The accumulator started injecting the safety coolant as the RCS pressure fell below the initial accumulator pressure around 640 seconds. The nitrogen gas in the accumulator tank expands and ejects the safety coolant to the RCS. The accumulator emptied of the water and the nitrogen began to enter the RCS at about 1750 seconds. These behaviors are well simulated in the M-RELAP5 calculation as shown in Figure 8.2.4-8 for the tank pressure, and in Figure 8.2.4-9 for the tank level, respectively. This validates the accumulator model implemented in M-RELAP5.

No fuel cladding heat-up was observed in the LOFT L3-1 test or calculated with M-RELAP5 as shown in Figure 8.2.4-10.

8.2.4.6 Conclusions

The LOFT L3-1 experiment was simulated by using M-RELAP5 to validate the code's ability to predict the plant response occurring under SBLOCAs. The primary purpose is to assess the M-RELAP5 models and noding scheme, which are also applied to the plant analysis, using the experimental test data.

M-RELAP5 attained reasonable agreement compared to the measured RCS pressure and the pressurizer, loop seal, and accumulator behaviors. A large core bypass fraction caused the loop seal in the crossover leg to not clear during the LOFT L3-1 test or in the M-RELAP5 calculation. In addition, M-RELAP5 predicted no cladding heat-up during the test, which was consistent with measured results.

Hence, it can be concluded that M-RELAP5 is able to reproduce the transient behavior, phenomena and processes of interest during the LOFT L3-1 SBLOCA test.

8.2.4.7 References

8.2.4-1. P. D. Bayless et al., "Experimental Data Report for LOFT Nuclear Small Break Experiment L3-1," NUREG/CR-1145, EGG-2007, January 1980.

8.2.4-2. K. G. Condie et al., "Four-Inch Break Loss-of-Coolant Experiments: Posttest Analysis of LOFT Experiment L3-1, L3-5 (Pumps Off), and L3-6 (Pumps On)," EGG-LOFT-5480, October 1981.

8.2.4-3. G. B. Wallis, "One Dimensional Two Phase Flow," McGraw-Hill, 1969.

8.2.4-4. C. L. Tien, et al., "Flooding in Two-Phase Countercurrent Flows," EPRI NP-1283, December 1979.

Table 8.2.4-1 Steady-State Parameter Checklist for Experiment L3-1

<u>Parameter</u>	<u>Experiment</u>	<u>M-RELAP5</u>
<u>Primary system pressure [MPa]</u>	<u>14.81 ± 0.04</u>	<u>14.81</u>
<u>Primary system mass flowrate [kg/s]</u>	<u>484.0 ± 6.3</u>	<u>484.0</u>
<u>Cold leg temperature [K]</u>	<u>554.0 ± 3</u>	<u>554.1</u>
<u>Hot leg temperature [K]</u>	<u>574.0 ± 1</u>	<u>573.1</u>
<u>Steam generator pressure [MPa]</u>	<u>5.43 ± 0.11</u>	<u>5.40</u>
<u>Steam generator mass flowrate [kg/s]</u>	<u>25.0 ± 0.4</u>	<u>25.4</u>
<u>Pressurizer level [m]</u>	<u>1.16⁴⁾ ± 0.01</u>	<u>1.16</u>
<u>Core bypass fraction (LP to UP)¹⁾ [%]</u>	<u>3.6</u>	<u>3.45</u>
<u>Core bypass fraction (DC to UP)²⁾ [%]</u>	<u>6.6</u>	<u>6.62</u>
<u>Core bypass fraction (RABV)³⁾ [%]</u>	<u>1.3</u>	<u>1.30</u>
<u>Core power [MW]</u>	<u>48.9 ± 1.0</u>	<u>48.9</u>

- 1) Core bypass fraction from lower plenum to upper plenum.
- 2) Core bypass fraction from downcomer to upper plenum.
- 3) Core bypass fraction through the reflood assist bypass valve.
- 4) Including the instrumentation offset

Table 8.2.4-2 Primary Test Chronology for Experiment L3-1

<u>Event</u>	<u>Experiment (sec)</u>	<u>M-RELAP5 (sec)</u>
<u>Reactor scram</u>	<u>-2.15</u>	<u>-2.15</u>
<u>LOCA initiated</u>	<u>0.0</u>	<u>0.0</u>
<u>Primary coolant pumps tripped</u>	<u>0.04 ± 0.01</u>	<u>0.04</u>
<u>Scaled HPIS initiated</u>	<u>4.6 ± 0.5</u>	<u>0.81¹⁾</u>
<u>Pressurizer empty</u>	<u>17.0 ± 1</u>	<u>23</u>
<u>Pump coastdown complete</u>	<u>19.0 ± 1</u>	<u>31²⁾</u>
<u>Accumulator injection initiated</u>	<u>633.6 ± 0.5</u>	<u>722.85</u>
<u>Accumulator liquid level below standpipe</u>	<u>1570.0 ± 1</u>	<u>1482</u>
<u>Accumulator line empty of fluid</u>	<u>1741.0 ± 1</u>	<u>1620</u>

1) Determined when the RCS pressure is less than 13.07 MPa.

2) Determined when the RCP head is less than 0.0m.

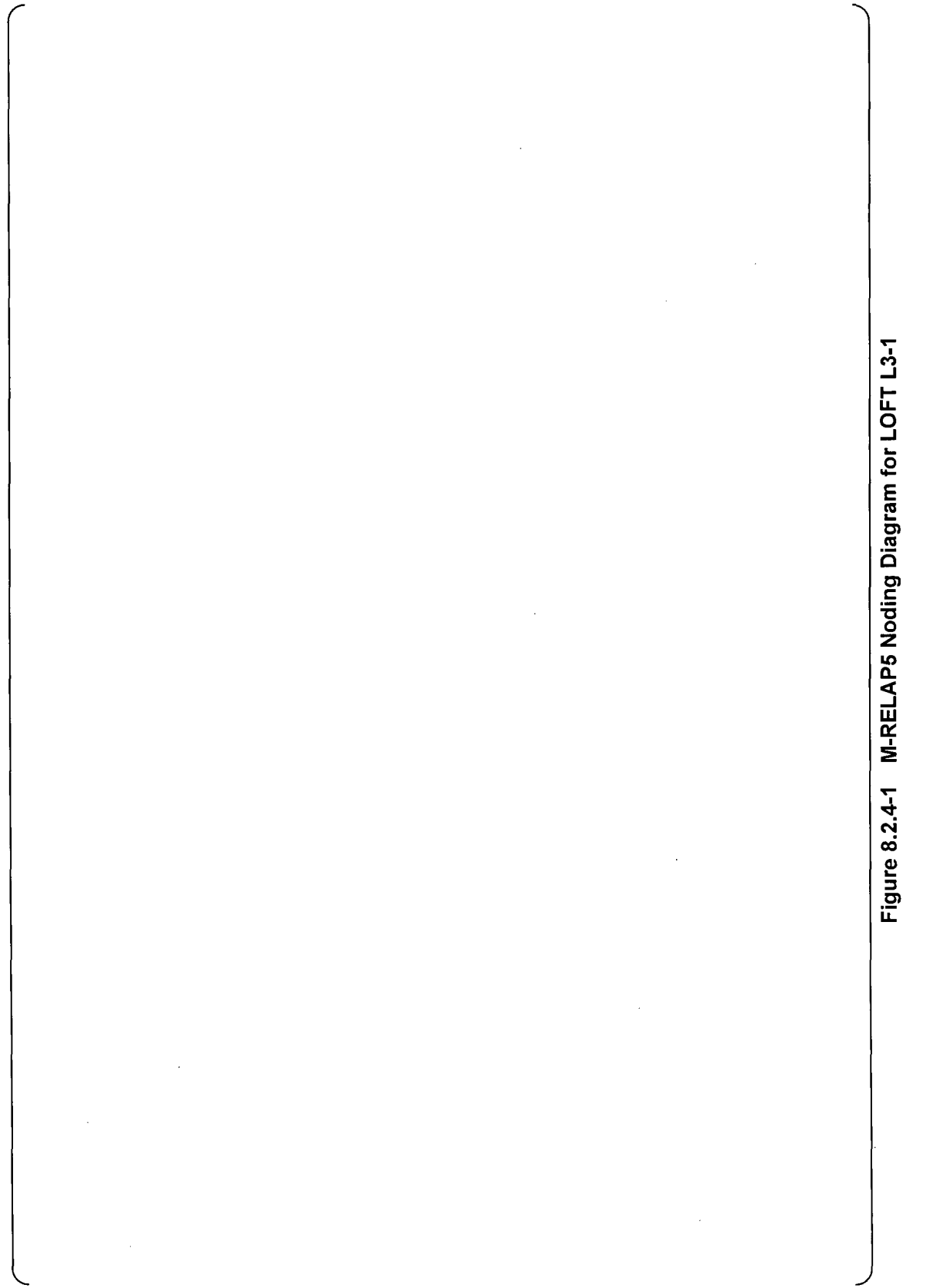


Figure 8.2.4-1 M-RELAP5 Noding Diagram for LOFT L3-1

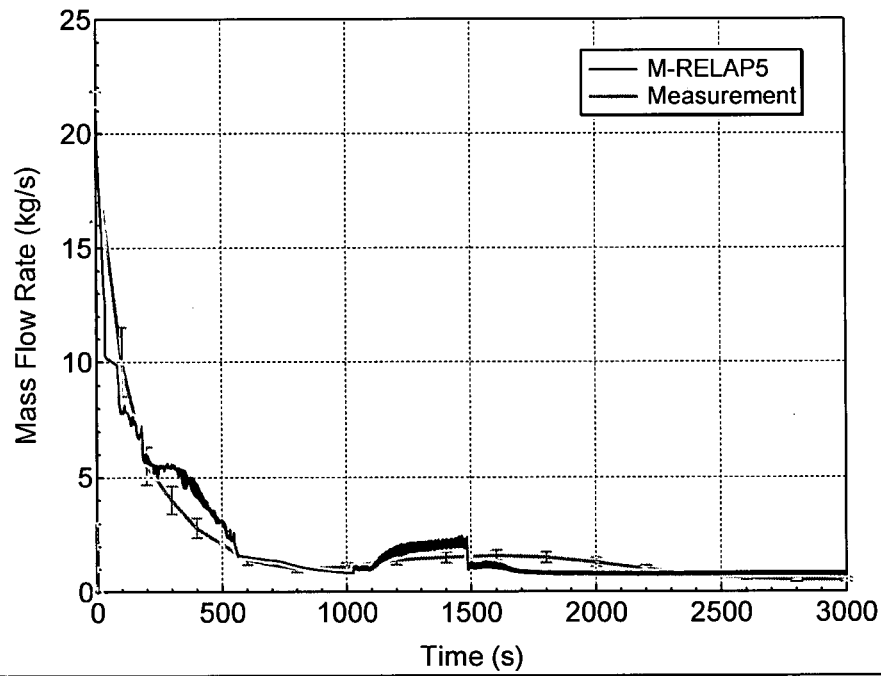


Figure 8.2.4-2 Break Flow Rate

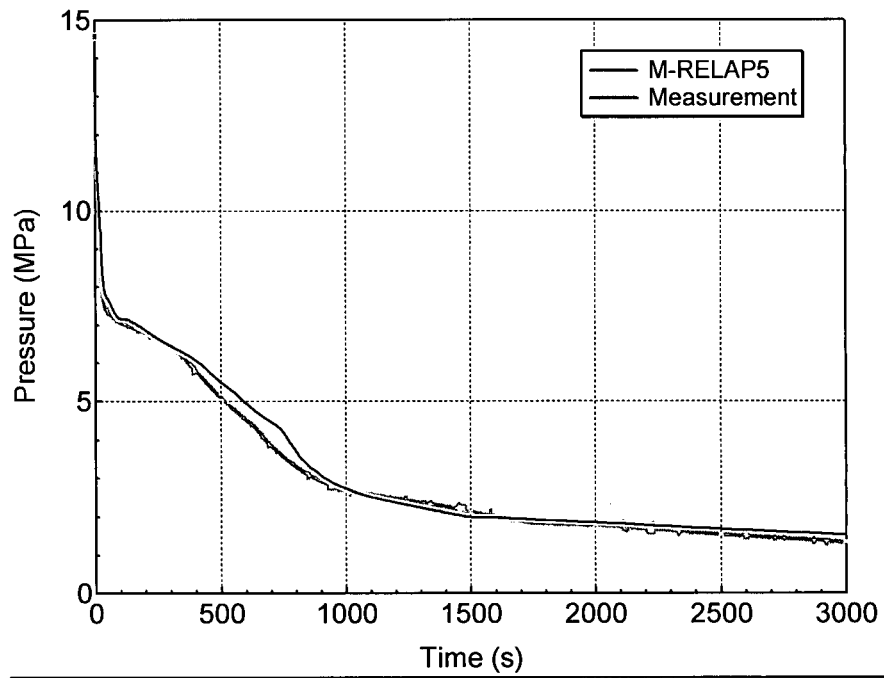


Figure 8.2.4-3 Primary System Pressures

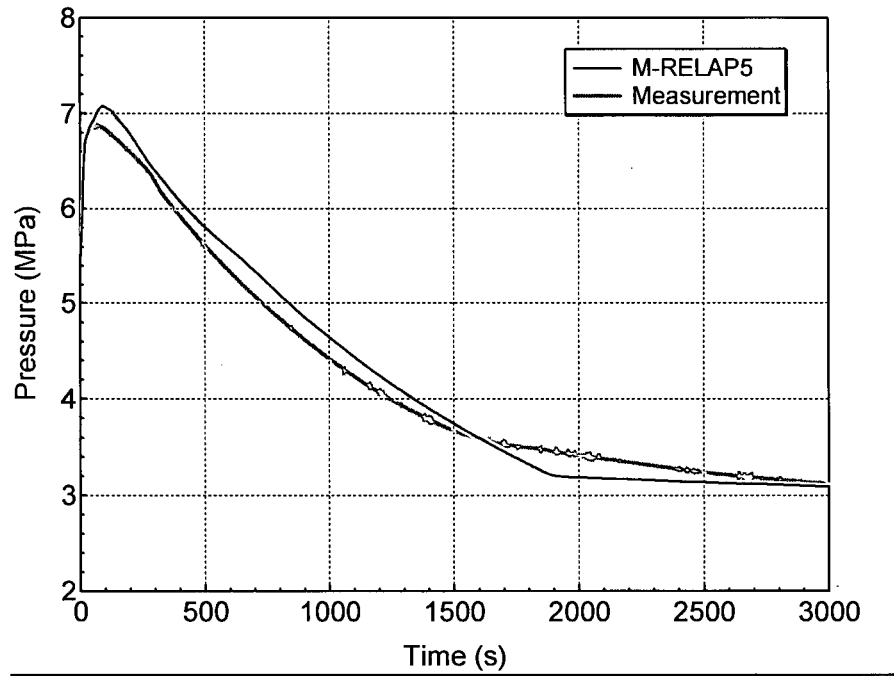


Figure 8.2.4-4 Secondary System Pressure

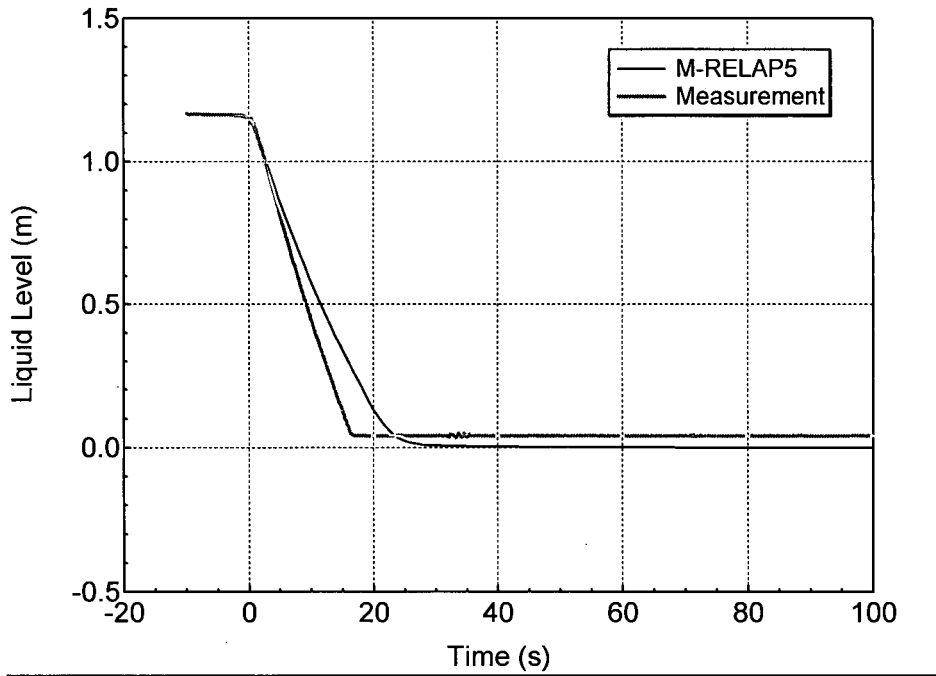


Figure 8.2.4-5 Pressurizer Liquid Level

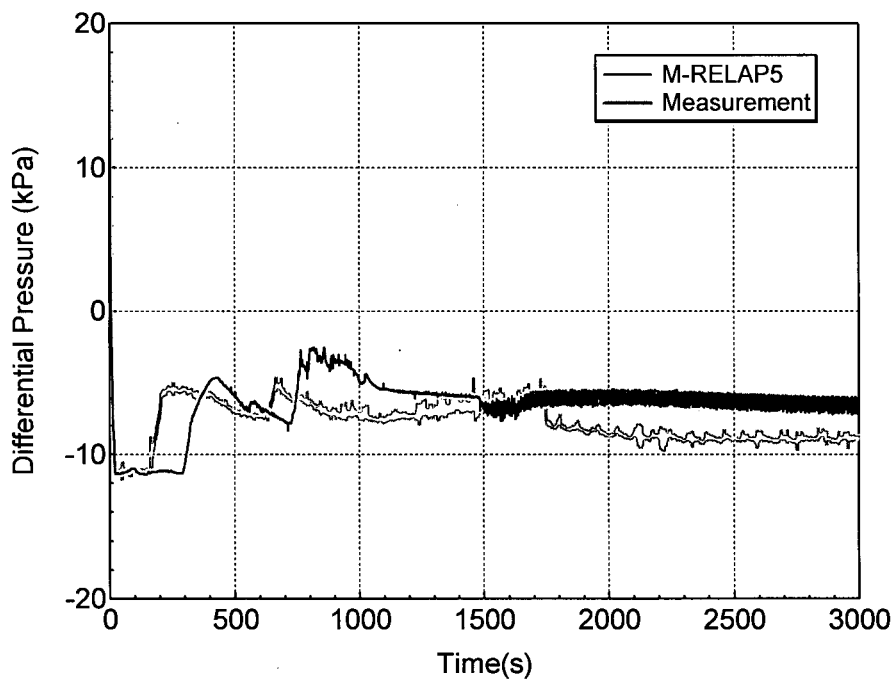


Figure 8.2.4-6 Intact Loop Cross-over Leg Downhill Side Differential Pressure

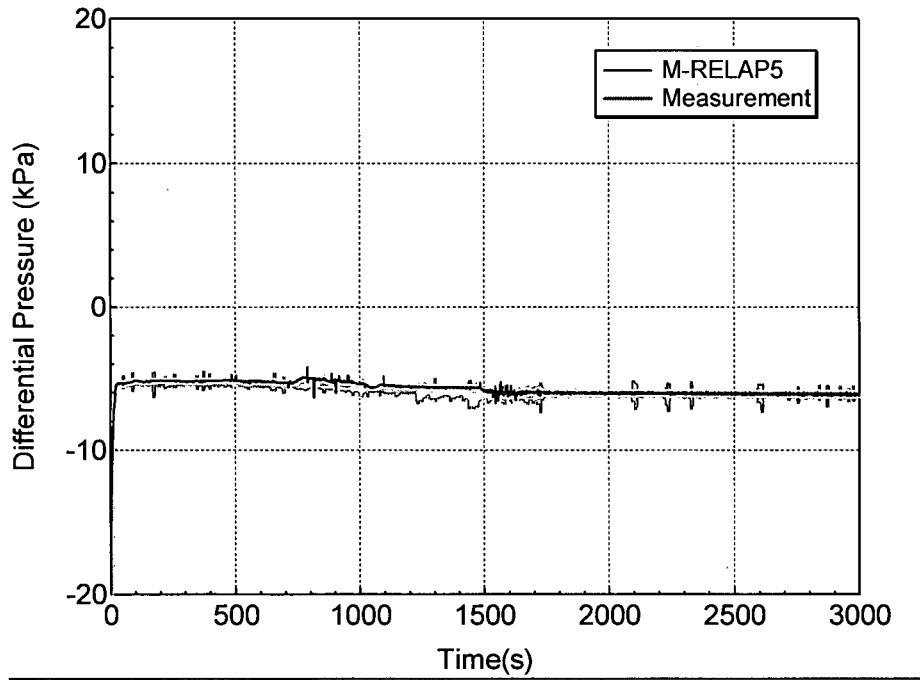


Figure 8.2.4-7 Intact Loop Cross-over Leg Uphill Side Differential Pressure

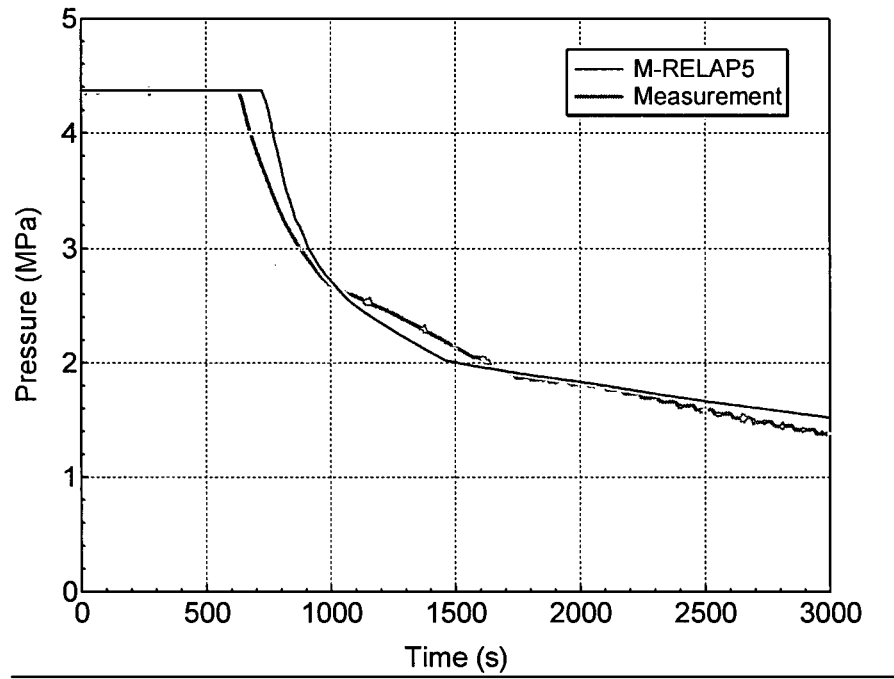


Figure 8.2.4-8 Accumulator Tank Pressure

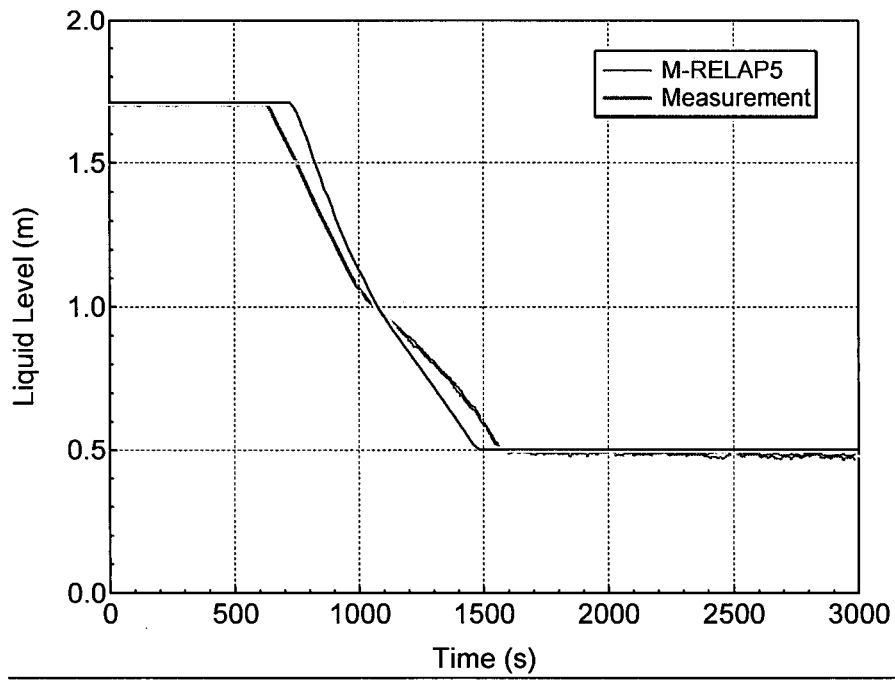


Figure 8.2.4-9 Accumulator Tank Liquid Level

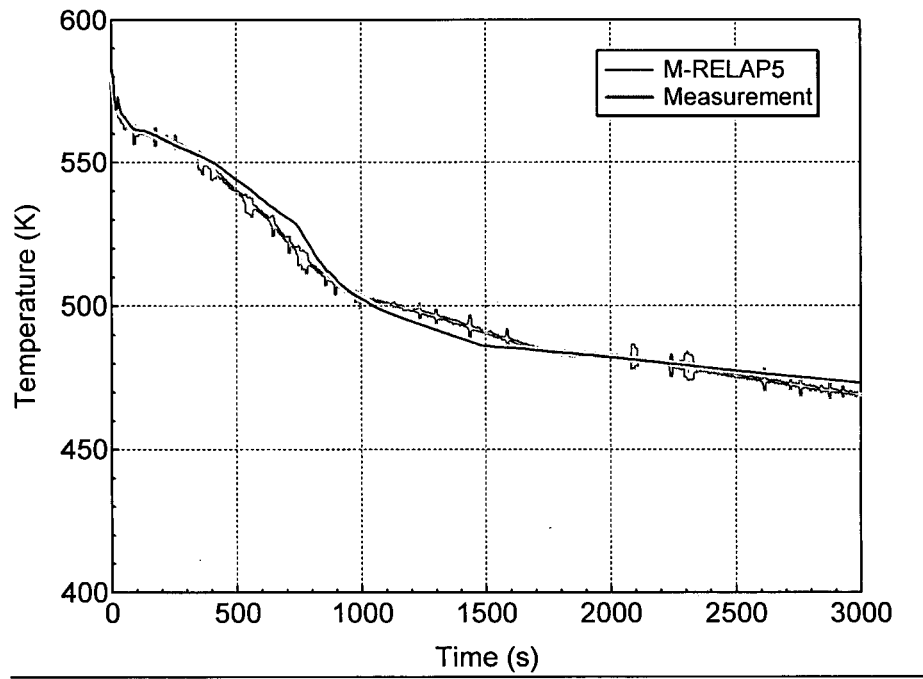


Figure 8.2.4-10 Fuel Cladding Surface Temperature at 62-in from Core Bottom

8.2.5 Semiscale small break (5%) LOCA test (S-LH-1)

8.2.5.1 Introduction

The Semiscale/S-LH-1 experiment (Ref. 8.2.5-1) was conducted in the Mod-2C test facility. The Semiscale Mod-2C is a small-scale, nonnuclear, experimental system with an electrically heated core. The S-LH-1 experiment simulated the 5% cold leg SBLOCA, where the upper head to downcomer bypass flow was calibrated to 0.9% of the recirculation flow to retard steam venting through the spray nozzle during the transient. The primary purpose of code validation using the Semiscale/S-LH-1 data is to assess the code's ability to predict the system response and the core heat-up behavior occurring during the loop seal period.

8.2.5.2 Selection of S-LH-1

The results of S-LH-1 could not be precise replications of full-scale PWR response due to inherent scaling distortions and facility limitations. The experiment, however, provided thermal-hydraulic behavior sufficiently representative of full-scale PWR behavior to preserve important phenomena and satisfy test objectives. Data from these experiments would provide the water reactor safety research community with an integral system database for benchmarking code calculations, specifically in the area of liquid "holdup" in the steam generator, manometrically-induced core liquid level depressions (loop seal formation and clearance), upper head drain characteristics, and the effect of downcomer to upper head bypass flow on the core liquid level depressions. The data also provided confirmation that the severe response observed during the S-UT-8 test (Ref. 8.2.5-2) was indeed repeatable and, thus, worthy of in-depth investigation.

The TMI action plan also requires assessing a computer code's ability to predict important phenomena and processes specific to SBLOCAs using experimental test data obtained in the Semiscale facility.

8.2.5.3 Test Condition

(a) Test Facility

A summary description of the Semiscale facility is provided in Section 5.2.2.5 of the present report.

(b) Test Procedure

The system was filled with de-mineralized water and vented to ensure a liquid-full-system. Instrumentation was calibrated and zeroed as necessary. The system was heated to initial conditions using core power and forced flow with the primary coolant pumps running. The secondary pressure stayed below the relief valve setpoints.

The experiment was initiated at 0 second by opening the block valve in the break assembly allowing primary fluid to blowdown through the break orifice. The break flow had allowed the primary system to depressurize to the low pressurizer pressure trip signal (12.6 MPa). Automatically occurring events were main steam isolation valve closure, core scram to the ANS decay curve, primary pump coastdown initiation, feedwater termination, and safety injection initiation.

The following assumptions were used in determining the sequence of events: a) feedwater flow was terminated at the low pressurizer pressure trip which coincided with a loss-of-offsite power, b) HPIS was delayed 25 seconds after the low pressurizer pressure trip to simulate starting of diesel generators and to achieve full operational status, c) core scram was delayed 3.4 seconds after the low pressurizer pressure trip to simulate control rod drop time, d) main steam isolation valve closure occurred at scram due to a steam turbine trip, and e) the pumps were tripped after a 2 seconds delay following the low pressurizer pressure trip. The experiment was terminated following the initiation of accumulator injection and a demonstration of an increasing vessel liquid level with all core heater rods quenched.

(c) Test Results

The transient was initiated at time zero (system pressure 15.5 MPa) by opening a block valve downstream of the break assembly causing a flow of subcooled primary flow out the break. This initiated a rapid depressurization due to the steam bubble in the pressurizer expanding as mass exited the system. When the primary pressure reached 12.6 MPa several automatically-occurring events transpired that greatly affected the depressurization rate, most importantly core scram and MSIV closure. There was a rapid increase in primary depressurization associated with these automatically-occurring events. Core scram reduced heat input to the fluid while the secondary remained a heat sink relative to the primary even though the MSIV in both loops was closed. By achieving saturation conditions in the cold leg at about 40 seconds, the depressurization rate was retarded, which countered the energy lost in the break flow. HPIS was insignificant when compared to the break flow and is a trivial component of the overall energy balance controlling depressurization.

The liquid level in the U-tubes of steam generators followed an apparent top-down drain complicated by the change from forced circulation to natural circulation as the pump coasted down. There was an interruption of drain in the U-tubes of both loops that lead to a "holdup" of liquid in the tubes. Reference 8.2.5-3 states that there was a differential drain rate between the intact and broken loop that resulted in more fluid "holdup" in the broken loop compared to the intact loop. And it was possible that the intact loop primary tube water drained through the bottom of the hot leg piping into the top of relatively hot core causing an increase in steam generation. This extra steam generation could have caused the holdup of broken loop.

As liquid drained out of the loop, liquid seals were left in the pump suctions of both loops. These liquid seals caused a blockage of steam flow generated in the core around the loop to the break. As a result, the vessel upper plenum and hot legs were pressurized causing manometric depressions in both the vessel liquid level. Two things greatly affected the amount of core liquid level depression during the loop seal formation: a) the amount of bypass steam flow from the vessel upper head to the downcomer, and b) the amount of liquid held in the loops prior to the seal formation. In the Semiscale simulation, the loop seals were essentially cleared of liquid allowing a steam relief path to the break and a relaxation of the manometric balance of pressure heads throughout the loop. The consequence and significance of this relaxation of heads is that the vessel liquid level increased thus mitigating a core heat-up. The intact loop cleared first followed later by the broken loop.

Clearing of the seals in the both intact and broken loops tended to increase the depressurization rate. Seal clearing is related to break uncover of liquid. As long as a pump suction liquid seal exists, a liquid plug extends throughout the cold leg to the break thus supplying liquid to the break. As a seal clears, steam is allowed to the break causing an increase in volumetric flow out the break but a decrease in mass flow rate. With more steam out the break, the depressurization is increased.

8.2.5.4 M-RELAP5 Calculation Procedure

(a) M-RELAP5 Model of Semiscale

The Semiscale Mod-2C system is numerically represented by the noding diagram illustrated in **Figure 8.2.5-1**. The primary feature is that the system is nodalized with the same manner as for US-APWR SBLOCA calculations. The M-RELAP5 Semiscale Mod-2C model primarily

consists of the a) reactor vessel, b) downcomer pipe, c) pressurizer, d) steam generator, e) intact loop, f) broken loop, and g) ECCS.

[

1

HPIS and accumulator injections are explicitly simulated in the present model in the same manner as the plant calculation. The characteristics of these safety injections are listed in Table 5.2.2.5-3.

(b) Calculation Conditions

Initial conditions:

Table 8.2.5-1 summarizes initial conditions prior to the blowdown, where the M-RELAP5 results are compared with the measurements. The comparisons demonstrate that the model is capable of reproducing the experimental steady state.

Boundary conditions:

The core fission power and decay power history are given through the input data table for the present calculation.

The break flow is explicitly simulated by using the Moody critical flow model with the atmospheric outer boundary condition. [

1

The secondary system pressure behavior is also explicitly simulated by modeling the main steam isolation and steam relief valves with the imposed boundary condition for the feedwater flow following the reactor trip.

Assumptions for analysis:

The CCFL occurring in the vertical piping with a smaller diameter is taken into account for the calculation, specifically, the vertical part of the hot leg and SG U-tubes. The CCFL in the SG U-tubes is modeled by using the Wallis correlation (Ref. 8.2.5-5), where $\beta=0.0$, $c=0.88$, and $m=1.0$ are applied. This modeling is identical to that for the US-APWR plant calculation, because the geometric scaling of the SG U-tubes is almost identical between the Semiscale and US-APWR. [

1

8.2.5.5 M-RELAP5 Calculation Result

The chronology during the Semiscale S-LH-1 test is listed in Table 8.2.5-2, where the experimental and calculated results are compared. The transient calculation was initiated by opening the break valve, and the simulated break flow is compared with the measurement in Figure 8.2.5-2. Although the Moody critical flow model tends to overestimate the two-phase break flow, the result indicates that the model reasonably reproduces the measured data without excess conservatism.

The secondary system pressures for the intact and broken loops are also compared with the measurements in Figure 8.2.5-3. In the experiment, the steam leak occurred in the steam generator secondary system, resulting in that the secondary system pressure remained below the relief valve opening pressure setpoint even after the main steam isolation valve was closed.

[

Figure 8.2.5-4 shows the calculated and measured primary system pressure response. Overestimation in the secondary system pressure induces slightly higher calculated pressure in the primary system during the natural circulation phase from about 50 to 170 seconds.

Figures 8.2.5-5 through 8.2.5-11 show collapsed liquid levels. The approach used here is consistent with that used in Reference 8.2.5-1, where the calculated values were obtained by integrating liquid volume fraction distributions and the measured values were obtained from differential pressure measurements. Differences between the two methods affect the level comparisons before 90 s, when the pumps finish coasting down, because the measured differential pressures are affected by flow.

A complicated loop seal behavior was observed in the Semiscale S-LH-1 test, where the coolant seal in the intact loop cleared first and the broken loop seal cleared later. This loop seal behavior can be simulated by M-RELAP5 as shown in Figures 8.2.5-5 and 8.2.5-6, which demonstrate the code's ability to predict the loop seal behavior during SBLOCAs accurately. It is noted that M-RELAP5 predicts transient decrease in the collapsed liquid level for the broken loop crossover leg (Figure 8.2.5-6) as core liquid level depression (Figure 8.2.5-11) during the loop seal period, while not observed in the measurement. However, the resultant core liquid level depression predicted by M-RELAP5 is deeper than the measurement, indicating that conservative prediction with respect to the loop seal PCT (Table 8.2.5-3 and Figure 8.2.5-12).

A severe reflux flooding occurred in the hot leg piping and steam generator U-tubes in the S-LH-1 test, and the core liquid level was significantly depressed during the loop seal phase. This was primarily caused by the small core bypass flow fraction between the upper head and downcomer, which prevented the steam from venting from the core. This cause was experimentally validated by comparing the two tests, S-LH-1 (0.9% bypass) and S-LH-2 (3.0% bypass) of the Semiscale Program (Ref. 8.2.5-1). M-RELAP5 results are compared with the

measurements from Figures 8.2.5-7 to 8.2.5-11 in terms of the hot leg and steam generator U-tubes for the intact and broken loops, and the core liquid level, respectively. The severe flooding and core liquid depression can be well simulated by M-RELAP5.

As a result of the core liquid depression, the heater rod experienced the dryout and heat-up during the loop seal phase. This temperature excursion was terminated by an increase in the core liquid level after the loop seal cleared as shown in Figure 8.2.5-11. Histories of the measured and calculated heater rod surface temperature are compared in Figure 8.2.5-12 and the peak values are listed in Table 8.2.5-3. The difference between the calculated and measured cladding temperatures shown in Figure 8.2.5-12 prior to scram is caused by the comparison of a calculated surface temperature with a measured temperature inside the heater rod.

Since M-RELAP5 predicts a deeper core liquid level depression, the highest heater rod cladding temperature is obtained at the elevation of 5.7-ft while at the 8.3-ft elevation in the experiment. The chopped-cosine axial power shape was implemented in the heater rod (12-ft length), and therefore, M-RELAP5 conservatively obtained a higher peak cladding temperature than measured during the loop seal phase. M-RELAP5 provides a conservative prediction in terms of the heater rod temperature even for the elevation where the highest experimental temperature was measured.

In the experiment, the heater rod heat-up was terminated when the seal cleared in the intact loop. In the calculation, the heat-up was terminated when the intact loop seal cleared, but started again at a higher elevation due to a larger liquid level depression in the core. The second heat-up was terminated around 250 seconds, after the broken loop seal cleared.

8.2.5.6 Conclusions

The simulation of Semiscale S-LH-1 was performed by M-RELAP5. The results demonstrate that M-RELAP5 well predicts the complicated plant responses, including the significant fluid holdup in the hot leg and in the steam generator U-tubes, and the loop seal behaviors. In particular, the severe core depression and heater rod temperature excursion during the loop seal phase were well reproduced by M-RELAP5, resulting in a conservative prediction for the heater rod cladding surface temperature. It is concluded M-RELAP5 is sufficiently capable to predict important phenomena occurring in SBLOCAs.

8.2.5.7 References

- 8.2.5-1. G. G. Loomis and J. E. Streit, "Results of Semiscale Mod-2C Small-Break (5%) Loss-of-Coolant Accident Experiments S-LH-1 and S-LH-2," NUREG/CR-4438, EGG-2424, R2, November 1985.
- 8.2.5-2. W. W. Tingle, "Experiment Operating Specifications for Semiscale Mod-2A 5% Break Experiment S-UT-8," EGG-SEMI-5685, December 1981.
- 8.2.5-3. G. G. Loomis and J. E. Streit, "Quick Look Report for Semiscale Mod-2C Experiments S-LH-1 and S-LH-2," EGG-SEMI-6884, May 1985.
- 8.2.5-4. G. G. Loomis, "Experiment Operating Specification for Semiscale Mod-2C 5% Small Break Loss-of-Coolant Experiment S-LH-1," EGG-SEMI-6813, February 1985.
- 8.2.5-5. G. B. Wallis, "One Dimensional Two Phase Flow," McGraw-Hill, 1969.
- 8.2.5-6. H. T. Kim and J. C. No, "Assessment of RELAP5/MOD3.2.2y against flooding database in horizontal-to-inclined pipes," Annals of Nuclear Energy, Vol. 29, Issue 7, May 2002.

Table 8.2.5-1 Steady-State Parameter Checklist for Experiment S-LH-1

<u>Parameter</u>	<u>Experiment</u>	<u>M-RELAP5</u>
<u>Pressurizer pressure [MPa]</u>	<u>15.47 ± 0.14</u>	<u>15.47</u>
<u>Core ΔT</u>	<u>37.65 +1.5/-0.6</u>	<u>37.37</u>
<u>Intact loop flow rate [kg/s]</u>	<u>7.13</u>	<u>7.13</u>
<u>Broken loop flow rate [kg/s]</u>	<u>2.35</u>	<u>2.35</u>
<u>Intact loop cold leg temperature [K]</u>	<u>562.12 ± 2</u>	<u>562.09</u>
<u>Broken loop cold temperature [K]</u>	<u>564.05 ± 2</u>	<u>563.98</u>
<u>Intact loop Steam generator pressure [MPa]</u>	<u>5.72 ± 0.07</u>	<u>5.72</u>
<u>Broken loop Steam generator pressure [MPa]</u>	<u>6.08 ± 0.07</u>	<u>6.08</u>
<u>Pressurizer level [cm]</u>	<u>395 ± 14</u>	<u>394.85</u>
<u>Core bypass fraction [%]</u>	<u>0.9</u>	<u>0.9</u>
<u>Core power [kW]</u>	<u>2014.75 ± 0.15</u>	<u>2014.75</u>

Table 8.2.5-2 Primary Test Chronology for Experiment S-LH-1

<u>Event</u>	<u>Experiment (sec)</u>	<u>M-RELAP5 (sec)</u>
<u>Pressurizer at 12.6MPa (trip level)</u>	<u>14.67</u>	<u>15.03</u>
<u>Core scram</u>	<u>19.57</u>	<u>19.93</u>
<u>Pump coastdown initiated</u>		
<u>Intact loop</u>	<u>21.35</u>	<u>21.71</u>
<u>Broken loop</u>	<u>20.76</u>	<u>21.12</u>
<u>HPIS initiated</u>		
<u>Intact loop</u>	<u>41.60</u>	<u>40.65</u>
<u>Broken loop</u>	<u>40.98</u>	<u>40.65</u>
<u>Minimum core liquid level reached</u>	<u>172.6</u>	<u>163</u>
<u>Intact loop pump suction cleared</u>	<u>171.4</u>	<u>167</u>
<u>Broken loop pump suction cleared</u>	<u>262.3</u>	<u>213</u>

Table 8.2.5-3 Summary of PCTs during Loop Seal for Experiment S-LH-1

	<u>Time (s)</u>	<u>PCT (K)</u>
<u>Measured PCT</u>	<u>182.4</u>	<u>624.4</u>
<u>M-RELAP5</u>	<u>173.3</u>	<u>659.0</u>

Note: The peak temperature was measured at 8.3-ft elevation, while M-RELAP5 predicts the highest temperature at 5.7-ft elevation.

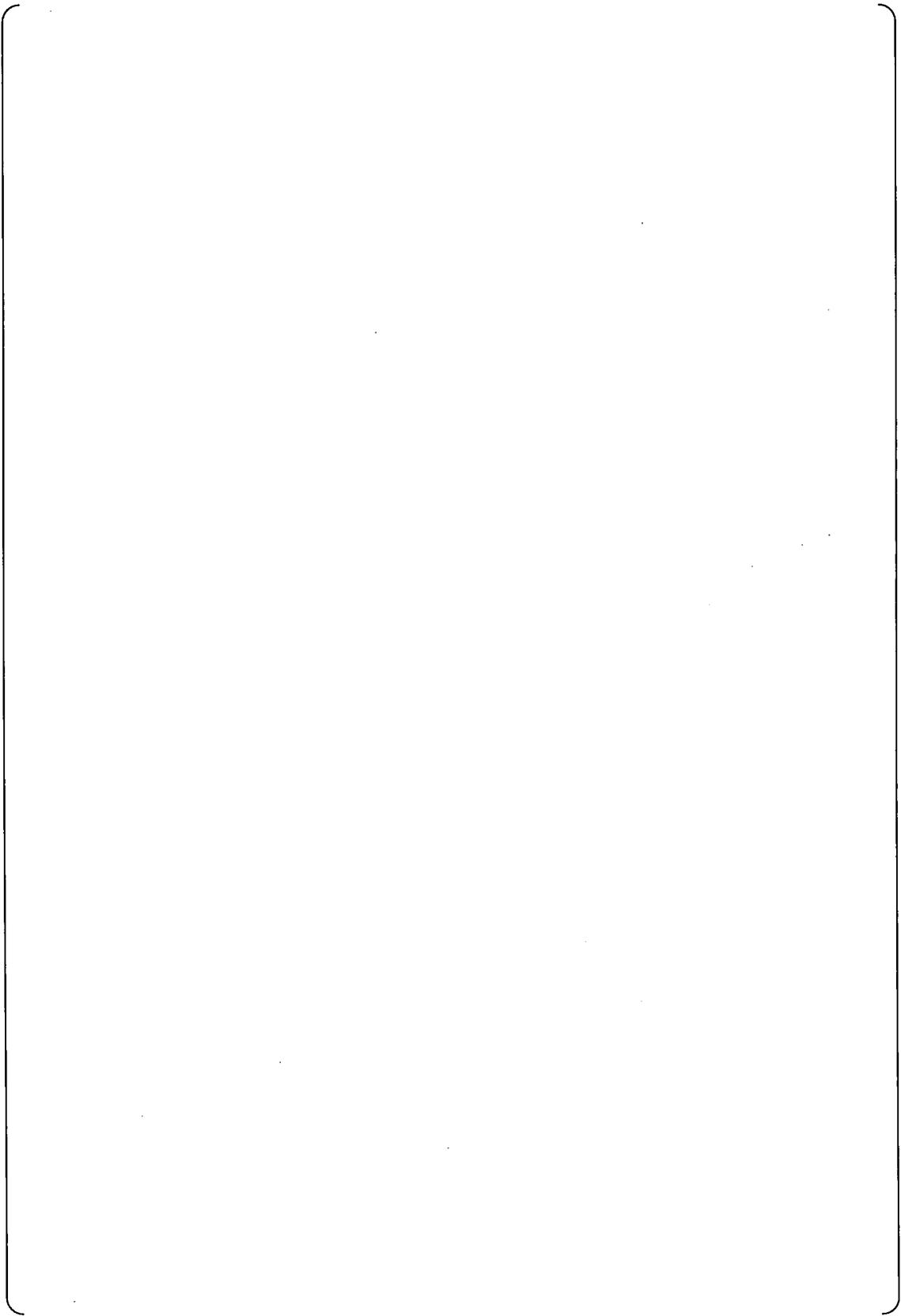


Figure 8.2.5-1 M-RELAP5 Noding Diagram for Semiscale S-LH-1

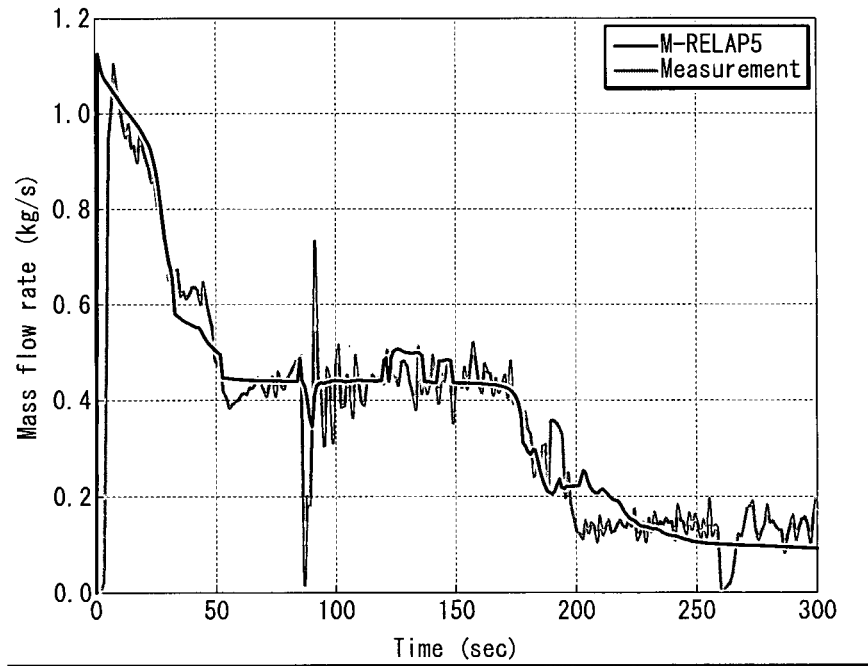


Figure 8.2.5-2 Break Flow Rate

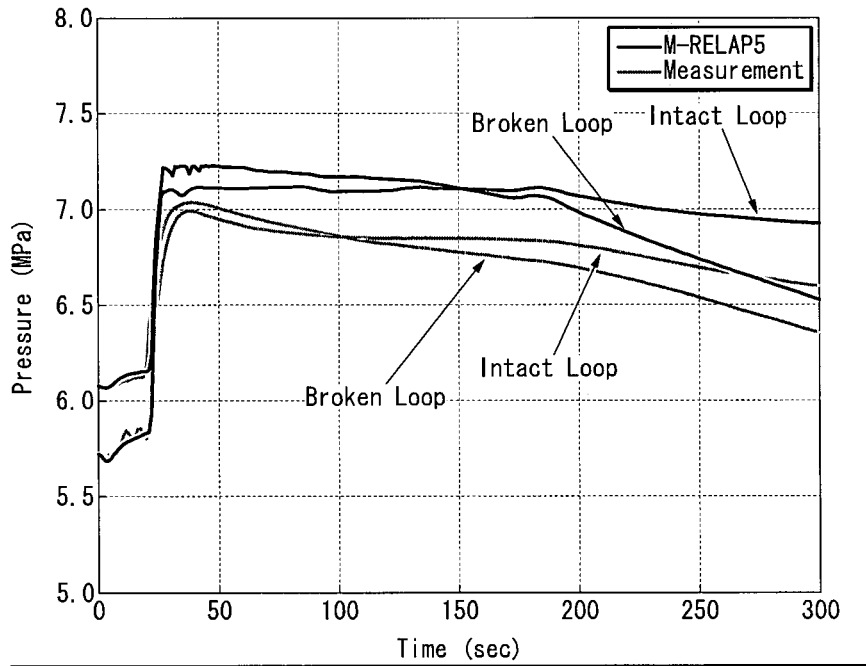


Figure 8.2.5-3 Secondary System Pressure

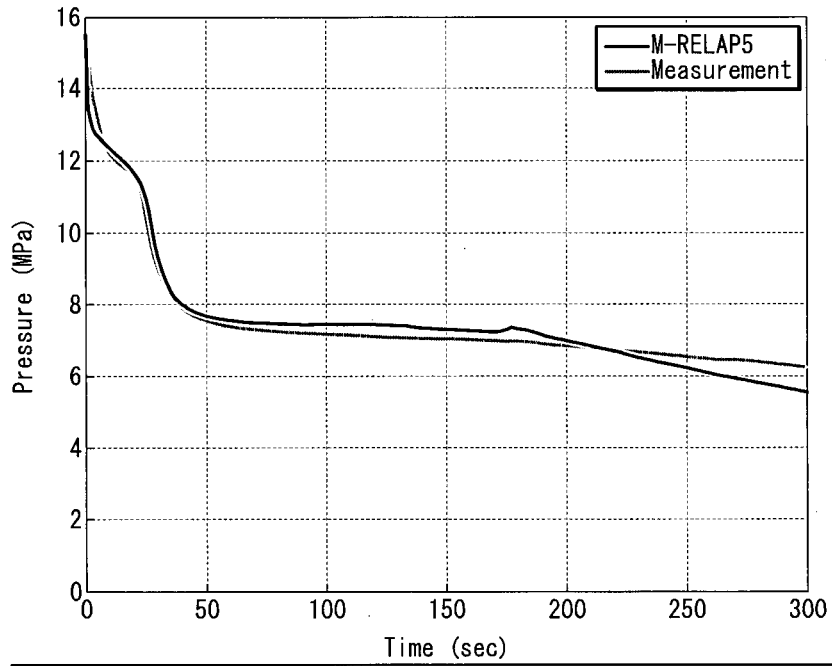


Figure 8.2.5-4 Primary System Pressure

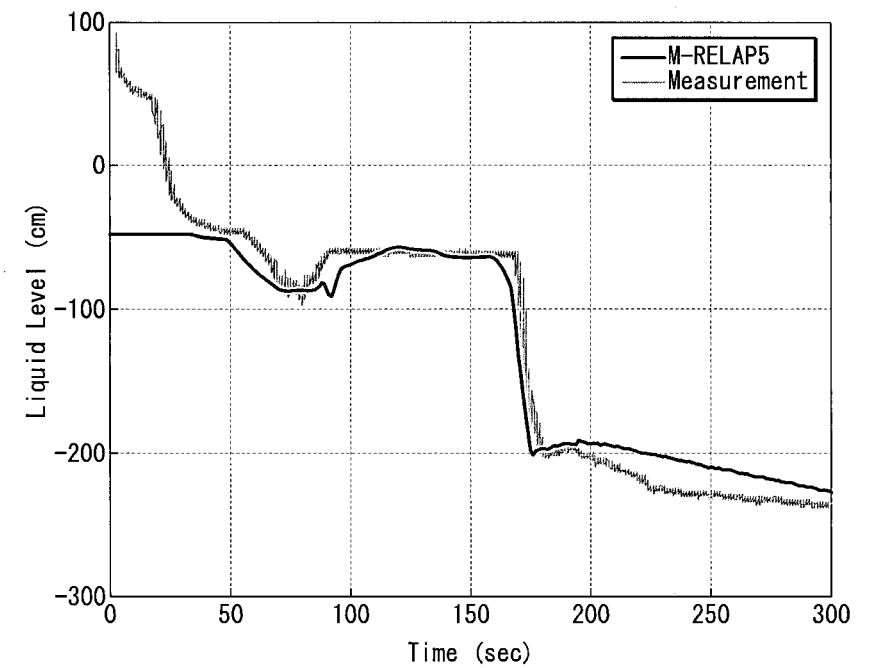


Figure 8.2.5-5 Collapsed Level in Uphill-Side of Intact Loop Crossover Leg

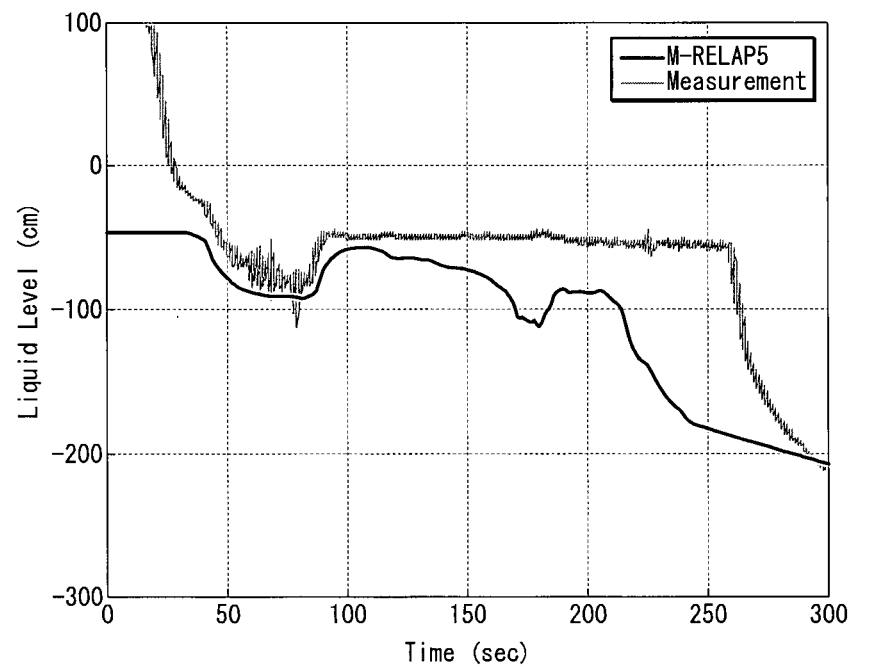


Figure 8.2.5-6 Collapsed Level in Uphill-Side of Broken Loop Crossover Leg

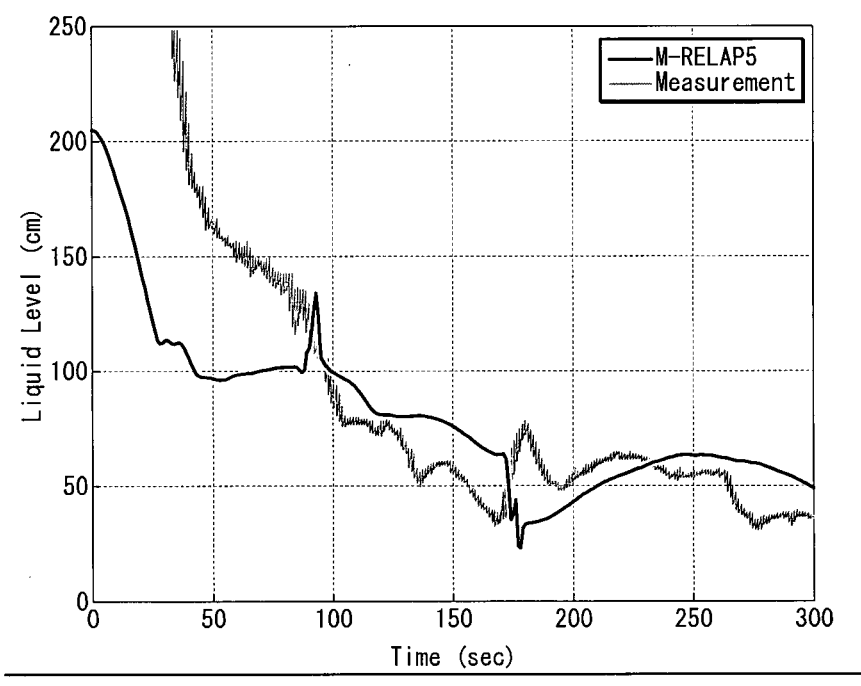


Figure 8.2.5-7 Collapsed Level in Intact Loop Hot Leg

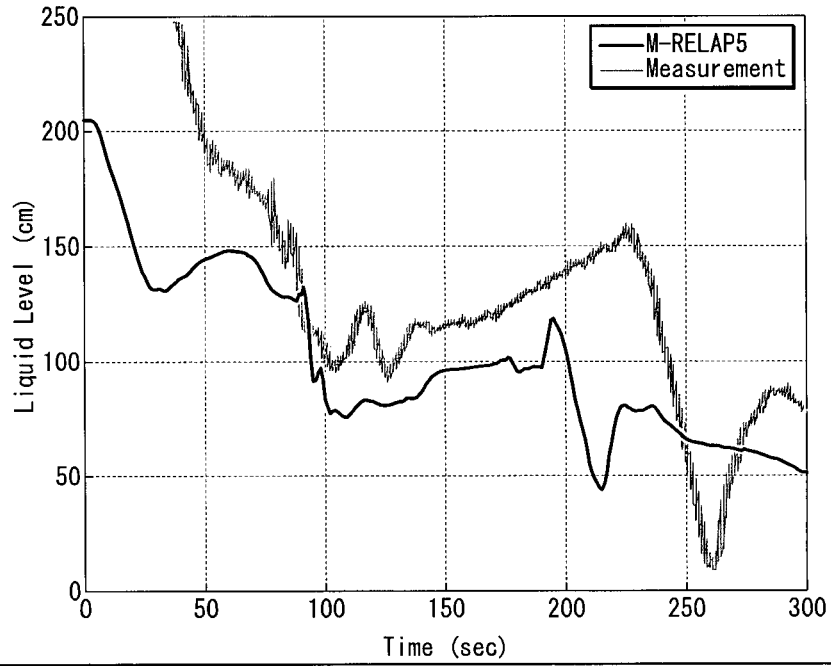


Figure 8.2.5-8 Collapsed Level in Broken Loop Hot Leg

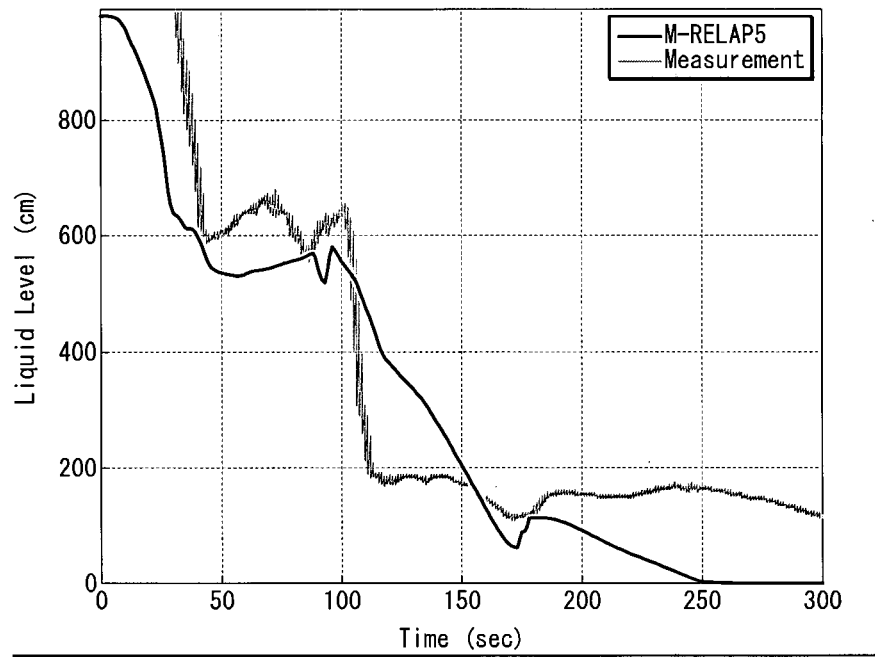


Figure 8.2.5-9 Collapsed Level in Uphill-Side of Intact Loop SG U-tubes

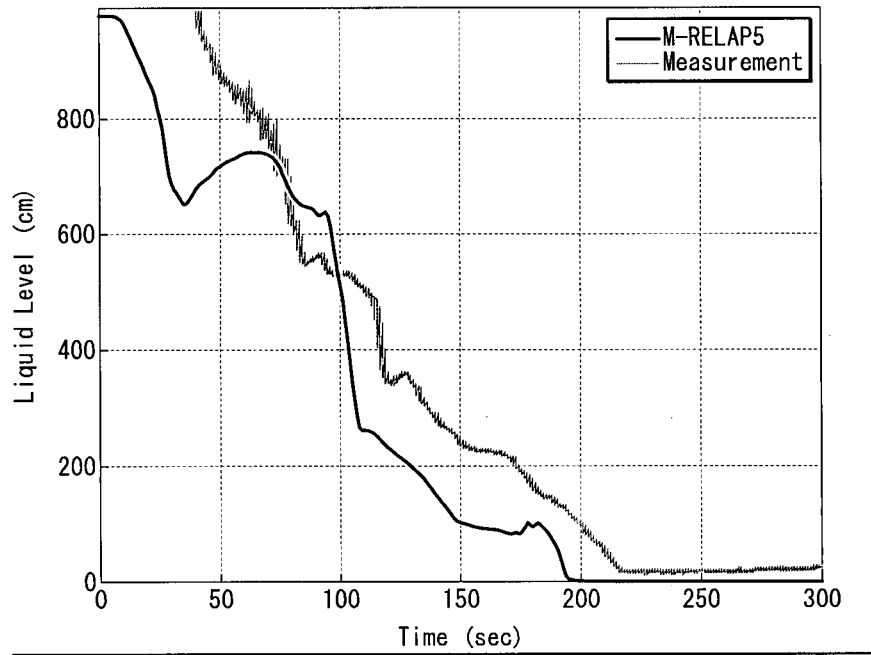


Figure 8.2.5-10 Collapsed Level in Uphill-Side of Broken Loop SG U-tubes

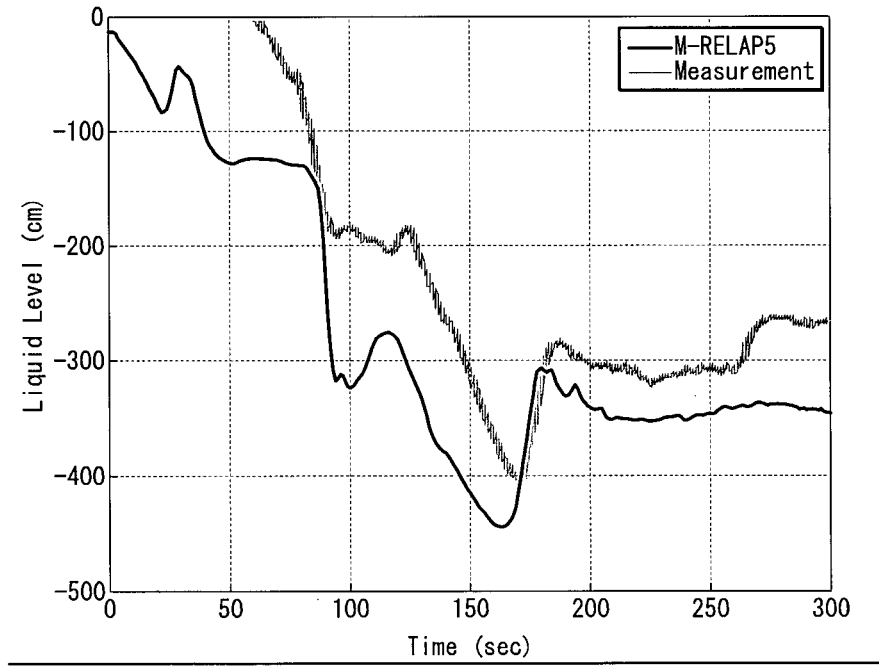


Figure 8.2.5-11 Core Collapsed Level

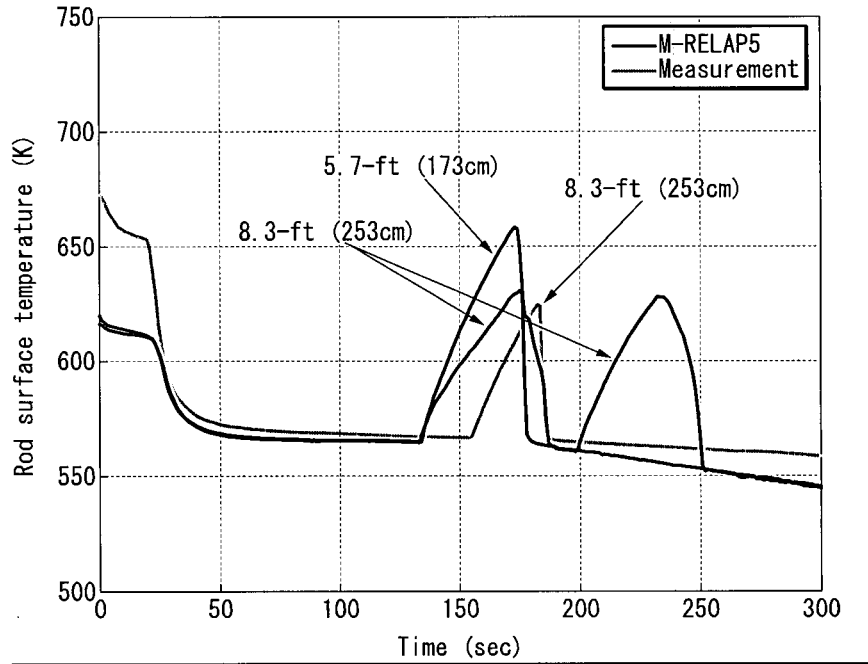


Figure 8.2.5-12 Heater Rod Cladding Temperature

8.3 Determine Capability of Field Equations to Represent Processes and Phenomena and Ability of Numeric Solution to Approximate Equation Set

8.3.1 The Field Equations Evaluation

The basic field equations for the two-fluid nonequilibrium model in M-RELAP5 consist of two phasic continuity equations, two phasic momentum equations, and two phasic energy equations. The phase change between the phases is calculated from the interfacial and wall heat and mass transfer models. In addition, the basic two-phase single-component model is extended to include a noncondensable component in the vapor/gas phase and a dissolved component in the liquid phase. State relationship equations and constitutive equations make up closure relations for the system of basic field equations. M-RELAP5 also has multidimensional fluid models besides 1-D models.

The modeling capabilities are required to calculate the transient phenomena of a small break LOCA as identified in the PIRT process described previously. The calculation capabilities of the phenomena shown in the PIRT depend on the system of equations composed of the basic field equations, state relationships and constitutive equations in M-RELAP5. The M-RELAP5 system of equations is applicable to the phenomena shown in the PIRT as follows.

8.3.1.1 Fuel Rod

1. Stored Energy / Initial stored energy:

The stored energy can be simulated with the heat structure model of M-RELAP5 using the appropriate material thermal properties, such as the heat capacity and thermal conductivity. Heat transfer to the both liquid and vapor phases is calculated by the wall heat transfer model included in the constitutive equation. The heat addition due to the heat transfer is taken into account as heat source terms in the phasic energy equations. Therefore, the field equations can properly account for the stored energy of the fuel rods and associated heat transfer to the vapor and liquid phases.

2. Core Kinetics, Reactor Trip (Fission Power):

The core power is calculated by the reactor kinetics model of M-RELAP5 with the appropriate core parameters. The core parameters include the reactivity curve at the reactor trip, doppler reactivity feedback, fuel temperature coefficient, moderator density coefficient, moderator temperature coefficient and boron reactivity. The core power is one of the heat sources in the

heat conduction equation. Fuel rod heat conduction is calculated with the heat structure model. The heat inputs due to core power are taken into account as heat source terms in the phasic energy equations via the wall heat transfer. Therefore, the field equations take into account fission power including any transients associated with reactor trip.

3. Decay heat:

Decay heat is calculated by the reactor kinetics model of M-RELAP5. The decay heat is one of the heat sources in the heat conduction equation. Heat conduction in the fuel rod is calculated with the heat structure model similar to the case of the fission power. The heat inputs due to decay power are taken into account as heat source terms in the phasic energy equations via the wall heat transfer. Therefore, the field equations take into account decay heat. The decay heat is ranked as high in the PIRT. The conservative nature of the decay heat calculation is ensured using 1.2 times the ANS-1971 standard as specified in Appendix K and as noted in Section 8.

4. Oxidation of Cladding:

The heat generation due to cladding oxidation is taken into account as a heat source in the heat conduction equation. Therefore, it is taken into account as a heat source terms in the phasic energy equations via the wall heat transfer model. The associated production of hydrogen is also considered in the noncondensable portion of the field equations.

5. Cladding Deformation (Creep / Burst):

In M-RELAP5, the cladding deformation is calculated with the heat structure model depending on the fuel rod internal gas pressure, reactor coolant system pressure, cladding burst temperature, and the cladding elastic and plastic strain limits. Then, in the basic field equations, the cladding deformation is modeled as a flow area change determined by the amount of deformation. Because the flow area is a parameter included in the field equations, the field equations are capable to simulate the effect of the cladding deformation.

6. Gap conductance:

Gap conductance is incorporated as a part of the heat structure model, considering the deformation of the fuel rod cladding and the thermal properties of the enclosed gas. The gap conductance model is modeled as a change of the thermal conductivity of the heat structural material in the heat conduction equation, and is taken into account as heat source terms in the phasic energy equations via the wall heat transfer model. Therefore, the field equations are capable to simulate the change of heat inputs by the gap conductance.

7. Local power:

The local power is modeled as the power distribution of the fuel rod in the axial direction and radial direction, which is defined by the input of the heat structure model. The effect on the fluid is simulated through the use of appropriate input to the heat structure model as well as associated heat transfer into the liquid and vapor phases by the wall heat transfer model. In order to simulate the distribution, a nodalization on the hydrodynamic component is required to correspond to the power distribution in the axial direction. The local power is ranked as high in the PIRT. The conservative evaluation of the local power is ensured by setting the peaking factor of the maximum power through appropriate input according to Appendix K.

8.3.1.2 Core**8. Heat transfer below the mixture level:**

Heat transfer below the mixture level can be calculated with the wall heat transfer model based on the various conditions of the core such as pressure, flow rate, wall temperature, and so on. The vapor generation rate is calculated from the interfacial and wall heat and mass transfer models. Therefore, M-RELAP5 field equations can properly account for the heat transfer below the mixture level.

8. CHF/Dryout:

In M-RELAP5, CHF is calculated with the wall heat transfer model based on the flow and structural wall conditions. The M-RELAP5 thermal-hydraulic model solves the properties such as phasic densities, phasic energies or temperatures, phasic mass flux, and so on. Using these properties, the CHF calculation is carried out with the wall heat transfer model. Because the field equations of M-RELAP5 can treat thermal nonequilibrium conditions between liquid and vapor, not only a single phase superheated vapor but also a superheated vapor in a two-phase state can be simulated. By the use of the RELAP5 flow regime map in combination with the appropriate interfacial heat transfer, the dryout can be calculated for corresponding flow regime and vapor properties. The dryout is ranked as high in the PIRT. The predictive capability of M-RELAP5 has been validated by analyzing ORNL/THTF void profile test and ORNL/THTF uncovered heat transfer test as SETs. The ROSA-IV/LSTF small break (5%) LOCA test has been used for the IET validation.

10. Uncovered Core Heat Transfer:

The uncovered core heat transfer is calculated with the wall heat transfer model based on the

flow and structural wall conditions. The flow and heat transfer conditions in the uncovered portion of the core is characterized by the superheated vapor and the flow regimes. As to the former, because the field equations of M-RELAP5 can treat thermal nonequilibrium between liquid and vapor, M-RELAP5 can calculate not only single phase superheated vapor but also superheated vapor in a two-phase state. As to the latter, the flow regimes in Post-CHF include inverted annular flow regime, inverted slug flow regime and mist flow regime so the flow and heat transfer in Post-CHF can be appropriately simulated. The uncovered core heat transfer is ranked as high in the PIRT. The modeling capability of M-RELAP5 has been validated by analyzing the (a) ORNL/THTF void profile, (b) ORNL/THTF uncovered heat transfer, and (c) ORNL/THTF reflood tests as SETs. The ROSA-IV/LSTF small break (5%) LOCA test has been used for the IET validation.

11. Rewet (Heat Transfer Recovery):

For the simulation of rewet, it is required to simulate the two-phase flow behavior in the core such as inflow at the core inlet, water droplets and reversal liquid flow at the core outlet. The inflow at the core inlet is driven by the pressure balance between the head in downcomer and the flow resistance through the core, which is taken into account in the momentum equations. The water droplets are modeled in mist flow regime and annular flow regime, which are determined by flow regime map, and the motion of droplets is calculated with the momentum equations. The reversal liquid flow is counter current flow against the vapor upward flow. The counter current flow can be simulated with the two-fluid nonequilibrium field equations using interfacial friction corresponding to the flow regime. After the distribution of liquid in the core is determined, the wall heat transfer model is capable to model the adequate heat transfer mode corresponding to the flow and fuel rod surface condition. Therefore, the rewet behavior can be simulated by the field equations system. The rewet is ranked as high in the PIRT. The modeling capability of M-RELAP5 has been validated by analyzing ORNL/THTF Reflood test as a SET and ROSA-IV/LSTF small break (5%) LOCA test as an IET.

12. Entrainment / De-entrainment:

M-RELAP5 can model the droplets in vapor flow using the flow regimes and the entrainment correlation equation. The effect of droplet entrainment is calculated based on interfacial friction and interfacial heat transfer. The field equations do not have an independent model for droplets; their velocities are defined as those of liquid phase.

13. 3-D Flow:

Because M-RELAP5 has multidimensional fluid models besides 1-D models, the influence of

the 3-D flow distribution can be determined where appropriate by simulating the 3D flow and heat transfer. In addition, the influence of the 3-D flow distribution can be simulated in a conservative manner by the use of a hot channel model and 1D flow and heat transfer models.

14. Mixture Level:

The M-RELAP5 two-fluid nonequilibrium field equations track the liquid and vapor separately, allowing the formation of the appropriate liquid and mixture levels in the core. The two phase regions, and thus the height of the mixture level in the core, are determined from the interface and wall mass, momentum, and energy transfer constitutive models. The resulting mixture level can be refined using the M-RELAP5 mixture level tracking model. The mixture level tracking model is applied through user input when a water level is formed by gravity.

The mixture level is ranked as high in the PIRT. The modeling capability of M-RELAP5 has been validated by analyzing ORNL/THTF void profile test and ROSA-IV/LSTF void profile test as SETs. The ROSA-IV/LSTF small break (5%) LOCA test has been used for the IET validation.

15. Flow resistance:

The wall friction term and form loss term are taken into account in the phasic momentum equation. The wall friction in two-phase flow is calculated with the two-phase friction multipliers, and it is distributed into liquid and vapor phase using the Lockhart-Martinelli parameter.

16. 3-D Power Distribution:

The spatial power distribution in the core is defined as the input of the axial power distribution and radial power distribution for the heat structure model. Therefore, the effect on the liquid and vapor is modeled using the appropriate input to the heat structure models in combination with the calculation of heat transfer via the wall heat transfer model. Because M-RELAP5 has multidimensional fluid models besides 1-D models, the influence of the 3-D power distribution can be determined where appropriate by simulating the 3D flow and heat transfer. In addition, the influence of the 3-D power distribution can be simulated in a conservative manner by the use of a hot channel model and 1D flow and heat transfer models. The 3-D power distribution is ranked as high in the PIRT. The conservative evaluation is ensured by setting the peaking factor of the maximum power according to Appendix K.

17. Top Nozzle / Tie Plate CCFL:

The two-fluid nonequilibrium field equations of M-RELAP5 can simulate a liquid/vapor counter

flow, since the flows of liquid and vapor are determined separately through the two fluid model. Therefore, liquid drainage against an upward flow of vapor can be simulated. In addition, M-RELAP5 can simulate the phenomenon in which the steam generated in the core prevents the counter current drainage from the upper plenum, because Counter-Current Flow Limitations (CCFL) model is taken into account in the phasic momentum equations.

8.3.1.3 Neutron Reflector

18. Steam and Droplet Generation in Flow Holes:

Steam and droplets may be generated in the flow holes of the neutron reflector due to boiling caused by heat input into the coolant from the reflector. The heat input from the reflector is calculated as heat transfer to each phase with the wall heat transfer model included in the constitutive equation. Because the heat transfer to each phase is taken into account as heat source terms in the phasic energy equations, the field equations can simulate the heat input from the reflector. In addition, the droplets in vapor flow can be modeled using the flow regime map, the entrainment correlation, and associated momentum equations.

19. Water Storage and Boiling in Back Region:

Water storage and boiling in back region can be simulated by modeling the region as a channel. A flow in the channel can be simulated with the field equations.

20. Heat Transfer between Back Region and Core Barrel:

Heat transfer between back region and the core barrel can be simulated by modeling with heat structure model. Energy exchange with fluid is simulated with the wall heat transfer model. The resulting heat transfer is included as heat source terms in the phasic energy equations. Therefore, the field equations are capable to simulate the change of energy as heat input.

21. Core Bypass Flow:

Core bypass flow can be simulated by modeling the region as a channel. The flow in the channel can be simulated with the field equations.

8.3.1.4 Upper Head

22. Drainage to Core / Initial Fluid Temperature:

Initial fluid temperature in the upper head is determined by a balance of inflow of low temperature coolant from the downcomer, inflow of high temperature coolant from the center

part of the upper plenum, and outflow of mixed coolant to the peripheral part of the upper plenum. Because the flow of each channel depends on the pressure difference and flow resistance between upstream and downstream, it can be simulated with the field equations of M-RELAP5. The flow mixing at the upper plenum can be also simulated with the field equations. Therefore, the field equations are capable to simulate the fluid initial temperature in the upper head.

23. Bypass Flow between Upper Head and Downcomer (Cold Leg):

The bypass path between the downcomer and upper head becomes an alternative steam flow path connecting the cold leg and the hot leg during the loop seal clearing period. Thus, the flow resistance of the path affects the core mixture level depression. Because the field equations take into account the flow resistance for single phase or two phase flow, the flow resistance at the upper head bypass can be simulated with appropriate input values.

24. Metal Heat Release:

Metal heat release is taken into account as a heat source term in the phasic energy equations via the wall heat transfer model. Therefore, the field equations are capable to simulate the effect of heat input from the vessel wall and structure.

8.3.1.5 Upper Plenum

25. Mixture Level:

The M-RELAP5 two-fluid nonequilibrium field equations track the liquid and vapor separately, allowing the formation of the appropriate liquid and mixture levels in the upper plenum. ~~The two phase regions, and thus the height of the mixture level in the upper plenum, are determined from the interface and wall mass, momentum, and energy transfer constitutive models. The resulting mixture level can be refined using the M-RELAP5 mixture level tracking model. The mixture level tracking model is applied through user input when a water level is formed by gravity.~~ Although M-RELAP5 has a level tracking model that can determine the location of a mixture level within a control volume, the model is not used in the US-APWR SBLOCA calculations because an adequate representation of the void fraction distribution can be obtained using an appropriate number of control volumes.

26. Drainage to Core:

During the period of loop seal clearing, drainage is possible but the steam generated in the core may limit the liquid draining from the upper plenum. The two-fluid nonequilibrium field

equations of M-RELAP5 can simulate a liquid/vapor counter flow, since the flows of liquid and vapor are calculated separately. Therefore, liquid drainage against an upward flow of vapor can be simulated. In addition, M-RELAP5 can simulate the phenomenon which the steam generated in the core prevents the counter current drainage from the upper plenum, because Counter-Current Flow Limitations (CCFL) model is taken into account in the phasic momentum equations.

27. Entrainment / De-entrainment:

M-RELAP5 can model the droplets in vapor flow using the flow regimes and the entrainment correlation equation. The effect of droplet entrainment is calculated based on interfacial friction and interfacial heat transfer. The field equations do not have an independent model for droplets; their velocities are defined as those of liquid phase.

28. Bypass Flow / Hot Leg – Downcomer Gap:

A leak path between hot leg nozzles and the downcomer upper region becomes a steam flow path connecting the cold leg and the hot leg during the loop seal clearing period. Thus, the flow resistance of the path affects the core mixture level depression. Because the field equations take into account the flow resistance for single phase or two phase flow, the flow resistance at the leak path can be simulated with appropriate input values.

29. Metal Heat Release:

Metal heat release is taken into account as heat source terms in the phasic energy equations via the wall heat transfer model. Therefore, the field equations are capable to simulate the effect of heat input from the structure.

8.3.1.6 Hot Leg**30. Horizontal Stratification / Counter-flow:**

The stratified flow regime is determined by the horizontal flow regime map. Interfacial friction for the stratified flow is calculated according to the flow condition. In addition, the two-fluid nonequilibrium field equations of M-RELAP5 can simulate a liquid/vapor counter flow according to the interfacial friction, since the flows of liquid and vapor are calculated separately. Therefore, the field equations allow either the vapor to slip from the upper plenum into the SGs or counter current flow in reflux cooling condition.

31. Entrainment / De-entrainment:

M-RELAP5 can model the droplets in vapor flow using the flow regimes and the entrainment correlation equation. The effect of droplet entrainment is calculated based on interfacial friction and interfacial heat transfer. The field equations do not have an independent model for droplets; their velocities are defined as that of liquid phase.

32. Metal Heat Release:

Metal heat release is taken into account as heat source terms in the phasic energy equations via the wall heat transfer model. Therefore, the field equations are capable to simulate the effect of heat input from the piping.

8.3.1.7 Pressurizer and Surge Line

33. Mixture Level:

The M-RELAP5 two-fluid nonequilibrium field equations track the liquid and vapor separately, allowing the formation of the appropriate liquid and mixture levels in the pressurizer. ~~The two phase regions, and thus the height of the mixture level in the pressurizer, are determined from the interface and wall mass, momentum, and energy transfer constitutive models. The resulting mixture level can be refined using the M-RELAP5 mixture level tracking model. The mixture level tracking model is applied through user input when a water level is formed by gravity.~~ Although M-RELAP5 has a level tracking model that can determine the location of a mixture level within a control volume, the model is not used in the US-APWR SBLOCA calculations because an adequate representation of the void fraction distribution can be obtained using an appropriate number of control volumes.

34. Out-Surge by Depressurization:

The discharge flow to the hot leg depends on the pressure difference between the pressurizer and the hot leg. The discharge flow, including the effect of the pressure difference, inertia and flow resistance, is taken into account with the field equations.

35. Metal Heat Release / Heater:

Metal heat release and heat input by heater are taken into account as heat source terms in the phasic energy equations via the wall heat transfer model. Therefore, the field equations are capable to simulate the effect of heat input from the pressurizer wall and the heater.

36. Location / Proximity to the Break:

The behavior of coolant flowing out from the pressurizer to the hot leg is calculated with the field

equations according to the flow path. Because the location of pressurizer determines the connection of flow path, the effect of location of the pressurizer can be modeled.

8.3.1.8 Steam Generator

37. Water Hold-Up in SG Inlet Plenum:

Liquid holdup in SG inlet plenum, including the inclined pipes from the hot legs, is caused by a Counter-Current Flow Limitations (CCFL) in this region. The two-fluid nonequilibrium field equations of M-RELAP5 can simulate a liquid/vapor counter flow, since the flows of liquid and vapor are calculated separately. Therefore, the field equations are capable to simulate the liquid flow return to the upper plenum from the SG inlet plenum against the vapor flow. In addition, M-RELAP5 can simulate a liquid holdup caused by a CCFL, which the steam flow prevents the counter current drainage from the SG inlet plenum, because CCFL model is taken into account in the phasic momentum equations. Once liquid holdup occurs, the core mixture level depression is calculated according to the pressure balance between the head caused by the liquid holdup in SG inlet plenum and the head caused by downcomer mixture, since the phasic momentum equations take into account the head. The liquid holdup in SG inlet plenum is ranked as high in the PIRT. The applicability of M-RELAP5 has been validated by analyzing UPTF SG plenum CCFL test as an SET and ROSA-IV/LSTF small break (5%) LOCA test as an IET.

38. Water Hold-up in U-Tube Uphill Side:

Liquid holdup on the primary side of the SG tubes is caused by a CCFL in the U-tubes. The two-fluid nonequilibrium field equations of M-RELAP5 can simulate a liquid/vapor counter flow, since the flows of liquid and vapor are calculated separately. Therefore, the field equations are capable to simulate the liquid flow return to the SG inlet plenum from the U-tube uphill side against the vapor flow. In addition, M-RELAP5 can simulate a liquid holdup caused by a CCFL, which the steam flow prevents the counter current drainage from the U-tube, because CCFL model is taken into account in the phasic momentum equations. Once liquid holdup occurs, the core mixture level depression is calculated according to the pressure balance between the head caused by the liquid holdup in U-Tube uphill side and the head caused by downcomer mixture, since the phasic momentum equations take into account the head. The liquid holdup in U-Tube uphill side is ranked as high in the PIRT. The applicability of M-RELAP5 has been validated by analyzing Dukler Air-Water Flooding test as a SET and ROSA-IV/LSTF small break (5%) LOCA test as an IET.

39. Primary side Heat Transfer:

Heat transfer at the U-tube is modeled as an energy exchange between the primary side and the secondary side with the heat structure model bounded by both sides. The heat transfer from the U-tube to the liquid and vapor is calculated with the wall heat transfer model included in the constitutive equation. Because the heat transfers to the each phase are taken into account as heat source terms in the phasic energy equations, the field equations are capable to simulate the primary side heat transfer. The primary side heat transfer is ranked as high in the PIRT. The applicability of M-RELAP5 has been validated by analyzing the ROSA-IV/LSTF small break (5%) LOCA test as an IET.

40. Secondary side heat transfer (Water Level):

Heat transfer at the U-tube is modeled as an energy exchange between the primary side and the secondary side with the heat structure model bounded by both sides. The heat transfer from the U-tube to the liquid and vapor is calculated with the wall heat transfer model included in the constitutive equation. Because the heat transfers to the each phase are taken into account as heat source terms in the phasic energy equations, the field equations are capable to simulate the secondary side heat transfer. The secondary side heat transfer is ranked as high in the PIRT. The applicability of M-RELAP5 has been validated by analyzing the ROSA-IV/LSTF small break (5%) LOCA test as an IET.

41. Metal heat release:

Metal heat release is taken into account as a heat source term in the phasic energy equations via the wall heat transfer model. Therefore, the field equations are capable to simulate the effect of heat input from the steam generator wall and structure.

42. Multi-U-tube Behavior:

In order to simulate multiple U-tubes, a modeling capability of branch flow paths is required to model the multiple flow paths from the SG plenum to U-tubes. M-RELAP5 has a flexible modeling capability for branch flow paths to simulate multiple U-tubes. For the US-APWR SBLOCA safety analysis, however, the SG U-tube flow behavior is modeled with a single flow path.

43. Auxiliary Feed Water Flow:

Injection characteristics and enthalpy of the AFW can be modeled with the combination of the time-dependent junction component and time-dependent volume component. The injection characteristics can be modeled with a table of flow rate as a function of pressure on the

downstream side of the injection point using the time-dependent junction. The injection enthalpy is modeled with a table of enthalpy as a function of time or integral of the injection flow rate using the time-dependent volume component. The injection flow rate and injection enthalpy modeled with these components are treated as boundary conditions of the field equations, and can be simulated as changes of mass, momentum and energy.

8.3.1.9 Crossover Leg

44. Water Level in SG Outlet Piping:

The field equations determine the distribution of liquid and vapor in the primary coolant system. Because the field equations of M-RELAP5 treat liquid and vapor separately, they are capable to simulate the distribution of liquid and vapor in the primary coolant system. Therefore they are capable to calculate the amount of water in SG outlet piping as an initial condition of a loop seal formation. The water level in SG outlet piping is ranked as high in the PIRT. The ROSA-IV/LSTF small break (5%) LOCA test has been used as an IET validation.

45. Loop Seal Formation and Clearance (Entrainment/Flow regime/Interfacial drag/Flow resistance):

A loop seal forms when the two phase natural circulation loop flow is not sufficient to carry the steam down through the pump suction piping. The M-RELAP5 two-fluid nonequilibrium field equations track the liquid and vapor separately, allowing the formation of the appropriate liquid and mixture levels in the loop seal. ~~The two phase regions, and thus the height of the mixture level in the loop seal, are determined from the interface and wall mass, momentum, and energy transfer constitutive models. The resulting mixture level can be refined using the M RELAP5 mixture level tracking model. The mixture level tracking model is applied through user input when a water level is formed by gravity.~~ Accurate predictions of the water head and the void distribution are required in evaluating the loop seal behavior. Accurate predictions of both can be accomplished by dividing the region into an appropriate of control volumes.

After the loop seal forms, the core mixture level depression is calculated according to the pressure balance between the head in the crossover leg and the head in the downcomer mixture. The loop seal clears when the liquid level in the crossover leg becomes lower, because the vapor flows into the lowermost part of the crossover leg and the liquid is carried by vapor to the pump side. The field equations of M-RELAP5 consider the momentum exchange between liquid and vapor phases based on interfacial friction and describe the carry over of liquid by high velocity vapor flow. In addition, interfacial friction is calculated appropriately for

horizontal stratified flow regime or annular mist flow regime, which is determined by flow regime map. Therefore, the field equations are capable to simulate the loop seal clearing. After the loop seal clearing, the head in the crossover leg is lost and the core mixture level increased through the pressure adjustment described by the field equations.

The loop seal formation and clearance is ranked as high in the PIRT. The modeling capability of M-RELAP5 has been validated by analyzing ROSA-IV/LSTF small break (5%) LOCA test as an IET.

46. Metal Heat Release:

Metal heat release is taken into account as heat source terms in the phasic energy equations via the wall heat transfer model. Therefore, the field equations are capable to simulate the effect of heat input from the piping.

8.3.1.10 RCP

47. Coastdown Performance:

The coastdown performance of the RCPs is modeled with angular momentum equation included in the pump component model. The phasic momentum equations take into account the pump head as a change of head term.

48. Two-phase Flow Performance:

The two-phase flow performance of the RCPs is modeled as the degradation of pump performance in two-phase state included in the pump component model. The phasic momentum equations take into account the pump head as a change of head term.

49. Reversal Flow of ECC Water:

Reversal flow of ECC water to the RCP suction pipes could interfere with the steam flow toward the break and reduce the core liquid level. The two-fluid nonequilibrium field equations of M-RELAP5 can simulate a liquid/vapor counter flow according to the interfacial friction, since the flows of liquid and vapor are calculated separately. Therefore, the field equations are capable to simulate the reversal liquid flow to the RCP against the vapor flow. [

]

50. Metal heat release:

Metal heat release is taken into account as heat source terms in the phasic energy equations via the wall heat transfer model. Therefore, the field equations are capable to simulate the effect of heat input from the pump structure.

8.3.1.11 Cold Leg**51. Stratified Flow:**

The stratified flow regime is determined by the horizontal flow regime map and interfacial friction for the stratified flow is calculated according to the flow condition. In addition, the two-fluid nonequilibrium field equations of M-RELAP5 can simulate a liquid/vapor counter flow according to the interfacial friction, since the flows of liquid and vapor are calculated separately. Therefore, the field equations allow either the co-current flow or counter current flow at the stratified flow condition.

52. Condensation by ACC water:

M-RELAP5 uses a combination of wall and interfacial heat and mass transfer constitutive equations to model the phase change by the evaporation/condensation. Using these equations, the phase change terms are calculated, which are included in the phasic continuity equations, phasic momentum equations and phasic energy equations. The heat transfer from vapor phase to ACC water in the cold leg is simulated with the interfacial heat transfer model. The condensation is determined from the interfacial mass and heat transfer models.

53. Non-condensable Gas Effect:

The nitrogen gas is not injected into the primary system until the accumulator injection almost terminates. In the field equations of M-RELAP5, the mass conservation equation of noncondensable gas in vapor phase is included in the basic field equations. Thus, behavior of noncondensable gas can be simulated. The presence of noncondensable gases is also taken into account in the state equations and constitutive models.

54. Metal heat release:

Metal heat release is taken into account as a heat source term in the phasic energy equations via the wall heat transfer model. Therefore, the field equations are capable to simulate the effect of heat input from the piping.

8.3.1.12 Accumulator

55. Large Flow Injection/Flow Resistance:

The injection rate of the advanced accumulator is controlled with a flow damper. The advanced accumulator model incorporated in M-RELAP5 enables the code to model the characteristics of the flow damper. Because the flow resistance of the flow damper is added to the loss terms in the phasic momentum equations, the injection can be appropriately simulated.

56. Small Flow Injection/Flow Resistance:

As discussed in the preceding section, because the flow resistance of the flow damper is added to the loss terms in the phasic momentum equations, the injection can be appropriately simulated.

57. Interfacial Heat Transfer:

The accumulator component model of M-RELAP5 is capable to model the interfacial heat transfer between nitrogen gas and liquid. Therefore, the enthalpy of injection water and the pressure of nitrogen gas are appropriately simulated, and the effect on the injection rate can be simulated with the field equations.

58. Metal heat release:

The accumulator component model of M-RELAP5 is capable to model the heat transfer between liquid and the tank wall. Therefore, the enthalpy of injection water and pressure of nitrogen gas are appropriately simulated, and the effect on the injection rate can be simulated with the field equations. In addition, because heat transfer with the tank wall can be set to be zero (adiabatic conditions) as an option, the injection rate could be conservatively evaluated.

59. Injection of Nitrogen gas Effects:

Non-condensable gas effect might affect when accumulator nitrogen cover gas is discharged into the RCS. In the field equations of M-RELAP5, the mass conservation equation of noncondensable gas in vapor phase is included in the basic field equations. Thus, behavior of noncondensable gas can be simulated. The presence of noncondensable gases is also taken into account in the state equations and constitutive models.

8.3.1.13 Downcomer / Lower Plenum**60. Mixture Level/Void Distribution:**

The M-RELAP5 two-fluid nonequilibrium field equations track the liquid and vapor separately,

allowing the formation of the appropriate liquid and mixture levels in the downcomer and lower plenum. ~~The two phase regions, and thus the height of the mixture level in the downcomer and lower plenum, are determined from the interface and wall mass, momentum, and energy transfer constitutive models. The resulting mixture level can be refined using the M-RELAP5 mixture level tracking model. The mixture level tracking model is applied through user input when a water level is formed by gravity. Although M-RELAP5 has a level tracking model that can determine the location of a mixture level within a control volume, the model is not used in the US-APWR SBLOCA calculations because an adequate representation of the void fraction distribution can be obtained using an appropriate number of control volumes.~~

The flashing or condensation in the downcomer region is determined from the interface and wall heat and mass transfer models. Even if flashing does not occur in the downcomer or lower plenum, void generated in the hot legs is carried to the downcomer by convective or natural circulation.

The mixture level is ranked as high in the PIRT. The applicability of M-RELAP5 has been validated by analyzing ROSA-IV/LSTF small break (5%) LOCA test as an IET.

61. Metal heat release:

Metal heat release is taken into account as heat source terms in the phasic energy equations via the wall heat transfer model. Therefore, the field equations are capable to simulate the effect of heat input from the vessel wall and structure.

62. ECC Water/Mixing:

The mixing of safety pump injection and accumulator water occurs with the remaining fluid in the downcomer. The mixing is simulated with the phasic continuity equations, phasic momentum equations and phasic energy equations.

63. 3-D Flow:

~~Because the field equations of M-RELAP5 have multidimensional fluid models besides 1-D models, 3-D flow can be simulated. M-RELAP5 has a multidimensional component that can simulate 3-D flow.~~ In addition, a pseudo spatial effect can be simulated by combining 1-D models. However, the 1-D model is considered to give a conservative evaluation because the liquid in the downcomer easily flows out to the break in the model. adopted for the downcomer in the US-APWR SBLOCA analyses because the experimental validation using the ROSA/LSTF test data showed that the 1-D modeling is well suited to the SBLOCA analysis.

including an ability to predict the downcomer liquid level.

64. DVI/SI Water/Flowrate:

Injection characteristics of DVI can be modeled with a table of flow rate as a function of pressure on the downstream side of the injection point using the time-dependent junction. The injection flow rate modeled with the time-dependent junction is treated as a boundary condition of the field equations, and can be simulated as changes of mass, momentum and energy. The DVI/SI water/flow rate is ranked as high in the PIRT. A single failure of the apparatus that has the most significant influence is assumed according to Appendix K.

65. DVI/SI Water/Condensation:

M-RELAP5 uses a combination of wall and interfacial heat and mass transfer constitutive equations to model the phase change by the evaporation/condensation. Using these equations, the phase change terms are calculated, which are included in the phasic continuity equations, phasic momentum equations, and phasic energy equations. The condensation is calculated from the interfacial and wall heat and mass transfer models.

66. DVI/SI Water/Injection Temperature:

Injection enthalpy of DVI is modeled with a table of enthalpy as a function of time or integral of the injection flow rate using the time-dependent volume component. The injection enthalpy modeled with the time-dependent volume is treated as a boundary condition of the field equations, and can be simulated as a change of energy. US-APWR uses the in-containment RWSP as the injection water source. It eliminates the sump switchover and improves the reliability. Injection water enthalpy increases as the amount of break flow to the containment vessel increases. The enthalpy rise can be simulated by the table of enthalpy as a function of time or integral of the injection flow rate. The effect of the enthalpy rise caused by the in-containment RWSP is minor effect in the period of the PCT evaluation. Therefore, the conservative evaluation is ensured by evaluating the enthalpy of injection water conservatively.

8.3.1.14 Break

67. Critical Flow:

In M-RELAP5, the break flow velocities of each phases is calculated with the critical flow model, and the velocities are reflected on the field equations. Therefore, the break flow is appropriately simulated with the critical flow model. Appendix K specifies that Moody's critical

flow model should be applied for the evaluation of a discharge under a two phase flow conditions at a break location. Moody's critical flow model incorporated to M-RELAP5 enables the code to evaluate the discharge flow according to Appendix K. The critical flow is ranked as high in the PIRT. Moody's critical flow model is applied according to Appendix K.

The offtake entrainment and pullthrough vapor carryover in the break flow for each of top, bottom and side breaks are of interest when the flow regime transits to the stratified flow in the horizontal piping. M-RELAP5 employs an offtake/pullthrough model identical to that implemented into RELAP5-3D. The model has been validated using ROSA/LSTF test data simulating various break sizes and orientations in addition to the original model verification, showing its adequate applicability to the small break.

68. Break Flow Enthalpy:

Because a critical flow is calculated with the field equations using thermal properties in the upstream side, break flow enthalpy is appropriately simulated. The break flow enthalpy is ranked as high in the PIRT. The applicability of M-RELAP5 has been validated by analyzing ROSA-IV/LSTF small break (5%) LOCA test as an IET.

8.3.1.5 Capability of Field Equations to Represent Processes and Phenomena

The modeling capabilities are examined for the transient phenomena of a small break LOCA as identified in the PIRT. The results show that the M-RELAP5 system of equations is applicable to the phenomena shown in the PIRT with the constitutive equations. For the phenomena ranked as high in the PIRT excluding the phenomena modeled conservatively based on the Appendix-K requirements, the modeling capability of M-RELAP5 has been validated by SETs and IETs analyses.

8.3.2 The Numeric Solution Evaluation

The M-RELAP5 thermal-hydraulic model solves eight field equations for eight primary dependent variables. These are the equations describing mass conservation, momentum conservation, and energy conservation for each phase of liquid and vapor, and the equations describing mass conservation for the noncondensable gas contained in vapor and for the boron dissolved in liquid. The independent variables are time and the spatial distance in the one dimensional model. The independent variables are time and the three dimensional spatial distance (x, y and z in a Cartesian coordinate system, and r, θ and z in a cylindrical coordinate system) in the three dimensional model. The eight primary dependent variables are pressure, phasic specific internal energies, void fraction, phasic velocities, noncondensable quality, and boron density. The secondary dependent variables used in the equations are phasic densities, phasic temperatures, saturation temperature, and noncondensable mass fraction in noncondensable gas phase for the each noncondensable species.

A more convenient set of differential equations upon which to base the numerical scheme is obtained through a process of substitution and transformation. For this equation system, the M-RELAP5 adopts the staggered spatial mesh as a spatial finite difference scheme, the donor formulation for mass and energy flux, and the donor-like formulation for momentum. In addition, the code allows the semi-implicit scheme or the nearly-implicit scheme to be selected as time integral scheme. The staggered spatial mesh consists of a mass and energy control volume, in which scalars such as pressure, mass, energy and void fraction are defined, and a momentum control volume, which defines their boundary velocity. The momentum control volume is defined at the center between the adjacent two mass and energy control volumes. The donor formulation for mass and energy flux is a method that uses the thermal properties in the upstream side depending on the flow direction. The donor-like formulation for momentum applies a donor formulation for a quantity obtained by adding a numerical viscosity term to a spatial velocity gradient.

The numerical solution of the M-RELAP5 is characterized by the selection of the primary dependent variables which are directly obtained by solving the equation system, and the staggered spatial mesh as a spatial finite difference scheme. The time step control depends on these features and thus influences the accuracy of numerical solutions obtained by a time integral.

At first, the time step control uses a mass error occurring because the phasic densities are not treated as the primary dependent variables. The phasic densities are secondary dependent variables and are approximately determined by an expansion to a Taylor's series of them as a function of the primary dependent variables such as pressure, phasic specific internal energies and noncondensable quality. Therefore, they might be different from the phasic densities directly determined by a mass conservation equation due to the reason of numerical solution methodology in some cases. The difference is defined as a mass error.

There are two types of mass error measures time used by time step controls. The first one is designed to check the validity of the density linearization by the Taylor's series expansion and evaluates the mass error for every volume. The second one is a measure of overall system mass error defined as a root mean square value. If either relative error is greater than 8×10^{-3} , the time step is rejected and repeated with one half of the time step size.

The material Courant limit check is made before a hydrodynamic advancement takes place. Thus, it may reduce the time step, but it does not cause a time step to be repeated. The material Courant limit is a ratio of a volume length to velocity, which depends on the spatial finite difference method, and hence provides a time step, during which the fluid in a volume is wholly replaced. In order to evaluate the material Courant limit, the N volumes are divided into five subsets, i.e., the 1st, 6th, 11th, ... volumes belong to the first subset, the 2nd, 7th, 12th, ... volumes belong to the second subset, etc. Then, the minimum Courant limits for each of the five subsets are rearranged in ascending order. For the semi-implicit scheme, the second smallest Courant limit is used for limiting the time step size. Thus, partial violation of the material Courant limit is allowed for this scheme. For the nearly-implicit scheme, 20 times of the second smallest Courant limit is used for limiting the time step size for the transient mode, and 40 times the second smallest Courant limit is used for limiting the time step size for the steady-state mode.

Because of the above method to control a time step, M-RELAP5 prediction accuracy depends on the geometry of a volume which is defined by the noding method. If there are few volumes much smaller than the others, the material Courant limit could not be applied properly for such the volumes and cause an excessive error. On the other hand, if a two phase condition changes significantly in a small volume, the density linearization by the Taylor's series expansion will cause an excessive mass error. Thus, a careful consideration is necessary for the noding model of the object as well as the choice of the maximum time step

Especially in IET analysis, the noding model was examined to avoid the excessive errors due to the small volumes, and the maximum time step was chosen to be less than the minimum Courant limit. Time step sensitivity analyses were performed ROSA-IV small break LOCA (SB-CL-18). The Core differential pressures and heater rod surface temperatures are compared in Figure 8.3.2-1 and Figure 8.3.2-2. [

] The results show that the time step control is able to control the numerical error to be sufficiently small in M-RELAP5.



Figure 8.3.2-1 Core Differential Pressure



Figure 8.3.2-2 Heater Rod Surface Temperature (2.23m)

8.4 Determine Applicability of Evaluation Model to Simulate System

Section 8 presents an assessment of the general application of the code to the US-APWR for SBLOCA conditions including an assessment of the different systems and components, constituents and phases, field equations, and numerics. This section describes the overall applicability of M-RELAP5 to simulate the US-APWR during a SBLOCA.

The general assessment of M-RELAP5 for the analysis of SBLOCA in the US-APWR, covered in this section, focuses on the US-APWR systems and components and how those systems are represented in the US-APWR input model. The RELAP5 approach using a non-equilibrium, non-homogenous hydrodynamics models was not changed in M-RELAP5. In addition, the basic nature of the SBLOCA in the US-APWR will be much like that of current operating four-loop PWRs. As a result, the general discussion and assessment of the RELAP5 approach, included in Section 6, regarding constituents and phases, field equations, and numerics for RELAP5 would also be applicable to M-RELAP5 and the US-APWR, so that discussion and assessment is not repeated.

M-RELAP5 is used to model the following subsystems for the US-APWR for the SBLOCA analysis:

- Primary System (Reactor and Core, Reactor Coolant System, Emergency core cooling system)
- Secondary System (Main steam system, Main feedwater system, Emergency feedwater system)
- Containment Vessel

The primary system includes the reactor internals and vessel walls, the steam generators, the reactor coolant pumps, the pressurizer, the reactor coolant pipe and pressurizer surge line, the accumulators and direct vessel injection (DVI) system. The secondary system includes the SG secondary side – main feedwater, main steam and emergency feedwater lines, and safety valves.

Nodalization of the SBLOCA analysis in the US-APWR for M-RELAP5 is depicted in Figure 8.4-1. The definition of the symbols used in the nodalization diagram is the following:

- **Component type** is expressed by the first alphabetic characters such as AN for annulus, P for pipe, B for branch, SV for single volume, and SJ for single junction. ACC for accumulator, TV for time dependent volume, TJ for time dependent junction, MJ for multiple junction, and SP for separator.
- **Component number** is expressed by the three-digit number following the component type such as ~~AN102~~ AN103 which means an annular component numbered ~~102~~103. The same scheme is applied to single volumes and junctions such as ~~SV172~~ SV170 and ~~SJ124~~ SJ203.
- **Component internal volume numbers** are expressed by the two-digit number enclosed in parentheses. For example, P116, pipe component numbered 116, has 20 internal volumes numbered from 01 to 20.

(These reference numbers are used extensively through RELAP5 and allow the user to select a particular volume or component for output, for use in the control system, or to connect to different heat structures.)



Figure 8.4-1 Overall Nodalization of Primary System for US-APWR SBLOCA Analysis

8.4.1 Reactor Vessel Modeling

[] as shown in Figure 8.4.1-1. During normal operation Flow enters from the cold legs into the downcomer, goes downward to the lower plenum and enters the bottom of the core with splitting small fraction into the neutron reflector channel. Then the coolant is heated in the core region before mixing in the upper plenum, and is discharged to the hot legs.

The corresponding vessel nodalization of M-RELAP5 is shown in Figure 8.4.1-2. An expanded view of the downcomer and core region is shown in Figure 8.4.1-3. []

]

The downcomer is annular region between the reactor vessel inner surface and outer surface of the core barrel from the bottom of the lower core support plate to the top of the upper core support plate flange. []

]

[]

.]

[

|
|

|

|

|

]

[

]

Figures 8.4.1-4 and 8.4.1-5 show a comparison of the vessel and core hydrodynamic nodalization with the minimum recommended nodalization for the Westinghouse PWR, section 5.1.1 in Reference 8.4-3. [

] These guidelines and underlying rationale are summarized below.

“The desired flow splits through the various reactor vessel bypasses generally are attained in the model by adjusting the calculated flow losses (forward and reverse loss coefficients) as needed to best represent the actual losses associated with orifices and complex geometries. To minimize iterations, this process should proceed from the flow paths with the largest flows to those with the smallest flows. In general, when representing small leakage paths between large volumes, the modeler should not use a highly reduced junction flow area (e.g., that of the orifice itself). Instead, a junction flow area equal to that of the smaller of the two adjacent volumes should be used along with an increased loss coefficient as needed to limit the flow to the desired value. The noding for the reactor vessel shown in the left diagram of Figure 8.4.1-4 represents the standard nodalization scheme used at the INL for small break LOCA simulations. The elevations of the junctions between nodes are consistent between parallel flow paths (such as the downcomer, bypass, and core regions); this scheme was developed to prevent numerical oscillations between parallel channels during early development of the code. Nodalizing the core with six axial cells is a compromise scheme allowing observation of core uncovering, yet being relatively economical. If an accurate simulation of the core uncovering process is needed, then the user is advised to use a finer nodalization near the top of the core. ...Nodalization of the upper plenum and upper head regions provides sufficient resolution of flashing phenomena and liquid levels in these regions during accident simulations.”

The US-APWR core is similar in design to that of a current 4-loop PWR. Both core designs are based on a standard fuel rod design arranged in a 17X17 array. For the US-APWR, the active fuel height has been increased from 12 feet used in the current standard 4-loop PWR to about 14 feet and the number of fuel assemblies has been increased to 257 from 193 used in the current 4-loop plant.

[

]

The standard RELAP5 modeling options for fuel rods such as gap conductance and cladding deformation are not used for the M-RELAP5 calculations since these models have been replaced by the conservative Appendix K methods described in Section 7 of this report.

An expanded view of the upper and lower portions of the reactor vessel nodalization diagrams is presented in Figure 8.41-6. [

]

The reactor internals consist of two major assemblies, the lower core support assembly and the upper core support assembly. The lower core support assembly consists of the core barrel, the lower core support, the neutron reflector, the diffuser plate, and the energy absorber. The lower core support sustains all the fuel assemblies, the neutron reflector, the diffuser plate and the energy absorber. Four flow holes are provided for each fuel assembly. The neutron reflector is located between the core barrel and core, and forms the core cavity. The upper core support assembly consists of the upper core support, the upper core plate, the upper support columns and the guide tubes. The upper core support structure separates the upper plenum of the core barrel from the reactor vessel upper head plenum, and supports the guide tubes and the upper support columns.

[

]

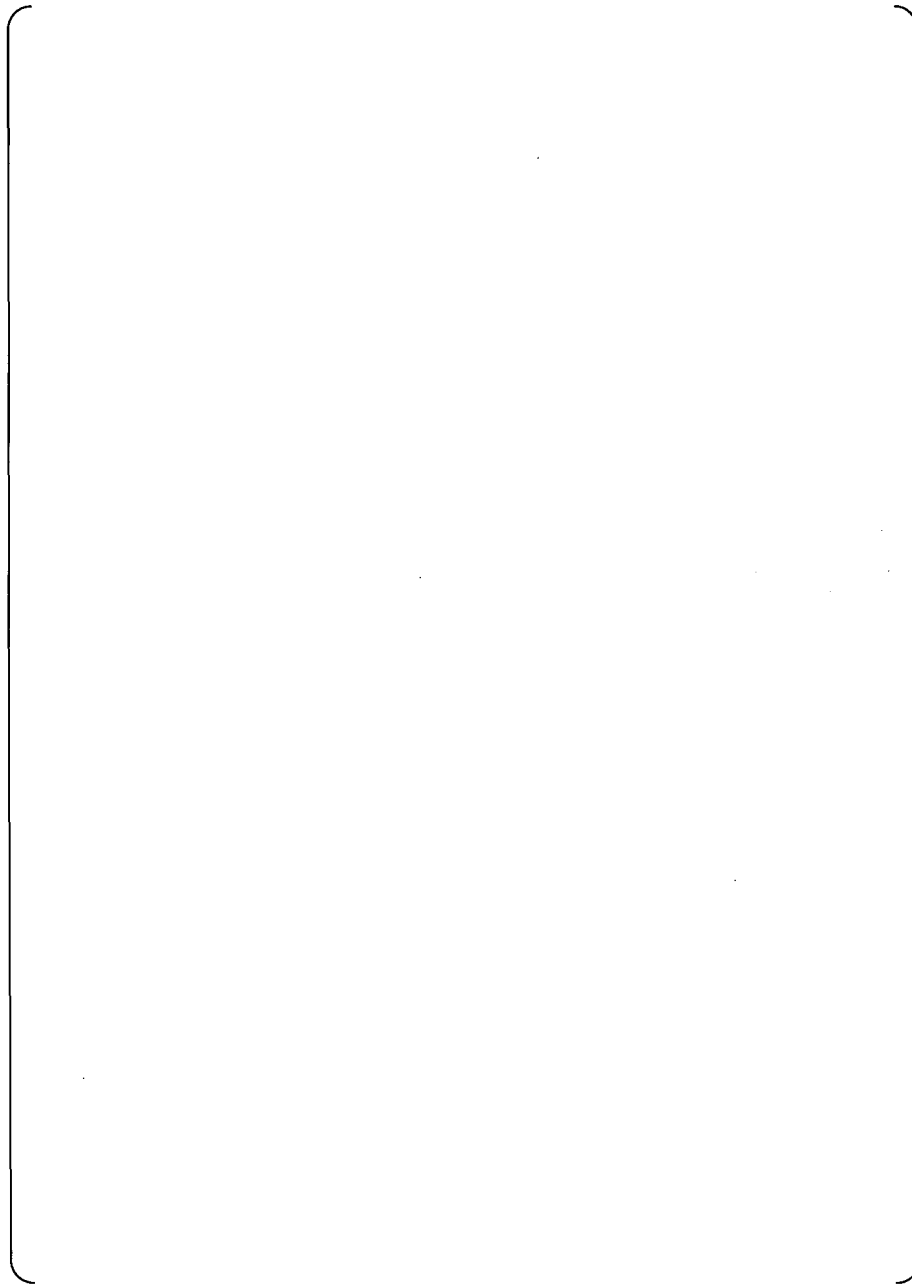


Figure 8.4.1-1 Modeling Regions of Reactor Vessel and Internals

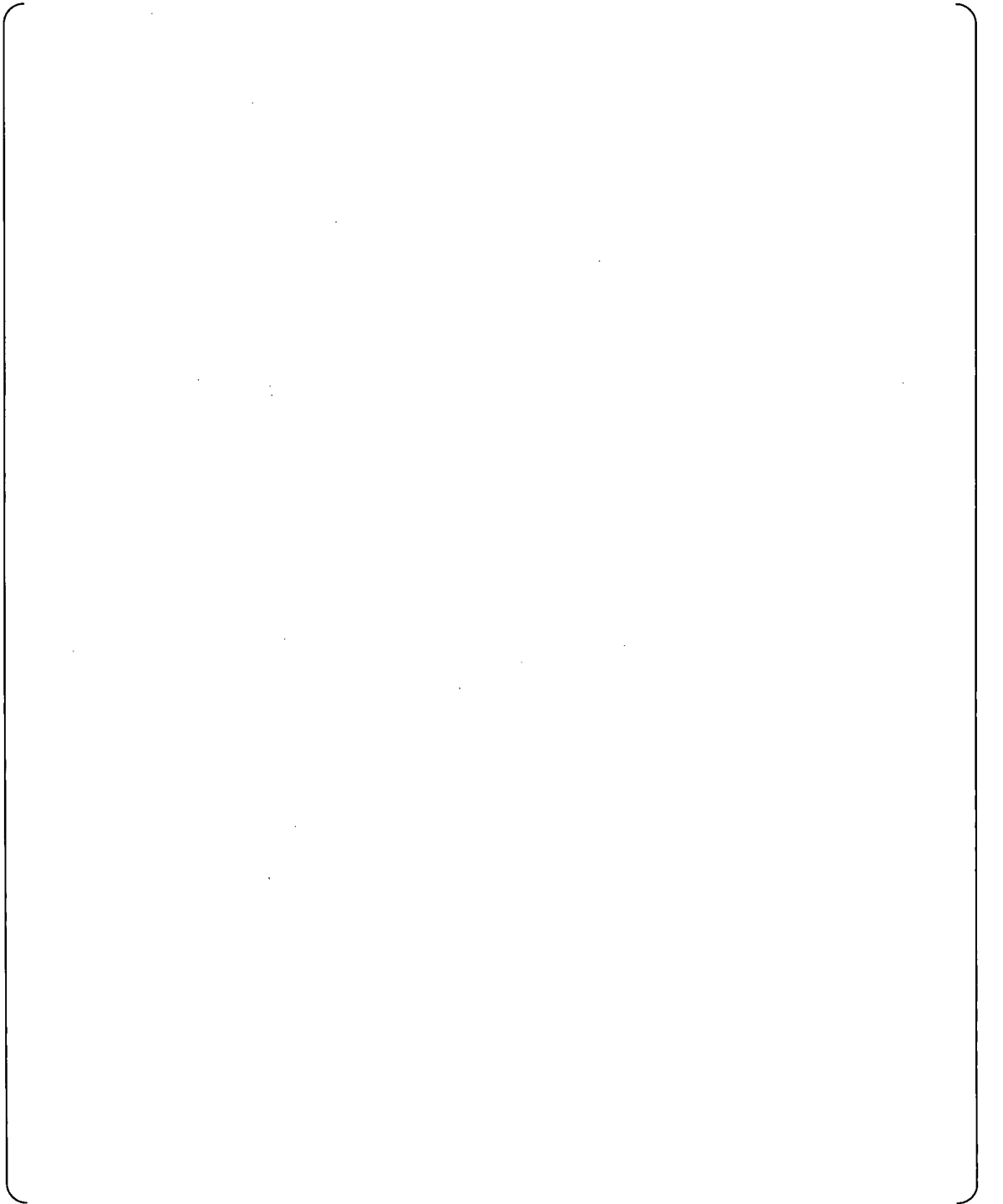
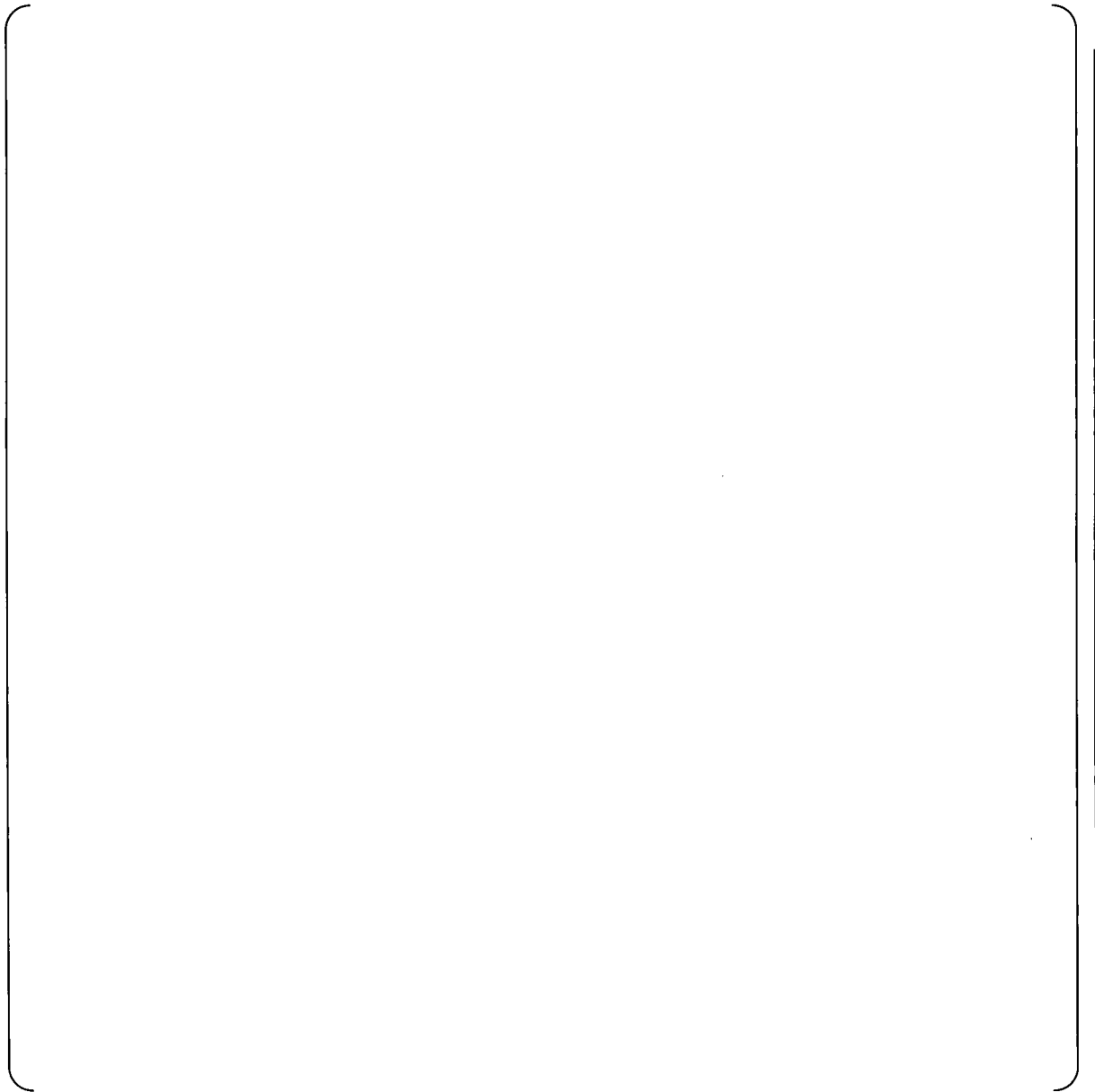


Figure 8.4.1-2 Nodalization of Reactor Vessel for US-APWR



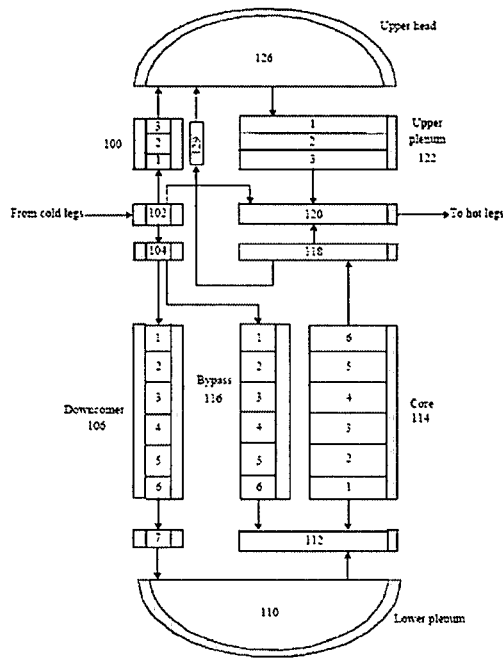


Figure 8.4.1-4 Comparison of US-APWR and RELAP5-3D Guidelines for Reactor Vessel Nodalization

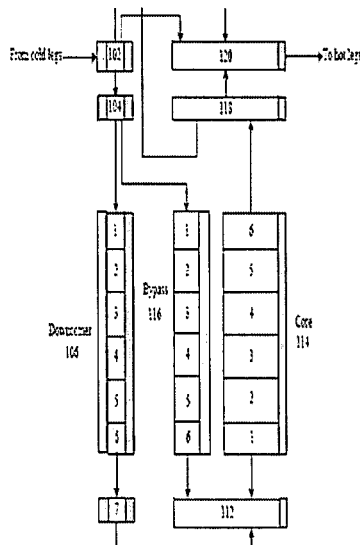


Figure 8.4.1-5 Comparison of US-APWR and RELAP5-3D Guidelines for Core and Downcomer Nodalization



Figure 8.4.1-6 Expanded View of Nodalization of Upper and Lower Plenum Regions of Reactor Vessel

8.4.2 Reactor Coolant System Modeling

The reactor coolant system (RCS) provides the reactor cooling and energy transport functions. The RCS consists of the reactor vessel, the steam generators, the reactor coolant pumps, the pressurizer, the reactor coolant pipes, and valves. The corresponding hydrodynamic nodalization is shown in Figure 8.4-1 with expanded views of the two representative loops, one with the pressurizer and one without included as Figures 8.4.2-1 and 8.4.2-2.

Steam Generator

The modeled regions of the Steam generator (SG) primary and secondary sides are illustrated in Figure 8.4.2-3. [

.]

[

.]

Reactor Coolant Pump

[

]

Reactor Coolant Pipe

[

]

Pressurizer and Surge Line

[

]

Figures 8.4.2-4 shows the corresponding nodalization diagrams provided in the advanced user guidelines (Ref. 8.4-3) for Westinghouse PWRs. Figure 8.4.2-5 shows a comparison of the US-APWR pressurized hydrodynamic nodalization with the advanced user guidelines nodalization. Figure 8.4.2-6 shows a similar comparison for the steam generator nodalization.

[

] These guidelines and underlying rationale are summarized below.

“Standard INL nodalization for one of the primary coolant loops is shown in Figure 8.4.2-4. ...Pipe 408 (steam generator tube primary side) represents the many thousands of steam generator tubes. ... Representing the steam generator tube primaries with an 8-cell pipe component is a nodalization scheme that compromises between calculational fidelity and expense. This scheme has proven generally useful, however the modeler should individually consider the nodalization requirements for the problem to be modeled. The tube nodalization scheme shown may not be sufficiently detailed to model phenomena associated with reflux cooling and greatly reduced secondary-side levels. ..Pipe 412 represents the pump suction cold leg. To ensure proper simulation of behavior in the loop seal region, cell 4 of this pipe is input as horizontal. This orientation allows the formation of horizontally stratified flows at the bottom of the loop seal. It is recommended that at least one horizontal cell be used for simulating loop seal phenomena. Cells 1, 2, 3, and 5 of pipe 412 provide sufficient vertically-oriented calculational cells for simulating the formation of liquid levels in the loop seal region and for simulating countercurrent flow limiting phenomena. ...The pump discharge cold leg is modeled with branches 416 and 418 and pipe 420. This nodalization scheme has proven suitable for simulating horizontal stratification of fluid within the cold legs during loss of coolant accidents.”

“Heat structures are employed to model the hot and cold leg piping walls, the steam generator plena heads, the plena separation plate, the tubesheet, and the steam generator tubes.”

The US-APWR steam generator is a vertical shell U-tube evaporator with integral separator. The reactor coolant enters the channel head via the hot side primary coolant nozzle, flows through the inverted U-tubes, transferring heat from the primary side to the secondary side, and leaves from the channel head through the cold side primary coolant nozzle. Steam generated on the shell side (secondary side), flows upward, and exits through the outlet nozzle at the top of the vessel. Feedwater enters the steam generator at an elevation above the top of the U-tubes through a feedwater nozzle. The feedwater enters a feed-ring and is distributed through nozzles attached to the top of the feed-ring. After exiting the nozzles, the feedwater mixes with the saturated water removed by the moisture separators. The flow then enters the downcomer annulus between the wrapper and the shell.

The US-APWR pressurizer is a vertical vessel with hemispherical top and bottom heads. Electrical immersion-type heaters are installed vertically through the bottom head of the vessel while the spray nozzle, and relief line connected to relief and safety valves are located on the top head of the vessel.

The emergency core cooling system (ECCS) includes the accumulator system and high-head injection system. [

] As discussed in the Section 6, the time dependent volumes are used to specific time dependent (scalar) boundary conditions such as pressures and temperatures of the fluid. The time dependent junctions provide vector or directional quantities such as mass flow rates. [

]]

The advanced accumulators are modeled with the accumulator components [

]

The break is also shown on Figure 8.4.2-7. [

]

The secondary system consists of the main feedwater system, the main steam system and the emergency feedwater system. Figure 8.4.2-8 shows the nodalization used. [

]

In summary, there are three key components in the assessment that M-RELAP5, and the US-APWR SBLOCA input model, are able to provide a realistic framework for the use of the conservative Appendix K methodology to analyze the SBLOCA for the US-APWR.

- M-RELAP5, which uses the widely accessed RELAP5 general framework and modeling approach, can correctly describe the system and components of the US-APWR. The RELAP5-based non-equilibrium, non-homogenous approach including the phases and constituents, the basic field equation, and numerics has been widely assessed by the US Nuclear Regulatory Commission and the international community for the application to SBLOCA conditions in PWRs. In addition, the analysis of the US-APWR should be well with the range of existing SBLOCA conditions that have been analyzed using

RELAP5. There are two important considerations for that judgment. One, since the US-APWR shares the general design features and physical characteristic of currently operating 4-loop PWRs, the general nature of the SBOCA transient will mimic those analyzed by the international community with RELAP5. Second, because the US-APWR has a reduced fuel linear heat rating compared to current PWRs as well as advanced emergency core cooling systems, the general thermal response of the core to a SBLOCA should be benign and fall well within the existing assessment data base for SBLOCAs.

- The US-APWR SBLOCA input model was designed following the INL RELAP5-3D advanced user guidelines (Ref. 8.4-3) for the analysis of Westinghouse PWRs with the suitable improvements to increase the accuracy of the basic numerical techniques. For example, [

] The

structures in the system were also modeled using the standard RELAP user guidelines. For example, [

-]
- The standard RELAP5 modeling approach including standard models and correlations will provide a realistic prediction of the thermal hydraulic response of those regions of the plant not directly impacted by the conservative Appendix K methods.

Sample calculation of US-APWR with M-RELAP5 is shown in the Appendix E.

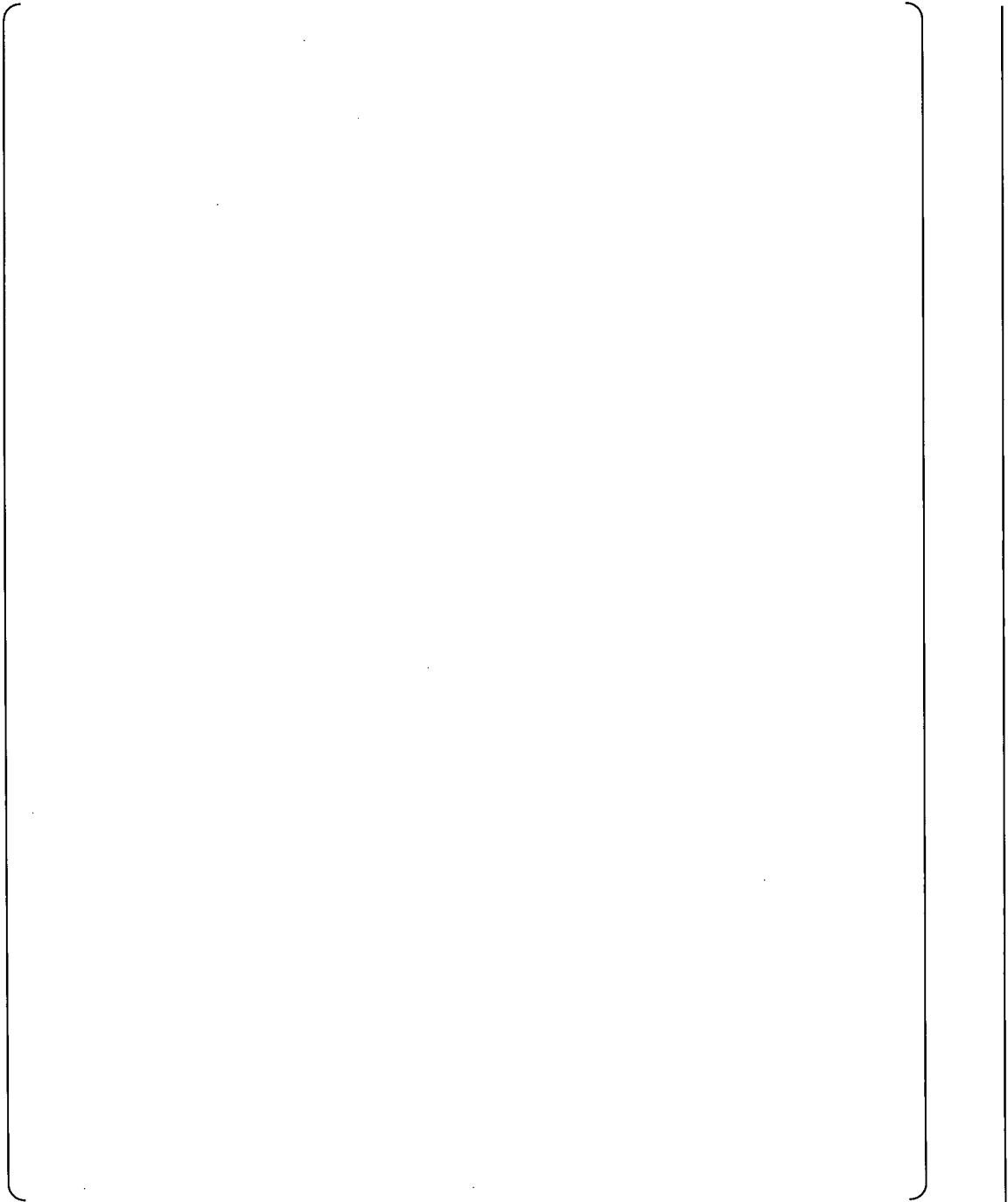


Figure 8.4.2-1 Expanded View of Nodalization for Loop with Pressurizer

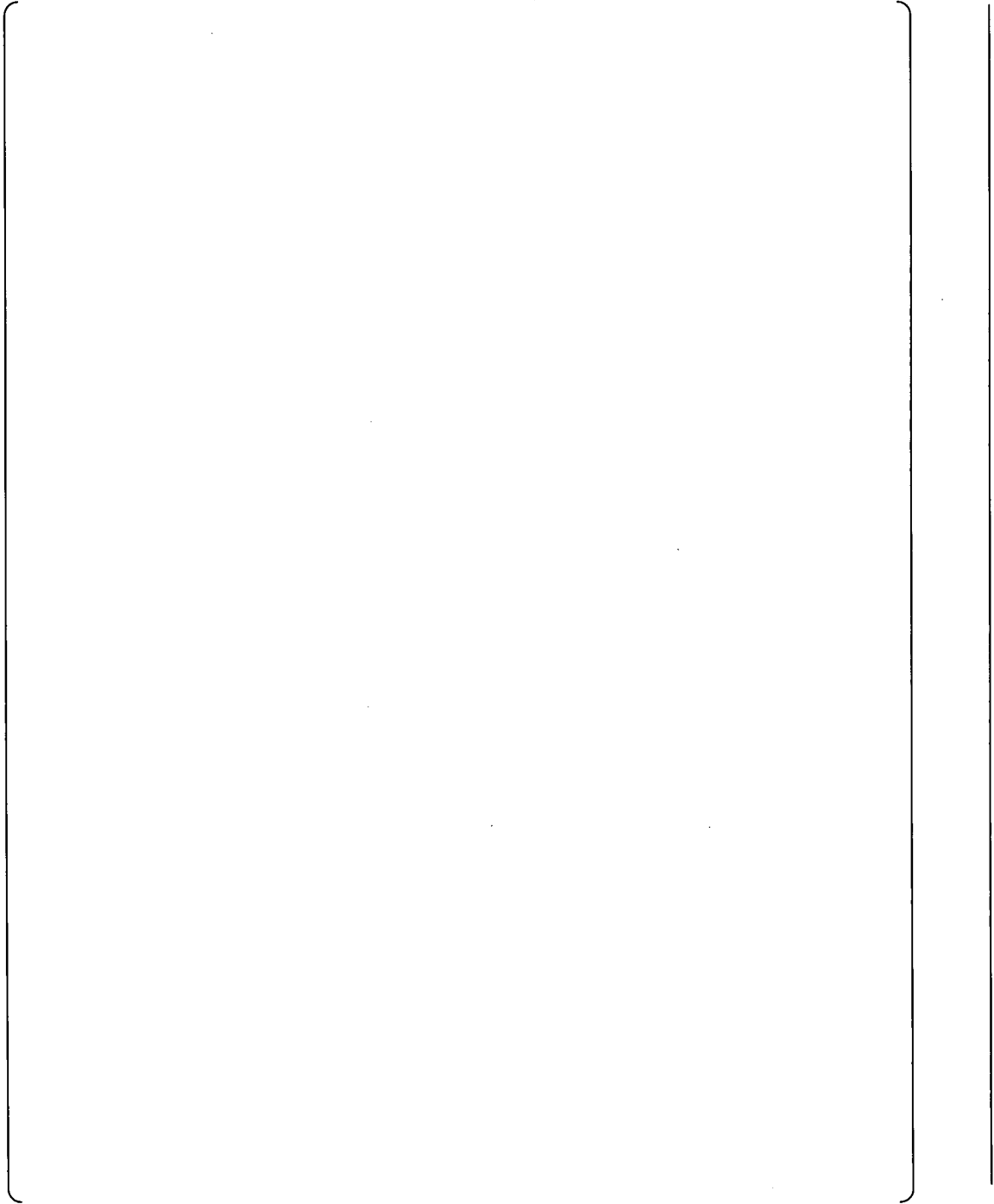


Figure 8.4.2-2 Expanded View of Nodalization for Loops without Pressurizer

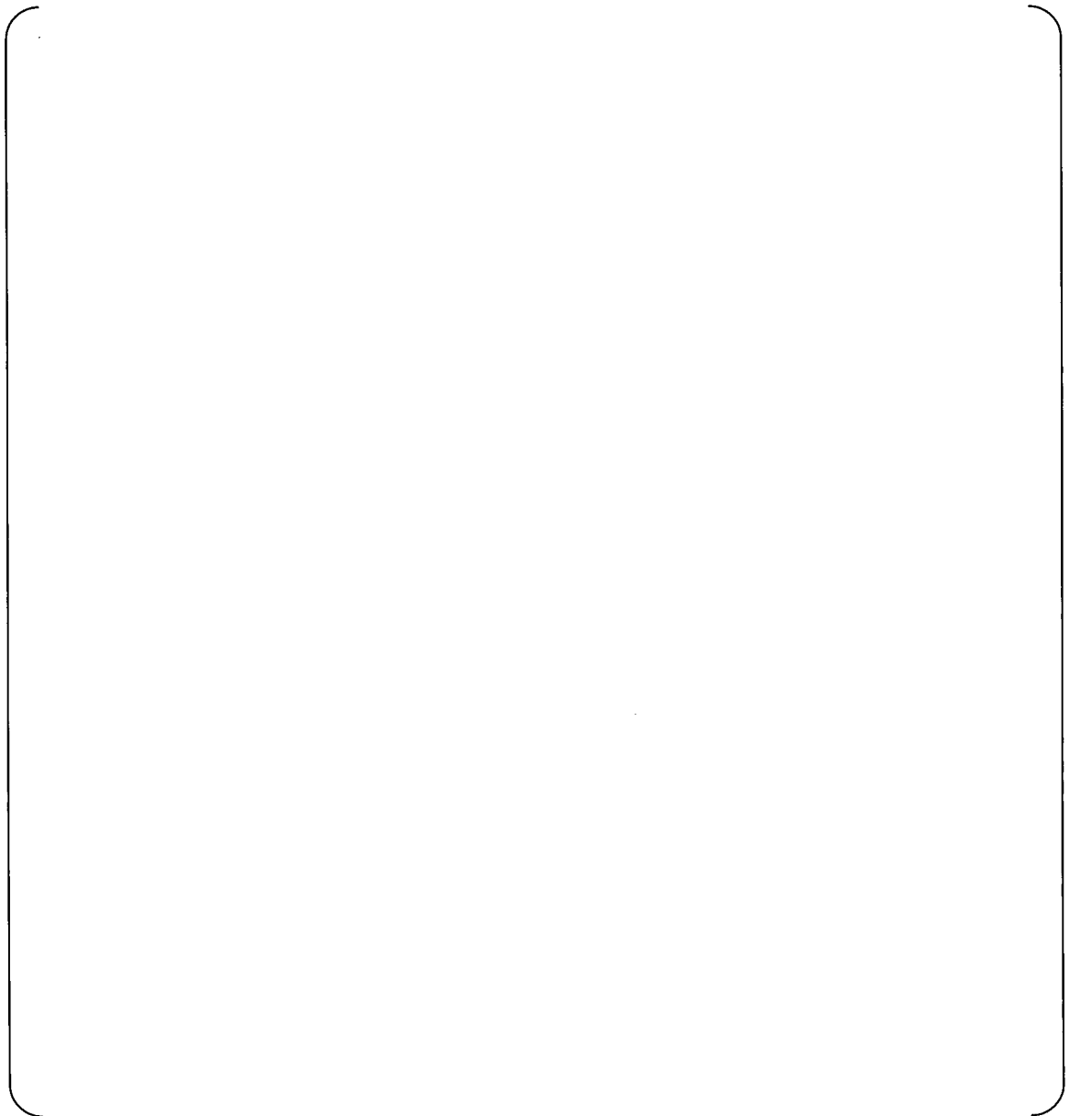


Figure 8.4.2-3 Modeling Regions of Steam Generator

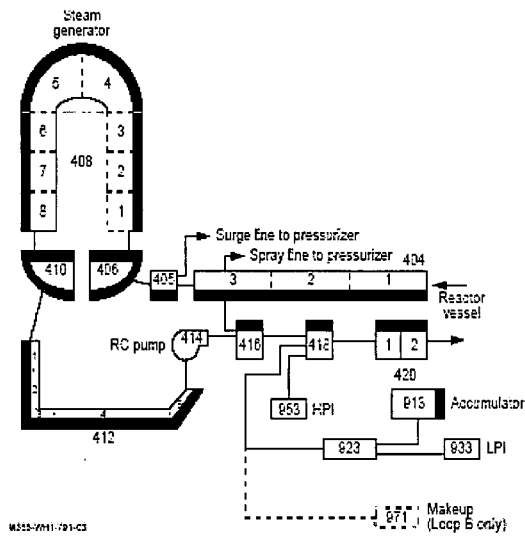


Figure 8.4.2-4 RELAP5-3D Guidelines for Primary Loop Nodalization

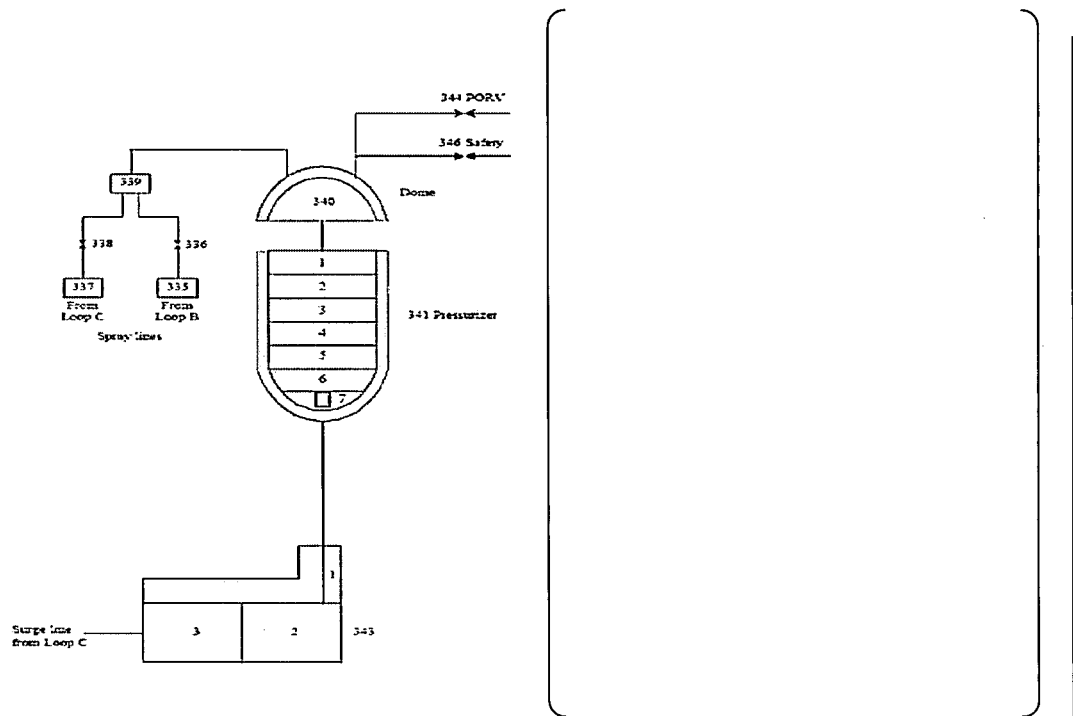


Figure 8.4.2-5 Comparison of US-APWR and RELAP5-3D Guidelines for Pressurizer Nodalization

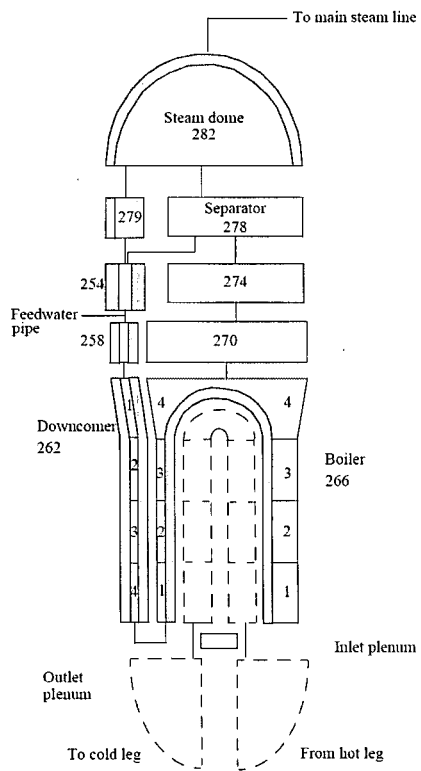


Figure 8.4.2-6 Comparison of US-APWR and RELAP5-3D Guidelines for Steam Generator Nodalization



Figure 8.4.2-7 ECCS Injection Nodalization

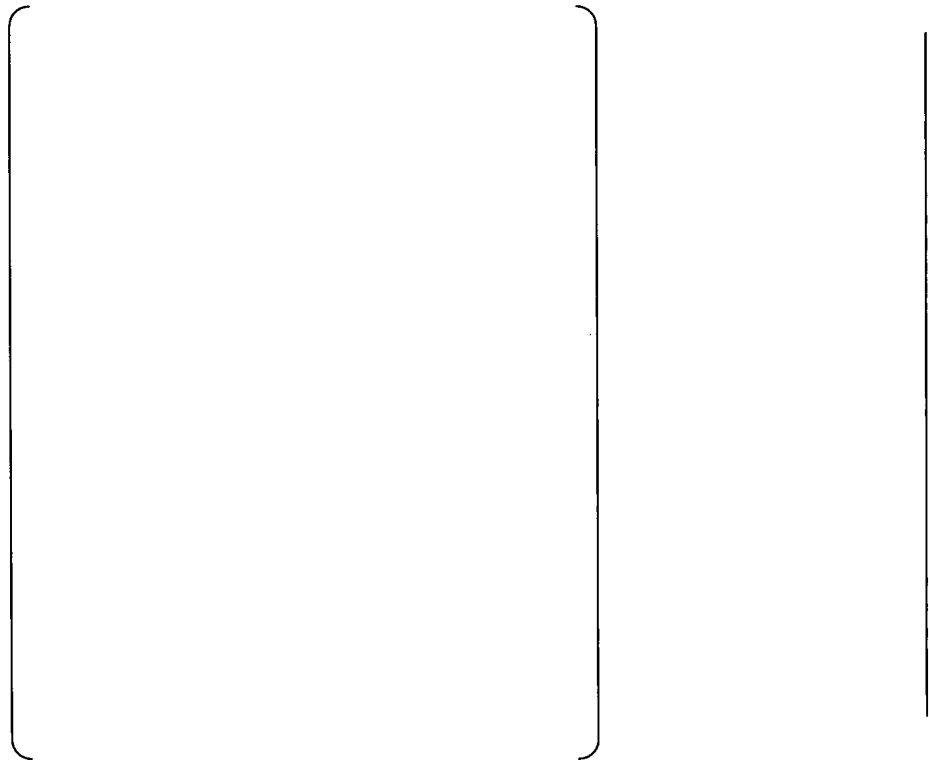


Figure 8.4.2-8 Nodalization of Feedwater and Steam Systems

8.4.3 References

- 8.4-1 RELAP5-3D[®] CODE MANUAL VOLUME I: CODE STRUCTURE, SYSTEM MODELS, AND SOLUTION METHODS, INEEL-EXT-98-00834, Revision 2.4, June 2005.
- 8.4-2 RELAP5-3D[®] CODE MANUAL VOLUME II: USER'S GUIDE AND INPUT REQUIREMENTS, INEEL-EXT-98-00834, Revision 2.4, June 2005.
- 8.4-3 RELAP5-3D[®] CODE MANUAL VOLUME V: USER'S GUIDELINES, INEEL-EXT-98-00834, Revision 2.4, June 2005.

8.5 Determination of Evaluation Model

The PIRT for SBLOCA of the US-APWR is developed as described in Section 4.3. M-RELAP5 was assessed with regard to the following phenomena that are ranked High in the PIRT by the test calculations: CHF/core dryout, uncovered core heat transfer, rewet, core mixture level, water hold up in SG primary side, SG primary and secondary heat transfer, water level in the SG outlet piping, loop seal formation and clearance, downcomer mixture level/downcomer void distribution. Six Separate Effect Tests (SETs) and one Integral Effects Test (IET) were analyzed with M-RELAP5.

The calculation result for the ROSA/LSTF void profile test using M-RELAP5 show good agreement with the test data for both the axial void fraction profile and the averaged void fraction. M-RELAP5 was assessed by the comparison with the ORNL/THTF two-phase mixture level swell test and the uncovered-bundle heat transfer test. The assessment shows that the M-RELAP5 code reasonably predicts these parameters. Rewetting modeling was assessed against the ORNL/THTF high-pressure reflood tests. M-RELAP5 conservatively predicts the rod heat transfer and rewet behavior during reflood. M-RELAP5 was assessed by the comparison with the UPTF CCFL test data and Dukler Air-Water Flooding Test. It is confirmed that M-RELAP5 with the CCFL parameters is applicable to CCFL behavior of the hot leg and the SG plenum, and SG U-tube in the US-APWR.

M-RELAP5 was assessed by the comparison with the ROSA/LSTF small break (5% and 10%) LOCA integral tests (SB-CL-18 and SB-CL-09) for confirmation of integral system behavior. A cold leg break (17%) test, scaled to the 1-ft² break of US-APWR, has been newly performed using the ROSA/LSTF with technical support of JAEA, which was used to assess M-RELAP5 applicability to SBLOCAs with relatively larger break sizes. In addition, M-RELAP5 was validated using small break LOCA test data obtained in the LOFT (L3-1, 2.5%) and Semiscale (S-LH-1, 5%) facilities in compliance to requirement specified in the TMI Action Plans. Against these various experimental tests performed in the different test facilities, M-RELAP5 predicted excellently the following important parameters: water hold up in SG primary side, condensation drainage to inlet plenum, SG primary and secondary heat transfer, water level in SG outlet piping, and loop seal formation and clearance.

The modeling capabilities of M-RELAP5 are concluded to be applicable to the important phenomena specified in the PIRT with the constitutive equations. Time step sensitivity

analyses also show that M-RELAP5 is able to control the numerical error to be sufficiently small. Finally, modeling and nodalization of M-RELAP5 for the US-APWR SBLOCA analysis were discussed in detail.

Based on the discussion above, M-RELAP5 is concluded to be suitable to determine the performance of the designed ECCS for the design-basis SBLOCAs in the US-APWR.

9.0 CONCLUSIONS

For the US-APWR small-break LOCA analysis, MHI specifically selected RELAP5-3D and modified it as M-RELAP5 in order to meet the requirements in 10CFR Part 50 Appendix K, "ECCS Evaluation Models". (Ref. 9-1)

First, the PIRT for small break LOCA of the US-APWR was developed for the modification and validation plans of M-RELAP5. The approach used for the US-APWR SBLOCA PIRT was to utilize the expertise at MHI and also the independent experts. For conservative M-RELAP5, some Appendix K requirements was achieved through the implementation of new models or the modification, although RELAP5-3D has a number of models that enable it to meet many of the Appendix K requirements with no modification, .

Then, M-RELAP5 capability to analyze the small Break LOCA was confirmed by the validation analyses with integral effect tests and separate effect tests focused on the models related to the important phenomena identified in the PIRT as follows: CHF/core dryout, uncovered core heat transfer, rewet, core mixture level, water hold up in SG primary side, SG primary and secondary heat transfer, water level in the SG outlet piping, loop seal formation and clearance, downcomer mixture level/downcomer void distribution. The results show that M-RELAP5 well predicts key phenomena that are ranked high.

The modeling capabilities of M-RELAP5 were also examined and concluded to be applicable to the important phenomena specified in the PIRT with the constitutive equations. Time step sensitivity analyses also show that M-RELAP5 is able to control the numerical error to be sufficiently small. Finally, modeling and nodalization of M-RELAP5 for the US-APWR SBLOCA analysis were discussed in detail.

With these results, M-RELAP5 is concluded to be able to applicable to the Chapter 15 small break LOCA analysis of the US-APWR against the acceptance criteria specified in 10 CFR Part 50 Section 50.46, "Acceptance Criteria for Emergency Core Cooling System for Light-Water Nuclear Power Reactors." (Ref. 9-2)

9.1 References

9-1 10 CFR Part 50, Appendix K, "ECCS Evaluation Models."

9-2 10 CFR 50.46, "Acceptance Criteria for Emergency Core Cooling System for Light-Water Nuclear Power Reactors."

Appendix A Resumes of peer reviewers for PIRT

One of the most important steps in developing an analysis methodology is the identification of phenomena and processes that provide the most dominant influence on the specific transient of interest. A Phenomena Identification and Ranking Table (PIRT) lists key processes and specifies at which stage in the transient the process or phenomenon occurs.

The approach used for the US-APWR SBLOCA PIRT was to utilize the expertise at MHI to develop the initial SBLOCA PIRT. There were five individuals involved at MHI which had a total of 110 years of experience in analyzing PWRs, performing safety related experiments, and accident analysis experience for model development and plant analysis.

Once this Preliminary SBLOCA PIRT was completed, it was reviewed independently and separately by Dr. Thomas George from Numerical Applications Incorporated, and Dr. L.E. Hochreiter from The Pennsylvania State University. Once the review comments were assembled, a specific meeting was held between MHI, Dr. George and Dr. Hochreiter to review comments and resolve differences.

Attachments are the resumes of Dr. George and Dr. Hochreiter.

LAWRENCE EDWARD HOCHREITER

Professor of Nuclear and Mechanical Engineering

The Pennsylvania State University

615 Berkshire Drive

State College, PA 16803

Ph. (Office): (814) 854-6198

Ph (Home): (814) 235-2267

Email (Office): lehnuc@engr.psu.edu

Email: (Home): lehoch@aol.com

EDUCATION

1971	Ph.D.	Nuclear Engineering, Purdue University, W. Lafayette, Indiana
1967	M.S.	Nuclear Engineering, Purdue University, W. Lafayette, Indiana
1963	B.S.	Mechanical Engineering, University of Buffalo, Buffalo, New York

OVERVIEW OF EXPERIENCE

After receiving his Ph.D. in Nuclear Engineering at Purdue University, Dr. Hochreiter spent 26 years working in the Nuclear Energy Systems Division at Westinghouse in the Nuclear Safety area. He initially worked with others in developing the THINC-IV PWR sub-channel analysis code for thermal-hydraulic analysis. In 1972 he was appointed Manager of Safeguards Development (first level manager) and supervised light water reactor safety research, as applied to Pressurized Water Reactors. These experiments included large full-length rod bundle blowdown film boiling, level swell, and reflood heat transfer tests, the NRC/W Full Length Emergency Core Heat Transfer (FLECHT) reflooding experiments, the 1/14 and 1/3 scale cold-let steam/water mixing tests, and the Westinghouse Transient DNB tests. He helped develop models and correlations for Westinghouse Appendix K LOCA Safety Analysis codes and licensed the codes and models with the USNRC, made numerous presentations to the NRC and to the ACRS.

In 1977 he was appointed to Advisory Engineer and was the Principal Technical Investigator for the NRC/EPRI/W Full Length Emergency Core Heat Transfer-Systems Effects and Separate Effects Tests (FLECHT-SEASET) program which examined reflood heat transfer effects in unblocked and blocked rod bundle arrays as well as steam generator effects during reflooding. These experiments also examined the different modes of natural circulation cooling for a PWR following a small-break LOCA with different inventories within the reactor system. In addition to the experimental effort, heat transfer models were developed for spacer grids and flow blockages for the COBRA-TF computer code. He also helped develop an analysis and licensing plan for Westinghouse BWR reload fuel assembly designs. He developed and modified the COBRA-TF code to analyze combined radiation and film boiling heat transfer situations for rod bundles with top spray cooling for BWR LOCA situations. He also designed, performed, and analyzed BWR tieplate counter flow experiments. He also designed downflow two-phase pressure drop experiments on reactor

structures for the Advanced PWR in Japan that verified the blowdown pressure drop models in the Westinghouse safety analysis code for this design.

He served as Westinghouse's safety analysis technical expert for the Three-Mile Island accident. Participated and directed an independent Westinghouse analysis of the accident for the President's Commission on TMI. A detailed presentation was made to the Commission on the analysis performed at Westinghouse. He also served as the Westinghouse representative on the TMI clean-up activities.

He participated in the United Kingdom Reactor Safety Case for the Sizewell PWR application with National Nuclear Corporation and helped develop the safety case. He helped develop the safety analysis models that were used in the Sizewell safety analysis and made several presentations to the UK safety authorities as well as the CEGB utility.

In 1987 he was appointed as a Consulting Engineer, the highest technical position at Westinghouse Electric Corporation. He led Westinghouse engineers to develop a model for the Chernobyl RBMK reactor which was used to explain the accident and the differences in the RBMK design relative to a PWR. These results were presented to the USNRC and the Department of Energy.

He led and participated with engineers to develop a Best-Estimate Thermal Hydraulic Methodology, using WCOBRA/TRAC to analyze Westinghouse two-loop reactors with upper plenum injection. As part of this effort, he developed the code assessment and code uncertainty efforts that were applied to the WCOBRA/TRAC code. He also led and participated with a team of Westinghouse engineers in completing the Best Estimate Loss-of-Accident Thermal-Hydraulic Safety Analysis Methodology to all pressurized water reactors. This was the first application of the revised 1988 Appendix K rule allowing the Application of Best Estimate Computer models for Loss-of-Coolant Accident Analysis for PWRs. He developed the code uncertainty, helped develop the initial PIRT for the Westinghouse plants, Performed analysis to address the scaling uncertainty issues, prepared, with others, the five volume Code Qualification Document for the Westinghouse methodology. He made a significant number of presentations to the USNRC staff and their consultants as well as the ACRS, discussing and explaining the PIRT, code models, code uncertainty, analysis methods, and the plant results.

He was responsible for the development and integration of the AP600 (an advanced PWR design) safety testing and analysis efforts which supported the AP600 design certification and licensing. He was directly involved in the model development, refinement, and validation of the Westinghouse safety analysis computer codes for small break LOCA, large break LOCA, long term cooling, and containment analysis for this passive plant design. He developed several of the initial PIRTs for the AP600 LBLOCA, SBLOCA, transient analysis, and containment analysis. He also performed the scaling analysis for the CMT tests; he worked with Dr. Jose Reyes on the scaling for the Oregon State University APEX low pressure integral systems effects tests for the AP600. He reviewed and participated in the scaling analysis for the AP600 containment experiments, the SPES full pressure AP600 integral systems experiments, and the ADS experiments. He led a team of

engineers in the data analysis of these experiments. He also co-authored the AP600 Scaling and PIRT Closure Report. He also authored and co-authored several of the safety analysis computer code applicability reports which showed that the Westinghouse computer codes were applicable for the AP600 passive safety system design. He also co-authored several of the AP600 safety analysis reports for the LBLOCA, SBLOCA, Long Term Cooling, and code validation reports were submitted to the NRC and ACRS.

Since joining The Pennsylvania State University in January 1997, Dr. Hochreiter has continued to work in the safety analysis and development, reactor thermal-hydraulics, reactor safety, and two-phase flow and heat transfer areas. He is the Principal Investigator for the NRC sponsored Rod Bundle Heat Transfer Program which is designed to provide more fundamental experimental data and model development for the NRC advanced computer codes. He is also the Principal Investigator for the Bettis Atomic Power Laboratory Laminar Flow heat Transfer studies, modeling two-phase reactor coolant pump behavior, and validation analysis of the LOFT experiments. He is involved with the Framatome-ANF (Siemens Power Corporation) developing models and analysis methods for new fuel assembly designs and is investigating modeling the effects of spacer grids on dryout in BWR bundles. He is also involved with modeling the EPR reactor design with MELCOR severe accident code.

While at Penn State, he has consulted with Framatome-ANF (Siemens Power Corporation), on the development of their LBLOCA PIRT and code validation; US Nuclear Regulatory Commission on the development of the High Burnup PIRT, Bettis Atomic Power Laboratory, Idaho Nuclear Laboratory on the development of the LBLOCA PIRT for the Korean KNGR design, Canadian Owners Group on the CANDU BE LOCA and PIRT as well as a High Temperature Fuel Phenomena LOCA PIRT for CANDU fuel and with the Canadian Nuclear Safety Commission in developing guidelines for Best-Estimate LOCA reviews..

PROFESSIONAL EXPERIENCE

1997 – Present Professor of Nuclear and Mechanical Engineering,
The Pennsylvania State University, Department of Mechanical and
Nuclear Engineering, 233 Reber Building, University Park, PA
16802

PUBLICATIONS

Authored and co-authored over 160 publications in journals, transactions, and proceedings. Also authored and co-authored 90 Westinghouse Reports.

Member American Society of Mechanical Engineers (29 years), ASME Fellow (1994), K-13 Committee, Heat Transfer Division.
Member American Nuclear Society

THOMAS L. GEORGE
Principal and Senior Consulting Engineer
Numerical Applications, Inc.

Education

Ph.D. Mechanical Engineering, Oregon State University, 1982
 MS Mechanical Engineering, Montana State University, 1975
 MA Mathematics, University of Wisconsin, Madison, 1973
 BA Mathematics, Carroll College, Helena, Montana, 1972

Experience

Dr. George joined Numerical Applications, Incorporated, in 1984 to develop software for engineering mechanics applications. Previously, he worked at Battelle Northwest Laboratory in the Fluid & Thermal Engineering section. Dr. George specializes in numerical modeling in engineering mechanics. His experience includes the development of large computer codes to model a variety of problems in heat transfer, single- and multi-phase thermal hydraulics, and elastic/plastic analysis in solid mechanics. He has extensive experience in both finite-difference and finite-element numerical methods and simulation of multiphase phenomena. He has been responsible for, or a major participant in, the following projects:

- **Multiphase Flow Modeling.** Participated or led the development of major codes used in the nuclear industry, including COBRA for in core analysis, COBRA-TRAC for combined core and loop analysis, COBRA-WC for core analysis in liquid metal reactors and GOTHIC for general purpose multiphase flow and heat transfer analysis. Developed and validated models for drop entrainment, deposition, vapor/liquid drag in bubbly, stratified and film regimes, interphase heat and mass transfer including condensation, evaporation, boiling and flashing.
- **Expert Review.** Participated in a peer review for the Westinghouse AP600 containment response. Participated in the development of a PIRT (Phenomena Identification and Ranking Table) for BWR design basis and operating transients.
- **Reactor Safety Analysis.** Primary developer for the GOTHIC code for nuclear containment and general-purpose thermal-hydraulic analysis. GOTHIC is a hybrid CFD/lumped parameter code that features multiphase flow and heat transfer, and incorporates engineered safety equipment such as pumps, heat exchangers, valves and an extensive Graphical User Interface (GUI) to simplify complex modeling tasks. GOTHIC is used worldwide in the nuclear industry. He is responsible for an ongoing program to develop, document and assess the GOTHIC code. He has been involved in numerous projects to develop and apply GOTHIC models for BWR and PWR containments, auxiliary buildings, primary loops and system components. The models are used to address a variety of safety issues including containment integrity, Equipment Qualification and equipment performance and loop performance. GOTHIC has been used by many utilities for safety and reactor licensing issues, including submittals to the US NRC.
- **Fire and Smoke Modeling.** Developed a computer program to track smoke propagation and fire growth in buildings. The model includes aerosol transport, agglomeration and deposition, fire ignition, spreading and decay, fuel and oxidant depletion and radiant heat transfer with participating media.
- **Solid Mechanics Modeling.** Developed a mechanical response model that predicts the elastic and plastic properties of restructuring sphere-pac nuclear fuel and the stress-strain distribution in the fuel and cladding. Property models are based on principles from solid mechanics and the theory of composite materials. The analysis package models thermal, creep, swelling, elastic, and plastic strains. He also has expertise in the thermal aspects of sphere-pac fuel including restructuring and fission gas behavior.
- **Heat and Mass Transfer Modeling.** Developed models and methods to accurately predict condensation on cold walls in the presence of noncondensing gases. Developed models for

interfacial heat and mass transfer including drop entrainment and deposition and evaporation and condensation on drops, films and pools. Developed a model to predict the performance of fan cooler (condensing heat exchanger) over a wide range of operating conditions.

- **CFD Analysis.** Developed numerical techniques for thermal-hydraulic analysis in three-dimensional curvilinear or generalized coordinate systems for complex geometries. In conjunction with this, he has developed a method for generating three-dimensional curvilinear computational grids. He has extended the capabilities of the GOTHIC code for CFD analysis in a wide range of multiphase and single-phase flow applications.
- **Hydrogen Mixing and Combustion.** GOTHIC includes models to predict the propagation of a hydrogen flame in a coarse mesh grid. It also includes models to predict the distribution of hydrogen including a two-equation turbulence model and molecular diffusion.

Publications

George, T. L. "Oxidation of Iridium in CO₂ at High Temperatures," M. A. Thesis, Montana State University, August 1975.

Stewart, C. W., et. al., "Core Thermal Model: COBRA-IV Development and Applications," BNWL-2212, Pacific Northwest Laboratory, Richland, Washington, January 1977.

Stewart, C. W., and T. L. George. "A Eulerian Computation Method for Fluid Flows with Large Density Gradients at all Speeds," Nuc. Sci. Eng., 64: 2, October 1977.

Donovan, T. E., T. L. George, and C. L. Wheeler, "COBRA-IV Wire-Wrap Data Comparisons," PNL-2938, Pacific Northwest Laboratory, Richland, Washington, February 1979.

Khan, E. U., T. L. George, and C. L. Wheeler. "COBRA and CORTRAN Code Thermal-Hydraulic Models for LMFBR Core-Wide Temperature Distribution During a Natural Circulation Transient," IAEA Specialists Meeting, Karlsruhe, Germany, February 5-7, 1979.

George, T. L., et. al., "COBRA-WC: A Version of COBRA for Single-Phase Multiassembly Thermal-Hydraulic Transient Analysis," PNL-3257, Pacific Northwest Laboratory, Richland, Washington, July 1980.

Thurgood, M. J., et. al., "COBRA-TF, a Three-Field Two-Model for Reactor Safety Analysis," ASME HTD-Vol 7, 19th National Heat Transfer Conference, Orlando, Florida, July 1980.

George, T. L., K. L. Basehore, and W. A. Prather, "COBRA-WC Model and Predictions for a Fast Reactor Natural Circulation Transient," AIChE Symposium Series, Vol. 76, 19th National Heat Transfer Conference, Orlando, Florida, July 1980.

Khan, E. U., et. al., "A Validation Study of the COBRA-WC Computer Program for LMFBR Core Thermal-Hydraulic Analysis," PNL-4138, Pacific Northwest Laboratory, Richland, Washington, 1981.

Thurgood, M. J., and T. L. George. "COBRA/TRAC - A Thermal-Hydraulic Code for Transient Analysis of Nuclear Reactor Vessels and Primary Coolant Systems: Volume 2, COBRA/TRAC Numerical Solution Methods," NUREG/CR-3046, PNL-4385, November 1982.

George, T. L. "A Model for the Mechanical Behavior of Irradiated Mixed Carbide Sphere Pac Fuel Pins," Ph.D. Thesis, Oregon State University, December 1982.

Stewart, C. W., et. al., "VIPRE-01, A Thermal-Hydraulic Analysis Code for Reactor Cores: Volume 1, Mathematical Modeling," Electric Power Research Institute, Palo Alto, California, NP-2511, December, 1982.

Khan, E. U., Et. A., "COBRA-WC Pretest Predictions and Post-Test Analysis of the FOTA Temperature Distribution during FFTF Natural Circulation Transients," PNL-4141, Pacific Northwest Laboratory, Richland, Washington, 1982.

George, T. L., "Improved Two-Fluid Numerics for VIPRE-2" FATE-83-114, Pacific Northwest Laboratory, Richland, Washington, May 1983.

George, T. L., "An Implicit Two-Fluid Numerical Scheme for VIPRE-2," FATE-83-100, Pacific Northwest Laboratory, Richland, Washington, January 1983.

George, T. L., "Two Fluid Model for the Tube Side of an LMFBR Steam Generator," FATE-83-118, Pacific Northwest Laboratory, Richland, Washington, August 1983.

George, T. L., T. C. Kennedy, and K. L. Peddicord. "An Elastic Stress-Strain Relation for Sphere Arrays Undergoing Initial Stage Sintering," Journal of Applied Mechanics Paper No. 84-WA/APM-49, December 1984.

Peddicord, K. L., T. L. George, and T. C. Kennedy. "A Model for the Thermal-Mechanical Behavior of Mixed Carbide Sphere Pac Fuel Pins," Nuclear Science and Engineering, Vol. 86, No. 3, March 1984.

Kennedy, T. C., T. L. George, and K. L. Peddicord, "Thermoplastic Analysis of a Sphere Pac Fuel Pin," Nuclear Engineering and Design, Vol. 75, 1983.

George T. L., and C. W. Stewart, "A Fast, Implicit Two-Fluid Solution Technique for Subchannel Geometries," AIChE Symposium Series, 23rd National Heat Transfer Conference, Denver, Colorado, August 1985.

George, T. L., "Numerical Thermal Hydraulics in Curvilinear Coordinates," FATE-84-118, Pacific Northwest Laboratory, Richland, Washington, October 1984.

George, T. L., "PLEXUS: Mesh Generator for Finite Difference Applications," FATE-84-119, Pacific Northwest Laboratory, Richland, Washington, October 1984.

George, T. L., and M. J. Thurgood, "COBRA-NC Analysis for a Main Steamline Break in The Catawba Unit 1 Ice Condenser Containment," NAI-TN-8502, September 1985.

George, T. L., and M. J. Thurgood, "An Assessment of the N-Reactor Hydrogen Mitigation System Effectiveness," NAI-8707-02, January 1988.

George, T. L., and M. J. Thurgood, "CAP Containment Analysis Package User's Manual," May 1988.

George, T. L., "Hydrogen Mitigation System Effectiveness in the N-Reactor Pressurizer Penthouse," NAI-8909-02, September 1989.

George, T. L., "GOTHIC Modeling Guidelines," NAI-8907-04, October 1989.

George, T. L., "Generalized Coordinates for GOTHIC," NAI-9117-1, March 1992.

George, T. L., et al., "Containment Analysis with GOTHIC", ASME 27th National Heat Transfer Conf. Proceedings, July 1991.

George, T. L., "Fire Module Technical Manual", NAI-9118-01, March 1993. 1991.

McLeod, J. N., D. Ghosh and T. L. George, "Application of the Gothic Nuclear Containment Analysis Code to Natural Convection Analysis", 1993 ASHRAE winter meeting, New Orleans.
George, T. L., "Separate Effects Assessment for GOTHIC", Third International Conference on Containment Design and Operation, Toronto, October 1994.

George, T. L. and A. Singh, "Separate Effects Tests for GOTHIC Condensation and Evaporative Heat Transfer Models", Nuclear Engineering and Design, 166, 1966.

George, T. L., et al., "GOTHIC Containment Analysis Package: User's Manual," NAI-8907-02, January 2006.

George, T. L., et al., "GOTHIC Containment Analysis Package: Technical Manual," NAI-8907-06, January 2006.

Wiles, L. E., T. L. George and S. W. Claybrook, "GOTHIC Containment Analysis Package: Qualification Report for GOTHIC_S," NAI-8907-09, January 2006.

George, T. L., et al., "GOTHIC Containment Analysis Package: Programmer's Manual," NAI-8907-10, January 2006.

Wiles, L. E. and T. L. George, "Thermal-Hydraulic Analysis of the Nuclear Power Engineering Corporation Containment Experiments with GOTHIC", Nuclear Technology, Vol. 142, No. 1, April 2003.

Appendix B Cladding Swelling and Rupture Effect on Cladding Heat Conduction Calculation

The temperature of heat structure is calculated at the fixed mesh points by the heat conduction equation in RELAP5-3D. In the case the cladding geometry is greatly changed by the plastic hoop strain or rupture, its effect on the heat conduction calculation should be taken into account.

In the one-dimensional cylindrical coordinate system, Equations B-1 to B-3 give the differential equations of heat conduction at the interior, the inner surface and the outer surface of the cladding respectively when the cladding deformation is not considered. Figure B-1 shows temperature calculation mesh points and intervals between them.

$$(\rho c_p)_j V_j \frac{T_j - T_j^{n-1}}{\Delta t} = 2\pi r_{j-1/2} k_{j-1/2} \frac{T_{j-1} - T_j}{\Delta r_{j-1,j}} - 2\pi r_{j+1/2} k_{j+1/2} \frac{T_j - T_{j+1}}{\Delta r_{j,j+1}} + V_j S_j \quad (B-1)$$

$$(\rho c_p)_i V_i \frac{T_i - T_i^{n-1}}{\Delta t} = 2\pi r_{i-1/2} h_{gap} (T_p - T_i) - 2\pi r_{i+1/2} k_{i+1/2} \frac{T_i - T_{i+1}}{\Delta r_{i,i+1}} + V_i S_i \quad (B-2)$$

$$(\rho c_p)_o V_o \frac{T_o - T_o^{n-1}}{\Delta t} = 2\pi r_{o-1/2} k_{o-1/2} \frac{T_{o-1} - T_o}{\Delta r_{o-1,o}} - 2\pi r_o h_f (T_o - T_f) + V_o S_o \quad (B-3)$$

where (ρc_p) is specific heat of cladding, V is volume per unit length, T is temperature, Δt is time step size, r is radius, Δr is distance, k is thermal conductivity of cladding, S is heat source due to metal water reaction, h_{gap} is gap heat transfer coefficient and h_f is wall heat transfer coefficient.

When the cladding plastic strain begins or the cladding rupture occurs, temperature calculation mesh points, considering the cladding geometry change due to deformation, can be determined so that the volume represented by each calculation mesh point is preserved. When the radii of calculation mesh points, the radii of the middle of them and the distances between them after the cladding deformation are denoted by \hat{r}_j , $\hat{r}_{j+1/2}$, $\Delta \hat{r}_{j,j+1}$ and so on, Equations B-1 to B-3 are converted to Equations B-4 to B-6 respectively.

$$(\rho c_p)_j V_j \frac{T_j - T_j^{n-1}}{\Delta t} = 2\pi \hat{r}_{j-1/2} k_{j-1/2} \frac{T_{j-1} - T_j}{\Delta \hat{r}_{j-1,j}} - 2\pi \hat{r}_{j+1/2} k_{j+1/2} \frac{T_j - T_{j+1}}{\Delta \hat{r}_{j,j+1}} + V_j S_j \quad (B-4)$$

$$(\rho c_p)_i V_i \frac{T_i - T_i^{n-1}}{\Delta t} = 2\pi \hat{r}_{i-1/2} h_{gap} (T_p - T_i) - 2\pi \hat{r}_{i+1/2} k_{i+1/2} \frac{T_i - T_{i+1}}{\Delta \hat{r}_{i,i+1}} + V_i S_i \quad (B-5)$$

$$(\rho c_p)_o V_o \frac{T_o - T_o^{n-1}}{\Delta t} = 2\pi \hat{r}_{o-1/2} k_{o-1/2} \frac{T_{o-1} - T_{out}}{\hat{\Delta} r_{o-1,o}} - 2\pi \hat{r}_o h_f (T_o - T_f) + V_o S_o \quad (B-6)$$

Cladding thermal conductivity, gap heat transfer coefficient and wall heat transfer coefficient after deformation are defined as follows:

$$k_{j+1/2}^* = k_{j+1/2} \frac{\hat{r}_{j+1/2}}{r_{j+1/2}} \frac{\Delta r_{j,j+1}}{\Delta \hat{r}_{j,j+1}} \quad (B-7)$$

$$h_{gap}^* = h_{gap} \frac{\hat{r}_{i-1/2}}{r_{i-1/2}} \quad (B-8)$$

$$h_f^* = h_f \frac{\hat{r}_o}{r_o} \quad (B-9)$$

Substituting them into the Equations B-4 to B-6, the cladding temperature after deformation can be evaluated based on the calculation mesh points before cladding deformation when the corrected thermal cladding conductivity, the corrected gap heat transfer coefficient and the corrected wall heat transfer coefficient defined by Equation B-7 to B-9 are applied. In this manner, the cladding temperature after deformation can be evaluated without changing the calculation mesh points of the heat conduction difference equations in M-RELAP5.

The cladding deformation caused by thermal expansion or elastic deformation by the pressure difference between the inner and outer surfaces is considered to have little effect on the temperature distribution in the fuel. Therefore, these deformation effects are to be neglected in the heat conduction calculations as the original RELAP5-3D.

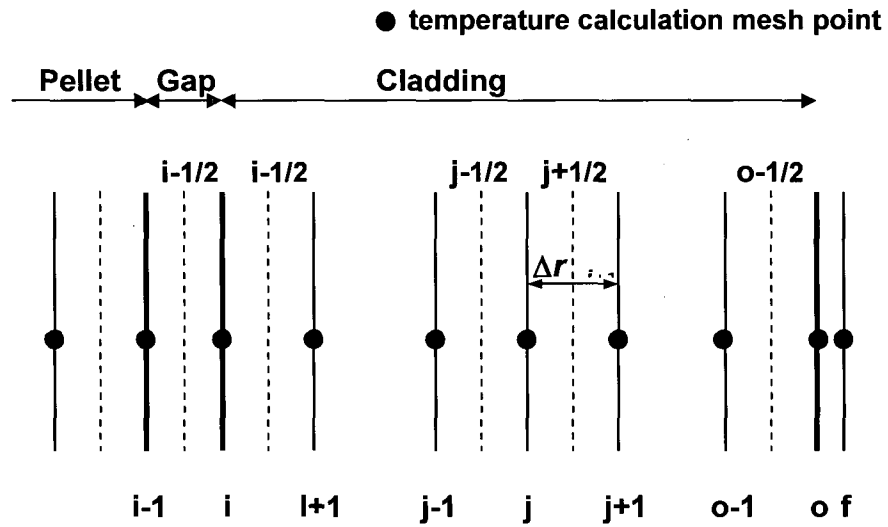


Figure B-1 Temperature Calculation Mesh Points and Intervals between them

Appendix-C Validation of Discharge Model

C.1 Validation of Moody's Critical Flow Model

The Moody's critical flow model (Ref. C-1) incorporated into M-RELAP5 was validated by calculating a critical flow for the system shown in Figure C-1 and then comparing the results with the aforementioned Figure C-2 from the Moody original paper.

The boundary conditions specified were the pressure and the quality for an upstream volume. For a downstream volume the pressure and quality were fixed at 1 psia and 0.0 respectively. The pressures and the qualities selected for the upstream volume are as follows:

Pressure : 25 psia, 50 psia, 100 psia, 200 psia, 300 psia, 400 psia, 500 psia, 600 psia, 700 psia, 800 psia, 1000 psia, 1200 psia, 1400 psia, 1600 psia, 1800 psia, 2000 psia, 2200 psia, 2400 psia, 2600 psia, 2800 psia, 3000 psia.

Quality : 0.0, 0.0101, 0.05, 0.1, 0.15, 0.2, 0.25, 0.3, 0.35, 0.4, 0.45, 0.5, 0.55, 0.6, 0.65, 0.7, 0.8, 0.9, 0.997, 1.0.

After carrying out the analysis using M-RELAP5, the upstream pressure, the upstream mixture enthalpy and the critical flow rate at the time of 1.0 second were extracted to plot from the restart file. Figure C-3 shows these values compared with the values shown in the Moody paper (Ref. C-1). The results agree with those shown in Figure C-2 from the Moody paper.

Moody's critical flow model has an applicable range of $0.01 \leq x_e \leq 1.00$ for equilibrium quality. In the subroutine jchoke, the equilibrium quality is calculated from the following equation

$$x_e = \frac{h_{mix} - h_f}{h_g - h_f}$$

The calculated equilibrium quality is then used as a applicable condition for a critical flow model. To investigate the difference the Moody-Henry-Fauske model from the other critical flow models in RELAP5-3D in the applicable range, the critical flow rates at $x_e = 0.0$ and $x_e = 1.0$, which are out of the applicable range, were investigated under the conditions similar to those used to produce Figure C-3.

Figure C-4 shows plots of the critical flow rates calculated using $x_e = 0.0$ and $x_e = 1.0$.

These values were added to the results shown in Figure C-3. From the calculation results, the critical flow rate was extracted from the restart file at a time of 1.0 seconds, the Henry-Fauske's model for a liquid single phase was then applied at the left end point since $x_e < 10^{-6}$. On the other hand, the equation for a compressible single phase fluid of steam was applied at the right end point, since $x_e = 1.0$.

The difference in the critical flow rate between the results obtained using the Moody model at $x_e = 0.01$ and the results obtained using the Henry-Fauske model at $x_e = 0.0$ is about 25%. On the other hand, the difference between the critical flow rate obtained using the Moody model at $x_e = 0.998$ and the results obtained using the equation for the compressible single phase fluid of steam single phase at $x_e = 1.0$ is about 9%.

C.2 References

- C-1 Moody, F. J., "Maximum Flow Rate of a Single Component, Two-Phase Mixture," J. of Heat Transfer, Trans. ASME, Series C, Vol. 87, No. 1, February 1965, PP. 134–142.

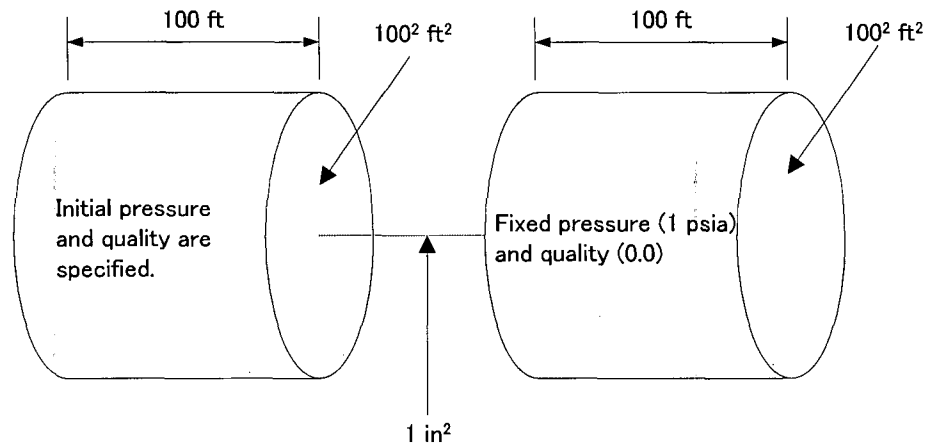


Figure C-1 Noding Diagram of Moody Critical Flow Model Test Problem

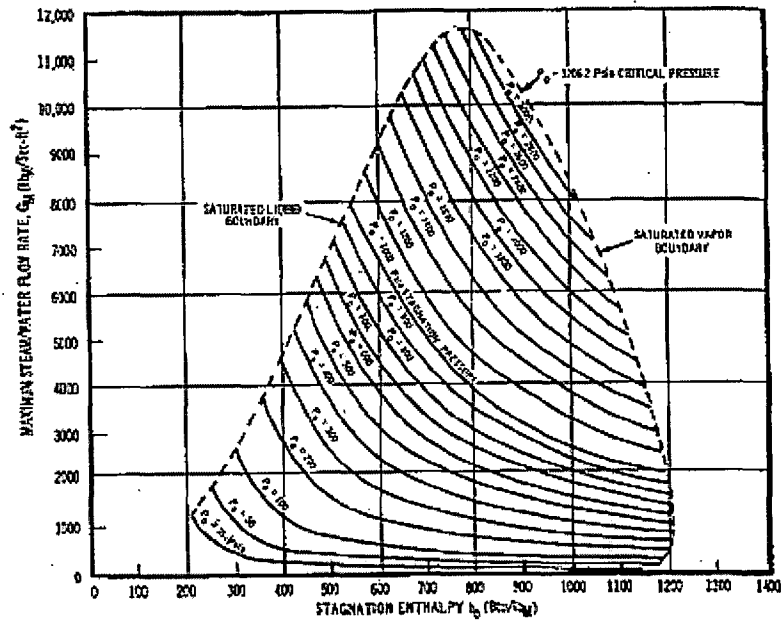


Figure C-2 Maximum Steam/Water Flow Rate and Local Stagnation Properties

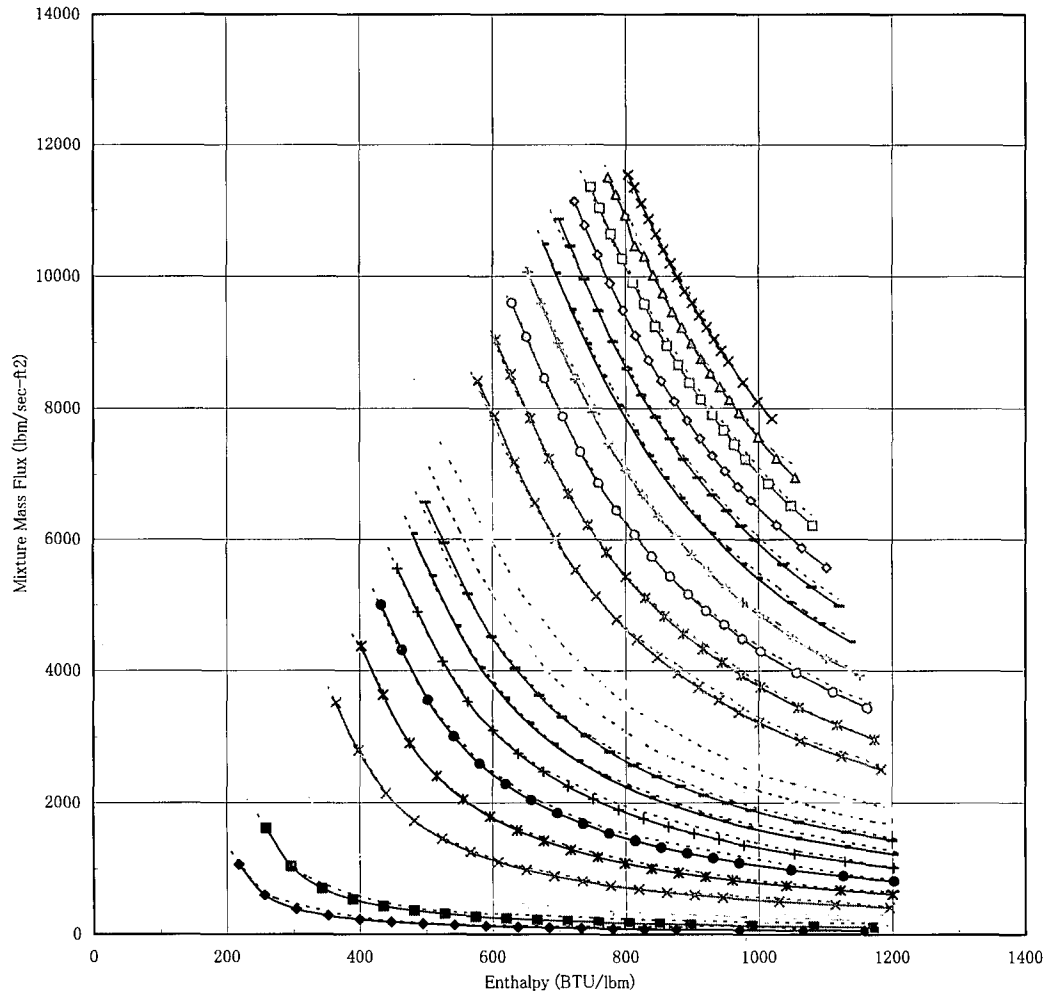


Figure C-3 Comparison of the Calculation Results with the Moody's Paper

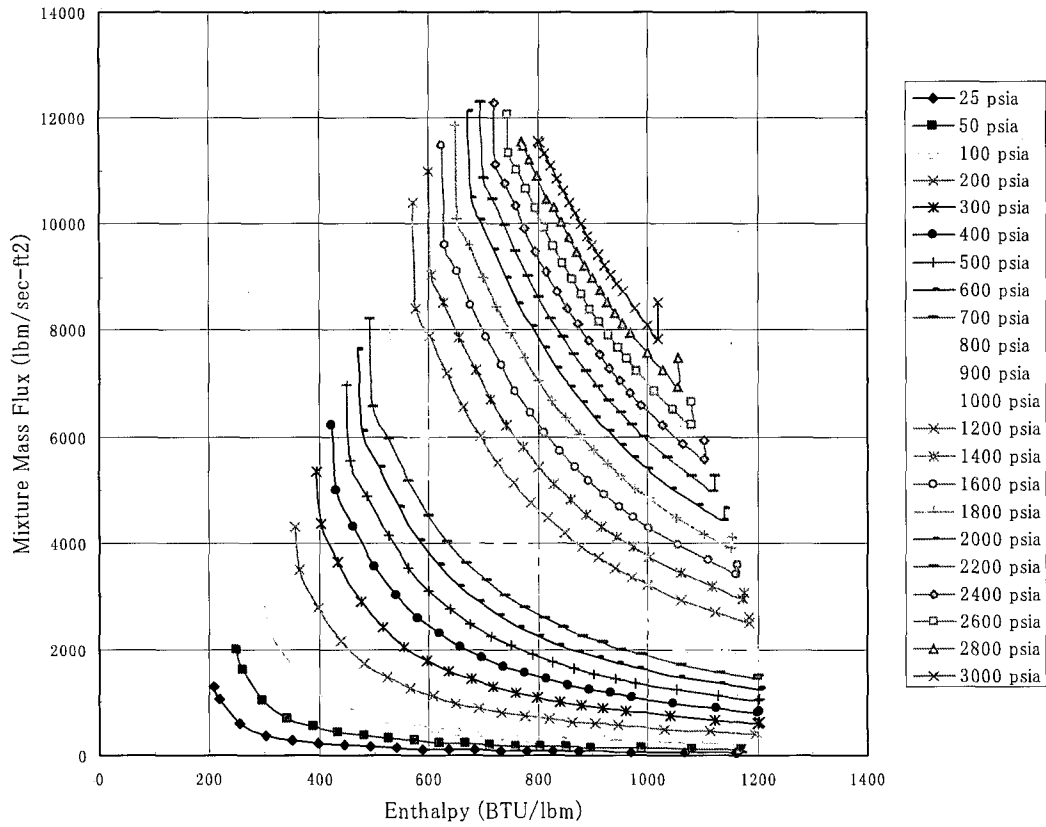


Figure C-4 Connection of Moody's Critical Flow Model and Other Models

The left end points were obtained with Henry-Fauske and the right end points were obtained with the equation for the compressible single phase fluid of steam single phase.

Appendix D Implementation of Advanced Accumulator Model

D.1 Advanced Accumulator Model

The total resistance coefficient K_{ACC} , is determined from the ACC flow rate coefficient, C_v and the resistance coefficient from the injection piping. (Ref. D-1) The flow rate coefficient is a function of the cavitation factor σ_v , and the water level in the ACC. The total resistance coefficient is calculated as follows.

(1) σ_v is calculated from the flow condition at flow damper

$$\sigma_v = \frac{P_D + P_{at} - P_v}{(P_A + \rho g H) - \left(P_D + \frac{\rho V_D^2}{2} + \rho g H' \right)} \quad (D-1)$$

- σ_v : Cavitation factor
- P_{at} : Atmospheric pressure (abs)
- P_D : Flow damper outlet pressure (gage)
- P_A : Gas pressure in accumulator (gage)
- P_v : Vapor pressure (abs)
- ρ : Density of water
- g : Acceleration of gravity
- H : Distance between ACC water level and vortex chamber
- H' : Distance between outlet pipe and vortex chamber
- V_D : Velocity of injection pipe

(2) The flow rate coefficient C_v is calculated using the following correlations obtained from test data that covers the range of applicability for the US-APWR design. The empirical correlations of C_v are derived separately for large and small flow rate injections as a function of the cavitation factor of σ_v .

$$\text{For large flow rate: } C_v = 0.7787 - 0.6889 \exp(-0.5238 \sigma_v) \quad (D-2)$$

$$\text{For small flow rate: } C_v = 0.07197 - 0.01904 \exp(-6.818 \sigma_v) \quad (D-3)$$

(3) C_v is converted to K_D

$$K_D = 1/C_v^2 \quad (D-4)$$

(4) Total resistance coefficient is calculated by;

$$K_{acc} = K_D + K_{pipe} \quad (D-5)$$

Where

K_{acc} : Total resistance coefficient of flow damper and injection piping

K_{pipe} : Total resistance coefficient of injection piping

D.2 Accumulator Model in RELAP5-3D for Existing PWRs

In RELAP5, an accumulator for an existing three or four loop PWR is modeled as a lumped-parameter component (black box model), because the spatial distribution in the accumulator tank does not make any difference in the system transient analysis, and a special treatment of the state equation becomes possible. The following is the outline of the accumulator model excerpted from RELAP5-3D© Code Manual VOLUME (Ref. D-2).

An accumulator model is included that features mechanistic relationships for the hydrodynamics, heat transfer from the tank wall and liquid surface, condensation in the vapor/gas dome, and vaporization from the liquid surface to the vapor/gas dome. The geometry of the tank may be cylindrical or spherical. The accumulator model also includes the surge line and an outlet check valve junction.

The accumulator model and associated notations are shown in Figure D-1 a) for the case of a cylindrical tank, and Figure D-1 b) for the case of a spherical tank. The basic model assumptions are:

- Heat transfer from the accumulator walls and heat and mass transfer from the liquid are modeled using natural convection correlations, assuming similarity between heat and mass transfer from the liquid surface.
- The vapor/gas in the vapor/gas dome is modeled as a closed expanding system composed of an ideal gas with constant specific heat. The vapor in the dome exists at a very low partial pressure; hence, its effect on the nitrogen state is neglected. However, energy transport to the vapor/gas dome as a result of vaporization/condensation is included.

- Because of the high heat capacity and large mass of liquid below the interface, the liquid is modeled as an isothermal system.
- The model for liquid flow includes inertia, wall friction, form loss, and gravity effects.

Using these assumptions, the basic equations governing the thermal-hydraulics of the tank and discharge line are as follows:

The conservation of mass for the nitrogen dome is

$$M_N = \text{const} = \rho_n V_D \dots\dots\dots(D-6)$$

where M_N is nitrogen gas mass, ρ_N is nitrogen gas density, and V_D is vapor/gas dome volume. The conservation of energy for the nitrogen gas in the dome is

$$M_N \frac{dU_N}{dt} = -P \frac{dV_D}{dt} + \dot{Q}_D \dots\dots\dots(D-7)$$

where U_N is nitrogen specific internal energy, P is vapor/gas dome pressure, and \dot{Q}_D is net heat transfer rate to the vapor/gas dome from all sources. The conservation of energy for the tank wall is

$$M_{\text{wall}} C_{V,\text{wall}} \frac{dT_{\text{wall}}}{dt} = -\dot{Q}_{\text{wall}} \dots\dots\dots(D-8)$$

where M_{wall} is metal mass in the tank wall, $C_{V,\text{wall}}$ is metal specific heat, T_{wall} is mean metal temperature, and \dot{Q}_{wall} is heat transfer rate to the wall. The conservation of momentum for the accumulator tank and surge line is

$$\rho A \left(L \frac{dv}{dt} + \frac{1}{2} v^2 \right) + Fv = A(P - P_{\text{exit}}) + A \Delta P_z \dots\dots\dots(D-9)$$

where A is flow channel cross-sectional area, L is discharge line flow channel length, v is velocity in discharge line, F is frictional loss coefficient, P_{exit} is pressure at exit of surge line, ΔP_z is elevation pressure differential between discharge line entrance and liquid surface. This equation is the combined tank and discharge line momentum equation. The equations of state for the nitrogen gas in the dome are

$$PV_D = M_N R_N T \dots\dots\dots(D-10)$$

$$U_N = M_N C_{V,n} T_g \dots\dots\dots(D-11)$$

Using Eq. (D-11), Eq. (D-7) the nitrogen energy equation, can be rewritten as

$$M_N C_{V,N} \frac{dT_g}{dt} = -P \frac{dV_D}{dt} + \dot{Q}_D \dots\dots\dots(D-12)$$

Differentiating Eq. (D-10), eliminating the constant term $M_n R_n$, and substituting the result into Eq. (D-12) yields

$$P \left(1 + \frac{R_N}{C_{V,N}} \right) \frac{dV_D}{dt} + V_D \frac{dP}{dt} = \frac{R_N}{C_{V,N}} \dot{Q}_D \dots\dots\dots(D-13)$$

Eqs. (D-9), (D-12) and(D-13) comprise the system of three differential equations used in the accumulator hydrodynamic model. They are used to numerically advance T_g , V_D and P in time.

The numerical scheme used for the accumulator model includes special features for coupling the solution scheme to the main code in such a way that it is time step independent. This scheme is semi-implicit, and special considerations are employed to preserve the nitrogen energy and mass. Since a spherical accumulator has a variable cross-sectional area, the momentum equation is generalized to the case of a variable flow area.

The numerical scheme uses finite-difference techniques to solve the differential equations. The momentum equation is formulated by integrating Eq. (D-9) over space and writing the time variation in difference form as

$$\begin{aligned} & \left[\rho_f (L_{fL} + L_{fTK}) \left(\frac{A_L}{A_f} \right) + F_f \Delta t + \rho_g (L_{gL} + L_{gTK}) \left(\frac{A_L}{A_g} \right) + F_g \Delta t \right] v_{fL}^{n+1} = \\ & - (P^{n+1} - P^n) \Delta t + \Delta P_z \Delta t + \left[\rho_f (L_{fL} + L_{fTK}) \left(\frac{A_L}{A_f} \right) + \rho_g (L_{gL} + L_{gTK}) \left(\frac{A_L}{A_g} \right) \right] v_{fL}^n \dots\dots\dots(D-14) \\ & - CONVF - CONVG \end{aligned}$$

where P^{n+1} is the pressure downstream from the accumulator junction. The inertia term is represented by

$$\rho_f (L_{fL} + L_{fTK}) \left(\frac{A_L}{A_f} \right) + \rho_g (L_{gL} + L_{gTK}) \left(\frac{A_L}{A_g} \right) \dots\dots\dots(D-15)$$

where L_{fL} , L_{fTK} , L_{gL} and L_{gTK} are the lengths of the liquid and vapor/gas in the discharge

line and tank, respectively, A_L is the area of the discharge line, and A_f and A_g are the mean flow areas in the tank and discharge line of the liquid and vapor/gas, respectively. In the case of a spherical tank, A_g used in the vapor/gas inertia term is obtained from the relation

$$L_{gTK} A_g = V_{gTK} \dots\dots\dots(D-16)$$

and A_f used in the liquid inertia term is obtained from the relation

$$L_{fTK} A_f = V_{fTK} \dots\dots\dots(D-17)$$

where V_{gTK} and V_{fTK} are the vapor/gas and liquid volumes, respectively. The volume of vapor/gas in the tank is

$$V_{gTK} = \frac{\pi}{3} L_{gTK}^2 (3R - L_{gTK}) \dots\dots\dots(D-18)$$

and the available volume of liquid in the tank is

$$V_{fTK} = \frac{4\pi}{3} R^3 - V_{gTK} - \frac{\pi}{3} L_{min}^2 (3R - L_{min}) \dots\dots\dots(D-19)$$

where L_{min} is the minimum liquid level that is determined by the position of the discharge line which may protrude into the tank. The inertia terms are computed at each time step and vary explicitly with time; as the accumulator blows down, the inertia term changes from a liquid-dominant to a vapor/gas-dominant term. R is the radius of the spherical tank.

The liquid and vapor/gas friction terms, respectively, are formulated as

$$F_f = \frac{\rho_f}{2} \left(\lambda \frac{L_{fL} + L_{fTK}}{D} + K_L \frac{L_{fL}}{L_L} \right) v_{fL}^n \left(\frac{A_L}{A_f} \right)^2 \dots\dots\dots(D-20)$$

for the liquid, and

$$F_g = \frac{\rho_g}{2} \left(\lambda \frac{L_{gL} + L_{gTK}}{D} + K_L \frac{L_{gL}}{L_L} \right) v_{gL}^n \left(\frac{A_L}{A_g} \right)^2 \dots\dots\dots(D-21)$$

for the vapor/gas, where the friction is calculated for the tank and the line. The line friction factor λ is assumed to be the constant turbulent-turbulent Darcy friction factor given as

$$\lambda = \left[1.74 - 2 \log_{10} \left(\frac{2\varepsilon}{D} \right) \right]^{-2} \dots\dots\dots (D-22)$$

The loss factor term, K_L , is assumed to be distributed over the discharge line length, L_L , and it is neglected in the tank. If the surge line length is 0, the loss factor term is not used. The term D is the average tank and surge line hydraulic diameter, and ε is the input wall roughness.

The elevation head term, ΔP_Z , is formulated as

$$\Delta P_Z = - \frac{g \Delta z_{TK} \left(\rho_f + \frac{1}{2} \rho_g L_{gTK} \right)}{L_{TK}} - \frac{g \Delta z_L \left(\rho_f L_{fL} + \rho_g L_{gL} \right)}{L_L} \dots\dots\dots (D-23)$$

where Δz_{TK} and Δz_L are the tank and surge line elevation changes, respectively, and g is the gravitational acceleration.

The liquid and vapor/gas momentum flux terms, $CONVF$ and $CONVG$, respectively, are formulated in linear implicit form as

$$CONVF = \frac{1}{2} \rho_f \left[1 - \left(\frac{A_L}{A_f} \right)^2 \right] \Delta t v_{fL}^n \left(2v_{fL}^{n+1} - v_{fL}^n \right) \dots\dots\dots (D-24)$$

if there is liquid in the tank,

$$CONVF = 0.0 \dots\dots\dots (D-25)$$

where there is no liquid in the tank,

$$CONVG = \frac{1}{2} \rho_g \left[1 - \left(\frac{A_L}{A_g} \right)^2 \right] \Delta t v_{gL}^n \left(2v_{gL}^{n+1} - v_{gL}^n \right) \dots\dots\dots (D-26)$$

if there is vapor/gas in the discharge line, and, finally

$$CONVG = 0.0 \dots\dots\dots (D-27)$$

where there is no vapor/gas in the discharge line. In the case of a spherical tank, the value of A_{TK} used in $CONVF$ is the flow area at the liquid-vapor/gas interface, and the value of A_{TK} used in $CONVG$ is the mean flow area of the tank. In this formulation, the momentum equation is solved over the pressure gradient from the centroid of the vapor/gas dome to the accumulator junction. However, the momentum of the fluid downstream from the accumulator junction is not included. Flow begins when the pressure, gravity, and friction forces result in

positive flow out of the accumulator; and flow ceases when these forces result in reverse flow. Also, since fluxing of the vapor/gas through the junction is not allowed,

$$v_{gL}^n = v_{fL}^n \dots\dots\dots(D-28)$$

until the accumulator empties of liquid. The effect of this formulation is that as the accumulator blows down, the liquid-vapor/gas interface moves out of the accumulator tank and surge line. Thus, the centroid of the vapor/gas dome moves towards the centroid of the combined tank and surge line.

The pressure solution is obtained by combining Eqs. (D-7) and (D-11), and multiplying by $R_N/C_{V,N}$, which results in

$$M_N R_N \frac{dT}{dt} = -\frac{R_N P}{C_{V,N}} \frac{dV_D}{dt} + \frac{R_N}{C_{V,N}} \dot{Q}_D \dots\dots\dots(D-29)$$

Since the liquid is incompressible, we obtain

$$\frac{dV_D}{dt} = -\frac{dV_f}{dt} = A_L v_{fL} \dots\dots\dots(D-30)$$

substitution into Equation Eq. (D-13), and expanding in nonconservative finite difference form gives

$$P^n \left(1 + \frac{R_N}{C_{V,N}} \right) A_L \Delta t v_{fL}^{n+1} + V_D^n (P^{n+1} - P^n) = \frac{R_N}{C_{V,N}} \dot{Q}_D \Delta t \dots\dots\dots(D-31)$$

The energy equation may then be solved directly for the new time vapor/gas temperature by combining Eqs. (D-5), (D-8) and (D-26) and integrating, which gives

$$T_g^{n+1} = T_g^n \exp \left[\frac{R_N}{C_{V,N}} \ln \frac{V_D^n}{V_D^{n+1}} + \Delta t \frac{R_N}{C_{V,N}} \frac{\dot{Q}_D}{P^n V_D^n} \right] \dots\dots\dots(D-32)$$

The algorithm used to track the liquid level is based on the tank mass balance which is given by

$$A_L v_{fL} = -A_{TK} \frac{dL_{gTK}}{dt} \dots\dots\dots(D-33)$$

In the case of a spherical tank, A_{TK} is given by

$$A_{TK} = \pi L_{gTK} (2R - L_{gTK}) \dots\dots\dots(D-34)$$

Given L_{gTK}^n , Eq. (D-33) is solved by explicit numerical integration to obtain L_{gTK}^{n+1} , which is of the form

$$L_{gTK}^{n+1} = L_{gTK}^n - \frac{A_L v_{fL}^{n+1} \Delta t}{\pi L_{gTK}^n (2R - L_{gTK}^n)} \dots\dots\dots(D-35)$$

In RELAP5, the following heat transfers to the nitrogen gas enclosed in the accumulator are considered.

- Heat transfer from the accumulator wall
- Heat transfer from the liquid phase
- Energy transfer from the liquid phase by mass transfer

If “heat transfer flag,” which is one of the input options, is set to “1”, all the heat transfer calculations are skipped in the program, and the heat transfers to the nitrogen gas is not calculated. That is to say, the state change of the nitrogen gas is treated as an adiabatic expansion process by setting the “heat transfer flag” to “1.”

D.3 Implementation of Advanced Accumulator Model

The injection characteristic of the advanced accumulator is simulated by calculating C_v using the correlations of cavitation coefficient σ_v and flow coefficient C_v obtained from the experiments, converting C_v into the resistance coefficient K value and adding it to the friction terms. By adding the resistance coefficient K_D to the loss factor term, K_L indicated in Eqs. (D-20) and (D-21) in RELAP5-3D, the injection characteristics of the advanced accumulator are modeled. The calculation procedure is as follows.

Based on the configuration of the advanced accumulator shown in Figure D-2, the new time step value of the vortex damper outlet pressure, P_D , is

$$P_D = P_{INJ} - \rho_f g H_{INJ} + PLOSS - \frac{\rho_f V_D^2}{2} \dots\dots\dots(D-36)$$

where P_{INJ} is the pressure at the injection point which is the downstream volume pressure, $\rho_f g H_{INJ}$ is the head loss due to the elevation change from the injection point to the flow damper outlet, $PLOSS$ is the friction terms in discharge line, and V_D is the velocity at the flow damper outlet which is the old time step value of junction velocity representing the

discharge line velocity. As the elevation change H_{inj} is not included in the input data of RELAP5-3D, the input method is provided by the new additional input card. The velocity at the vortex damper outlet, V_D , must be calculated based on the discharge line flow area, the junction area should set to the discharge line flow area as same as the conventional input of RELAP5-3D. Using λ and K_L used in Eqs. (D-20) and (D-21), $PLOSS$ is given by

$$PLOSS = \frac{\rho_f}{2} \left(\lambda \frac{L_L}{D} + K_L \right) V_D^2 \dots\dots\dots(D-37)$$

If it is required that the pressure loss of the surge pipe should be set to the loss factor term only, the option is set using the volume flag of the accumulator so that the pipe friction is not calculated. This insures the consistency between the design values obtained from the experiments using the loss factor term and the calculation by RELAP5-3D.

Using the flow damper outlet pressure, P_D , the cavitation factor σ_v is

$$\sigma_v = \frac{P_D - P_v}{(P_g - P_D) - \frac{\rho_f V_D^2}{2} + \rho g H} \dots\dots\dots(D-38)$$

where the variables and constants are

- P_D : Flow damper outlet pressure (abs) (calculated for new time step advancement)
- P_g : Gas pressure in accumulator (abs) (volume pressure at the old time step)
- P_v : Vapor pressure (abs) (vapor partial-pressure at the old time step)
- ρ_f : Density of water (volume liquid phase density at the old time step)
- g : Acceleration of gravity (a constant)
- H : Distance between accumulator water level and vortex chamber (calculated based on the geometry)
- V_D : Velocity of injection pipe (junction flow velocity at the old time step).

In order to calculate the elevation change from the tank water level to the vortex damper outlet, the water level and the elevation of the vortex damper outlet, H , are required. The water level is calculated by subtracting the dead water volume V_{noinj} from the volume of liquid phase. As the dead water volume, V_{noinj} , and the elevation of the vortex damper outlet, H , are not included in the input data of RELAP5-3D, the input method is provided by the new additional input card.

Using the cavitation coefficient, σ_v , the flow rate coefficient C_v is given by

$$C_v = 0.7787 - 0.6889 \exp(-0.5238\sigma_v) \dots\dots\dots(D-39)$$

for large flow rate and

$$C_v = 0.07197 - 0.01904 \exp(-6.818\sigma_v) \dots\dots\dots(D-40)$$

for small flow rate.

The residual water volume of the tank, V_s is used as the condition to select the equation, and is not included in the input data of RELAP5-3D, it is entered using the option card.

The resistance coefficient K_D is calculated by Eq. (D-4) using the flow coefficient C_v . The resistance coefficient obtained is added to the configurational loss in Eqs. (D-20) and (D-21). Consequently, the loss term of the liquid phase is given by the equation below:

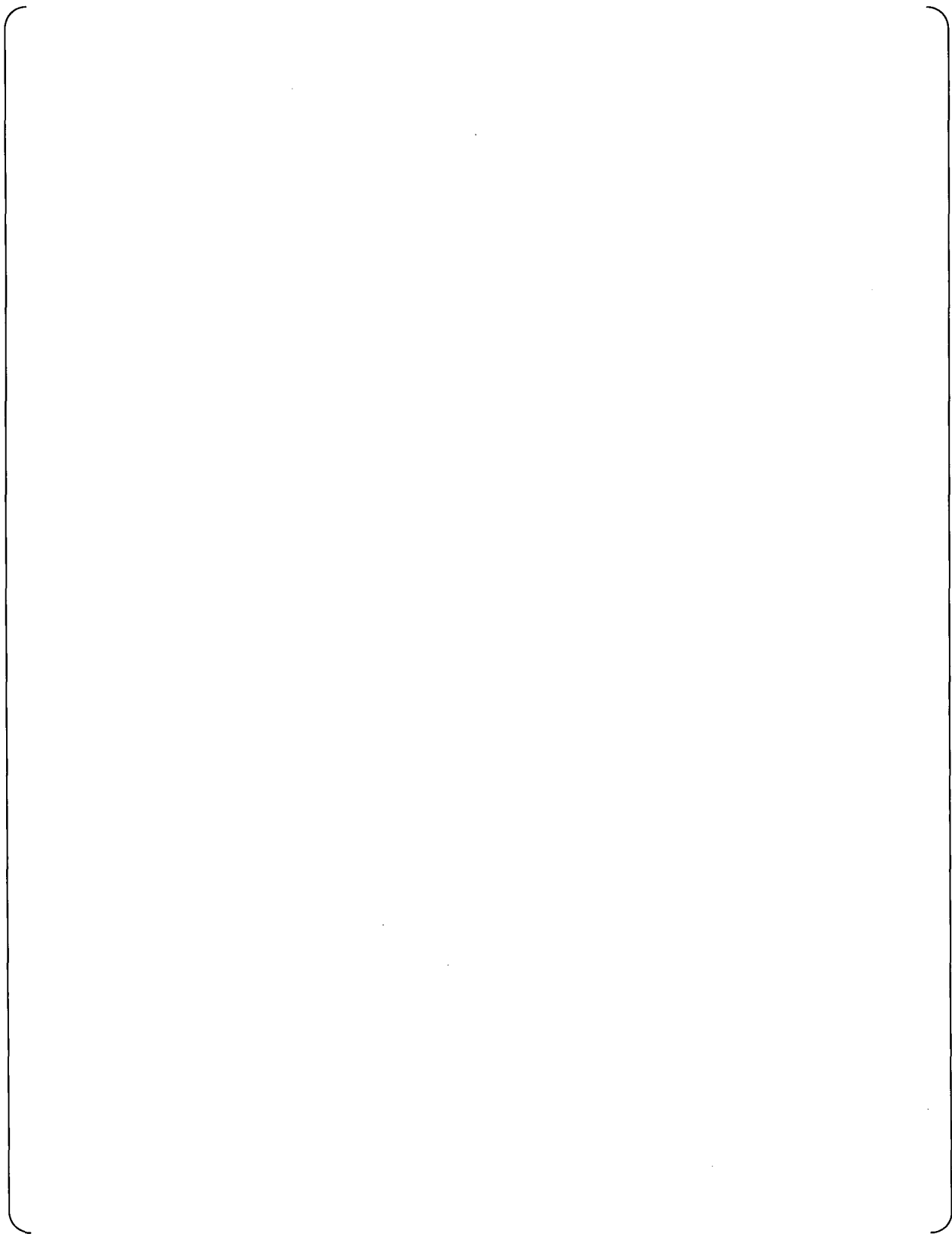
$$F_f = \frac{\rho_f}{2} \left(\lambda \frac{L_{fL} + L_{fTK}}{D} + (K_L + K_D) \frac{L_{fL}}{L_L} \right) v_{fL}^n \left(\frac{A_L}{A_f} \right)^2 \dots\dots\dots(D-41)$$

while the loss term of the gas phase is given by the equation below:

$$F_g = \frac{\rho_g}{2} \left(\lambda \frac{L_{gL} + L_{gTK}}{D} + (K_L + K_D) \frac{L_{gL}}{L_L} \right) v_{gL}^n \left(\frac{A_L}{A_g} \right)^2 \dots\dots\dots(D-42)$$

D.4 Treatment of Uncertainty







Uncertainties of Water Level for Switching Flow Rates for US-APWR



D.5 References

- D-1. T. Ogino, et al., THE ADVANCED ACCUMULATOR, MUAP-07001-P(R1), Mitsubishi Heavy Industries, 2007.

D-2. RELAP5-3D© Code Manual VOLUME I: CODE STRUCTURE, SYSTEM MODELS,
AND SOLUTION METHODS, INEEL-EXT-98-00834 Revision 2.4, June 2005

Table D-1 Total Uncertainty of Experimental Equation for Safety Analysis of US-APWR



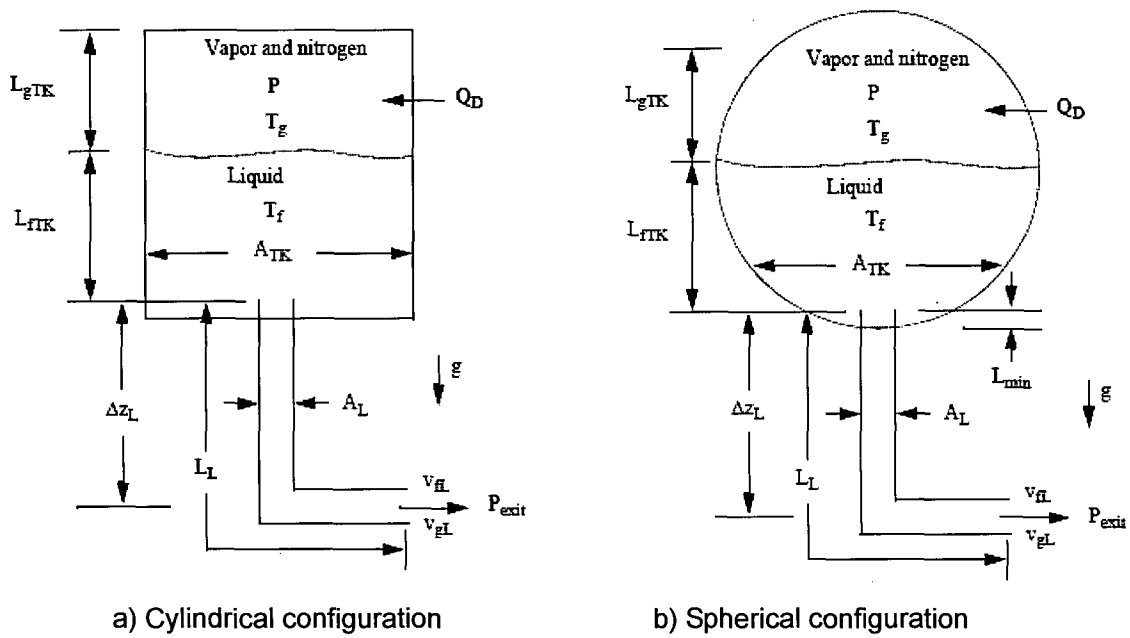


Figure D-1 Accumulator model

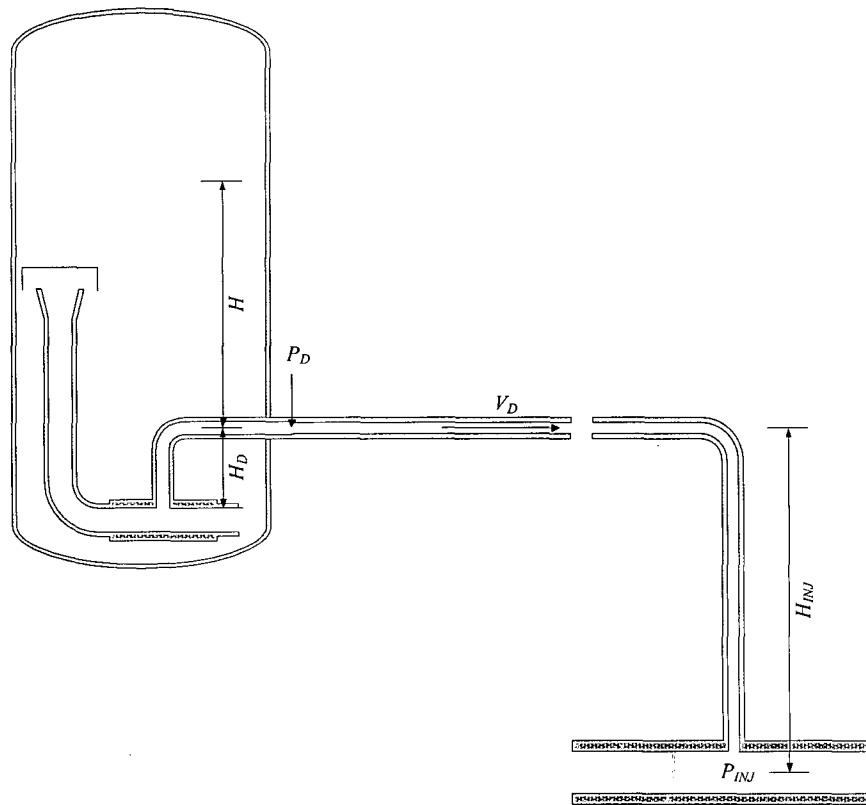


Figure D-2 Parameters required for the calculation of P_D

Appendix E Sample Analysis of Small Break LOCA

E.1 Introduction

The analysis of a small break loss-of-coolant accident (SBLOCA) for US-APWR was performed using M-RELAP5 in accordance with the requirements specified in 10 CFR Part 50 Section 50.34, "Contents of Applications; Technical Information" (Ref. E-1) and the acceptance criteria specified in 10 CFR Part 50 Section 50.46, "Acceptance Criteria for Emergency Core Cooling System for Light-Water Nuclear Power Reactors" (Ref. E-2). The purpose of the analysis is to examine the thermal-hydraulics and fuel rod behavior of US-APWR in the design-basis small break LOCA using M-RELAP5 and thereby to show that M-RELAP5 has sufficient capability to properly analyze the US-APWR design-basis small break LOCA. A cold leg 67.5-inch break LOCA is selected as a typical small break LOCA for US-APWR. The analysis models are described in Section 8.4 of the body of the report. Sections E.2 and E.3 present conditions and results of the analysis, respectively. The conclusion is given in Section E.4.

E.2 Analysis Conditions

E.2.1 Calculation Procedure

Steady-State Calculation

Before transient calculation a steady-state calculation with no break is performed to set desired initial plant operating conditions. Major parameters such as core power, primary system pressure, temperatures, primary system flow and secondary side pressure from the steady-state calculation are confirmed to be sufficiently steady and that steady-state values of these parameters are sufficiently close to the desired values.

Transient Calculation

Transient calculation is performed subsequently after the steady-state calculation. For the transient calculation, a postulated split break is assumed to occur in one of the cold legs. Reactor trip due to the pressurizer low pressure signal and SI signal from the pressurizer low-low pressure are modeled. Subsequent component actuations from these signals are also

modeled.

E.2.2 Description of Analysis Conditions

Sample plant analysis conditions of the US-APWR for M-RELAP5 are listed in Table E-1. The followings are the assumptions in major small break LOCA input parameters for the US-APWR sample analysis.

E.2.2.1 Core and Fuel Rod Conditions

- a. Initial Core Average Linear Heat Rate: The core power assumed for the sample analysis is 102 percent of the rated power considering calorimetric uncertainty.
- b. Hot Rod Peaking Factor, F_Q : The technical specification limit value (2.6) of hot rod peaking factor is assumed
- c. Hot Channel Enthalpy Rise Factor, $F_{\Delta H}$: The technical specification limit value (1.78) is assumed. 1.59 is used for hot assembly average power factor.
- d. Axial Power Shape: Top-Skew (double-hump) power shape is adopted. Such a distribution is limiting for SBLOCA since it minimizes core level swell while maximizing vapor superheating and fuel rod heat generation at the uncovered elevation. Axial peaking factor of the shape is given so as to be consistent with F_Q and $F_{\Delta H}$ of the hot rod.
- e. Hot Assembly Burnup: Beginning of life (BOL) conditions in the hot assembly is assumed in the sample analysis. The fuel temperature is calculated by the fuel design code based on the burnup condition.

E.2.2.2 Plant Operating Conditions

- a. Fraction of Steam Generator Tube Plugged: The highest average tube plugging likely to occur during the next several cycles is expected to be less than 10 percent. For the sample analysis, a tube plugging fraction of 10 percent is assumed.
- b. Primary coolant average temperature: Nominal value plus 4°F, measurement uncertainties, is assumed.
- c. RCS pressure: Nominal values plus 30psi, measurement uncertainties, is assumed.
- d. Primary coolant flow rate: Thermal design flow in case of the above SG plugging ratio is assumed.
- e. Upper head temperature: Cold leg temperature as the best estimate value is assumed.

- f. Pressurizer water level: A nominal value of pressurizer level is assumed.
- g. Accumulator water temperature: The highest value within the operating condition is assumed as a constant value through transient.
- h. Accumulator pressure: The lowest value of accumulator pressure is assumed.
- i. Accumulator water volume: A nominal value of accumulator water volume is assumed.

E.2.2.3 Accident Boundary Conditions

- a. Break location: A break is assumed to occur near the middle point of the cold leg in the loop with the pressurizer is assumed. Pressurizer location in the analysis model is considered to have a small influence on PCT.
- b. Break type: The split break with top orientation is assumed.
- c. Break size: 67.5-inch diameter break area is assumed.
- d. Offsite power: Loss of offsite power is assumed to occur simultaneous with the turbine trip.
- e. Reactor Protection System: Reactor trip signal by the pressurizer low-pressure is assumed. Reactivity insertion due to control rod with signal delay time ~~and rod drop delay time~~ is considered.
- f. Turbine Trip: Turbine trip concurrent with the pressurizer low-pressure is assumed. Steam generators are assumed to be isolated on turbine trip in order to maximize stored energy in the SGs.
- g. Reactor Coolant Pump (RCP) Operation: RCP trip occurs by the signal of the safety injection and the turbine trip with delay time in the US-APWR design. Start of RCP coast-down is assumed 10-3 seconds after ~~turbine reactor~~ trip during which RCP is assured to be powered even if loss of offsite power occurs.
- h. Safety Injection Signal: SI signal by the pressurizer low-low-pressure are modeled. Uncertainty of the pressure setpoint is conservatively considered.
- i. Safety injection delay time: Maximum value consistent with loss of offsite power assumption is used.
- j. Number of available safety injection pumps: 2 pumps are assumed.
- k. Safety injection water temperature: ~~The highest temperature of RWST water in the normal operation is assumed.~~ Higher bounding temperature throughout the LOCA transient is assumed. [

]

Accumulator water temperature is assumed to be equal to the highest containment atmospheric temperature, 120°F, allowed in the normal plant operation for conservatism. The temperature is also assumed to be constant throughout the transient. These treatments give a conservative condition to calculate the PCT.

- I. Auxiliary feed-water flow: Minimum auxiliary feed-water flow is assumed.

E.3 Analysis Results

Transient calculation is initiated from the end of the steady state calculation with the break model applied to the break location. The sequence of events in the transient is shown in Table E-2.

Figure E-1 shows pressurizer pressure. Pressurizer pressure decreases rapidly to the saturation pressure right after the break before and then primary coolant begins to boil. Reactor trip signal is issued when the pressure reaches the set point at 9.99.3 seconds. Figure E-2 shows SG secondary side pressure. The secondary side pressure increases to the set point of the safety valve in both broken loop and intact loop after the reactor trip because secondary side is isolated immediately after the reactor trip. Figure E-3 shows normalized core power. After 2-1.8 seconds from the reactor trip signal, control rods begin to drop and core power decreases rapidly.

RCPs begin to coast-down 40-3 seconds after reactor trip signal. Figure E-4 shows average core channel/hot assembly flow rate. Average and hot channel flow which decreases along with RCP coast-down.

SI signal is generated when the pressurizer pressure reached the set point at 16-11.9 seconds and DVI injection begins at 134-130 seconds. As the system pressure decreases, the accumulator begins to discharge at 547-315 seconds. Injection flows of the DVI and the accumulator are shown in Figure E-5

Figure E-6 shows break flow. Break flow decreases as the primary pressure decreases and quality of the break location increases.

Core collapsed level (Figure E-7) decreases as the coolant is lost from the break and hot fuel rod in the upper region begins to heat up at 483-122 seconds due to temporal core uncover by

the loop seal formation in the cross over leg. Figure E-8 shows cladding the maximum temperature of the all elevations of hot rod at the peak cladding temperature (PCT) location. Figure E-9 shows heat transfer coefficient of the hot fuel rod at the PCT location. The peak cladding temperature is 699775 °F at 202136 seconds. Core collapsed level begins to recover due to DVI and accumulator injection after about 550s300 seconds and thereafter no core uncover occurs. Cladding temperature of hot fuel rod is kept near the saturation temperature of the coolant.

E.4 Conclusion

In the sample analysis, the small break LOCA of 67.5-inch size break is analyzed by M-RELAP5 and reasonable transient behavior is obtained. Temporal core uncover occurs due to the loop seal formation and fuel rods are heated up. The PCT is 699775 °F and is much lower than the acceptance criteria of 2200°F. The DVI injection and the accumulator injection keep the core covered after the temporal core uncover.

This sample analysis demonstrates that M-RELAP5 has sufficient capability to analyze the design basis small break LOCA for US-APWR.

E.5 References

- E-1 10 CFR 50.34, "Contents of Application; Technical Information."
- E-2 10 CFR 50.46, "Acceptance Criteria for Emergency Core Cooling System for Light-Water Nuclear Power Reactors."
- E-3 NUREG-0800, "Standard Review Plan 15.6.5 Loss-of-Coolant-Accident Resulting from Spectrum of Postulated Piping Breaks within the Reactor Coolant Pressure Boundary," Revision 3 –March 2007.

Table E-1 Analysis Conditions for US-APWR

Parameter	Values
Core and Fuel Rod Conditions	
a) Core power	102% of rated power (4540 MWt)
b) Peaking factor	Tech Spec ($F_Q=2.6$)
c) Hot channel enthalpy rise factor	Tech Spec ($F_{\Delta H}=1.78$)
d) Hot assembly average power factor	1.59
e) Axial power shape	Top-Skew (double hump)
f) Hot assembly burnup	Beginning of life (BOL)
g) Fuel assembly type	17x17 ZIRLO™ cladding
Plant Operating Conditions	
a) Fraction of SG tube plugged	Maximum (10%)
b) Tavg	Nominal value +4 F (587.8 F)
c) Pressurizer pressure	Nominal value + 30 psi (2280 psia)
d) Primary coolant flow	Thermal design flow (112000 gpm/loop)
e) Upper Head Temperature	Nominal (Tcold)
f) Pressurizer level	Nominal
g) Accumulator temperature	Maximum (120 F)
h) Accumulator pressure	Minimum (600.0 psia)
i) Accumulator volume	Nominal (2152.45 ft ³)
Accident Boundary Conditions	
a) Break location	Cold leg in the loop with pressurizer
b) Break type	Split (top orientation)
c) Break size	67.5-inch diameter size (28.2744.18-inch ²)
d) Offsite power	Not available
e) Reactor trip signal	Pressurizer low-pressure
f) Reactor trip signal delay time	2-1.8 seconds
g) Control rod drop delay time	3 seconds
hg) Turbine trip	Reactor trip signal
lh) RCP trip	Safety injection signal and 40-3 seconds after turbine reactor trip (LOOP)
ji) Safety injection signal	Pressurizer low-low-pressure
kj) Safety Injection delay	Maximum (118 seconds)
lk) Number of available safety injection pump	2
ml) Safety injection flow	Minimum
nm) Safety injection water temperature	RWST maximum temperature during normal operation (120 F) [

Table E-2 Sequence of Events in US-APWR Sample Analysis

<u>Event</u>	<u>Time (sec)</u>
<u>Break occurs; blowdown initiation</u>	<u>0.0</u>
<u>Reactor trip (loss-of-offsite power is assumed)</u>	<u>9.3</u>
<u>Control rod insertion starts</u>	<u>11.1</u>
<u>Main steam isolation</u>	<u>11.1</u>
<u>ECCS actuation signal</u>	<u>11.9</u>
<u>RCP trip</u>	<u>12.3</u>
<u>Main feedwater isolation</u>	<u>17.3</u>
<u>Main steam safety valve open</u>	<u>81</u>
<u>Emergency Power Source initiates</u>	<u>115</u>
<u>Fuel cladding starts heating up</u>	<u>122</u>
<u>High Head Injection System begins</u>	<u>130</u>
<u>Peak Cladding Temperature occurs</u>	<u>136</u>
<u>Fuel cladding rewets</u>	<u>143</u>
<u>Emergency feedwater flow begins</u>	<u>145</u>
<u>Accumulator injection begins</u>	<u>315</u>

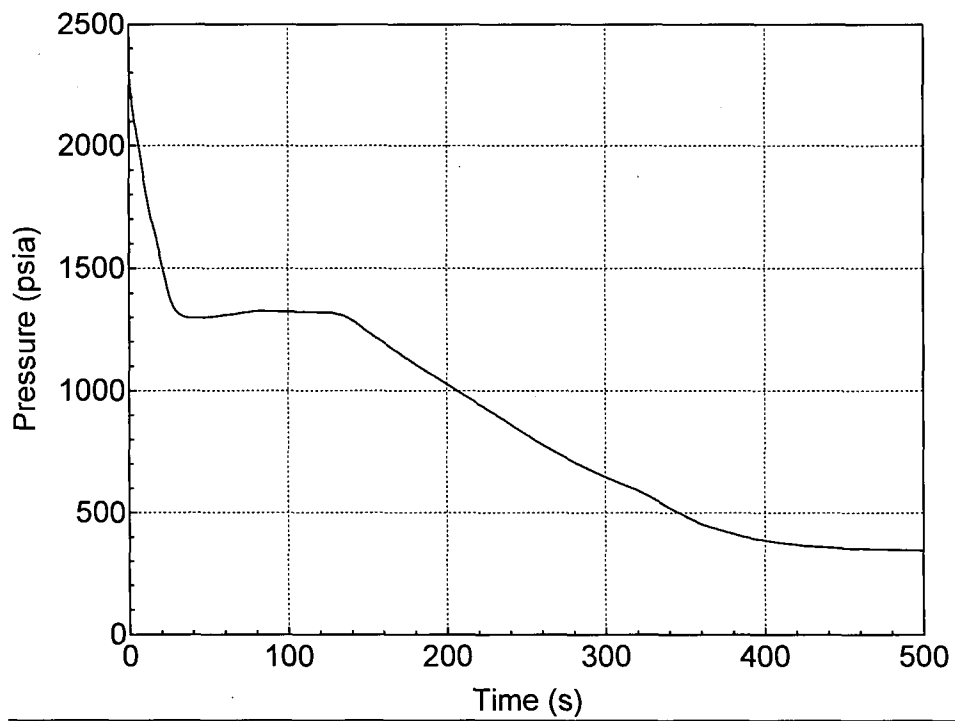


Figure E-1 Pressurizer Pressure

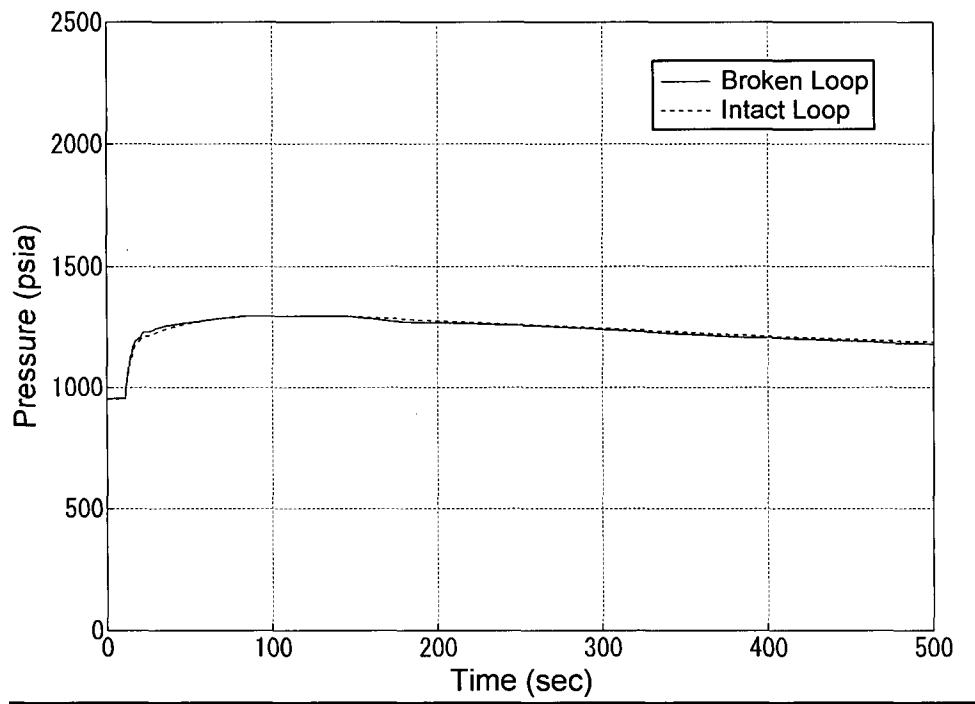


Figure E-2 SG Secondary Side Pressure

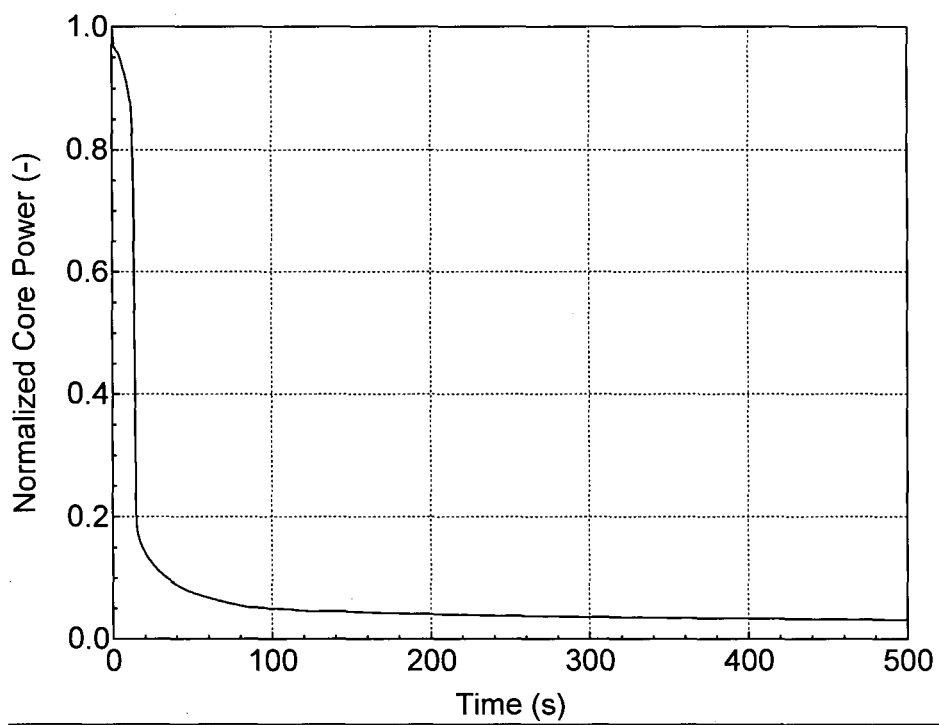


Figure E-3 Normalized Core Power

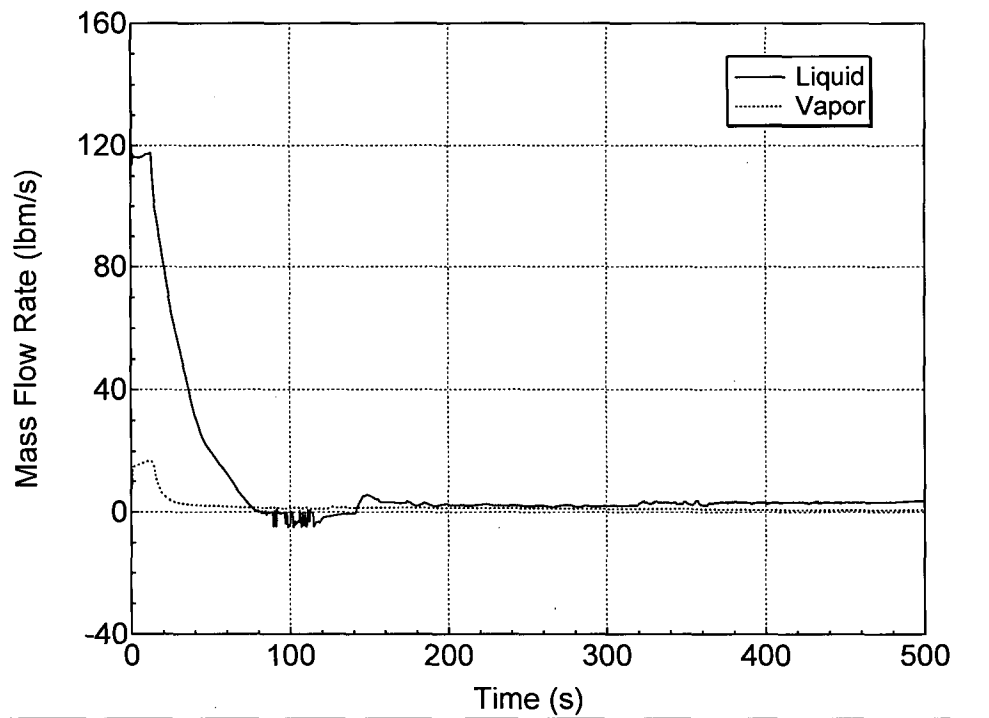


Figure E-4 Average Core Channel Flow Rate Hot Assembly Exit Vapor and Liquid Mass Flowrates

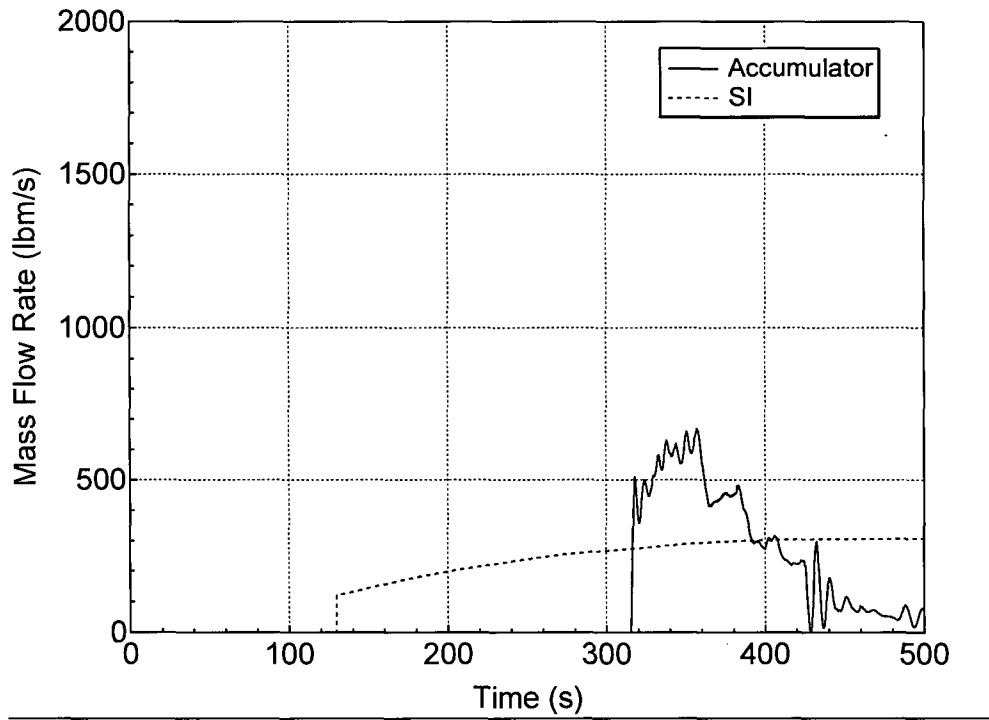


Figure E-5 DVI and Accumulator Injection Flow Rate

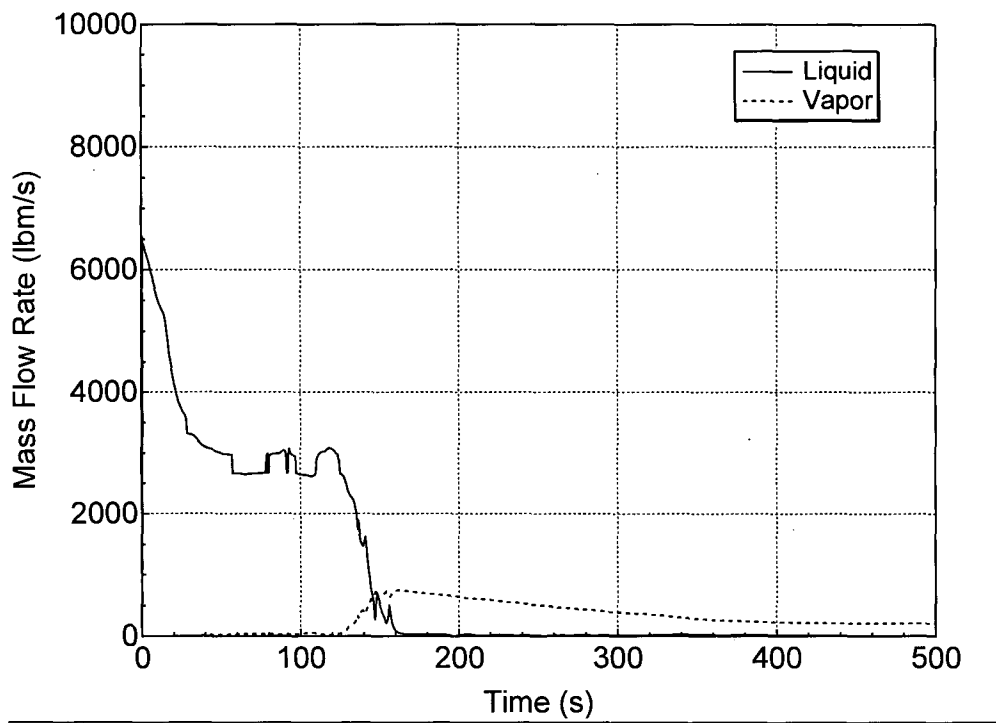


Figure E-6 Break Flow

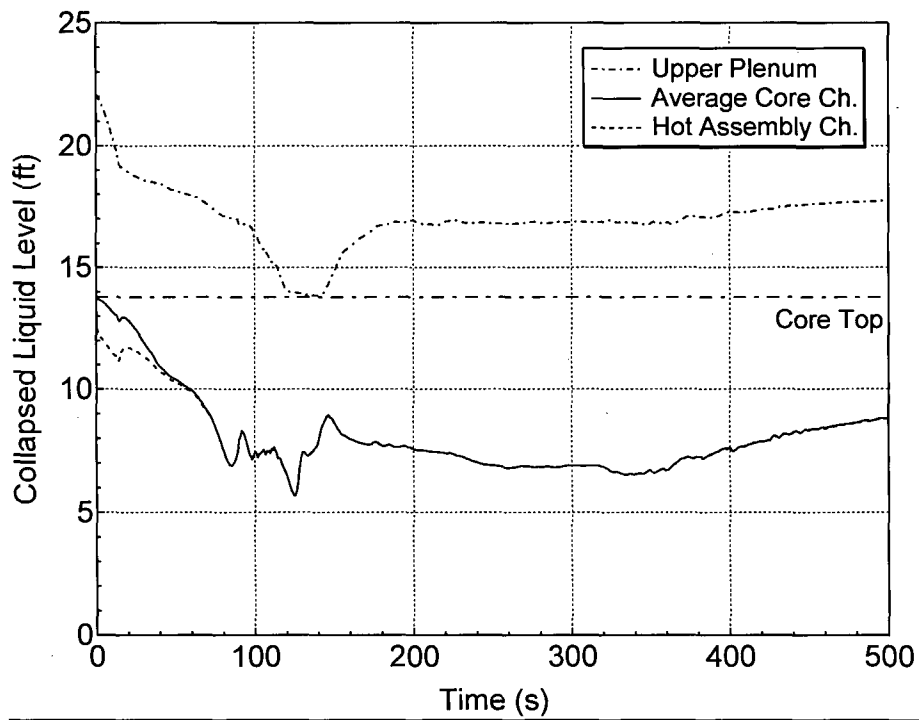


Figure E-7 Core and Upper Plenum Collapsed Level (Hot Channel)

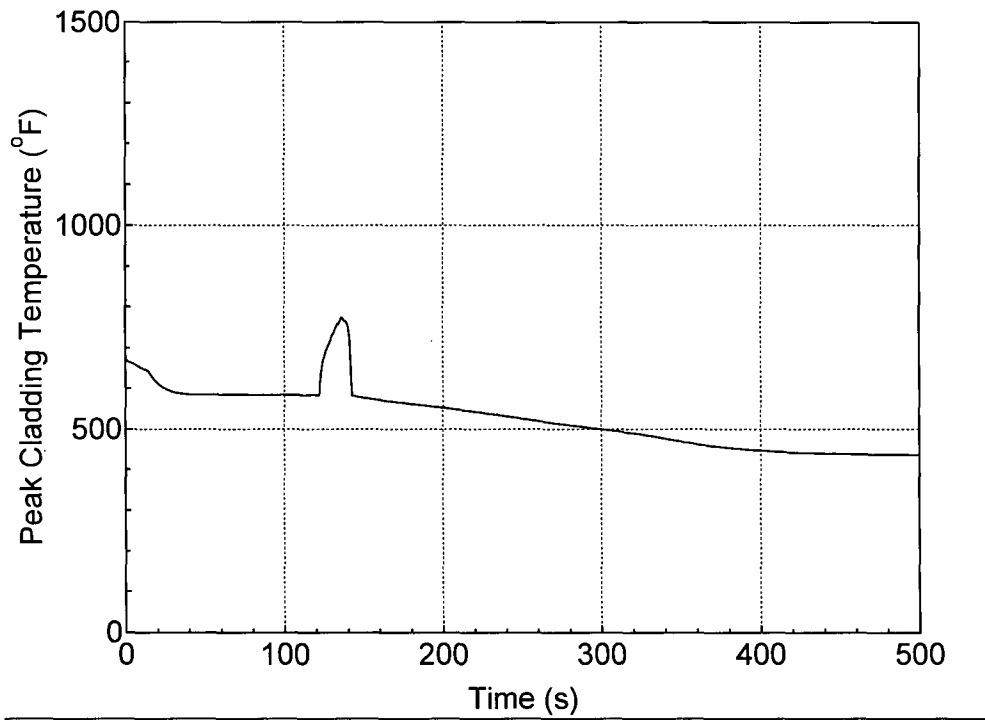


Figure E-8 Cladding Temperature of Hot Rod at PCT Location All Elevations

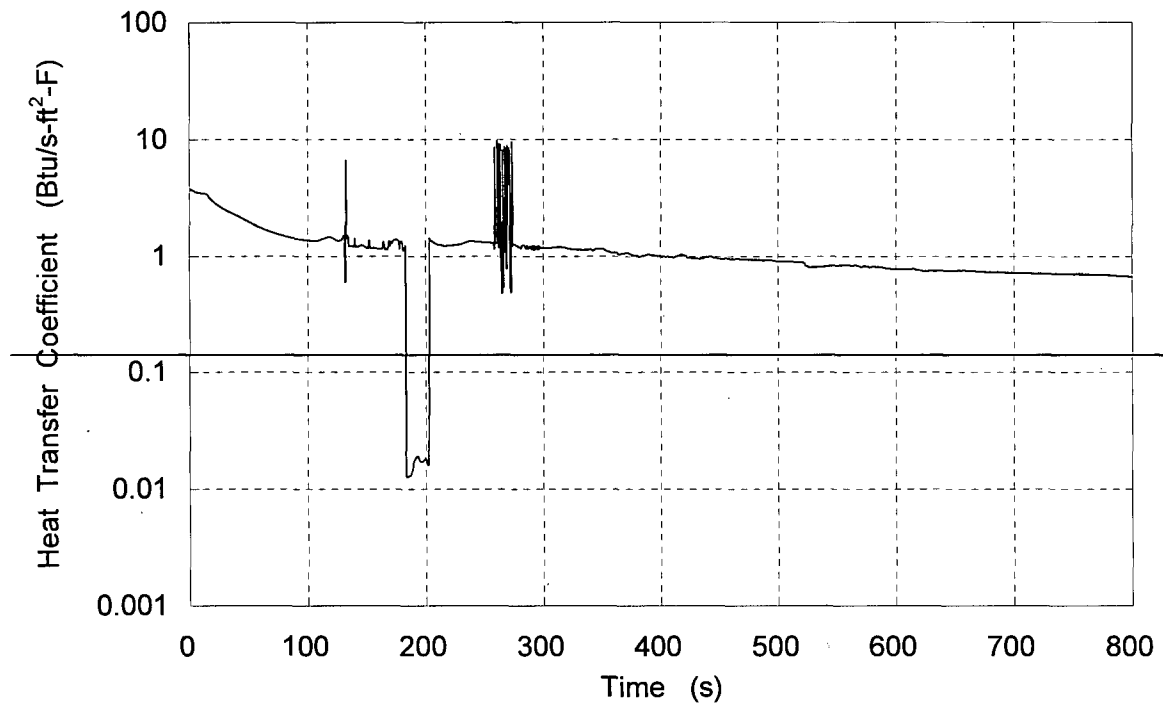


Figure E-9 Heat Transfer Coefficient of Hot Rod at PCT Location